

ANALYSIS OF SCALING OF ENERGY AND BARYON
DENSITIES IN RELATIVISTIC
HEAVY-ION COLLISIONS

by
DANIEL S. ZACHARY

B.S. MASSACHUSETTS INSTITUTE OF TECHNOLOGY (1985)
M.S. MASSACHUSETTS INSTITUTE OF TECHNOLOGY (1986)

Submitted to the Department of Physics
in partial fulfillment of the requirements for the degree of

Doctor of Philosophy
at the

MASSACHUSETTS INSTITUTE OF TECHNOLOGY
May 1994

©Massachusetts Institute of Technology 1994

Signature of Author _____
Department of Physics
May 1994

Certified by _____
Stephen G. Steadman
Department of Physics
Thesis Supervisor

Accepted by _____
George F. Koster
Chairman, Physics Graduate Committee

MASSACHUSETTS INSTITUTE
OF TECHNOLOGY

MAY 25 1994

LIBRARIES

Science

Analysis of Scaling of Energy and Baryon Densities in Relativistic Heavy-Ion Collisions

by

Daniel S. Zachary

Submitted to the Department of Physics
on April 27, 1994, in partial fulfillment of the
requirements for the degree of
Doctor of Philosophy

Abstract

This work focuses on understanding the trends of particle production in heavy-ion collisions. We investigate the physics of multiple scattering and rescattering in $A + A$ reactions. By varying the number of participants in $^{16}\text{O} + A$, $^{28}\text{Si} + A$ systems at 14.6 $A \cdot \text{GeV}/c$ and the $^{197}\text{Au} + ^{197}\text{Au}$ system at 11.6 $A \cdot \text{GeV}/c$, we vary the size of the reaction zone as well as the mean number of binary collisions, $\langle N_{BC} \rangle$. With the full E802/E866 data available, we have been able to determine and compare shapes and magnitudes of the rapidity distributions for reactions of varying number of participants. Measured fiducial yields for pions and kaons have been determined as a function of the participants in the reaction. Pion production increases linearly as a function of participants, averaging $n_\pi = (1.1 \pm .1) \times (\text{total participants})$. Production of K^+ from fiducial yields is shown to increase linearly for $^{197}\text{Au} + ^{197}\text{Au}$ reactions by, $n_{K^+} = (0.050 \pm .005) \times (\text{total participants})$. Energy and baryon densities vs. the number of participants have also been examined assuming thermal sources. The meson number densities range from $(0.29 \pm .03 \pm .04) - (.48 \pm .05 \pm .06) / \text{fm}^3$ for the oxygen and silicon projectiles. The meson number density for the gold projectile is $(.56 \pm .03 \pm .04) / \text{fm}^3$. The proton number densities range from $(.18 \pm .02 \pm .03) - (0.39 \pm .04 \pm .06) / \text{fm}^3$ for the oxygen and silicon projectiles. The proton number density for the gold projectile is $(.66 \pm .07 \pm 0.1) / \text{fm}^3$. Proton number densities are twice the meson densities in $^{197}\text{Au} + ^{197}\text{Au}$ collisions. This large discrepancy and the large measured baryon "temperatures" may indicate collective effects such as hydrodynamic expansion. Total energy densities reach $(1.4 \pm 0.1 \pm 0.2) \text{ GeV}/\text{fm}^3$ in central $^{197}\text{Au} + ^{197}\text{Au}$ collisions.

Thesis Supervisor: Dr. Stephen G. Steadman
Title: Senior Research Scientist, Department of Physics

Contents

1	Introduction	19
1.1	A Brief History of Relativistic Heavy-Ion Collisions	19
1.2	A Closer Look at Heavy-Ion Collisions	20
1.3	Why Study Heavy-Ion Collisions?	25
1.4	Heavy-Ion Collisions Models	27
1.5	Questions to be Answered in this Thesis	28
1.6	Techniques of the Analysis	29
1.6.1	Scaling	30
1.7	The Data Sets	31
1.8	Summary of this Thesis	32
2	Models	33
2.1	Kinematic Variables	34
2.2	Energy and Baryon Density	35
2.2.1	Techniques to Extract Energy and Baryon Density	35
2.2.2	A Thermodynamic Approach	35
2.2.3	The Landau Fireball Model	37
2.2.4	Thermodynamic Approximation Using Fit Parameters	45
2.3	Cascade Models	48
2.3.1	Specific Dynamical Models	48
2.4	Summary	52

3	Experimental Setup	53
3.1	The AGS and Tandem Facilities at Brookhaven National Laboratories . .	53
3.2	Experiment E802/E866	55
3.2.1	Beam Counters and Target	55
3.2.2	The Target Multiplicity Array	57
3.2.3	The Zero Degree Calorimeter	58
3.2.4	The Spectrometer	61
3.2.5	The Data Acquisition	66
3.3	Data Sets	66
3.4	Data Analysis	67
3.5	Summary	68
4	Nuclear Geometry	70
4.1	A Geometric Model	70
4.1.1	Collision Participants	71
4.1.2	A Simple Geometric Model of Participant Nucleons	73
4.2	Nuclear Geometry and the ZCAL	81
4.3	Summary	84
5	Cross-Section Analysis	86
5.1	Introduction	86
5.2	Definitions	87
5.3	Procedure	88
5.3.1	CSPA W: Acceptance Generation	91
5.3.2	CSPA W: Filtering	95
5.3.3	CSPA W: Differential Yield Generation	97
5.3.4	CSPA W: Error Handling	101
5.4	Data Quality	102
5.4.1	Track Statistics	102

5.4.2	Accuracy of the Measurements	104
5.4.3	Summary of Fixes.	105
5.4.4	Inelastic Cross-Sections.	106
5.5	ZCAL Software Cuts	106
5.5.1	Participants	112
5.6	Summary	112
6	Results	115
6.1	Particle Differential Yields	116
6.1.1	Pions: Ratios and Multiplicity Dependencies	117
6.2	Rapidity Distributions	122
6.2.1	K^+/π^+ Ratios	134
6.3	Inverse Slope Parameters.	134
6.4	Integrated Yields	138
6.5	Summary	150
7	Density	152
7.1	Energy and Baryon Densities	152
7.2	Thermal Fits	153
7.3	Coulomb Corrections	156
7.4	Densities and Participants	158
8	Conclusion	165
A	Yield Summary: $^{16}\text{O} + ^{27}\text{Al} : \pi$	170
B	Yield Summary: $^{16}\text{O} + ^{64}\text{Cu} : \pi$	181
C	Yield Summary: $^{16}\text{O} + ^{197}\text{Au} : \pi$	194
D	Yield Summary: $^{16}\text{O} + ^{27}\text{Al} : \text{Kaons}$	207

E	Yield Summary: $^{16}\text{O} + ^{64}\text{Cu}$: Kaons	212
F	Yield Summary: $^{16}\text{O} + ^{197}\text{Au}$: Kaons	221
G	Yield Summary: $^{16}\text{O} + \text{A}$ Protons	231
H	Yield Summary: $^{28}\text{Si} + ^{27}\text{Al}$: π	249
I	Yield Summary: $^{28}\text{Si} + ^{64}\text{Cu}$: π	258
J	Yield Summary: $^{28}\text{Si} + ^{197}\text{Au}$: π	267
K	Yield Summary: $^{28}\text{Si} + ^{27}\text{Al}$: Kaons	276
L	Yield Summary: $^{28}\text{Si} + ^{64}\text{Cu}$: Kaons	281
M	Yield Summary: $^{28}\text{Si} + ^{197}\text{Au}$: Kaons	286
N	Yield Summary: $^{28}\text{Si} + \text{A}$: Protons	291
O	Yield Summary: $^{197}\text{Au} + ^{197}\text{Au}$: π	304
P	Yield Summary: $^{197}\text{Au} + ^{197}\text{Au}$: Kaons	321
Q	Yield Summary: $^{197}\text{Au} + ^{197}\text{Au}$: Protons	335

List of Tables

1.1	Summary of items in and outside experimental control.	29
1.2	Data summary of this thesis work.	31
2.1	Landau Fireball predictions for different collisions.	42
2.2	Table of the Landau fireball energy and baryon densities.	44
3.1	Characteristic of the tracking chambers.	63
3.2	Drift chamber dimensions.	64
3.3	Summary of analysis passes	69
4.1	Scaling variables	74
4.2	Extended WNM collision scenarios.	75
4.3	An extended WNM for the cascade mode ARC.	78
5.1	Summary of minimum-bias data used in this thesis.	90
5.2	Table of acceptance weights.	92
5.3	Summary of the track status used in the data.	96
5.4	A typical list of run information for a June 88 $^{16}\text{O} + ^{197}\text{Au}$ run.	103
5.5	Inelastic cross-sections	110
5.6	Table of energy ranges for the oxygen and silicon projectiles.	111
5.7	Table of energy ranges for the gold projectile.	111
5.8	Table of mean participants: ^{16}O and ^{28}Si ions	113
5.9	Table of mean number of participants: $^{197}\text{Au} + ^{197}\text{Au}$	114

6.1	Summary of K^+/π^+ ratios for ^{16}O , ^{28}Si , and ^{197}Au collisions.	134
6.2	Summary of integrated yields for $^{197}\text{Au} + ^{197}\text{Au}$ reactions.	142
6.3	Fit parameters for total integrated yields.	145
6.4	Fit parameters for fiducial yields.	150
7.1	Sensitivity of Proton Densities to μ and T	156
7.2	Density calculations for measured species.	159
7.3	Mesons Density Summary.	160
7.4	Baryon Density Summary.	162
7.5	Total energy density summary.	163

List of Figures

1-1	Regions of vanishing baryon density.	22
1-2	Rapidity loss for pPb collisions.	22
1-3	Nuclear Matter phase diagram.	25
1-4	A Gedanken experiment	28
2-1	Geometry of a non-symmetric heavy-ion reaction.	38
2-2	Sketch of a possible heavy-ion scenario for a symmetric collision.	39
2-3	Summary of fireball model predictions.	43
3-1	AGS layout	54
3-2	E802 layout	56
3-3	Front sketch of ZCAL.	60
3-4	Energy vs. transverse distance across the ZCAL.	62
4-1	Woods-Saxon density profile for several nuclei.	71
4-2	Comparison of sizes for nuclei used in this analysis.	72
4-3	Total number of participant vs. the impact parameter (and ZCAL).	76
4-4	Number of binary collisions vs. the impact parameter.	80
4-5	Spatial distribution of the energy deposited in ZCAL.	83
4-6	Impact parameter vs. energy in the ZCAL	85
5-1	Bad slats for oxygen and gold running periods.	91
5-2	Acceptance in $\theta_{particle}$ vs. $\theta_{bend-particle}$ space.	93

5-3	θ_{bend} Diagram.	94
5-4	Cross-section flow chart in the PAW environment.	99
5-5	Cross-section vs. run for the p + A, ^{16}O + A, ^{28}Si + A and ^{197}Au + ^{197}Au data sets.	107
5-6	Raw ZCAL spectra for ^{16}O + A, ^{28}Si + A, and ^{197}Au + A reactions.	108
5-7	ZCAL target-out spectra for ^{16}O , ^{28}Si , and ^{197}Au projectiles.	109
6-1	Central rapidity π^+ 's for ^{16}O , ^{28}Si , and ^{197}Au collisions.	118
6-2	Central rapidity π^- 's for ^{16}O , ^{28}Si , and ^{197}Au + A collisions.	119
6-3	K^+ for ^{16}O , ^{28}Si , and ^{197}Au + A collisions.	120
6-4	Protons for ^{16}O , ^{28}Si , and ^{197}Au + A collisions.	121
6-5	π^+ / π^- - ratios as a function of p_t	123
6-6	π^\pm multiplicity comparisons.	124
6-7	Full π^+ dN/dy comparison for ^{16}O , ^{28}Si , and ^{197}Au + A collisions.	126
6-8	Full π^- dN/dy comparison for ^{16}O , ^{28}Si , and ^{197}Au + A collisions.	127
6-9	Full K^+ dN/dy comparison for ^{16}O , ^{28}Si , and ^{197}Au + A collisions.	128
6-10	Full K^- dN/dy comparison for ^{16}O , ^{28}Si , and ^{197}Au + A collisions.	129
6-11	Full proton dN/dy comparison for ^{16}O , ^{28}Si , and ^{197}Au + A collisions.	130
6-12	Full dN/dy comparison for ^{197}Au + ^{197}Au central collisions.	131
6-13	K^+ / π^+ ratios for ^{16}O , ^{28}Si , and ^{197}Au + A collisions.	135
6-14	Inverse slope parameters for central collisions.	136
6-15	Fiducial yields for π^+ and π^- in ^{28}Si + ^{27}Al collisions.	139
6-16	Fiducial yields for π^+ and π^-	140
6-17	Total integrated yields for π^+ and π^-	143
6-18	Total integrated yields for π^+ and π^-	144
6-19	Fiducial yields for K^+ in ^{28}Si + ^{27}Al collisions.	146
6-20	Fiducial yields for K^+	147
6-21	Normalized fiducial yields for π^+ and π^-	148
6-22	Fiducial Yield K^+ / π^+ Ratios	149

7-1	Thermal fits for π^\pm and protons.	154
7-2	Sensitivity to thermal fits for $^{197}\text{Au} + ^{197}\text{Au}$ protons.	157
7-3	n_π, n_K , and n_{Prot} densities and participants.	161
A-1	Yield Summary for $^{16}\text{O} + ^{27}\text{Al}$ INEL: π^+	171
A-2	Yield Summary for $^{16}\text{O} + ^{27}\text{Al}$ INEL: π^-	172
A-3	Yield Summary for $^{16}\text{O} + ^{27}\text{Al}$ TMA: π^+	173
A-4	Yield Summary for $^{16}\text{O} + ^{27}\text{Al}$ TMA: π^-	174
A-5	Yield Summary for $^{16}\text{O} + ^{27}\text{Al}$ CENT2: π^+	175
A-6	Yield Summary for $^{16}\text{O} + ^{27}\text{Al}$ CENT2: π^-	176
A-7	Yield Summary for $^{16}\text{O} + ^{27}\text{Al}$ MID: π^+	177
A-8	Yield Summary for $^{16}\text{O} + ^{27}\text{Al}$ MID: π^-	178
A-9	Yield Summary for $^{16}\text{O} + ^{27}\text{Al}$ PERP1: π^+	179
A-10	Yield Summary for $^{16}\text{O} + ^{27}\text{Al}$ PERP1: π^-	180
B-1	Yield Summary for $^{16}\text{O} + ^{64}\text{Cu}$ INEL: π^+	182
B-2	Yield Summary for $^{16}\text{O} + ^{64}\text{Cu}$ INEL: π^-	183
B-3	Yield Summary for $^{16}\text{O} + ^{64}\text{Cu}$ TMA: π^+	184
B-4	Yield Summary for $^{16}\text{O} + ^{64}\text{Cu}$ TMA: π^-	185
B-5	Yield Summary for $^{16}\text{O} + ^{64}\text{Cu}$ CENT1: π^+	186
B-6	Yield Summary for $^{16}\text{O} + ^{64}\text{Cu}$ CENT1: π^-	187
B-7	Yield Summary for $^{16}\text{O} + ^{64}\text{Cu}$ CENT2: π^+	188
B-8	Yield Summary for $^{16}\text{O} + ^{64}\text{Cu}$ CENT2: π^-	189
B-9	Yield Summary for $^{16}\text{O} + ^{64}\text{Cu}$ MID: π^+	190
B-10	Yield Summary for $^{16}\text{O} + ^{64}\text{Cu}$ MID: π^-	191
B-11	Yield Summary for $^{16}\text{O} + ^{64}\text{Cu}$ PERP1: π^+	192
B-12	Yield Summary for $^{16}\text{O} + ^{64}\text{Cu}$ PERP1: π^-	193
C-1	Yield Summary for $^{16}\text{O} + ^{197}\text{Au}$ INEL: π^+	195
C-2	Yield Summary for $^{16}\text{O} + ^{197}\text{Au}$ INEL: π^-	196

C-3	Yield Summary for $^{16}\text{O} + ^{197}\text{Au}$ TMA: π^+	197
C-4	Yield Summary for $^{16}\text{O} + ^{197}\text{Au}$ TMA: π^-	198
C-5	Yield Summary for $^{16}\text{O} + ^{197}\text{Au}$ CENT1: π^+	199
C-6	Yield Summary for $^{16}\text{O} + ^{197}\text{Au}$ CENT1: π^-	200
C-7	Yield Summary for $^{16}\text{O} + ^{197}\text{Au}$ CENT2: π^+	201
C-8	Yield Summary for $^{16}\text{O} + ^{197}\text{Au}$ CENT2: π^-	202
C-9	Yield Summary for $^{16}\text{O} + ^{197}\text{Au}$ MID: π^+	203
C-10	Yield Summary for $^{16}\text{O} + ^{197}\text{Au}$ MID: π^-	204
C-11	Yield Summary for $^{16}\text{O} + ^{197}\text{Au}$ PERP1: π^+	205
C-12	Yield Summary for $^{16}\text{O} + ^{197}\text{Au}$ PERP1: π^-	206
D-1	Yield Summary for $^{16}\text{O} + ^{27}\text{Al}$ INEL: K^-	208
D-2	Yield Summary for $^{16}\text{O} + ^{27}\text{Al}$ TMA: K^+	209
D-3	Yield Summary for $^{16}\text{O} + ^{27}\text{Al}$ TMA: K^-	210
D-4	Yield Summary for $^{16}\text{O} + ^{27}\text{Al}$ CENT2: K^+	211
E-1	Yield Summary for $^{16}\text{O} + ^{64}\text{Cu}$ INEL: K^+	213
E-2	Yield Summary for $^{16}\text{O} + ^{64}\text{Cu}$ INEL: K^-	214
E-3	Yield Summary for $^{16}\text{O} + ^{64}\text{Cu}$ TMA: K^+	215
E-4	Yield Summary for $^{16}\text{O} + ^{64}\text{Cu}$ TMA: K^-	216
E-5	Yield Summary for $^{16}\text{O} + ^{64}\text{Cu}$ CENT1: K^+	217
E-6	Yield Summary for $^{16}\text{O} + ^{64}\text{Cu}$ CENT1: K^-	218
E-7	Yield Summary for $^{16}\text{O} + ^{64}\text{Cu}$ CENT2: K^+	219
E-8	Yield Summary for $^{16}\text{O} + ^{64}\text{Cu}$ MID: K^+	220
F-1	Yield Summary for $^{16}\text{O} + ^{197}\text{Au}$ INEL: K^+	222
F-2	Yield Summary for $^{16}\text{O} + ^{197}\text{Au}$ INEL: K^-	223
F-3	Yield Summary for $^{16}\text{O} + ^{197}\text{Au}$ TMA: K^+	224
F-4	Yield Summary for $^{16}\text{O} + ^{197}\text{Au}$ TMA: K^-	225
F-5	Yield Summary for $^{16}\text{O} + ^{197}\text{Au}$ CENT1: K^+	226

F-6	Yield Summary for $^{16}\text{O} + ^{197}\text{Au}$ CENT1: K^-	227
F-7	Yield Summary for $^{16}\text{O} + ^{197}\text{Au}$ CENT2: K^+	228
F-8	Yield Summary for $^{16}\text{O} + ^{197}\text{Au}$ CENT2: K^-	229
F-9	Yield Summary for $^{16}\text{O} + ^{197}\text{Au}$ MID: K^+	230
G-1	Yield Summary for $^{16}\text{O} + ^{27}\text{Al}$ INEL: Protons	232
G-2	Yield Summary for $^{16}\text{O} + ^{27}\text{Al}$ TMA: Protons	233
G-3	Yield Summary for $^{16}\text{O} + ^{27}\text{Al}$ CENT2: Protons	234
G-4	Yield Summary for $^{16}\text{O} + ^{27}\text{Al}$ MID: Protons	235
G-5	Yield Summary for $^{16}\text{O} + ^{27}\text{Al}$ PERP1: Protons	236
G-6	Yield Summary for $^{16}\text{O} + ^{64}\text{Cu}$ INEL: Protons	237
G-7	Yield Summary for $^{16}\text{O} + ^{64}\text{Cu}$ TMA: Protons	238
G-8	Yield Summary for $^{16}\text{O} + ^{64}\text{Cu}$ CENT1: Protons	239
G-9	Yield Summary for $^{16}\text{O} + ^{64}\text{Cu}$ CENT2: Protons	240
G-10	Yield Summary for $^{16}\text{O} + ^{64}\text{Cu}$ MID: Protons	241
G-11	Yield Summary for $^{16}\text{O} + ^{64}\text{Cu}$ PERP1: Protons	242
G-12	Yield Summary for $^{16}\text{O} + ^{197}\text{Au}$ INEL: Protons	243
G-13	Yield Summary for $^{16}\text{O} + ^{197}\text{Au}$ TMA: Protons	244
G-14	Yield Summary for $^{16}\text{O} + ^{197}\text{Au}$ CENT1: Protons	245
G-15	Yield Summary for $^{16}\text{O} + ^{197}\text{Au}$ CENT2: Protons	246
G-16	Yield Summary for $^{16}\text{O} + ^{197}\text{Au}$ MID: Protons	247
G-17	Yield Summary for $^{16}\text{O} + ^{197}\text{Au}$ PERP1: Protons	248
H-1	Yield Summary for $^{28}\text{Si} + ^{27}\text{Al}$ CENT1: π^+	250
H-2	Yield Summary for $^{28}\text{Si} + ^{27}\text{Al}$ CENT1: π^-	251
H-3	Yield Summary for $^{28}\text{Si} + ^{27}\text{Al}$ CENT2: π^+	252
H-4	Yield Summary for $^{28}\text{Si} + ^{27}\text{Al}$ CENT2: π^-	253
H-5	Yield Summary for $^{28}\text{Si} + ^{27}\text{Al}$ MID: π^+	254
H-6	Yield Summary for $^{28}\text{Si} + ^{27}\text{Al}$ MID: π^-	255

H-7	Yield Summary for $^{28}\text{Si} + ^{27}\text{Al}$ PERP1: π^+	256
H-8	Yield Summary for $^{28}\text{Si} + ^{27}\text{Al}$ PERP1: π^-	257
I-1	Yield Summary for $^{28}\text{Si} + ^{64}\text{Cu}$ CENT1: π^+	259
I-2	Yield Summary for $^{28}\text{Si} + ^{64}\text{Cu}$ CENT1: π^-	260
I-3	Yield Summary for $^{28}\text{Si} + ^{64}\text{Cu}$ CENT2: π^+	261
I-4	Yield Summary for $^{28}\text{Si} + ^{64}\text{Cu}$ CENT2: π^-	262
I-5	Yield Summary for $^{28}\text{Si} + ^{64}\text{Cu}$ MID: π^+	263
I-6	Yield Summary for $^{28}\text{Si} + ^{64}\text{Cu}$ MID: π^-	264
I-7	Yield Summary for $^{28}\text{Si} + ^{64}\text{Cu}$ PERP1: π^+	265
I-8	Yield Summary for $^{28}\text{Si} + ^{64}\text{Cu}$ PERP1: π^-	266
J-1	Yield Summary for $^{28}\text{Si} + ^{197}\text{Au}$ CENT1: π^+	268
J-2	Yield Summary for $^{28}\text{Si} + ^{197}\text{Au}$ CENT1: π^-	269
J-3	Yield Summary for $^{28}\text{Si} + ^{197}\text{Au}$ CENT2: π^+	270
J-4	Yield Summary for $^{28}\text{Si} + ^{197}\text{Au}$ CENT2: π^-	271
J-5	Yield Summary for $^{28}\text{Si} + ^{197}\text{Au}$ MID: π^+	272
J-6	Yield Summary for $^{28}\text{Si} + ^{197}\text{Au}$ MID: π^-	273
J-7	Yield Summary for $^{28}\text{Si} + ^{197}\text{Au}$ PERP1: π^+	274
J-8	Yield Summary for $^{28}\text{Si} + ^{197}\text{Au}$ PERP1: π^-	275
K-1	Yield Summary for $^{28}\text{Si} + ^{27}\text{Al}$ CENT1: K^+	277
K-2	Yield Summary for $^{28}\text{Si} + ^{27}\text{Al}$ CENT1: K^-	278
K-3	Yield Summary for $^{28}\text{Si} + ^{27}\text{Al}$ CENT2: K^+	279
K-4	Yield Summary for $^{28}\text{Si} + ^{27}\text{Al}$ MID: K^+	280
L-1	Yield Summary for $^{28}\text{Si} + ^{64}\text{Cu}$ CENT1: K^+	282
L-2	Yield Summary for $^{28}\text{Si} + ^{64}\text{Cu}$ CENT1: K^-	283
L-3	Yield Summary for $^{28}\text{Si} + ^{64}\text{Cu}$ CENT2: K^+	284
L-4	Yield Summary for $^{28}\text{Si} + ^{64}\text{Cu}$ MID: K^+	285

M-1	Yield Summary for $^{28}\text{Si} + ^{197}\text{Au}$ CENT1: K^+	287
M-2	Yield Summary for $^{28}\text{Si} + ^{197}\text{Au}$ CENT1: K^-	288
M-3	Yield Summary for $^{28}\text{Si} + ^{197}\text{Au}$ CENT2: K^+	289
M-4	Yield Summary for $^{28}\text{Si} + ^{197}\text{Au}$ CENT2: K^-	290
N-1	Yield Summary for $^{28}\text{Si} + ^{27}\text{Al}$ CENT1: Protons	292
N-2	Yield Summary for $^{28}\text{Si} + ^{27}\text{Al}$ CENT2: Protons	293
N-3	Yield Summary for $^{28}\text{Si} + ^{27}\text{Al}$ MID: Protons	294
N-4	Yield Summary for $^{28}\text{Si} + ^{27}\text{Al}$ PERP1: Protons	295
N-5	Yield Summary for $^{28}\text{Si} + ^{64}\text{Cu}$ CENT1: Protons	296
N-6	Yield Summary for $^{28}\text{Si} + ^{64}\text{Cu}$ CENT2: Protons	297
N-7	Yield Summary for $^{28}\text{Si} + ^{64}\text{Cu}$ MID: Protons	298
N-8	Yield Summary for $^{28}\text{Si} + ^{64}\text{Cu}$ PERP1: Protons	299
N-9	Yield Summary for $^{28}\text{Si} + ^{197}\text{Au}$ CENT1: Protons	300
N-10	Yield Summary for $^{28}\text{Si} + ^{197}\text{Au}$ CENT2: Protons	301
N-11	Yield Summary for $^{28}\text{Si} + ^{197}\text{Au}$ MID: Protons	302
N-12	Yield Summary for $^{28}\text{Si} + ^{197}\text{Au}$ PERP1: Protons	303
O-1	Yield Summary for $^{197}\text{Au} + ^{197}\text{Au}$ INEL: π^+	305
O-2	Yield Summary for $^{197}\text{Au} + ^{197}\text{Au}$ INEL: π^-	306
O-3	Yield Summary for $^{197}\text{Au} + ^{197}\text{Au}$ ZCALBAR: π^+	307
O-4	Yield Summary for $^{197}\text{Au} + ^{197}\text{Au}$ ZCALBAR: π^-	308
O-5	Yield Summary for $^{197}\text{Au} + ^{197}\text{Au}$ 0 - 4 % σ_{inel} : π^+	309
O-6	Yield Summary for $^{197}\text{Au} + ^{197}\text{Au}$ 0 - 4 % σ_{inel} : π^-	310
O-7	Yield Summary for $^{197}\text{Au} + ^{197}\text{Au}$ 0 - 10 % σ_{inel} : π^+	311
O-8	Yield Summary for $^{197}\text{Au} + ^{197}\text{Au}$ 0 - 10 % σ_{inel} : π^-	312
O-9	Yield Summary for $^{197}\text{Au} + ^{197}\text{Au}$ 10 - 30 % σ_{inel} : π^+	313
O-10	Yield Summary for $^{197}\text{Au} + ^{197}\text{Au}$ 10 - 30 % σ_{inel} : π^-	314
O-11	Yield Summary for $^{197}\text{Au} + ^{197}\text{Au}$ 30 - 50 % σ_{inel} : π^+	315

O-12	Yield Summary for $^{197}\text{Au} + ^{197}\text{Au}$ 30 - 50 % $\sigma_{inel} : \pi^-$	316
O-13	Yield Summary for $^{197}\text{Au} + ^{197}\text{Au}$ 50 - 70 % $\sigma_{inel} : \pi^+$	317
O-14	Yield Summary for $^{197}\text{Au} + ^{197}\text{Au}$ 50 - 70 % $\sigma_{inel} : \pi^-$	318
O-15	Yield Summary for $^{197}\text{Au} + ^{197}\text{Au}$ 70 - 90 % $\sigma_{inel} : \pi^+$	319
O-16	Yield Summary for $^{197}\text{Au} + ^{197}\text{Au}$ 70 - 90 % $\sigma_{inel} : \pi^-$	320
P-1	Yield Summary for $^{197}\text{Au} + ^{197}\text{Au}$ INEL: K^+	322
P-2	Yield Summary for $^{197}\text{Au} + ^{197}\text{Au}$ INEL: K^-	323
P-3	Yield Summary for $^{197}\text{Au} + ^{197}\text{Au}$ ZCALBAR: K^+	324
P-4	Yield Summary for $^{197}\text{Au} + ^{197}\text{Au}$ ZCALBAR: K^-	325
P-5	Yield Summary for $^{197}\text{Au} + ^{197}\text{Au}$ 0 - 4 % $\sigma_{inel} : \text{K}^+$	326
P-6	Yield Summary for $^{197}\text{Au} + ^{197}\text{Au}$ 0 - 4 % $\sigma_{inel} : \text{K}^-$	327
P-7	Yield Summary for $^{197}\text{Au} + ^{197}\text{Au}$ 0 - 10 % $\sigma_{inel} : \text{K}^+$	328
P-8	Yield Summary for $^{197}\text{Au} + ^{197}\text{Au}$ 0 - 10 % $\sigma_{inel} : \text{K}^-$	329
P-9	Yield Summary for $^{197}\text{Au} + ^{27}\text{Al}$ 10 - 30 % $\sigma_{inel} : \text{K}^+$	330
P-10	Yield Summary for $^{197}\text{Au} + ^{197}\text{Au}$ 30 - 50 % $\sigma_{inel} : \text{K}^+$	331
P-11	Yield Summary for $^{197}\text{Au} + ^{27}\text{Al}$ 30 - 50 % $\sigma_{inel} : \text{K}^-$	332
P-12	Yield Summary for $^{197}\text{Au} + ^{197}\text{Au}$ 50 - 70 % $\sigma_{inel} : \text{K}^+$	333
P-13	Yield Summary for $^{197}\text{Au} + ^{197}\text{Au}$ 70 - 90 % $\sigma_{inel} : \text{K}^+$	334
Q-1	Yield Summary for $^{197}\text{Au} + ^{197}\text{Au}$ INEL: Protons	336
Q-2	Yield Summary for $^{197}\text{Au} + ^{197}\text{Au}$ ZCALBAR: Protons	337
Q-3	Yield Summary for $^{197}\text{Au} + ^{197}\text{Au}$ 0 - 4 % $\sigma_{inel} : \text{Protons}$	338
Q-4	Yield Summary for $^{197}\text{Au} + ^{197}\text{Au}$ 0 - 10 % $\sigma_{inel} : \text{Protons}$	339
Q-5	Yield Summary for $^{197}\text{Au} + ^{197}\text{Au}$ 10 - 30 % $\sigma_{inel} : \text{Protons}$	340
Q-6	Yield Summary for $^{197}\text{Au} + ^{197}\text{Au}$ 30 - 50 % $\sigma_{inel} : \text{Protons}$	341
Q-7	Yield Summary for $^{197}\text{Au} + ^{197}\text{Au}$ 50 - 70 % $\sigma_{inel} : \text{Protons}$	342
Q-8	Yield Summary for $^{197}\text{Au} + ^{197}\text{Au}$ 70 - 90 % $\sigma_{inel} : \text{Protons}$	343

Chapter 1

Introduction

1.1 A Brief History of Relativistic Heavy-Ion Collisions

Initial work in the field of relativistic heavy-ion physics started with the early experiments at the Bevalac (Berkeley, California) in 1974. Experiments using ions as large as ^{197}Au , with incident momentum $p_{beam} \approx 1 \text{ A}\cdot\text{GeV}/c$, were collided with fixed targets. This work focused on understanding the nuclear equation of state. This experimental effort clarified that relativistic heavy-ion collisions were not simple superpositions of pp collisions, but rather hosted global phenomena that occurred in the many-body collisions of these reactions. Experiments were designed to study these phenomena in reactions of increasing size and incident momentum.

Theoretical work continued simultaneously. In particular, there were predictions of a new state of nuclear matter [Lee76], [Wei76], an excitation when nuclear matter is heated to extreme conditions. It soon became clear that relativistic heavy-ion collisions were the technique to systematically push nuclear matter to these extreme conditions. At very high densities and/or at very high temperatures, the nature of the QCD vacuum is modified [QM83-Ja], [Shur80]. The Relativistic Heavy-ion Collider (RHIC) was proposed

to provide the needed incident momentum for these extreme conditions. Collisions at RHIC would have high energy densities yet a baryon free region at mid-rapidity. The experimental effort at the Brookhaven Alternating Gradient Synchrotron (AGS) grew as a predecessor to RHIC. The AGS has hosted collisions of oxygen ($A=16$) and silicon ($A=28$) at $14.6 A \cdot \text{GeV}/c$ with various targets, and in 1992 gold nuclei ($A=197$) have been accelerated to $11.6 A \cdot \text{GeV}/c$.

Heavy-ions have been accelerated at *Le Conseil European pour la Recherche Nucléaire* (CERN's) SPS ring concurrently with the AGS program. Oxygen and sulfur ($A=32$) have been accelerated to $200 A \cdot \text{GeV}/c$, and Pb beams will become available in late 1994. Higher energy densities may be achieved at CERN; however, higher baryon densities in the central rapidity regions are found at the AGS, as will be explained in the following section.

Future work at RHIC [QM91-Gu], scheduled to begin experimental work in 1999, will provide collisions of $^{197}\text{Au} + ^{197}\text{Au}$ with a center of mass momentum of $200 A \cdot \text{GeV}/c$. The Large Hadron Collider (LHC), proposed for the next decade at CERN, will collide $^{208}\text{Pb} + ^{208}\text{Pb}$ with a center of mass energy of $8 A \cdot \text{TeV}$ [Nat92-Gu].

1.2 A Closer Look at Heavy-Ion Collisions

In the last eight years, relativistic heavy-ion collisions have been performed at two sites: the AGS and the SPS ring at CERN. Heavy-ion reactions at both locations are similar, both violent in nature. Both projectile and target nuclei are disintegrated in a central collision. Collisions at the AGS will be described in this work where the incoming projectiles essentially “stop” in the target nucleus. This produces a cored-out volume of a hot, dense mass of nucleons. Once the density of nuclear matter exceeds that of about 5 – 6 times normal nuclear matter, nucleons overlap to such an extent that one cannot treat quarks confined to isolated nucleons. Under these conditions, it is hoped that a transition to a new state of nuclear matter, the Quark Gluon Plasma (QGP), will be

possible. This is discussed further in the next chapter.

There are a few important differences in heavy-ion collisions at the AGS compared to the higher energy CERN collisions. Baryons that multiple scatter with other nucleons are more likely to populate the mid-rapidity regions of AGS collisions. The larger cross-sections for nucleons at lower momentum also increase the amount of multiple scattering. We will take advantage of this important difference as we try to understand how multiple scattering plays a role in redistributing the incoming beam energy to the target nucleons.

Rescattering of produced mesons off nucleons is also more important at the AGS than at higher beam momentum. Particle cross-sections are much higher due to resonance effects [PPDB80]. The cross-sections for pp and np reactions increase enormously below about 1 GeV/c momentum, increasing from approximately $\sigma_{pp} \approx 50$ millibarns at 100 GeV/c to $\sigma_{pp} \approx 1000$ millibarns at 200 MeV/c incident momentum.

Relativistic heavy-ion collisions may also be described in a region of rapidity space, namely the projectile, the target, and the central rapidity region. Figure 1-1 [QM91-Sa] shows a sketch of the regions of vanishing baryon density. Collisions at the AGS are in the baryon rich region. The smaller rapidity at the AGS ($y_{lab} = 3.44$) for oxygen and silicon compared to SPS ($y_{lab} \approx 6$), makes it easier for nuclear matter to fill the mid-rapidity region.

In a central $^{16}\text{O} + ^{197}\text{Au}$ collision at the AGS, for example, kinetic energy from the projectile nucleons is transferred to the target nucleons. Energy is deposited to the target nucleons, and a clump of matter, composed of projectile and target nucleons, is created. This comoving mass of nucleons moves approximately at a common velocity. The common velocity is a weighted average velocity of the participant nucleons. This excited matter exists for only a few fm/c. In earlier experiments, it was found that protons incident on lead nuclei have a rapidity loss of about $\Delta y \approx 2 - 3$ (Fig. 1-2). Once the incoming nuclei have an incident momentum greater than a few GeV, projectile nuclei lose a constant amount of rapidity, regardless of the incident energy. At 100 A-GeV/c, for example, fast nuclei impinging on target nuclei lose up to 2 to 3 units of rapidity

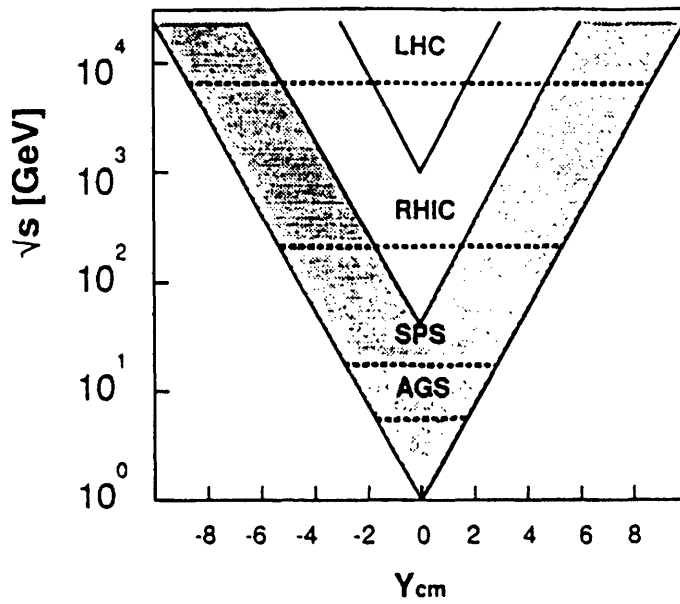


Figure 1-1: Simplified diagram showing the regions of vanishing baryon density (inner white and light shaded triangles). The AGS and SPS energies do not produce a baryon free region [QM91-Sa].

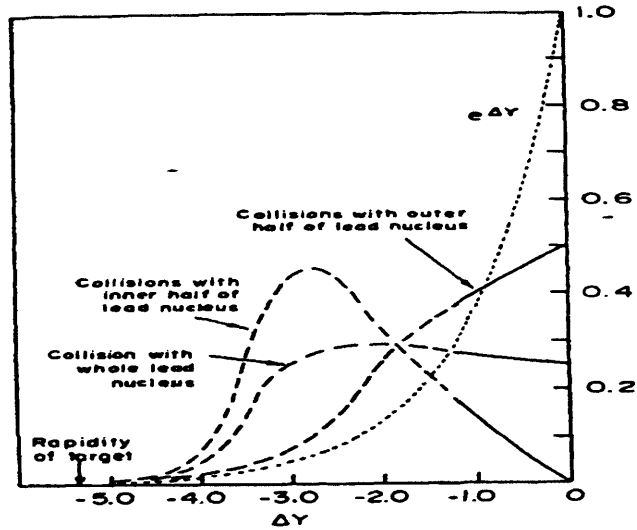


Figure 1-2: Rapidity loss for pPb collisions of various impact parameters [Bus88]. The vertical axis shows the probability that the rapidity loss for baryons is Δy for protons with incident momentum of 100 A-GeV/c. There is a limiting rapidity shift $\Delta y \approx 2 - 3$ for pA collisions as the size of the target mass is increased. We therefore expect a maximum limit to baryon densities in A + A collisions, occurring when the rapidities of the projectile and target nucleons shift to a common rapidity.

[Bus84]. This finding implies that the ideal beam rapidity for maximum baryon densities would then be ≈ 5 . Mid-rapidity ($y = 2.5$) would then be situated at the peak rapidity loss. The AGS beam rapidity of 3.44 is close to this value and therefore hosts collisions where the highest baryon densities may be produced in the laboratory.

There is a trade-off in obtaining a large degree of stopping and in reaching an equilibrated state with the larger $^{197}\text{Au} + ^{197}\text{Au}$ reaction. Though the lighter projectiles have fewer overall participants, these projectiles achieve greater mean rapidity loss. The nucleons of an oxygen ion, for example, in a central $^{16}\text{O} + ^{197}\text{Au}$ collision, will undergo relatively more collisions than the peripheral nucleons of a gold ion in a central $^{197}\text{Au} + ^{197}\text{Au}$ collision. The larger gold-gold collisions provide for more nucleon-nucleon interactions and probably achieve a greater degree of equilibration in the center of the collision. But, even in the most central $^{197}\text{Au} + ^{197}\text{Au}$ collisions there are still many single pp collisions near the periphery of the nuclei that do not achieve a high degree of equilibration. Furthermore, it may be easier to understand the explicit dynamical processes in collisions of smaller nuclei than in the more complicated $^{197}\text{Au} + ^{197}\text{Au}$ collisions.

There are still no unambiguous theoretical signatures that predict an unconfined QGP at any incident beam energy. Furthermore, there are no clear indications that the QGP phase transitions is a first order or second order transition. In either case, there are many predictions that an increase in the strange particle multiplicity will accompany the onset of a QGP phase [Chi79], [Fah79], [Witt84], [Koc86].

Nearly 10 years ago, predictions of increased strange matter production [Raf82] in heavy-ion collisions were made. The fermi momentum of u and d quarks in protons and neutrons depends on the density. After summing over the momentum, the density becomes: $\rho = N/V = g/h^3 \int_0^{p_F} d^3p$. The fermi momentum may be written as

$$p_F(u, d) \approx (3)^{1/3} (\rho/\rho_0)^{1/3} p_0, \quad (1.1)$$

where $p_0 = 260 \text{ MeV}/c$ is the fermi momentum for nucleons in normal nuclear matter. An increase in density by a factor of 5 in a heavy-ion collision will push $p_F(u,d) \approx 600\text{-}700$

MeV/c [Nag92], well above the 200 MeV s-quark mass. It is energetically more favorable to produce strange quarks in low p states instead of producing more u and d quarks in high p states.

At AGS energies, since stopping is essentially achieved, in thermal equilibrium the ratio of strange to non-strange particle production, for example, may be predicted. We begin using a Maxwell-Boltzmann distribution for two particle species (strange and non-strange) s and q . For a given energy and temperature, the strange to non-strange ratio is simply $R = f_s^{MB}/f_q^{MB}$, where the fugacity is $f_i = e^{\mu_i/T}$. Then,

$$R = \frac{e^{\mu_s/T}}{e^{\mu_q/T}}. \quad (1.2)$$

In equilibrium, if $T = 150$ MeV, and $\mu_s = 200$ MeV and $\mu_q = 313$ MeV, we get $R = 0.47$. In ideal conditions, the strange to non-strange meson ratio ($K^+(u\bar{s})/\pi^+(u\bar{d})$), would provide such a measurement of R . Both mesons share the abundant u quarks and either a created \bar{d} or \bar{s} quark. The highest ratio is observed in central $^{197}\text{Au} + ^{197}\text{Au}$ reactions where $K^+/\pi^+ \approx 0.25$.

As heavy-ion collisions increase in size, we might also expect to increase the degree of equilibration. Experimentally, we can measure the K^+/π^+ ratio for systems of different sizes to determine if we are at least moving in the right direction towards a QGP phase.

The microscopic processes of individual nucleon-nucleon collisions can also be understood in the context of cascade models. This thesis will examine multiple scattering and rescattering in heavy-ion collisions at the AGS at BNL. Experimentally, we only measure particle yields and the number of reaction participants. We understand how particle yields depend on multiple scattering and rescattering with cascade models. Hopefully, we will better understand how secondary interactions affect particle yields.

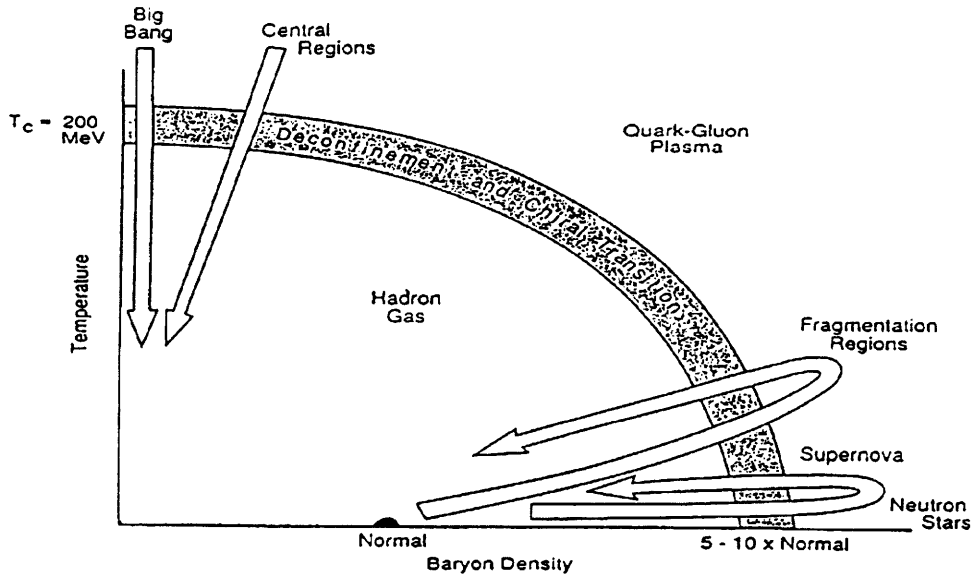


Figure 1-3: Nuclear Matter phase diagram, showing the point of normal matter and possible trajectories of various reaction scenarios at RHIC energies. A heavy-ion collision at AGS energies could hopefully follow a track similar to the one labeled “Fragmentation Region” in the figure.

1.3 Why Study Heavy-Ion Collisions?

Figure 1-3 shows a schematic nuclear matter phase diagram. Normal nuclear matter is shown as a point on the diagram and the trajectory for a hypothetical heavy-ion collision at the AGS is shown.

The Quark Gluon Plasma (QGP) is a prediction of lattice gauge calculations for baryon free nuclear matter under extreme conditions. Physicists are interested in determining the shape of the transition boundary as well as the location of the transition. The temperature vs. density phase diagram shown in Figure 1-3 indicates a transition at $5 - 10 \rho_0$, where ρ_0 is the normal nuclear matter density.

We note that the phase diagram includes a rather broad deconfinement boundary. Based on present understanding of heavy-ion collisions at the AGS it is hoped that a collision trajectory could be traced out such as that labeled “Fragmentation Region” in Figure 1-3. If a phase transition of nuclear matter occurs, it should manifest itself in the

dependence of particle production on the density of participant nucleons.

As mentioned in the previous section, the AGS beam momentum implies that secondary collisions play an important role in heavy-ion collisions. Multiple scattering and rescattering are both important aspects of the collision since we are interested not only in creating a high baryon density in the central region of heavy-ion collisions, but also in equilibrating the reaction as much as possible in the few fm/c duration of a heavy-ion reaction. The total time for the reaction may be estimated by the time it takes a 14.6 GeV/c nucleon to traverse a nucleus, approximately a few to 10 fm/c. Most nucleons that participate in the collision have an opportunity to collide only a few times with other nucleons or with produced particles within the duration of the collision.

The thermodynamic conditions in a heavy-ion collision are quite different than a gas at room temperature where there are a very large number of participants interacting over a long period of time. It is natural to ask to what degree heavy-ion collisions are equilibrated. In other words, what degree of initial momentum *memory* of the beam nucleons is lost when they impact the target nucleons? It would be interesting to understand the degree of equilibrium reached in the collision as well as the participant number densities for a variety of projectile-target combinations.

This work builds on the earlier analysis efforts of Matt Bloomer [Blo90]. Bloomer examined rapidity distributions and baryon densities for Si + Al, Cu, and Au reactions using the E802 spectrometer and examined pA reactions at higher energies with the Fermilab Hybrid Spectrometer E565/570. This analysis will use improved E802 spectrometer calibrations as well as a more complete data set, examining the ^{16}O and ^{28}Si + A reactions as well as $^{197}\text{Au} + ^{197}\text{Au}$ data from the first E866 run. With three projectiles (A=16,28,197) and three targets (A=27,64,197), this data set offers a much larger range in size and number of participants than the earlier analysis.

As in the previous analysis, we use a zero-degree calorimeter (ZCAL) to measure the number of participants in the above reactions. With the new data set, we hope to piece together a yield vs. participant function (see Chapter 6) over a wide range of

participants. We also hope to understand better how multiple scattering plays a role in heavy-ion reactions. With the zero-degree calorimeter and the ensemble of projectiles and targets, we are free to vary the number of participants that we examine. Using a simple model of two colliding spheres, we effectively vary the impact parameter of the collision and therefore the geometry of the collision. When we do this, we also vary the amount of multiple scattering that can take place in a collision as we vary the mass of the spectator material that surrounds the initial hot reaction participants. Thus with the ensemble of collisions, we hope to understand how particle production varies over the size of the reaction system as well as the surrounding environment.

1.4 Heavy-Ion Collisions Models

We examine several models in this thesis. The focus of the model comparison in this thesis is twofold;

1. Understanding to what extent the present cascade models match the yields of π 's over the full range of total participants determined in ^{16}O , ^{28}Si , and ^{197}Au collisions.
2. Understanding the degree of equilibration, i.e., understanding the amount of secondary collisions for heavy-ion collisions at AGS energies.

This thesis uses models at three levels. First, we compare one of the simplest models, the isotropic fireball model [Land53], [Land56], [Nat92-He] with central AA data. This model is a useful starting point and simple in conception. Secondly, we will use geometric models (as those used in the input to FRITIOF [And87] and [Nil87]) to calculate participants in heavy-ion collisions of various impact parameter ranges. In Chapter 4 we will discuss clean-cut collisions in terms of hard spheres with a skin depth determined by a Woods-Saxon potential. Thirdly, we look at the cascade codes, Relativistic Quantum Molecular Dynamics (RQMD), and A Relativistic Cascade (ARC). A comparison of yields for pions and kaons will be made with this model in Chapter 6.

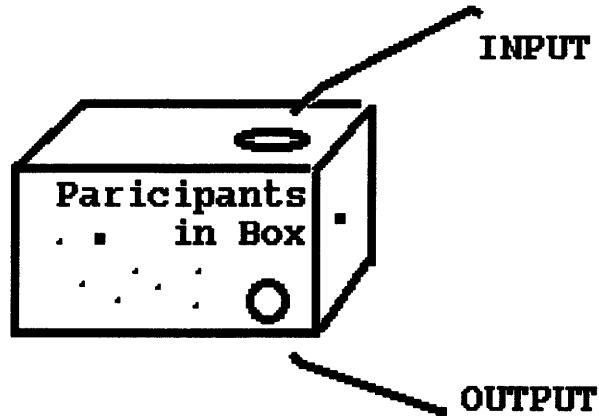


Figure 1-4: A Gedanken experiment to allow nucleons to interact in a controlled environment. Ideally, one would like to vary several physics parameters and then observe particle yields and inverse slope parameters (temperatures).

1.5 Questions to be Answered in this Thesis

We would like to understand if and why heavy-ion collisions differ from a simple superposition of many pp collisions. Do nuclear collisions with many participants differ from collisions with relatively few participants?

Consider a Gedanken experiment as in the simple box experiment in Figure 1-4. Suppose we can add nucleons at a specified energy E_0 and momentum p_0 , and observe the overall particle yields and inverse slope parameters that emerge from a hole in the side of the box to be detected. In light of this figure, the following list of parameters, those within and out of our control, are described in Table 1.1.

The systems under observation after a heavy-ion collision of type $A_1 + A_2$ are very transient. We can change the number of initial participants by varying the impact parameter and size of the projectile. Some nucleon participants will scatter only one time, others as many as ≈ 10 times, for nucleons in central $^{197}\text{Au} + ^{197}\text{Au}$ collision (see Chapter 4). In addition, our collision zone is unlikely to be homogeneous. For these two regions, heavy-ion collisions may not approach the level of control implied by Figure 1-4. Therefore, we must be careful in the interpretation of the experimental results.

ITEMS IN EXPERIMENTAL CONTROL

Within experimental control	Outside experimental control
1. Size of the box.	1. Homogeneity of number of collisions within the box.
2. Number of nucleons in the box.	
3. Longevity of the box**.	2. Filter between box and detector.*

Table 1.1: Summary of items in and outside experimental control. * By varying the number of forward going spectators with the zero-degree calorimeter in this experiment, we effectively change the impact parameter of the collision and therefore the amount of surrounding material (i.e., filter). ** This variable is however only loosely controlled as the longest collision durations are only $\approx 10fm/c$.

The goals of this thesis are four-fold:

1. We will determine the particle yields and inverse slope parameters for a large selection of heavy-ion collisions. Collision systems of $^{16}\text{O} + \text{A}$ and $^{28}\text{Si} + \text{A}$ will be compared to the $^{197}\text{Au} + ^{197}\text{Au}$ reactions.
2. We will compare the total yields for the above reactions vs. the number of participants in the reaction. Yields for π 's and kaons will be compared with the number of participants in the reaction. The participants are determined using the calorimeter.
3. We will perform an in-depth analysis of how secondary collisions affect particle production. We will examine the RQMD code and tag particles that undergo at least one collision after the initial collision in a heavy-ion reaction. This analysis will be described in Chapter 4.
4. Finally, we will address trends in dN/dy and discuss the inverse slope parameter for the full range of collision systems.

1.6 Techniques of the Analysis

We address the first question in Section 1.5 using the E802 spectrometer to measure particle yields. The particle invariant differential yields, $d^2n/2\pi p_t dp_t dy$, will be plotted

as a function of p_t for π^\pm , K^\pm , and protons over the measured ranges in rapidity. The E802 spectrometer (in particular the time-of-flight wall) differentiates pions from the lighter electrons up to a momentum of 0.7 GeV/c, pions and kaons up to 2.2 GeV/c and kaons from protons up to 3.7 GeV/c using the particle's time of flight and the path length. The cross-sections are fit with exponential functions and Boltzmann functions in both m_t and p_t and an inverse slope parameter is measured for each particle as well as the integrated yield, dN/dy . The specific technique to determine these values will be discussed later in Chapter 5 and the data presented in their entirety in the appendices.

We use the zero-degree calorimeter to measure the mean number of projectile participants $\langle N_{part}^{proj} \rangle$. In symmetric collisions, the mean number of target participants is $\langle N_{part}^{targ} \rangle = \langle N_{part}^{proj} \rangle = \langle N_{part}^{tot} \rangle / 2$. The number of participants is related to the energy deposited in the calorimeter:

$$\text{Participants} = A_{proj}(1 - E_{ZCAL}/T_{beam}). \quad (1.3)$$

Our procedure is to make software cuts of varying energy deposited in the ZCAL and to examine the corresponding particle rapidity distributions for pions, kaons, and protons. With the full E802 data set and the first running period of E866 data available, we are able to compare shapes and magnitudes of the rapidity distributions for reactions of varying impact parameters but with fixed $\langle N_{part}^{tot} \rangle$. We are more interested in the global trends of the data in this analysis, i.e., trends in average particle yields.

1.6.1 Scaling

Though the term scaling is widely used in the field of heavy-ion reactions, we will use this term to imply the invariance of an observable, normalized to some parameter and measured over some phase space appropriate to the experiment. A simple example of a scaling observable is a linearly scaled variable. For example, over a limited number of participants, the production of π 's appears to be a linear function with the number of

DATA SUMMARY

Projectile	Runs	Target	θ_{spec}	Field (kG)	Comments
^{16}O	Jun 88	$^{27}\text{Al}, ^{64}\text{Cu}, ^{197}\text{Au}$	5,14,24,34,44	$\pm 2, \pm 4, \pm 6$	full analysis
^{28}Si	Dec 88	$^{27}\text{Al}, ^{64}\text{Cu}, ^{197}\text{Au}$	5,14,24,34,44	$\pm 2, \pm 4, \pm 6$	reanalysis of ZCAL data
^{197}Au	Apr 92	$^{27}\text{Al}, ^{64}\text{Cu}, ^{197}\text{Au}$	24,34,44	$\pm 2, \pm 4$	full analysis

Table 1.2: This table shows a quick summary of the data that was analyzed in this work, including the projectile, the run period, the target, and the spectrometer angle setting.

participants. This linearity occurs up to about 100 total participants, representing central $^{28}\text{Si} + \text{A}$ collisions. Do collisions of more participants follow this linear dependence? We will examine this scaling in Chapter 6 and determine pion, and more crudely kaon scaling over a much larger range of participants, using $^{197}\text{Au} + ^{197}\text{Au}$ data.

Protons, though not created in these reactions, are an excellent means of measuring how energy is distributed in these collisions as one varies the size of the reacting system as well as varying the surrounding target material. We measure hadron yields with respect to: (1) the number of total participants and (2) the rapidity.

1.7 The Data Sets

The nature of this analysis is to examine as wide a variety of heavy-ion collisions over as wide a range of reactions participants as were available at AGS energies. We combine E802 data including the lighter-ion running, oxygen data (June 1988) and silicon data (December 1988) with the heavy-ion gold beam data E866 (April and May 1992). Table 1.2 gives a brief listing of the data taken, including the running period, targets, and trigger conditions.

The oxygen and silicon data were taken at a beam momentum of $14.6 \text{ A} \cdot \text{GeV}/c$ while the gold running was done at $11.6 \text{ A} \cdot \text{GeV}/c$.

The entire data set has been analyzed using a cross-section routine written by Chuck Parsons and modified by several students, [Par92], [PZ,91], [MRSZ,92]. Chapter 5 contains details of creating differential yields and cross-sections and explains data filtering

and quality.

1.8 Summary of this Thesis

This thesis is organized in eight chapters. Chapter 2 discusses the models used in this thesis. The discussion focuses on simple descriptions of the nuclei in violent collisions. We discuss the fireball model of heavy-ion collisions as well as the cascade models, Relativistic Quantum Molecular Dynamics (RQMD) and A Relativistic Cascade (ARC). Chapter 3 describes of the E802 spectrometer. Chapter 4 describes the event characterizations and interpretation of the centrality measurements with the ZCAL.

Chapter 5 describes the cross-section analysis. We discuss data quality and filtering and correct for inefficiencies. Chapter 6 discusses the particle yields, results of dN/dy , and inverse slope parameters for the various reactions. Chapter 7 discusses energy and baryon densities in these collisions. Finally, Chapter 8 draws the conclusions reached in this thesis.

The appendices contain particle invariant yields, dN/dy , and inverse slope parameters for semi-inclusive spectra. Minimum-bias and hardware triggered spectra of π^\pm , K^\pm and protons from O + A, Si + A, and Au + Au reactions are shown.

Chapter 2

Models

We begin this section with a very simple geometric collision model between two nuclei, each having approximate uniform density in the center and falling off at the edges according to a Woods-Saxon potential. This picture of the nucleus (a Glauber model) treats the protons and neutrons classically because of the high relative momentum between the projectile and the target nuclei. The beam momentum $p_{beam} = 14.6 A \cdot \text{GeV}/c \gg 200 \text{ MeV}/c$, the Fermi momentum associated with the nucleons in cold nuclear matter.

We are also able to estimate theoretically the number of participants in a heavy-ion collision at the AGS, given the impact parameter of the projectile with this model. Figure 2-2 shows a typical symmetric heavy-ion collision somewhere between a central and peripheral collision. The produced particles are created in this dense, hot region, formed in rapidity space (see Section 2.1) somewhere between the target and the projectile rapidity ($y = 3.44$ at the AGS for oxygen and silicon running and $y = 3.2$ for gold running).

Kinematic variables are needed in the discussion of particle cross-sections and yields. Therefore, a discussion of the appropriate kinematic variables is now presented.

2.1 Kinematic Variables

Kinematic variables for high energy collisions are often described in terms of rapidity y and perpendicular momentum p_t , or transverse mass m_t :

$$m_t = \sqrt{p_t^2 + m_o^2}, \quad (2.1)$$

and

$$y = \frac{1}{2} \ln \left(\frac{E + p_{\parallel}}{E - p_{\parallel}} \right) = \tanh^{-1}(\beta_{\parallel}), \quad (2.2)$$

where m_o is the mass of the measured particle, E is the energy of the particle and $\beta_{\parallel} = v_z/c$ or the velocity along the beam axis. Transverse and parallel momentum are also related by $p = \sqrt{p_t^2 + p_{\parallel}^2}$, where p is the total momentum of the particle. Energy and longitudinal momentum may also be expressed in terms of m_t and y :

$$E = m_t \cosh(y), \quad (2.3)$$

$$p_{\parallel} = m_t \sinh(y). \quad (2.4)$$

Observed particles from high energy collision are often described in terms of an invariant cross-section, defined such that the quantity σ_{inv} is frame invariant:

$$\sigma_{inv} = E \cdot \frac{d^3\sigma}{dp^3}. \quad (2.5)$$

The invariance of this quantity makes it useful when comparing cross-sections of data sets from various collision energies. In this analysis, we discuss the invariant yield instead of the cross-section. When using a trigger that selects events of interest, we may define the invariant yield as

$$\frac{d^2 n_i}{2\pi p_t dp_t dy} = \frac{1}{\sigma_{trig}} \cdot \frac{d^3 \sigma_{trig}}{dp^3}. \quad (2.6)$$

where n_i is the yield for a particular particle.

2.2 Energy and Baryon Density

2.2.1 Techniques to Extract Energy and Baryon Density

Ultimately, we would like to construct a picture of the heavy-ion collision so that we may be able to extract the important quantities from these transient, heated and compressed states of nuclear matter. Where on the (T, ρ) nuclear phase diagrams of Fig. 1-3 are heavy-ion collisions at the AGS? The details of determining the temperature¹ will be described later. For the moment, we focus on techniques to determine the energy and baryon densities, ϵ and ϵ_B . We discuss ϵ and ϵ_B in terms of a thermal model.

2.2.2 A Thermodynamic Approach

How relevant is a thermodynamic discussion for heavy-ion collisions at AGS energies? There are several parameters that could be addressed in order to answer this question. Some important parameters may include:

- available energy
- collision time
- redistribution of energy.

There is certainly sufficient energy available at the AGS such that incident nucleons are able to interact numerous times. Measured proton yields in central $^{197}\text{Au} + ^{197}\text{Au}$ colli-

¹We actually measure the inverse slope parameter, not the temperature. Some of these transient states of matter are probably not in thermodynamic equilibrium.

sions, for example, do peak at mid-rapidity and suggest a large degree of secondary scattering. Incident nuclei are so energetic that nuclear transitions and more subtle effects need not be considered. The more relevant issues are collision times and redistributions of energy.

A heavy-ion collision occurs in approximately the time needed for a nucleus to transverse another nucleus. At the AGS this is a few fm/c. In classical equilibrium, a large period of time is allowed for particles in the system to interact. In these heavy-ion collisions at the AGS, the more relevant question may be asked: Is there sufficient time for participant baryons and produced particles to exchange enough momentum with other particles such that the initial momentum information is lost? In other words, what particle spectra are expected if thermal equilibrium is reached? A general expression is obtained that must be satisfied for particles which are in thermodynamic equilibrium [Nat92-He],

$$dN/dy = Cm^2Te^{-m\cosh(y)/T}\left[1 + 2\frac{T}{m\cosh(y)} + \left(\frac{T}{m\cosh(y)}\right)^2\right], \quad (2.7)$$

where C is a constant. This expression reduces for $m \gg T$ to

$$dN/dy \sim e^{-m(y-y_{FB})^2/2T}, \quad (2.8)$$

where y_{FB} is the fireball rapidity. Equation 2.7 reduces to

$$dN/dy \sim \frac{1}{\cosh^2 y}, \quad (2.9)$$

for massless particles. Equation 2.8 describes rapidity spectra for a thermal fireball for light particles (pions and kaons). Protons in central $^{197}\text{Au} + ^{197}\text{Au}$ collisions are also well fit by Equation 2.8. Satisfying Eq. 2.8 does not necessarily imply that the particles come from a thermal source. Not satisfying this equation would most certainly preclude any analysis using a thermodynamic approach.

It is also reassuring that protons display dramatic changes in their dN/dy shape as the size of the collisions increase from peripheral $^{197}\text{Au} + ^{197}\text{Au}$ collisions (reminiscent of ^{16}O and $^{28}\text{Si} + A$ proton distributions) to central collisions. Cascade calculation (see Chapter 4) show that protons and neutrons in $^{197}\text{Au} + ^{197}\text{Au}$ collisions dramatically increase in the mean number of total scattering events from peripheral to central collisions. The mean number of binary collisions increases from $\langle N_{BC} \rangle \sim 1$ to about 10. Baryons in the center of the central collisions certainly undergo even more collisions. Particles that undergo these many collisions lose any initial momentum information as they are “stopped” at central rapidities.

By no means do these observations prove that equilibrium exists for any collision system under observation; but together, these observations indicate that a thermal approach may be reasonable, especially for central $^{197}\text{Au} + ^{197}\text{Au}$ collisions.

Next we examine two cases of thermodynamic collisions. First, the Landau fireball model is examined. This model assumes that all initial kinetic energy is transferred to participants in the fireball. This then determines the temperature of the system.

An alternative approach is to determine the temperature and chemical potentials from thermal fits to the particle spectra, weighted appropriately with quantum statistical functions. These temperatures and chemical potentials can then be used to determine densities.

2.2.3 The Landau Fireball Model

The Landau model is one of the earliest models that attempts to explain some of the basic physics in a very high density hot hadronic or quark matter fireball [Land53], [Land56]. The model is also one of the simplest pictures of the heavy-ion collision. A good discussion of the model is found in the Ph. D. thesis work by Bloomer [Blo90]. It is worthwhile to briefly describe the basis of the model here and to predict the physics parameters, such as number of participants, temperature, and kinematics for central $^{16}\text{O} + A$, $^{28}\text{Si} + A$, and $^{197}\text{Au} + ^{197}\text{Au}$ collisions.

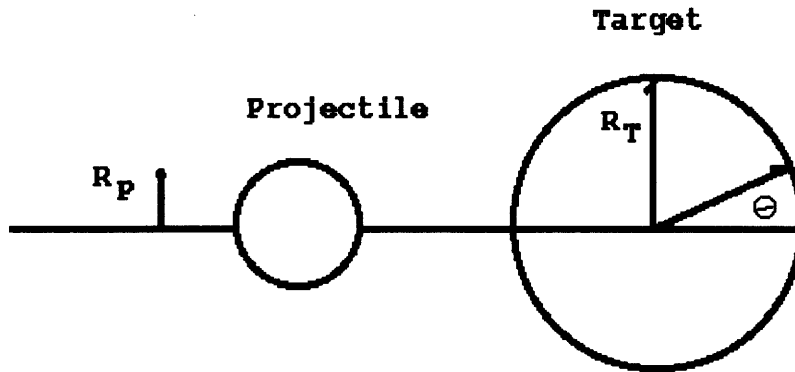


Figure 2-1:

A sketch of a heavy-ion collision where the projectile is smaller than the target. θ is defined as $\arcsin(R_T/R_P)$.

The model assumes that the projectile collides with the target nucleus and that the intercepted volume gives the size of the fireball. The comoving mass radiates energy via particle production. The volume and total energy are both calculable from the fireball model. The volume of the overlap of the projectile on the target nucleus may be calculated for central collisions. A clean-cut collision gives the following geometrical relationship from Figure 2-1 [E802-17]:

$$V_{overlap} = \frac{4\pi}{3} R_{targ}^3 (1 - \cos^3 \theta). \quad (2.10)$$

The value θ is shown in the sketch of Figure 2-1 and the following geometrical constructs are apparent:

$$\sin \theta = R_{proj} / R_{targ} \quad (2.11)$$

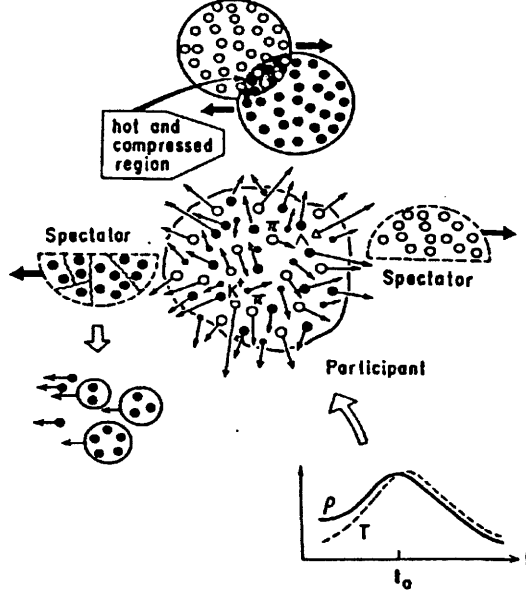


Figure 2-2:

Sketch of a possible heavy-ion scenario for a symmetric collision. The hottest and most compressed portion of the collision takes place very soon after the initial impact.

and,

$$\cos\theta = \sqrt{1 - R_{proj}^2/R_{targ}^2}. \quad (2.12)$$

In the center of mass frame, \sqrt{s} may be written for a two body system as

$$\sqrt{s} = \sqrt{m_{proj}^2 + m_{targ}^2 + 2E_{proj}E_{targ} - 2\vec{p}_{proj}\vec{p}_{targ}}. \quad (2.13)$$

Further simplification can be made as we let the target 3-momentum $\vec{p}_{targ} = 0$. The masses of the two systems are:

$$m_{proj} = m_o N_{proj} ; \quad m_{targ} = m_o N_{targ}, \quad (2.14)$$

where N_{proj} = number of projectile nucleons and N_{targ} = number of target nucleons. The number of target nucleons may be determined from the atomic number, $N_{targ} = A'_{targ}$,

where A'_{targ} is defined as

$$A'_{targ} = A_{targ} \cdot (1 - \cos^3\theta). \quad (2.15)$$

The second factor of 2.15 represents the ratio of overlapped volume to total volume of the target nucleus as defined in Figure 2-1. We let $m_o = 0.938 \text{ GeV}/c^2$ for both protons and neutrons. The total kinetic energy available in the fireball is

$$T_{cm}^{fb} = \sqrt{s} - m_{proj} - m_{targ}. \quad (2.16)$$

The energy density is determined by dividing the total fireball kinetic energy by the volume of the fireball. Because of the Lorentz contraction along the beam direction, one writes $V = V_o\gamma$. Using $\rho_o = 0.17 \text{ GeV}/\text{fm}^3$, the normal nuclear density, the volume

$$V^{fb} = \frac{N_{targ}}{\gamma\rho_o}. \quad (2.17)$$

The energy and baryon density for a heavy-ion collision are calculated separately for the projectile and the target. We begin with the energy density and write it in terms of the atomic numbers of the target and projectile: A_{targ} , A_{proj} . Then,

$$\epsilon = T_{cm}^{fb} \cdot \frac{\gamma\rho_o}{A_i \cdot (1 - \cos^3\theta)} \quad (2.18)$$

and,

$$\epsilon_B = 2\gamma\rho_o. \quad (2.19)$$

The geometric factor used here is only for the larger nucleus. The γ factors are used to describe the density in these approximations and are defined as

$$\gamma_{proj} = \cosh(y_{beam} - y_{FB}), \quad (2.20)$$

and

$$\gamma_{targ} = \cosh(y_{FB}). \quad (2.21)$$

The number of participants is easily determined in a central fireball calculation. All the nucleons from the projectile are assumed to interact as long as the projectile is smaller than the target nucleus (or the same size), which is always the case for the collisions in this analysis. The number of participants involved in the target nuclei may be determined from Equation 2.15. The rapidity of the fireball is related to the fireball mass using Equation 2.13:

$$m_{fb} = \sqrt{s} = \frac{E_{cm}^{fb}}{\cosh(y_{fb})}. \quad (2.22)$$

Table 2.1 shows the number of participants with the respective thermal fireball predictions for each collision reaction and Figure 2-3 sketches the various reactions of Table 2.1. The thermal fireball rapidity

$$y_F = \cosh^{-1}(E_{cm}^{fb}/m_{fb}). \quad (2.23)$$

Finally, we may estimate the fireball model's energy and baryon densities from Equation 2.18 and 2.19:

$$\epsilon = \epsilon_{proj} + \epsilon_{targ} = T_{cm}^{fb} \cdot \frac{\gamma_{proj}\rho_o}{A_{proj}} + T_{cm}^{fb} \cdot \frac{\gamma_{targ}\rho_o}{A_{targ}}, \quad (2.24)$$

and

$$\epsilon_B = \epsilon_B^{proj} + \epsilon_B^{targ} = \gamma_{proj}\rho_o + \gamma_{targ}\rho_o. \quad (2.25)$$

Table 2.2 shows the predictions of the fireball model that complement the predictions from the earlier analysis [Blo90].

Figure 2-3 plots the results of the fireball predictions for γ_{FB} , T_{FB} , ϵ , and ϵ_B for the projectile, target, and total participants. Later, we compare these predictions with

LANDAU FIREBALL MODEL PREDICTIONS

Proj.	Targ	$\langle N_{proj}^{part} \rangle$	$\langle N_{targ}^{part} \rangle$	$\langle N_{total}^{part} \rangle$	m_{fb} GeV	T_{fb} GeV	y_F
p	8Be	1	1	2	3.99	3.32	1.72
	${}^{27}Al$	1	3.11	4.11	3.93	5.52	0.84
	${}^{64}Cu$	1	4.59	5.59	5.63	6.29	0.63
	${}^{197}Au$	1	6.20	7.20	4.49	6.90	0.48
${}^{16}O$	${}^{27}Al$	16	17.2	33.2	89.0	58.1	1.66
	${}^{64}Cu$	16	30.8	46.8	122.7	78.1	1.18
	${}^{197}Au$	16	52.2	68.2	159.2	95.3	0.81
${}^{28}Si$	${}^{27}Al$	28	27.0	55.0	151.1	99.	1.72
	${}^{64}Cu$	28	40.7	68.7	194.6	125.	1.40
	${}^{197}Au$	28	75.6	103.6	251.5	156.	1.27
${}^{197}Au$	${}^{27}Al$	89.4	27	116.4	244.6	135.0	2.45
${}^{197}Au$	${}^{197}Au$	197	197	394	954.3	678.6	1.6

Table 2.1: Predictions for the Landau fireball model for the range of collisions that will be analyzed in this thesis. For the non-symmetric collisions the number of participants were generated with the geometric algorithm used as an input to FRITIOF. The center of mass energy available for a pp type collision with $p_{beam}=14.6$ A·GeV/c is $\sqrt{s} = 5.4$ and for a pp collision with $p_{beam}=11.6$ A·GeV/c, $\sqrt{s} = 4.81$.

FIREBALL CENTRAL COLLISION SUMMARY

Central collisions p,O,Si,Au Projectiles

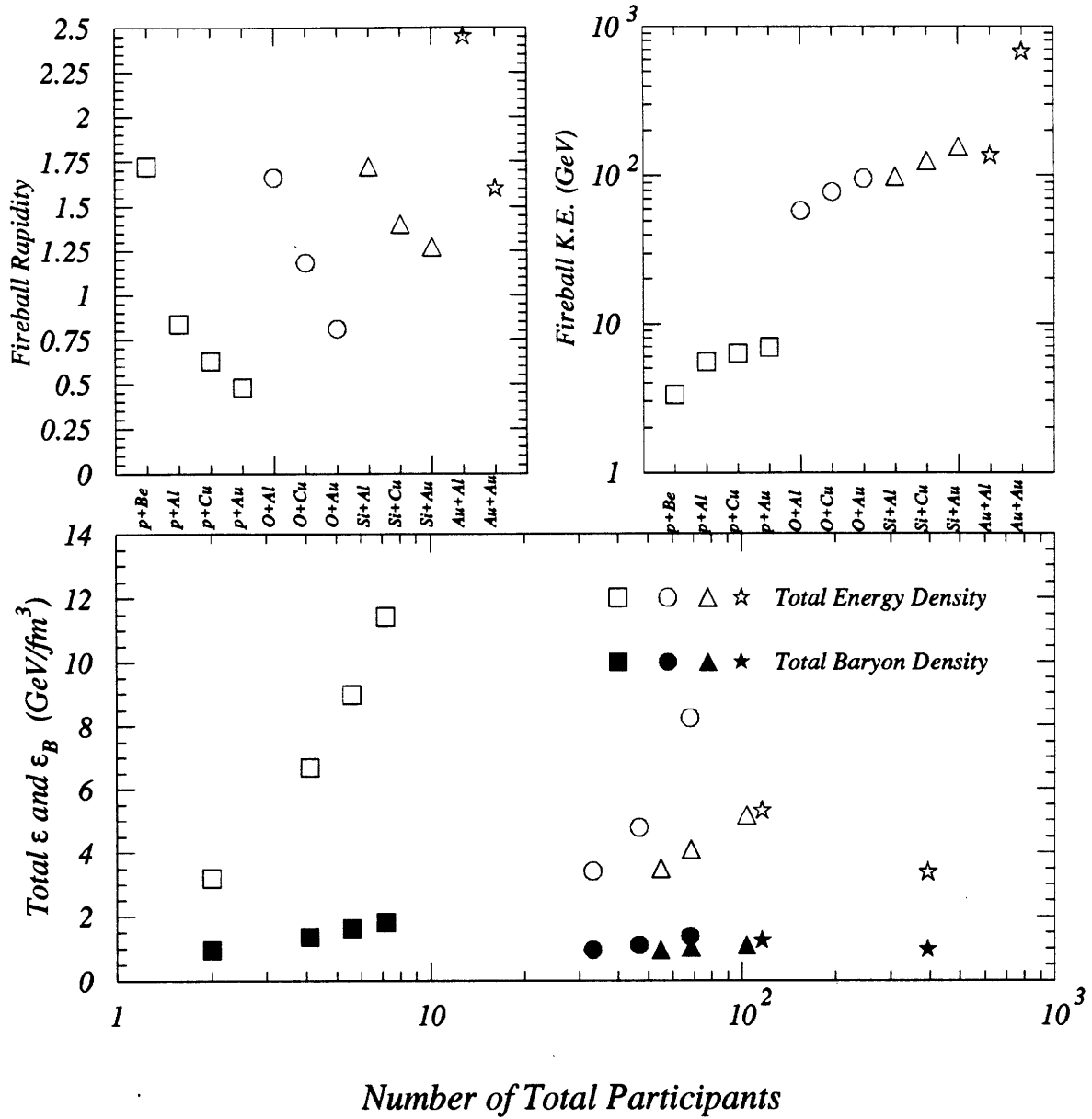


Figure 2-3:

Predictions of the Landau fireball model plotted as a function of numbers of participants. The plot shows the energy and baryon densities for the total number of participants. The data for the graph comes from Table 2.1. The above calculations use the beam momentum appropriate for the AGS; $p_{beam} = 14.6 \text{ GeV}/c$ for proton, oxygen, and silicon projectiles and $p_{beam} = 11.6 \text{ GeV}/c$ for the gold projectile.

DENSITIES FROM THE LANDAU FIREBALL MODEL

Projectile	Target	y_{beam}	γ_{proj}	γ_{targ}	ϵ_{proj}	ϵ_{targ}	ϵ_B^{proj}	ϵ_B^{targ}	ϵ_B
p	8Be	3.44	2.88	2.88	1.62	1.57	0.48	0.48	.96
	${}^{27}Al$	3.44	6.76	1.37	6.28	.41	1.14	0.23	1.37
	${}^{64}Cu$	3.44	8.33	1.25	8.70	.280	1.41	0.21	1.62
	${}^{197}Au$	3.44	9.67	1.17	11.2	.221	1.63	0.19	1.82
${}^{16}O$	${}^{27}Al$	3.44	3.04	2.72	1.87	1.54	0.51	0.45	.96
	${}^{64}Cu$	3.44	4.84	1.78	4.01	.76	0.81	0.30	1.11
	${}^{197}Au$	3.44	6.92	1.34	7.92	.31	1.17	0.22	1.39
${}^{28}Si$	${}^{27}Al$	3.44	2.88	2.88	1.73	1.77	0.48	0.48	.96
	${}^{64}Cu$	3.44	3.91	2.15	2.95	1.14	0.66	0.36	1.02
	${}^{197}Au$	3.44	4.75	1.88	4.49	.66	0.80	0.31	1.11
${}^{197}Au$	${}^{27}Al$	3.2	1.59	5.83	.408	4.9	0.27	0.99	1.26
${}^{197}Au$	${}^{197}Au$	3.2	3.22	2.57	1.88	1.5	0.54	0.43	.97

Table 2.2: Predictions of the energy and baryon densities for the Landau fireball model for a wide range of central collisions. Densities are measured here in units of GeV/fm^3 .

the values from the data. We note that the energy and baryon densities that have been predicted by this model overestimate ϵ and ϵ_B obtained with the data. The density is overestimated partly because the model assumes the participants completely “stop”. A more realistic picture is that only partial “stopping” occurs, with some of the incident longitudinal momentum not equilibrated (i.e., more longitudinal than transverse momentum). The Landau fireball model shows a decrease in ϵ for larger systems. This results because of the large transferred energy for small projectile systems and their small volumes.

It is also interesting to note that the baryon densities from this calculation remain fairly constant, $\epsilon_B^{targ} \approx .2 \text{ GeV}/\text{fm}^3$ and $\epsilon_B^{proj} \approx .5 \text{ GeV}/\text{fm}^3$. Thermal parameters, determined by fitting the data, produce very different results when they are used to determine the densities of particle species. This comparison will be discussed next.

2.2.4 Thermodynamic Approximation Using Fit Parameters

Perhaps a better approach to estimating the densities in AGS collisions in the context of a thermal model is to determine densities using temperatures and chemical potentials determined from fitting the momentum spectrum. The invariant spectrum for a fireball has the form

$$E \frac{d^3 N}{d^3 p} = \frac{C}{(2\pi^3)} m_t \cosh(y - y_{FB}) e^{-m_t \cosh(y - y_{FB})/T}, \quad (2.26)$$

where C is a constant. Typically, the temperature is written in terms of an effective temperature, $T_{eff} = T/\cosh(y - y_{FB})$. In a small rapidity slice, Δy , the invariant spectrum takes on the form [Nat92-He]

$$\frac{dN}{dy dm_t^2} \sim m_t e^{-m_t/T}. \quad (2.27)$$

At low momentum, particle species are expected to show evidences of quantum statistical effects. Further refinement to Eq. 2.27 gives

$$\frac{dN}{dy dm_t^2} \sim \frac{m_t}{e^{(E-\mu)/T} \pm 1}, \quad (2.28)$$

where the denominator accounts for the Bose or Fermi statistical dependency.

At low momentum, pion spectra are observed to rise above a Boltzmann distribution [Par92], [HIP93-go].² One possibility to explain the shape of the pion spectra at low momentum may be decaying Δ resonances. However, some studies have shown that decaying Δ 's do not reproduce the low momentum rise seen for the pions [Par92]. Other possibilities include decaying baryons and Bose statistics to explain the rise in pion yields at low momentum.

In this section, we will examine the possibility of Bose and Fermi statistics to describe the low momentum pion and proton behavior.

²The most recent pion spectra taken with low magnetic field settings in E859 also show that pion spectra rise above a Boltzmann distribution [Sun94].

The distribution function for Bose-Einstein (BE) particles, and Fermi-Dirac (FD) particles may be expressed as

$$f = \frac{1}{e^{(E-\mu)/T} \pm A} \text{ with } A = \begin{cases} \pm 1 & \text{FD/BE distribution} \\ 0 & \text{MB distribution, } \mu = +0. \end{cases}$$

The chemical potential may be considered as a potential energy term and is equivalent to the energy required to create one more particle in thermodynamic equilibrium:

$$\mu_i = \frac{\partial E}{\partial N_{i,S,V}}. \quad (2.29)$$

The shape of the pion spectra and differences between π^+ and π^- may, in part, be affected by the chemical potential [Gor91]. In one model a Coulomb term, μ_Q , is added to the chemical potential to account for the nuclear charge:

$$\mu_{\pi^-} = \mu_{\pi} - \mu_Q; \quad \mu_{\pi^+} = \mu_{\pi} + \mu_Q.$$

In a similar manner, the chemical potential for the baryons

$$\mu_p = \mu_B + \mu_Q; \quad \mu_n = \mu_B.$$

Because of the Coulomb effect the invariant cross-section, or differential yield, is altered. The Coulomb effect and the contributions to the cross-section will be discussed in Chapter 7. Equation 1.2 may also be used to predict μ_Q in AGS A + A data. Pion abundances, determined with chemical potentials using μ_{π^+} and μ_{π^-} , are

$$R = e^{-\mu_Q/T}, \quad (2.30)$$

assuming $\mu_Q = \mu_{Q^+} = -\mu_{Q^-}$. Later we will show that central $^{197}\text{Au} + ^{197}\text{Au}$ collisions, where $R = .6 - .7$, are reasonably accounted for in this model for low momentum pions $p_t < 200 \text{ GeV}/c$. After correcting for the expected π^- abundances for the neutron rich

$^{197}\text{Au} + ^{197}\text{Au}$ collisions, the excess π^- may be accredited to a Coulomb contribution to the chemical potential on the order of $\mu_Q \approx 15$ MeV. The chemical potential for pions that are determined by fitting Bose functions for $A + A$ collisions gives a reasonable explanation to the abundances of π^- at low momentum and provides another way to describe the differences in pion abundances along with conservation of isospin. This ratio will be discussed more in Chapter 6.

We expect that particles detected in the E802/E866 spectrometer come from a source distribution where Bose-Einstein effects for pions and kaons and Fermi-Dirac effects for protons occur. By modeling the heavy-ion collisions as a thermal system, we may extract the densities by summing over the number of states and obtain

$$\rho = \frac{N}{V} = \frac{g}{V} \int f d^3x d^3p / h^3. \quad (2.31)$$

The degeneracy-spin factor g is also included here. A good discussion of energy and baryon density in a thermal model may be found in a lecture by Zimányi [Nat92-Zi].

The invariant spectra are fitted to the Bose-Einstein or Fermi-Dirac form, as appropriate. For π 's, we have

$$\rho = \frac{4\pi g}{(2\pi\hbar)^3} \int_0^\infty \frac{p^2 dp}{e^{(\sqrt{m_\pi^2 + p^2} - \mu)/T} - 1}. \quad (2.32)$$

This expression may be integrated over p to give a number density of each particle species at freeze-out. The thermal fits to the data are treated later in the discussion of this thesis. Results of the thermal fits to the data will be described in Chapter 7.

Work continues at the AGS to determine the true contribution of resonance decays and quantum statistical effects to low momentum particle yields.

2.3 Cascade Models

Cascade models are a general class of event generators that allow particles to progress through a series of collisions. These models fall into several categories of varying complexity. We begin with the simplest model, FRITIOF. Later, we discuss the RQMD and ARC models.

2.3.1 Specific Dynamical Models

FRITIOF: The FRITIOF [And87] model is a form of Wounded Nucleon Model (WNM). Wounded nucleon models are a general class of models that assume that particle production is directly proportional to the number of participants in a heavy-ion collision. This model has first been treated in pA collisions, invoking the simple linear relationship for pion production [Bial74]:

$$N_\pi = a + bN_{tot}^{part}. \quad (2.33)$$

Macroscopically, the FRITIOF model collides pp, pA, and AA collisions. Both target and projectile fill a nuclear volume with an average intra-nuclear spacing of 1.13 fm between adjacent nucleons. The boundaries of a nucleus are not sharp, but are described by a Woods-Saxon distribution. A projectile bores out a cylindrical core, similar to that described in the fireball model, and nucleons in this core become the collision participants. The mean number of collisions per participant, ν , is determined in this bored cylinder. Each subsequent collision transfers momentum to the target nucleons via Monte-Carlo collision processes. Once a projectile nucleon interacts, in pA and AA collisions, they are free to interact with subsequent target nuclei in the bored core. For A + A collisions, the target nuclei are free to interact multiple times after they initially interact by a leading nucleon; they multiple scatter. On the other hand, target and projectile spectators and participants never interact with created hadrons. These spectators are untreated in FRITIOF.

Individual nucleons in FRITIOF are described as massless strings [And87]. A collision of two quarks excites a QCD color string that figuratively stretches between the two quarks. Hadronization occurs as a color string de-excites.

FRITIOF is modeled for high energy experiments (i.e., CERN energies), where the interaction duration is small compared to the hadronization time. Produced hadrons generally do not rescatter since the projectile has long since bored through the nucleus before the produced particles could interact with the spectators. At AGS energies, it is likely that produced particles have an opportunity to interact with target and projectile nucleons.

In summary, the FRITIOF model provides a good starting point for understanding nuclear collisions, but neglects the rescattering.

RQMD: The RQMD (Relativistic Quantum Molecular Dynamics) model [Sor89] was designed to study the space-time evolution of heavy-ion collisions over a very wide range of energies, starting from the lowest incident momentum at the BEVALAC ($p_{beam} = 2$ GeV/c), DUBNA ($p_{beam} = 3$ GeV/c), AGS ($p_{beam} = 14.6$ GeV/c and 11.6 GeV/c), and finally CERN ($p_{beam} = 200$ GeV/c). The model assigns an eight dimensional phase space for each particle, the 4-position and 4-momentum vectors. The model includes a soft many body collective potential that may be turned off if desired. Studies have shown that particle production is not greatly affected by this potential [Mosk92], [Sol94].

The baryon-baryon, baryon-meson, and meson-meson cross-sections are taken from experimental data when available. The RQMD uses a 1 fm/c mean formation time in the center of mass frame of the two particles. Quantum effects are also included. They are:

1. Quantum stochastic scattering of hadrons and quarks.

2. Pauli blocking in collisions.

The RQMD model approaches particle production in three different energy regions. The lowest energy regime is (quasi-) elastic scattering of hadrons in heavy-ion collisions (relevant up to a few GeV/c incident momentum per nucleon). Next there is the region of resonance production and subsequent particle formation, the most relevant region at AGS energies. Finally, there is the high energy region characterized by hard quark-quark scattering.

The most important resonances created in the intermediate particle production process arise from the following baryon-baryon, meson-meson, and baryon-meson interactions:

$$\pi N \rightarrow \Delta(1232),$$

$$\pi\pi \rightarrow \rho(770),$$

$$NN \rightarrow N\Delta(1232) .$$

At higher energies (CERN energies), contributions from direct quark-quark interactions also become important.

ARC : The ARC model [Pan92] is also an intra-nuclear cascade model. The ARC model has been developed recently to specifically study many body interactions of heavy-ion collisions at AGS energies. The ARC model excites masses to higher resonance states and then allows them to decay. After the original collision, subsequent collisions are possible if the trajectory of a nucleon comes within a critical distance of another nucleon, determined by the nucleon-nucleon inelastic cross-section.

After a collision, particle production may occur via two types of mechanisms in ARC: Direct (DIR) and Resonance (RES) production and scattering.

- **DIR**: Mode that handles intranuclear inelastic nucleon collisions as if they occurred in free space.
- **RES**: Mode of particle production via low-lying baryonic and mesonic resonances as intermediate states within nuclear matter.

Mesons may be produced from both DIR and RES modes. A 1 fm/c formation time is required for hadronization in the DIR mode. It has been shown that the RES mode gives a quantitatively better description to the E802 data [Pan92]. DIR production, on the other hand, has been shown to produce more stopping, too high of a pion yield and too low a K^+ yield as well as too low a nucleon effective temperature [HIP93:-ka].

Energy is shared by resonant states as well as produced particles, and this results in a dissipation of the energy within a few fm/c's after the start of the collision.

The cascade model has shown to be a very powerful and effective analysis tool in understanding heavy-ion collisions at the AGS. Some caveats and limitations of the model include:

- No Fermi momentum is assigned to the nucleons in either the projectile or target nucleons. This initial Fermi momentum is assigned to each particle once a collision occurs.
- Nucleons travel in straight line trajectories since there is no nuclear mean field in this model. Tests done with the RQMD model [Mosk92] with the mean field turned off show that the mean field plays no significant role in particle production at AGS energies.
- The lack of knowledge of resonance-resonance cross-sections is a weakness to the model.

The ARC model will be compared to the measured yields of pions and K^+ in $^{28}\text{Si} + ^{27}\text{Al}$ and $^{197}\text{Au} + ^{197}\text{Au}$ reactions.

2.4 Summary

We have examined the fireball model in the context of heavy-ion collisions at the AGS. A thermal model is also examined. The temperatures and chemical potentials are obtained by fitting the particle's momentum distributions with thermal functions. Chapter 7 contains a comparison of these two approaches.

Two cascade models RQMD and ARC are also discussed. These two models are compared in Chapter 6 to the measured yields of pions and kaons in $^{28}\text{Si} + ^{27}\text{Al}$ and $^{197}\text{Au} + ^{197}\text{Au}$ collisions.

Chapter 3

Experimental Setup

This chapter describes the E802/E866 experimental layout. A brief overview of the AGS and Tandem Van de Graaff facilities is described as well as the experimental floor layout. Data for this thesis was obtained from three experimental running periods from June 1988 through April 1992. Apparatus changes which affect the analysis are described. This chapter emphasizes the spectrometer and the zero-degree calorimeter (ZCAL), which were used extensively in this analysis.

3.1 The AGS and Tandem Facilities at Brookhaven National Laboratories

The AGS has long been used for high energy acceleration of protons to 30 GeV/c on fixed targets. The acceleration of heavy-ions came after the Tandem Van de Graaff Facility was constructed in the early 1970's and used to accelerate heavy-ions to a few MeV/c per nucleon [Abb89]. In 1986, a transfer line was completed between the Tandem facility and the AGS. Thus, heavy-ions from the Tandem could be injected into the AGS at a momentum of $p \approx 120 A \cdot \text{MeV}/c$. Ions of ^{16}O and ^{28}Si were chosen; with a charge-to-mass ratio $Z/A = 1/2$ for oxygen and silicon, they could be accelerated to a momentum of about half that of the proton ($Z/A=1$) to 14.6 A·GeV/c. Heavy-ion beams from the

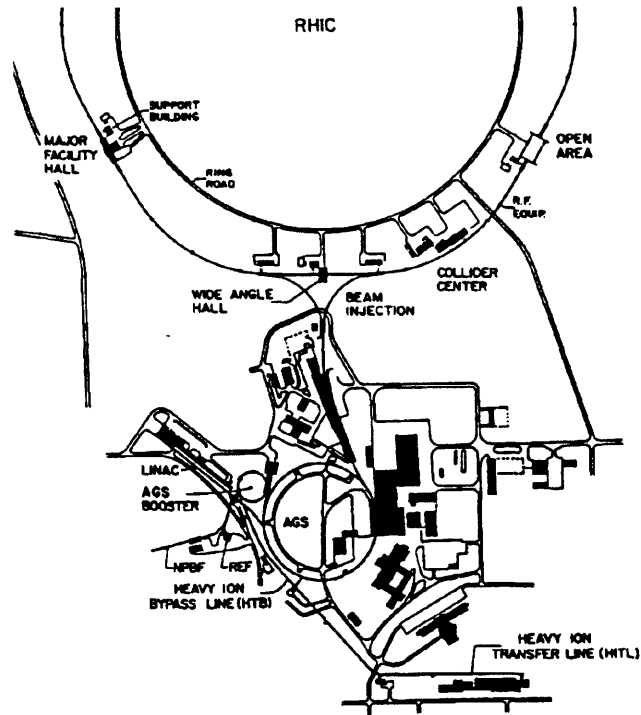


Figure 3-1: Layout of the AGS Accelerator facility.

AGS are extracted to several experimental beam lines. Figure 3-1 shows a map of the AGS/Tandem layout.

In the spring of 1992, the gold beam was commissioned. A booster in front of the AGS allows for the acceleration of partially stripped gold ions to a high enough velocity to strip the remaining electrons. The gold ions are then injected into the AGS ring. The smaller charge-to-mass ratio of the gold ions allows for their acceleration only to 11.6 A·GeV/c. The highest baryon densities achievable are expected to be reached with the AGS gold program.

Experiment E802 was the first of three series of experiments and started in 1986. Ongoing work has included spectrometer upgrades and improved rare-particle triggering (E859). A forward spectrometer, new multiplicity array, and a data acquisition system are changes that are implemented for gold running in E866. The forward spectrometer is needed for measuring particles in the forward high multiplicity regions of $^{197}\text{Au} +$

^{197}Au collisions. This thesis data includes the $^{16}\text{O} + \text{A}$ reactions taken during June 1988 and $^{28}\text{Si} + \text{A}$ data during December 1988. Finally, $^{197}\text{Au} + ^{197}\text{Au}$ reactions measured during April 1992 are analyzed here and compared to the lighter-ion data.

3.2 Experiment E802/E866

We will refer mostly to the partitions of experiment E802 in this section. The experimental discussion is divided into roughly two parts: (1) a discussion of event characterization and (2) a discussion of particle identification with the E802 spectrometer. Event characterization is done by the ZCAL, the TMA (Target Multiplicity Array), and Lead Glass Array. Particle identification is done primarily with the E802 spectrometer. Figure 3-2 shows the spectrometer arm and the event characterizing partitions.

3.2.1 Beam Counters and Target

The beam counters comprise four scintillators that are used to define the trigger for beam interactions as well as to provide the start signal for all other partitions. Several beam scintillators are used to define the beam profile and collimate the beam, including UDEW BVETO, AND BTOF (see below).

The beam scintillators are responsible for making sure that the beam shape is reasonable and to supply a minimum bias INT trigger. A logical BEAM signal is defined as:

$$BEAM = \overline{PRE} \cap \overline{UDEW} \cap BTOF \cap BTOT \cap \overline{BVETO}. \quad (3.1)$$

The beam counter scintillators function in the following roles:

1. **PRE:** A digital busy that prevents beam pile-up by rejecting beam events that are preceded by another beam event by less than $3\mu\text{s}$.
2. **UDEW:** The most upstream scintillator set that defines the beam horizontal and

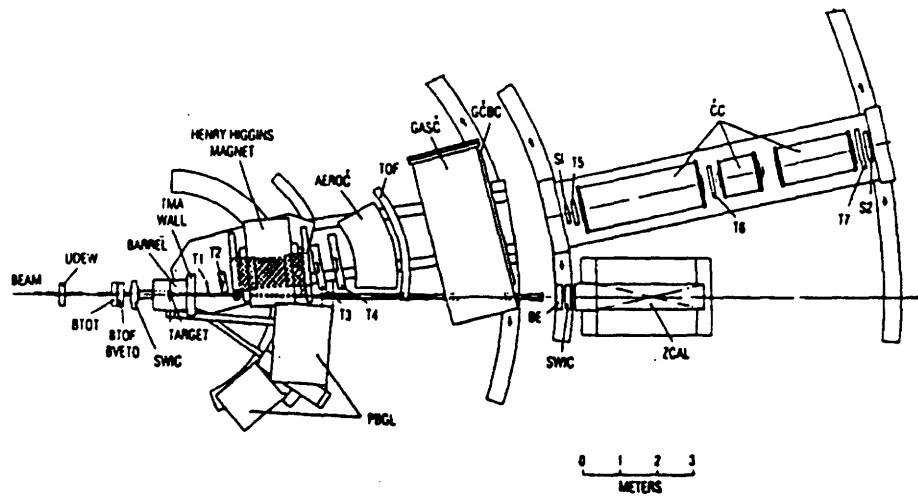
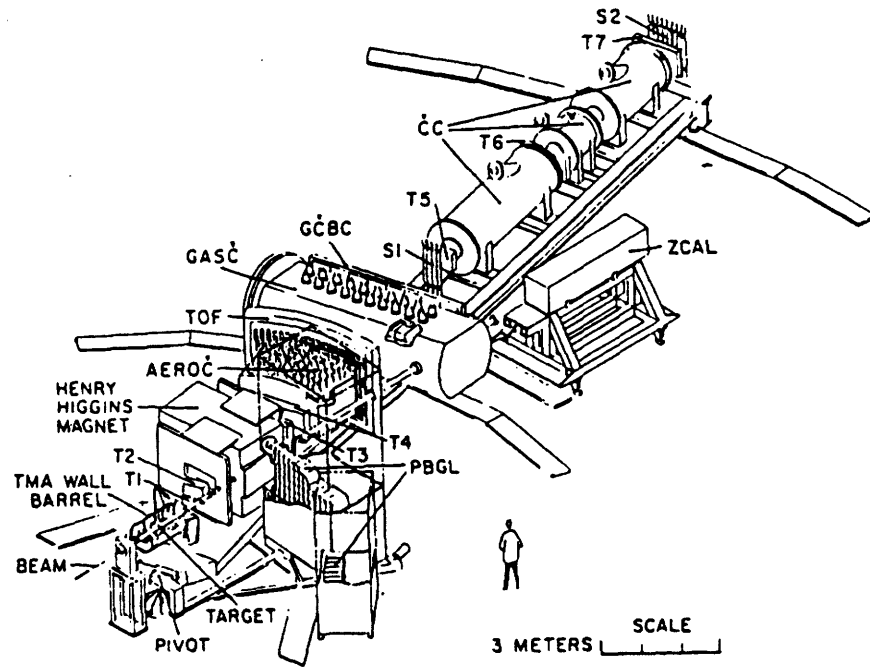


Figure 3-2: E802 Layout, showing the Spectrometer, ZCAL, TMA, and Lead Glass array. The beam counters are also shown.

vertical position.

3. **BTOT**: Measures the charge of each beam particle with a resolution of 0.5 charge units (for silicon).
4. **BTOF**: A scintillator that defines the starting time, T_0 , for the TOF partition and all other partitions. BTOF has a time resolution of $\Delta t = 30 - 40$ ps for E802 running.
5. **BE**: The “Bull’s Eye” counter is a downstream scintillator, sitting 10.6m from the target directly in front of the zero-degree calorimeter. The bull’s eye scintillator forms one part of the interaction trigger, defined as:

$$INT = BEAM \cap \overline{BE} \quad (3.2)$$

The BE scintillator measures charge carried by the beam fragments . Charge thresholds for the three beams were fixed at $Z = 6.5, 12.4$ and 75 for oxygen, silicon and gold beams. An interaction is considered to have occurred when $Z_{BE} < Z_{thres}$. The bull’s eye counter is only sensitive to charge, so that interactions in which only neutrons are lost from the projectile will not result in a detected interaction. The measured cross-sections for $A + A$ collisions will be smaller than the actual inelastic cross-section. One must take this into account when determining the error associated with the measured inelastic cross-section.

3.2.2 The Target Multiplicity Array

The target multiplicity array (TMA) is an array of resistive plastic tubes operated in the proportional mode and read out from signals induced on copper cathode pads [Abb89]. The TMA surrounds the target completely in azimuthal angles as well as forward angles from 6° to 140° . The array consists of two parts, a *barrel* and *wall* . The barrel is a cylindrical array (1520 pads) of tubes surrounding the target ($\theta = 40^\circ$ to 149° and $\phi = 0$

to 2π). The wall is placed at forward angles ($\theta = 6^\circ$ to 40°) and is designed with higher segmentation (1728 pads) for larger multiplicities in the forward direction. The TMA's large coverage allows it to be used as a central trigger. The online TMA central trigger is defined as an event where the total charge multiplicities are approximately the upper 7% in multiplicity for a given A + A collision. The barrel covers 2π and ranges from 40° to 149° in θ .

With only a couple of exceptions, the TMA is not used in this analysis. TMA triggered oxygen data are shown for completeness with the minimum bias and spectrometer triggered data set. The reader is referred to Ph. D. theses where the TMA was used as a central trigger for event characterization (see T. Abbott's thesis [Abb90th] and C. Parson's thesis [Par92]). Contributions to the overall accuracy of the TMA include;

- Uncertainty of the multiplicity due to hits on two or more adjacent pads. These clusters are counted as only one hit, since hits near the edges of pads may fire adjacent pads.
- There are small inefficiencies due to two or more particles hitting one pad. These double events are counted as one particle track.
- The TMA cannot distinguish events that do and do not come from the target. Target out subtraction can be done offline, however, only on an "average" basis.

3.2.3 The Zero Degree Calorimeter

The ZCAL is the principle event characterizing detector in this work and functions to measure the projectile spectators. The ZCAL is located 11.7m downstream from the target and is a rectangular shaped box filled with a sandwich of 138 layers of 60×60 cm of scintillator and iron sheets. Very forward produced particles will also be absorbed in the ZCAL, although they represent only a very small fraction of the energy deposited. The ZCAL converts kinetic energy of the beam fragments to photons. Because of the high efficiency of the detector, a simple conversion relates the energy deposited in the ZCAL to

the number of projectile nucleons as described in Equation 1.3. The calorimeter provides 8.9 interaction lengths and therefore essentially all the incident spectators' kinetic energy is measured by the calorimeter.

The size of the calorimeter's opening angle (1.47°) was determined from the root-mean-square angles expected for fragments from Bevalac energies [Gre75]. A simple calculation also shows that the inscribed opening angle of the ZCAL is sufficiently large so as to absorb spectators that move in transverse directions to the beams with a Fermi momentum of $.27 \text{ GeV}/c$:

$$\theta_{spec-max} = \text{Arctan}\left(\frac{.27}{14.6}\right) = 1.06^\circ < 1.47^\circ \quad (3.3)$$

Light is channeled to the 16 wavelength shifters that are mounted on the side of ZCAL and then is channeled to phototubes in one of two hadronic sections, H1(front) or H2(rear). Each hadronic section is composed of 8 locations (see Figure 3-3) and each location has two air-gap-coupled wave-length-shifter plates (WLS), $5\text{mm(thick)} \times 24.5 \text{ cm} \times 24.5 \text{ cms}$. The ZCAL was used for ^{16}O , ^{28}Si , and ^{197}Au projectiles and run in the mode where the energy output was roughly matched from H1 and H2. Figure 3-4 shows the energy response of the calorimeter as a function of transverse distance across the face. The figure also shows the total energy summed from the two sections as well as the resolution for ^{28}Si beams impinging on different x positions across the calorimeter.

The ZCAL is very linear in output to the number of incident nucleons [Abb89] for ^{16}O and ^{28}Si as well as for ^{197}Au projectiles. Limitations of the instrument include:

- The ZCAL accurately measures the projectile spectators. Once a projectile is completely occluded by the target, there is no forward energy. Thus, for asymmetric systems, the correlation between E_{ZCAL} and impact parameter is significantly reduced.
- The ZCAL aperture is collimated when the spectrometer is positioned at the most forward setting (5°). At this setting the beam pipe travels through the yoke of the

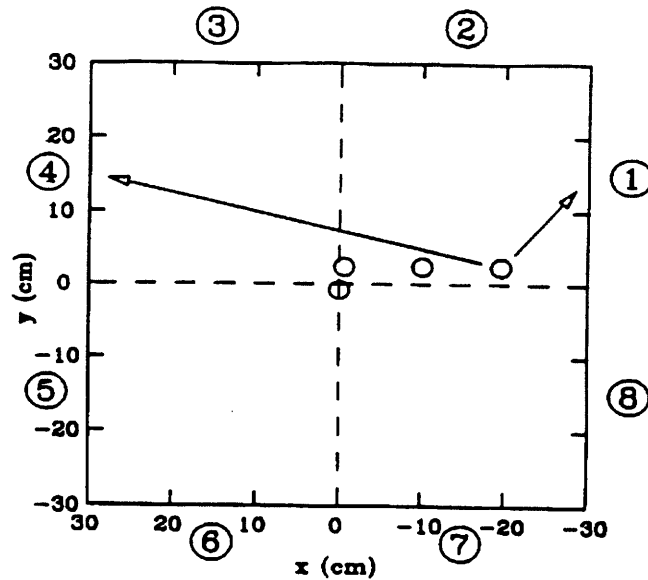


Figure 3-3: Beam-eye sketch of the ZCAL showing the eight locations for either hadronic sections H1 (front) for H2(back). Two air-gap-coupled wave-length-shifters (WLS) are at each of the eight locations for each hadronic section.(From [E802-40])

Henry Higgins magnet forcing the opening angle subtended at the calorimeter to be decreased from 1.5° to 0.8° [E802-40]. The effect of the beam pipe in this running mode is two-fold: collimation attenuates the beam but the influence of albedo from showering off from the beam pipe tends to offset this attenuation. The large incident angle of the fragments within the beam pipe allow for secondary particles to shower into the ZCAL. With this complication, several attempts were made to use the calorimeter so that comparisons with 14° data could be made. After these efforts, it was still realized that the severe non-linearity of the collimated beam and the ZCAL response do not allow us to use data at this most forward setting.

- The ZCAL's light output is 9 % larger at the periphery of the scintillator than at the center. Nucleons that impact at the scintillator create photons in the interaction with the scintillator. These photons will be partially absorbed before reaching the wave shifters and light-guides, reducing the signal. This correction is taken into account when simulating ZCAL response in Monte-Carlo generated collisions.

- The performance of the ZCAL changed between 1988 and 1992. The most notable change for this analysis came during the E866 phase. Prior to the gold projectile running a high intensity silicon run at a few times 10^6 per spill degraded the calorimeter resolution from $\sigma_{ZCAL}/\sqrt{E_{ZCAL}} = 76\%/\sqrt{E(\text{GeV})}$ (for oxygen and silicon running) to $\sigma_{ZCAL}/\sqrt{E_{ZCAL}} \approx 230\%/\sqrt{E(\text{GeV})}$.
- A very large target out subtraction was seen in the $^{197}\text{Au} + ^{197}\text{Au}$ data. A large target out contribution was seen for high values of ZCAL. Fig. 5-7 shows a large target out contribution for large values of ZCAL ($ZCAL > ZCAL_{BEAM}$). Target out subtraction eliminates most of this contribution.
- Ron Soltz also discovered that the peak of the ZCAL energy spectra shifted depending on the beam rate. This rate dependency was seen for the high intensity running of March 1992[Sol94b]. All gold running for E866 was done with a much reduced intensity and this specific problem is not seen.

Despite the aforementioned limitations, the ZCAL is the best device for determining the number of participants in the collision.

3.2.4 The Spectrometer

The spectrometer arm can be divided into 4 sections; (1) the Henry Higgins magnet, (2) the tracking chambers, (3) the time-of-flight wall, and (4) miscellaneous detectors. The spectrometer consists of a rotatable frame whose purpose is to provide a rigid support for the magnet and tracking chambers and other partitions. The length of the spectrometer is about 7m and is determined so that kaons would survive long enough to be detected. The spectrometer measures particles in the range of $0.5 < p_{lab} < 4.7\text{GeV}/c$, $5^\circ < \theta_{lab} < 51^\circ$.

Henry Higgins The Henry Higgins magnet is a variable strength dipole magnet mounted on the spectrometer arm. The magnet itself is 3600 kg and is designed to allow for a substantial solid angle of 25 msr and provides a homogeneous field at $\pm 0.2\text{T}$, $\pm 0.4\text{T}$, and

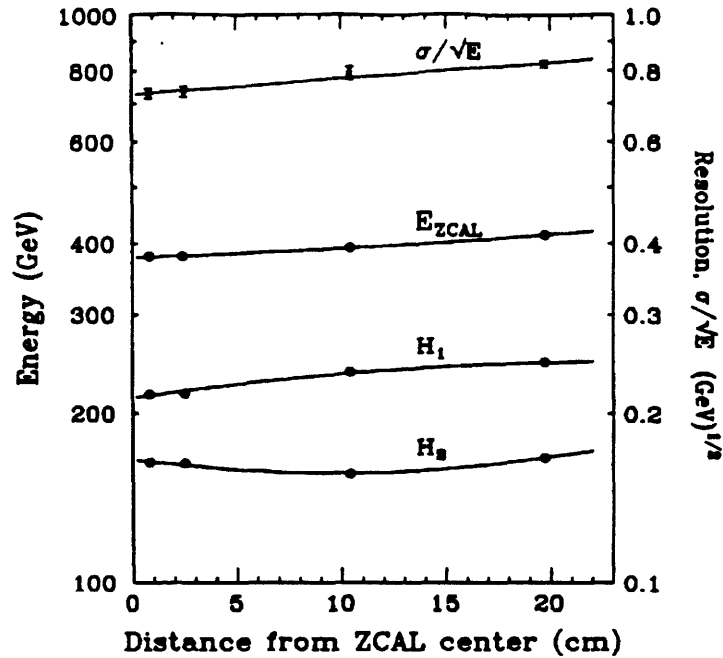


Figure 3-4: Dependence of energy deposited in H1 and H2 as a function of the transverse displacement across the face of the ZCAL. The total energy $E_{ZCAL} = H_1 + H_2$ is also plotted as well as the resolution σ/\sqrt{E} for incident ^{28}Si beams.

$\pm 0.6\text{T}$. The magnet is capable of going to $\pm 1.2\text{ T}$ but was never run in this mode. Large magnet-field clamps were mounted on the ends of the magnet to reduce the field to a few parts $\times 10^{-4}$ Tesla in the region adjacent to the magnet. The beam pipe passes through a hole bored through the beam side yoke when the spectrometer is in the most forward (5°) angle setting.

The tracking chambers The E802 tracking chambers T1, T2, T3, and T4 are drift chambers designed to identify events with multiplicities up to about 10. A total of 4 drift chambers, each with 10 planes in the original E802 setup, were arranged as shown in Table 3.1. Later, for E859 and E866, another 3 planes were added in the frame T3.5, but these additional planes were never used effectively to increase track trajectory information. A good discussion of the spectrometer's drift chambers is documented in several Ph.D. student theses (see the theses of M. Bloomer [Blo90] and H. Huang. [Hua90]). Tracking chamber T2 was replaced for E859 and E866 with a new chamber that has more planes and higher segmentation and is slightly larger to better match the spectrometer acceptance.

CHARACTERISTICS OF THE TRACKING CHAMBERS

chamber	Module	Wire Angle	Planes	Wires per Plane	Drift Length	Ionization Length
T1	X	0	2	32	4 mm	3 mm
	V	-45	2	32	4 mm	3 mm
	Y	-90	2	16	4 mm	3 mm
	U	45	2	32	4 mm	3 mm
	W	-26	2	32	4 mm	3 mm
Total T1			10	288		
T2(E802)	U	30	2	21/22	10.5 mm	7 mm
	X	0	3	20/19/19	10.5 mm	7 mm
	Y	-90	3	11/10/10	10.5 mm	7 mm
	V	-30	2	22/21	10.5 mm	7 mm
Total T2			10	175		
T2(E859) and T2(E866)	U	30	3	28/28/28	10.5 mm	7 mm
	X	0	3	28/27/27	10.5 mm	7 mm
	Y	-90	3	13/13/14	10.5 mm	7 mm
	V	-30	3	28/28/28	10.5 mm	7 mm
Total T2			12	290		
T3	U	30	2	36	16.1 mm	7 mm
	X	0	3	36	15.3 mm	7 mm
	Y	-90	3	16	15.3 mm	7 mm
	V	-30	2	36	16.1 mm	7 mm
Total T3			10	300		
T4	U	30	2	44	16.5 mm	7 mm
	X	0	3	40	17.5 mm	7 mm
	Y	-90	3	16	17.2 mm	7 mm
	V	-30	2	44	16.5 mm	7 mm
Total T4			10	344		

Table 3.1: Characteristic of the Tracking Chambers. Most of the information in this table is taken from [Abb89]. The additional information and changes in T2 are included.

T1	26.4 cm × 13.6 cm
T2(E802)	42.2 cm × 23.5 cm
T2(E859,E866)	39.5 cm × 20.4 cm
T3	113.7 cm × 52.1 cm
T4	143.5 cm × 58.7 cm

Table 3.2: Fiducial dimensions for the E802/E866 drift chambers. The thickness for each chamber is $\approx 21\text{cm}$.

Each chamber is composed of 10 “active” planes that are composed of alternating sense and field wires. Between each sense/field plane are cathode wire planes that are kept at high negative voltage (between 1000 and 2000 V depending on the chamber). The electric field in each chamber is “shaped” by field wires, positioned alternating between sense wires and kept at a negative voltage. As charged particles ionize the Argon-Isobutane gas mixture flowing through the chambers, the released electrons “drift” towards the sense wires that are held at large positive voltages.

Sense wires are $10\mu\text{m}$ in diameter and made of gold plated tungsten for the T1 chamber and $30\mu\text{m}$ diameter gold-plated tungsten for T2, T3, and T4 chambers. The field and cathode wires were somewhat larger, with a diameter of $100\mu\text{m}$, made of copper - beryllium alloy.

Drift chambers increase in size with distance from the target so that the solid angle (fixed by the aperture of the Henry Higgins magnet) is maintained. Figure 3-2 shows T1 and T2 positioned before the magnet and T3 and T4 after the magnet. The active area of the chambers are found in Table 3.2.

Using a offline *self-correcting* geometry algorithm [E802-54], [E859memip], the chamber geometry was maximized and a $200\mu\text{m}$ resolution was achieved. Two multiwire proportional trigger chambers (TR1 and TR2) were added for E859 running that would allow for pattern recognition behind the magnet and serve as an input to an online PID trigger.

The Time-of-flight Wall The TOF partition plays a critical role in the identification of particles. The wall sits 6.5m from the target, behind the tracking chambers. The survival rate for 1 GeV/c kaons at 6.5m from the source is 42 % [Abb89].

The TOF wall performs three principle functions concerning particle tracking and identification. First, it acts as a space-point hit detector for trajectory information, later used in tracking codes. Second, the TOF wall measures the time-of-flight of the particles so that offline particle identification may be done. Finally, the detector is also used to determine the particle charge by adding up the energy deposited in the phototubes at the top and bottom of each picket. The ADC value is obtained in the following way:

$$\langle ADC \rangle = \sqrt{ADC(UP) \cdot ADC(DOWN)}. \quad (3.4)$$

The TOF wall consists of 160 pickets that are 78cm \times 1.6 cm \times 1.6 cm in dimension. Two Hamamatsu R2083-subnanosecond phototubes receive light on each end of the plastic scintillator pickets. Both x and y positions may be determined with TOF. The x position is determined by the slat position. The y - position is determined by the difference in timing of the photomultiplier tubes positioned at the top and bottom of the TOF wall.

The TOF resolution steadily decreased over the three running periods. An 80ps resolution was obtained for oxygen and silicon runs and the resolution decreased to about 120ps for gold running.

The TOF slats were ORed together to form a TOF trigger. The SPEC trigger was made up of BEAM, TOF and T1Y:

$$SPEC = BEAM \cap TOF \cap T1Y. \quad (3.5)$$

The TOF information is capable of separating pions, kaons, and protons up to a momentum of 2.2 GeV/c.

3.2.5 The Data Acquisition

The data acquisition is described in great detail in several of the hardware notes and publications of the E802 collaboration; [Abb89], [Lev87], [Wad87]. There are about 6000 total channels in the E802 setup. Analog signals from the various detectors are digitized in CAMAC and FASTBUS modules (ADC's and TDC's). A 68020 microprocessor (the Chairman) is capable of handling data from all 6000 channels approximately every 20 milliseconds. Data is written to a 9-track tape on a VAX host computer once it is put in a standardized event bank structure called YBOS [CDF156]. Typically, one tape is used for each run and hundreds of runs make up each running period. Each running period will be described in the upcoming sections.

3.3 Data Sets

The data analyzed in this work cover several running periods. Essentially five types of hardware triggers are used over the data set for this thesis: BEAM, INT, SPEC, TMA, and $\overline{\text{ZCAL}}$. An offline ZCAL trigger is also used on INT and SPEC triggered data to select out events of a certain numbers of participants. A summary of the important considerations of data taking over the several running periods are listed below.

1. The gold running included the E859 changes in hardware. A new T2 replaced the T2 of E802. (See Section 3.2.4).
2. New trigger chambers are included in the E859 and E866 running. The addition of trigger chambers adjacent to drift chambers T3 and T4 for E859 and E866 also needed to be included in the acceptance calculations. (See Section 3.2.4).
3. 5° running forced the beam pipe to go through the magnet yoke. Interference with the magnet did not allow reliable comparisons with the ZCAL at this angle setting.
4. In this analysis, two different reconstruction codes were used. The reconstruction code RECONSTRUCT was used on the ^{16}O and ^{28}Si data set, [Hua90], [Sar89].

The AUSCON code [Roth94] made use of the E859 trigger chambers and was used on the $^{197}\text{Au} + ^{197}\text{Au}$ data set. The efficiency of the RECONSTRUCT code was determined using a hand scanning process. The total number of tracks reconstructed is compared to those that should have been reconstructed. The efficiency of RECONSTRUCT was determined to be $85 \pm 5\%$ [Hua90]. The efficiency for AUSCON was determined with Monte-Carlo generated tracks and was found to be $91 \pm 5\%$.

5. Both INT and SPEC triggers were used as minimum bias triggers for the oxygen data. The INT trigger was used for the majority of the oxygen running period. The SPEC trigger came online late in the oxygen running period and was merged appropriately with the INT triggered data for $\theta_{spec} = 34^\circ$ and 44° running. With only one exception, the rest of the oxygen data were triggered with the hardware SPEC trigger. TMA triggered data were included in this thesis only for completeness and for comparison with the offline ZCAL triggered oxygen data.

3.4 Data Analysis

The enormous quantity of data from E802/E866 has called for an analysis procedure to have a very generalized format and is broken up into different stages. Once again, some minor changes have occurred over the 4 running periods of this work. The raw data, once on tape, undergoes a series of data “passes”. The following list includes the main steps in the data analysis procedure.

PASS0 This is the first pass on the raw data set where initial calibrations are done. During this pass, pedestals and gains of ADC’s are determined for each detector as well as timing offsets of the TDC’s for the drift chambers and TOF wall.

PASS1 Physical quantities are determined during this pass. The zero-degree calorimeter energies are determined for every event as well as the values for the other event detectors including the TMA, Lead Glass, and Beam detectors.

PASS2 This phase of data analysis is essentially devoted to track reconstruction using

either the RECONSTRUCT or AUSCON codes. RECONSTRUCT was used with oxygen and silicon data sets. A complete discussion of this code may be found in Ph.D. theses of H. Huang [Hua90] and M. Sarabura [Sar89]. The gold data set was reconstructed with the AUSCON code. A complete discussion of the AUSCON code may be found in the thesis work of P. Rothschild [Roth94]. Particle tracks are reconstructed using information from the spectrometer’s drift chambers, trigger chambers and TOF wall.

PASS3 PASS3 was used to do particle identification. In this thesis π^\pm , K^\pm , and protons were analyzed and particle ID was done using the a particle’s time-of-flight, t , the track momentum, p , and the path length, l :

$$m = p\sqrt{1 - \beta^2}/\beta \text{ GeV}/c^2, \quad (3.6)$$

with

$$\beta = l/ct. \quad (3.7)$$

Table 3.3 shows the breakup of the data analysis stages up through the physics compression stage for all the running periods that were used in this analysis. Final data processing includes a physics compression stage where data that has particle ID is written to a file called an “ntuple”. Every run used in the analysis has an ntuple file. All the run ntuples are next compressed into a running period summary file. These summary files contain all the physics information to determine particle invariant cross-sections and yields. Invariant yields are the topic of Chapter 5.

3.5 Summary

The principle E802/E866 partitions are summarized in this section. The calorimeter is used for event characterization in this work and has proven to be a reliable means to measure incident collision spectators.

	pass 0	pass 1,2	pass 3	Physics compression (Summary File)
^{16}O	BNL	MIT, Columbia	MIT/author	MIT/author
^{28}Si	BNL	MIT	MIT/C. Parsons	MIT/C. Parsons
^{197}Au	BNL	MIT	MIT	MIT/author

Table 3.3: Summary of analysis passes.

Chapter 4

Nuclear Geometry

In this chapter we discuss the geometry of heavy-ion collisions and its effects on particle production. We attempt to understand heavy-ion collisions from a simple picture of colliding spheres.

Next, we discuss particle production using a simple wounded nucleon model. We also include a discussion of a more general wounded nucleon model that includes rescattering. We use the recently developed RQMD code and examine particle production in this model for $^{28}\text{Si} + ^{27}\text{Al}$ and $^{197}\text{Au} + ^{197}\text{Au}$ reactions. Finally, we study how the E802 calorimeter is used to determine the reaction participants.

4.1 A Geometric Model

A simple description of the time-independent nuclear density is given by the Woods-Saxon distribution,

$$P(r) = \frac{a}{1 + e^{(r-R_{1/2})/b}}. \quad (4.1)$$

The value a is a normalization constant. This value is determined by integrating the distribution $P(r)$ over all space to obtain the atomic mass of the nucleus. The value b is also determined empirically: $b = 0.545$ fm.

Woods Saxon Distributions (Normalized to Unity)

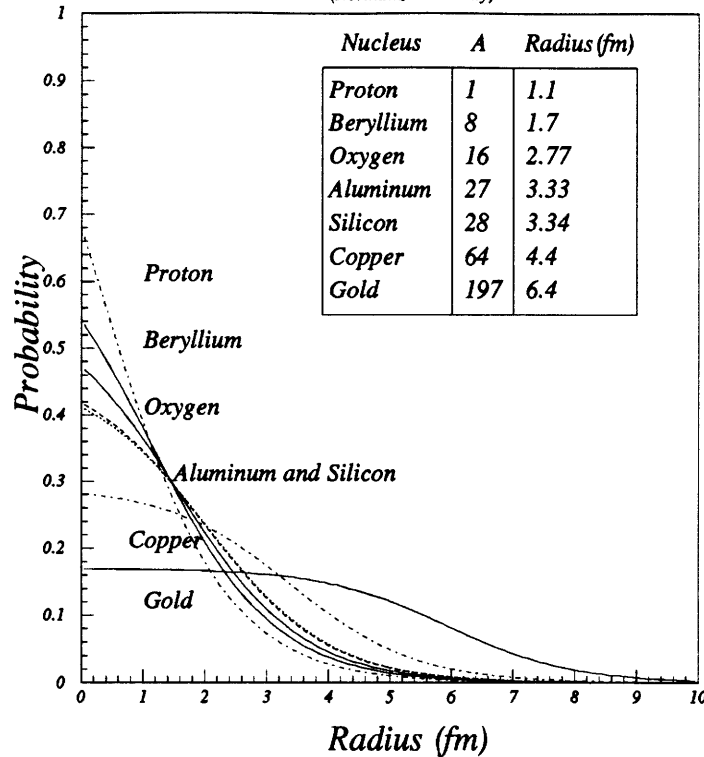


Figure 4-1: A Woods-Saxon density profile of several nuclei and a table of the half radii that are used in this model. The FRITIOF model uses these density profiles for determining the number of collisions that will take place as the projectile bores through the target nucleus.

The half-radius, $R_{1/2}$, is defined to be the radius where the density falls to half the central density. This radius is empirically determined to be $R_{1/2} = r_o A^{1/3}$. The parameter r_o is approximately 1.1 fm. The values of r_o used in FRITIOF are chosen to fit experimental nuclear inelastic cross sections, σ_{inel}^{pA} . Figure 4-1 shows density profiles (setting $a = 1$) for several nuclei used in this work. Figure 4-2 shows the relative sizes of oxygen, silicon, and gold.

4.1.1 Collision Participants

We begin with a few observations from earlier work.

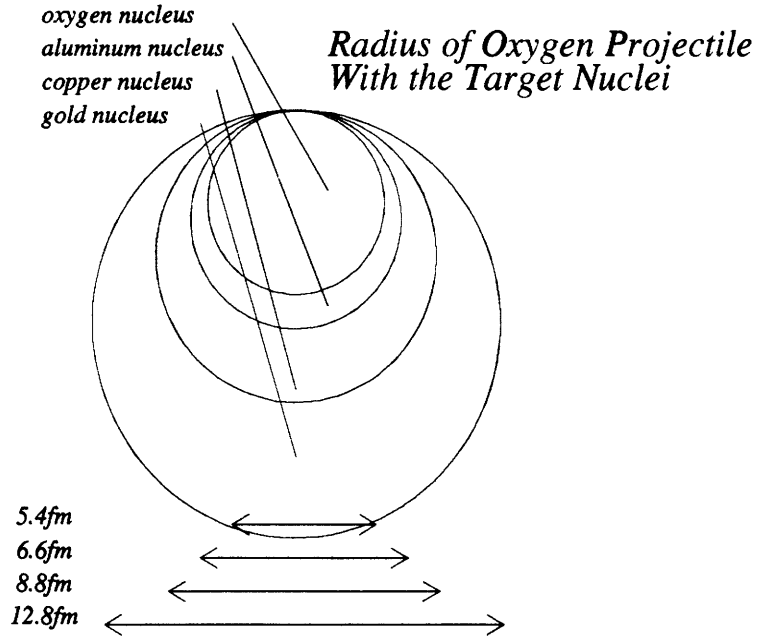


Figure 4-2: Relative sizes of nuclei used in this analysis.

- The median rapidity loss for protons in central p + Pb collisions at 100 A·GeV/c is $\Delta y \approx 2$ [Bus84].
- At AGS energies, a semiclassical approximation is used to determine the number of binary collisions, $\langle N_{BC} \rangle$, that a projectile nucleon makes with the target nucleons. $\langle N_{BC} \rangle$ is approximated by the number of times a projectile nucleon overlaps the target nucleons as it traverses straight through it. Specifically, $\langle N_{BC} \rangle = \langle \nu \rangle^{targ} \cdot N_{part}^{targ}$. A similar relation gives the projectile participants, $\langle N_{BC} \rangle = \langle \nu \rangle^{proj} \cdot N_{part}^{proj}$. The quantity $\langle \nu \rangle^{targ}$ and $\langle \nu \rangle^{proj}$ are the mean number of collisions for a target participant or projectile participant.
- Particle production for p + A reactions (200 GeV/c incident momentum) is proportional to the mean number of collisions per participant $\langle \nu \rangle^{tot}$ [Blo90].
- Pion production depends on both the rapidity loss of the projectile as well as the total size of the collision system. Results from N + N interactions demonstrate

that the pion production rate is ≈ 1.5 π 's per participant (assuming $\pi^0 = (\pi^+ + \pi^-)/2$) for $^{28}\text{Si} + ^{197}\text{Au}$ collisions at the AGS [Par92]. At $y = 1$, where target protons undergo a rapidity shift of 1, there is enough excitation energy available for resonance baryon production and subsequent decays.

- Kaons are produced in NN and NM collisions (N = nucleon and M = meson) and are produced at higher rates for larger systems [Abb94]. This increased rate is supposedly dependent on the effects of rescattering in the larger systems and will be the subject of investigation with the cascade model in the following section.

4.1.2 A Simple Geometric Model of Participant Nucleons

Before a discussion of particle production, we can ask, how does particles production depend on incident energy? The energy available per nucleon can be written

$$\sqrt{s} = \sqrt{(N_{proj}m_o)^2 + (N_{targ}m_o)^2 + 2E_{proj}N_{targ}m_o}, \quad (4.2)$$

where m_o is the nucleon mass. Clearly, the available energy in the reaction increases with the mass of the projectile and target and does not reach a maximum at some particular collision size.

Secondly, there may be complications from spectator matter that distort the particle yields. At AGS energies, there may be sufficient time during a collision for produced particles to interact with the spectator material. Consider a central $^{16}\text{O} + ^{197}\text{Au}$ collision that leads to the formation of a Delta. Consider a pion that is created by a Delta decay ($\Delta(1232)$). If the pion is created from a decaying resonance with transverse and longitudinal momentum $p_t = p_{||} = 1$ GeV/c, it will be emitted at $\theta_{particle} = 45^\circ$ in the center of mass frame. The Delta has a momentum of $\sqrt{2}$ GeV and a Lorentz corrected lifetime of 3.1 fm/c. The impinging oxygen nucleus at 14.6 A·GeV/c will pass through the gold target in about $t = 12$ fm/c. In this time, the produced pion should pass through some of the surrounding target matter. A full analysis of nuclear shadowing is

Physical Quantity	Scaling Variable	Measured	Simulated
Yield = $\int_y (dN/dy)dy$ Inverse Slope, T	E_{ZCAL}	x	
	$N_{part}^{tot} = N_{part}^{proj} + N_{part}^{targ}$	x	(see caption)
	b		x
	$\langle N_{BC} \rangle$		x
	$\langle \nu \rangle^{tot} = \langle \nu \rangle^{targ} + \langle \nu \rangle^{proj}$		x

Table 4.1: Possible scaling variable for particle production in heavy-ion collisions. Note that the number of target participants is only known for symmetric collisions. A geometric model is needed to determine the target and hence the total participants for asymmetric collisions.

required to fully study this effect.

There are several factors that affect particle production. A brief list of some of these variables (both measured and modeled) are shown in Table 4.1. The first two variables are experimentally measured. Symmetric collisions have an advantage, ($N_{part}^{proj} = N_{part}^{targ}$) and therefore N_{part}^{tot} may also be determined. In an asymmetric collision, N_{part}^{targ} and N_{part}^{tot} must be modeled. These measured variables will be discussed in more detail in Chapter 6, where yields and inverse slope parameters are presented as a function of the number of collision participants. In particular, yields and inverse slope parameters of π^\pm, K^\pm and protons are measured as a function of the energy deposited in the ZCAL (giving a direct measurement of N_{part}^{proj} and N_{part}^{tot}).

The relationship between the mean number of collisions, $\langle N_{BC} \rangle$, and particle production should also be considered. Is the number of participants or the mean number of collisions more important for particle production? For example, we might imagine a projectile nucleon that when struck by a target nucleon is excited to only one state and is then free to decay to a meson. We would then say that the number of participants (namely, the projectile nucleons plus the target nucleons) play a more important role than the number of collisions. In A + A collisions, the projectile nucleon could potentially be struck several times in an A + A collision and yet hadron production would

EXTENDED WOUNDED NUCLEON MODEL

Type of collision.	Representation
Initial collision: Both the unwounded target and the projectile nucleons undergo a first collision.	oo
A projectile nucleon has collided already but the target nucleon has not been struck.	•o
A target nucleon has collided already but the projectile nucleon is unstruck.	o•
Both the target and projectile nucleons have been struck at least once.	••
A nucleon that has rescattered off <i>at least</i> one meson.	o·
A nucleon struck by another nucleon has scattered off <i>at least</i> one produced meson.	•·

Table 4.2: Extended WNM collision scenarios

not be enhanced. The important scaling variables in that scenario would be the number of participants. We know that in a real nucleus, a nucleon can be struck several times. Delta resonances can be created and then further excited, thereby increasing the number of produced particles. In summary, we would expect that particle production actually depends in some complicated fashion on both the total number of participants and on the mean number of binary collisions. Unfortunately, it is impossible to measure the number (or even mean number) of binary collisions in a heavy-ion reaction. However the RQMD model does predict the mean number of binary collisions for a given impact parameter.

Before a discussion of this cascade model, it is informative to understand nuclear collision in terms of *clean-cut* geometry. The first three scaling variables can be understood with this model. From Chapter 1, the forward energy measured in the ZCAL is related to the number of total participants,

$$N_{\text{proj}}^{\text{part}} = A_{\text{proj}}(1 - E_{\text{ZCAL}}/T_{\text{beam}}). \quad (4.3)$$

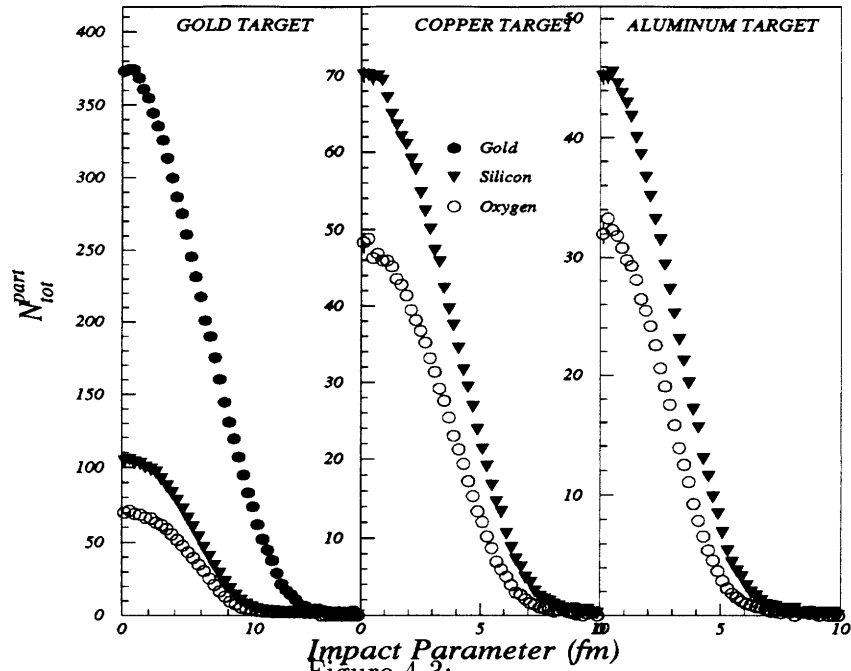


Figure 4-3:

Total number of participants vs. the impact parameter. The simple mapping from E_{ZCAL} to number of participants is done with Equation 1.3 with instrumentation resolution folded in. (Simulations done with a clean-cut geometry, an input to FRITIOF).

The energy deposited in the calorimeter is a measure of the number of projectile spectators and hence projectile participants.¹ With this assumption, the trends in the particle yields and slope parameters may be described in terms of N_{part}^{tot} , N_{part}^{proj} , and N_{part}^{targ} and not in terms of E_{ZCAL} .

Earlier, Matt Bloomer examined N_{part}^{tot} as well as N_{part}^{proj} and N_{part}^{targ} for ^{28}Si on gold and aluminum targets [Blo90]. We use this analysis as a starting point and examine the RQMD model in light of the number of participants and the number of binary collisions. Figure 4-3 shows the relationship between the total number of participants and impact parameter for $^{16}\text{O} + \text{A}$, $^{28}\text{Si} + \text{A}$ and $^{197}\text{Au} + ^{197}\text{Au}$ collisions from this geometric model.

In this picture, the impact parameter, b , is not the most fundamental physics parameter governing particle production. The more fundamental parameter for particle production, the number of total participants, does not vary as strongly at small and

¹Limitations to this assumption will be discussed at the end of this chapter. For example, some created mesons will also be detected in the calorimeter.

large impact parameters, especially for ^{16}O and ^{28}Si ions. Tables 5.8 and 5.9 give a full listing of impact parameters and number of participants for these collisions.

In the much more complex RQMD cascade model, different types of interactions are taken into account. Because of the complexity of the RQMD model, we make some simplifications in order to understand how binary collisions play a role in $A + A$ collisions. We keep the list of collision possibilities from the earlier analysis and extend the list as appropriate for including, at least in the simplest manner, rescattered events (see Table 4.3).

By using the RQMD model, we can extend the list of collision possibilities to include collisions where nucleons interact multiple times with each other (*multiple scattering*). Nucleons in the RQMD model are also free to interact with mesons (*rescattering*).

The additional collision possibilities give rise to an extended wounded nucleon model. A wounded nucleon model implies that nucleons are capable of producing particles when hit (wounded). A simple wounded nucleon model was used in the earlier analysis and allows for the first four cases in Table 4.2. An extended wounded nucleon model allows for many more collision possibilities. Table 4.3 shows a schematic of an extended wounded nucleon model. Table 4.3 shows more collision possibilities but lists only a fraction of the collision possibilities in the RQMD model. The extended wounded nucleon model does not differentiate *how many times* a particle has been multiply hit by other nucleons or mesons.

In the analysis by Bloomer, the number of binary collisions and the number of target and projectile participants are related in the following manner:

$$N_{BC} = N_{proj}^{part} \langle \nu^{part} \rangle = N_{targ}^{part} \langle \nu^{part} \rangle . \quad (4.4)$$

The number of binary collisions in a cascade scenario may be described as the total number of times a nucleon or meson collides with either another nucleon or with another meson. Using Table 4.3, we may express $\langle N_{BC} \rangle$ as

	○	●	○·	●·
○	○○	○●	○○·	○●·
●	●○	●●	●○·	●●·
○·	○·○	○·●	○·○·	○·●·
●·	●·○	●·●	●·○·	●·●·

Table 4.3:

A schematic diagram of the extended WNM for heavy-ion collisions used in the context of the cascade model, RQMD. The upper left four regions represent the collision space discussed under the analysis of M. Bloomer. The rest of the space is an extension of the Wounded Nucleon Model that accounts for collisions of either projectile nucleon with hadronic matter of the form of π^\pm, ρ^\pm, K^\pm , etc.

$$\begin{aligned}
 \langle N_{BC} \rangle = & \text{○○} + \text{○●} + \text{●○} + \text{●●} + \\
 & \text{○○·} + \text{○●·} + \text{●○·} + \text{●●·} + \\
 & \text{○·○} + \text{○·●} + \text{●·○} + \text{●·●} + \\
 & \text{○·○·} + \text{○·●·} + \text{●·○·} + \text{●·●·} .
 \end{aligned}$$

The RQMD model provides a tool for measuring the relative strengths of the contributions to $\langle N_{BC} \rangle$. Figure 4-4 is a plot of the number of binary collisions a proton or neutron undergoes in $^{28}\text{Si} + ^{27}\text{Al}$ and $^{197}\text{Au} + ^{197}\text{Au}$ collisions. There are a number of interesting details that we may learn from this picture. First, the lower curve in the left panel shows the number of binary collisions that protons and neutrons undergo if they interact only with other nucleons as they travel straight through the target. This simplest scheme is used in the FRITIOF model and represents only a fraction of the collisions $\text{○○} + \text{○●} + \text{●○} + \text{●●}$. The next higher curve, represented by the black circles is probably a more realistic representation of $\text{○○} + \text{○●} + \text{●○} + \text{●●}$ and is about 1.5 times greater in magnitude than the FRITIOF curve.

Rescattering events are then added to the multiple-scattering curve. The open diamonds and triangles show the effect of adding the contribution of the pions and kaons to the total number of binary collisions. This contribution is depicted in Table 4.3. The contribution to binary collisions from pions in $^{28}\text{Si} + ^{27}\text{Al}$ collisions is approximately 10

- 15% above the contribution from multiple-scattered nucleons.

For $^{197}\text{Au} + ^{197}\text{Au}$ data, there is a different result. Pions contribute to a slightly larger fraction of the total number of collisions compared to the $^{28}\text{Si} + ^{27}\text{Al}$ data. At $b \approx 0$, the pions from $^{197}\text{Au} + ^{197}\text{Au}$ collision represent about 1/3 of the total contribution to $\langle N_{BC} \rangle$.

Kaons do not contribute significantly to $\langle N_{BC} \rangle$, neither for $^{28}\text{Si} + ^{27}\text{Al}$ nor for $^{197}\text{Au} + ^{197}\text{Au}$ collisions. In both cases, they represent only about 1% of $\langle N_{BC} \rangle$.

Finally, the total number of binary collisions are added for comparison. The black stars in the figure represent the number of binary collisions that nucleons undergo with any other particle. These particles include Δ resonances and other short lived mesons such as the ρ and the η . Again, there are marked differences between the $^{28}\text{Si} + ^{27}\text{Al}$ and $^{197}\text{Au} + ^{197}\text{Au}$ collisions. The $^{28}\text{Si} + ^{27}\text{Al}$ collisions indicate that the number of collisions in addition to those already accounted for represent a constant 40% increase. In $^{197}\text{Au} + ^{197}\text{Au}$ collision, when $b < 8$ fm, collisions become more and more dominated by baryonic resonances and short-lived mesons. At $b = 0$, this contribution is equal in magnitude to the number of binary collisions that nucleons undergo from multiple scattering and rescattering.

We conclude from Figures 4-3 and 4-4 that

1. The number of total participants is flat once the projectile is shadowed by the target. This occurs for $b < 2$ fm for $^{16}\text{O} + ^{197}\text{Au}$ and $^{16}\text{O} + ^{64}\text{Cu}$ and for $b \leq 1.5$ fm for $^{28}\text{Si} + ^{197}\text{Au}$ and $^{28}\text{Si} + ^{64}\text{Cu}$ collisions. The target is partly opaque to the projectile in both of these models. Since $^{28}\text{Si} + ^{27}\text{Al}$ and $^{197}\text{Au} + ^{197}\text{Au}$ collisions are symmetric, this overlap does not occur.
2. The number of binary collisions play an important role in the equilibration of a system.

Mean Binary Collision vs. B : $Si+Al$ and $Au+Au$

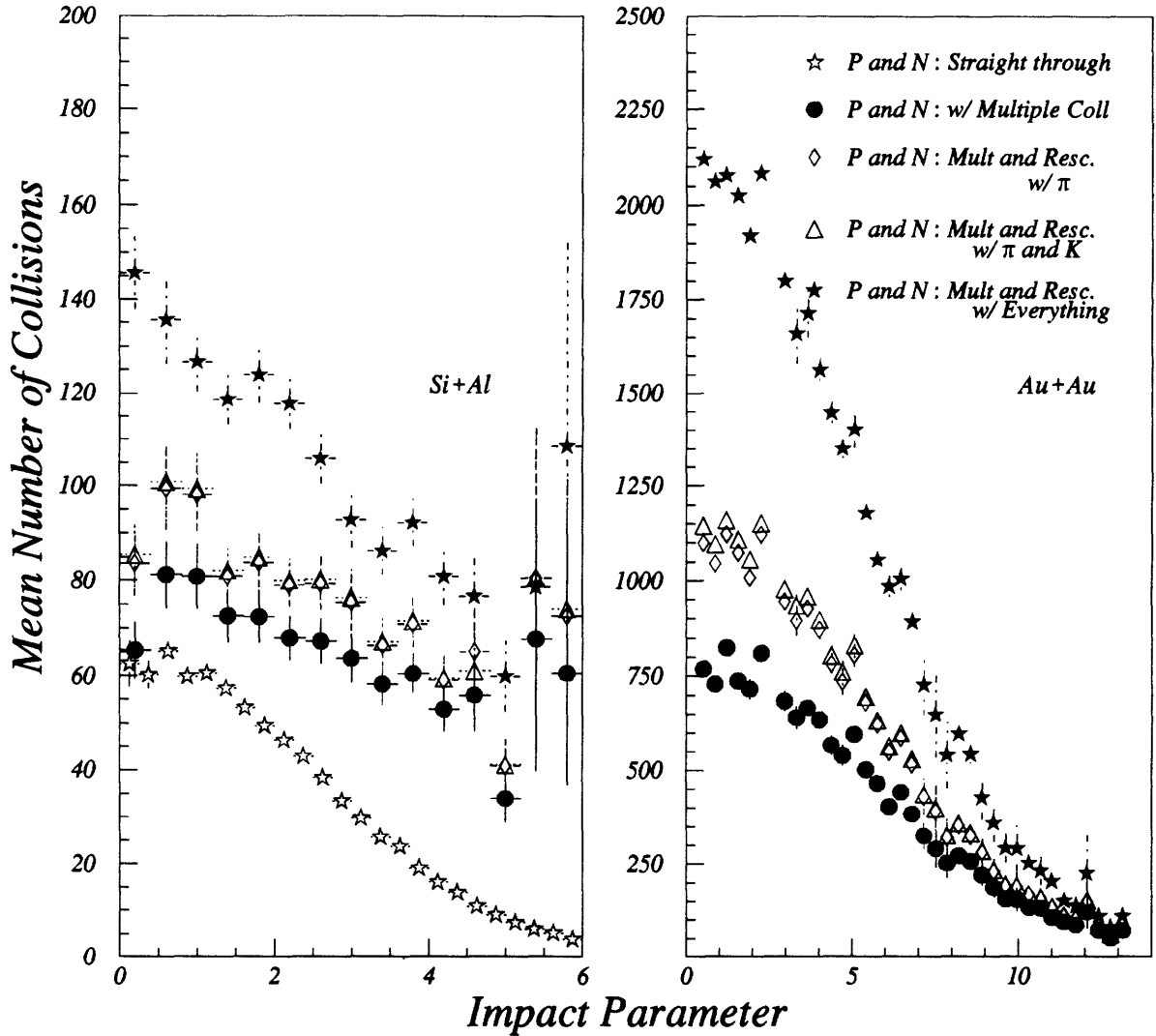


Figure 4-4: Number of binary collisions vs. the impact parameter for $^{28}Si + ^{27}Al$ and $^{197}Au + ^{197}Au$ collisions (RQMD and FRITIOF simulations). The incident beam momenta for the two projectiles are 14.6 and 11.6 A-GeV/c respectively. The contributions to $\langle N_{BC} \rangle$ from collisions calculated from a clean-cut geometry and a more realistic multiple scattering picture are made. The contribution from rescattering of pions and kaons is also shown. Note that the RQMD model shows large contributions of binary collisions at large impact parameters.

4.2 Nuclear Geometry and the ZCAL

The zero degree calorimeter plays a critical role in this analysis. The calorimeter's response to the collision fragments is relatively simple to interpret; however, some precautions must be considered. To begin, the calorimeter has an intrinsic resolution, dependent on the energy deposited. The resolution for each projectile is

$$\frac{\sigma_{ZCAL}}{\sqrt{E_{ZCAL}}} = \frac{76\%}{\sqrt{E(\text{GeV})}} \quad (^{16}\text{O} \text{ and } ^{28}\text{Si} \text{ projectiles}), \quad (4.5)$$

$$\frac{\sigma_{ZCAL}}{\sqrt{E_{ZCAL}}} \approx \frac{230\%}{\sqrt{E(\text{GeV})}} \quad (^{197}\text{Au} \text{ projectiles}). \quad (4.6)$$

At the full beam energy, oxygen and silicon nuclei result in a kinetic energy resolution, $\Delta E = 11.2$ and 11.4 GeV. This is better than a one nucleon resolution. The ZCAL is symmetric in ϕ around the beam. This condition assures that off central collisions ($b > 0$) will not be misinterpreted as long as all forward going spectators are seen by the ZCAL. These conditions are not simultaneously met by other detectors in the E802, E859 and E866 apparatus.

There are a few important questions to be considered before using Eq. 4.3. For example,

1. Is the calorimeter energy output linear with incident energy?
2. Is there a non-linear energy response across the face of the calorimeter?

Deviations from linearity are not seen for ^{16}O and ^{28}Si projectiles [Beav89] and the total output of the calorimeter is generally understood as being linear with incident energy. Unfortunately, no systematic study of the calorimeter response was made for very heavy-ions, near $A=197$. Unfragmented gold nuclei, injected into the calorimeter have been studied and the calorimeter's response is tuned to match the linear response extrapolated from the lighter-ion studies. Non-linearity in the response of the calorimeter in the region between $A=28$ and $A=197$ is not expected.

The second area of concern is the non-linearity of the calorimeter's response across its fiducial opening. There is an overall 9% drop in response to input energy near the center of the calorimeter. The gains of the hadronic sections of the calorimeter have been adjusted to offset this inefficiency and any spatial inefficiencies should be averaged out over many collisions. A decrease in the overall energy resolution is seen for $^{197}\text{Au} + ^{197}\text{Au}$ running. No large positional dependencies have been measured. Figure 4-5 shows a comparison of the average energy deposited in the ZCAL for BEAM and INT triggers for $^{197}\text{Au} + ^{197}\text{Au}$ collisions. A slightly wider distribution is seen for INT triggers as expected; however, both spatial distributions are fairly flat near the midpoint of the calorimeter face.

It is also important to ask to what degree do produced particles contaminate the ZCAL spectra? The calorimeter's acceptance subtends a 1.5° cone around the beam. Pseudorapidity is defined as $\eta = -\ln(\tan(\theta/2))$; Given $\theta=1.5^\circ$, then $\eta = 4.3$. The yields of π 's at this pseudorapidity (about one pion) are not expected to be greater than about 1% of the total yields. The contamination for central $^{16}\text{O} + ^{197}\text{Au}$ and $^{28}\text{Si} + ^{197}\text{Au}$ collisions will contribute $\Delta E = \sqrt{m_\pi^2 + p_\pi^2} \approx 1 \text{ GeV}$. We therefore expect contamination to be no greater than about one nucleon (probably much less) based on the measured yields for pions. Contamination from produced particles is worse for central $^{197}\text{Au} + ^{197}\text{Au}$ collisions. Up to 50 GeV due to produced particles may be deposited in the calorimeter. This contribution is approximately 20% of the signal.

Figures 5-6 and 5-7 show the calorimeter energy spectra for three projectiles and their respective targets. Lists of ranges in ZCAL energies used in each measurement are tabulated in Tables 5.6 and 5.7. The ranges for $^{197}\text{Au} + ^{197}\text{Au}$ collisions are superimposed on the spectra of Figure 5-6. The ZCAL is especially effective when measuring symmetric collisions ($^{27}\text{Al} + ^{28}\text{Si}$ and $^{197}\text{Au} + ^{197}\text{Au}$), since there will always be some forward projectile spectators producing a signal in the ZCAL. Asymmetric collisions are more difficult to interpret in terms of the number of participants. Both symmetric and asymmetric collisions are considered in this analysis. However, the projectile nuclei are

Spatial ZCAL Energy Dependence

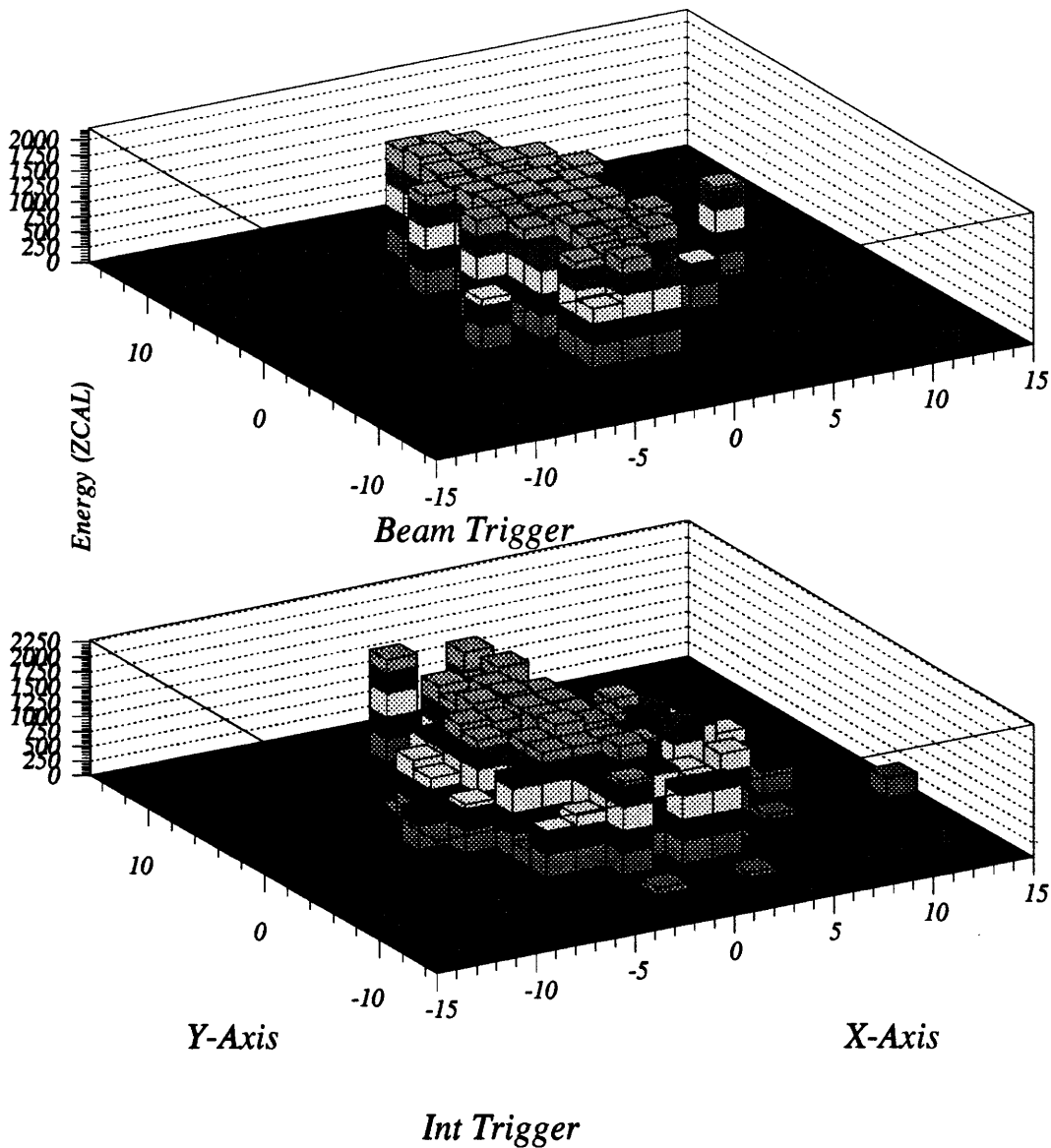


Figure 4-5: Spatial distribution of the energy deposited in ZCAL. A comparison is made between BEAM and INT triggers and show a slightly larger spread in deposited energy with INT triggers. Since light is detected only at the edges of the detector, any inefficiencies at the center will be averaged out.

never larger than the target nuclei. A large cross-section for central $^{16}\text{O} + ^{197}\text{Au}$ and $^{28}\text{Si} + ^{197}\text{Au}$ is apparent in Fig. 5-6. In these asymmetric cases, the more peripheral collisions are emphasized for two reasons:

1. The ZCAL is more sensitive to peripheral collisions, where the signal is not ambiguous.
2. Since we are comparing spectra as a function of the number of participants in the reaction, it is important to maximize the statistics for particle production in those collisions where statistics are poor. The large $^{197}\text{Au} + ^{197}\text{Au}$ collisions provide information for collisions with a large number of participants and must be compared to collisions at the opposite extreme. Peripheral non-symmetric collisions provide these needed statistics.

FRITIOF simulations show the relationship of the impact parameter with ZCAL energy (Fig. 4-6). Lines representing the centrality cuts have been superimposed. The scatter plot shows that the impact parameter is best determined at mid-rapidity and that the most central impact parameter for asymmetric collisions is somewhat distorted. The relationship between impact parameter and forward projectile energy is difficult to determine for these central collisions, see Fig. 4-6.

4.3 Summary

In this chapter we have briefly outlined the geometric considerations of heavy-ion collisions. The important scaling variables have been tabulated and will be referred to in the analysis of particle production participants. A discussion of binary collisions in heavy-ion reactions has been extended to include mesons and baryonic resonances. The details of Figure 4-4 will be important in light of particle production in $A + A$ collisions (Chapter 6). Finally, we highlight the calorimeter's capabilities and limitations in distinguishing the number of collision participants.

Impact Parameter vs. ZCAL

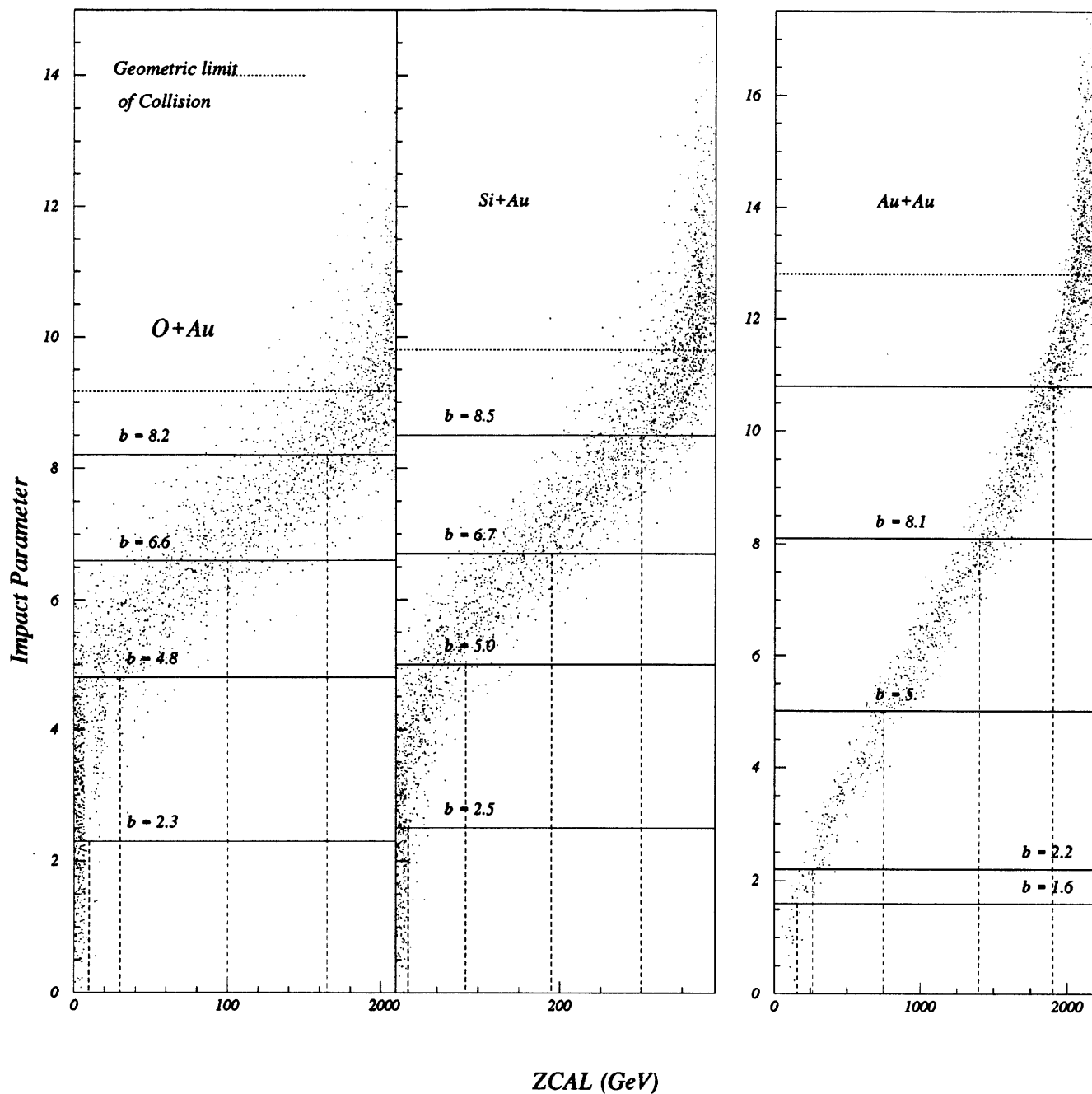


Figure 4-6: Impact parameter vs. energy in the ZCAL for $^{16}O + ^{197}Au$, $^{28}Si + ^{197}Au$, and $^{197}Au + ^{197}Au$ collisions. The cuts in centrality are superimposed on the plots. The values in impact parameter are determined from the mean in the distribution, where the ZCAL value intersects the distribution. Simulations done with FRITIOF.

Chapter 5

Cross-Section Analysis

5.1 Introduction

This chapter defines and discusses the Lorentz invariant semi-inclusive cross-section and differential yield. We also discuss the minimum bias and central triggered cross-section. By *semi-inclusive* we imply that a pion, for example, is created in a reaction $^{16}\text{O} + ^{197}\text{Au} \rightarrow \pi + X$, where X is any other particle or particles. Minimum bias in this context implies that no special triggering conditions need to be met other than an interaction has occurred (as defined by a bull's-eye beam scintillator) and/or that a particle has been detected in the spectrometer.

We begin the discussion on cross-section and differential yields with a few definitions. An *interaction* is defined as any inelastic collision of a beam particle with a target nucleus. For example, an INT event occurs when there is a beam particle after the collision with $Z \leq Z_{thres}$, $Z_{thres} = 6.5, 12.6,$ and 75 for ^{16}O , ^{28}Si , and ^{197}Au projectiles, respectively. The particle *cross-section* is defined as the number of outgoing particles per scatterer per incoming flux. The *differential yield* is the number of particles of a given type emitted per event. We will use the differential yield throughout the remaining discussion of this thesis work. Cross-sections are difficult to accurately determine in this analysis. By attempting to measure the upper 10% of σ_{inel} in a particular reaction, we may include

events that vary in the range 8 to 12 % σ_{inel} . This variation results in a 20% error in the measurement of the cross-section. The differential yields, on the other hand, do not vary dramatically from 8 to 12% σ_{inel} and therefore decrease the variations of the measurement. Particle cross-sections are therefore addressed only when necessary.

5.2 Definitions

A very simple definition of cross-section may be given in terms of a probability for having some species of particles be produced in a reaction per scattering particle per incident particle flux [E802-39],

$$\sigma = \frac{\text{number of outgoing particles per scatterer}}{\text{incoming flux}}. \quad (5.1)$$

This definition is sometimes useful and helps us to think about the cross-section in terms of a probability. A Lorentz invariant, momentum dependent cross-section for this analysis is appropriate for defining the cross-section in terms of the perpendicular and transverse momentum and mass,

$$\sigma_{inv} = E \frac{d^3\sigma}{dp^3} = \frac{E}{2\pi} \frac{d^2\sigma}{p_t dp_t dp_{||}} = \frac{E}{2\pi} \frac{d^2\sigma}{m_t dm_t dm_{||}}. \quad (5.2)$$

Both p_t and $p_{||}$ have been defined in Chapter 2. The transverse momentum is related to the rapidity by

$$\cosh(y) = \frac{E}{m_t}, \quad \sinh(y) = \frac{P_{||}}{m_t}. \quad (5.3)$$

Using $dp_{||} = E dy$, we can rewrite Equation 5.2 as

$$\sigma_{inv} = E \frac{d^3\sigma}{dp^3} = \frac{d^2\sigma}{2\pi p_t dp_t dy} = \frac{d^2\sigma}{2\pi m_t dm_t dy}. \quad (5.4)$$

The invariant cross-section is written in terms of the measurable quantities:

$$\frac{d^2\sigma}{2\pi p_t dp_t dy} = \frac{N \cdot \text{Acceptance} \cdot \text{Decay}}{2\pi p_t N_{BEAM} dp_t dy} \cdot \frac{10^{27} m_{targ}}{t \cdot A_{AV}}. \quad (5.5)$$

- $N = N(y, p_t)$ is the number of counts for a particular trigger and particle species.
- **Acceptance** is the particle-by-particle geometric acceptance correction for the ϕ coordinate, $2\pi/\delta\phi$.
- **Decay** is the particle-by-particle decay correction factor.
- dp_t is the differential transverse momentum. This variable is fixed in software at the value of 0.05 GeV/c.
- dy is the differential rapidity. This variable is a fixed constant in CSPAW in units of 0.05.
- A_{AV} is Avogadro's number, 6.023×10^{23} .
- t is the target thickness measured in gm/cm².
- m_{targ} is the Atomic Weight of the target in gm/mole.

In this thesis, we will present data in terms of the differential yield. This quantity is directly proportional to the particle cross-section of a particular particle species, i.e.,

$$\frac{d^2 n_i}{2\pi p_t dp_t dy} = \frac{1}{\sigma_i} \frac{d^2 \sigma_i}{2\pi p_t dp_t dy}. \quad (5.6)$$

The differential yields are displayed in the appendices for π^\pm , K^\pm , and protons for p + A, $^{16}\text{O} + \text{A}$, $^{28}\text{Si} + \text{A}$ and $^{197}\text{Au} + ^{197}\text{Au}$ reactions.

5.3 Procedure

Differential yields have been generated for three running periods in this thesis work. The software package for differential yield generation is a relatively flexible one that is

used in the Physics Analysis Workstation (PAW) environment. All four data sets have been analyzed with the same cross-section procedure called CSPAW, created by Chuck Parsons and modified by several students [PZ,91], [MRSZ,92]. This cross-section software package allows the user to make small detailed changes in the code, implementing certain trigger conditions and filters for a wide range running conditions. Physics information for each run is stored in the form of compressed ntuples, as explained in Chapter 3. These data files allow for very quick processing of information and determination of differential yields. Full data sets may be processed from the compressed ntuple stage to the finished differential yield histograms in about one hour on a VAX 3100 workstation.

We will briefly describe the process of creating a differential yield. The reader is referred to collaboration memos, [PZ,91] and [MRSZ,92], for more details on the procedure. One first starts with a reconstructed output file (see Chapter 3). Data that have been analysed up through the pass3 stage (particle ID) are translated into a form suitable for analysis in the PAW environment. A run-by-run ntuple file is created and contains track, event, and run information. The next stage creates a large ntuple summary file containing all the runs for a run period in one file. A typical run in a directory would be listed according to target, run angle, and magnetic field setting. This manner of storing information has proven to be very flexible and allows a very efficient way to analyze very large data sets in short periods of time.

Quality checks are next done on the data. First, trigger scaledowns are checked for consistency. One can determine if wrong scaledowns were typed into the database when created at run time. Inefficient TOF slats are flagged for correction later on. A list of runs that contains bad or inefficient TOF slats is generated. Figure 5-1 shows the run-by-run listing of bad TOF slats for oxygen and gold data sets (The reader is referred to Chuck Parson's thesis [Par92] for a slat-by-slat correction of the silicon data set).

The acceptance files are next created for each running period and are the topic of the following section.

SUMMARY OF MINB, CENTRAL ^{16}O and ^{197}Au DATA ANALYSED

Beam	Target	particle	5	14	24	34	44	Central
^{16}O	^{27}Al	π^+	16.9	14.3	14.8	10.8	6.2	73.9
		π^-	17.3	15.7	16.1	13.3	7.6	74.1
		K^+	3.5	1.5	0.91	0.56	0.28	12.6
		K^-	1.8	0.63	0.26	0.11	0.04	5.7
		Protons	17.3	16.7	21.3	23.9	15.6	84.3
	^{64}Cu	π^+	12.9	15.3	13.6	7.1	4.4	89.2
		π^-	14.8	14.5	14.7	8.9	5.9	96.4
		K^+	2.7	1.7	1.0	0.44	0.25	14.5
		K^-	1.2	0.5	0.21	0.08	0.04	5.1
		Protons	15.7	20.1	23.3	18.9	16.5	132.4
	^{197}Au	π^+	27.5	40.0	8.8	9.5	12.2	126.1
		π^-	28.8	41.3	9.8	11.8	13.4	133.2
		K^+	5.9	5.3	0.8	0.8	0.85	24.1
		K^-	2.4	1.6	0.16	0.13	0.13	8.1
		Protons	36.0	72.1	20.3	33.2	48.3	243.7
			14	21	24	34	44	
^{197}Au	^{197}Au	π^+	37.0	5.1	33.5	18.6	31.8	52.8
		π^-	39.3	8.9	50.2	22.1	34.9	61.1
		K^+	3.9	0.65	3.1	1.4	1.8	5.0
		K^-	0.73	0.11	0.59	0.83	0.26	0.8
		Protons	56.6	11.6	53.8	33.7	63.7	77.2

Table 5.1: Summary of minimum-bias data that were analyzed exclusively in this thesis. The statistics (multiply all numbers by 1000) were determined for identifiable particles found in the spectrometer for minimum bias data samples. The central-collision statistics are compressed to show all the spectrometer running angles. Statistics for ^{28}Si running may be found elsewhere, but are at least as good, and in many cases better than the minimum bias statistics for ^{16}O and ^{197}Au running. Offline ZCAL cuts are limited by the poorer statistics of the back angle minimum bias data samples.

Bad Slats for Oxygen and Gold Data Sets

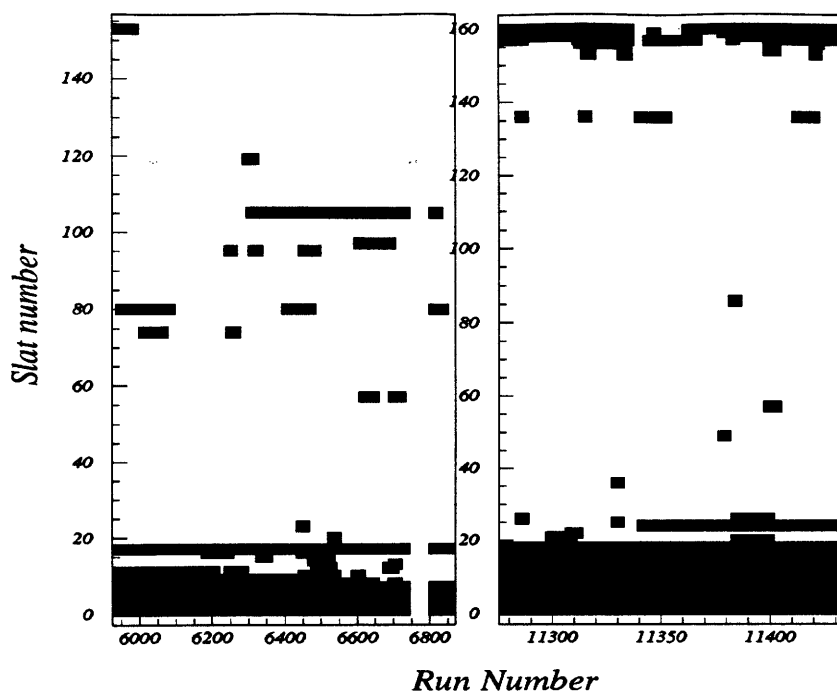


Figure 5-1: Bad Slats listed for each run. If slats were considered dead or only inefficient, they would be corrected when the acceptance is generated.

5.3.1 CSPAW: Acceptance Generation

The acceptance is generated on a run-by-run basis for each particle. Acceptance histograms are generated for each particle type and for all relevant running conditions (i.e., magnet field, spectrometer angle, etc.) prior to differential yield generation.

The acceptance boundaries are generated analytically using detector positions and then checked with data for consistency. Previously, the acceptance calculations required extensive Monte Carlo simulations of tracks through the spectrometer. This time consuming and clumsy process was stream-lined in CSPAW.

In CSPAW, the detector geometry is referenced at first to form the rough acceptance boundaries. Data are then superimposed on this acceptance and checked for voids or places where data falls outside the boundaries. This technique maximizes the acceptance for the experiment and is especially useful in regions of low p_t .

First, a database of geometric values that define the edges of the acceptance around chambers, the TOF wall and the boundaries of the magnet is generated. The routine **GENACC** is run in the PAW environment and loads the acceptance for each run.

I_{int}	81 interior points weighted by 1
I_{side-x}	18 x-side points weighted by 1/2
I_{side-y}	18 y-side points weighted by 1/2
I_{corner}	4 corner points weighted by 1/4

Table 5.2: Table of acceptance weights for each acceptance subbin. Weights are applied to each subbin depending on the fraction in the acceptance.

The run-by-run acceptance histograms are created in the routine **YPTACHST**. The actual values for the chamber boundaries and the TOF wall are contained in a file called **BUILD_ACCEPT**. This database file contains all the boundaries for all running periods as well as geometry shifts even over one running period. For example, for June 88 running, the target shift was seen. Particle tracks from different spectrometer settings pointed back to different target positions. This shift was incorporated on an angle-by-angle basis.

Data containing acceptance information are stored in two-dimensional histograms, binned in $y - p_t$ coordinates. Each bin is 0.05 units in rapidity as well as in transverse momentum. Each $y - p_t$ bin is checked at the time of acceptance generation in the routine **BIN_IN_ACCEPT** to determine if the acceptance is satisfied. Bins that are close to the edge of the acceptance are weighted appropriately. Acceptance bins are multiplied by a correction factor, depending on the fraction of the bin that lies within the geometric boundary. An algorithm divides each $y - p_t$ bin into 10×10 total subbins. The actual fraction that the subbin has in the acceptance is next calculated so that the contents in that bin may be weighted correctly. Each of these subbins are multiplied by a weighting factor F ,

$$F = \frac{1 \times I_{int} + .5 \times I_{side-x} + .5 \times I_{side-y} + .25 \times I_{corner}}{100}. \quad (5.7)$$

A second unique feature of CSPAW acceptance generation is the way that data are binned. Typically, the data are binned and acceptance is verified in $y - p_t$ space. In the CSPAW environment, bins are converted to $\theta_{particle}$ vs. $\theta_{bend-particle}$ space. The familiar θ coordinate is simply the polar coordinate measured from the beam direction.

Acceptance for Gold Target at $\Theta_{\text{spec}} = 44^\circ$

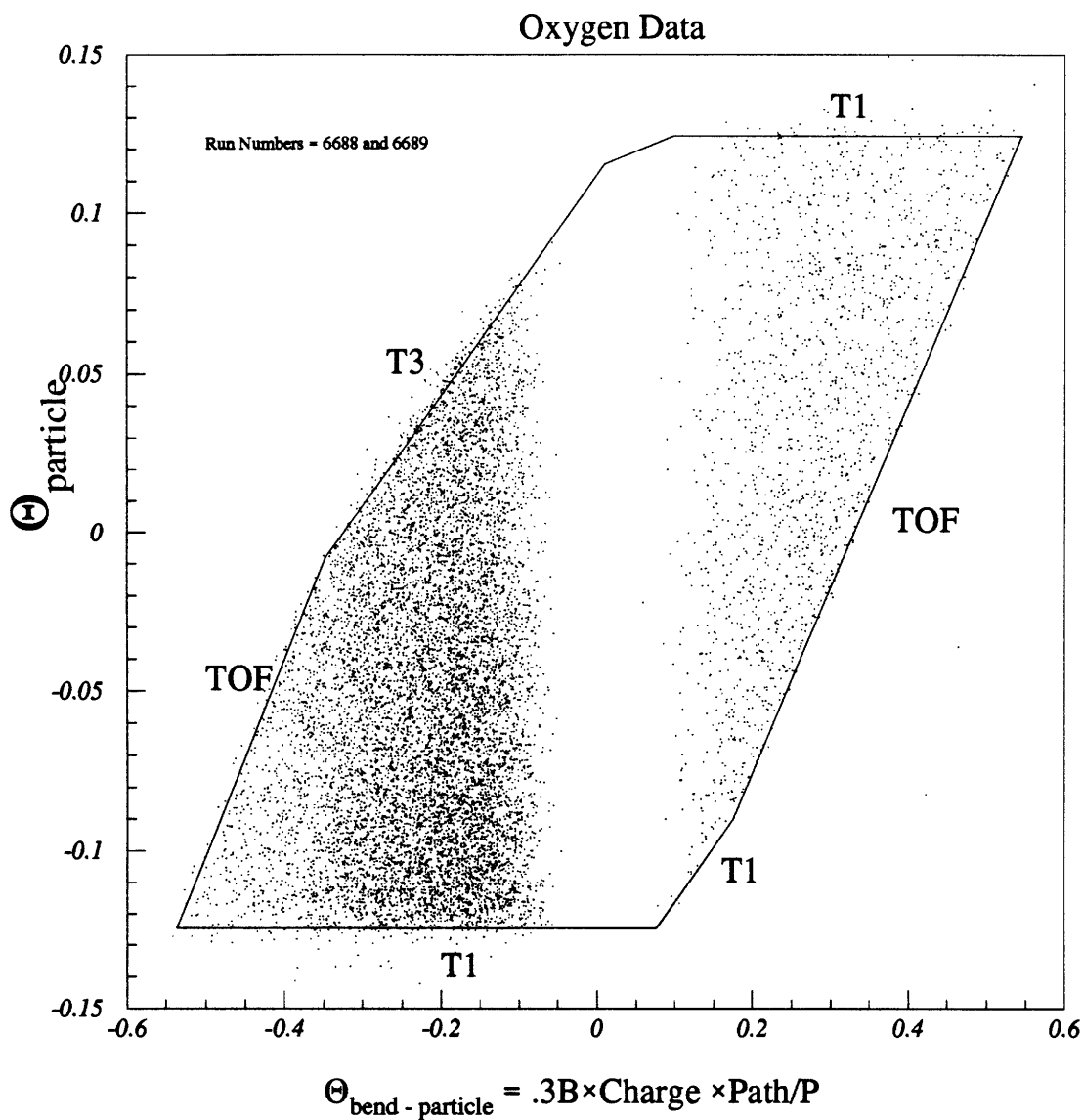


Figure 5-2: Acceptance plotted in θ_{particle} vs $\theta_{\text{bend-particle}}$ coordinates (see text). The side boundaries are sloped, since the physical chamber boundaries of T3 and T4 occur after the magnet. Slight modifications to this picture occur for E866 running, as two trigger chambers, TR1 and TR2, modify the acceptance boundary after the magnet.

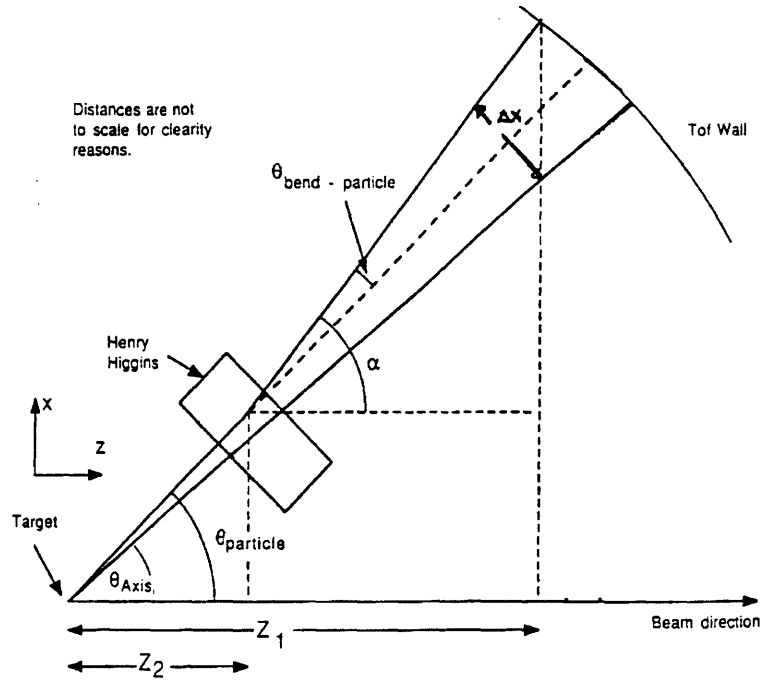


Figure 5-3: Diagram of $\theta_{bend-particle}$ after the HH magnet, showing the relationship to the particle's initial polar coordinate.

The θ_{bend} coordinate is determined from the particle's momentum. Assuming a constant magnetic field in the Henry Higgins magnet, we have the approximation,

$$\theta_{bend-particle} \approx \frac{0.3qBL}{p}, \quad (5.8)$$

where q is the charge of the particle, B is the magnetic field strength (assumed to be constant within the magnet interior) and L is the path length of the particle in the field and p is the particle's momentum. Figure 5-3 shows a schematic of the Henry Higgins spectrometer, depicting a possible trajectory of a charged particle, bent in the magnet by an angle, $\theta_{bend-particle}$.

A particle's deflection, Δx , is a measure of its displacement from an imaginary line emanating from the target and going straight through the magnet. The deflection may be determined from a small angle approximation. The mapping of all deflected positions fills in the acceptance boundary of Figure 5-2. The total deflection, $\Delta x = x_2 - x_1$, is given by

$$\Delta x \approx [\theta_{bend-particle}(z_1 - z_2) + (\theta_{particle} - \theta_{axis})(z_1)]/\cos(\theta_{particle}), \quad (5.9)$$

where we have used the small angle approximation, $\tan(\theta_{particle} - \theta_{axis}) \approx \theta_{particle} - \theta_{axis}$ and $\tan(\theta_{bend-particle}) \approx \theta_{bend-particle}$. Rearranging Equation 5.9, we have a linear relationship between $\theta_{bend-particle}$ and $\theta_{HH} = \theta_{axis} - \theta_{particle}$. The relation is:

$$\theta_{bend-particle} \approx \frac{z_1 \theta_{HH}}{(z_1 - z_2)} + \frac{\Delta x \cos\theta_{particle}}{(z_1 - z_2)}. \quad (5.10)$$

This linear relationship has the nice property that when data or objects are binned and plotted as a function of $\theta_{bend-particle}$, objects that vary linearly in θ (i.e., detector sides, TOF slats, etc.) also vary linearly in $\theta_{bend-particle}$. Changes in the acceptances due to geometry shifts appear as straight lines in this picture.

Bad TOF slats are also incorporated in the acceptance at this point. The routine **FIND_PHI_BADSLAT** is called when the acceptance for each bin is determined. The $\Delta\phi$ contribution due to the bad slat is calculated and the azimuthal angle contribution due to the badslat, ϕ_{bad} , is subtracted from the $\Delta\phi$ of the particle. Dead and inefficient TOF slats appear as streaks in Fig. 5-2. Details of the subtraction routine are rather complicated and the reader is referred to the memo by C. Parson and this author [PZ,91].

Finally, acceptance boundaries are verified for accuracy by superimposing the data on the geometric boundaries of the $\theta_{particle} - \theta_{bend-particle}$ polygon of Fig. 5-2.

5.3.2 CSPAW: Filtering

Cross-sections and differential yields created in CSPAW are generated using an event and particle track loop routine, **RUN3**, that will be described in the next section. At the start of each cross-section generation, runs are checked for quality and some are filtered. We enumerate a list of filters that are used before differential yields are determined. These filters eliminate events where there are large background contributions. For reference, Table 5.3 gives a listing of the possible track status.

Track Status	Description
88	T1T2 and TOF not verified. T3T4 verified.
94	T1T2T3T4 verified, but no TOF hit.
120	Verified with T3T4-TOF, but have no T1T2 verification.
126	Verified with T1T2T3T4-TOF but track does not point to target.
255	Good track.

Table 5.3: Summary of the track status used in the data.

1. Track Status 120. The ratio of 120 status track to 255 status tracks is kept to less than 1.6 for **INT** triggered events.
2. Track Status 126. The ratio of 126 status tracks to 255 status tracks is kept to less than 0.25 for **INT** triggered events.
3. PID Mass Checks. Particles that are detected in the spectrometer must pass upper and lower mass cuts, determined from momentum and time-of-flight information. (see Equation 3.6).
4. Inappropriate Runs Discarded. **ZERO FIELD**, **CC**, **LASER**, and **PULSER** runs were not used to produce differential yields and therefore must be filtered. Runs were also discarded when hardware and software tests were being done on certain trigger chambers. For example, runs were not used during the June 88 period where the T1 trigger chamber underwent hardware and software tests.
5. Bad Runs. Runs were discarded when high voltage trips were set during the run. This particular problem was seen for the June 88, oxygen runs and December 88 and June 89 silicon runs, especially when the spectrometer was set at 5° .
6. Follow Events. Beam events are corrected for at the final analysis stages. Typically bad beam and follow events account for $\leq 5\%$ of the total beam.

5.3.3 CSPAW: Differential Yield Generation

In this section, we discuss the production of invariant cross-sections and differential yields produced for each particle species.

The differential yield is the number of particles emitted per event. We therefore need to know the event rate, N_{INT} . N_{INT} is related to N_{BEAM} in the following way,

$$N_{INT} = N_{BEAM} \cdot C_{BEAM} \cdot TARGFRAC, \quad (5.11)$$

where

$$C_{BEAM} = \frac{\text{Good Beam Events}}{\text{All Beam Events}}. \quad (5.12)$$

REALFRAC is defined as the fraction of the inelastic cross-section for that event. The quantity TARGFRAC is the ratio of the interaction rate to the beam rate, with the background rate subtracted out. The term C_{BEAM} is the good beam fraction and is a number typically between 0.95 and 1.0. Not all of the live beam is useful. Events are rejected if another beam particle *follows* the event within a $1\mu\text{sec}$ period. Likewise, events are rejected if a beam particle is *preceded* by another event within a window of $3\mu\text{sec}$. The quantity N_{BEAM} is the number of (live beam events for an entire run) \times (Beam scaledown/Trigger scaledown). Only a small fraction of total beam events are written to tape and therefore the total number is calculated by multiplying the measured number by the beam scaledown. The trigger scaledown, (i.e., the spectrometer scaledown, etc.) is divided through here and has the same effect as multiplying N , the number of counts, by this factor.

The differential yield has a particle-by-particle geometric acceptance, $2\pi/\delta\phi$, correction. There is also a particle-by-particle decay correction. When dividing through by the transverse momentum and rapidity variables we obtain the differential yield. A complete discussion of the particle cross-section and differential yields may be found in the cross-section memos (see [PZ,91] and [MRSZ,92]).

The summary file is first loaded into PAW memory. The run, event, and particle track loop routine, **RUN3**, is executed in PAW. The differential yields for each run are determined and the results are merged together. The event looping routine, **RUN3**, calls the routine **RUNACC** at the start of every run. **RUNACC** performs several functions. A run-by-run filter database, **RUNFILT**, is also called. This routine throws out any runs that should not be included in the analysis. Secondly, the software triggers are defined here and finally acceptance histograms are loaded into memory at this stage.

Next, the routine **CSFILL** is called for every particle track. The routine fills $y-p_t$ histograms with particle track information. Decay corrections and any physics corrections are done at this time. Various other corrections associated with instrumentation and analysis, including chamber inefficiencies, particle ID inefficiencies, and track reconstruction inefficiencies are also done here.

The routine **MERGERUN** is called at the end of every run and calls the routine **RUNFACT** where event normalizations are determined. Finally, runs are merged together in the routine **CSMERGE**. Figure 5-4 shows these routines in a flow-chart schematic in the PAW environment.

Next, the rapidity distribution may be determined. The quantity dN/dy is determined by integrating over the differential yield:

$$dN/dy = \int_{p_t(1)}^{p_t(2)} \frac{d^2n}{2\pi p_t dp_t dy} 2\pi p_t dp_t. \quad (5.13)$$

The major component of dN/dy will come from the low p_t contribution and we must first make an appropriate fit to the distribution and extrapolate to $p_t = 0$. The momentum spectra may be fit in a functional form and integrated out so that a yield at a particular rapidity may be determined as in Equation 5.13.

The quality and statistics of the E802 and E866 data set allows one to fit the momentum spectra in terms of an exponential function,

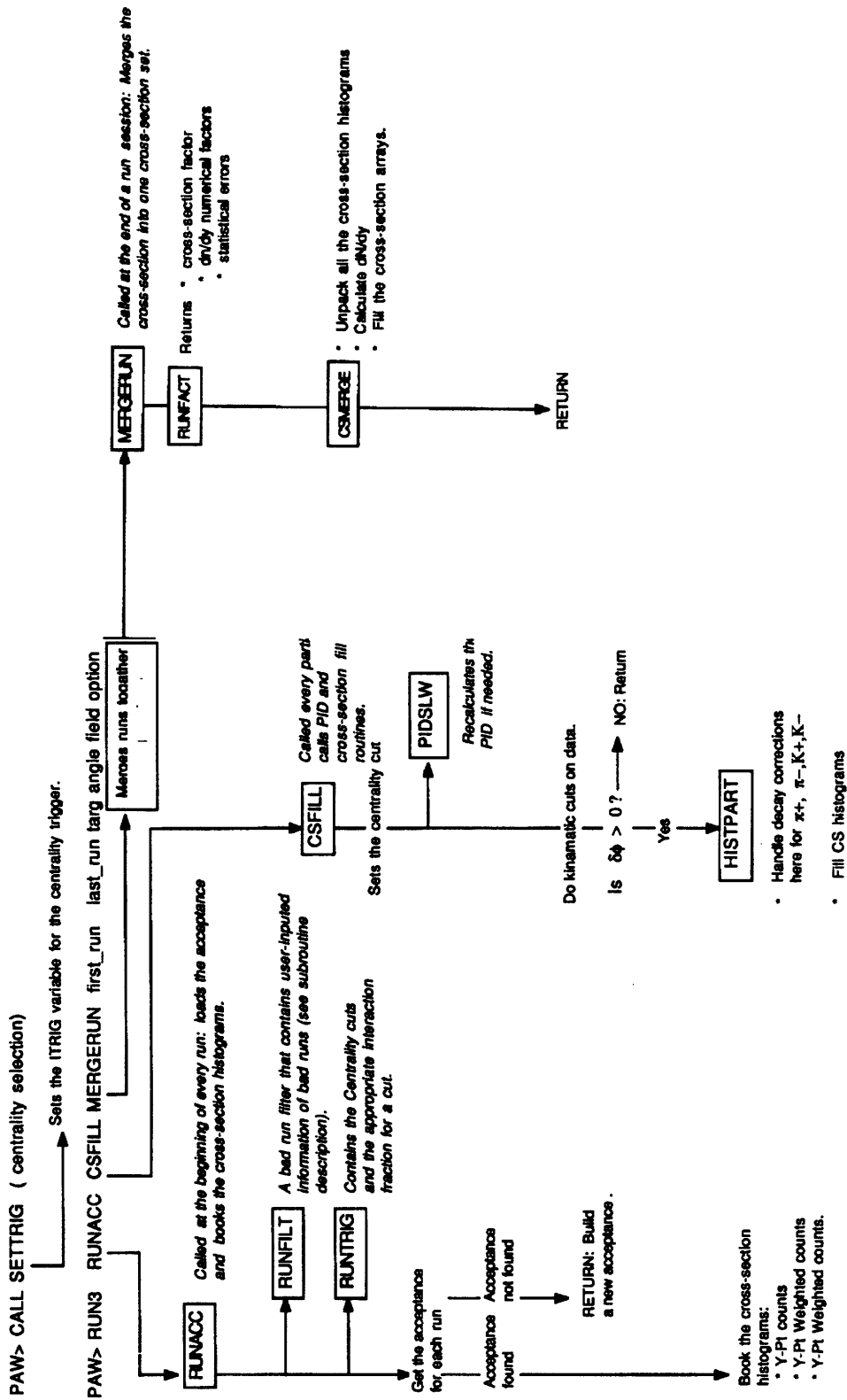


Figure 5-4: Cross-Section Flow Chart.

$$\frac{d^2n}{2\pi p_t dp_t dy} = A \cdot e^{-p_t/T}. \quad (5.14)$$

We are free to change variables of integration . The momentum spectrum has been plotted in terms of p_t and m_t because of the relations $m_t = \sqrt{m_o^2 + p_t^2}$ and $m_t dm_t = p_t dp_t$. Equation 5.14 may then be rewritten

$$\frac{d^2n}{2\pi m_t dm_t dy} = A \cdot e^{-m_t/T}. \quad (5.15)$$

Proton spectra were fit to either exponential or Boltzmann functions in m_t . For a Boltzmann distribution, $d^3n/dp^3 = A \cdot e^{-E/t}$, and therefore the differential yield may be written in terms of m_t and y . Using the relations $E = m_t \cosh(y)$ and $dy = dp_{||}/E$, we have

$$\frac{d^2n}{2\pi m_t dm_t dy} = A m_t \cosh(y) \cdot e^{-(m_t \cosh(y))/T}. \quad (5.16)$$

The differential yields are calculated in rapidity slices, typically .2 units of rapidity in width. The integrated yield is next determined. Event yields are determined by fitting a functional form to the rapidity distribution. Produced particles, pions and kaons, are fitted with a Gaussian distribution of the form

$$\frac{dn}{dy}_{\pi,K} = A \cdot e^{-(y - y_o)^2/2\sigma^2}. \quad (5.17)$$

The values for A and σ are tabulated in the following chapter. The value $y_o = y_{beam}/2$ for symmetric $^{28}\text{Si} + ^{27}\text{Al}$ and $^{197}\text{Au} + ^{197}\text{Au}$ collisions. Since protons are not abundantly produced in collisions at these energies, their rapidity distributions, not surprisingly, are different in form than the produced meson distributions.

5.3.4 CSPAW: Error Handling

Both statistical and systematic errors must be understood throughout the analysis. The differential yield may be written as

$$\frac{d^2n}{2\pi p_t dp_t dy} = \frac{N_W(y, p_t)}{DNDYFACT}. \quad (5.18)$$

The weighted counts, $N_W = N \cdot Acceptance \cdot Decay/2\pi p_t$. The value DNDYFACT is defined as $N_{INTREALFRAC} dp_t dy$. The error of the differential yield is

$$\sigma_{DY} = DY \sqrt{\frac{\sigma_{DNDYFACT}^2}{DNDYFACT^2} + \frac{\sigma_{N_W}^2}{N_W^2}}. \quad (5.19)$$

The error associated with counting independent events or a particular species is $\sigma_{N_W} = \sqrt{N}$ and therefore $\sigma_{N_W}^2/N_W^2 = 1/N_W$. The error resulting from the event normalization must be handled in more detail. The normalization factor, DNDYFACT, is composed of several terms, each contributing to the error of DNDYFACT.

The error associated with the normalization to the differential yield is a statistical error from counting the fraction of the “good” beam used. The terms REALFRAC and TARGFRAC are by definition exact quantities. The error from the normalization term arises in counting particles that satisfy the conditions imposed by these quantities. The error associated with counting the number of beam particles is therefore simplified to determining the error associated with counting the beam particles that pass all filters, $N_{Good\ beam}$. The relative error for this quantity is,

$$\frac{\sigma_{good\ beam\ fraction}^2}{(number\ of\ good\ beam\ events)^2} = \frac{(\sqrt{BEAM - GOOD\ BEAM})^2}{(BEAM - GOOD\ BEAM)^2}. \quad (5.20)$$

The above terms may be combined to give a summed relative error,

$$\frac{\sigma_{IY}^2}{IY^2} = \frac{1}{BEAM - GOOD\ BEAM} + \frac{1}{N_W}. \quad (5.21)$$

After determining the yields and errors, the momentum spectra are fit by one of several functional forms described in the previous sections. An exponential or Boltzmann form is fit to the momentum spectra. The constants A and T and their associated errors of Equation 5.14, 5.15, 5.16 are determined by minimizing chi-square in the **MINUIT** analysis package,

$$\chi^2 = \sum_{j=1}^n \frac{[f(x_j) - NP(x_j)]^2}{NP(x_j)}, \quad (5.22)$$

where $f(x_j)$ is the observed frequency distribution of possible observations x_j and $NP(x_j)$ is the proposed distribution function [Bev69]. For kaon data with very limited statistics, a log-likelihood function is used instead to determine A and T[Bak83].

The values for A and T are determined for each rapidity slice (see appendices).

5.4 Data Quality

5.4.1 Track Statistics

CSPAW carries event and track statistics that give a reasonably good indication of the quality of the run. Table 5.4 shows one of the early oxygen runs and a listing of information, including the number of particles, triggered events, and other track statistics.

In this work, only TRED status tracks, status ≥ 120 (see Table 5.3) are used. All tracks must be reconstructed with particle identification. Status 120 and 126 tracks are closely monitored and runs are not included in the analysis whenever status 120 tracks represent more than 10% of the identified tracks (typically at the most forward spectrometer setting). Most of the analysis did not use the most forward spectrometer setting and therefore this was never a major concern. Runs where the number of 126 status tracks were greater than 25% of the 255 status tracks were not included in the analysis.

Run Summary for #5950 , $^{16}\text{O} + ^{197}\text{Au}$ run

(1)	NEVENT	=	23104	(2)	N Passed Events	=	17331
(3)	FOLLOWS	=	5447	(4)	ZCUT Events	=	513
(5)	N Beam Triggers	=	943	(6)	INT Events	=	9331
(7)	TMA Events	=	10408	(8)	PB1 Events	=	5845
(9)	PB2 Events	=	5845	(10)	SPEC Events	=	0
(11)	CC Events	=	344	(12)	SPEC2 Events	=	0
(13)	# Pi+	=	1834	(14)	# Pi-	=	1272
(15)	# Protons	=	3239	(16)	# K+	=	261
(17)	# K-	=	97	(18)	N Beam with INT	=	48
(19)	N Good Tracks	=	8094	(20)	N Gd Trk Events	=	6032
(21)	N Track Events	=	8484	(22)	N Trip Events	=	0
(23)	120 Track Ratio	=	0.5325	(24)	126 Track Ratio	=	0.0216
(25)	88 Track Ratio	=	0.1782	(26)	Mean Target X	=	-0.3789
(27)	Mean Target Y	=	-0.0545	(28)	Mean tof SLAT	=	78.3818
(29)	Average Track P	=	1.8094	(30)	Mean Trck Theta	=	0.3364
(31)	Sigma Mass Pi+	=	0.0713	(32)	Mean Pi+ Mass	=	0.1420
(33)	Sigma Mass Pi-	=	0.0803	(34)	Mean Pi- Mass	=	0.1452
(35)	Sigma Mass K+	=	0.0737	(36)	Mean K+ Mass	=	0.5109
(37)	Sigma Mass K-	=	0.0943	(38)	Mean K- Mass	=	0.5018
(39)	Sigma Mass P	=	0.0570	(40)	Mean P Mass	=	0.9625
(41)	Mean TMA X Pos.	=	0.0677	(42)	Mean TMA Y Pos.	=	-0.0334
(43)	Avg TMA Eta Bin	=	1.8870	(44)	Avg TMA for INT	=	45.7834
(45)	7% Tma Trig	=	130.0000	(46)	Av ZCAL for INT	=	121.1783
(47)	10% ZCAL Trig	=	5.3000	(48)	Av ETOT for INT	=	6706.9937
(49)	10% ETOT Trig	=	16700.0000	(50)	Avg ET for INT	=	1930.3737
(51)	10% ET Trig	=	4900.0000	(52)	N Int Pass EVT	=	6884
(53)	N TMA Pass EVT	=	7883	(54)	N PB1 Pass EVT	=	4439
(55)	N PB2 Pass EVT	=	4439	(56)	N Spec Pass EVT	=	0
(57)	N CC Pass EVT	=	269	(58)	N SPC2 Pass EVT	=	0
(59)	N Int noFOL EVT	=	7124	(60)	N TMA noFOL EVT	=	7953
(61)	N PB1 noFOL EVT	=	4473	(62)	N PB2 noFOL EVT	=	4473
(63)	N Spec noFOL EV	=	0	(64)	N CC noFOL EVN	=	274
(65)	N SPC2 noFOL EV	=	0	(66)	Avg bm bullseye	=	7.7483
(67)	Avg int bulseye	=	2.9872	(68)	Avg INT ZBtof	=	8.0018
(69)	Avg INT ZBTOT	=	7.97838	(70)	Mean track Phi	=	-0.0052

Table 5.4: A typical list of run information for a June 88 $^{16}\text{O} + ^{197}\text{Au}$ run at $\theta_{spec}=14^\circ$.

5.4.2 Accuracy of the Measurements

The overall accuracy of the measurement for E802/E866 has been a topic of discussion since the early results of E802 were first presented. Particle yields, $d^2N/2\pi p_t dp_t dy$, are determined from three measured values, the yield, the momentum, and the rapidity,

N (yield of particles for a given number of events);

$p(\text{tof},d)$, d = path length;

y , rapidity.

The greatest uncertainty in determining the yield is in measuring N . When statistics are low, it is very difficult to determine the actual yields of particles. On the other hand, the overall accuracy for measured path length and time-of-flight are excellent, giving an accuracy of about 1%. Likewise, the uncertainty of the measured polar angle is about 2 - 4% at worst. The uncertainty in rapidity measurement is about 1 - 2%. Below is a list of sources for systematic errors in the analysis;

- BEAM Beam events are counted with scaler counters and a small fraction of the events are written to tape. The overall uncertainty of BEAM counting is small, less than 1%.
- INT The interaction trigger, the bull's-eye counter, does not measure the "total" inelastic cross-section. An unresolved single charge knockout for an interaction makes the determination of the total inelastic cross-section impossible. Event yields, not cross-sections, are determined in this analysis; therefore, the inaccuracies of INT do not present a great problem.
- ZCAL Particle yields are determined for various ranges in centrality of a collision. Particle yields do not rapidly vary with the number of baryon participants. Pion yields for oxygen and silicon projectiles range from 5 to about 50. A one nucleon resolution for oxygen and silicon running, for example, results in an inaccuracy of

pion yields of 2 - 10%. For central collisions, an inaccuracy as large as of 20% may occur.

- Reconstruction Efficiency. There are 5% uncertainties in determining reconstruction efficiencies [Roth94], [Hua90].
- PID Efficiency. Measured pions in the range $0.7 \text{ GeV}/c < p < 1 \text{ GeV}/c$ may be mistaken for electrons, 1 to 3% of the time [Par92]. Kaons measured in the range $p < 2.2 \text{ GeV}/c$ may be mistaken for pions < 1% of the time.
- Cross-Section (m_t vs. p_t). There is on average a 5 - 10 % systematic difference in yields that are determined by using m_t or p_t exponentials. In some cases, m_t and p_t exponentials fit the data equally well and we rely on current work (E859) to determine the best form.

The various uncertainties contribute to an overall systematic error of the measured yields. In summary, the overall sensitivity of the minimum bias data set is about 10 - 15%.

5.4.3 Summary of Fixes.

Data from E802, E859 and E866 have been the subject to ongoing corrections and re-analysis over the past several years. Many of the most recent corrections to the E802 data set that also apply to E859 and E866 data sets may be found in Chuck Parson's thesis [Par92]. Eighteen separate data corrections were recorded in his analysis for the silicon and proton data. All appropriate corrections have also been taken into account in this work. Some of the important corrections that have been done specifically for the oxygen and gold analysis are mentioned below.

1. Time-of-flight calibrations were redone for the June 88, oxygen data set.
2. Geometry changes have been incorporated in the E802 data as well as the E859 and E866 acceptance. The experimental positioning errors have been determined

to an accuracy of at best 1 - 2 mm. George Stephans is primarily responsible for the work on geometry correction routines. The procedure for the self-consistent geometry correction routines may be referred to in the E802 memo [E802-54]. The *self-consistent* geometry corrections were done early in the data analysis stage for both the oxygen and gold data sets. A similar geometric correction was also done by Chuck Parsons for the silicon data.

3. Dead TOF slats have been corrected for in the oxygen and gold analysis similar to the silicon analysis. Fig. 5-1 shows the dead TOF slats for the oxygen and gold runs over their respective running periods. Inefficient TOF slats (some as much as 25% inefficient) have been corrected for. An overall correction of 3 to 4 % in the yield has resulted. The reader is referred to [PZ,91] for the procedure to correct for dead TOF slats.

5.4.4 Inelastic Cross-Sections.

Data over three projectile running periods have been analysed and must pass consistency tests in several categories. The inelastic cross-sections of data from different targets are shown as a function of run number in Fig. 5-5. Only runs in the oxygen and silicon data sets that were analyzed in this thesis work are shown in the figure.

There were also numerous instrument problems in the first gold runs. These runs were not included in the analysis.

5.5 ZCAL Software Cuts

The forward calorimeter provides excellent event characterization, selecting events of varying centrality (and hence impact parameter). Particle yields may be measured as a function of collision size. In this section, we summarize the cuts made with the zero-degree calorimeter for various collision systems. Tables 5.6 and 5.7 list the energy limits for all software cuts for $^{16}\text{O} + \text{A}$, $^{28}\text{Si} + \text{A}$, and $^{197}\text{Au} + ^{197}\text{Au}$ collisions.

Inelastic Cross-Sections: O,Si,Au +A

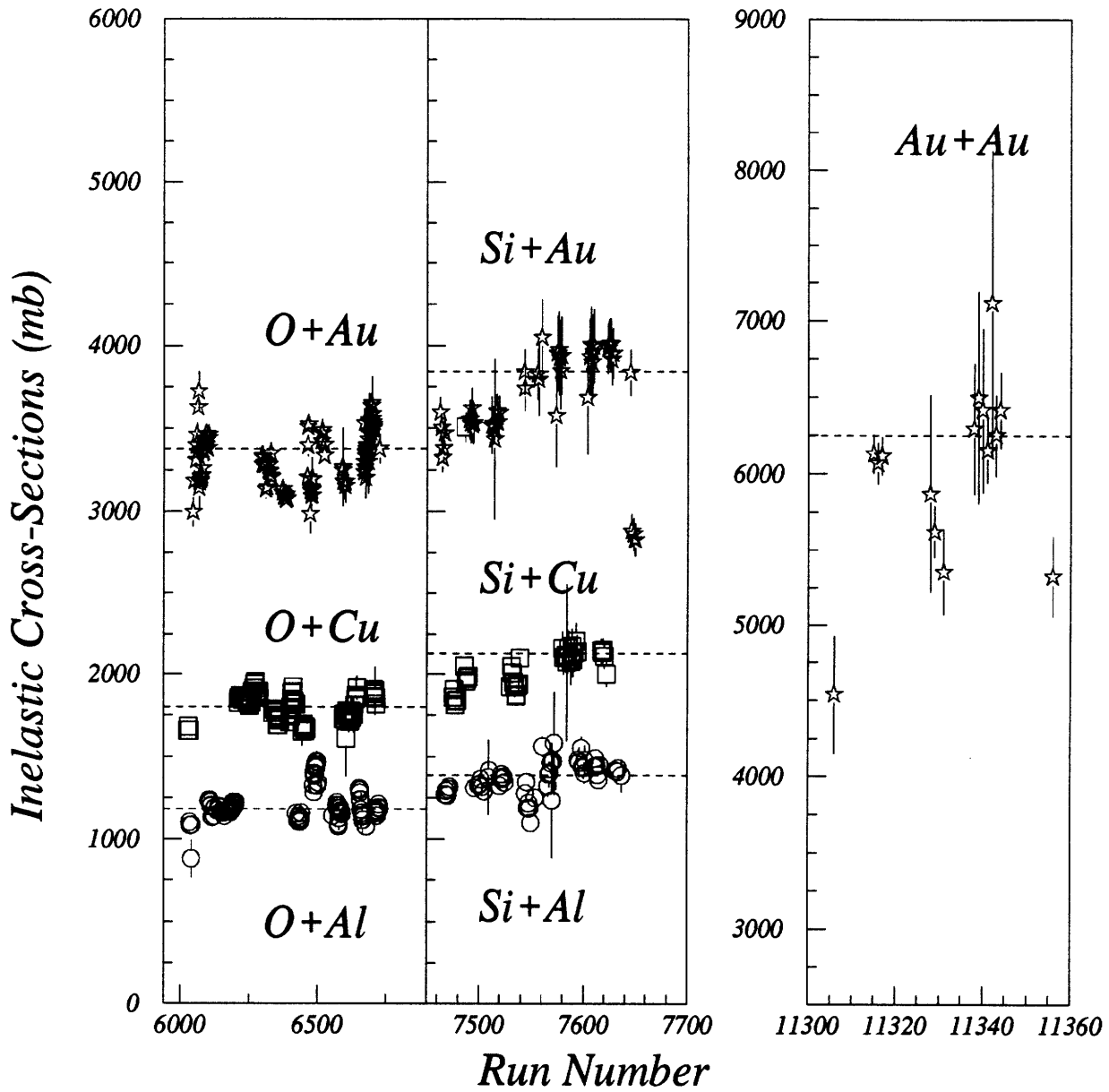


Figure 5-5: Cross-sections (background subtracted) for $^{16}\text{O} + \text{A}$, $^{28}\text{Si} + \text{A}$ and $^{197}\text{Au} + ^{197}\text{Au}$ data sets as a function of the run number.

Zero Degree Calorimeter Cuts

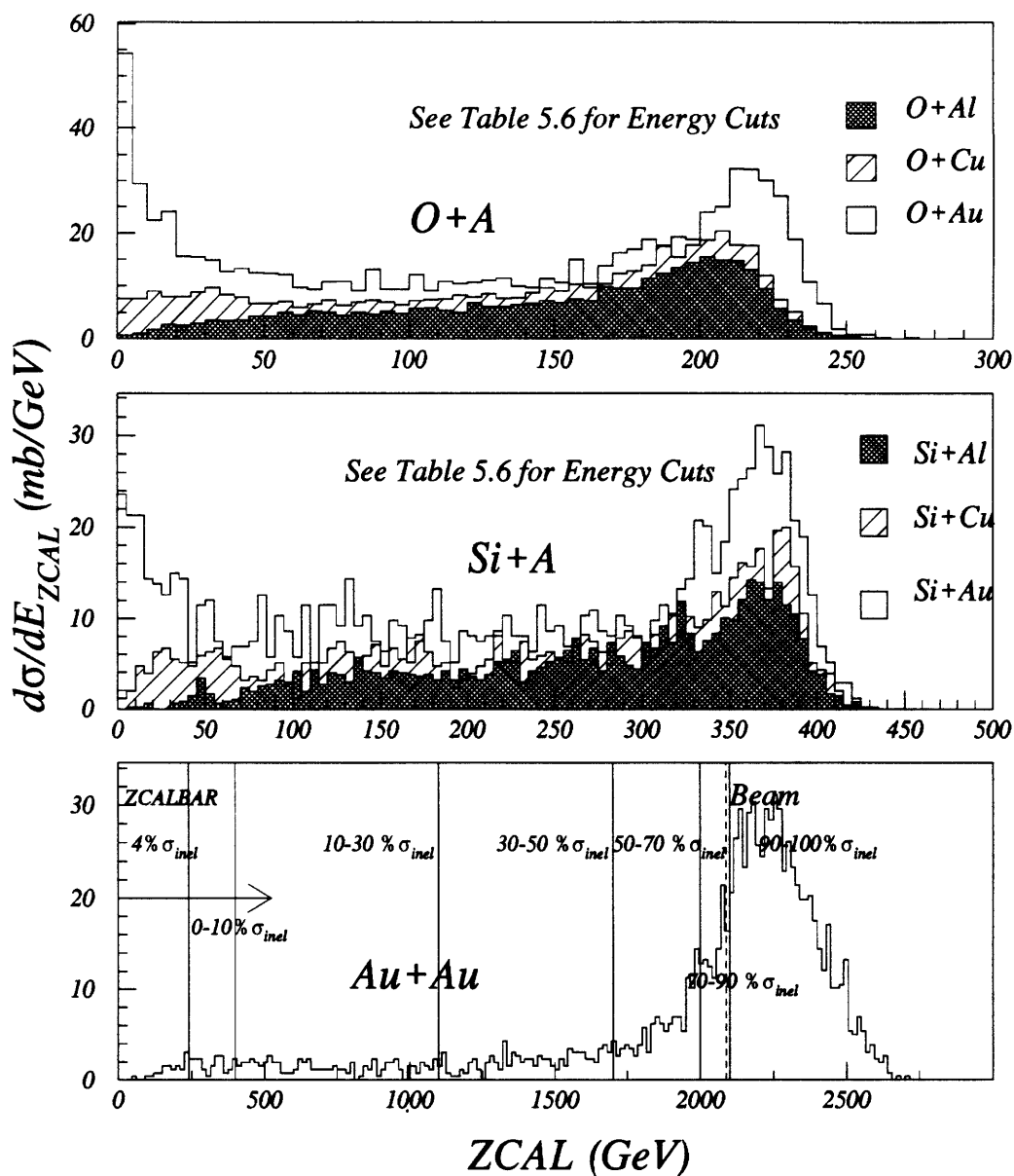


Figure 5-6: Raw ZCAL spectra for $^{16}O + A$, $^{28}Si + A$, and $^{197}Au + A$ reactions. ZCAL energy ranges are shown for $^{197}Au + ^{197}Au$ reactions. ZCAL ranges for ^{16}O and ^{28}Si projectiles may be found in Table 5.5. Note the large contribution to the cross-section for $^{197}Au + ^{197}Au$ events beyond the beam peak. This contribution is largely due to target out events; see Figure 5-7.

ZCAL Target-Out Comparison

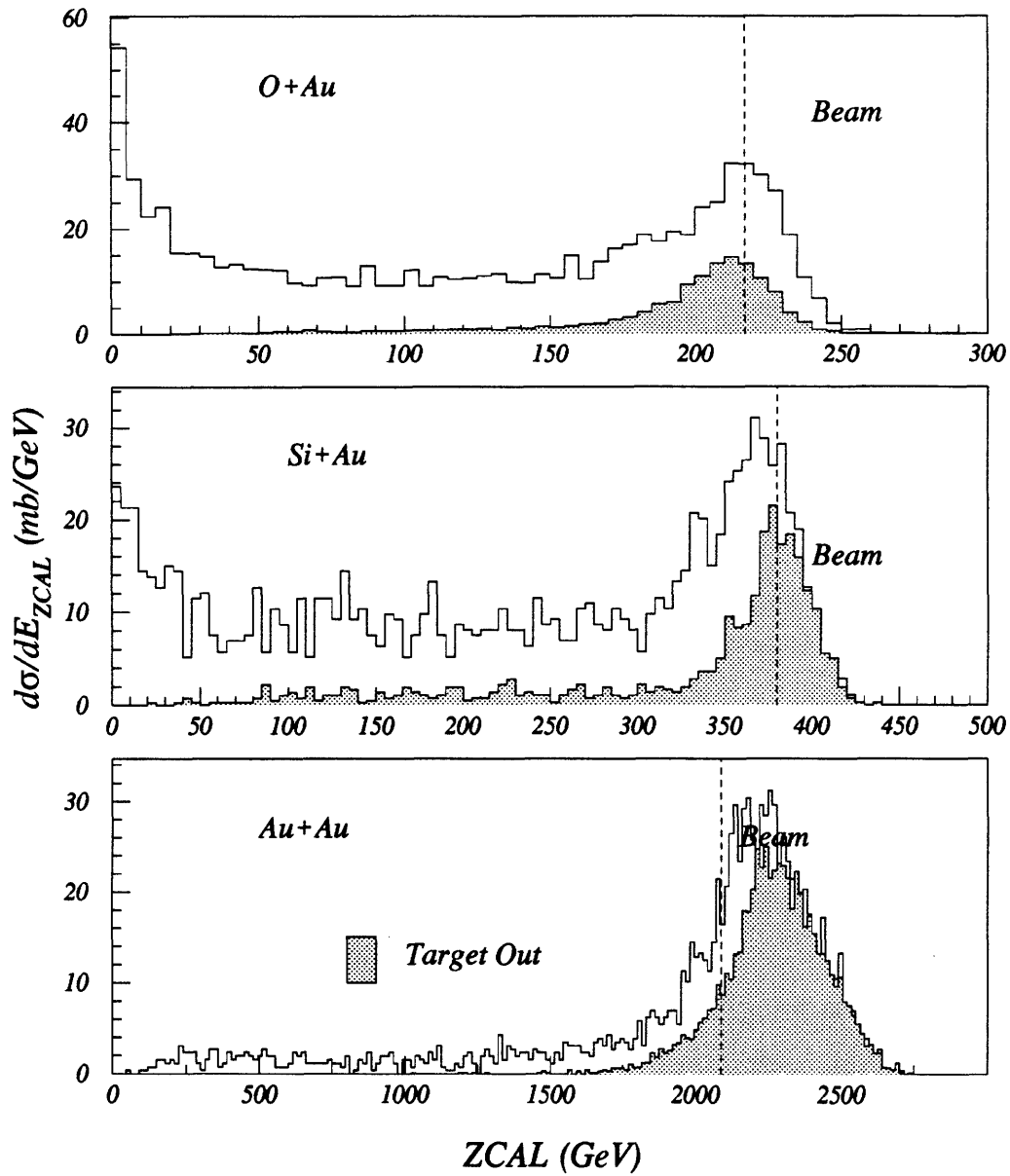


Figure 5-7: Target-out ZCAL comparison spectra for ^{16}O , ^{28}Si , and ^{197}Au projectiles superimposed on gold target spectra.

INELASTIC CROSS-SECTION AND INTERACTION RATES

System	σ_{inel} (millibarns)	INT Rate (target out subtracted)
$^{16}\text{O} + ^{27}\text{Al}$	1182 ± 76	$.0210 \pm .0016$
$^{16}\text{O} + ^{64}\text{Cu}$	1799 ± 133	$.0240 \pm .0016$
$^{16}\text{O} + ^{197}\text{Au}$	3378 ± 306	$.030 \pm .002$
^{16}O (empty)	—	$.0067 \pm .002$
$^{28}\text{Si} + ^{27}\text{Al}$	1386 ± 444	$.025 \pm .007$
$^{28}\text{Si} + ^{64}\text{Cu}$	2127 ± 51	$.028 \pm .001$
$^{28}\text{Si} + ^{197}\text{Au}$	3844 ± 831	$.034 \pm .007$
^{28}Si (empty)	—	$.0110 \pm .0004$
$^{197}\text{Au} + ^{197}\text{Au}$	6249 ± 818	$.017 \pm .001$
^{197}Au (empty)	—	$.026 \pm .001$

Table 5.5: Mean cross-sections and target-out subtracted interaction rates measured for $p + A$, $^{16}\text{O} + A$, $^{28}\text{Si} + A$ and $^{197}\text{Au} + ^{197}\text{Au}$ data used in this analysis.

Figures 5-6 and 5-7 show the ZCAL spectra for $^{16}\text{O} + A$, $^{28}\text{Si} + A$, and $^{197}\text{Au} + ^{197}\text{Au}$. A few remarks concerning the selection of the offline calorimeter triggers are needed before proceeding to the discussion of the data and the participant analysis.

- Oxygen and Silicon Software Triggering. The $^{16}\text{O} + A$ centrality triggers were selected with two primary considerations. First, the most central cuts were generally made to form a small fraction of the inelastic cross-section. These data, though shown in the analysis, are potentially more difficult to interpret because both the oxygen and silicon projectiles are completely occulted by their larger targets (see Fig. 4-2). Apart from the most central cuts, the ^{16}O and ^{28}Si data were divided into rather broad centrality ranges. These regions have statistically significant pion and proton yields and more marginal kaon statistics so that particle-to-particle comparisons may be made. Symmetric collisions are ideal for analyzing with the calorimeter since some forward projectiles are always deposited into the calorimeter and therefore event characterization is not ambiguous.

ZCAL ENERGY CUT INFORMATION:¹⁶O + A and ²⁸Si + A

System	Software Cut	Energy Range of ZCAL	Cut Name
¹⁶ O + ²⁷ Al	0 - 45% σ_{inel}	10 GeV < E_{ZCAL} < 120 GeV	CENT2
	40 - 75% σ_{inel}	120 GeV < E_{ZCAL} < 175 GeV	MID
	75 - 100% σ_{inel}	175 GeV < E_{ZCAL} < 210 GeV	PERP1
¹⁶ O + ⁶⁴ Cu	0 - 5% σ_{inel}	0 GeV < E_{ZCAL} < 10 GeV	CENT1
	5 - 45% σ_{inel}	10 GeV < E_{ZCAL} < 100 GeV	CENT2
	45 - 70% σ_{inel}	100 GeV < E_{ZCAL} < 160 GeV	MID
¹⁶ O + ¹⁹⁷ Au	70 - 100% σ_{inel}	160 GeV < E_{ZCAL} < 210 GeV	PERP1
	0 - 15% σ_{inel}	0 GeV < E_{ZCAL} < 10 GeV	CENT1
	15 - 40% σ_{inel}	10 GeV < E_{ZCAL} < 70 GeV	CENT2
	40 - 65% σ_{inel}	70 GeV < E_{ZCAL} < 130 GeV	MID
²⁸ Si + ²⁷ Al	65 - 100% σ_{inel}	130 GeV < E_{ZCAL} < 200 GeV	PERP1
	0 - 10% σ_{inel}	0 GeV < E_{ZCAL} < 100 GeV	CENT1
	10 - 40% σ_{inel}	100 GeV < E_{ZCAL} < 200 GeV	CENT2
	40 - 90% σ_{inel}	200 GeV < E_{ZCAL} < 340 GeV	MID
²⁸ Si + ⁶⁴ Cu	90 - 100% σ_{inel}	340 GeV < E_{ZCAL} < 370 GeV	PERP1
	0 - 5% σ_{inel}	0 GeV < E_{ZCAL} < 30 GeV	CENT1
	5 - 45% σ_{inel}	30 GeV < E_{ZCAL} < 170 GeV	CENT2
²⁸ Si + ¹⁹⁷ Au	45 - 70% σ_{inel}	170 GeV < E_{ZCAL} < 280 GeV	MID
	70 - 100% σ_{inel}	280 GeV < E_{ZCAL} < 370 GeV	PERP1
	0 - 15% σ_{inel}	0 GeV < E_{ZCAL} < 30 GeV	CENT1
	15 - 40% σ_{inel}	30 GeV < E_{ZCAL} < 140 GeV	CENT2
²⁸ Si + ¹⁹⁷ Au	40 - 55% σ_{inel}	140 GeV < E_{ZCAL} < 240 GeV	MID
	55 - 100% σ_{inel}	240 GeV < E_{ZCAL} < 360 GeV	PERP1

Table 5.6: Table of energy ranges for the oxygen and silicon projectiles.

 ZCAL ENERGY CUT INFORMATION:¹⁹⁷Au + ¹⁹⁷Au

System	Fraction of σ_{inel}	Energy Range of ZCAL	Cut Name
¹⁹⁷ Au + ¹⁹⁷ Au	0 - 4% σ_{inel}	E_{ZCAL} < 240 GeV	ZCALBAR
	0 - 10% σ_{inel}	0 GeV < E_{ZCAL} < 400 GeV	CENT1
	10 - 30% σ_{inel}	400 GeV < E_{ZCAL} < 1100 GeV	CENT2
	30 - 50% σ_{inel}	1100 GeV < E_{ZCAL} < 1700 GeV	MID
	50 - 70% σ_{inel}	1700 GeV < E_{ZCAL} < 1900 GeV	PERP1
	70 - 90% σ_{inel}	1900 GeV < E_{ZCAL} < 2100 GeV	PERP2
	90 - 100% σ_{inel}	2100 GeV < E_{ZCAL}	PERP3

Table 5.7: Table of energy ranges for the gold projectile.

- Gold Software Triggering. The $^{197}\text{Au} + ^{197}\text{Au}$ system is ideally suited for the calorimeter analysis. The symmetric system allows the forward projectile remnant to be detected in the calorimeter for all collision impact parameters and therefore distinct event characterization may be made. Because of the large pion multiplicities, comparable statistics to ^{16}O and ^{28}Si data were achieved over a much shorter running period. The large dynamic range of the ZCAL for the gold projectile also allowed the data to be divided by ZCAL cuts into slightly finer bins than the ^{16}O and ^{28}Si data sets.

5.5.1 Participants

This section tabulates the event information. Experimentally measured number of participants are tabulated for each collision system. All quantities for ^{16}O , ^{28}Si , and ^{197}Au systems are found in Tables 5.8 and 5.9. Participants were determined by a “clean-cut” collision of two nuclei.

5.6 Summary

We have outlined the steps in producing invariant cross-sections and differential yields in this section. Event characterization using the forward calorimeter has been used to select data at various centrality ranges by measuring the forward projectile spectators. Mean values of ZCAL for each range have been tabulated and are used in the following chapter to determine the particle yield as a function of collision participants. This analysis will naturally lead to a discussion of scaling variables in the upcoming chapters.

TABLE OF MEAN NUMBER OF PARTICIPANTS: ^{16}O and ^{28}Si IONS

System	Software Cut	$\langle \text{ZCAL} \rangle$ (GeV)	N_{part}^{targ}	N_{part}^{proj}	N_{part}^{tot}	$\langle b \rangle$ (fm's)
$^{16}\text{O} + ^{27}\text{Al}$	0 - 45% σ_{inel}	83	11.6 ± 5	9.8 ± 3	20.9 ± 8	2.7
	40 - 75% σ_{inel}	153	3.9 ± 2	3.7 ± 2	7.2 ± 3	4.6
	75 - 100% σ_{inel}	187	2.3 ± 1	2.2 ± 1	4.0 ± 2	5.6
$^{16}\text{O} + ^{64}\text{Cu}$	0 - 5% σ_{inel}	5	32.4 ± 4	16.1 ± 1	48.0 ± 4	1.
	5 - 45% σ_{inel}	40	18.1 ± 7	12.1 ± 3	29.7 ± 9	3.4
	45 - 70% σ_{inel}	140	6.6 ± 3	5.6 ± 2	11.7 ± 4	5.4
	70 - 100% σ_{inel}	185	1.6 ± 2	2.9 ± 1	5.6 ± 3	6.5
$^{16}\text{O} + ^{197}\text{Au}$	0 - 15% σ_{inel}	5	48.6 ± 7	$16. \pm 2$	64.6 ± 7	2.3
	15 - 40% σ_{inel}	30	31.3 ± 7	$15. \pm 1$	45.5 ± 8	4.8
	40 - 65% σ_{inel}	100	15.8 ± 5	10.4 ± 3	25.8 ± 7	6.6
	65 - 100% σ_{inel}	165	5.8 ± 3	4.8 ± 2	10.1 ± 5	8.2
$^{28}\text{Si} + ^{27}\text{Al}$	0 - 10% σ_{inel}	66	21.0 ± 2	21.3 ± 3	42.3 ± 4	1.4
	10 - 40% σ_{inel}	150	12.7 ± 4	12.8 ± 4	25.4 ± 7	3.2
	40 - 90% σ_{inel}	293	4.1 ± 3	4.1 ± 3	6.3 ± 4	5.3
	90 - 100% σ_{inel}	355	1.5 ± 1	1.5 ± 1	3.5 ± 2	6.2
$^{28}\text{Si} + ^{64}\text{Cu}$	0 - 5% σ_{inel}	15	41.6 ± 5	26.5 ± 1	68.1 ± 5	1.1
	5 - 45% σ_{inel}	100	23.0 ± 8	18.2 ± 5	41.1 ± 13	3.7
	45 - 70% σ_{inel}	225	7.4 ± 4	6.8 ± 3	14.2 ± 6	5.9
	70 - 100% σ_{inel}	325	3.1 ± 2	3.0 ± 2	6.3 ± 3	7.0
$^{28}\text{Si} + ^{197}\text{Au}$	0 - 15% σ_{inel}	15	67.0 ± 9	27.8 ± 1	94.5 ± 9	2.5
	15 - 40% σ_{inel}	85	41.0 ± 10	23.7 ± 3	64.0 ± 12	5.
	40 - 55% σ_{inel}	190	22.5 ± 6	16.4 ± 3	38.6 ± 7	6.7
	55 - 100% σ_{inel}	300	8.6 ± 5	7.0 ± 4	15.7 ± 9	8.5

Table 5.8: Table of mean number of participants for the various collision combinations for ^{16}O and ^{28}Si ions. The entire set of numbers are determined by counting the interaction events from $E_{\text{ZCAL}} = 0$ to the desired ZCAL value, represented by the fraction of the inelastic cross-section in the second column. The impact parameters for the range of collisions in this analysis are also shown and are determined from FRITIOF simulation (see Fig. 4-6).

TABLE OF MEAN NUMBER OF PARTICIPANTS: $^{197}\text{Au} + ^{197}\text{Au}$					
Software Cut	Mean ZCAL Value (GeV)	N_{part}^{targ}	N_{part}^{proj}	N_{part}^{tot}	$\langle b \rangle$ (fm's)
^{197}Au					
0 - 4% σ_{inel}	160	183.8 ± 5	183.8 ± 5	$364. \pm 10$	1.6
0 - 10% σ_{inel}	266	172.3 ± 10	172.3 ± 10	345.5 ± 23	2.2
10 - 30% σ_{inel}	750	123.2 ± 31	123.2 ± 31	$246. \pm 42$	5.
30 - 50% σ_{inel}	1400	65.9 ± 18	65.9 ± 18	$132. \pm 37$	8.1
50 - 70% σ_{inel}	1830	31.4 ± 12	31.4 ± 12	$63. \pm 19$	10.2
70 - 90% σ_{inel}	2030	5.2 ± 7	5.2 ± 7	$10. \pm 13$	12.5
90 - 100% σ_{inel}	—	—	—	—	—

Table 5.9: Table of mean number of participants for $^{197}\text{Au} + ^{197}\text{Au}$ reactions. The numbers are determined by counting the interactions events from $E_{ZCAL} = 0$ to the desired ZCAL value represent by the fraction of the inelastic cross-section in the second column. The simulated impact parameter range for each cut is also shown (see Fig. 4-6).

Chapter 6

Results

We summarize the analysis for the ^{16}O , ^{28}Si , and ^{197}Au data sets. These three data sets represent an enormous compilation of data taken over the E802 and E866 running periods and therefore the emphasis in this chapter will be on highlighting the results. The complete data sets are shown in the appendices. A discussion of the data will be made in three primary areas:

- Particle differential yields and the appropriate fitting functions will be described. The $^{197}\text{Au} + ^{197}\text{Au}$ collisions, which produce a larger “fireball”, will be discussed in greater detail. These collisions present the best opportunity to see “collective effects” in heavy-ion collisions.
- Integrated yields for the three reaction systems provide a comparison of physics quantities over a large range of collision participants. Some of the data sets have insufficient statistics, however, for trustworthy functional fits to be made. In these cases rapidity distributions must be integrated in a defined range. This restricted, fiducial range is defined as $\tilde{Y} = \Sigma(dN/dy)\delta y$, where y_1 and y_2 are minimum and maximum rapidities. The integrated yields for all systems will be discussed and compared.
- The inverse slope parameter will also be compared and discussed for all systems.

6.1 Particle Differential Yields

The complete presentation of all differential yields, rapidity spectra and inverse slope parameters for the three data sets are given in the appendices. In this section, we highlight the data. Figures 6-1 through 6-4 show spectra of five particle species. For each collision system, the differential yields are shown in slices of rapidity, .2 units in width at or near y_{nn} . For brevity, only central reactions are shown in the comparison. These comparisons cover the full range of collision size and are sufficient to show trends of the data sets. This presentation will also provide the context for a discussion of general observations.

- Pions Both π^+ and π^- momentum spectra are well described by an exponential parameterization of the form $A e^{-p_t/B}$. This parameterization works well for the smallest ($^{16}\text{O} + ^{27}\text{Al}$) to largest ($^{197}\text{Au} + ^{197}\text{Au}$) systems. The measured momentum range is $.12 \text{ GeV}/c < p_t < .75 \text{ GeV}/c$. The inverse slope parameters are similar, but not identical, $B \approx 160 \text{ MeV}$ for π^+ and range from 140 to 150 MeV for π^- data. There is a very slight trend towards smaller B as the system size increases; however, inverse slope measurements for all systems fall within 1σ error of 160 MeV.
- Kaons The statistics for K^+ are poorer than for the pions and are even worse for the K^- . Some general observations may still be made for kaons. Differential yields for K^+ over a range $.27 \text{ GeV}/c < p_t < 1. \text{ GeV}/c$. are fairly similar. The inverse slopes measured in this comparison are very similar. Kaon differential yields cannot be distinguished by exponentials in either m_t or p_t . Insufficient coverage at low momentum in this data does not allow a distinction between the two parameterizations.
- Protons The proton data have good statistics for all reaction systems. Protons are generally not produced in these collisions (protons are created at the same rate as anti-protons and their yields are a factor of 10^{-3} smaller than proton yields). The

momentum spectra of protons are therefore not expected to behave similarly to pion and kaon spectra. Protons are well fit by both exponentials in m_t as well as by Boltzmann functions in m_t . Proton data are compared in Figure 6-4. Protons are measured in a momentum range $.5 \text{ GeV}/c < p_t < 1.8 \text{ GeV}/c$ for oxygen and silicon data and in a range $.4 \text{ GeV}/c < p_t < 1.6 \text{ GeV}/c$ for gold data. Protons measured in $^{197}\text{Au} + ^{197}\text{Au}$ collisions show a statistically significant greater inverse slope parameter than for protons from lighter-ion reactions. This is especially true for comparisons with the smallest collision systems (mid-cut) $^{16}\text{O} + ^{27}\text{Al}$ where $B=158 \pm 10 \text{ MeV}$ determined with an exponential fit in m_t . Measurements of $^{197}\text{Au} + ^{197}\text{Au}$ proton inverse slope parameters near $y = y_{nn}$ ($y = 1.45$) show exceptionally high inverse slope parameters, $B = 320 \pm 40 \text{ MeV}$. These inverse slope parameters are the highest measured for any particles of any collision system at AGS energies.

6.1.1 Pions: Ratios and Multiplicity Dependencies

Pion ratios π^+/π^- for central collisions are shown in Fig. 6-5 as a functions of transverse momentum. These ratios provide another way to compare data sets and look for Coulomb effects in heavy-ion collisions. Pion ratios measured in oxygen and silicon reactions are typically flat and have a ratio near unity. There are initially an equal number of protons and neutrons in the lighter-ion collisions. Isospin conservation dictates that a net increase of π^- (isospin -1) occurs for the neutron rich collisions. The gold nuclei have a large net negative isospin, $p/n=79/118 = 0.66$ or $I_{tot} = -19 \frac{1}{2}$. This net negative isospin will enhance a net π^- production. Not surprisingly, we see that the π^+/π^- ratio is down by about 20 - 30 % from unity at small momenta. A line representing these isospin ratios is drawn for comparison with the data.

At small transverse momentum, there is generally good agreement with this ratio. At high p_t , the π^+/π^- ratio typically becomes unity. Another reasonable explanation for π^- excess at low momentum is Coulomb attraction of the π^- . Similarly there is a repulsion of π^+ from the large positive baryon participant source. Both effects are on the

Comparison of π^+ spectra for $y = y_{nn}$

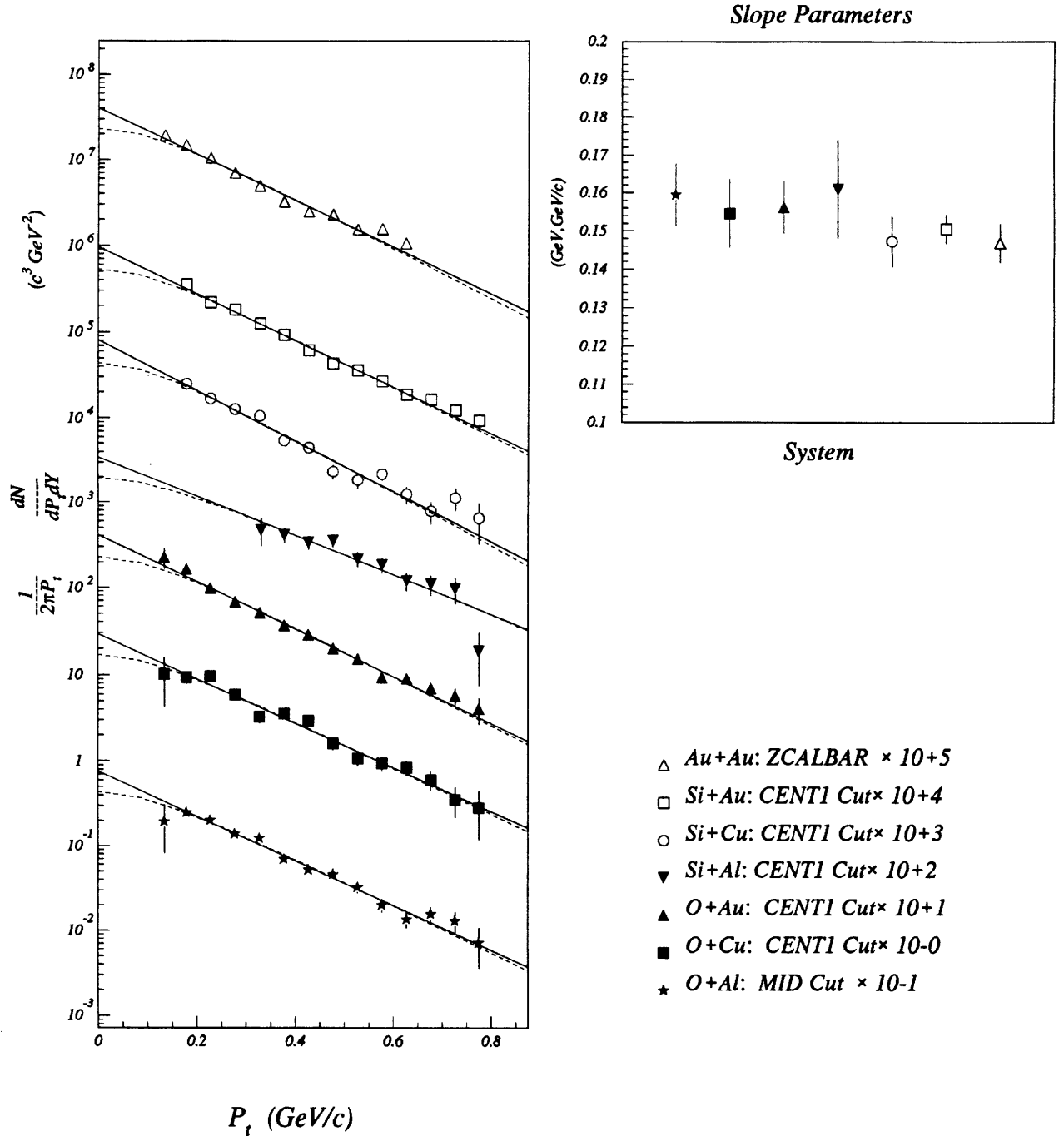


Figure 6-1: Comparison of differential yields for π^+ at y_{nn} in $^{16}\text{O} + \text{A}$, $^{28}\text{Si} + \text{A}$, and $^{197}\text{Au} + \text{A}$ collisions. All systems are fit by exponentials of the form $Ae^{-m_t/B}$ (dashed) and $Ae^{-p_t/B}$ (solid).

Comparison of π^- spectra for $y = y_{nn}$

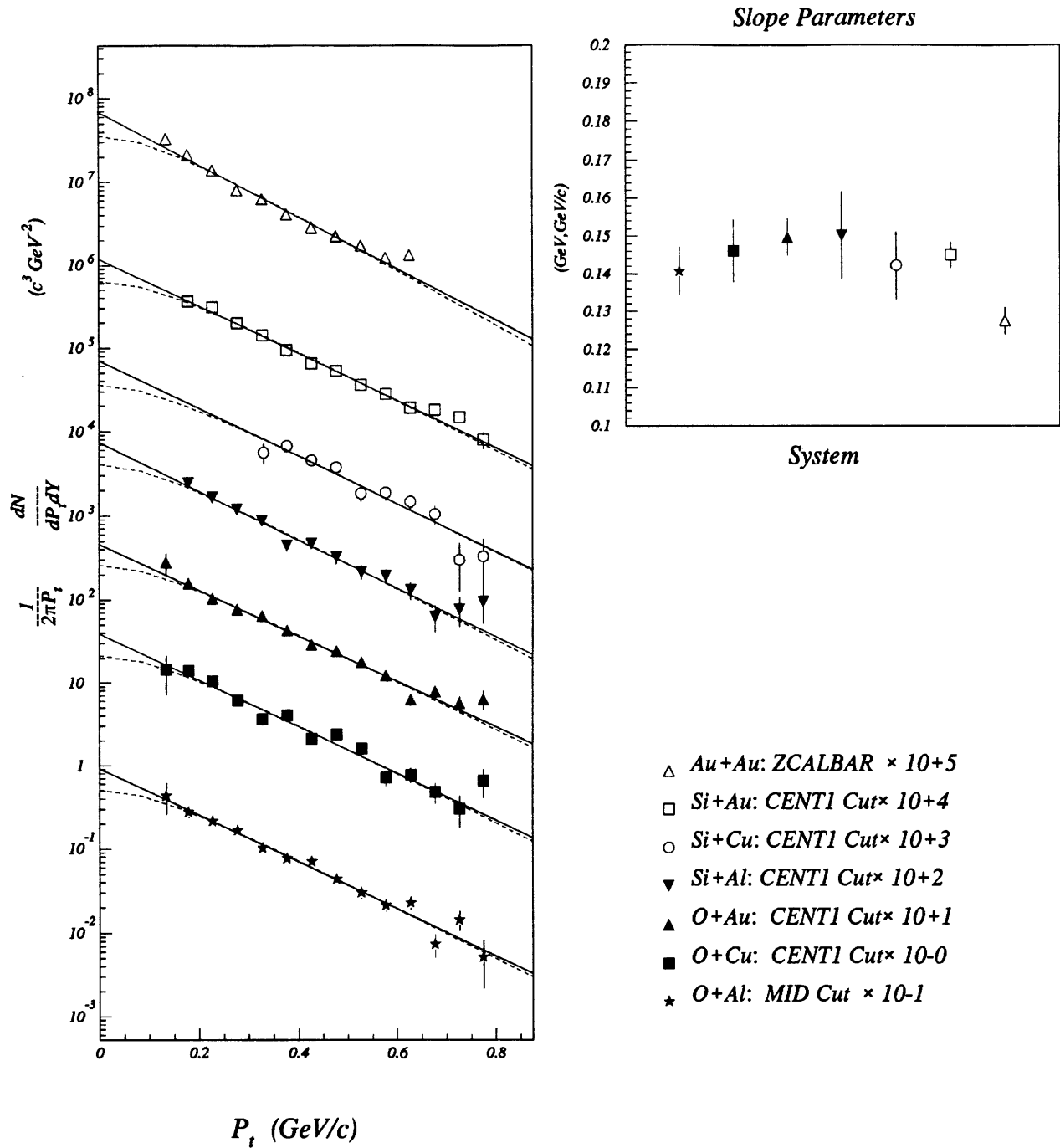


Figure 6-2: Comparison of differential yields for π^- at y_{nn} in $^{16}\text{O} + \text{A}$, $^{28}\text{Si} + \text{A}$, and $^{197}\text{Au} + \text{A}$ collisions. All systems are fit by exponentials of the form $Ae^{-m_t/B}$ (dashed) and $Ae^{-p_t/B}$ (solid).

Comparison of K^+ spectra for $y = 1.5$

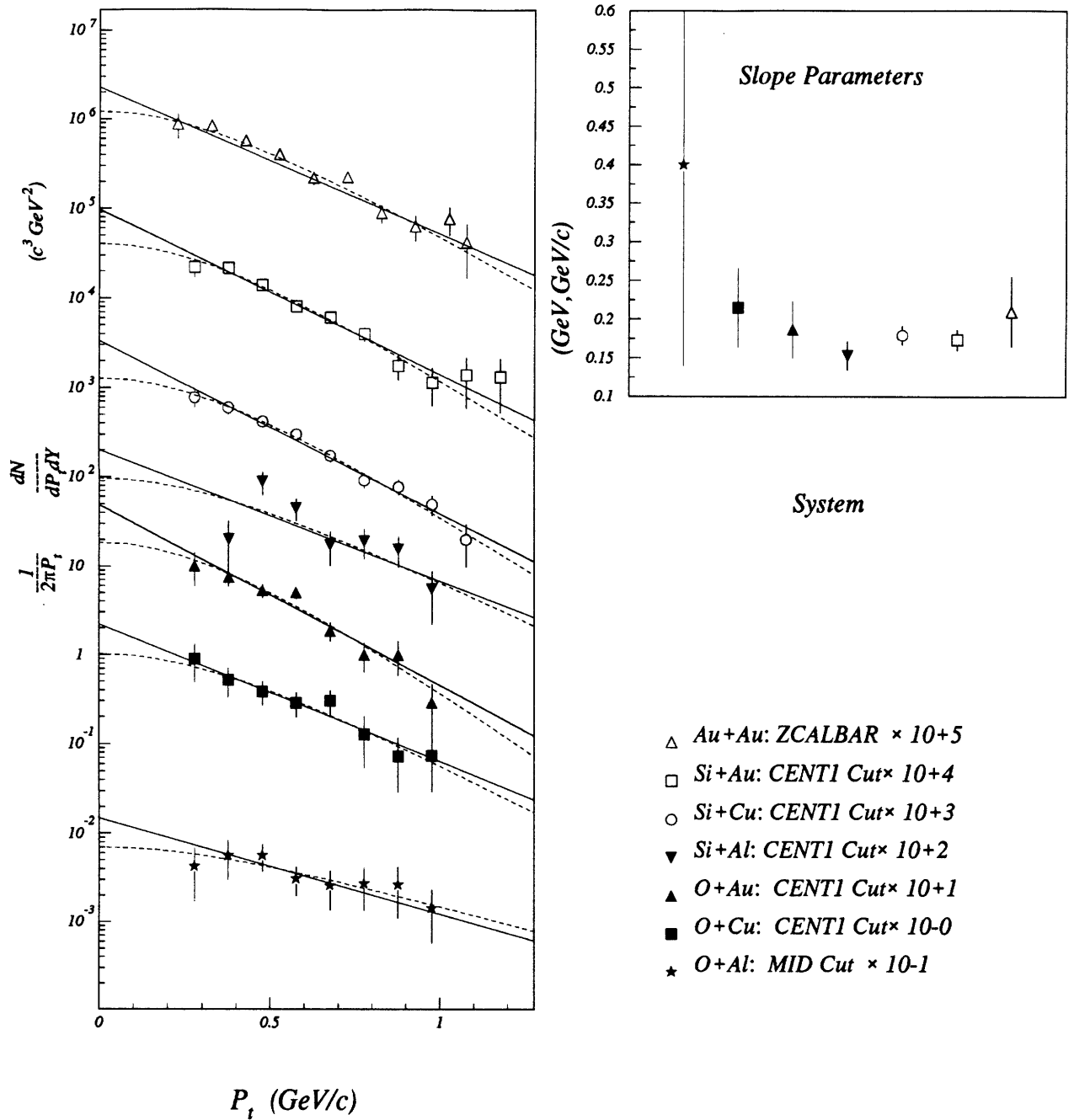


Figure 6-3: Comparison of differential yields for K^+ 's at $y = 1.5$ in $^{16}\text{O} + \text{A}$, $^{28}\text{Si} + \text{A}$, and $^{197}\text{Au} + \text{A}$ collisions. All systems are fit by exponentials of the form $Ae^{-m_t/B}$ (dashed) and $Ae^{-p_t/B}$ (solid). Rapidity slices were combined, due to insufficient statistics.

Comparison of Proton spectra for $y = 1.3$

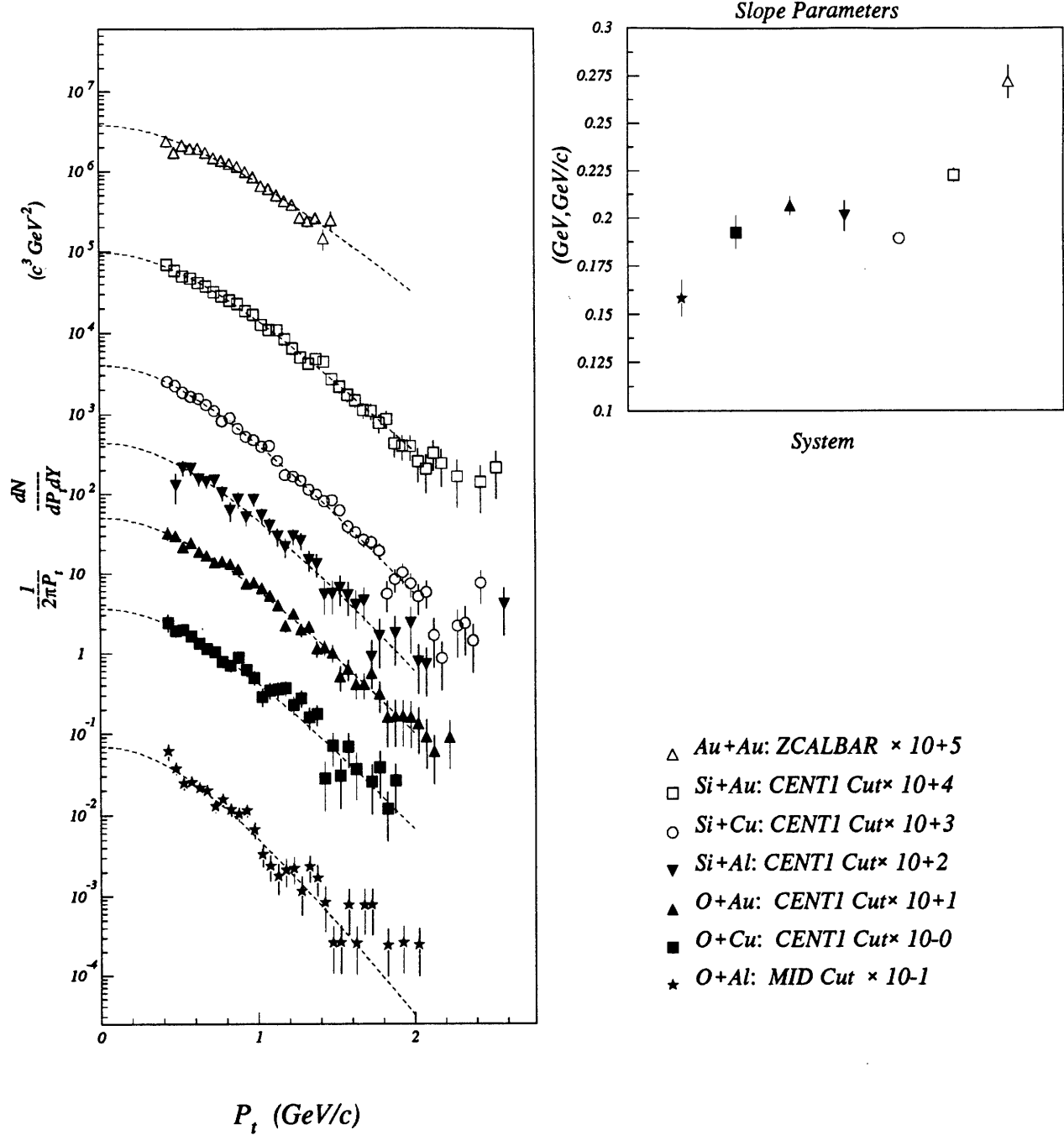


Figure 6-4: Comparison of differential yields for protons at $y = 1.3$ in $^{16}\text{O} + \text{A}$, $^{28}\text{Si} + \text{A}$, and $^{197}\text{Au} + \text{A}$ collisions. All systems are fit by exponentials of the form $Ae^{-m_t/B}$. Note the exceptionally high inverse slope parameters for central $^{197}\text{Au} + ^{197}\text{Au}$ collisions. Inverse slope parameters for $y=1.5$ are even higher in this reaction system ($B = 320 \pm 40$ MeV at $y = 1.5$).

order of 10 MeV.

Are there interesting collective effects occurring in central $^{197}\text{Au} + ^{197}\text{Au}$ collisions that may be observed in π^+ and π^- yields? To check this, a simple multiplicity dependant comparison of π^+ and π^- was performed for central $^{197}\text{Au} + ^{197}\text{Au}$ collisions. If there are regions of quark gluon plasma being formed in the large gold reactions, entropy is expected to be higher in these regions. Perhaps copious pion production would occur at low momentum as these systems hadronize. If this were the case, we might expect to observe anomalously high π^+ and π^- yields at low momentum for events with large multiplicities. A crude multiplicity measurement was done comparing central $^{197}\text{Au} + ^{197}\text{Au}$ collisions with central collisions when at least two pions were detected in the spectrometers, (see Fig. 6-6). There does not appear to be statistically significant differences in momentum spectra for either π^+ or π^- . A similar test was done for 3 pions in the spectrometer (again of either sign) and with poorer statistics. Again, no difference was found in comparison to the unbiased central data.

6.2 Rapidity Distributions

We would like to understand trends in particle yields with the size of the “fireball” produced in the collision for each particle species. We reach this goal in several steps. First, we construct the transverse momentum distribution for each particle species. We next obtain integrated yields for each rapidity slice. We first discuss the particle yields of separate particle species and then discuss π^+ / K^+ ratios.

There are some differences that need to be noted in this analysis in comparison to earlier work. This work has used the calorimeter as the event characterizer. Most central data presented in earlier publications are TMA triggered data (events of high multiplicity). Some differences in rapidity spectra will be noted, as appropriate in the discussion. Most differences are small and fall within systematic errors of the measurements. Figures 6-7 through 6-12 show complete rapidity distributions for π^\pm , K^\pm , and protons. These

π^+/π^- Ratio for $y = y_{part}$

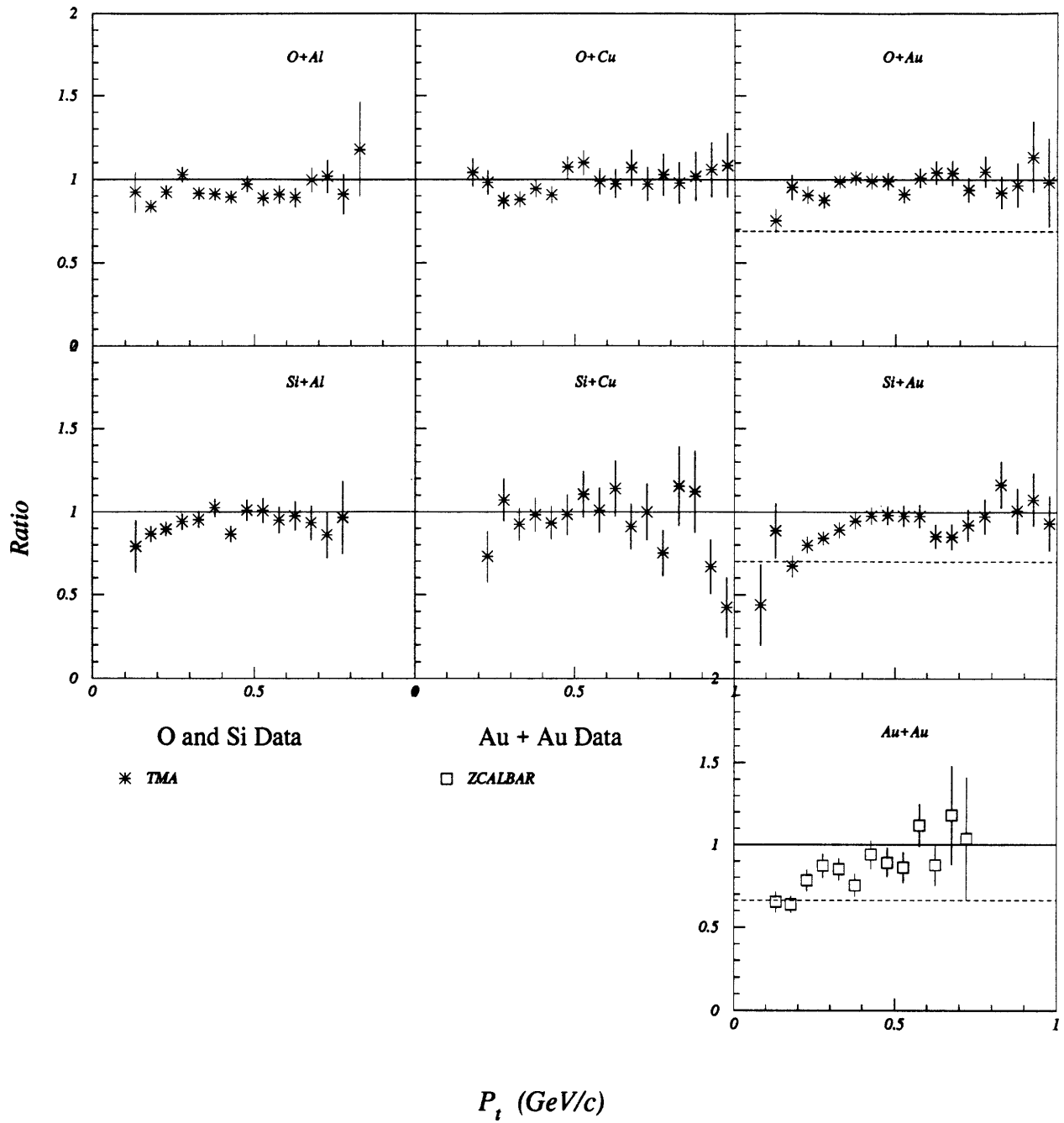


Figure 6-5: π^+/π^- ratios for central collision data as a function of p_t for $^{16}\text{O} + \text{A}$, $^{28}\text{Si} + \text{A}$, and $^{197}\text{Au} + \text{A}$ collisions. All data are taken at mid-rapidity in a rapidity slice, $\Delta y = .2$.

Multiplicity dependant π cross-sections: $y=y_{nn}$

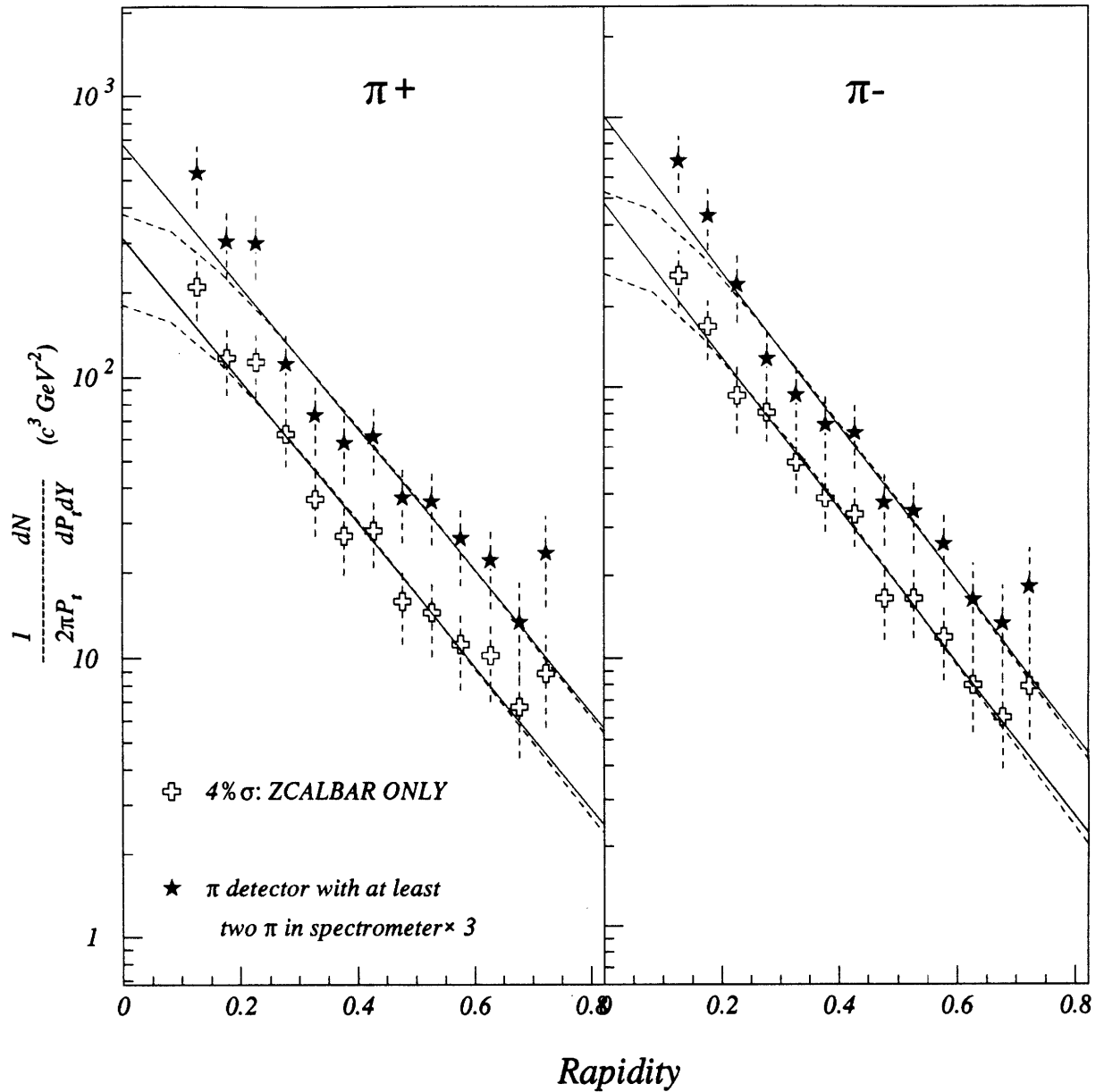


Figure 6-6: π^\pm multiplicity comparison. Pions at y_{nn} measured when there were at least two pions in the spectrometer (either charge) are compared to the unbiased central (ZCALBAR: 4% σ_{inel}) $^{197}\text{Au} + ^{197}\text{Au}$ pions. There are no striking differences in shape of the two spectra.

distributions are created by integrating the differential yields in each rapidity slice.

Pions Both π^+ and π^- rapidity distributions are displayed for all offline software cuts on minimum bias data. Oxygen data sets are shown with TMA triggered data. $^{28}\text{Si} + ^{27}\text{Al}$ and $^{197}\text{Au} + ^{197}\text{Au}$ data sets have been reflected about mid-rapidity as they are symmetric systems. Some general observations may be made.

- π yields increase with centrality for all systems.
- Most π distributions are Gaussian-like in shape.
- The π yields from the most central cuts for lighter-ions are ≈ 10 times greater than the most peripheral cuts. Pion yields from central $^{197}\text{Au} + ^{197}\text{Au}$ collisions are 100 times greater than pion yields from peripheral $^{16}\text{O} + ^{27}\text{Al}$ collisions.
- More peripheral offline cuts are flatter and non-Gaussian in shape when compared to the more central data sets. Part of this effect may be due to poorer determinations of yields with fewer statistics in peripheral cuts. We probably can rule out a difference in shape attributed to less kinetic randomization of π 's in peripheral collisions. Pion yields from pBe reactions, for example, are also Gaussian in shape [Abb92a].
- The yields for π 's from mid-central and peripheral offline cuts of data do *not* drop around rapidity $y \approx 1.8 - 2.0$ as do the central data. There is no known reason for this as fits to the momentum distributions appear to be good, despite the smaller lever-arm in p_t range. The p_t coverage is typically $200 \text{ MeV} < p_t < 600 \text{ MeV}$ for $y = 1.8 - 2.0$ for lighter-ion data. Any small systematic errors in fitting this limited distribution range may preferentially distort the yields.

It would be interesting to further study non-central π production in “shadowing” experiments with large asymmetric $^{197}\text{Au} + \text{A}$, $\text{A} < 197$ collisions, where there are great abundances of non-participant matter to distort the pion distributions.

dN/dY Summary : π^+

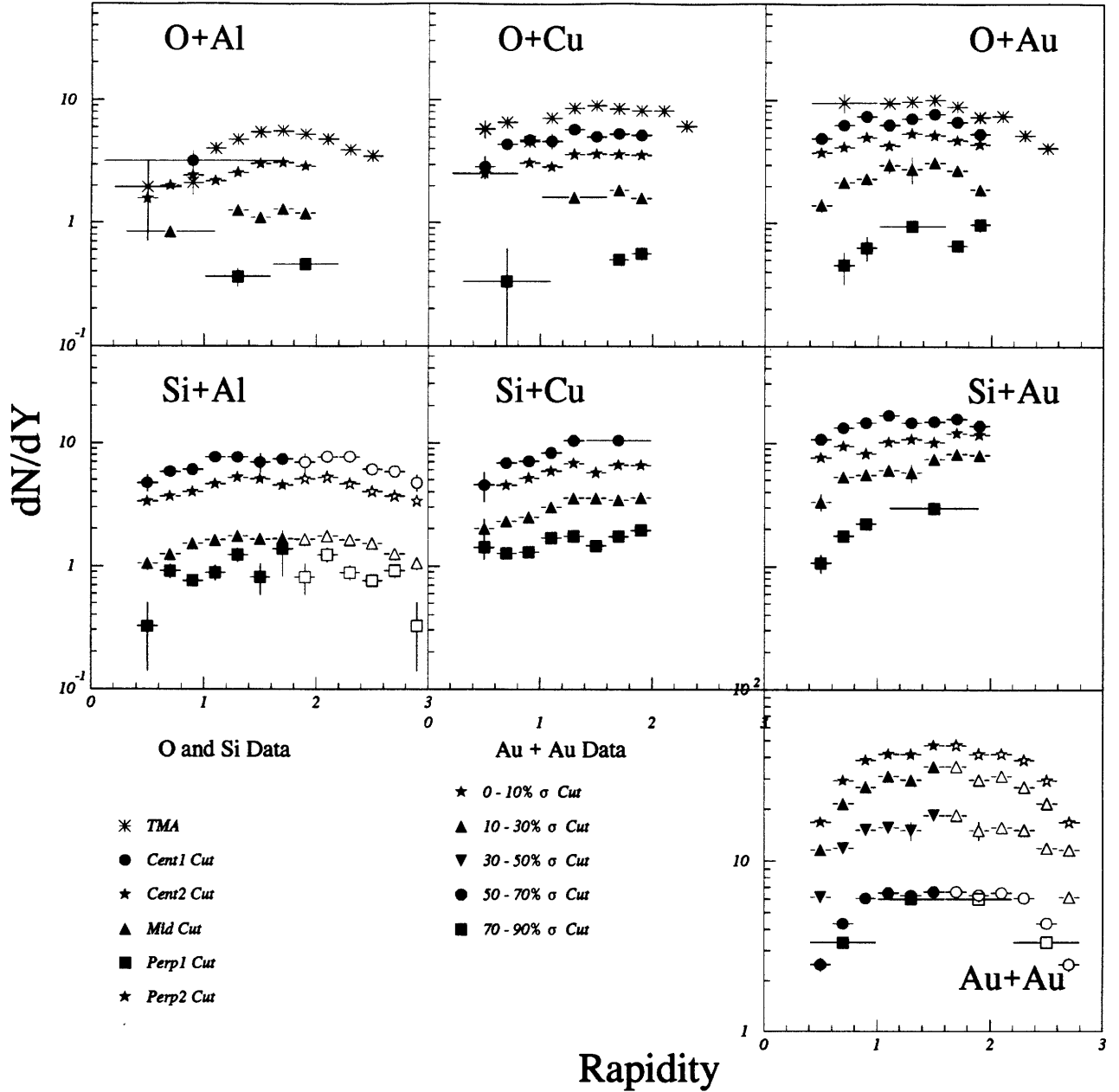


Figure 6-7: Full dN/dy comparison for π^+ in $^{16}\text{O} + \text{A}$, $^{28}\text{Si} + \text{A}$, and $^{197}\text{Au} + \text{A}$ collisions. Exponentials in p_t are fit to the momentum spectra and integrated to give dN/dy . Horizontal error bars represent rapidity bin widths. Tables 5.6 and 5.7 give values for the fraction of σ_{inel} for offline calorimeter cuts. The open points are reflected data about Y_{nn} .

dN/dY Summary : π^-

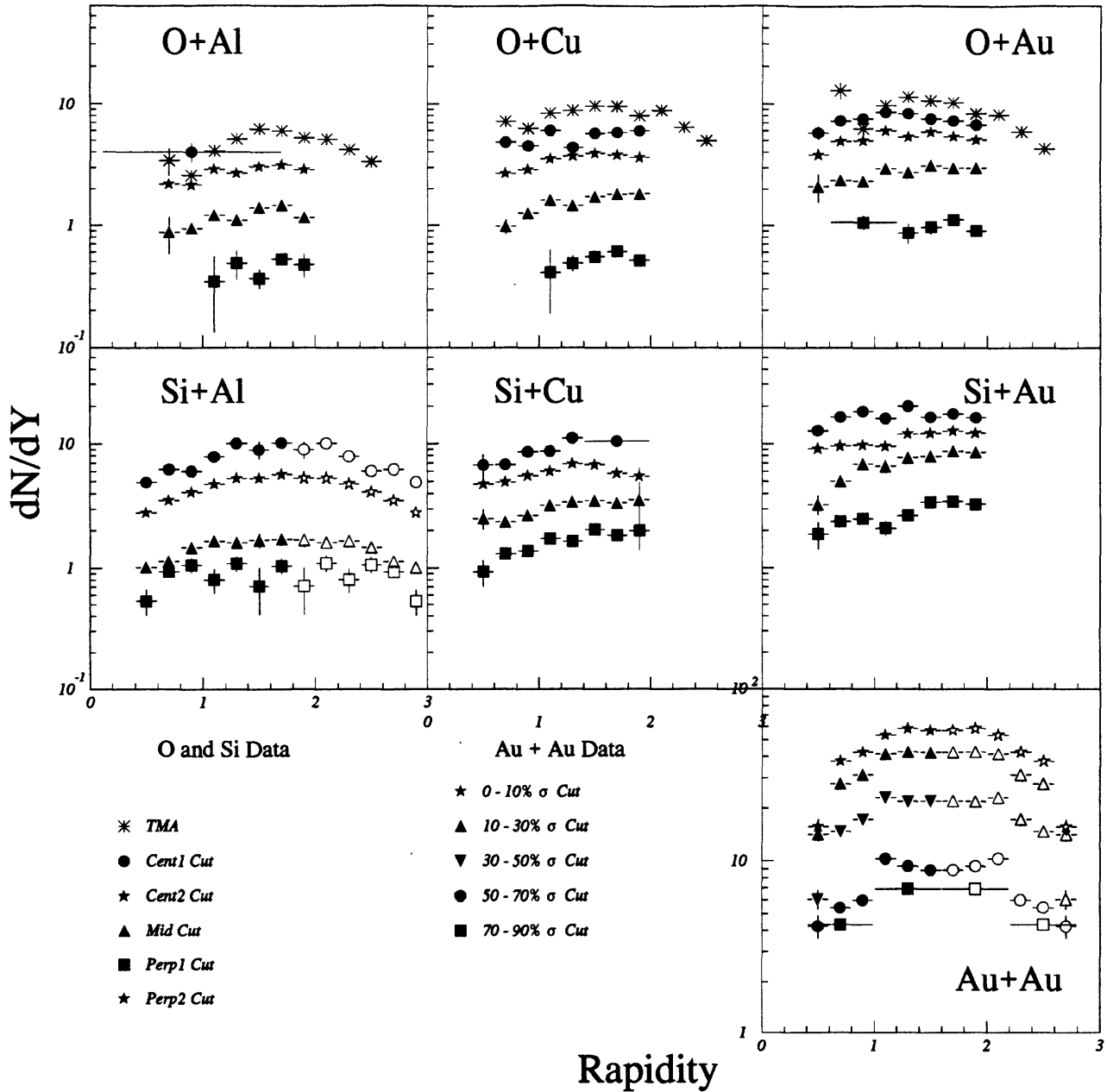


Figure 6-8: Full dN/dy comparison for π^- in $^{16}\text{O} + \text{A}$, $^{28}\text{Si} + \text{A}$, and $^{197}\text{Au} + \text{A}$ collisions. Exponentials in p_t are fit to the momentum spectra and integrated to give dN/dy . Horizontal error bars represent rapidity bin widths. Tables 5.6 and 5.7 give values for the fraction of σ_{inel} for offline calorimeter cuts. The open points are reflected data about y_{nn} .

dN/dY Summary : K⁺

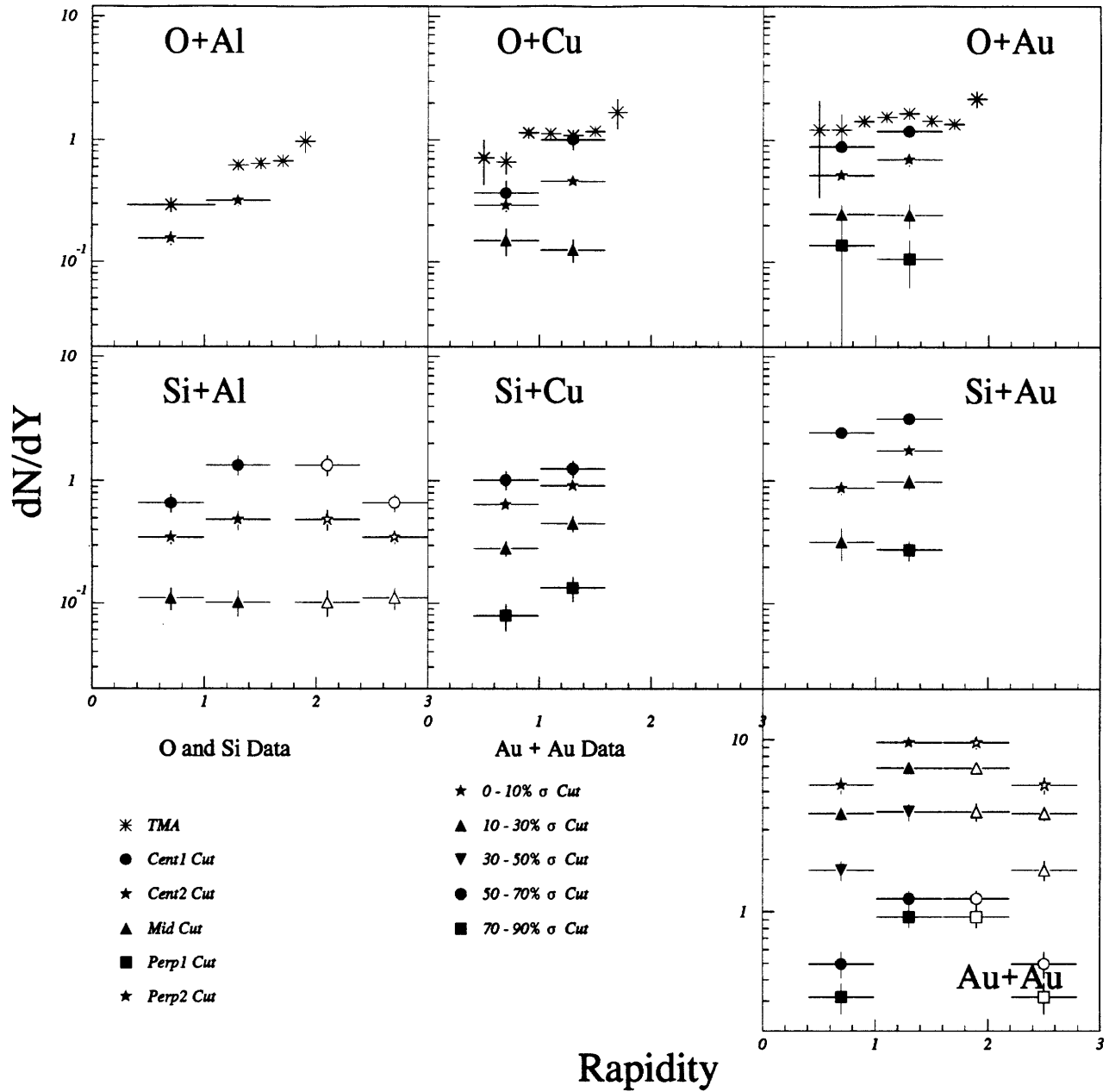


Figure 6-9: Full dN/dy comparison for K⁺ in ¹⁶O + A, ²⁸Si + A, and ¹⁹⁷Au + A collisions. Exponentials in m_t are fit to the momentum spectra and integrated to give dN/dy. Horizontal error bars represent rapidity bin widths. Tables 5.6 and 5.7 give values for the fraction of σ_{inel} for offline calorimeter cuts. The open points are reflected data about y_{nn} .

dN/dY Summary : K-

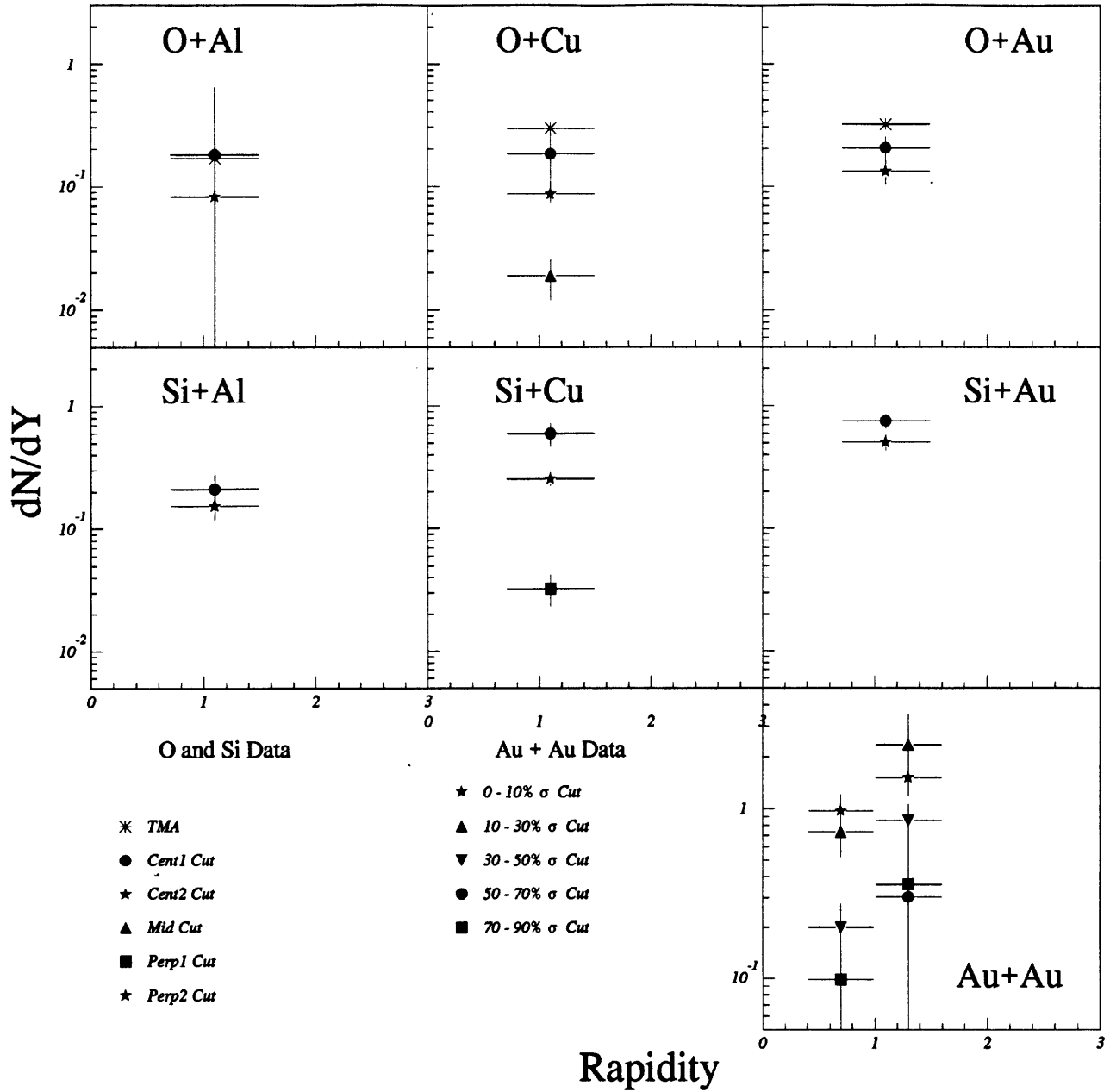


Figure 6-10: Full dN/dy comparison for K^- in $^{16}\text{O} + \text{A}$, $^{28}\text{Si} + \text{A}$, and $^{197}\text{Au} + \text{A}$ collisions. Exponentials in m_t are fit to the momentum spectra and integrated to give dN/dy . Horizontal error bars represent rapidity bin widths. Tables 5.6 and 5.7 give values for the fraction of σ_{inel} for offline calorimeter cuts. The open points are reflected data about y_{nn} .

dN/dY Summary : Proton

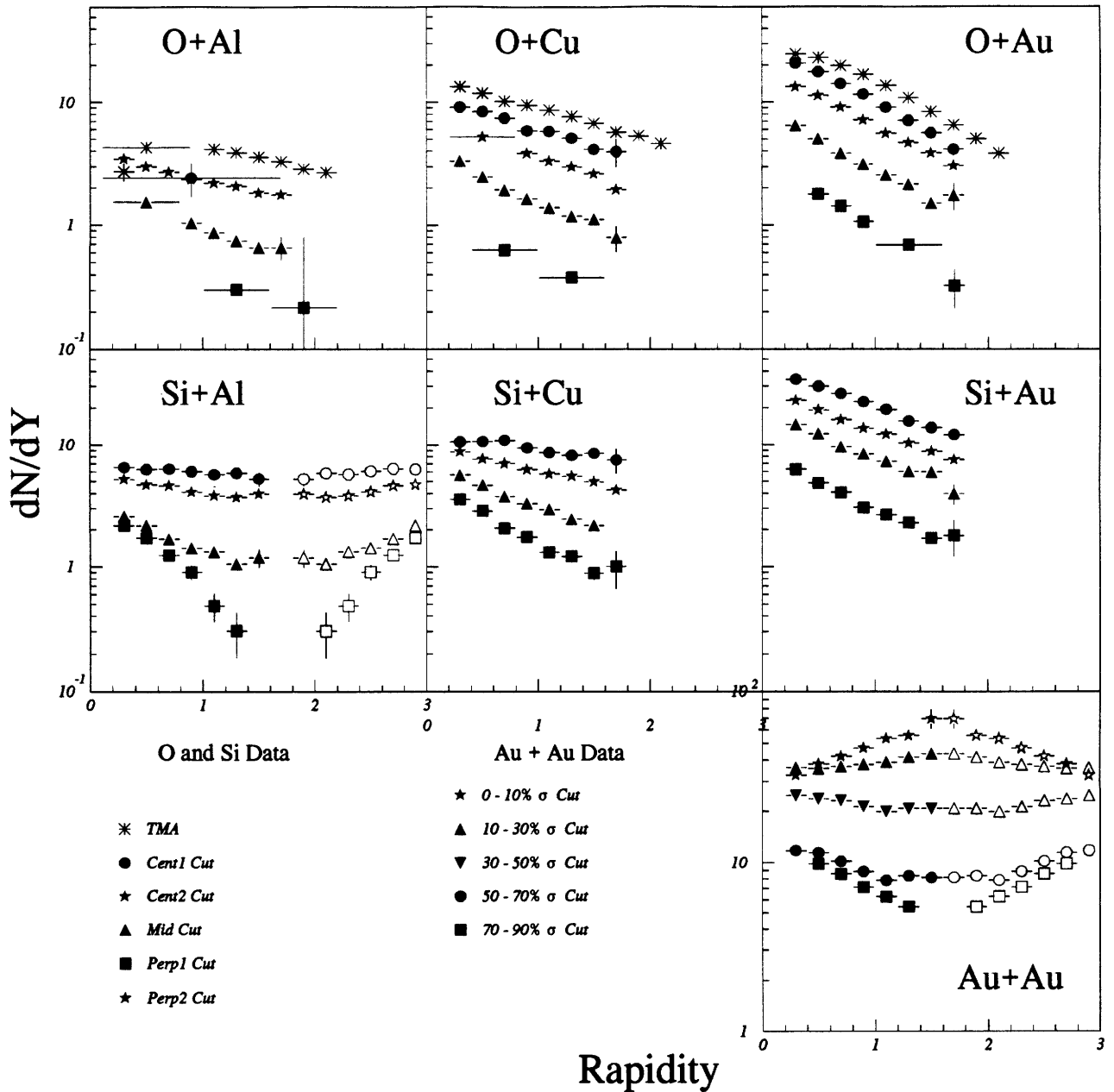


Figure 6-11: Full dN/dy comparison for protons in $^{16}\text{O} + \text{A}$, $^{28}\text{Si} + \text{A}$, and $^{197}\text{Au} + \text{A}$ collisions. Exponentials in m_t are fit to the momentum spectra and integrated to give dN/dy . Horizontal error bars represent rapidity bin widths. Tables 5.6 and 5.7 give values for the fraction of σ_{inel} for offline calorimeter cuts. The open points are reflected data about y_{nn} .

dN/dY Summary Central $^{197}\text{Au} + ^{197}\text{Au}$

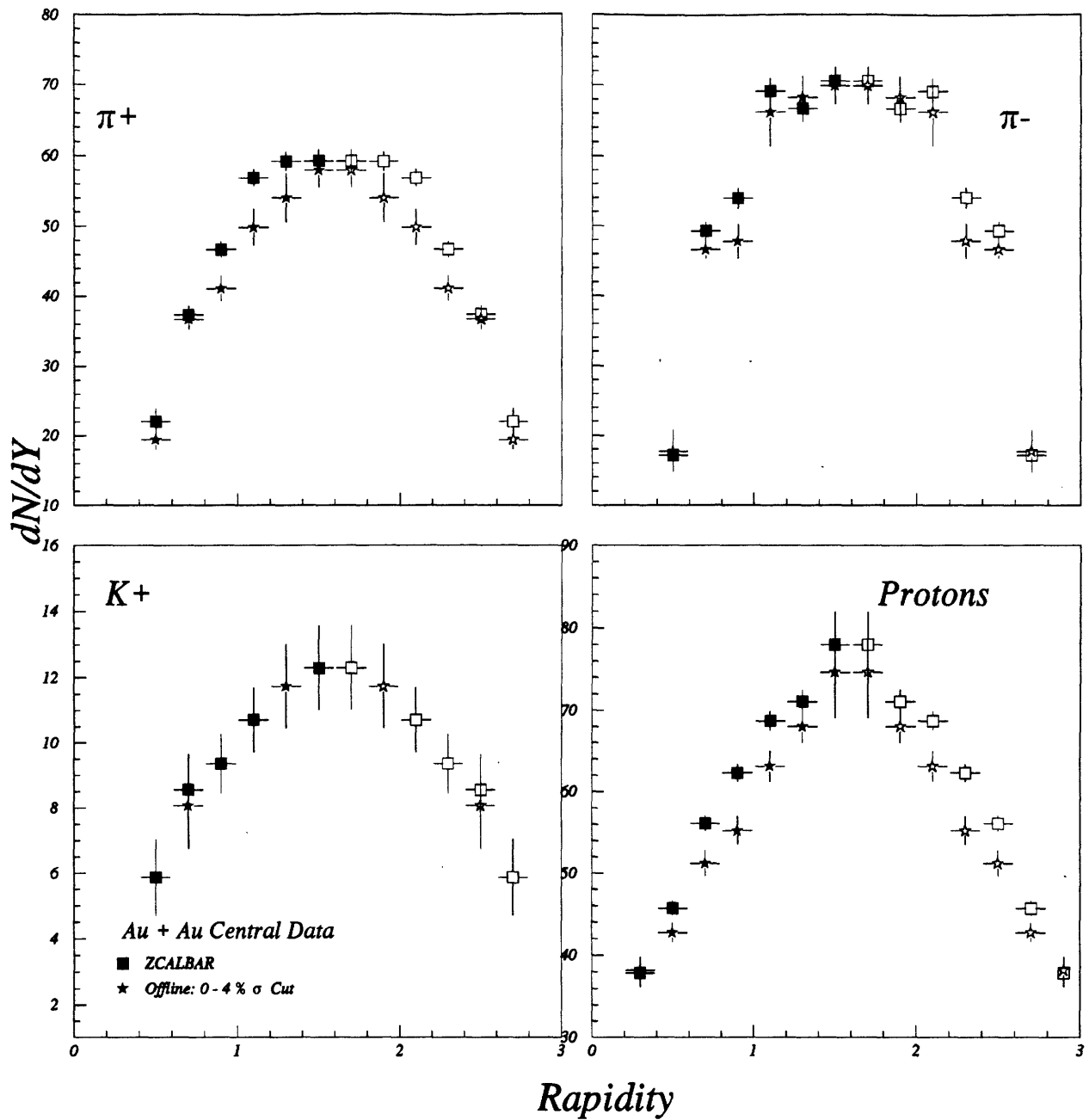


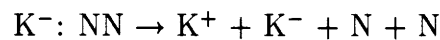
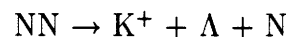
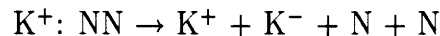
Figure 6-12: Full dN/dy comparison for central $^{197}\text{Au} + ^{197}\text{Au}$ collisions. Distributions are formed by fitting exponentials in m_t to the differential yields. Horizontal errors represent rapidity bin widths. The systematic errors are typically $\pm 15\%$.

Pions from central and middle cuts (CENT1 and MID) for $^{28}\text{Si} + ^{27}\text{Al}$ collisions roughly match the fractions of inelastic cross-section for cuts made in recent E802 publications. Pion yields from central (upper 7% TMA) and peripheral (lower 50% TMA) collisions are consistent to the 5% level with pion yields measured in this analysis with CENT1 (upper 10% σ_{inel}) and MID (40 - 90% σ_{inel}) collisions. Pion yields in central $^{28}\text{Si} + ^{64}\text{Cu}$ and $^{28}\text{Si} + ^{197}\text{Au}$ collisions are also consistent to the 5% level with pion yields of recently publishes E802 $^{28}\text{Si} + \text{A}$ results [Abb94].

Kaons Kaon rapidity distributions are shown in Figures 6-9 and 6-10. Some general observations are made for the kaon data.

- The kaon yields from the most central cuts for lighter-ions are ≈ 10 times greater than the most peripheral cuts. Kaon yields from central $^{197}\text{Au} + ^{197}\text{Au}$ collisions are 100 times greater than the kaon yields from peripheral $^{16}\text{O} + ^{27}\text{Al}$ collisions.
- Both K^+ and K^- yields increase with the size of the system and with the centrality of the collision.
- Only rough comparisons can be made with the K^- data sets because of very poor statistics. Current work with K^- triggering for $^{197}\text{Au} + ^{197}\text{Au}$ data (as well as with lighter-ions) will better determine the centrality dependence of K^- .

Yields for K^+ are about 5 times greater than for K^- . Most of the difference is accounted for by the different production mechanisms available for the two particles. Associated production of K^+ has a smaller threshold than has pair production for K^- . Typical production reactions include,



Protons Figure 6-12 shows the complete proton data set. Proton data have good

statistics, even for the most peripheral cuts in ZCAL. Very different rapidity distributions are seen for protons.

- Asymmetric lighter-ion proton data are characterized by decreasing yields, falling nearly exponentially in rapidity. This decreasing trend is apparent in both central, mid-central and peripheral data sets. The symmetric central $^{28}\text{Si} + ^{27}\text{Al}$ system does show a flatter dN/dy distribution, compared to the other lighter-ion data sets and are similar to proton distributions from central TMA data sets.
- Mid-central and peripheral $^{28}\text{Si} + ^{27}\text{Al}$ protons are more characteristic of the asymmetric lighter-ion data sets, where yields are high at target rapidities and low at central rapidities.
- Mid-central (30-50 % σ_{inel}) and peripheral (70-90% σ_{inel}) $^{197}\text{Au} + ^{197}\text{Au}$ protons are flat and decreasing towards y_{nn} , much like central and peripheral lighter-ion protons.

Protons from central $^{28}\text{Si} + ^{27}\text{Al}$ collisions are in agreement within statistical errors with proton yields from TMA triggered data presented in a recent E802 publication [Abb94]. Proton yields from central $^{28}\text{Si} + ^{64}\text{Cu}$ and $^{28}\text{Si} + ^{197}\text{Au}$ collisions are also in good agreement (at the 5% level) with published results.

The central $^{197}\text{Au} + ^{197}\text{Au}$ protons rise at mid-rapidity. This is the only system that displays proton yields that are peaked at y_{nn} . Figure 4-4 shows a RQMD simulation of minimum bias $^{197}\text{Au} + ^{197}\text{Au}$ data. The contribution to the mean number of binary collisions changes dramatically for $y \leq 7$. This corresponds approximately to the upper 30 - 50 % σ_{inel} range, see Table 5.7. The protons observed in this range exhibit peaking distributions at y_{nn} . Contributions from secondary collisions with pions and other baryons are probably responsible for shifting protons from the original $y=0$ (target rapidity) and $y=3.2$ (beam rapidity) to central rapidities.

K⁺/π⁺ RAPIDITY DEPENDENT RATIOS

System	Trigger	Ratio
¹⁶ O + ²⁷ Al	TMA	.14 ± .05
¹⁶ O + ⁶⁴ Cu	TMA	.145 ± .05
¹⁶ O + ¹⁹⁷ Au	TMA	.175 ± .04
²⁸ Si + ²⁷ Al	CENT1	.105 ± .02
²⁸ Si + ⁶⁴ Cu	CENT1	.178 ± .04
²⁸ Si + ¹⁹⁷ Au	CENT1	.195 ± .03
¹⁹⁷ Au + ¹⁹⁷ Au	<i>ZCAL</i>	.22 ± .04

Table 6.1: Summary of ¹⁶O, ²⁸Si, and ¹⁹⁷Au K⁺/π⁺ ratios using central (TMA) oxygen data and central (CENT1) ²⁸Si data. Comparisons are made with central ¹⁹⁷Au data.

6.2.1 K⁺/π⁺ Ratios

Several features of heavy-ion collisions may be learned from studying the rapidity dependant K⁺/π⁺ ratios. Figure 6-13 shows K⁺/π⁺ ratios for ¹⁶O + A, ²⁸Si + A, and ¹⁹⁷Au + ¹⁹⁷Au central collisions. One of the more significant features of the comparison is the increasing ratios for larger collisions. The ratio almost doubles from the smallest to largest collisions and all values are enumerated in Table 6.1. Furthermore, the K⁺/π⁺ ratios are relatively flat in rapidity for all data sets. The K⁺/π⁺ ratios of central ²⁸Si + A reactions are consistent with ratios from recently published results [Abb94].

6.3 Inverse Slope Parameters.

Before discussing integrated yields, we look at the inverse slope parameters for the various collisions. Exponential fits are determined by minimizing χ^2 for the parameters A and B as in the form $Ae^{-p_t/B}$. We use exponentials in p_t for pions and exponentials in m_t for kaons and for protons. Some general observations are made for the comparisons in Figure 6-14 .

Pions

- Both π⁺ and π⁻ inverse slope distributions have a similar rapidity dependence, very broadly peaked and Gaussian-like in shape. This is true for all targets and

K^+/π^+ Ratio

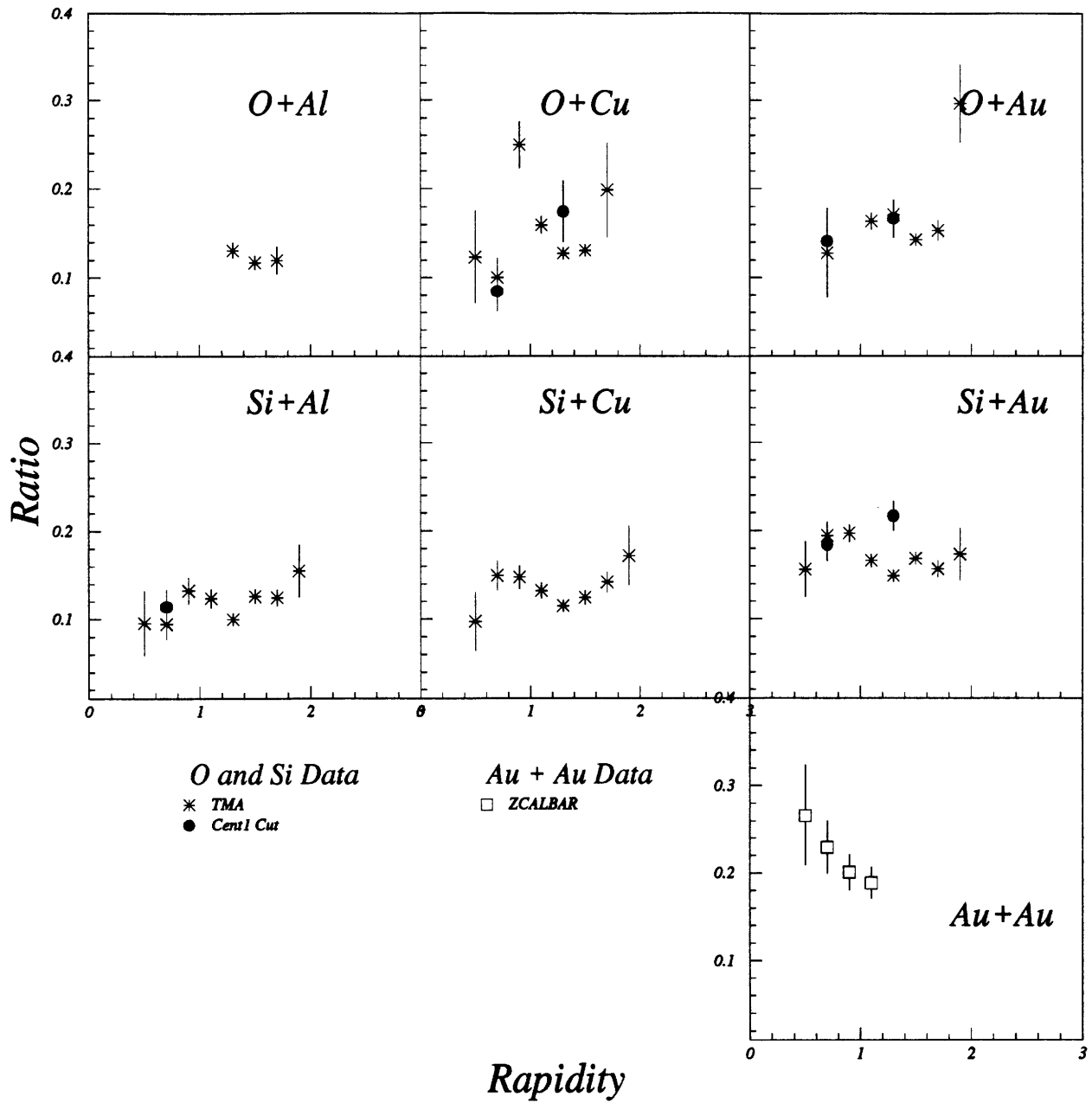


Figure 6-13: K^+/π^+ ratios for ^{16}O , ^{28}Si , and $^{197}Au + A$ collisions. Distributions are flat in rapidity and systematically increase from about 12 - 23 % from $^{16}O + ^{27}Al$ to $^{197}Au + ^{197}Au$ collisions.

Slope Parameters: Central Events

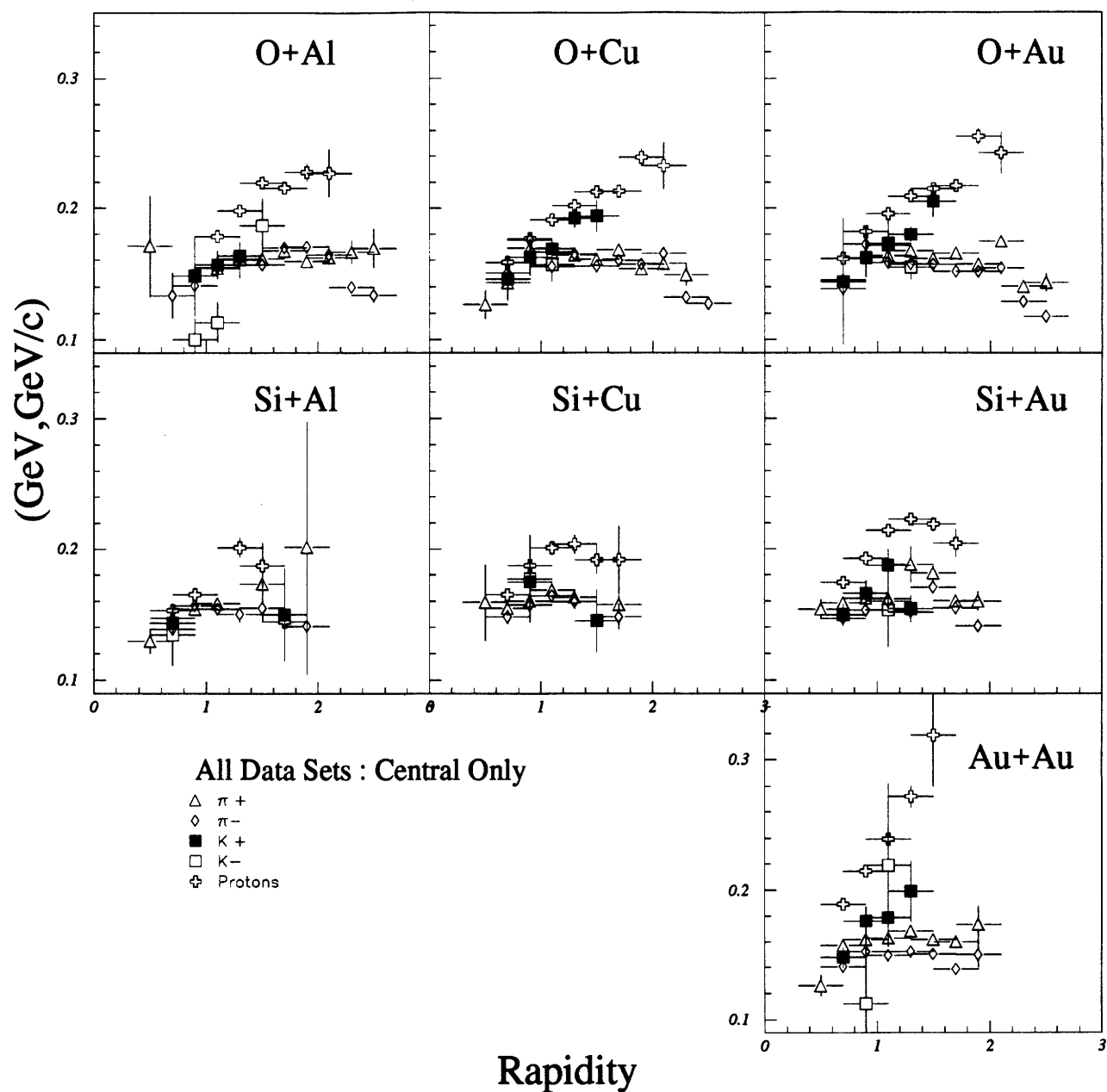


Figure 6-14: Inverse slope parameters for π^+ , π^- , K^+ , K^- and protons in central $^{16}\text{O} + \text{A}$, $^{28}\text{Si} + \text{A}$, and $^{197}\text{Au} + \text{A}$ collisions. $^{16}\text{O} + \text{A}$ central data sets are defined with the TMA and the $^{28}\text{Si} + \text{A}$ data sets are defined with an offline CENT1 cut. The $^{197}\text{Au} + ^{197}\text{Au}$ data points are measured using hardware $\overline{\text{ZCAL}}$ data.

centrality ranges for data shown (see appendices). This Gaussian-like distribution is expected from the thermal emission of a hot fireball.

- Pion inverse slope parameter distributions are similar from peripheral $^{16}\text{O} + ^{27}\text{Al}$ to central $^{197}\text{Au} + ^{197}\text{Au}$ collisions.
- Pion inverse slope parameters have a weak rapidity dependence.

Pion inverse slope distributions from central $^{28}\text{Si} + \text{A}$ reactions are all consistent (to the 10% level) with recently published TMA results [Abb94].

Kaons

- Kaon inverse slope parameters are more sharply peaked than pion inverse slope parameters.
- Kaon inverse slope parameters range from ≈ 160 MeV for peripheral $^{16}\text{O} + ^{27}\text{Al}$ collisions to 180 MeV for central $^{197}\text{Au} + ^{197}\text{Au}$ collisions.
- Statistics for K^- are too poor to make any definitive statement with these data.

Protons

- Proton inverse slope parameters are more sharply peaked than either pion or kaon inverse slope parameters.
- Proton inverse slope parameters range from a peak value of ≈ 200 MeV for central $^{16}\text{O} + ^{27}\text{Al}$ collisions to 320 ± 40 MeV for central $^{197}\text{Au} + ^{197}\text{Au}$ collisions.

The effects of multiple scattering and rescattering are once again evident in the comparison. Figure 4-4 gives evidence of the number of collisions for $^{28}\text{Si} + ^{27}\text{Al}$ and $^{197}\text{Au} + ^{197}\text{Au}$ reactions. A proton from a central $^{28}\text{Si} + ^{27}\text{Al}$ collision undergoes about 100 to 120 /53 or about $2 \sim 3$ total collisions. A proton from a $^{197}\text{Au} + ^{197}\text{Au}$ central collision undergoes about $2000/394 \sim 5$ collisions on average. Protons in the center of the collision

will undergo many more than this. The net effect is that protons “heat up”, or more quantitatively, their average transverse momentum increases with the number of binary collisions [Blo90], [Par92].

6.4 Integrated Yields

We integrate dN/dy distributions to determine a single yield for each collision system. Yields of π^+ , π^- , and K^+ are determined and plotted as a function of participants in the collision. We choose two methods to determine the participants in the collision; (1) integrated yields are plotted in terms of a mean experimental participant number defined as

$$\text{PROJ. PARTICIPANT} = \frac{(\text{TOTAL BEAM ENERGY} - \langle \text{ZCAL} \rangle)}{(\text{KINETIC ENERGY PER NUCLEON})}, \quad (6.1)$$

and (2) integrated yields are plotted in terms of a mean number of participants as determined with “clean-cut geometry” (input to FRITIOF). We emphasize the comparison between $^{28}\text{Si} + ^{27}\text{Al}$ and $^{197}\text{Au} + ^{197}\text{Au}$ pions and kaons using the two methods and then discuss a comparison of results with the RQMD and ARC models.

Fiducial yields are defined as ($\tilde{Y} = \int_{y_1}^{y_2} (dn/dy) dy$) and are examined first. Total yields are also determined by parameterizing the yields with a Gaussian distribution. Figures 6-15 and 6-16 show the fiducial yields for pions from $^{28}\text{Si} + ^{27}\text{Al}$ and $^{197}\text{Au} + ^{197}\text{Au}$ systems.

Comparisons are made with 5000 minimum bias RQMD and 10000 ARC events. The ZCAL acceptance is used to determine projectile participants in a similar fashion for measured data. Integrated pion yields are determined by parameterizing the simulated yields using exponentials in p_t in the experimental acceptance. Pion yields from RQMD are 30 to 40% larger than measured yields for the most central gold collisions. Yields from $^{28}\text{Si} + ^{27}\text{Al}$ collisions and more peripheral $^{197}\text{Au} + ^{197}\text{Au}$ collisions better match

Fiducial Yields π^+ and π^-

(Silicon Projectile)

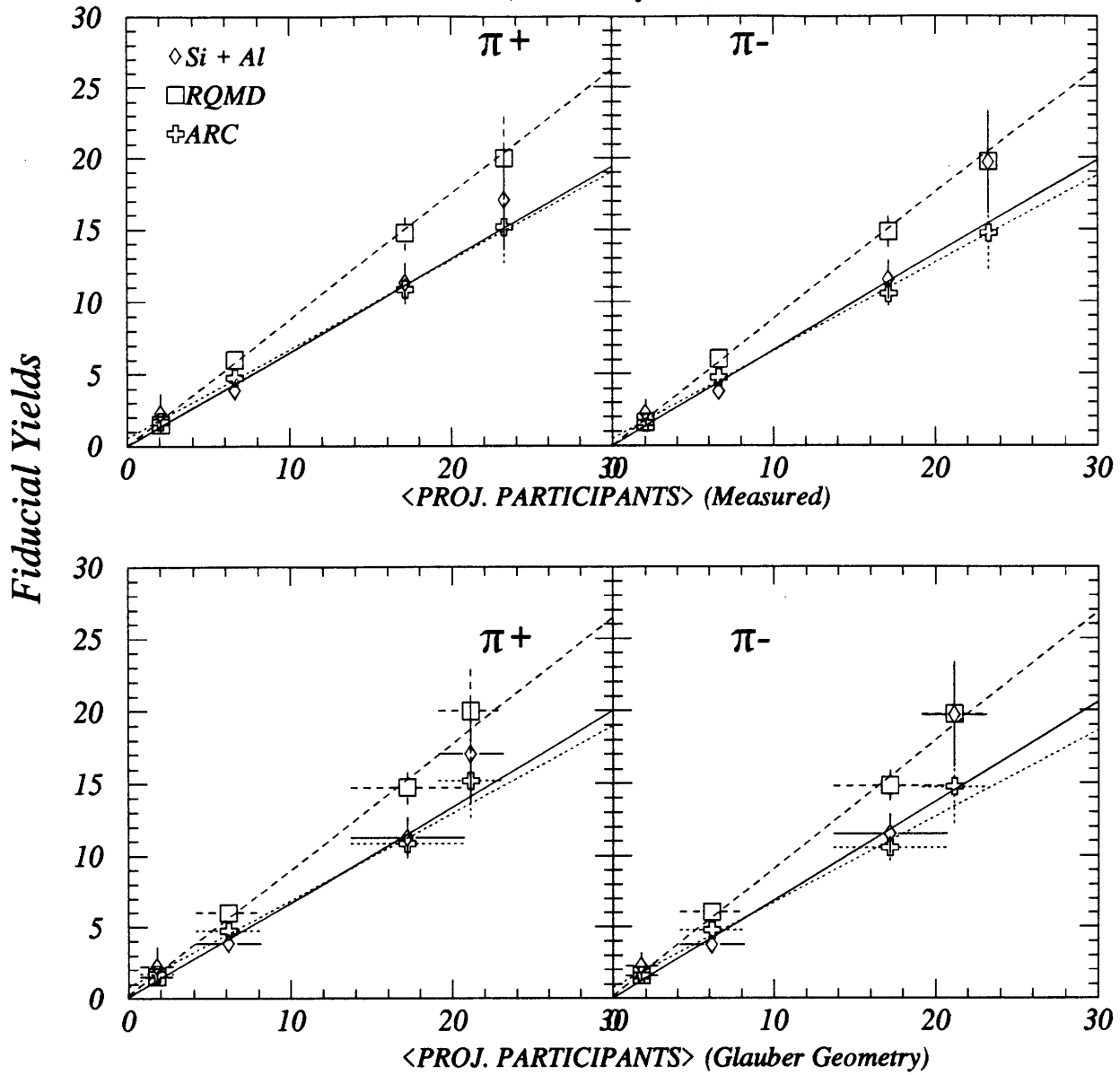


Figure 6-15: Fiducial yields for π^+ and π^- in $^{28}\text{Si} + ^{27}\text{Al}$ collisions. Yields are defined in a fiducial range, with $y_{min} = 0.4$ and $y_{max} = 3.0$ (reflected value) for $^{28}\text{Si} + ^{27}\text{Al}$ data. The abscissa for the top two panels are experimentally determined projectile participants. Projectile participants for the bottom panels are determined with a Glauber calculation. Comparisons are made with the RQMD and ARC models. (data: solid line), (dashed line: RQMD), (dotted line: ARC)

Fiducial Yields π^+ and π^-

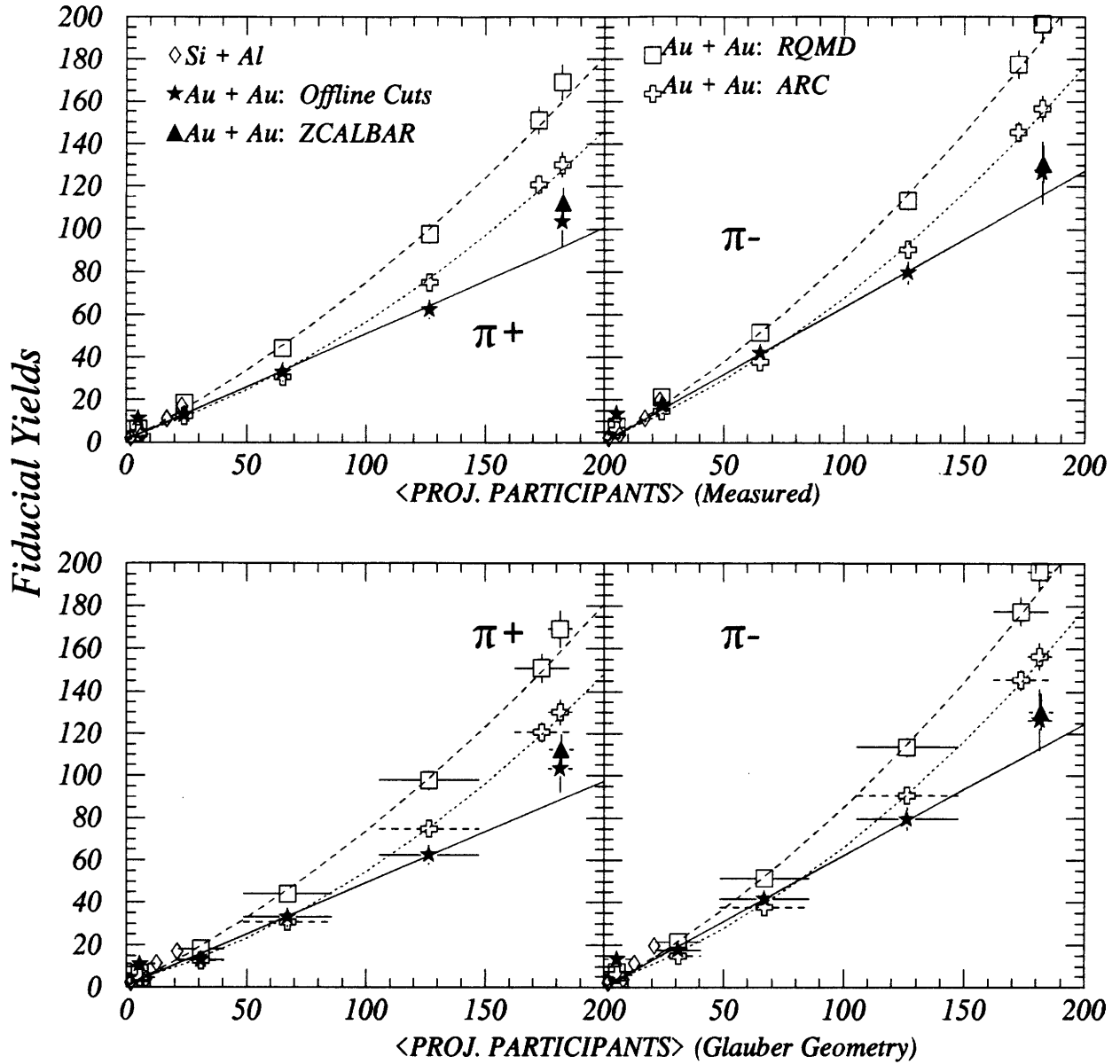


Figure 6-16: Fiducial yields for π^+ and π^- . Yields are defined in a fiducial range, with $y_{min} = 0.4$ and $y_{max} = 3.0$ (reflected value) for $^{28}\text{Si} + ^{27}\text{Al}$ data and $y_{min} = 0.4$ and $y_{max} = 2.8$ (reflected value) for $^{197}\text{Au} + ^{197}\text{Au}$ data. The abscissa for the top two panels are experimentally determined projectile participants. Projectile participants for the bottom panels are determined with a Glauber calculation. (data: solid line), (dashed line: RQMD), (dotted line: ARC)

the measured yields.

In recent conferences, pion yields from the RQMD model were compared with $^{28}\text{Si} + ^{197}\text{Au}$ data at AGS energies [HIP93-sor]. The comparisons have shown that predicted pion yields are higher than measured pion yields by 20 to 30 %. Comparisons with measured pion yields show good agreement for a small number of participants. The RQMD yields grow increasing greater than measured yields with the number of participants. The results are plotted in Figures 6-15, 6-16 and 6-17.

ARC calculation agree well with pion data for both $^{28}\text{Si} + ^{27}\text{Al}$ and peripheral $^{197}\text{Au} + ^{197}\text{Au}$ collisions. The results are plotted in Figure 6-15, 6-16 and 6-17 ARC calculations give larger pion yields for central $^{197}\text{Au} + ^{197}\text{Au}$ data.

Corrections are also made for the differences in incident beam energies of the silicon and gold beam. Studies with pp reactions at various energies show that an empirical relationship for the \sqrt{s} behavior for the production of charged mesons[Ant73] can be written as

$$\langle n_{\pi^+} \rangle = -1.7(\pm.3) + .84(\pm.007)\ln(s) + 1.(\pm.5)/s^{1/2}, \quad (6.2)$$

$$\langle n_{\pi^-} \rangle = -2.6(\pm.2) + .87(\pm.005)\ln(s) + 2.7(\pm.4)/s^{1/2}, \quad (6.3)$$

$$\langle n_{K^+} \rangle = -0.5(\pm.003) + .13(\pm.001)\ln(s) + .65(\pm.05)/s^{1/2}. \quad (6.4)$$

The energy corrected values are plotted for comparison with the uncorrected values in Fig. 6-21. Both π^+ and π^- yields exhibit linear dependency with either the experimentally measured participants or the participants determined with a Glauber model.

Not surprisingly, similar trends in pion behavior are seen for total integrated yields, determined by fitting a Gaussian function to the pion yields. We expect these similarities because the fiducial yields encompass most (80 to 90%) of the pions once the data are reflected about y_{nn} . Table 6.3 shows the fit parameters and yields for these two data

SUMMARY OF INTEGRATED YIELDS FOR $^{197}\text{Au} + ^{197}\text{Au}$ DATA

Type	Part.	Yield					
		0-4%	0-10 %	10-30 %	30-50 %	50-70 %	70-90 %
		σ_{inel}	σ_{inel}	σ_{inel}	σ_{inel}	σ_{inel}	σ_{inel}
Data	π^+	120 ± 4	101 ± 3	$73. \pm 4$	$39. \pm 2$	$15. \pm 1$	$12. \pm 1$
	π^-	159 ± 5	$131. \pm 3$	$99. \pm 2$	$51. \pm 1$	$20. \pm 1$	$16. \pm 1$
RQMD*	π^+	184 ± 7	$159. \pm 4$	$109. \pm 2$	$51. \pm 2$	$24. \pm 2$	$8. \pm 2$
	π^-	215 ± 8	$193. \pm 5$	$127. \pm 3$	$62. \pm 2$	$27. \pm 2$	$13. \pm 2$
ARC*	π^+	152 ± 5	141 ± 3	93 ± 2	44 ± 2	23 ± 2	6 ± 1
	π^-	182 ± 5	174 ± 3	117 ± 2	60 ± 2	28 ± 2	21 ± 13

Table 6.2: Summary of Gaussian fits to $^{197}\text{Au} + ^{197}\text{Au}$ data. Comparisons are made to the RQMD model run with 5000 $^{197}\text{Au} + ^{197}\text{Au}$ minimum bias events. * Acceptance corrected simulated data.

sets.

A pion production function can be determined from the total integrated yields. A best linear fit to the pion yield in $^{28}\text{Si} + ^{27}\text{Al}$ collisions is

$$n_{\pi^+} = .9(\pm .05) \times \text{PROJ. PARTICIPANTS} \quad (6.5)$$

$$n_{\pi^-} = .9(\pm .04) \times \text{PROJ. PARTICIPANTS.} \quad (6.6)$$

Similarly, a pion production function can be determined from the total integrated yields. A best linear fit to the pion yield in $^{197}\text{Au} + ^{197}\text{Au}$ collisions is

$$n_{\pi^+} = .6(\pm .07) \times \text{PROJ. PARTICIPANTS} \quad (6.7)$$

$$n_{\pi^-} = .8(\pm .04) \times \text{PROJ. PARTICIPANTS.} \quad (6.8)$$

Assuming that $\pi^0 = (\pi^+ + \pi^-)/2$, the average pion production for $^{197}\text{Au} + ^{197}\text{Au}$ collisions is $(1.1 \pm .05) \pi/(\text{participant})$.

Kaons are also plotted in a similar fashion. Kaon yields vs. participants are deter-

Integrated Yields π^+ and π^-

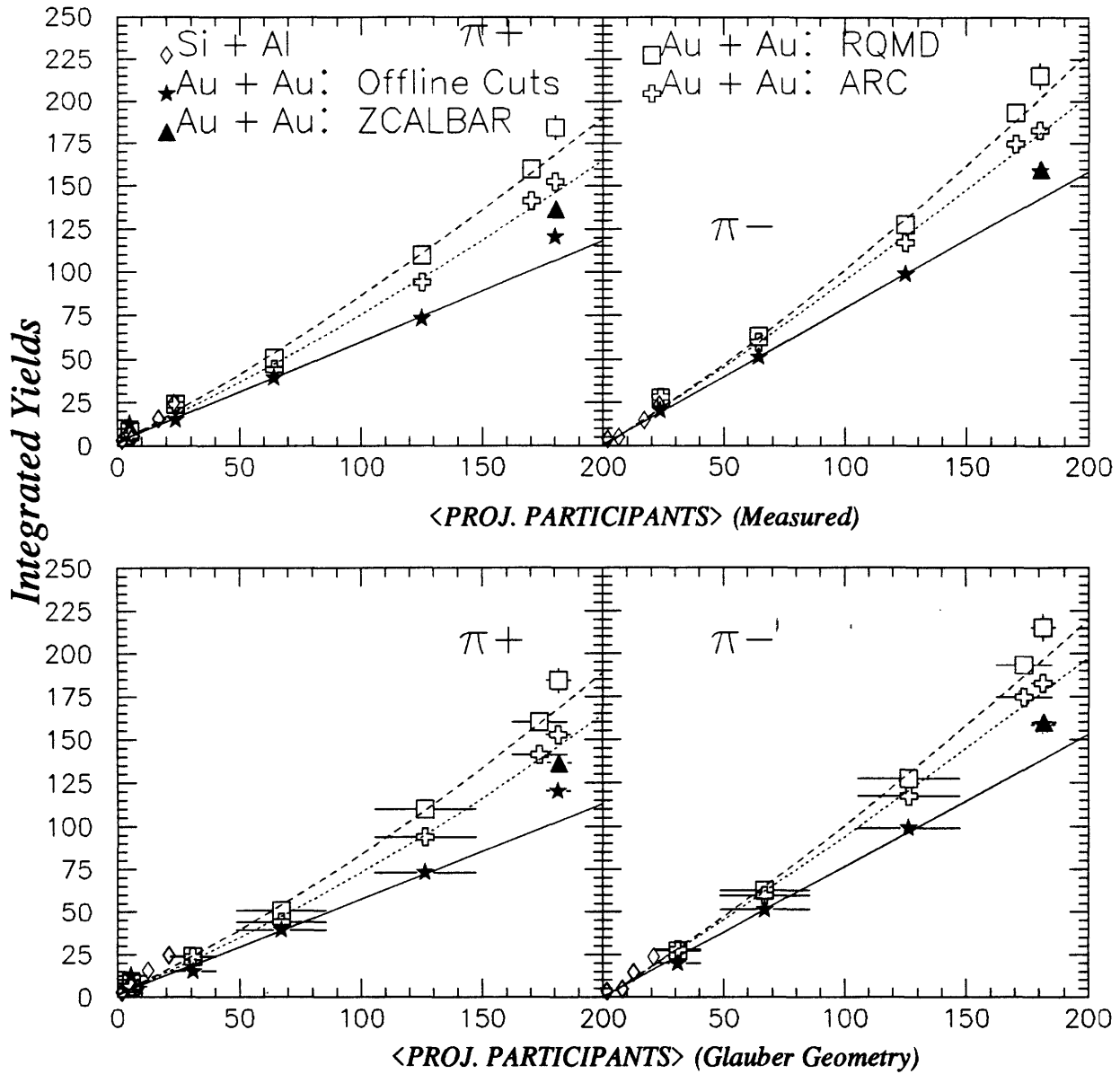


Figure 6-17: Total integrated yields for π^+ and π^- for $^{28}\text{Si} + ^{27}\text{Al}$ and $^{197}\text{Au} + ^{197}\text{Au}$ data. Rapidity distribution are fit to a Gaussian parameterization and then integrated from $y = -1$ to $y = 4$. (data: solid line), (dashed line: RQMD), (dotted line: ARC)

Summary Integrated Yields π^+ and π^-

(Oxygen and Silicon comparison)

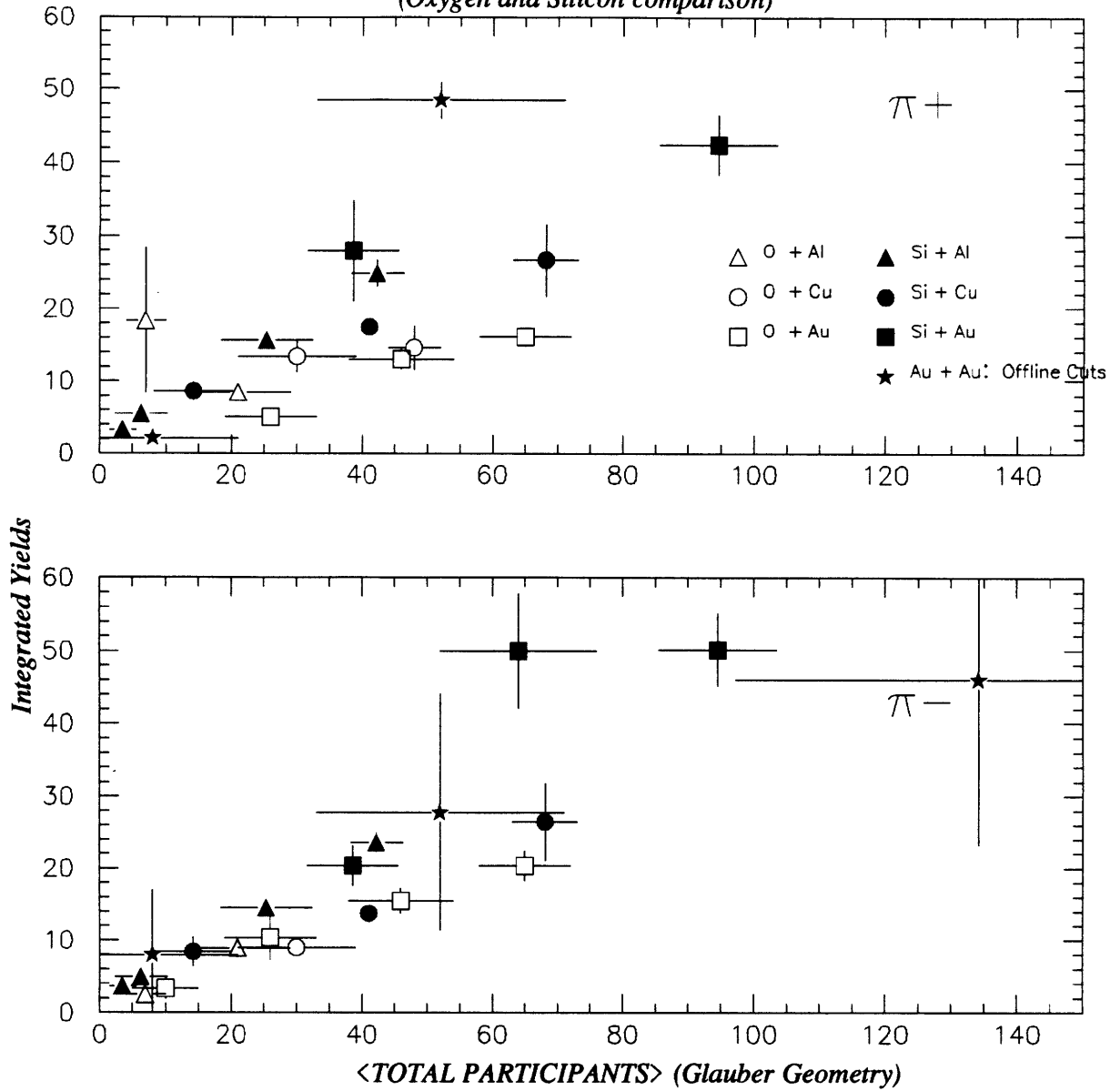


Figure 6-18: Total integrated yields for π^+ and π^- for ^{16}O , ^{28}Si , and ^{197}Au data. Rapidity distributions are fit to a Gaussian parameterization and then integrated over rapidity.

GAUSSIAN FIT PARAMETERS

System	Cut	A	y_0	σ
$^{28}\text{Si} + ^{27}\text{Al}$	CENT1	7.8	1.72	1.25
	CENT2	4.5	1.72	1.04
	MID	2.3	1.72	1.02
	PERP1	1.3	1.72	1.01
$^{197}\text{Au} + ^{197}\text{Au}$	\overline{ZCAL}	63.6	1.6	.85
	0 - 4 % σ_{inel}	60.1	1.6	.80
	0 - 10 % σ_{inel}	49.2	1.6	.82
	10- 30 % σ_{inel}	37.1	1.6	.78
	30- 50 % σ_{inel}	19.6	1.6	.79
	50- 70 % σ_{inel}	7.2	1.6	.83
	70- 90 % σ_{inel}	6.4	1.6	.78
	90- 100% σ_{inel}	—	1.6	—

Table 6.3: Fit parameters for total integrated yields for $^{28}\text{Si} + ^{27}\text{Al}$ and $^{197}\text{Au} + ^{197}\text{Au}$ collisions using a Gaussian function.

mined with both linear and quadratic fits. The poor K^+ statistics do not allow Gaussian fits to be performed on rapidity distributions. We expect a similar dependency with projectile participants since kaon fiducial yields capture most of the kaons. Kaon yields grow with a linear dependency with projectile participants for a large range of participants.

Kaon yields from RQMD and ARC $^{28}\text{Si} + ^{27}\text{Al}$ collisions are in good agreement with the data. Kaon yields from RQMD and ARC $^{197}\text{Au} + ^{197}\text{Au}$ collisions increase faster than a linear dependency. The RQMD and ARC models both show integrated kaon yields that are smaller than measured yields for $^{197}\text{Au} + ^{197}\text{Au}$ collisions.

Both pion and kaon fiducial yields are divided through by the measured projectile participants. This normalized fiducial yield is plotted in Figure 6-21.

The measured kaon yields have a linear dependency for a large range of projectile participants (from 50 to 180 participants). The linear and quadratic fit parameters are listed in Table 6.4.

K^+/π^+ ratios are shown in Figure 6-22. The ratio increases for $^{28}\text{Si} + ^{27}\text{Al}$ data but remains flat for $^{197}\text{Au} + ^{197}\text{Au}$ data. Both the RQMD and ARC models show increasing K^+/π^+ ratios.

Fiducial Yields K^+

(Silicon Projectile)

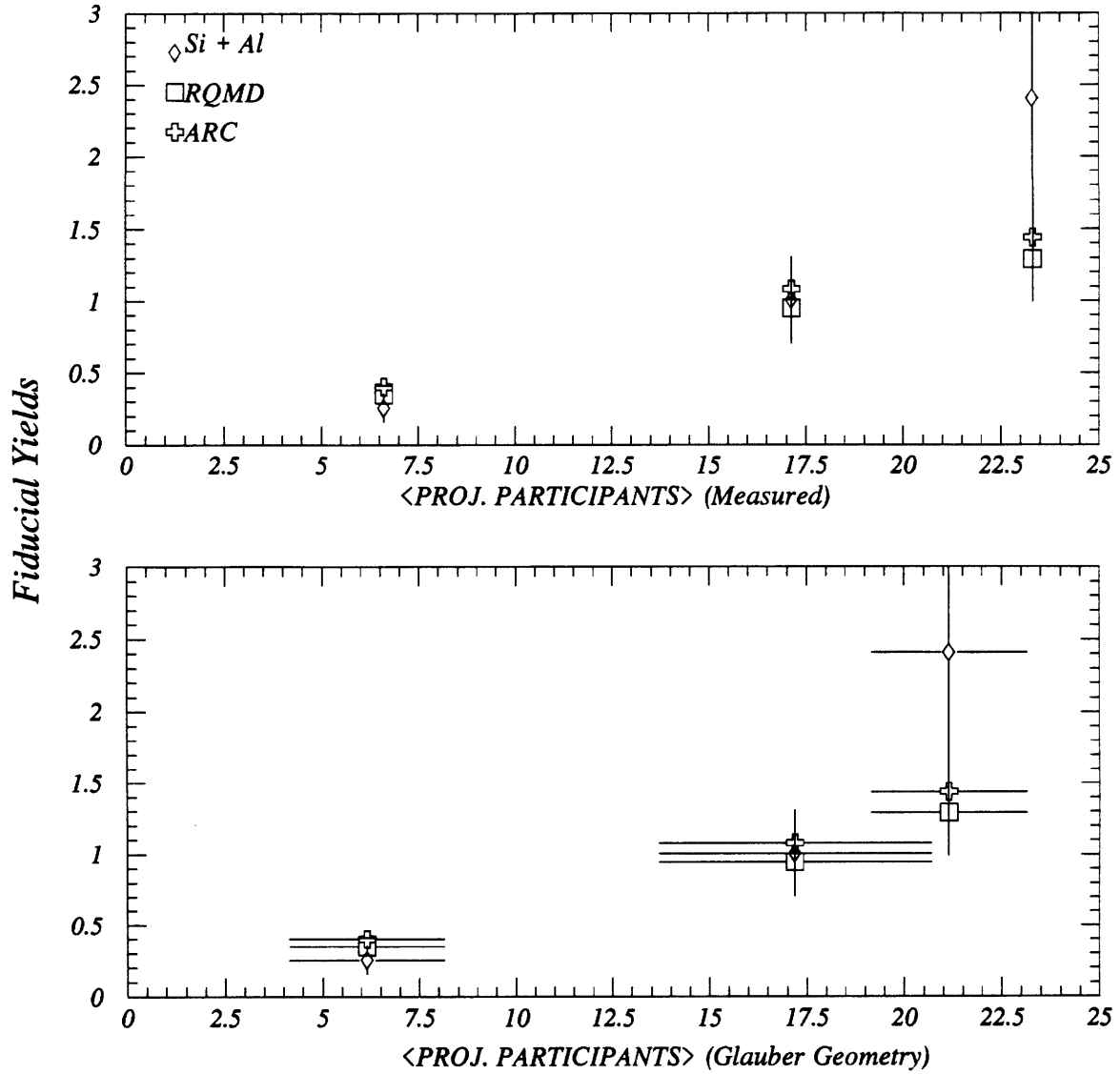


Figure 6-19: Fiducial yields for K^+ in $^{28}\text{Si} + ^{27}\text{Al}$ collisions. Yields are defined in a fiducial range, with $y_{min} = 0.4$ and $y_{max} = 3.0$ (reflected value). The abscissa represents an experimental measurement of the projectile participants. Comparisons are made with the RQMD and ARC models.

Fiducial Yields K^+

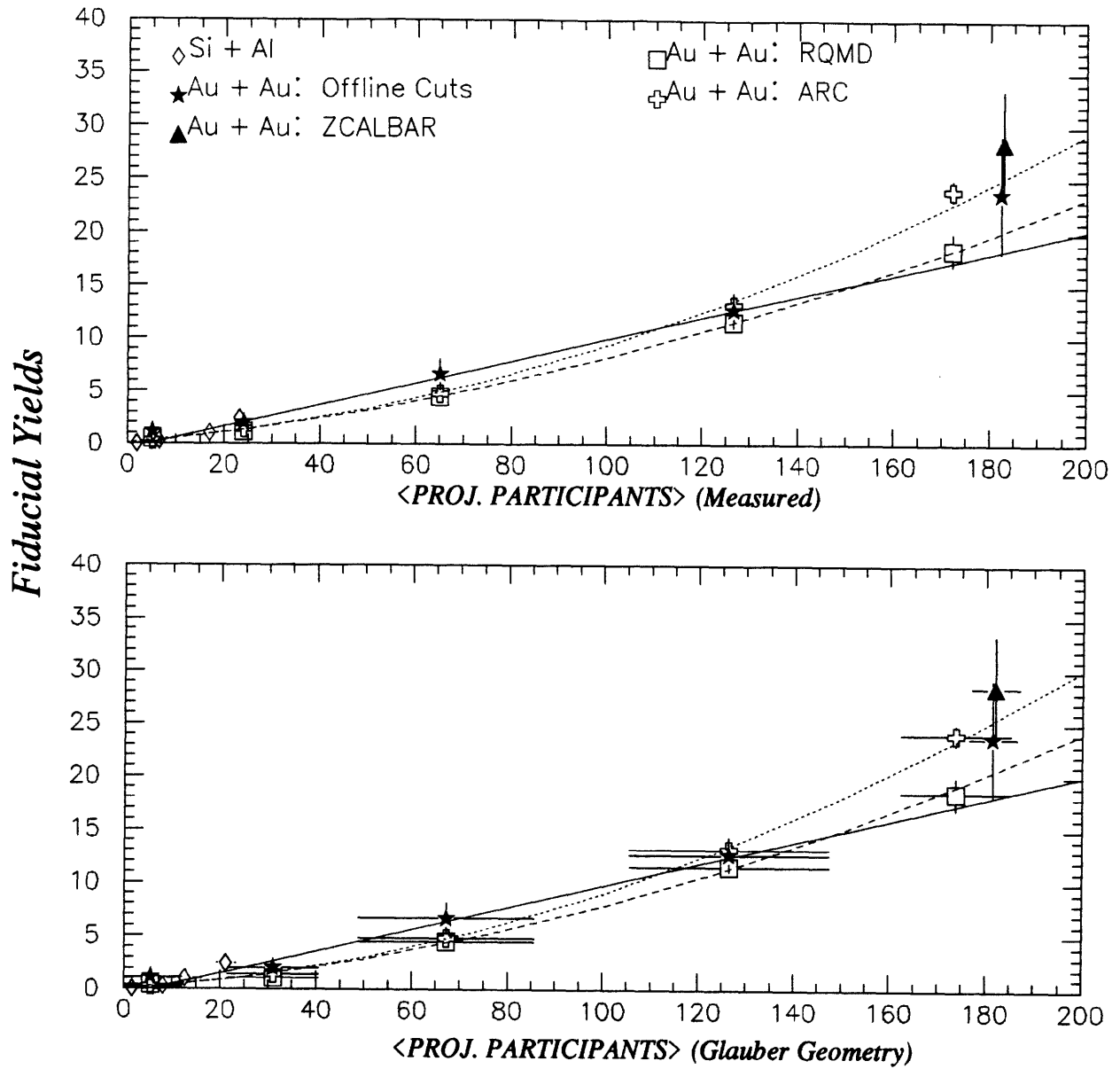


Figure 6-20: Fiducial yields for K^+ . Yields are defined in a fiducial range, with $y_{min} = 0.4$ and $y_{max} = 3.0$ (reflected value) for $^{28}\text{Si} + ^{27}\text{Al}$ data and $y_{min} = 0.4$ and $y_{max} = 2.8$ (reflected value) for $^{197}\text{Au} + ^{197}\text{Au}$ data. The abscissa represents an experimental measurement of the projectile participants. Comparisons are made with the RQMD(dashed line) and ARC(dotted line) models. Linear and quadratic fit parameters are shown in Table 6.4.

Normalized Fiducial Yields π^+ , π^- , and K^+

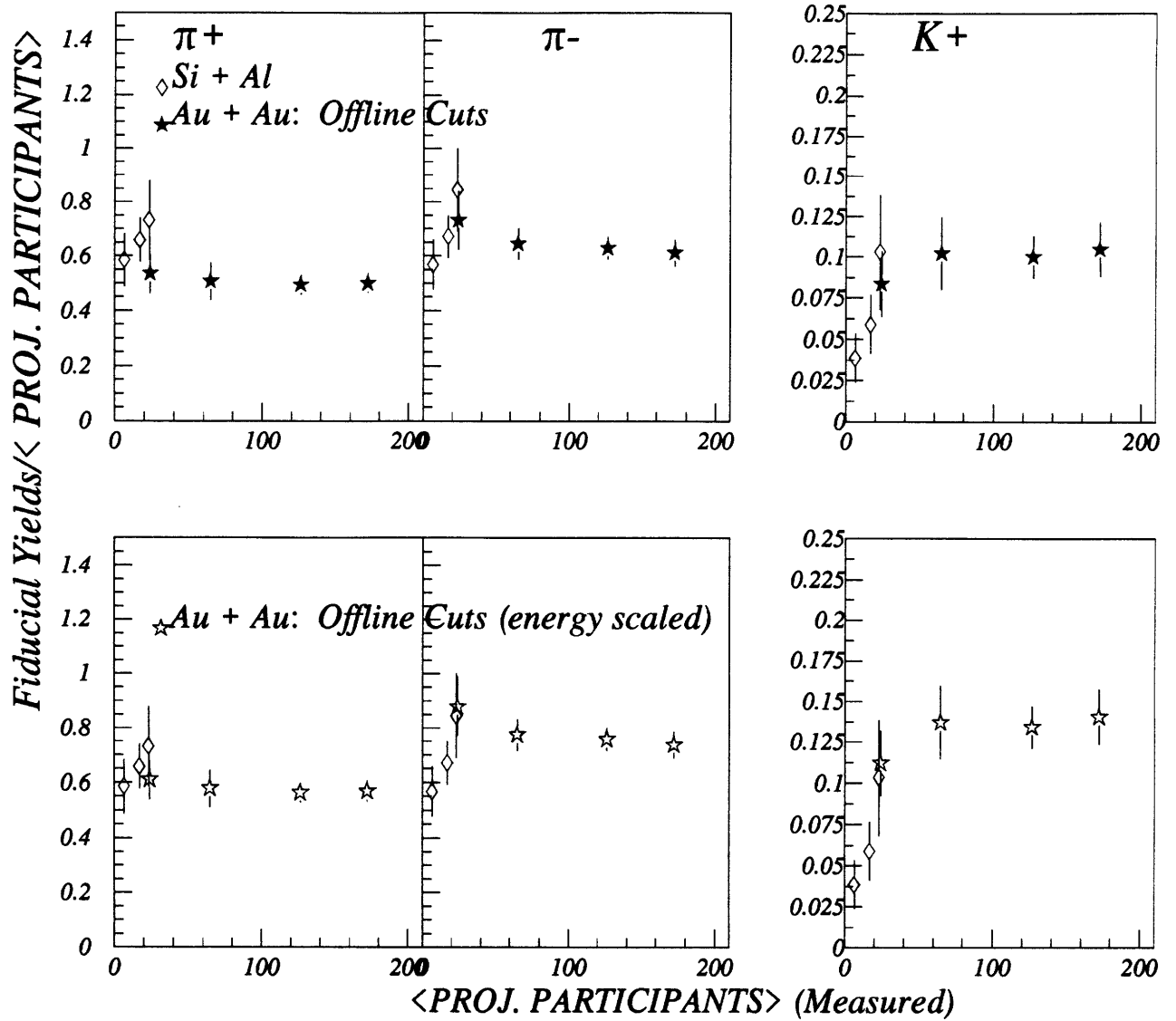


Figure 6-21: Normalized fiducial yields for π^+ and π^- . The top three panels show π^\pm and K^+ data as a function of projectile participants and normalized by the number of projectile participants. Gold data in the bottom three panels are multiplied by correction factors from equations 6.2 to 6.4.

K^+ / π^+ Ratio (From Fiducial Yields)

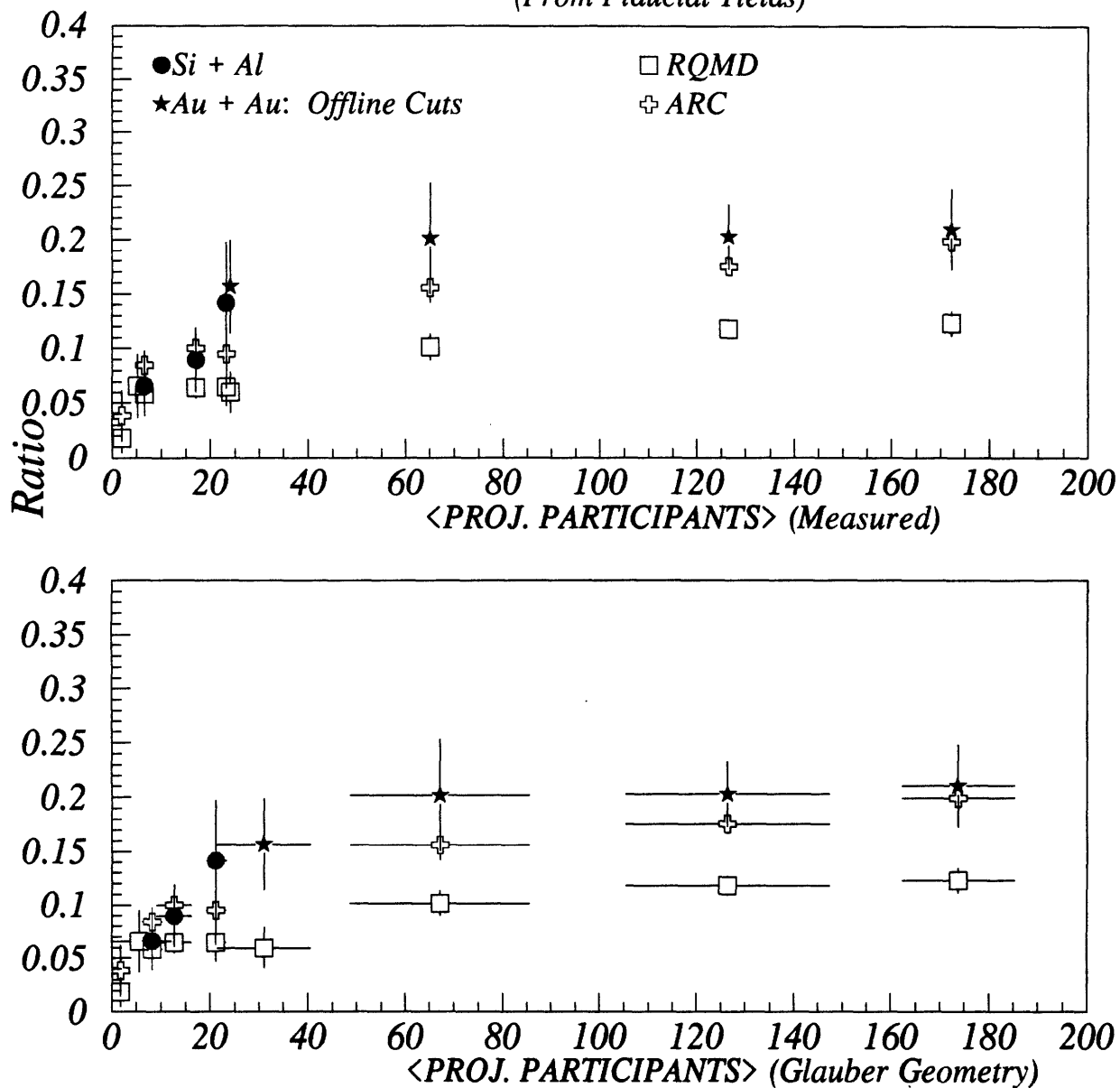


Figure 6-22: K^+ / π^+ Ratio for $^{28}\text{Si} + ^{27}\text{Al}$ and $^{197}\text{Au} + ^{197}\text{Au}$ data obtained from fiducial yields.

FIT PARAMETERS FOR FIDUCIAL YIELDS

Particle	$a + bN_{part}^{proj}$		$\frac{\chi^2}{(N-2)}$	$a + bN_{part}^{proj} + cN_{part}^{proj\ 2}$			$\frac{\chi^2}{(N-2)}$
	a	b	(linear)	a	b	c	(quad)
π^+	.54(.56)	.54(.02)	.86	1.1(.6)	.49(.05)	3×10^{-4} (3×10^{-4})	.24
π^-	0.(3)	.66(.06)	.14	.08(1.1)	.64(.05)	$8. \times 10^{-5}$ ($3. \times 10^{-4}$)	.17
K^+	-.5(.12)	.11(.01)	.23	-.25(.19)	.07(.02)	.0003(.0002)	.17
π^+ (ARC)	-.2(.6)	.61(.02)	.81	1.9(.7)	.36(.05)	.002(.0004)	.28
π^+ (RQMD)	-1.3(.6)	.79(.02)	.31	.31(.8)	.58(.07)	.002(.0001)	.1
π^- (ARC)	-.94(.5)	.74(.02)	1.0	1.15(.6)	.46(.05)	.002(.0003)	.26
π^- (RQMD)	-1.9(.5)	.93(.02)	.61	-.06(.7)	.65(.07)	.002(.0005)	.16
K^+ (ARC)	-1.6(.4)	.10(.005)	1.4	.04(.1)	.04(.01)	5×10^{-4} ($.5 \times 10^{-4}$)	.3
K^+ (RQMD)	-1.9(.22)	.19(.002)	1.4	-.06(.1)	.04(.01)	.003(10^{-4})	.14

Table 6.4: Fit parameters for normalized fiducial yields vs. projectile participants for $^{197}\text{Au} + ^{197}\text{Au}$ collisions. Errors to fits are in parenthesis.

We are now ready to use the particle yield results of this chapter to investigate energy and baryon densities in heavy-ion collisions at the AGS.

6.5 Summary

In this section we have presented a summary and comparison of $^{16}\text{O} + \text{A}$, $^{28}\text{Si} + \text{A}$ and $^{197}\text{Au} + ^{197}\text{Au}$ data. Integrated yields of pions from the various reactions allow one to determine pion production as a function of the number of participants.

Inverse slope parameters are also shown for π^\pm , K^+ , and protons for central collisions. Pion inverse slope parameters are very similar for all systems and fairly flat over rapidity. Light pions are more easily spread in momentum than the heavier kaons and protons. Pions are created in decaying resonances (for example, $\Delta^+ \rightarrow N\pi$) and receive most of the kinetic energy from the parent particles.

Proton inverse slope parameters, on the other hand, change on the order of 150 MeV, (ranging from 170 MeV to 320 MeV) over the range of collision reactions. Kaon inverse slope parameters measured at mid-rapidity range from 150 to 200 MeV over the range of collisions.

There is a linear dependency of π^+ and π^- production with projectile participants. Pions yields for $^{197}\text{Au} + ^{197}\text{Au}$ collisions from RQMD calculations are consistently higher than measured yields. Pion yields for $^{197}\text{Au} + ^{197}\text{Au}$ collisions from ARC calculations are in agreement with the data for peripheral collision but are larger by about 10 - 20% for central gold collisions.

Production of K^+ is also examined. The limited statistics for K^+ force making fiducial cuts in rapidity. Kaon yields are linear with the number of participants for a large range of participants (from 50 to 180).

Strange to non-strange meson ratios, K^+/π^+ , are determined for the $^{28}\text{Si} + ^{27}\text{Al}$ and $^{197}\text{Au} + ^{197}\text{Au}$ reactions. The K^+/π^+ ratio increases for $^{28}\text{Si} + ^{27}\text{Al}$ data and then is flat over a large range of participants. The most central $^{197}\text{Au} + ^{197}\text{Au}$ data point gives a K^+/π^+ ratio of $.26 \pm .05$.

Protons, although not produced in the collision reactions, provide much information that describes reaction violence and homogeneity. Protons from central and peripheral $^{16}\text{O} + \text{A}$, $^{28}\text{Si} + ^{64}\text{Cu}$, and $^{28}\text{Si} + ^{197}\text{Au}$ data are peaked in dN/dy at target rapidities. The symmetric $^{28}\text{Si} + ^{27}\text{Al}$ central collisions show flatter proton distributions, where larger $^{28}\text{Si} + ^{197}\text{Au}$ central proton distributions are peaked towards $y=0$.

Protons from $^{197}\text{Au} + ^{197}\text{Au}$ collisions show a very different behavior. There is a gradual change in the shape of the proton rapidity distributions from peripheral to central collisions. Proton distributions from central $^{197}\text{Au} + ^{197}\text{Au}$ collisions may show evidence for "stopping". Proton distributions from the upper 50 % σ_{inel} become peaked at mid-rapidity in $^{197}\text{Au} + ^{197}\text{Au}$ collisions. In these ranges of centrality, the cascade model RQMD shows very large contributions for multiple scattering and rescattering and may explain qualitatively the increasing yields at mid-rapidity for protons in central $^{197}\text{Au} + ^{197}\text{Au}$ collisions.

Chapter 7

Density

How do particle yields contribute to energy and baryon densities in heavy-ion collisions? We continue the discussion of thermal models from Chapter 2 and approximate the densities in these collisions. Densities are calculated as a function of collision participants. A simple model for a Coulomb correction to a particle's kinetic energy is also discussed. Finally, we make comparisons to the thermal fireball models.

7.1 Energy and Baryon Densities

Recalling Equation 2.31, densities are determined by summing over the phase space for a particle species and weighting it with the correct quantum statistics. From Chapter 2, the number density for particle species i is

$$\rho_i = \frac{g_i}{(2\pi)^2 \hbar^3} \int \frac{2\pi p_t dp_t dp_z}{e^{(E-\mu)/T} \pm 1}, \quad (7.1)$$

where \pm are used appropriately for fermions and bosons. There are two principle steps in determining ρ . First, the chemical potential, μ , and temperature, T , must be determined. Secondly, we must determine E in terms of transverse momentum and include a reasonable Coulomb correction. Coulomb corrections are especially important for slow protons where the magnitude of the Coulomb correction is on the order of the kinetic

energy of the proton.

We divide this discussion into two parts. We determine the contribution to the meson densities by determining the number densities for pions and kaons. Likewise, we determine the baryon densities by measuring the proton densities. Since we do not measure neutrons in this experiment, reasonable assumptions must be made in order to estimate the neutron densities and hence, total baryon densities.

Each density must be determined with the appropriate Coulomb correction and quantum statistical form. First, we fit the temperature and chemical potentials to the particle spectra in a thermal model.

7.2 Thermal Fits

The comparisons of particle yields to thermal models dates to the beginnings of the field. We determine densities for several particle types, for π^\pm , K^+ , and protons. Particle spectra may be fitted with Bose (for π 's and K 's) or Fermi (for protons) fits. Figure 7-1 shows fits for π^\pm , and proton data in central $^{197}\text{Au} + ^{197}\text{Au}$ collisions.

The pion momentum spectra are first normalized by a Boltzmann fit. The low momentum enhancement is clearly seen in Fig.7-1. Next, a Bose function is fit to this spectra. The temperature and chemical potential are then extracted. Protons are similarly fit to Fermi functions.

There is evidence indicating that protons are thermalized in central $^{197}\text{Au} + ^{197}\text{Au}$ collision:

- Proton momentum spectra are well fit by Boltzmann functions (see Appendix H, O, and R). Protons in thermodynamic equilibrium are fit by $d^2N/m_t dm_t \sim m_t e^{-m_t/T}$ [Nat92-He].
- Proton rapidity spectra are well fit by a Gaussian function. Rapidity distributions of protons in thermodynamic equilibrium are described by, $dN/dy \sim e^{-(y-y_{FB})^2/2T}$ [Nat92-He].

Bose and Fermi Fits to Central Au+Au Data

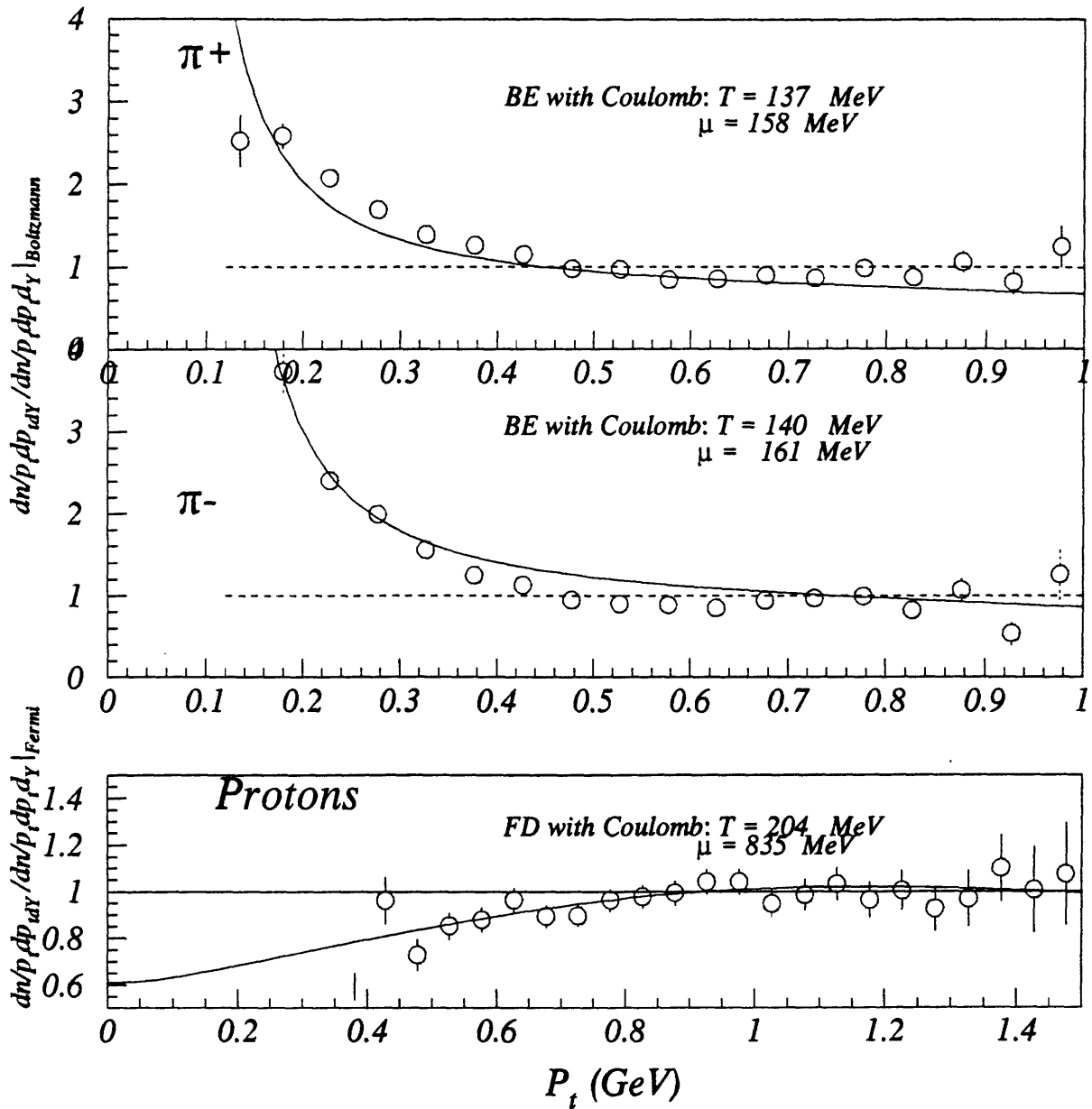


Figure 7-1: Thermal fits π^\pm and protons in central $^{197}\text{Au} + ^{197}\text{Au}$ reactions. This invariant momentum spectra has been divided by Boltzmann fits and refit using appropriate statistical functions. All fits have been Coulomb corrected.

- Protons are peaked at mid-rapidity in central $^{197}\text{Au} + ^{197}\text{Au}$ collisions. This rapidity distribution suggests stopping of the beam projectile with the target nuclei. The peaking at mid-rapidity also suggests that protons from target and beam nuclei suffer at least 2 collisions. We expect that each collision shifts the rapidity by about 2 units of rapidity from pA studies [Bus88].
- Cascade models show that protons in central $^{197}\text{Au} + ^{197}\text{Au}$ collisions suffer as many as 5 - 6 collisions (see Fig. 4-4) .

Even if protons are really thermalized in $^{197}\text{Au} + ^{197}\text{Au}$ collisions, there remains difficulties in interpreting their spectra. The proton temperatures are different than the kaon and pion temperatures. Some possible explanations for these differences include:

- Some fraction of the protons come from Δ resonance decays according to the ARC model [HIP93:-ka]. The decaying Δ 's impart most of their momentum to the protons. There will be distortions to the proton momentum spectra because some of the momentum will be carried off by the pions from the decay. Therefore, the temperatures determined using the protons may not reflect the parent resonance temperatures. Monte Carlo studies have shown that Deltas at a rapidity of 1.6, for example, decay to protons with smaller inverse slopes [Sun]. Delta's with inverse slopes of 200MeV give proton inverse slopes of 170MeV.
- Hydrodynamic expansion of a thermal gas will also distort the proton temperature.
- The densities determined from thermal fits are very sensitive to the proton behavior at low momentum. Figure 7-2 shows several fits and the resulting temperatures and chemical potentials. The proton numbers are given in Table 7.1.

The first two of these contributions distort the proton momentum spectra and all three contributions make the interpretation of the actual proton density difficult. We conclude that the density is very sensitive to the low momentum behavior of the proton. Table 7.1 shows the ranges of densities for various temperatures and chemical potentials

PROTON DENSITIES AND SENSITIVITIES TO μ AND T

Rapidity	μ (fixed) (MeV)	T (MeV)	n_{prot} fm^{-3}	$\chi^2/(N-2)$
1.5	200	262 ± 10	$0.1 \pm .06$.110
1.5	1000	210 ± 10	$1.2 \pm .06$.110
1.5	1100	190 ± 6	$1.6 \pm .05$.110
1.3	150	204 ± 4	$.02 \pm .04$.040
1.3	200	188 ± 4	$.02 \pm .04$.043
1.3	500	209 ± 4	$.16 \pm .04$.047
1.3	1100	187 ± 4	$1.6 \pm .04$.108
1.1	500	198 ± 2	$.13 \pm .01$.035
1.1	750	191 ± 2	$.42 \pm .01$.040
1.1	900	182 ± 3	$.80 \pm .01$.040
1.1	1000	182 ± 3	$1.1 \pm .01$.060

Table 7.1: Sensitivity of Proton Densities to μ and T.

for protons of central $^{197}\text{Au} + ^{197}\text{Au}$ collisions. Though the density is sensitive to the low momentum proton behavior it is insensitive to the rapidity. Protons, on the other hand, contribute most to the overall density. Protons also need to be treated with more care as the correction to their momentum due to Coulomb effects can become large.

Kaons are also treated. These particles also freeze out at a different, typically smaller source radius than protons or pions [Morr90], [Sol94], [Cian93] and therefore the density measured should be a better indicator of the conditions at the hot center.

7.3 Coulomb Corrections

We model a classic Coulomb correction to central A + A collisions using energy conservation, [Gyul81], [Goss78]. Energy conservation dictates that for particles escaping from the participant matter

$$\langle E_{obs} \rangle = \langle E_{K.E.} \rangle_{init} + \langle E_{Coul} \rangle. \quad (7.2)$$

We rewrite this as

Au+Au Protons

(Sensitivity of Density to T and μ)

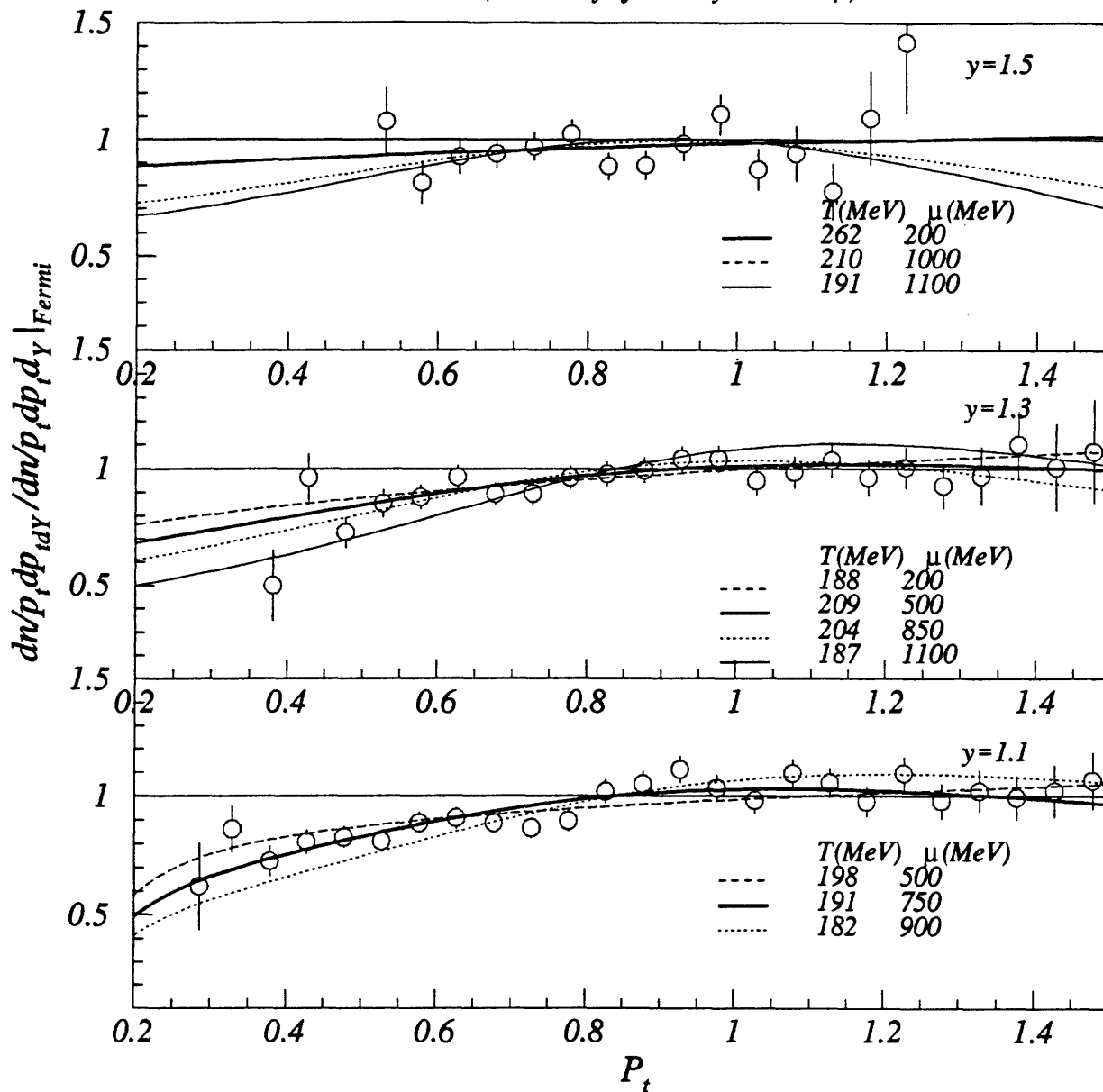


Figure 7-2: Sensitivity to thermal fits for $^{197}\text{Au} + ^{197}\text{Au}$ protons. Various values of chemical potential are chosen and the temperature is fit for $y=1.1$, 1.3 , and 1.5 . Temperature is not very sensitive to changes in chemical potential in these fits. However, the number density is very sensitive to particle yields at low momentum.

$$\frac{p_f^2}{2m} = \frac{p_i^2}{2m} \pm \frac{kq_1q_2}{r_i}. \quad (7.3)$$

In this model, $q_1 = \pm 1$, as appropriate for pions, kaons or protons escaping from the positive charge source potential, q_2 . The modification to the Coulomb cross-section becomes

$$\sigma = \sigma_o(r)e^{E_{Coul}/T} \left(1 \pm \frac{2mE_{Coul}}{p^2}\right), \quad (7.4)$$

where

$$E_{Coul} = k \frac{q_i q_{part}}{r} \quad \text{with } k = 1.44 \text{ MeV} - \text{fm}. \quad (7.5)$$

We model the correction for charged particles emitted from a spherical distribution, with q_{part} , defined as the charge of the participants in a Glauber model for central $^{16}\text{O} + \text{A}$, $^{28}\text{Si} + \text{A}$, and $^{197}\text{Au} + ^{197}\text{Au}$ collisions. We allow the comoving positive charge to be moving forward at $y = y_{part}$. Furthermore, we assume that emitted particles originate at some radius and use measured radii when available from correlation studies. The Coulomb corrections for pions are negligible, since the freezeout radius is large, ranging from 3 - 6 fm. The more massive protons are typically non-relativistic and have smaller kinetic energies. The most complete correction for protons must be a time-dependant correction, applied throughout the collision. This analysis is beyond the scope of this work. The corrections E_{Coul} at freezeout are shown in Table 7.2.

7.4 Densities and Participants

Finally, we calculate the densities in central A + A collisions using the thermal model described in the previous section. The particle number densities n_π , n_K , and n_{Prot} are very dependent on the behavior of particles at low momentum. The difficulty in measuring particle yields at low momentum contributes to the overall uncertainty of

DENSITY CALCULATIONS FOR MEASURED SPECIES

Particle	System	y	μ^{**} (MeV)	T^{**} (MeV)	Coulomb (MeV)	n (1/fm ³)
π^+	¹⁶ O + ²⁷ Al	1.66	111	125	11.7	.07
π^-	¹⁶ O + ²⁷ Al	1.66	113	127	11.7	.07
Kaons	¹⁶ O + ²⁷ Al	1.66	656	173	11.7	.08
Protons	¹⁶ O + ²⁷ Al	1.66	653	182	9.6	.22
π^+	¹⁶ O + ⁶⁴ Cu	1.18	151	135	21.3	.16
π^-	¹⁶ O + ⁶⁴ Cu	1.18	109	129	21.3	.07
Kaons	¹⁶ O + ⁶⁴ Cu	1.18	257	146	21.3	.08
Protons	¹⁶ O + ⁶⁴ Cu	1.18	275	181	13.2	.24
π^+	¹⁶ O + ¹⁹⁷ Au	0.81	127	139	30.9	.10
π^-	¹⁶ O + ¹⁹⁷ Au	0.81	128	124	30.9	.07*
Kaons	¹⁶ O + ¹⁹⁷ Au	0.81	494	173	30.9	.08
Protons	¹⁶ O + ¹⁹⁷ Au	1.3	500	171	13.1	.37*
π^+	²⁸ Si + ²⁷ Al	1.72	105	124	11.1	.06
π^-	²⁸ Si + ²⁷ Al	1.72	140	129	11.1	.11
Kaons	²⁸ Si + ²⁷ Al	1.72	173	153	11.1	.05
Protons	²⁸ Si + ²⁷ Al	1.72	775	174	11.7	.39
π^+	²⁸ Si + ⁶⁴ Cu	1.41	115	129	18.9	.07
π^-	²⁸ Si + ⁶⁴ Cu	1.41	142	134	18.9	.13
Kaons	²⁸ Si + ⁶⁴ Cu	1.41	260	180	18.9	.09
Protons	²⁸ Si + ⁶⁴ Cu	1.41	591	185	15.1	.18
π^+	²⁸ Si + ¹⁹⁷ Au	1.27	145	132	25.9	.17
π^-	²⁸ Si + ¹⁹⁷ Au	1.27	127	131	25.9	.09
Kaons	²⁸ Si + ¹⁹⁷ Au	1.27	260	173	25.9	.09
Protons	²⁸ Si + ¹⁹⁷ Au	1.1	750	171	14.2	.33*
π^+	¹⁹⁷ Au + ¹⁹⁷ Au	1.6	158	137	44.3	.18
π^-	¹⁹⁷ Au + ¹⁹⁷ Au	1.6	161	140	44.3	.13
Kaons	¹⁹⁷ Au + ¹⁹⁷ Au	1.6	340	161	44.3	.10
Protons	¹⁹⁷ Au + ¹⁹⁷ Au	1.6	998	184	44.3	1.1
Protons	¹⁹⁷ Au + ¹⁹⁷ Au	1.3	835	204	44.3	0.66
Protons	¹⁹⁷ Au + ¹⁹⁷ Au	1.1	906	186	44.3	0.79

Table 7.2: The energy and proton number densities measured for ¹⁶O, ²⁸Si, and ¹⁹⁷Au projectiles on various targets. All densities are Coulomb corrected. (*) Poor statistics forced larger binning of data in order to determine these fits.(**) Fit errors to μ and T are on the order of 5-10%. All densities are very sensitive to low momentum behavior. The best estimate of the systematic error of the density is $\sim 20\%$.

MESON DENSITY SUMMARY

SYSTEM	y_{part}	n_{meson} (1/fm ³)	$\langle m_t \rangle_{\pi}$ (GeV)	$\langle m_t \rangle_{K^+}$ (GeV)	$\epsilon_{meson} = \sum n_i \langle E_i \rangle$ (GeV/fm ³)
¹⁶ O + ²⁷ Al	1.66	.29	.32	.71	.12
¹⁶ O + ⁶⁴ Cu	1.18	.42	.32	.67	.17
¹⁶ O + ¹⁹⁷ Au	.81	.33	.33	.71	.16
²⁸ Si + ²⁷ Al	1.72	.30	.32	.68	.12
²⁸ Si + ⁶⁴ Cu	1.4	.39	.33	.73	.14
²⁸ Si + ¹⁹⁷ Au	1.27	.48	.33	.71	.19
¹⁹⁷ Au + ¹⁹⁷ Au	1.6	.56	.34	.72	.23

Table 7.3: Meson Density Summary. Statistical errors for the densities are 5-10% for all systems. Note that $y_{part} = y_{FB}$.

these calculations.

Figure 7-3 shows the trends of meson and baryon densities for nuclear matter using the fireball model and the thermal model discussed here. The meson number densities for ¹⁶O + A and ²⁸Si + A reactions range from $(0.29 \pm .03) - (.48 \pm .05) / \text{fm}^3$. The meson number density for the ¹⁹⁷Au projectile is $.56 \pm .03 / \text{fm}^3$. Energy densities are also calculated using a mean energy per particle species. The mean energy in the frame of the fireball is

$$\langle E \rangle = \langle m_t \rangle \cosh(y - y_{FB}). \quad (7.6)$$

With exponential parameterization of the differential yields, $Ae^{-m_t/T}$, we may analytically determine $\langle m_t \rangle$,

$$\langle m_t \rangle = T \frac{(m_o/T)^2 + 2(m_o/T) + 2}{1 + (m_o/T)}. \quad (7.7)$$

With this expression, a mean energy density is determined for mesons,

$$\epsilon_{meson} = \sum n_i \langle m_t \rangle_i. \quad (7.8)$$

We sum over pions and K⁺ to determine a total energy density. We do not include the

Meson and Baryon Densities

Central O,Si, Au Collisions

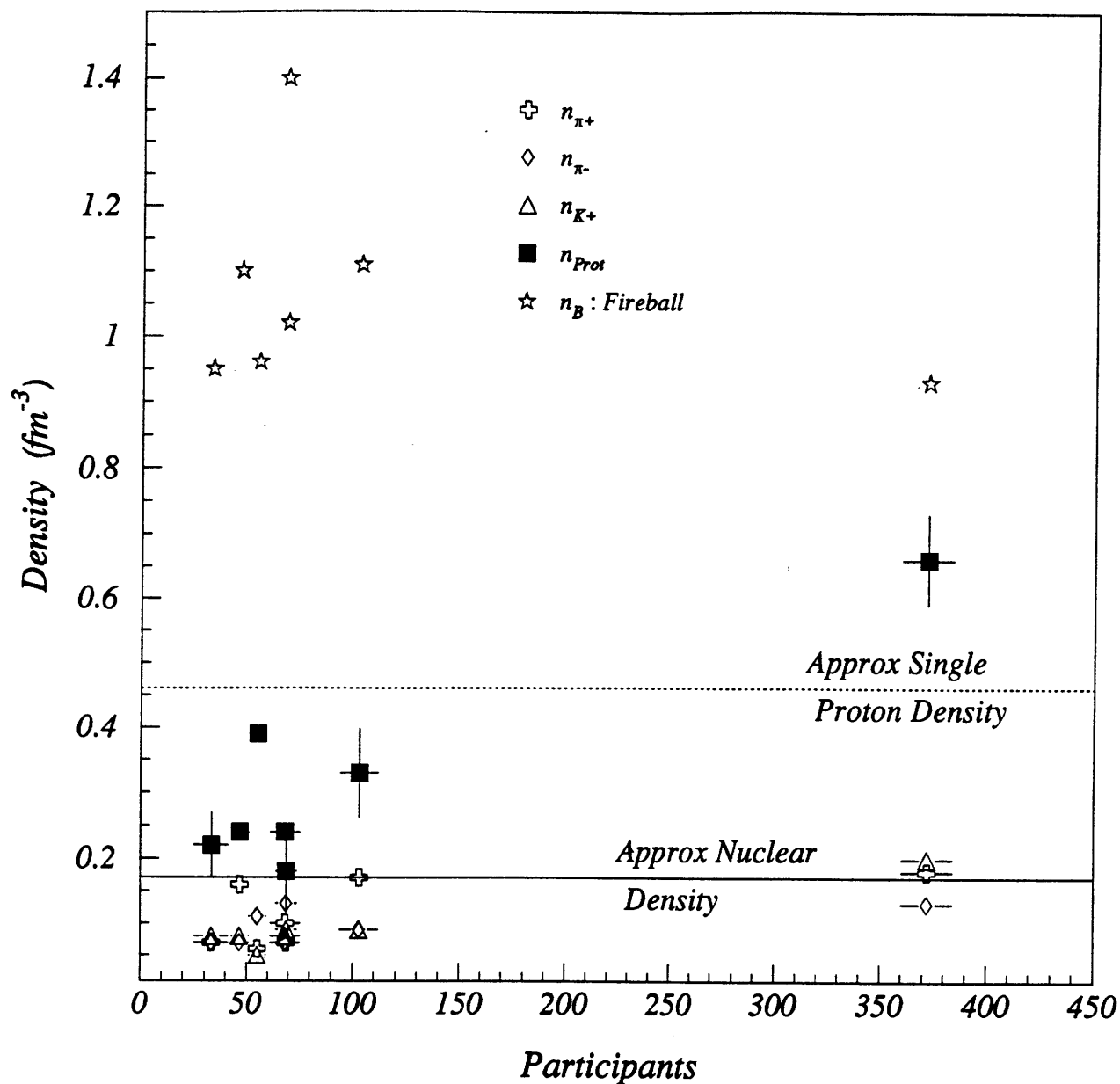


Figure 7-3:

Results of n_{π} , n_K , and n_{Prot} vs. participants. The lines at the bottom of the picture represent approximate nuclear (solid) and proton (dashed) densities in normal nuclear matter. We use a proton radius of .8 fm and nuclear density $\rho_o = .17/fm^3$. The cluster of points at the left, represent central ^{16}O and ^{28}Si collisions. See Section 2.2.3 for fireball calculations.

BARYON DENSITY SUMMARY

SYSTEM	y_{part}	n_{prot} (1/fm ³)	$\langle m_t \rangle_{prot}$ (GeV)	$\epsilon_{prot} = n_{prot} \langle E_{prot} \rangle$ (GeV/fm ³)	$\epsilon_B = \epsilon_{prot} \frac{(A_{targ} + A_{proj})}{(Z_{targ} + Z_{proj})}$ (GeV/fm ³)
¹⁶ O + ²⁷ Al	1.66	.22	1.15	.68	.48
¹⁶ O + ⁶⁴ Cu	1.18	.24	1.15	.49	.57
¹⁶ O + ¹⁹⁷ Au	.81	.37	1.14	.56	1.0
²⁸ Si + ²⁷ Al	1.72	.39	1.14	1.2	.74
²⁸ Si + ⁶⁴ Cu	1.4	.18	1.18	.64	.55
²⁸ Si + ¹⁹⁷ Au	1.27	.33	1.18	.72	.88
¹⁹⁷ Au + ¹⁹⁷ Au	1.6	1.1	1.15	3.2	3.1
¹⁹⁷ Au + ¹⁹⁷ Au	1.3	.66	1.17	1.53	1.2
¹⁹⁷ Au + ¹⁹⁷ Au	1.1	.79	1.15	1.52	1.2

Table 7.4: Baryon Density Summary. Statistical errors for the densities are 5-10% for all systems. Note that $y_{part} = y_{FB}$.

contribution of K^- in these calculations. Table 7.3 gives the values of $\langle m_t \rangle$ and ϵ_{meson} for the various collisions. Energy densities from mesons range from $(.12 \pm .02) - (.23 \pm .02)$ GeV/fm³.

Baryon number densities are also determined. Proton number densities range from $(.18 \pm .02) - (0.39 \pm .04)$ /fm³ for ¹⁶O and ²⁸Si projectiles. A larger proton density is determined for ¹⁹⁷Au + ¹⁹⁷Au collisions. Calculations where fits were reliable ($y = 1.3$) give a proton density of $(.66 \pm .07)$ /fm³. Proton densities are determined in a similar manner as the meson energy densities. Baryon densities are determined using $\epsilon_B = E_{prot}(A/Z)$. Baryon densities are determined for ¹⁶O and ²⁸Si projectiles and range from $(0.48 \pm .05) - (1.0 \pm .1)$ GeV/fm³. A baryon density of $(1.2 \pm .2)$ GeV/fm³ is determined for central ¹⁹⁷Au + ¹⁹⁷Au collisions.

There are a number of caveats that need to be discussed with these calculations. First, the thermal model as presented assumes that all particle species are at the same temperature. This is not the case. The temperature determined for protons is higher than the pion temperature. The number densities are determined only using the temperature and chemical potentials.

There are a number of possible explanations for the different proton temperatures.

TOTAL ENERGY DENSITY SUMMARY

SYSTEM	$\epsilon_{tot} = \epsilon_{meson} + \epsilon_B$ GeV/fm ³
¹⁶ O + ²⁷ Al	.6 ± .06
¹⁶ O + ⁶⁴ Cu	.74 ± .07
¹⁶ O + ¹⁹⁷ Au	1.2 ± .2
²⁸ Si + ²⁷ Al	.86 ± .09
²⁸ Si + ⁶⁴ Cu	.69 ± .07
²⁸ Si + ¹⁹⁷ Au	1.1 ± .1
¹⁹⁷ Au + ¹⁹⁷ Au	1.4 ± .1

Table 7.5:

One possible explanation for the differences in pion and proton temperatures is hydrodynamic expansion of a thermal source. Hydrodynamic expansion may distort the particle spectra [Hein89], [Lee88] and yet keep the thermal properties of the source. A simple “blast wave” mechanism has been studied [Cos90]. This mechanism distorts the exponential momentum spectra and may be written as

$$E \frac{d^3N}{dp^3} = AE \int_{Volume} e^{\frac{-\gamma E}{T}} \left[\left(1 + \frac{T}{\gamma E}\right) \frac{\sinh \alpha}{\alpha} - \frac{T}{\gamma E} \cosh \alpha \right] d^3r, \quad (7.9)$$

where A is a constant. Pion, kaon and proton momentum spectra have been fit by J. Costales using this blast wave form for ²⁸Si + ²⁷Al and ²⁸Si + ¹⁹⁷Au collisions. Pion temperature were determined to be 75 to 80 MeV at y_{part} . Proton temperatures were determined to be 90 MeV. Protons from central ¹⁹⁷Au + ¹⁹⁷Au collisions were fit with this functional form and resulted in temperatures of 123 MeV. This mechanism was used to fit the momentum spectra of the above particle species. This method did not give similar temperatures for all species. The blast wave mechanism does determine temperatures that are significantly lower than the temperatures determined from simple exponential fitting.

Approximately 1 pion is created for each baryon participant according to Figure 6-17. If the source size for pions is about the same as protons then we expect that $n_\pi \approx n_B$. We do not see this result. We measure a baryon number density that is approximately

twice the meson number density. This discrepancy indicates that this model cannot be used reliably, that perhaps collective effects are present.

There are other limitations to this analysis. The thermal calculations presented in this chapter assume that the source is time invariant. The measured “temperature” is really a weighted average of temperatures of particles that originate from many different regions of the collision at different times. The calculated densities are at best only an average quantity.

On the other hand, we assume that pions, for example, freeze-out at a critical density. Therefore, it may be irrelevant that we are measuring particles that originate from different points and from different times along the history of the collision.

In summary, this technique provides a method for seeing trends in the number densities and is insensitive to the details of the collision geometry and the history of the collision. However, the analysis yields inconsistent results.

Chapter 8

Conclusion

We now address the following questions: What have we learned about particle yields in heavy-ion collisions? Does particle production scale with the number of participants? Do secondary collisions play a role in these collisions? What densities do we achieve and how do they depend on the size of the target and projectile? To begin, we look at a comparison of differential yields.

Differential Yields

How do differential yields compare between $A + A$ collisions in heavy-ion reactions? We have made comparisons of the most abundant particle species with good statistics in ^{16}O , ^{28}Si , and ^{197}Au reactions. The good statistics of pions and protons near mid-rapidity in these reactions allow one to parameterize the momentum distributions. We choose exponential parameterization in p_t to describe the pions and exponential parameterization in m_t to describe the protons. Pion inverse slopes are similar, independent of rapidity, target size or projectile size. All pion spectra exhibit very similar inverse slope parameters, $145 \text{ MeV} \leq B \leq 155 \text{ MeV}$, obtained with exponential fitting in p_t .

Positive kaons are also measured in this analysis. Kaon differential yields can be described as exponential in m_t or p_t . Insufficient coverage at low momentum in this data does not allow a distinction between the two parameterizations.

Proton momentum distributions are parameterized by exponentials in m_t . Proton inverse slope parameters increase with the reaction size. Proton inverse m_t slope parameters range from (160 ± 8) MeV for $^{16}\text{O} + ^{27}\text{Al}$ collisions to (320 ± 40) MeV for central $^{197}\text{Au} + ^{197}\text{Au}$ collisions. This is a dramatic increase and likely reflects a substantial increase in secondary collisions in central $^{197}\text{Au} + ^{197}\text{Au}$ collisions.

Rapidity Distributions Rapidity distributions are determined for π^\pm , K^\pm and protons. Pions are measured from $0.3 \leq y \leq 2.0$ for the minimum bias data and from $0.3 \leq y \leq 2.5$ for the TMA data. All measured particle species show increasing yields for reactions of increasing centrality. Pion rapidity distributions are well parameterized by Gaussian functions.

Proton rapidity distributions change dramatically over the range in reaction sizes. Proton distributions generated in ^{16}O and ^{28}Si reactions show decreasing yields towards central rapidity. Distributions from symmetric $^{28}\text{Si} + ^{27}\text{Al}$ data show flatter proton distributions but still decrease at mid-rapidity. Protons from the most central $^{197}\text{Au} + ^{197}\text{Au}$ collisions are peaked at mid-rapidity, consistent with large shifting of rapidity of target and projectile protons due to secondary collisions (see Figure 4-4).

Integrated yields We measure both pion and kaon integrated yields in a fiducial range of rapidity over a large range of collision participants. Yields of both π^+ and π^- increase linearly with the number of participants. Detailed comparisons were done with symmetric systems. Particle yields may be plotted against either projectile, target or total participants since $N_{part}^{tot} = 2N_{part}^{proj} = 2N_{part}^{targ}$. Measurements of K^+ show that their fiducial yields may increase faster than a linear dependence for the $^{28}\text{Si} + ^{27}\text{Al}$ system. A linear increase in yield with projectile participants is seen in $^{197}\text{Au} + ^{197}\text{Au}$ collisions.

Total integrated yields of pions were determined using Gaussian functional fitting in $^{16}\text{O} + \text{A}$, $^{28}\text{Si} + \text{A}$, and $^{197}\text{Au} + ^{197}\text{Au}$ collisions. A linear dependence was measured for pions in $^{28}\text{Si} + ^{27}\text{Al}$ collisions with the form:

$$n_{\pi^+} = .9(\pm.05) \times \text{PROJ. PARTICIPANTS}, \quad (8.1)$$

$$n_{\pi^-} = .9(\pm.04) \times \text{PROJ. PARTICIPANTS}. \quad (8.2)$$

A linear dependence was measured for pions in $^{197}\text{Au} + ^{197}\text{Au}$ collisions with the form:

$$n_{\pi^+} = .6(\pm.07) \times \text{PROJ. PARTICIPANTS}, \quad (8.3)$$

$$n_{\pi^-} = .8(\pm.04) \times \text{PROJ. PARTICIPANTS}. \quad (8.4)$$

Total pion production may be estimated from the above $^{197}\text{Au} + ^{197}\text{Au}$ reactions. Summing the pions, $\pi^0 = 1/2(\pi^+ + \pi^-)$ there are $(1.1 \pm .05)$ π 's/participant.

Kaons are also measured, albeit with wider rapidity binning, and integrated over a fiducial range. K^+/π^+ ratios are determined measuring fiducial yields for pions and kaons in a rapidity range $y \in (.4,3)$ for $^{28}\text{Si} + ^{27}\text{Al}$ and $y \in (.4,2.8)$ for $^{197}\text{Au} + ^{197}\text{Au}$ collisions. Kaon production increases linearly with the number of participants. The fiducial yields vs. the number of participants gives

$$n_{K^+} = .1(\pm.02) \times \text{PROJ. PARTICIPANTS}. \quad (8.5)$$

K^+/π^+ ratios are also determined as a function of participants. We find an increasing ratio for $^{28}\text{Si} + ^{27}\text{Al}$ reactions, ranging from $(.07 \pm .02)$ to $(0.14 \pm .05)$. We find a constant ratio for $^{197}\text{Au} + ^{197}\text{Au}$ reactions, $\approx 0.2 \pm .04$.

Densities Densities are determined for A + A collisions using a thermal model. Temperature and chemical potentials are extracted via thermal fits to the data. The calculated densities are compared to the number of participants in the collision. Meson

number densities range from $(0.29 \pm .03 \pm .04) - (.48 \pm .05 \pm .06) /\text{fm}^3$ for oxygen and silicon projectiles. The meson number density for the gold projectile is $(.56 \pm .03 \pm .04) /\text{fm}^3$. Proton number densities for oxygen and silicon central collisions range from $(.18 \pm .02 \pm .03) - (0.39 \pm .04 \pm .06) /\text{fm}^3$. The proton density for the gold projectile is $(.66 \pm .07 \pm 0.1) /\text{fm}^3$.

Energy densities are also determined. Meson energy densities range from $(0.12 \pm .02 \pm .03) - (0.19 \pm .02 \pm .03) \text{ GeV}/\text{fm}^3$ for oxygen and silicon projectiles and $(.23 \pm .02 \pm .03) \text{ GeV}/\text{fm}^3$ for the gold projectile. Baryon energy densities are also determined and range from $(0.48 \pm .05 \pm .08) - (1.0 \pm .1 \pm .2) \text{ GeV}/\text{fm}^3$ for oxygen and silicon projectiles. Baryon energy densities are $(1.2 \pm .2 \pm .3) \text{ GeV}/\text{fm}^3$ for the gold projectiles.

These large baryon number densities, $\approx 4 n_{nuc}$, are difficult to interpret. A stationary fireball model does not explain the AGS collisions. Each particle species has a different temperature and therefore other mechanisms, for example, some form of hydrodynamic expansion, may need to be invoked to explain these differences.

One of the most prominent signatures for the QGP is increasing kaon production, possibly increasing in a non-linear fashion with collision participants. We have not seen any non-linear (K^+) production for $^{197}\text{Au} + ^{197}\text{Au}$ reactions.

Two immediate analysis efforts would greatly enhance the reliability of this result. First, a more detailed analysis of kaon yields (both K^+ and K^-) as a function of participants is needed. This particular analysis will be pursued with online particle-ID triggering (level II triggering) and an improved coverage at the most central rapidities. A forward spectrometer is currently being used with E866 and will greatly enhance the confidence of measuring particle yields at the most forward angles, $\theta_{spec} < 14^\circ$. The restacking of the ZCAL scintillator plates should also improve the measurement of participants in current E866 data.

There are no striking signatures that show the onset of a QGP at this stage. We expect a K^+ yield increasing faster than linear dependence with the number of participants. This is not seen in the data. Kaons increase with a linear dependence with the number of

projectile participants for $^{197}\text{Au} + ^{197}\text{Au}$ collisions. This linear dependence with projectile is contradictory to the current models for kaon production in heavy-ion collisions.

Meson densities are determined from a thermal model and remain fairly constant for ^{16}O , ^{28}Si , and ^{197}Au collisions. Large proton densities are seen in the $^{197}\text{Au} + ^{197}\text{Au}$ collisions. Densities are very sensitive to small changes in the yields at low-momentum. Much better coverage is needed to determine the proton density for gold data. Furthermore, a better understanding of resonance decays is needed to interpret the “temperature” of the protons in central gold collisions.

We conclude that if a deconfined plasma is created in $^{197}\text{Au} + ^{197}\text{Au}$ collisions at the AGS, the measured particle yields are insensitive to any known signature. We are left at the moment with no striking signs of the QGP onset from these first measurements of $^{197}\text{Au} + ^{197}\text{Au}$ collisions. Detailed studies of particle production in gold collisions is currently underway. Regardless of the creation of a deconfined plasma, this new area of research has provided some surprising results.

Appendix A

Yield Summary: $^{16}\text{O} + ^{27}\text{Al} : \pi$

We summarize the differential yields for ^{16}O , ^{28}Si , and ^{197}Au reactions. Differential yields are plotted vs. p_t and fits are made in exponentials of p_t , $f \sim e^{-p_t/B}$ and m_t , $f \sim e^{-m_t/B}$ for pions and kaons. Protons are fit with exponentials in m_t and Boltzmann functions in m_t , $f \sim m_t e^{-m_t/B}$.

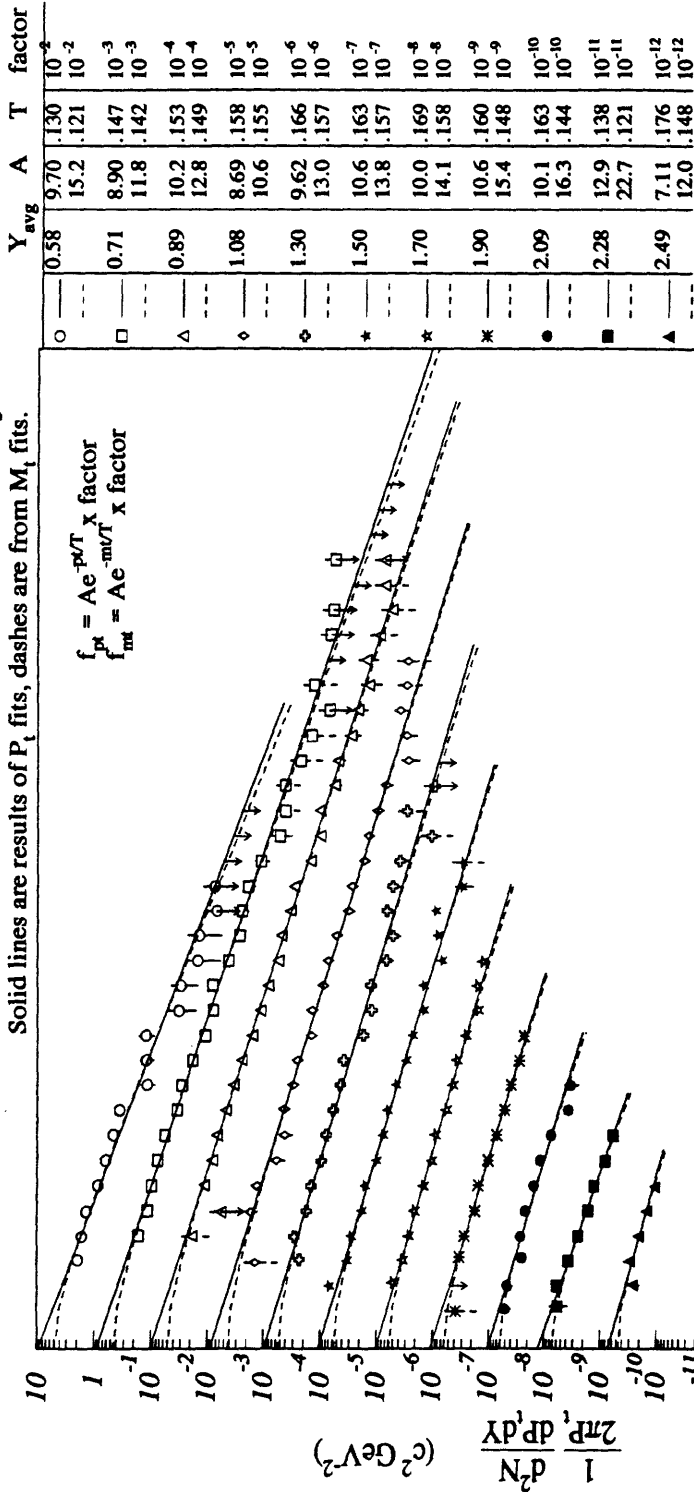
Inverse slope parameters and yields are shown for each particle species and slices in ZCAL.

The quality of the fits for each rapidity slice are shown for each summary page in terms of $\chi^2/(N - 2)$, where N =number of points for each fit (see Section 5.3.4).

Momentum bins that have only one count in them are indicated with an arrow that points down. Empty bins are indicated simply by an arrow pointing down, originating from the curve.

$^{16}\text{O} + \text{Al}$ Inelastic Cross-Section Summary for π^+

Solid lines are results of P_t fits, dashes are from M_t fits.



Y	Y _{avg}	A	T	factor
0	0.58	9.70	.130	10^{-4}
1	0.71	15.2	.121	10^{-2}
2	0.89	8.90	.147	10^{-3}
3	1.08	11.8	.142	10^{-3}
4	1.30	10.2	.153	10^{-4}
5	1.50	12.8	.149	10^{-4}
6	1.70	8.69	.158	10^{-5}
7	1.90	10.6	.155	10^{-5}
8	2.09	9.62	.166	10^{-6}
9	2.28	13.0	.157	10^{-6}
10	2.49	10.6	.163	10^{-7}
11		13.8	.157	10^{-7}
12		10.0	.169	10^{-8}
13		14.1	.158	10^{-8}
14		10.6	.160	10^{-9}
15		15.4	.148	10^{-9}
16		10.1	.163	10^{-10}
17		16.3	.144	10^{-10}
18		12.9	.138	10^{-11}
19		22.7	.121	10^{-11}
20		7.11	.176	10^{-12}
21		12.0	.148	10^{-12}

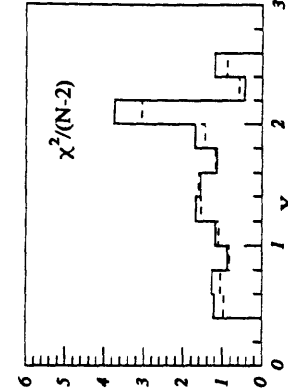
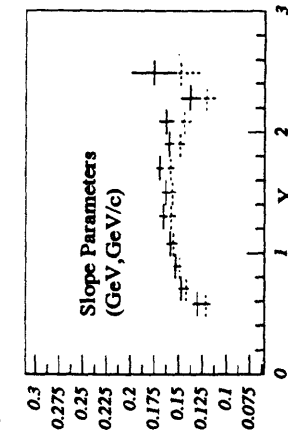
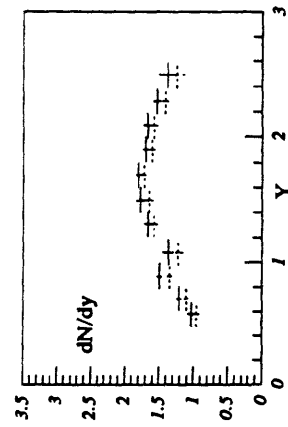
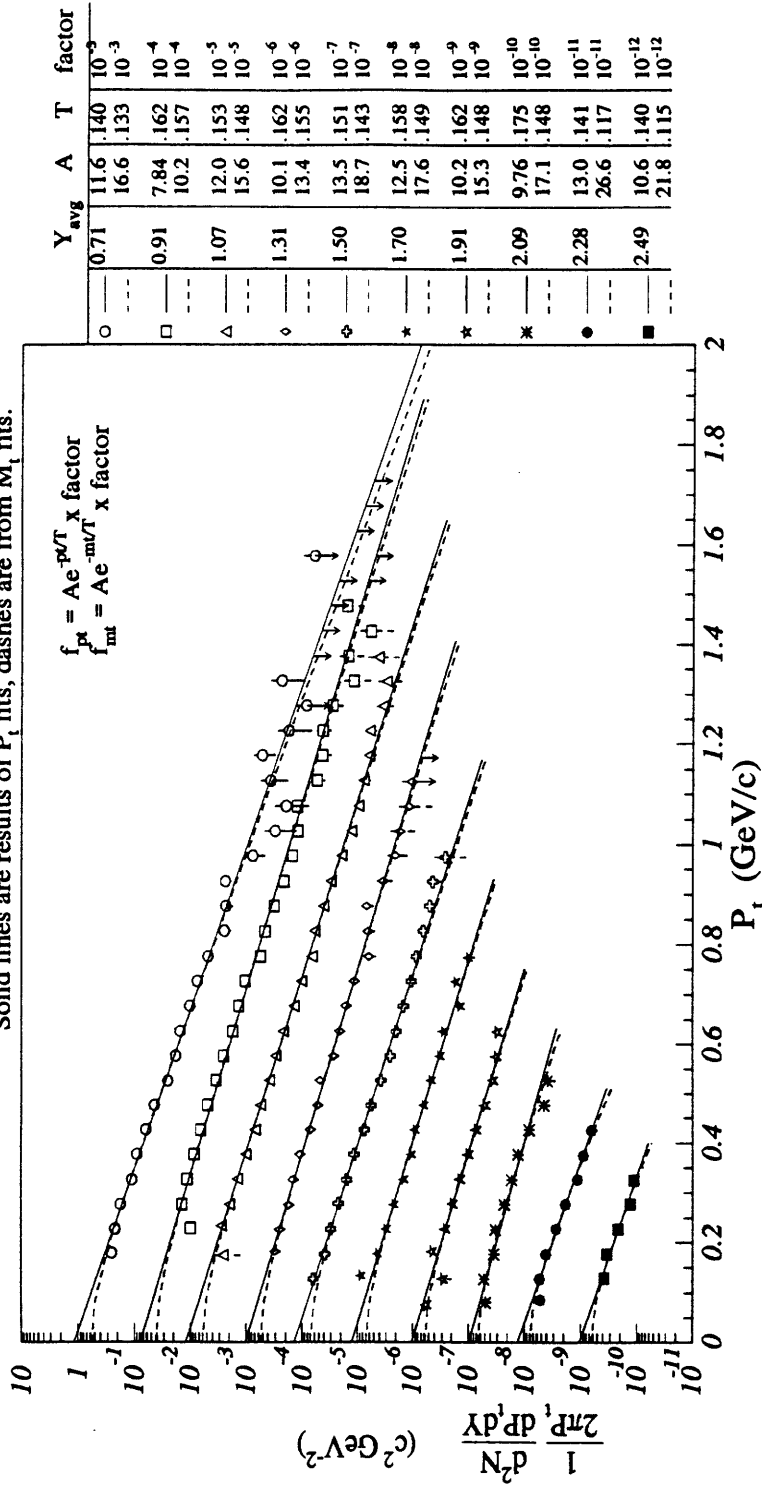


Figure A-1: Yield Summary for $^{16}\text{O} + ^{27}\text{Al}$ INEL: π^+

$^{16}\text{O} + \text{Al}$ Inelastic Cross-Section Summary for π^-

Solid lines are results of P_t fits, dashes are from M_t fits.



Y	Y _{avg}	A	T	factor
○	0.71	11.6	.140	10 ⁻⁹
□	0.91	16.6	.133	10 ⁻³
△	1.07	7.84	.162	10 ⁻⁴
◇	1.31	10.2	.157	10 ⁻⁴
◇	1.31	12.0	.153	10 ⁻³
◇	1.31	15.6	.148	10 ⁻⁵
◇	1.31	10.1	.162	10 ⁻⁶
◇	1.31	13.4	.155	10 ⁻⁶
◇	1.50	13.5	.151	10 ⁻⁷
◇	1.50	18.7	.143	10 ⁻⁷
*	1.70	12.5	.158	10 ⁻⁸
*	1.70	17.6	.149	10 ⁻⁸
*	1.91	10.2	.162	10 ⁻⁹
*	1.91	15.3	.148	10 ⁻⁹
*	2.09	9.76	.175	10 ⁻¹⁰
*	2.09	17.1	.148	10 ⁻¹⁰
●	2.28	13.0	.141	10 ⁻¹¹
●	2.28	26.6	.117	10 ⁻¹¹
■	2.49	10.6	.140	10 ⁻¹²
■	2.49	21.8	.115	10 ⁻¹²

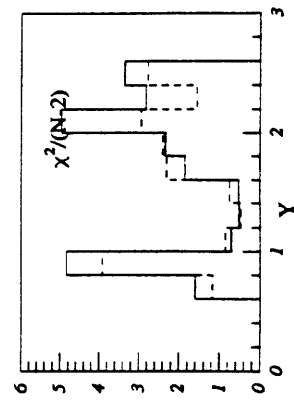
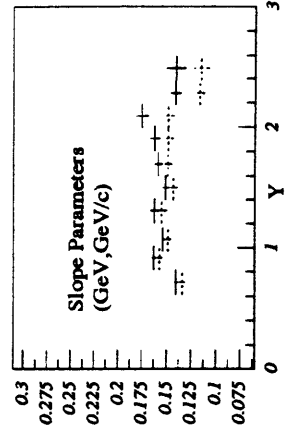
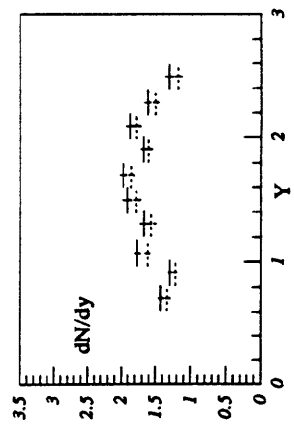
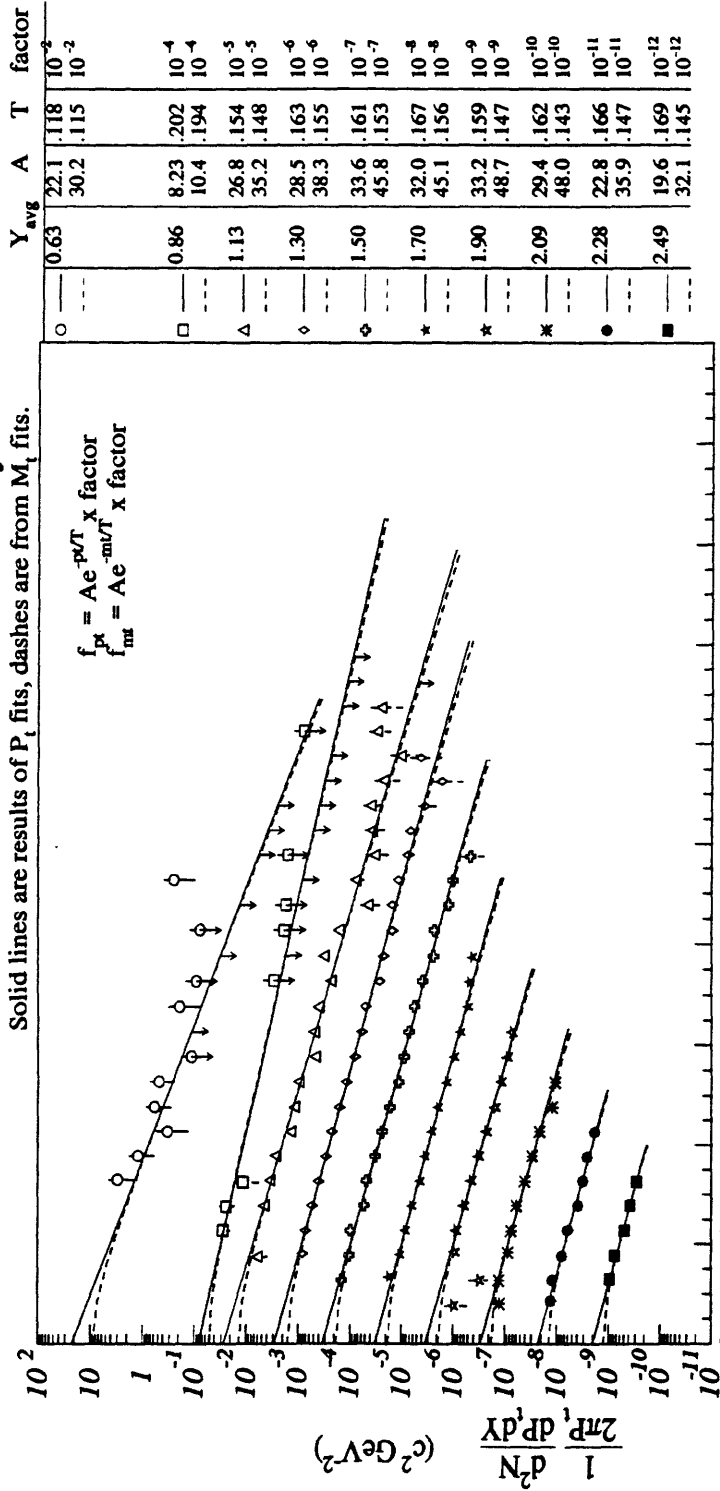


Figure A-2: Yield Summary for $^{16}\text{O} + ^{27}\text{Al}$ INEL: π^-

$^{16}\text{O} + \text{Al TMA} : \text{Yield Summary } \pi^+$

Solid lines are results of P_t fits, dashes are from M_t fits.



$$f_{\text{fit}}^{\text{pt}} = A e^{-p_t/T} \times \text{x factor}$$

$$f_{\text{fit}}^{\text{mt}} = A e^{-m_t/T} \times \text{x factor}$$

Symbol	Y_{avg}	A	T	factor
○	0.63	22.1	.118	10^{-2}
□	0.86	30.2	.115	10^{-2}
△	1.13	8.23	.202	10^{-4}
◇	1.30	10.4	.194	10^{-4}
◇	1.50	26.8	.154	10^{-5}
◇	1.70	35.2	.148	10^{-5}
◇	1.90	28.5	.163	10^{-6}
◇	2.09	38.3	.155	10^{-6}
◇	2.28	33.6	.161	10^{-7}
◇	2.49	45.8	.153	10^{-7}
◇	2.49	32.0	.167	10^{-8}
◇	2.49	45.1	.156	10^{-8}
◇	2.49	33.2	.159	10^{-9}
◇	2.49	48.7	.147	10^{-9}
◇	2.49	29.4	.162	10^{-10}
◇	2.49	48.0	.143	10^{-10}
◇	2.49	22.8	.166	10^{-11}
◇	2.49	35.9	.147	10^{-11}
◇	2.49	19.6	.169	10^{-12}
◇	2.49	32.1	.145	10^{-12}

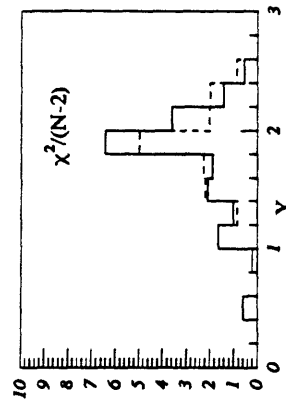
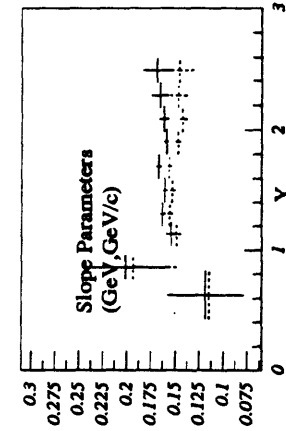
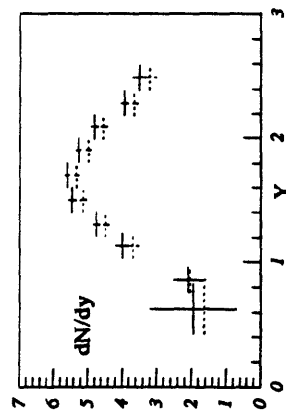
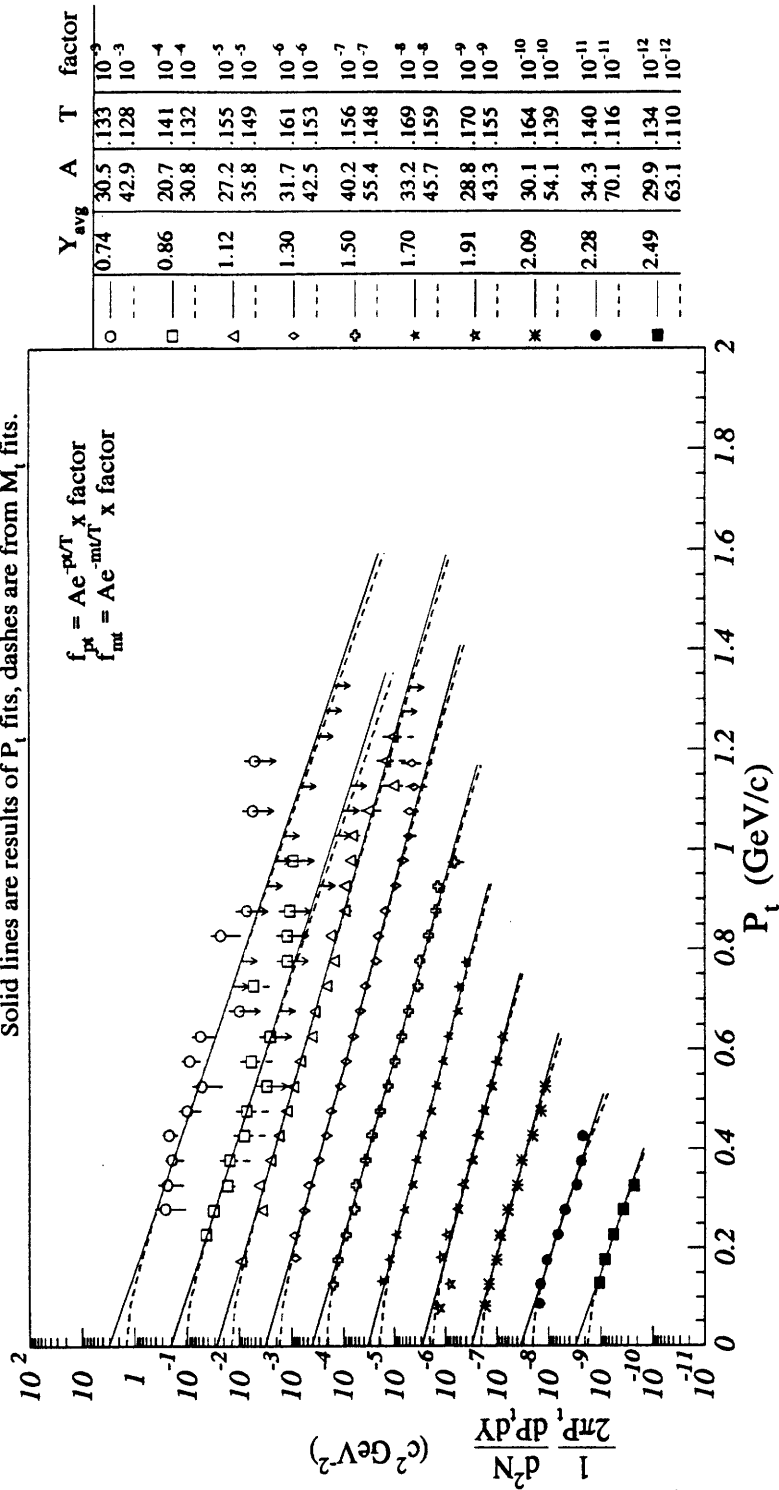


Figure A-3: Yield Summary for $^{16}\text{O} + ^{27}\text{Al TMA}: \pi^+$

$^{16}\text{O} + \text{Al TMA}$: Yield Summary π^-

Solid lines are results of P_t fits, dashes are from M_t fits.



$$f_{pt} = A e^{-P_t/T} \times \text{x factor}$$

$$f_{mt} = A e^{-m_t/T} \times \text{x factor}$$

Y	Y _{avg}	A	T	factor
0	0.74	30.5	.133	10^{-3}
1	0.86	42.9	.128	10^{-3}
2	1.12	20.7	.141	10^{-4}
3	1.30	30.8	.132	10^{-4}
4	1.50	27.2	.155	10^{-5}
5	1.70	35.8	.149	10^{-5}
6	1.91	31.7	.161	10^{-6}
7	2.09	42.5	.153	10^{-6}
8	2.28	40.2	.156	10^{-7}
9	2.49	55.4	.148	10^{-7}
10	2.74	33.2	.169	10^{-8}
11	3.01	45.7	.159	10^{-8}
12	3.43	28.8	.170	10^{-9}
13	4.02	43.3	.155	10^{-9}
14	4.54	30.1	.164	10^{-10}
15	5.41	54.1	.139	10^{-10}
16	70.1	34.3	.140	10^{-11}
17	70.1	70.1	.116	10^{-11}
18	29.9	29.9	.134	10^{-12}
19	63.1	63.1	.110	10^{-12}

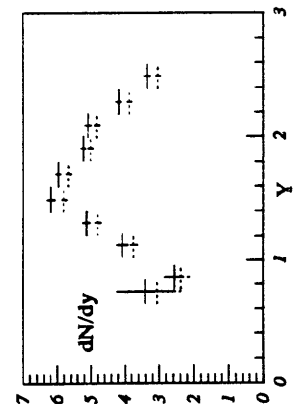
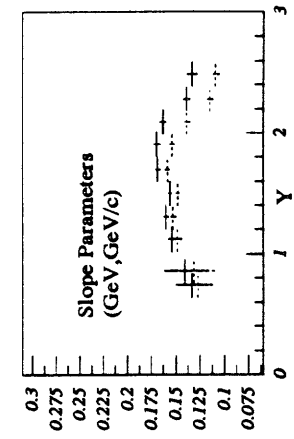
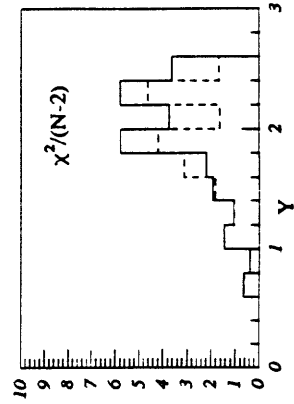
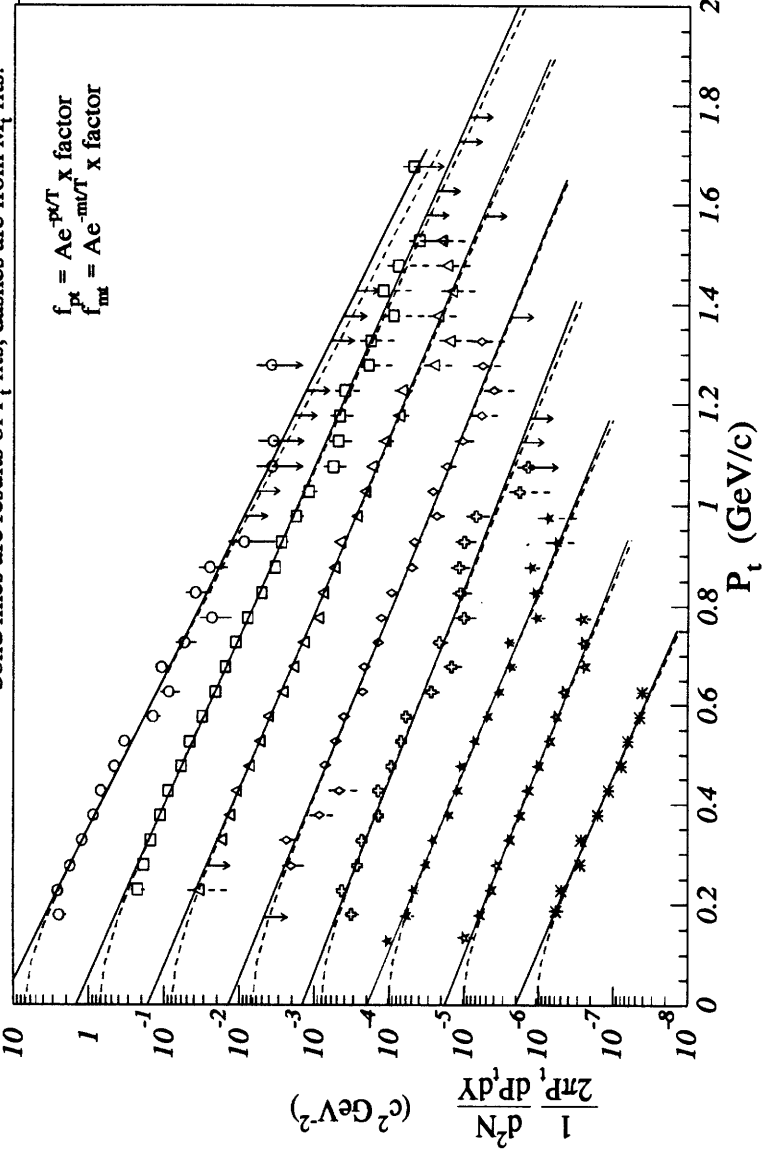


Figure A-4: Yield Summary for $^{16}\text{O} + ^{27}\text{Al TMA}$: π^-

$^{16}\text{O} + \text{Al CENT2} : \text{Yield Summary } \pi^+$

Solid lines are results of P_t fits, dashes are from M_t fits.



$$f_{\pi^+} = A e^{-p_t/T} \times \text{x factor}$$

$$f_{\text{m}} = A e^{-m p_t/T} \times \text{x factor}$$

Symbol	Y_{avg}	A	T	factor
○	0.58	14.3	.132	10^{-2}
○	0.70	21.3	.125	10^{-2}
□	0.88	14.6	.148	10^{-3}
□	1.08	19.0	.143	10^{-3}
△	1.30	16.3	.154	10^{-4}
△	1.50	20.3	.150	10^{-4}
◇	1.70	13.8	.159	10^{-5}
◇	1.87	16.4	.156	10^{-5}
⊕	1.50	14.3	.168	10^{-6}
⊕	1.70	19.3	.159	10^{-6}
★	1.50	19.3	.158	10^{-7}
★	1.70	26.3	.150	10^{-7}
★	1.70	17.9	.165	10^{-8}
★	1.87	25.1	.155	10^{-8}
★	1.87	20.1	.151	10^{-9}
★	1.87	28.8	.141	10^{-9}

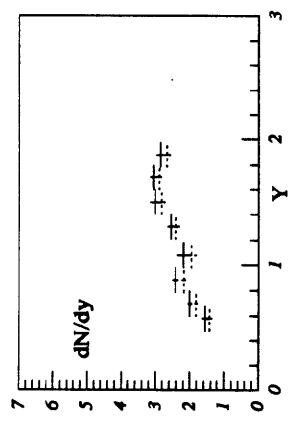
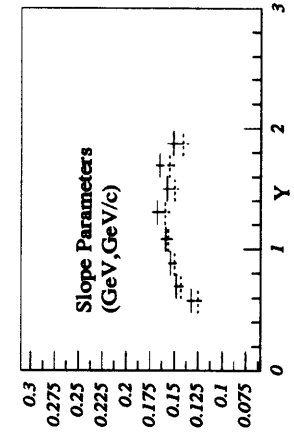
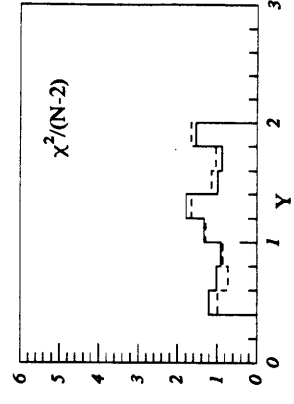
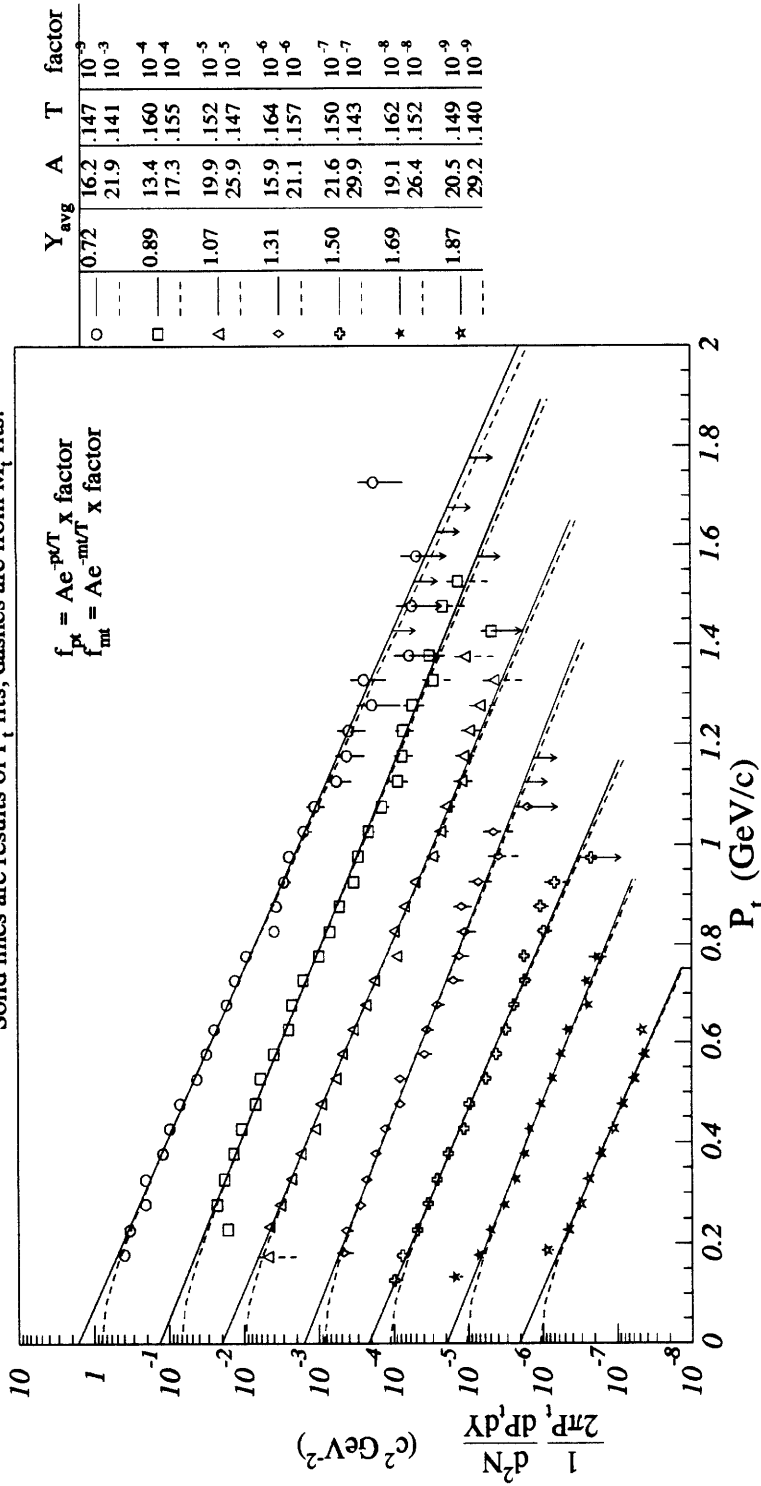


Figure A-5: Yield Summary for $^{16}\text{O} + ^{27}\text{Al CENT2} : \pi^+$

$^{16}\text{O} + \text{Al CENT2}$: Yield Summary π^-

Solid lines are results of P_t fits, dashes are from M_t fits.



Y	avg	A	T	factor
○	0.72	16.2	.147	10^{-9}
□	0.89	21.9	.141	10^{-3}
△	1.07	13.4	.160	10^{-4}
◇	1.31	17.3	.155	10^{-4}
◇	1.07	19.9	.152	10^{-5}
◇	1.31	25.9	.147	10^{-5}
◇	1.31	15.9	.164	10^{-6}
◇	1.31	21.1	.157	10^{-6}
◇	1.50	21.6	.150	10^{-7}
◇	1.50	29.9	.143	10^{-7}
◇	1.69	19.1	.162	10^{-8}
◇	1.69	26.4	.152	10^{-8}
◇	1.87	20.5	.149	10^{-9}
◇	1.87	29.2	.140	10^{-9}

$$f_{pt} = A e^{-p_t/T} \times \text{factor}$$

$$f_{mt} = A e^{-m_t/T} \times \text{factor}$$

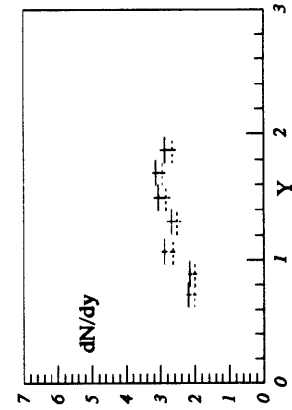
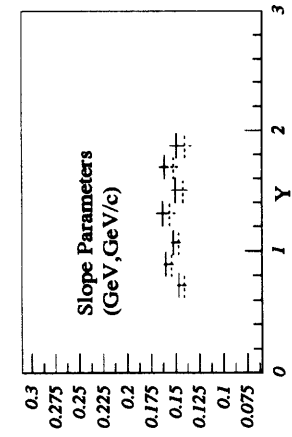
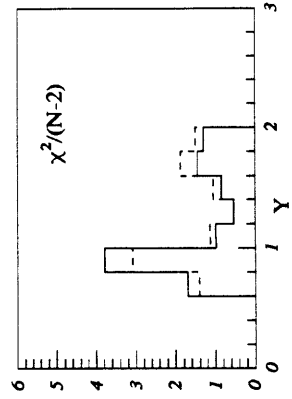
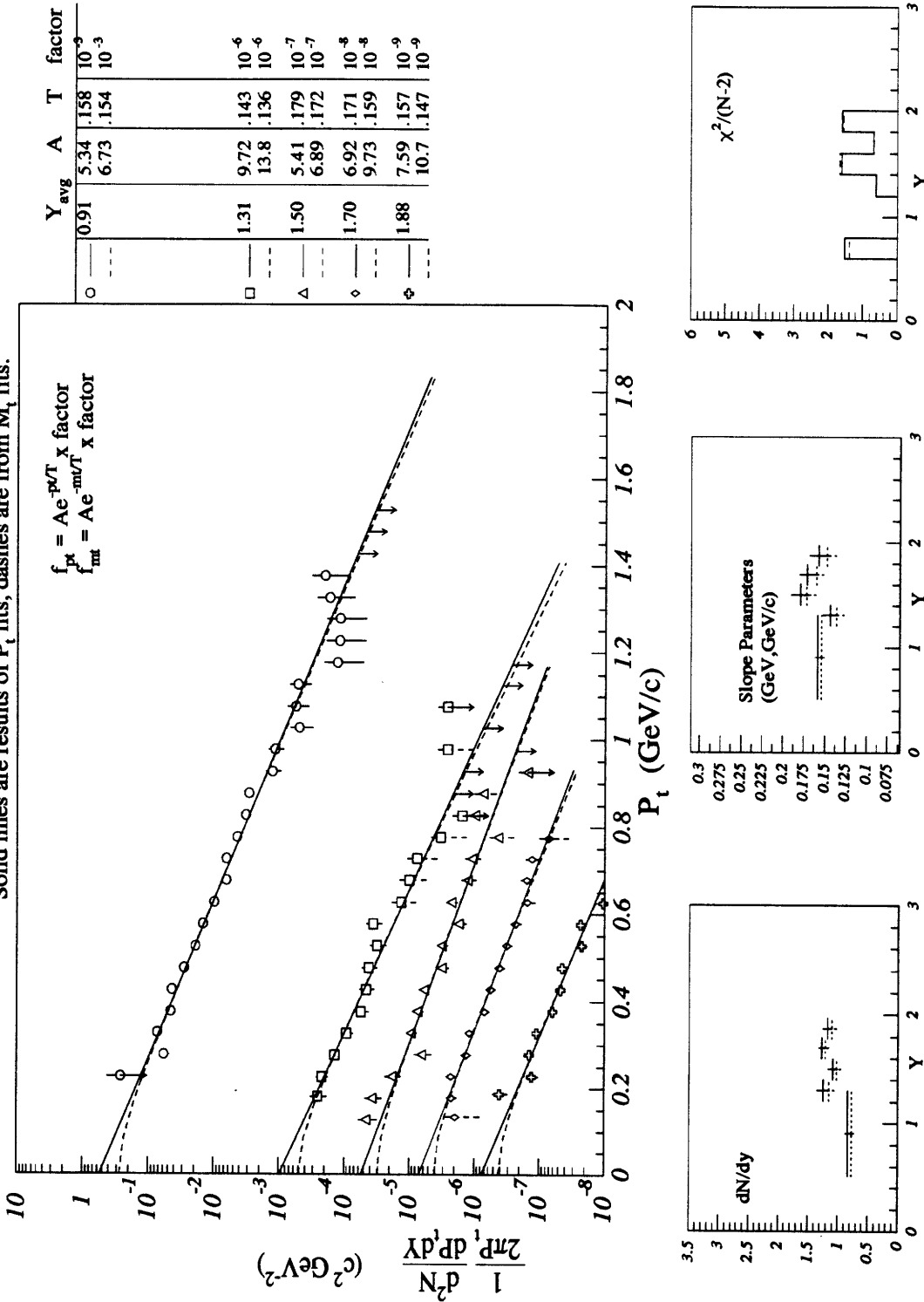


Figure A-6: Yield Summary for $^{16}\text{O} + ^{27}\text{Al CENT2}$: π^-

$^{16}\text{O} + \text{Al MID} : \text{Yield Summary } \pi^+$

Solid lines are results of P_t fits, dashes are from M_t fits.



	Y_{avg}	A	T	factor
○	0.91	5.34	.158	10^{-3}
○	---	6.73	.154	10^{-3}
□	1.31	9.72	.143	10^{-6}
□	---	13.8	.136	10^{-6}
△	1.50	5.41	.179	10^{-7}
△	---	6.89	.172	10^{-7}
◇	1.70	6.92	.171	10^{-8}
◇	---	9.73	.159	10^{-8}
⊕	1.88	7.59	.157	10^{-9}
⊕	---	10.7	.147	10^{-9}

Figure A-7: Yield Summary for $^{16}\text{O} + ^{27}\text{Al MID} : \pi^+$

$^{16}\text{O} + \text{Al MID} : \text{Yield Summary } \pi^-$

Solid lines are results of P_t fits, dashes are from M_t fits.

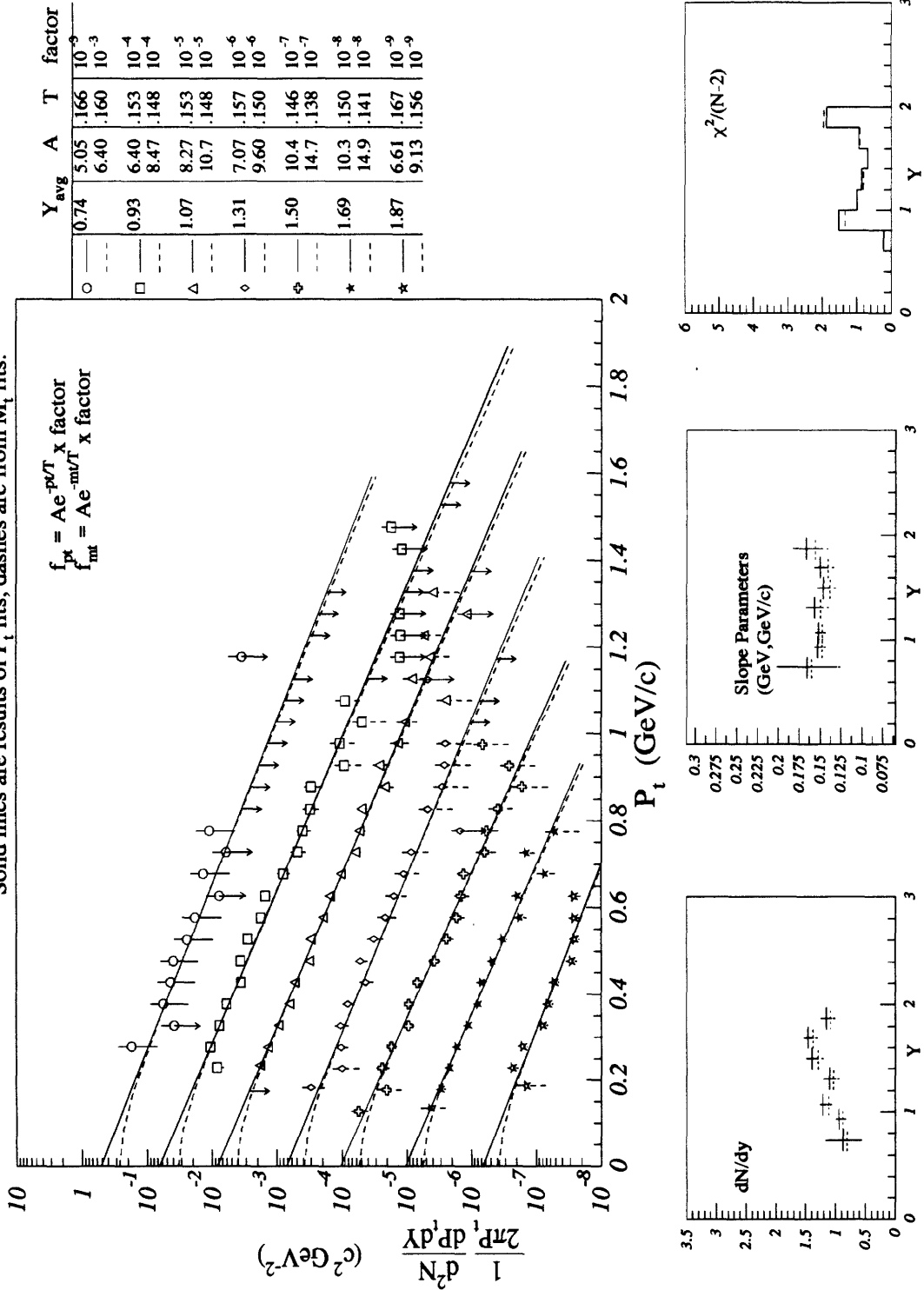


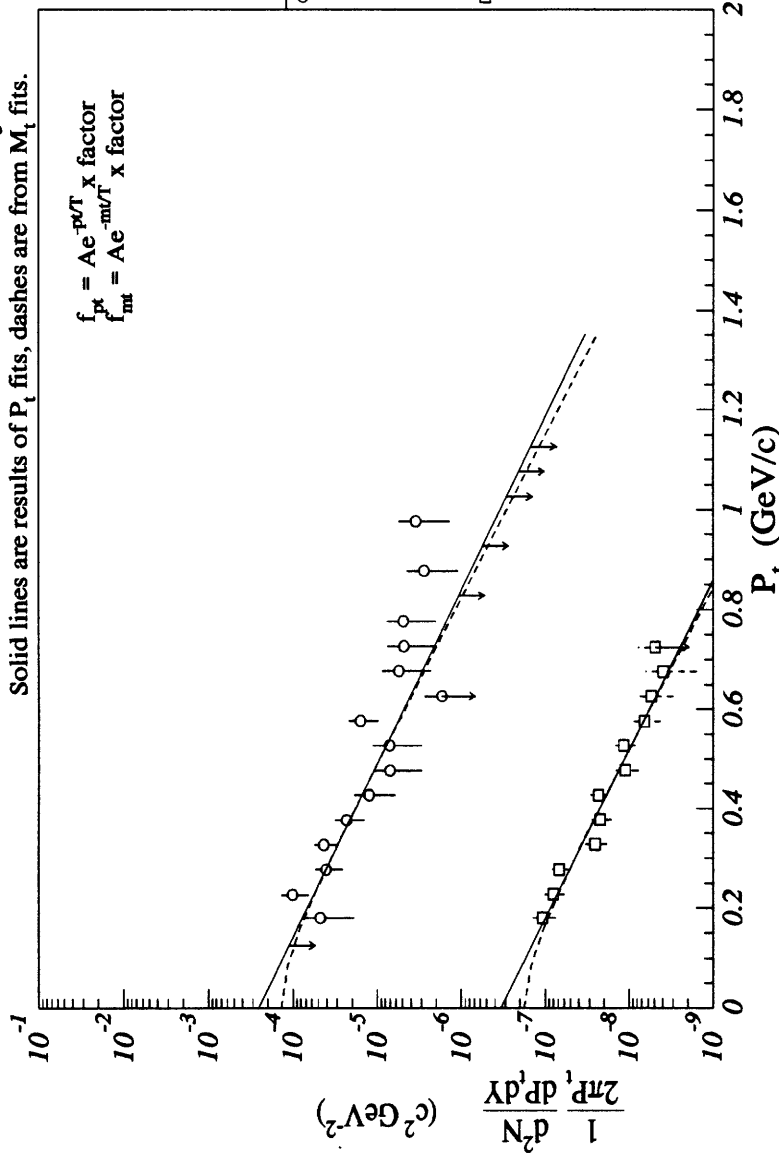
Figure A-8: Yield Summary for $^{16}\text{O} + ^{27}\text{Al MID} : \pi^-$

$^{16}\text{O} + \text{Al}$ PERP1 : Yield Summary π^+

Solid lines are results of P_t fits, dashes are from M_t fits.

$$f_{pt} = A e^{-pT/T} \times \text{x factor}$$

$$f_{mt} = A e^{-mT/T} \times \text{x factor}$$



	Y avg	A	T	factor
○	1.34	2.51	.151	10^{-6}
---		3.69	.141	10^{-6}
□	1.81	3.35	.147	10^{-9}
---		4.84	.138	10^{-9}

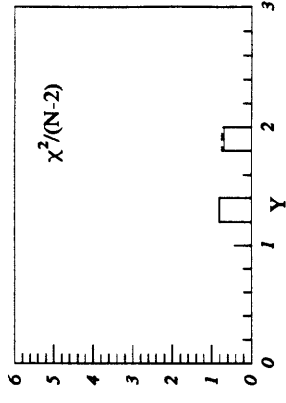
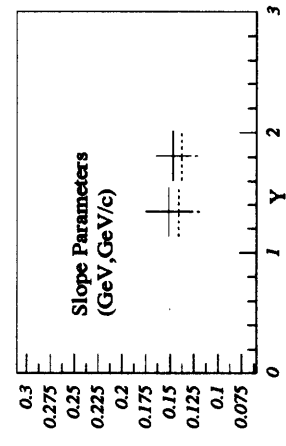
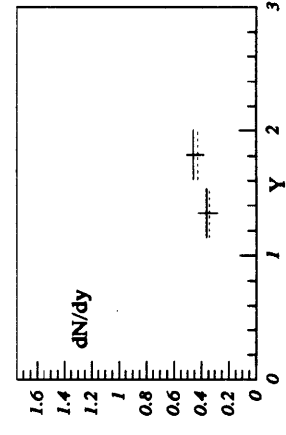


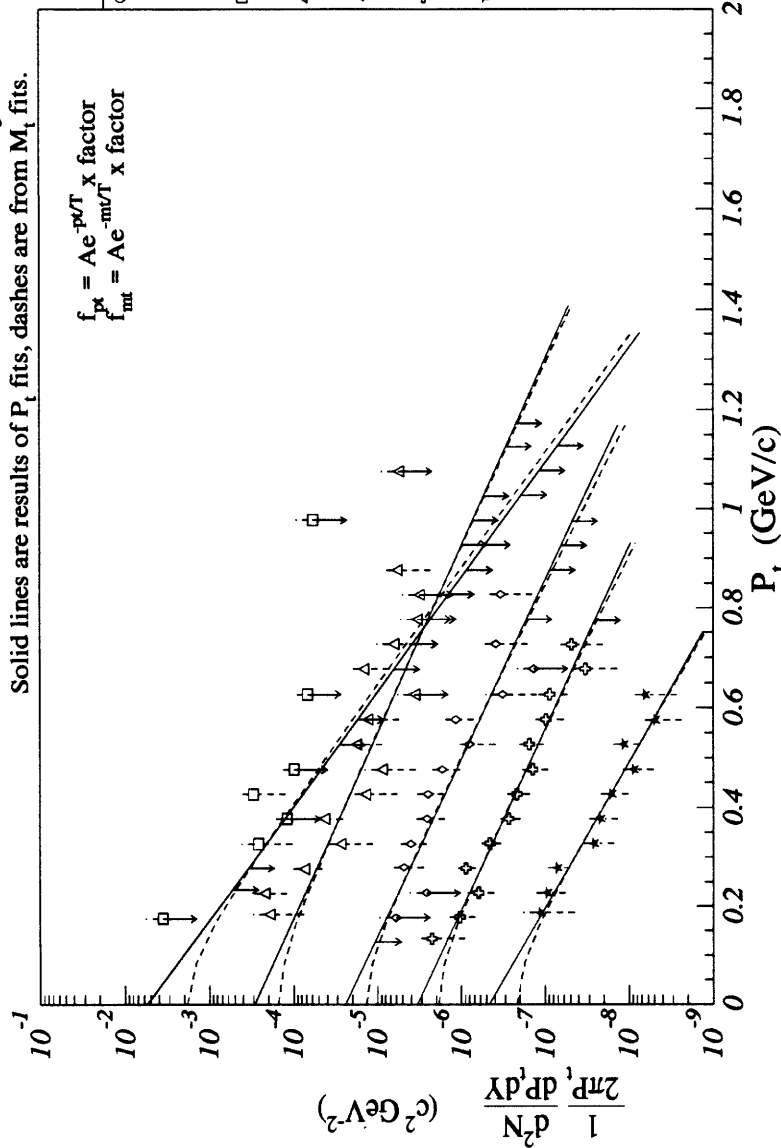
Figure A-9: Yield Summary for $^{16}\text{O} + ^{27}\text{Al}$ PERP1: π^+

$^{16}\text{O} + \text{Al PERP1}$: Yield Summary π^-

Solid lines are results of P_t fits, dashes are from M_t fits.

$$f_{pt} = A e^{-pT} \times \text{factor}$$

$$f_{mt} = A e^{-mT} \times \text{factor}$$



Y	Y_{avg}	A	T	factor
○	0.00	.000	.000	10^{-3}
□	1.11	5.45	.100	10^{-5}
△	1.31	7.37	.100	10^{-5}
◇	1.50	2.89	.163	10^{-6}
◆	1.69	3.62	.158	10^{-6}
★	1.87	2.36	.157	10^{-7}
		3.49	.146	10^{-7}
		3.31	.159	10^{-8}
		4.71	.148	10^{-8}
		4.56	.128	10^{-9}
		6.83	.121	10^{-9}

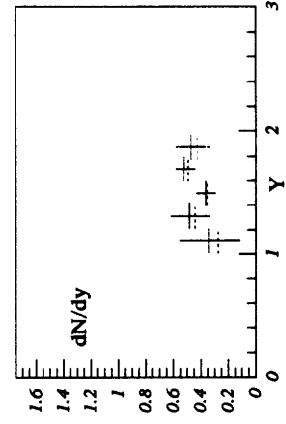
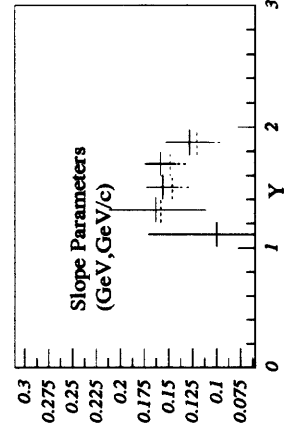
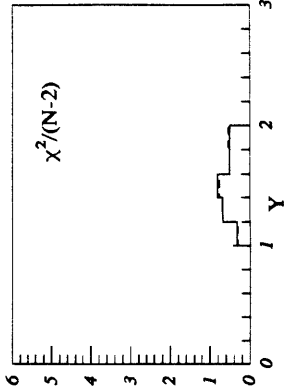


Figure A-10: Yield Summary for $^{16}\text{O} + ^{27}\text{Al PERP1}$: π^-

Appendix B

Yield Summary: $^{16}\text{O} + ^{64}\text{Cu} : \pi$

$^{16}\text{O}+\text{Cu}$ Inelastic Cross-Section Summary for π^+

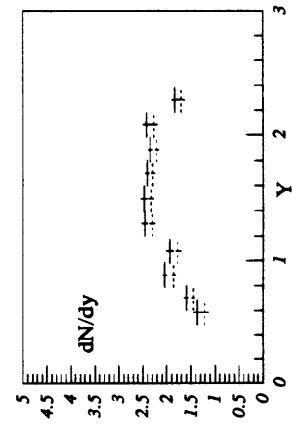
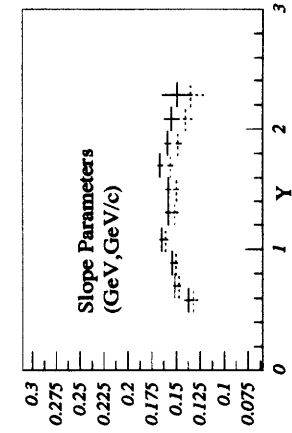
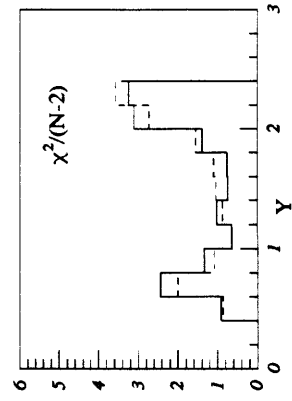
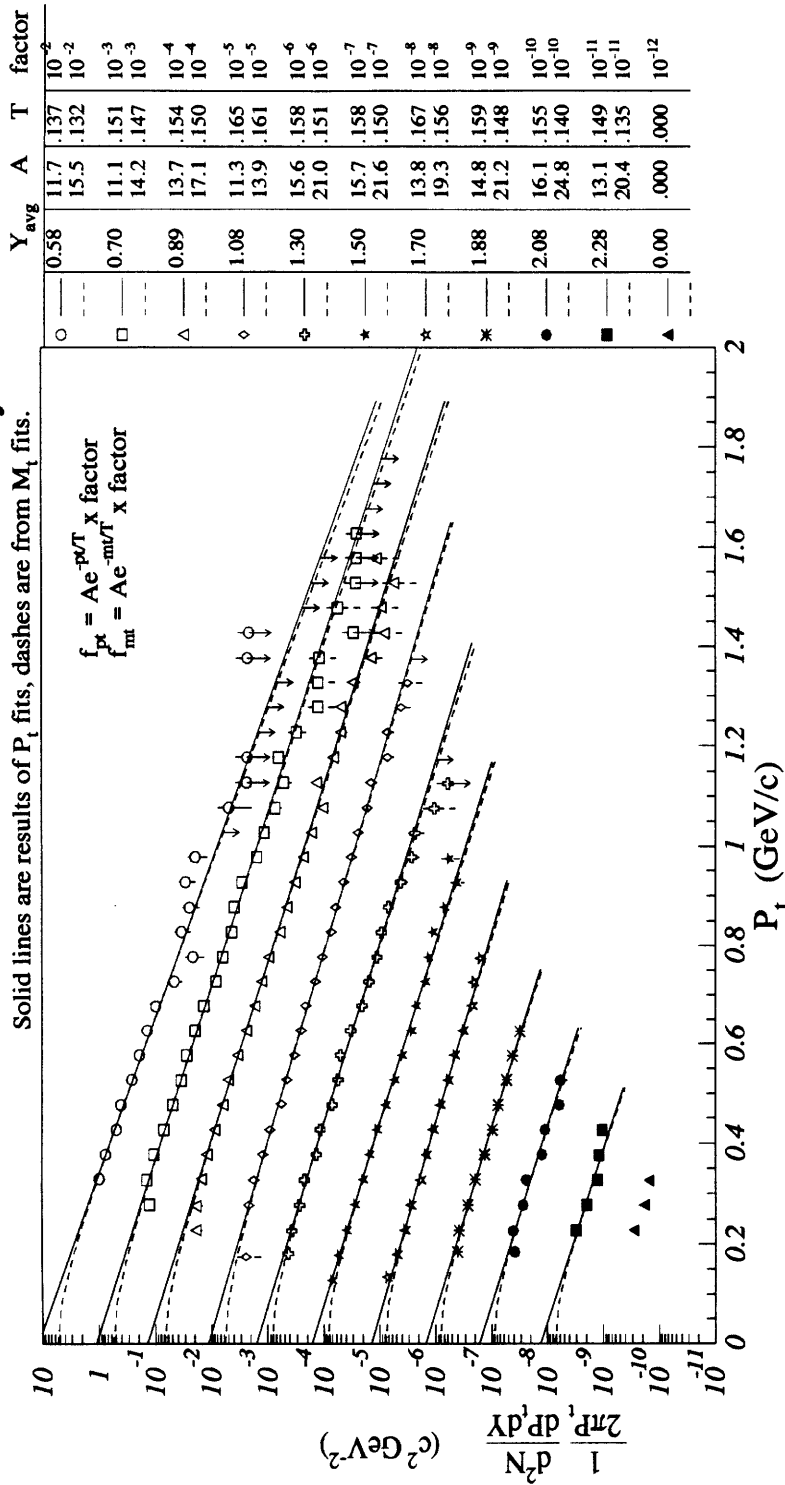
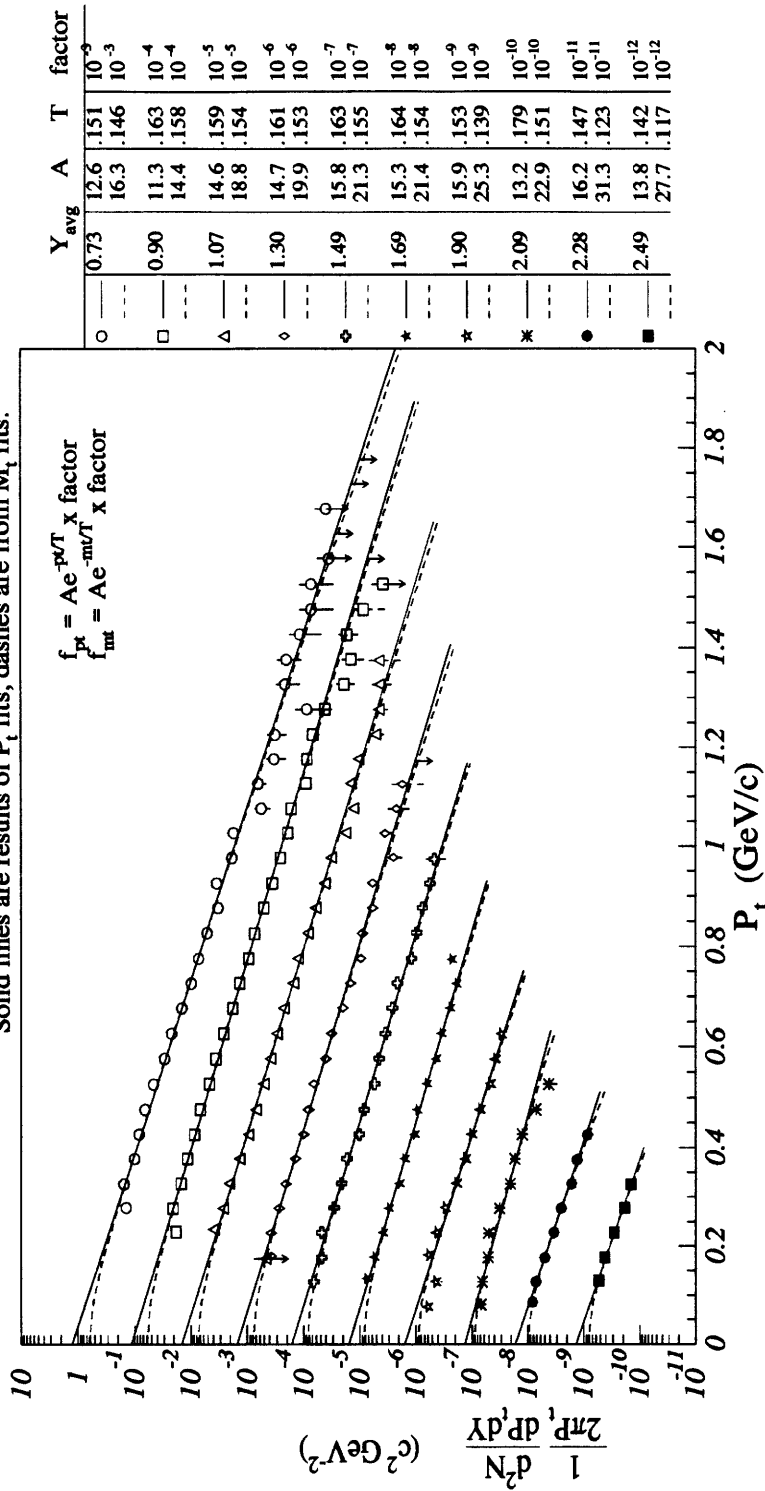


Figure B-1: Yield Summary for $^{16}\text{O} + ^{64}\text{Cu}$ INEL: π^+

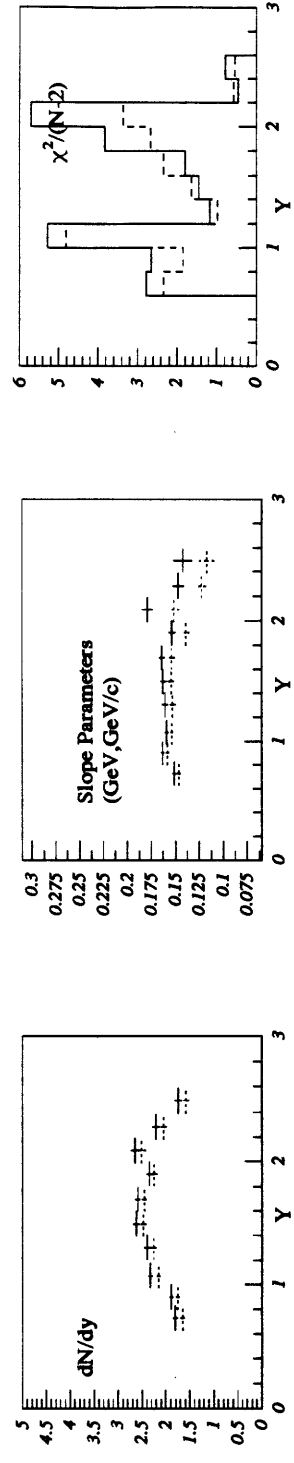
$^{16}\text{O} + \text{Cu}$ Inelastic Cross-Section Summary for π^-

Solid lines are results of P_t fits, dashes are from M_t fits.



Y	Y _{avg}	A	T	factor
○	0.73	12.6	.151	10 ⁻⁹
□	0.90	16.3	.146	10 ⁻³
△	1.07	11.3	.163	10 ⁻⁴
◇	1.30	14.4	.158	10 ⁻⁴
◆	1.49	14.6	.159	10 ⁻⁵
♣	1.69	18.8	.154	10 ⁻⁵
★	1.90	14.7	.161	10 ⁻⁶
✱	2.09	19.9	.153	10 ⁻⁶
✳	2.28	15.8	.163	10 ⁻⁷
✴	2.49	21.3	.155	10 ⁻⁷
✵	2.77	15.3	.164	10 ⁻⁸
✶	2.99	21.4	.154	10 ⁻⁸
✷	3.22	15.9	.153	10 ⁻⁹
✸	3.45	25.3	.139	10 ⁻⁹
✹	3.68	13.2	.179	10 ⁻¹⁰
✺	3.91	22.9	.151	10 ⁻¹⁰
✻	4.14	16.2	.147	10 ⁻¹¹
✼	4.37	31.3	.123	10 ⁻¹¹
✽	4.60	13.8	.142	10 ⁻¹²
✾	4.83	27.7	.117	10 ⁻¹²

Figure B-2: Yield Summary for $^{16}\text{O} + ^{64}\text{Cu}$ INEL: π^-

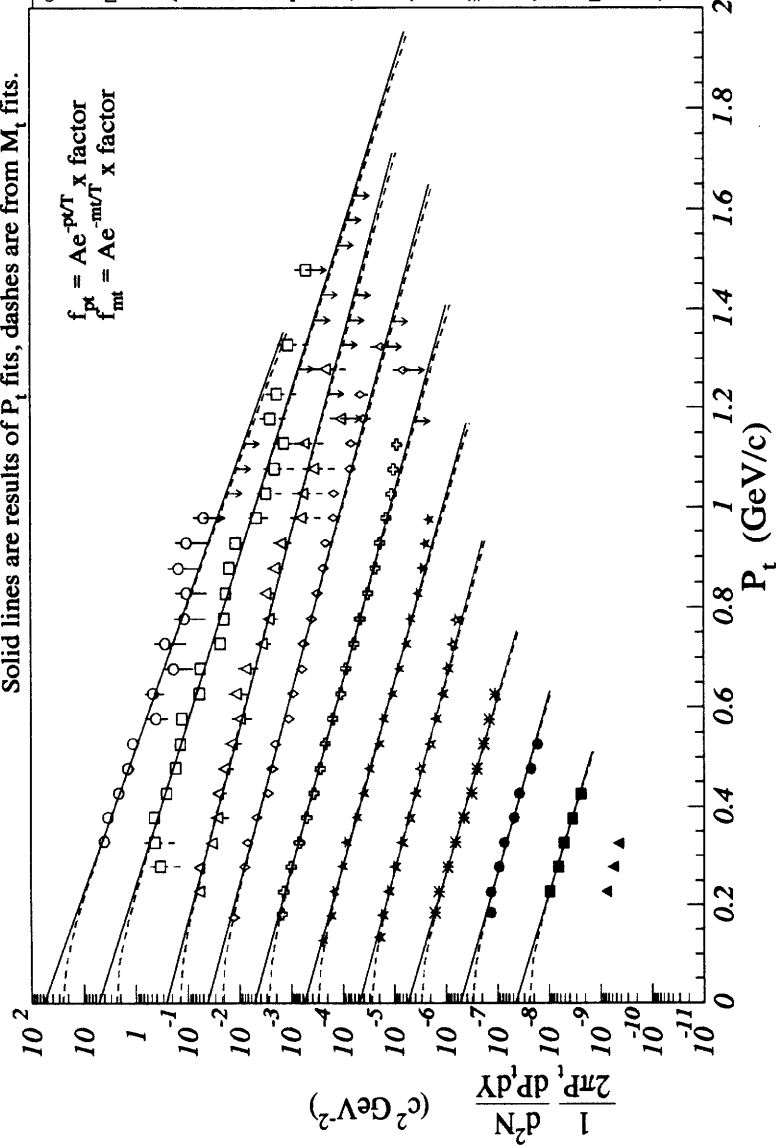


$^{16}\text{O} + \text{Cu TMA}$: Yield Summary π^+

Solid lines are results of P_t fits, dashes are from M_t fits.

$$f_{pt} = Ae^{-pT/T} \times \text{x factor}$$

$$f_{mt} = Ae^{-mT/T} \times \text{x factor}$$



Symbol	Y _{avg}	A	T	factor
○	0.58	57.5	.127	10 ⁻²
□	0.70	79.9	.122	10 ⁻²
△	0.87	51.1	.143	10 ⁻³
◇	1.12	64.9	.139	10 ⁻³
☆	1.30	25.7	.169	10 ⁻⁴
★	1.50	33.7	.163	10 ⁻⁴
✱	1.70	41.0	.166	10 ⁻⁵
✶	1.88	52.1	.161	10 ⁻⁵
●	2.08	50.8	.164	10 ⁻⁶
■	2.28	67.4	.157	10 ⁻⁶
▲	0.00	55.6	.161	10 ⁻⁷
		76.5	.152	10 ⁻⁷
		48.1	.168	10 ⁻⁸
		67.6	.157	10 ⁻⁸
		54.9	.154	10 ⁻⁹
		79.2	.143	10 ⁻⁹
		52.4	.157	10 ⁻¹⁰
		80.1	.143	10 ⁻¹⁰
		43.9	.149	10 ⁻¹¹
		68.7	.135	10 ⁻¹¹
		.000	.000	10 ⁻¹²

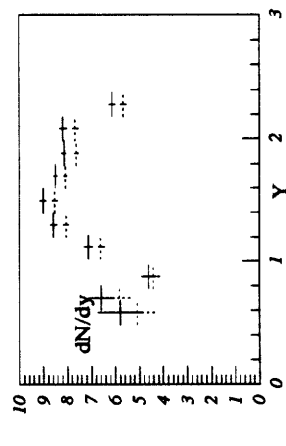
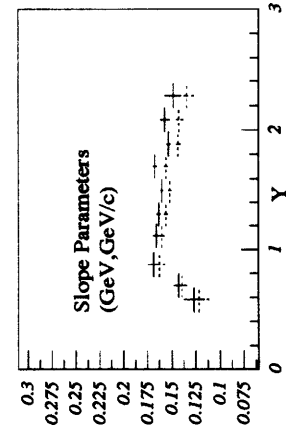
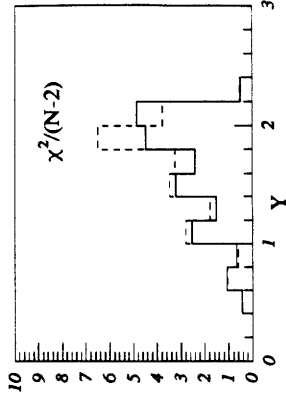
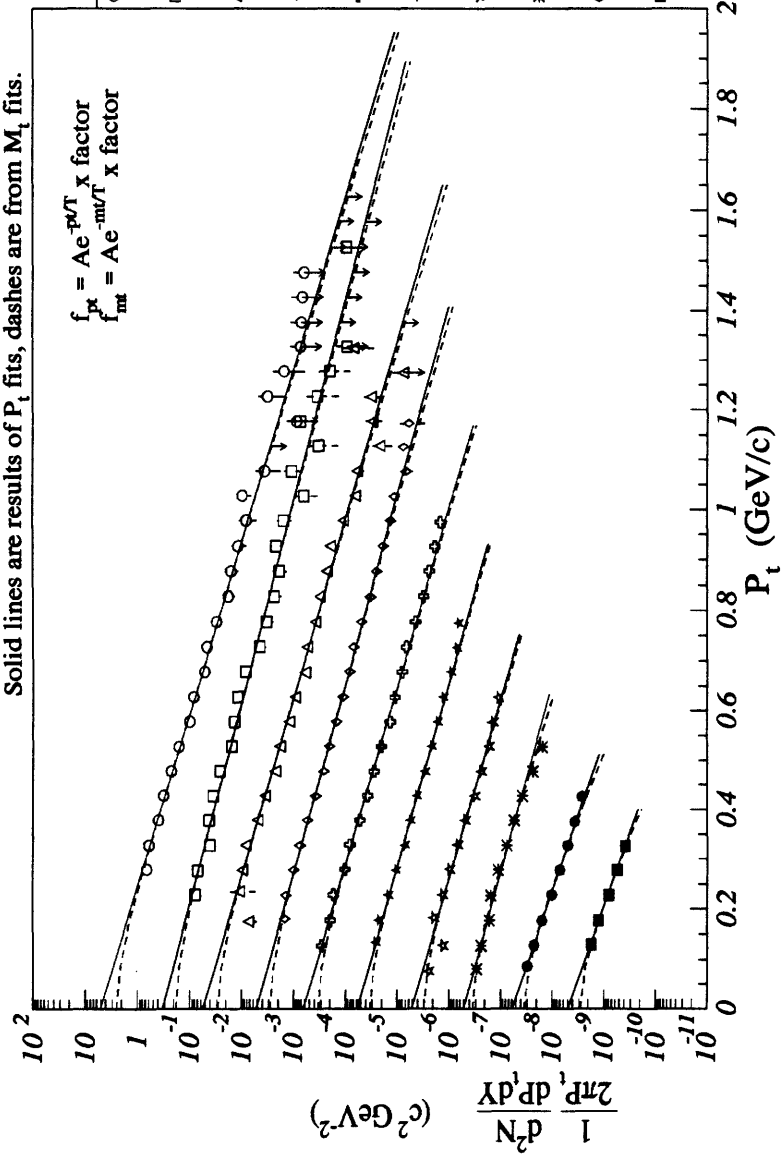


Figure B-3: Yield Summary for $^{16}\text{O} + ^{64}\text{Cu TMA}$: π^+

¹⁶O+Cu TMA : Yield Summary π^-

Solid lines are results of P_t fits, dashes are from M_t fits.



Symbol	Y_{avg}	A	T	factor
○	0.74	50.2	.150	10^{-9}
□	0.86	64.5	.146	10^{-3}
△	1.12	32.3	.176	10^{-4}
◇	1.30	41.3	.169	10^{-4}
◇	1.49	55.2	.155	10^{-5}
◇	1.49	73.0	.149	10^{-5}
◇	1.69	51.4	.164	10^{-6}
◇	1.69	68.7	.157	10^{-6}
◇	1.90	63.0	.155	10^{-7}
◇	1.90	85.8	.148	10^{-7}
◇	2.09	59.1	.160	10^{-8}
◇	2.09	83.0	.150	10^{-8}
◇	2.28	51.3	.157	10^{-9}
◇	2.28	79.0	.143	10^{-9}
◇	2.49	51.5	.165	10^{-10}
◇	2.49	91.8	.141	10^{-10}
◇	2.49	58.4	.132	10^{-11}
◇	2.49	121.	.111	10^{-11}
◇	2.49	48.8	.127	10^{-12}
◇	2.49	106.	.105	10^{-12}

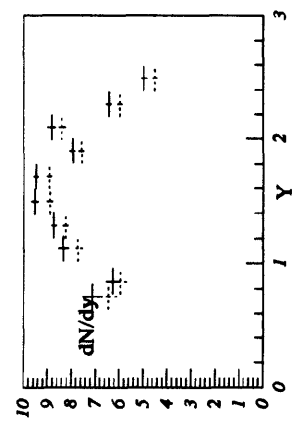
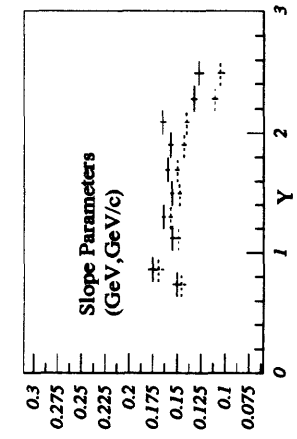
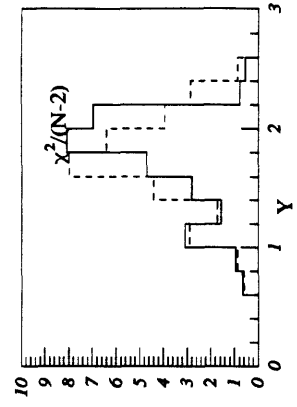
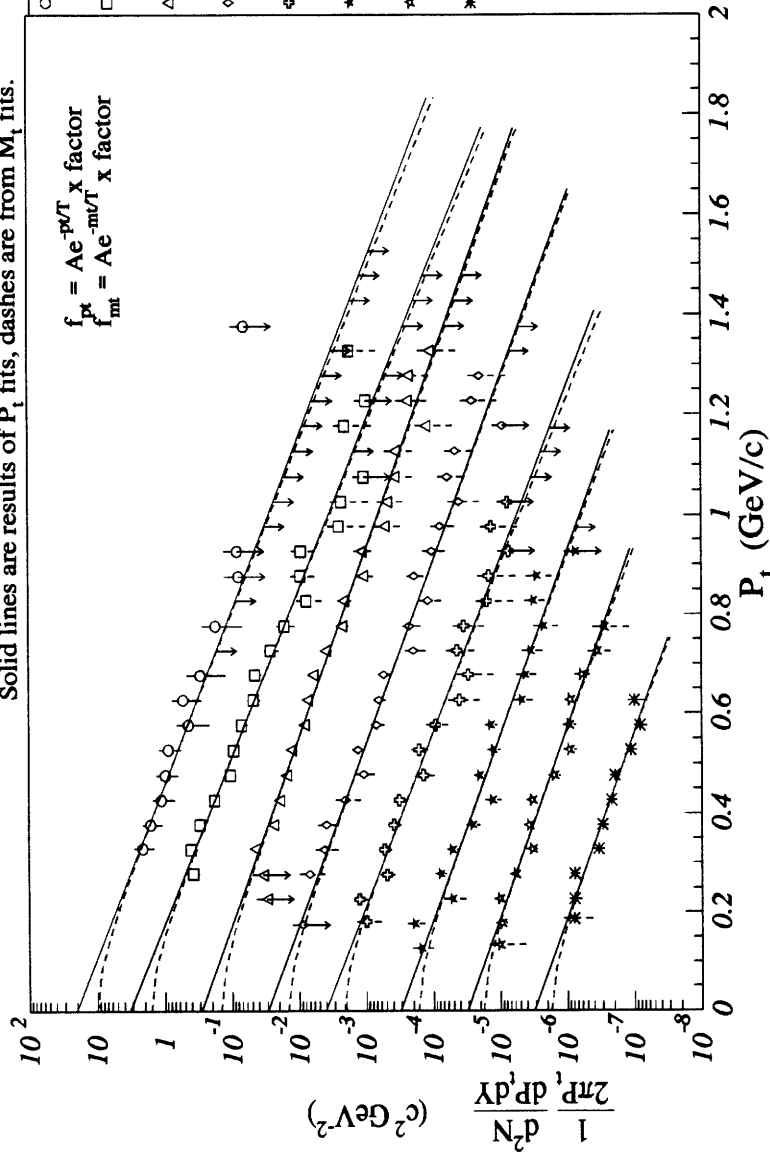


Figure B-4: Yield Summary for ¹⁶O + ⁶⁴Cu TMA: π^-

$^{16}\text{O} + \text{Cu}$ CENT1 : Yield Summary π^+

Solid lines are results of P_t fits, dashes are from M_t fits.



$$f_{pt} = A e^{-p_t/T} \times \text{x factor}$$

$$f_{mt} = A e^{-m_t/T} \times \text{x factor}$$

Centrality	Symbol	Y_{avg}	A	T	factor
0	○	0.58	19.9	.152	10^{-2}
1	□	0.71	25.8	.146	10^{-2}
2	△	0.89	32.6	.146	10^{-3}
3	◇	1.08	42.5	.142	10^{-3}
4	◇	1.30	28.0	.165	10^{-4}
5	◇	1.30	34.5	.160	10^{-4}
6	◇	1.30	29.1	.159	10^{-5}
7	◇	1.30	35.6	.156	10^{-5}
8	◇	1.30	39.9	.152	10^{-6}
9	◇	1.30	55.7	.144	10^{-6}
0	*	1.50	30.7	.161	10^{-7}
1	*	1.70	41.5	.154	10^{-7}
2	*	1.70	30.8	.166	10^{-8}
3	*	1.87	43.6	.155	10^{-8}
4	*	1.87	30.9	.163	10^{-9}
5	*	1.87	42.9	.153	10^{-9}

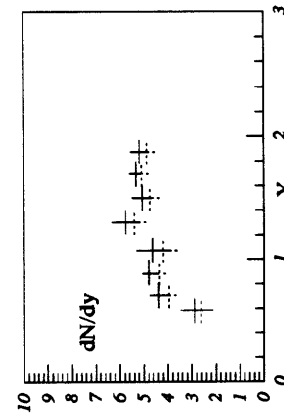
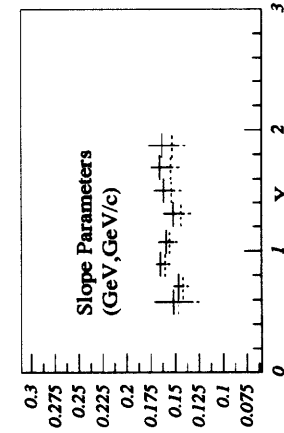
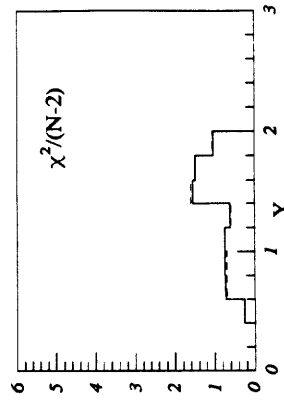
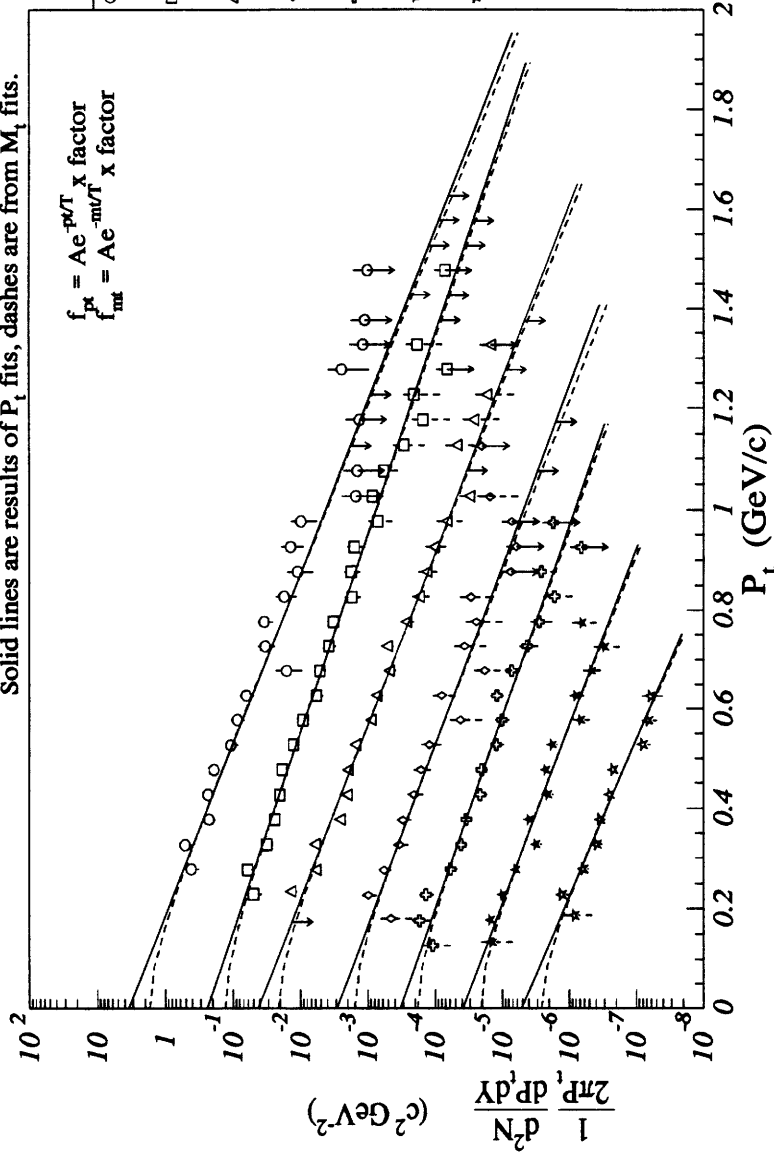


Figure B-5: Yield Summary for $^{16}\text{O} + ^{64}\text{Cu}$ CENT1: π^+

¹⁶O+Cu CENT1 : Yield Summary π^-

Solid lines are results of P_t fits, dashes are from M_t fits.



Symbol	Y_{avg}	A	T	factor
○	0.74	34.3	.149	10^{-9}
□	0.90	44.5	.144	10^{-3}
△	1.07	23.8	.174	10^{-4}
◇	1.31	29.6	.169	10^{-4}
◆	1.50	42.1	.151	10^{-5}
♣	1.69	54.4	.146	10^{-5}
★	1.87	28.4	.157	10^{-6}
★	1.87	40.2	.147	10^{-6}
★	1.87	32.5	.167	10^{-7}
★	1.87	43.3	.159	10^{-7}
★	1.87	38.1	.155	10^{-8}
★	1.87	53.7	.146	10^{-8}
★	1.87	51.0	.137	10^{-9}
★	1.87	76.6	.128	10^{-9}

$$f_{pt} = Ae^{-pt/T} \times \text{factor}$$

$$f_{mt} = Ae^{-mv/T} \times \text{factor}$$

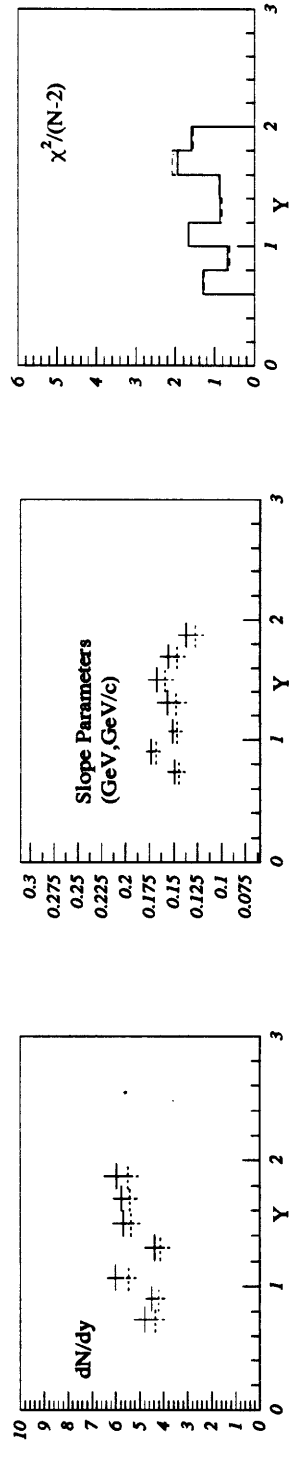


Figure B-6: Yield Summary for ¹⁶O + ⁶⁴Cu CENT1: π^-

$^{16}\text{O} + \text{Cu}$ CENT2 : Yield Summary π^+

Solid lines are results of P_t fits, dashes are from M_t fits.

$$f_{pt} = A e^{-pT/T} \times \text{factor}$$

$$f_{mt} = A e^{-mT/T} \times \text{factor}$$

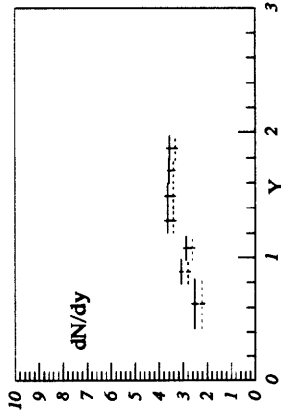
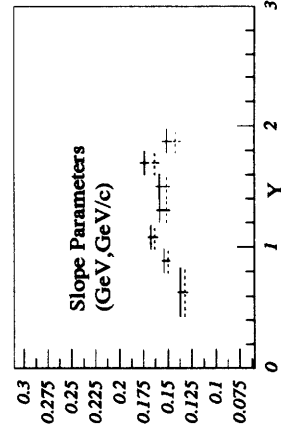
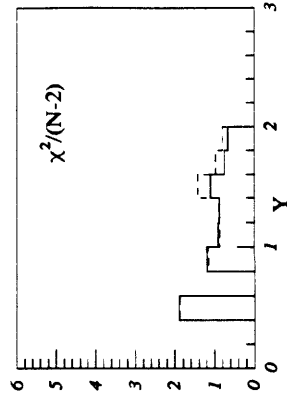
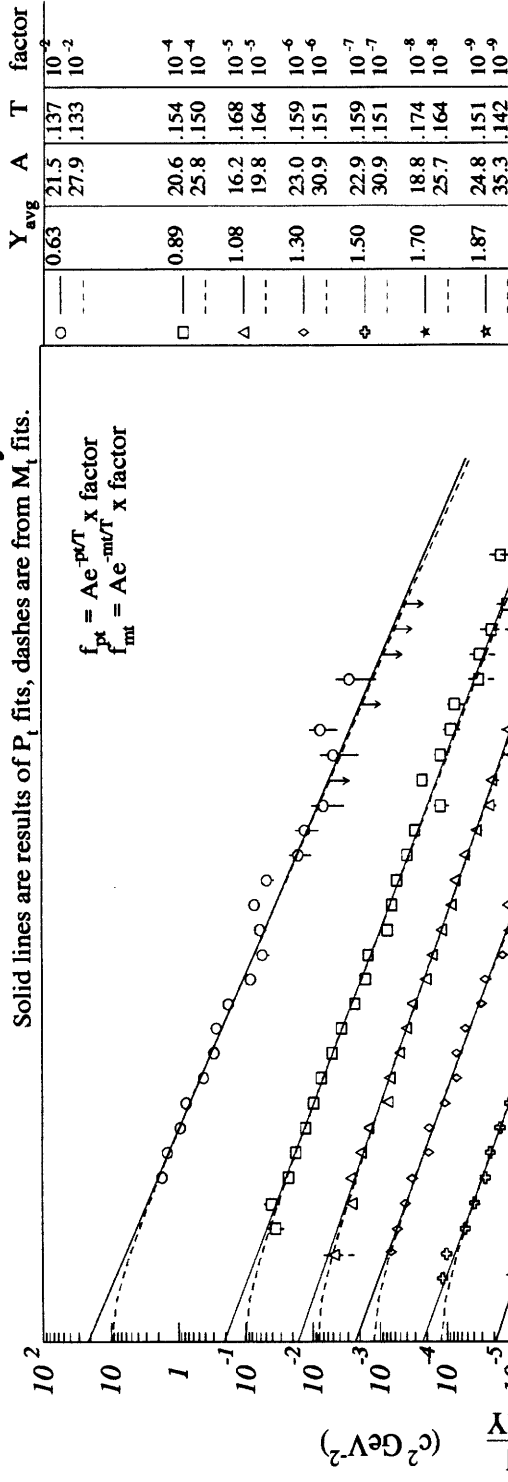
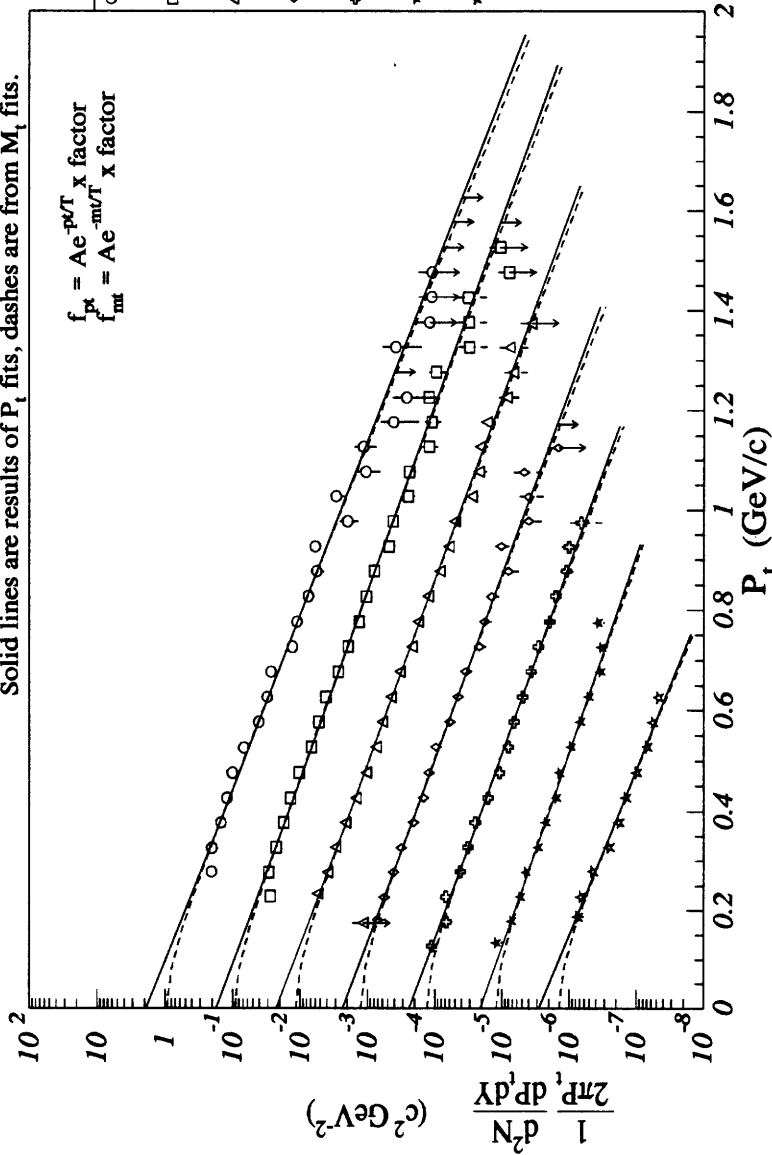


Figure B-7: Yield Summary for $^{16}\text{O} + ^{64}\text{Cu}$ CENT2: π^+

$^{16}\text{O} + \text{Cu}$ CENT2 : Yield Summary π^-

Solid lines are results of P_t fits, dashes are from M_t fits.



$$f_{pk} = Ae^{-pT/T} \times \text{factor}$$

$$f_{mt} = Ae^{-mT/T} \times \text{factor}$$

Symbol	Y_{avg}	A	T	factor
○	0.74	18.7	.151	10^{-9}
□	0.90	24.0	.147	10^{-3}
△	1.07	17.3	.163	10^{-4}
◇	1.30	22.1	.157	10^{-4}
◆	1.50	22.1	.159	10^{-5}
★	1.69	28.5	.154	10^{-5}
★	1.87	23.0	.160	10^{-6}
★	1.87	30.9	.153	10^{-6}
★	1.87	23.6	.162	10^{-7}
★	1.87	31.9	.154	10^{-7}
★	1.87	20.9	.170	10^{-8}
★	1.87	28.8	.159	10^{-8}
★	1.87	27.5	.145	10^{-9}
★	1.87	39.5	.136	10^{-9}

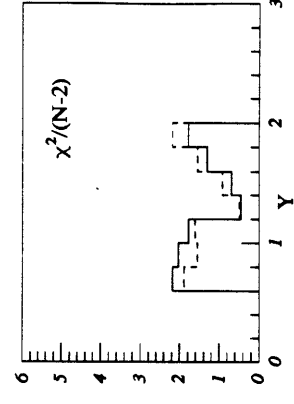
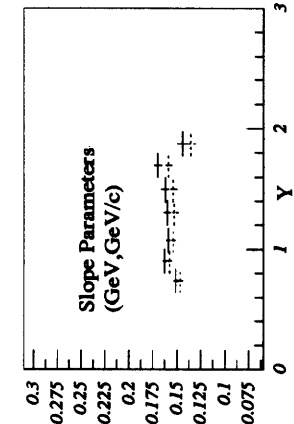
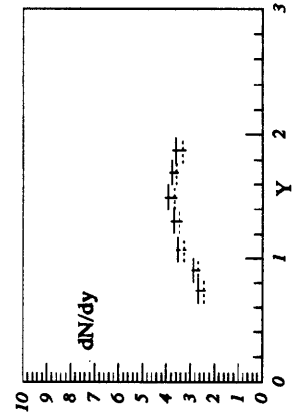


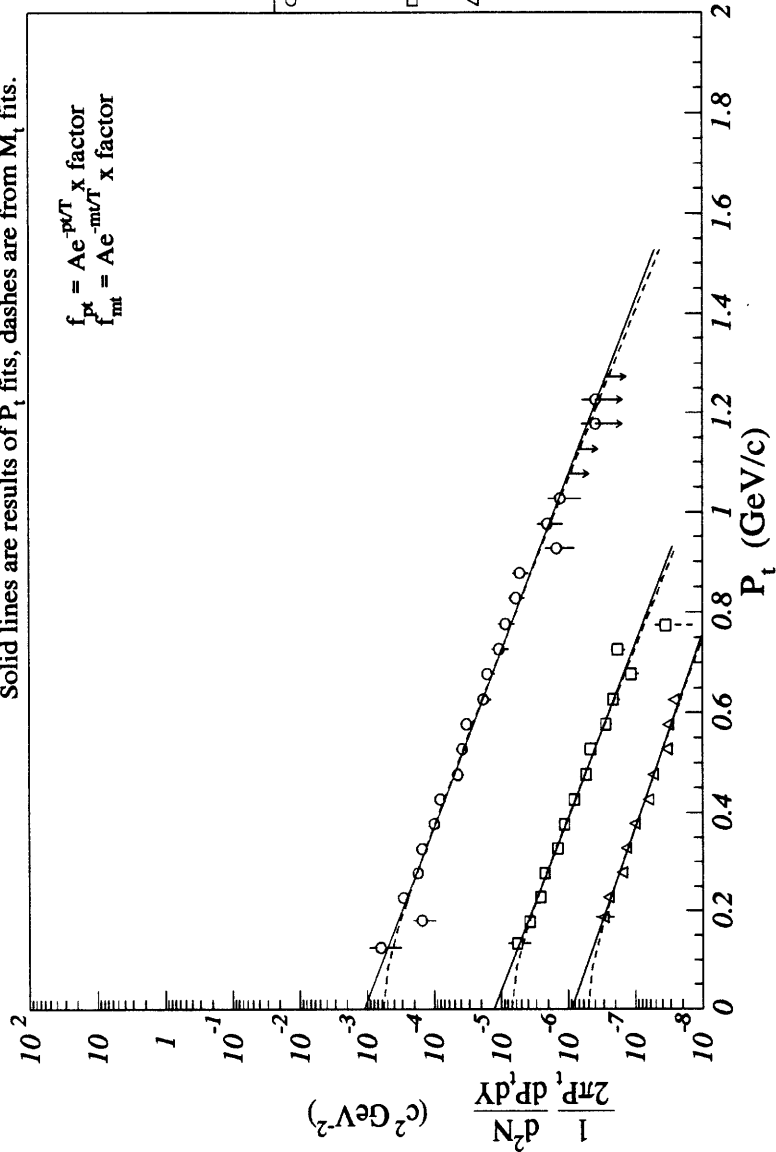
Figure B-8: Yield Summary for $^{16}\text{O} + ^{64}\text{Cu}$ CENT2: π^-

$^{16}\text{O} + \text{Cu}$ MID : Yield Summary π^+

Solid lines are results of P_t fits, dashes are from M_t fits.

$$f_{pt} = A e^{-p_t/T} \quad x \text{ factor}$$

$$f_{mt} = A e^{-m_t/r} \quad x \text{ factor}$$



	Y_{avg}	A	T	factor
○	1.27	11.0	.153	10^{-6}
○	---	14.9	.147	10^{-6}
□	1.70	12.7	.152	10^{-8}
□	---	18.5	.142	10^{-8}
△	1.87	8.90	.168	10^{-9}
△	---	12.2	.158	10^{-9}

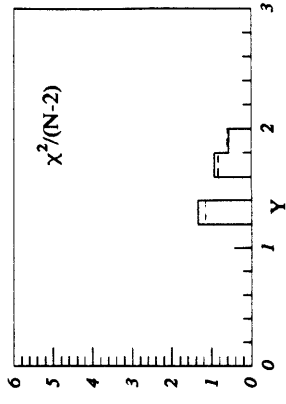
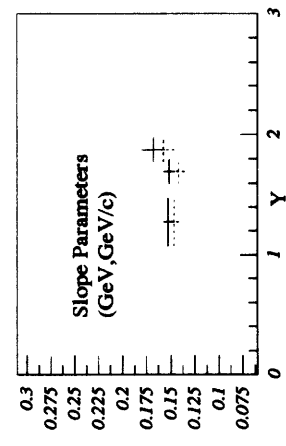
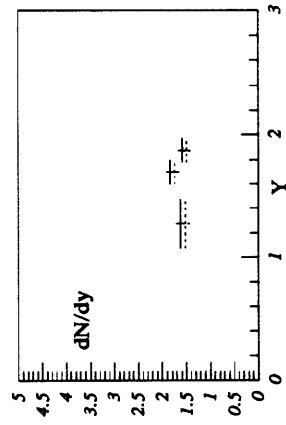
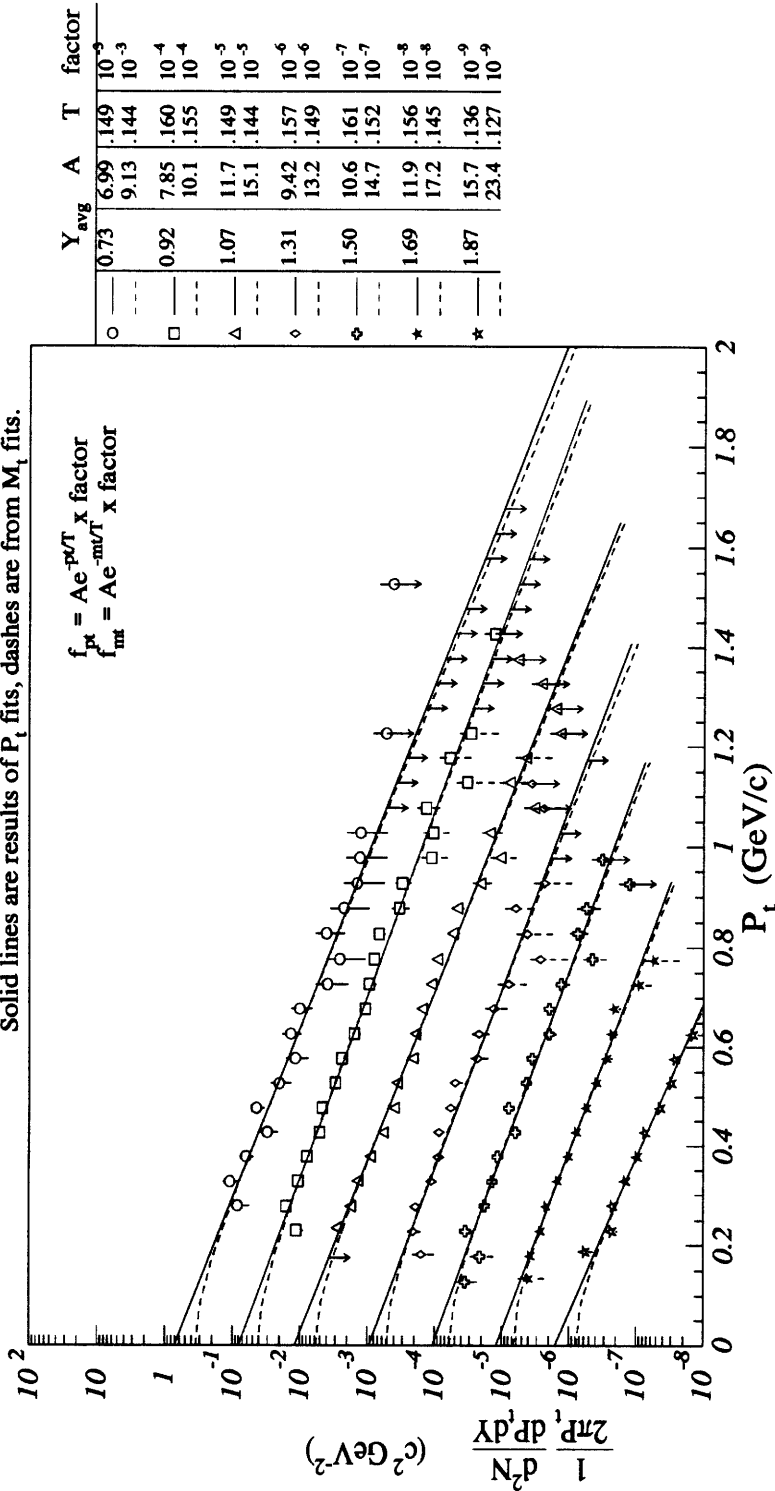


Figure B-9: Yield Summary for $^{16}\text{O} + ^{64}\text{Cu}$ MID: π^+

$^{16}\text{O} + \text{Cu}$ MID : Yield Summary π^-

Solid lines are results of P_t fits, dashes are from M_t fits.



	Y_{avg}	A	T	factor
○	0.73	6.99	.149	10^{-3}
□	0.92	9.13	.144	10^{-3}
△	1.07	7.85	.160	10^{-4}
◇	1.31	10.1	.155	10^{-4}
◇	1.31	11.7	.149	10^{-5}
◇	1.31	15.1	.144	10^{-5}
◇	1.31	9.42	.157	10^{-6}
◇	1.31	13.2	.149	10^{-6}
◇	1.50	10.6	.161	10^{-7}
◇	1.50	14.7	.152	10^{-7}
★	1.69	11.9	.156	10^{-8}
★	1.69	17.2	.145	10^{-8}
★	1.87	15.7	.136	10^{-9}
★	1.87	23.4	.127	10^{-9}

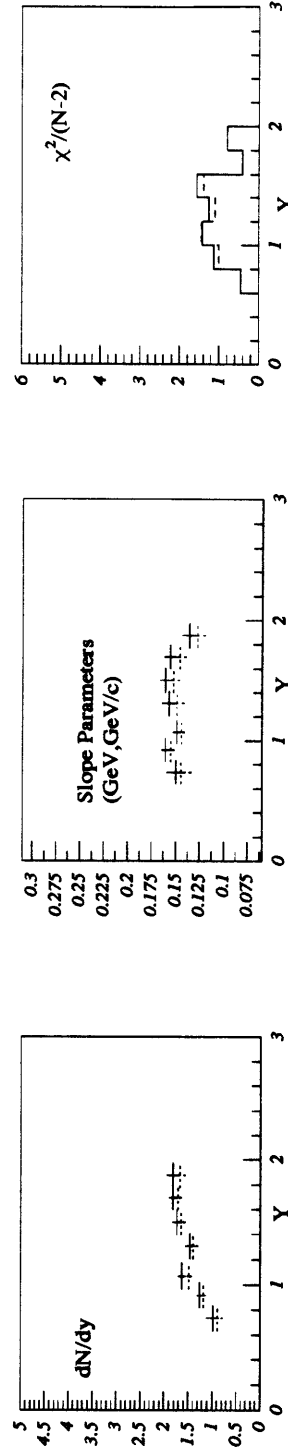
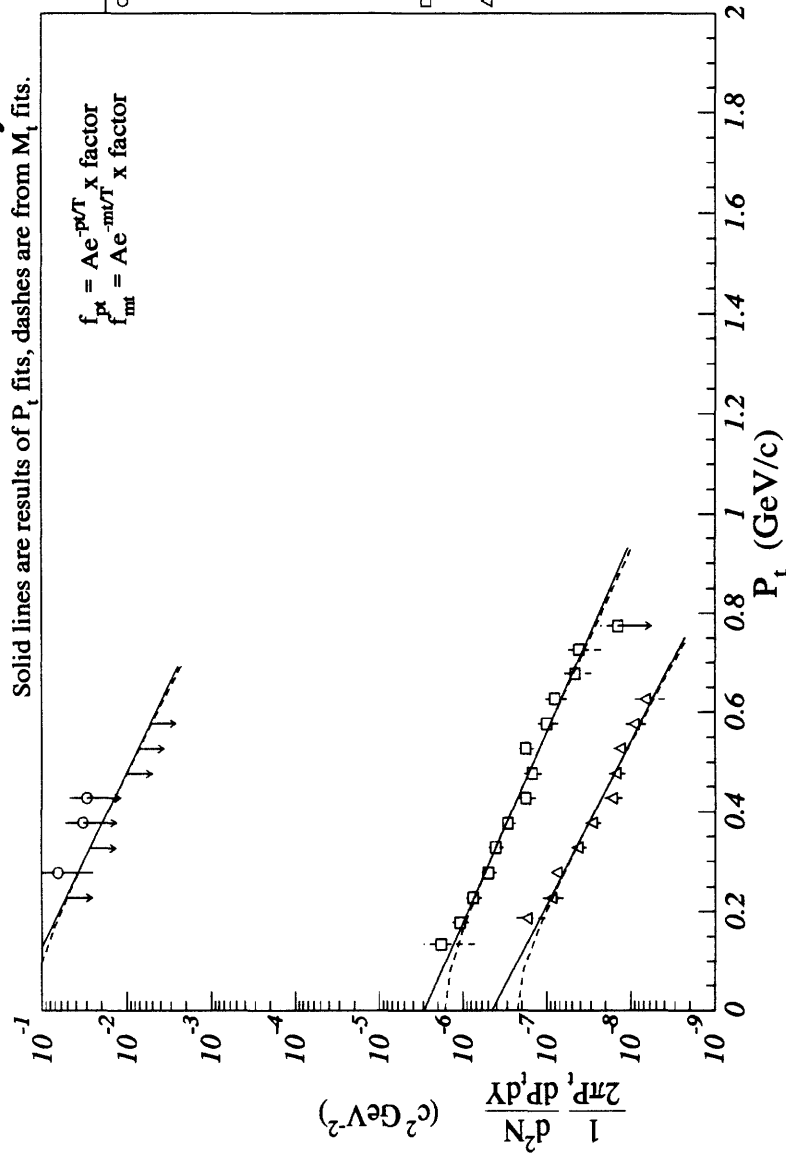


Figure B-10: Yield Summary for $^{16}\text{O} + ^{64}\text{Cu}$ MID: π^-

$^{16}\text{O} + \text{Cu}$ PERP1 : Yield Summary π^+

Solid lines are results of P_t fits, dashes are from M_t fits.



$$f_{\pi^+} = A e^{-pT} \times \text{factor}$$

$$f_{\text{fit}} = A e^{-mT} \times \text{factor}$$

Symbol	Y _{avg}	A	T	factor
○	1.04	2.27	.153	10 ⁻³
□	---	---	---	---
△	1.70	2.90	.166	10 ⁻⁸
□	---	3.98	.156	10 ⁻⁸
△	1.87	4.42	.142	10 ⁻⁹
□	---	6.34	.134	10 ⁻⁹

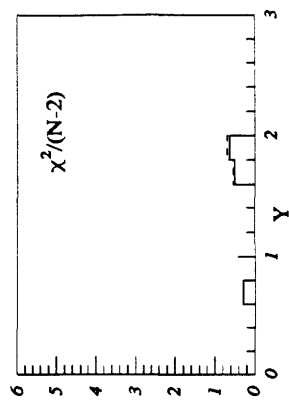
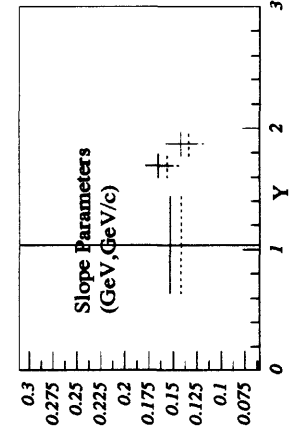
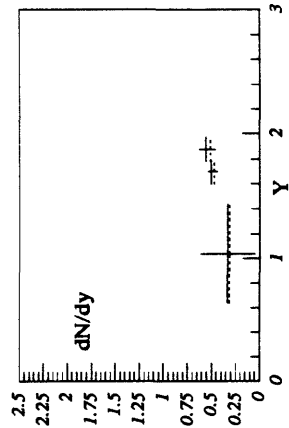
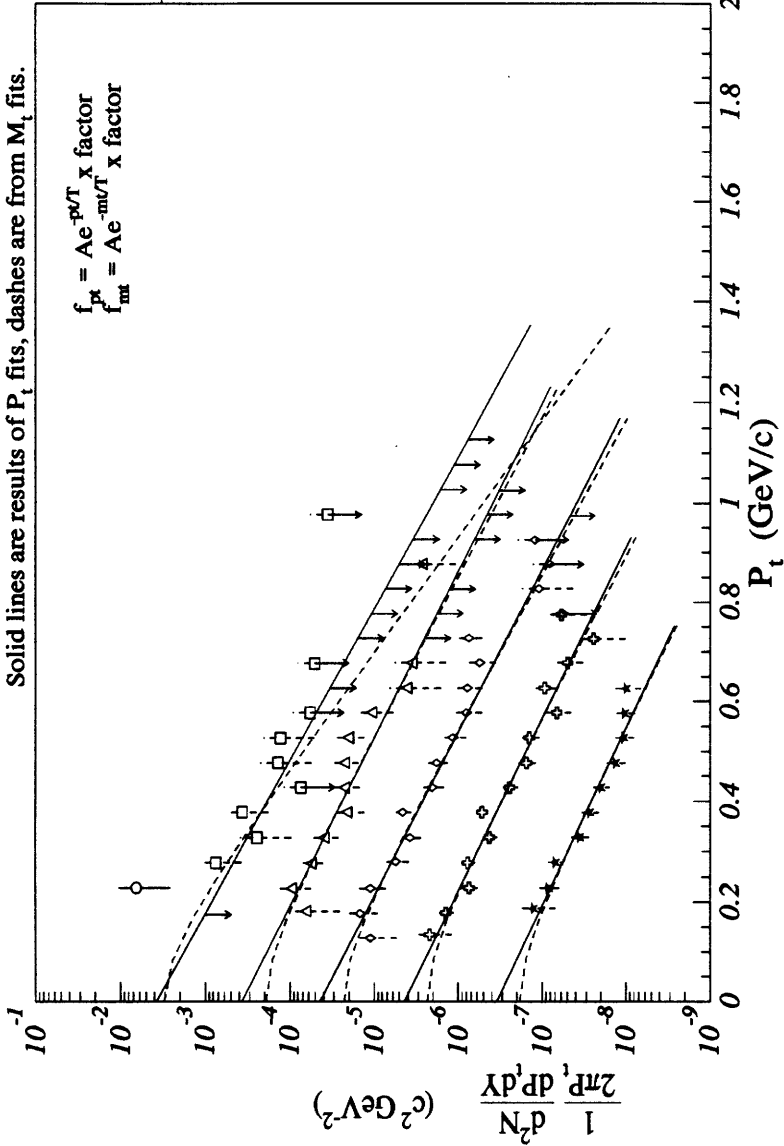


Figure B-11: Yield Summary for $^{16}\text{O} + ^{64}\text{Cu}$ PERP1: π^+

¹⁶O+Cu PERP1 : Yield Summary π^-

Solid lines are results of P_t fits, dashes are from M_t fits.



$$f_{pt} = Ae^{-pT/T} \times \text{x factor}$$

$$f_{mt} = Ae^{-mT/T} \times \text{x factor}$$

Symbol	Y _{avg}	A	T	factor
○	0.00	.000	.000	10 ⁻⁴
□	1.13	3.70	.133	10 ⁻⁵
△	1.32	12.3	.100	10 ⁻⁵
◇	1.50	3.64	.146	10 ⁻⁶
◇	1.50	5.20	.138	10 ⁻⁶
◇	1.50	4.32	.143	10 ⁻⁷
◇	1.50	6.42	.134	10 ⁻⁷
◇	1.69	4.31	.150	10 ⁻⁸
◇	1.69	6.30	.140	10 ⁻⁸
◇	1.87	3.43	.154	10 ⁻⁹
◇	1.87	4.80	.145	10 ⁻⁹

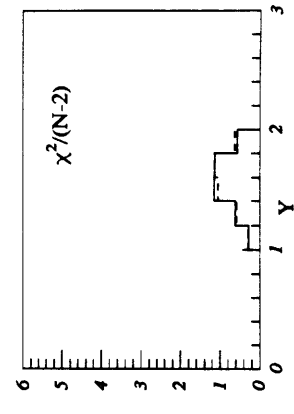
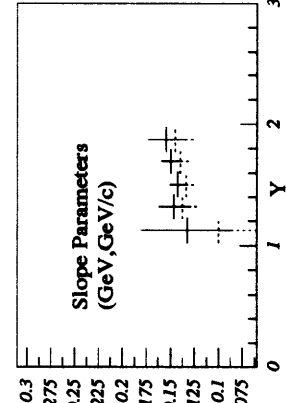
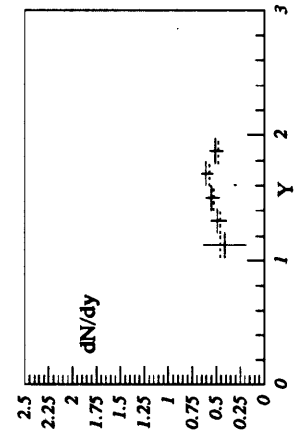


Figure B-12: Yield Summary for ¹⁶O + ⁶⁴Cu PERP1: π^-

Appendix C

Yield Summary: $^{16}\text{O} + ^{197}\text{Au} : \pi$

$^{16}\text{O} + \text{Au}$ Inelastic Cross-Section Summary for π^+

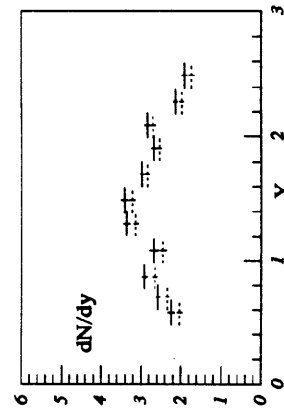
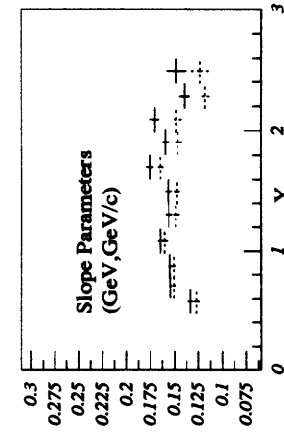
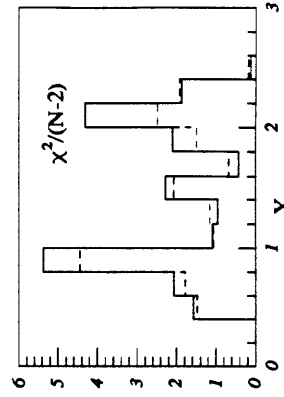
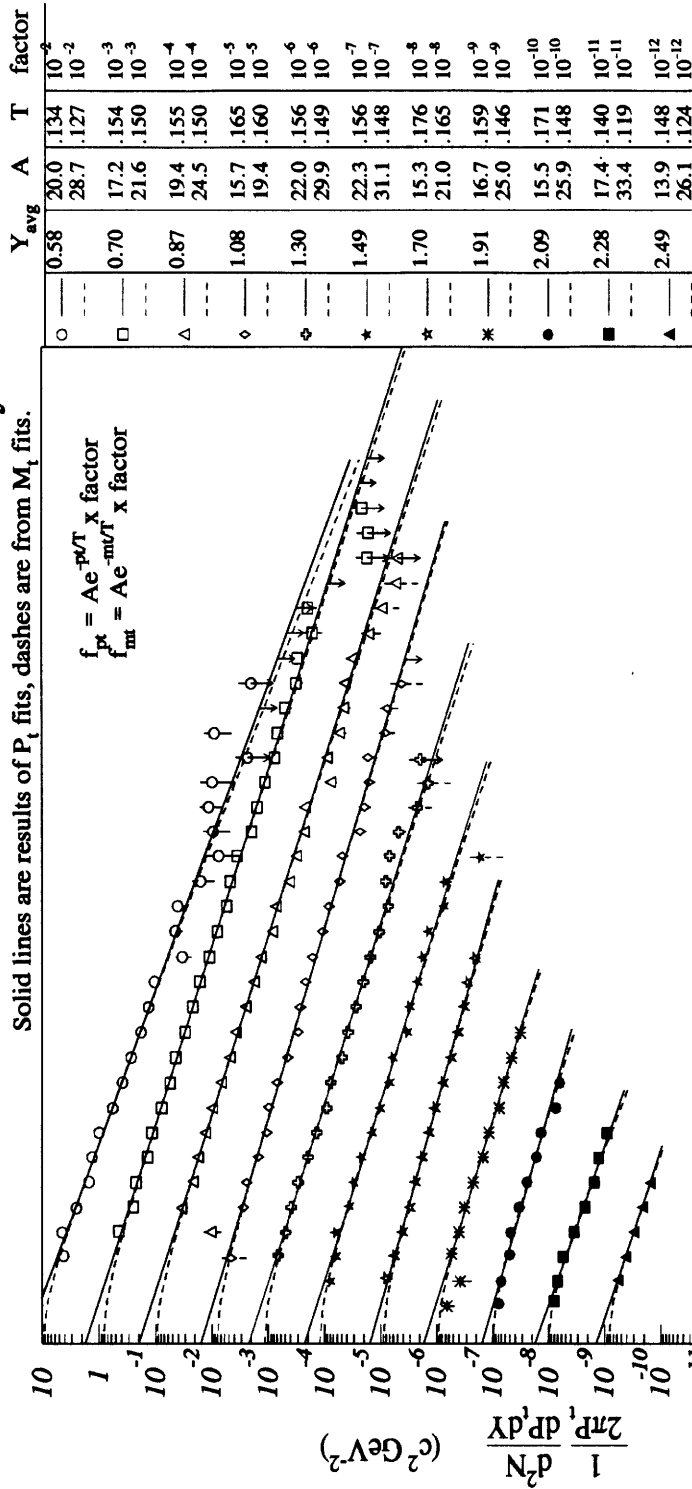


Figure C-1: Yield Summary for $^{16}\text{O} + ^{197}\text{Au}$ INEL: π^+

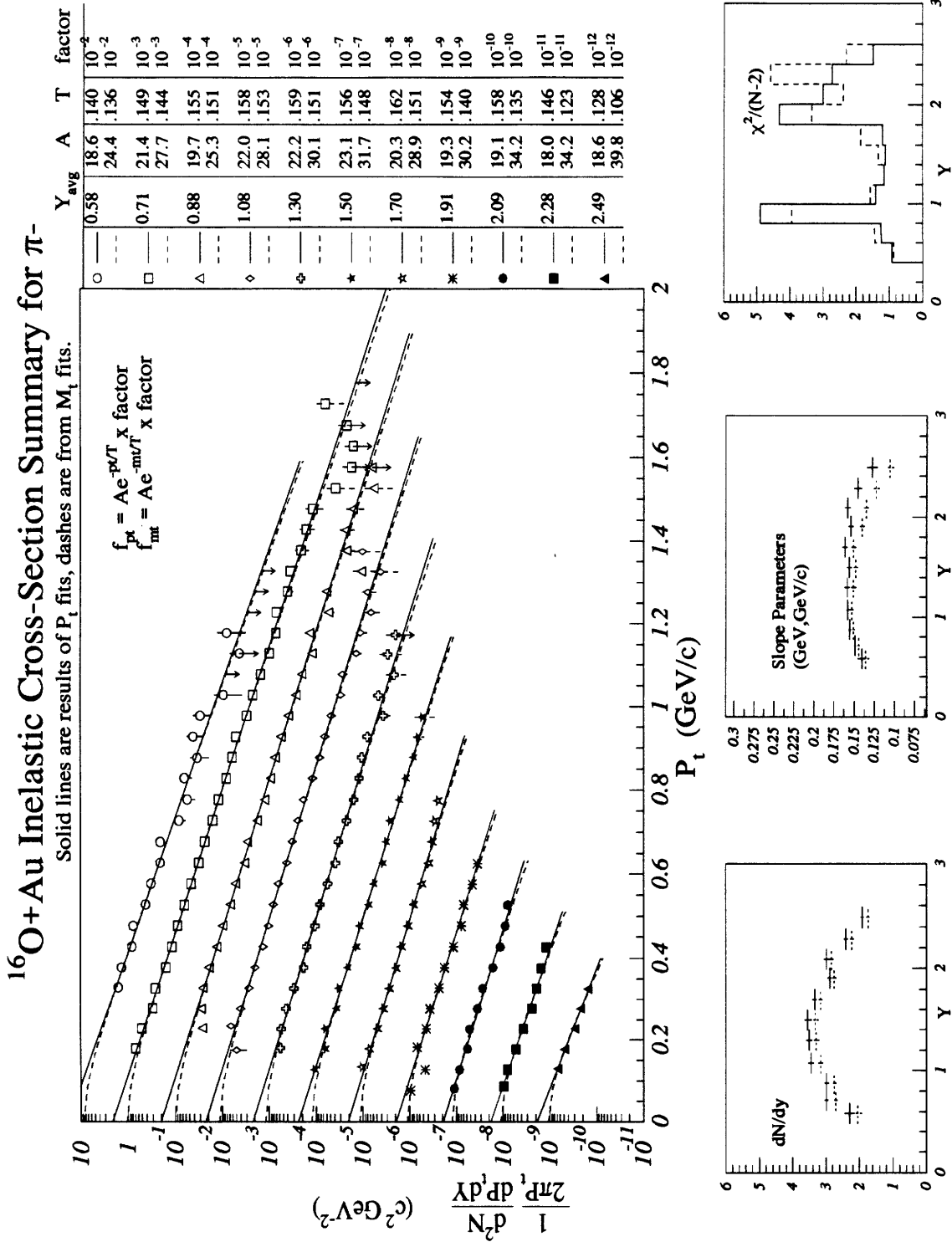
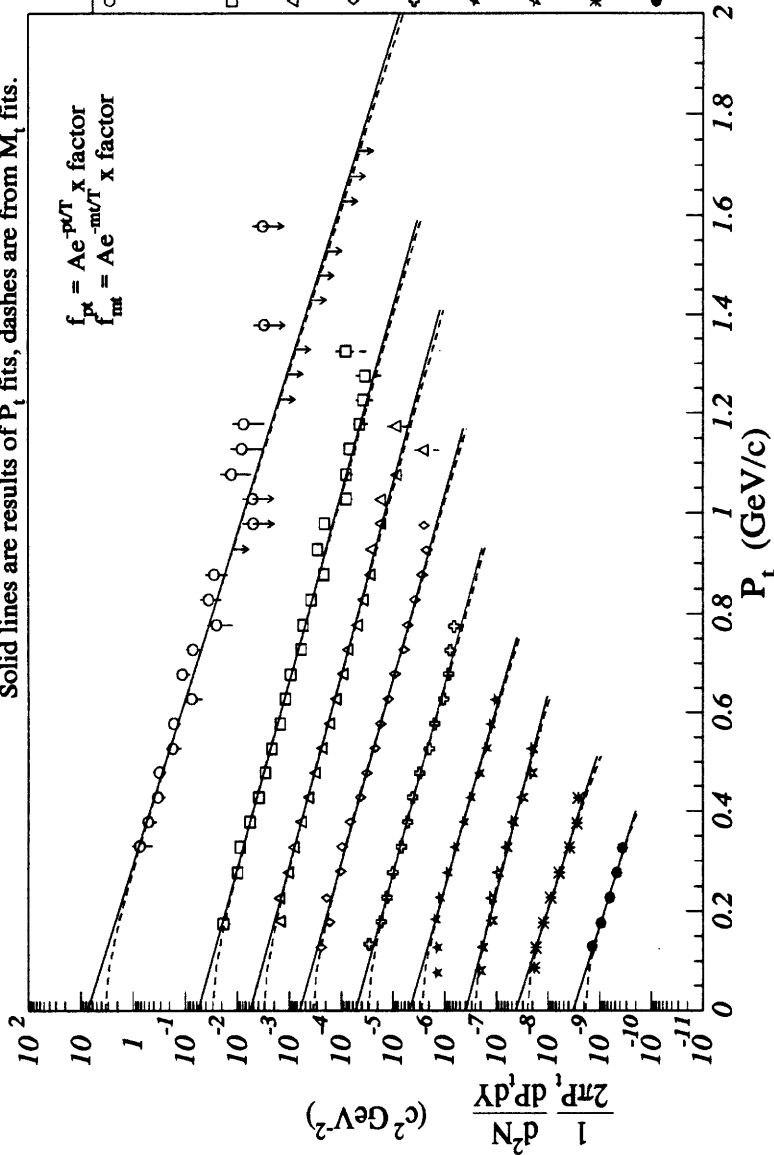


Figure C-2: Yield Summary for $^{16}\text{O} + ^{197}\text{Au}$ INEL: π^-

$^{16}\text{O} + \text{Au TMA} : \text{Yield Summary } \pi^+$

Solid lines are results of P_t fits, dashes are from M_t fits.



Symbol	Y_{avg}	A	T	factor
○	0.69	72.2	.145	10^{-9}
		91.6	.141	10^{-3}
□	1.13	56.4	.163	10^{-5}
		72.0	.158	10^{-5}
△	1.30	55.4	.167	10^{-6}
		73.3	.159	10^{-6}
◇	1.49	61.5	.161	10^{-7}
		85.3	.152	10^{-7}
◇	1.70	51.9	.165	10^{-8}
		73.3	.154	10^{-8}
★	1.91	47.4	.157	10^{-9}
		73.0	.143	10^{-9}
★	2.09	38.9	.174	10^{-10}
		64.1	.151	10^{-10}
★	2.28	42.0	.140	10^{-11}
		80.9	.119	10^{-11}
●	2.49	32.0	.143	10^{-12}
		60.5	.121	10^{-12}

$$f_{\text{fit}}^{\pi^+} = A e^{-p_t/T} \times \text{factor}$$

$$f_{\text{fit}}^{\text{mt}} = A e^{-m_t/T} \times \text{factor}$$

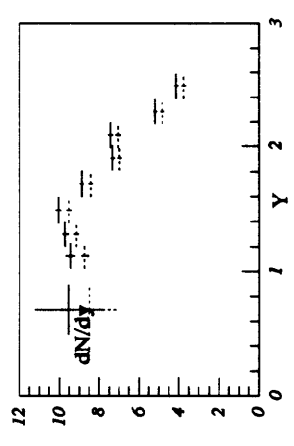
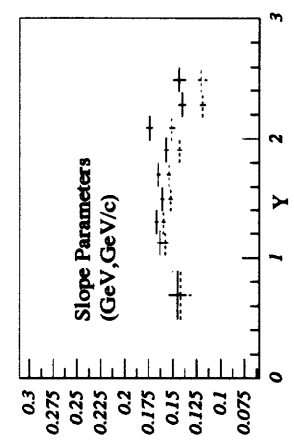
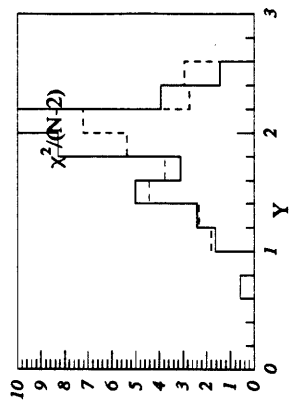
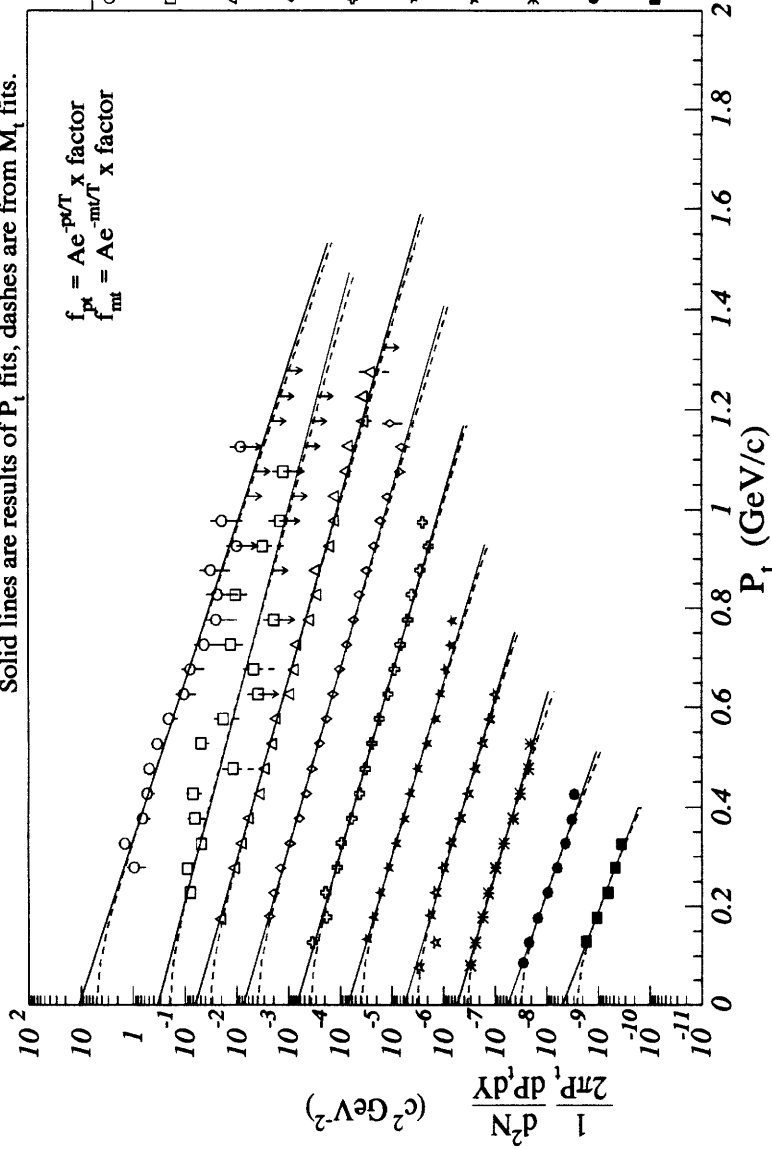


Figure C-3: Yield Summary for $^{16}\text{O} + ^{197}\text{Au TMA}: \pi^+$

$^{16}\text{O} + \text{Au TMA} : \text{Yield Summary } \pi^-$

Solid lines are results of P_t fits, dashes are from M_t fits.



Symbol	Y_{avg}	A	T	factor
○	0.74	108.	.138	10^{-3}
□	0.86	146.	.133	10^{-3}
△	1.13	33.6	.172	10^{-4}
◇	1.30	45.7	.163	10^{-4}
◇	1.49	62.3	.158	10^{-5}
◇	1.70	80.4	.152	10^{-5}
◇	1.70	73.6	.157	10^{-6}
◇	1.70	99.3	.150	10^{-6}
◇	1.70	69.1	.157	10^{-7}
◇	1.70	94.5	.149	10^{-7}
◇	1.70	71.4	.151	10^{-8}
◇	1.70	105.	.141	10^{-8}
◇	1.91	57.3	.151	10^{-9}
◇	2.09	90.6	.137	10^{-9}
◇	2.09	54.1	.154	10^{-10}
◇	2.09	100.	.131	10^{-10}
◇	2.28	55.8	.129	10^{-11}
◇	2.28	117.	.108	10^{-11}
◇	2.49	48.7	.118	10^{-12}
◇	2.49	104.	.100	10^{-12}

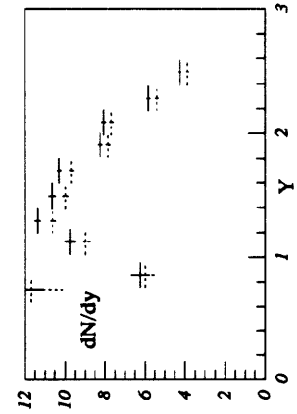
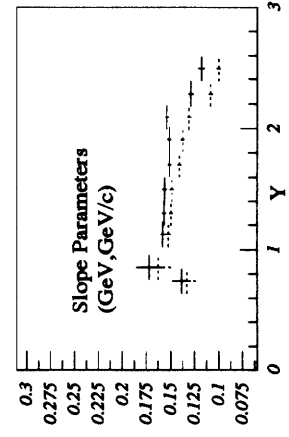
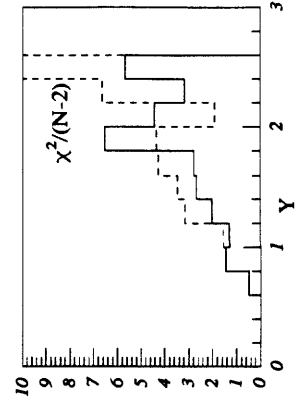
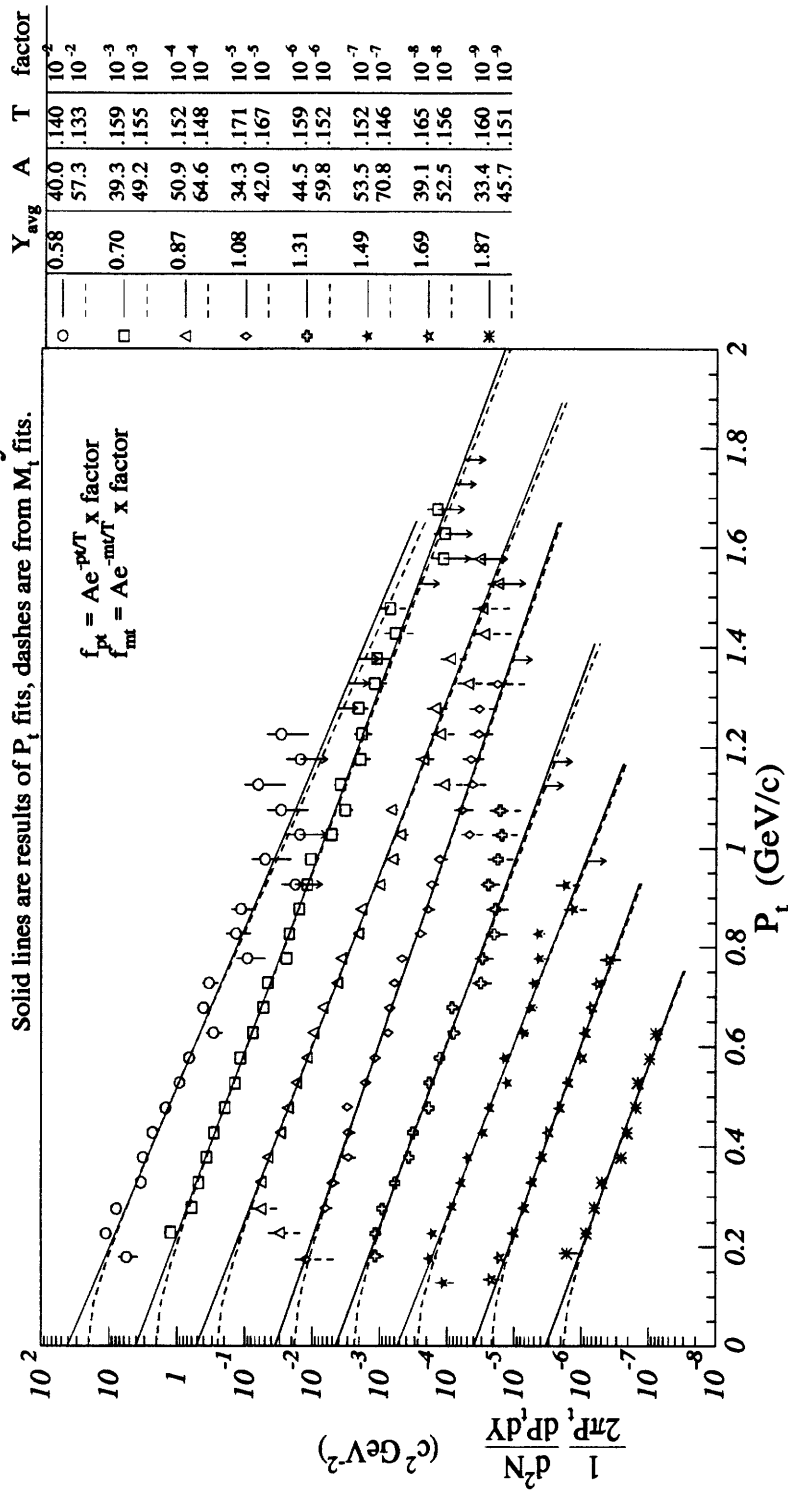


Figure C-4: Yield Summary for $^{16}\text{O} + ^{197}\text{Au TMA}: \pi^-$

$^{16}\text{O} + \text{Au}$ CENT1 : Yield Summary π^+

Solid lines are results of P_t fits, dashes are from M_t fits.



$$f_{pt} = Ae^{-pT/T} \times \text{x factor}$$

$$f_{mt} = Ae^{-mT/T} \times \text{x factor}$$

Symbol	Y _{avg}	A	T	factor
○	0.58	40.0	.140	10 ⁻²
□	0.70	57.3	.133	10 ⁻²
△	0.87	39.3	.159	10 ⁻³
◇	0.87	49.2	.155	10 ⁻³
◇	1.08	50.9	.152	10 ⁻⁴
◇	1.08	64.6	.148	10 ⁻⁴
◇	1.31	34.3	.171	10 ⁻⁵
◇	1.31	42.0	.167	10 ⁻⁵
◇	1.49	44.5	.159	10 ⁻⁶
◇	1.49	59.8	.152	10 ⁻⁶
◇	1.69	53.5	.152	10 ⁻⁷
◇	1.69	70.8	.146	10 ⁻⁷
◇	1.87	39.1	.165	10 ⁻⁸
◇	1.87	52.5	.156	10 ⁻⁸
◇	1.87	33.4	.160	10 ⁻⁹
◇	1.87	45.7	.151	10 ⁻⁹

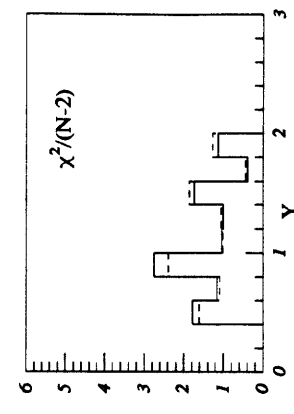
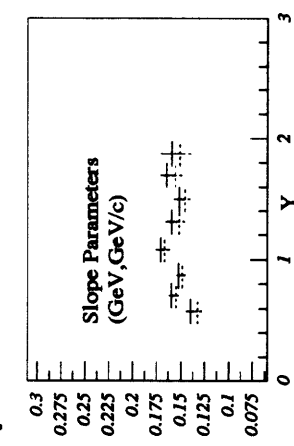
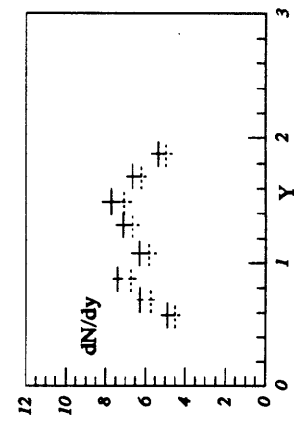


Figure C-5: Yield Summary for $^{16}\text{O} + ^{197}\text{Au}$ CENT1: π^+

$^{16}\text{O} + \text{Au}$ CENT1 : Yield Summary π^-

Solid lines are results of P_t fits, dashes are from M_t fits.

	Y _{avg}	A	T	factor
○	0.58	49.5	.137	10^{-2}
□	0.71	65.8	.132	10^{-2}
△	0.88	49.0	.153	10^{-3}
◇	1.07	62.6	.149	10^{-3}
◇	1.30	50.0	.155	10^{-4}
◇	1.30	63.7	.150	10^{-4}
◇	1.50	54.5	.158	10^{-5}
◇	1.50	69.9	.153	10^{-5}
◇	1.70	56.9	.153	10^{-6}
◇	1.70	79.6	.145	10^{-6}
◇	1.88	49.3	.156	10^{-7}
◇	1.88	65.9	.149	10^{-7}
◇	1.88	44.9	.160	10^{-8}
◇	1.88	64.1	.150	10^{-8}
◇	1.88	55.8	.138	10^{-9}
◇	1.88	83.3	.129	10^{-9}

$$f_{\pi^-} = A e^{-pT} \times \text{factor}$$

$$f_{\text{mt}} = A e^{-mT} \times \text{factor}$$

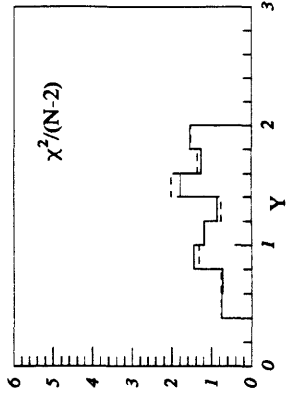
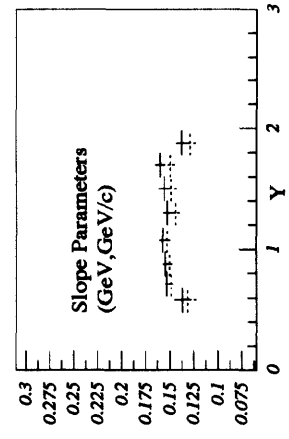
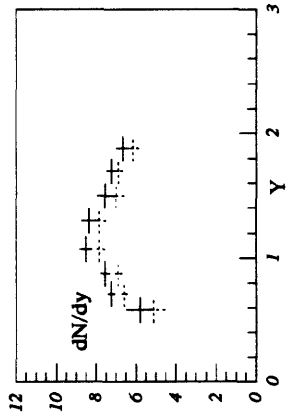
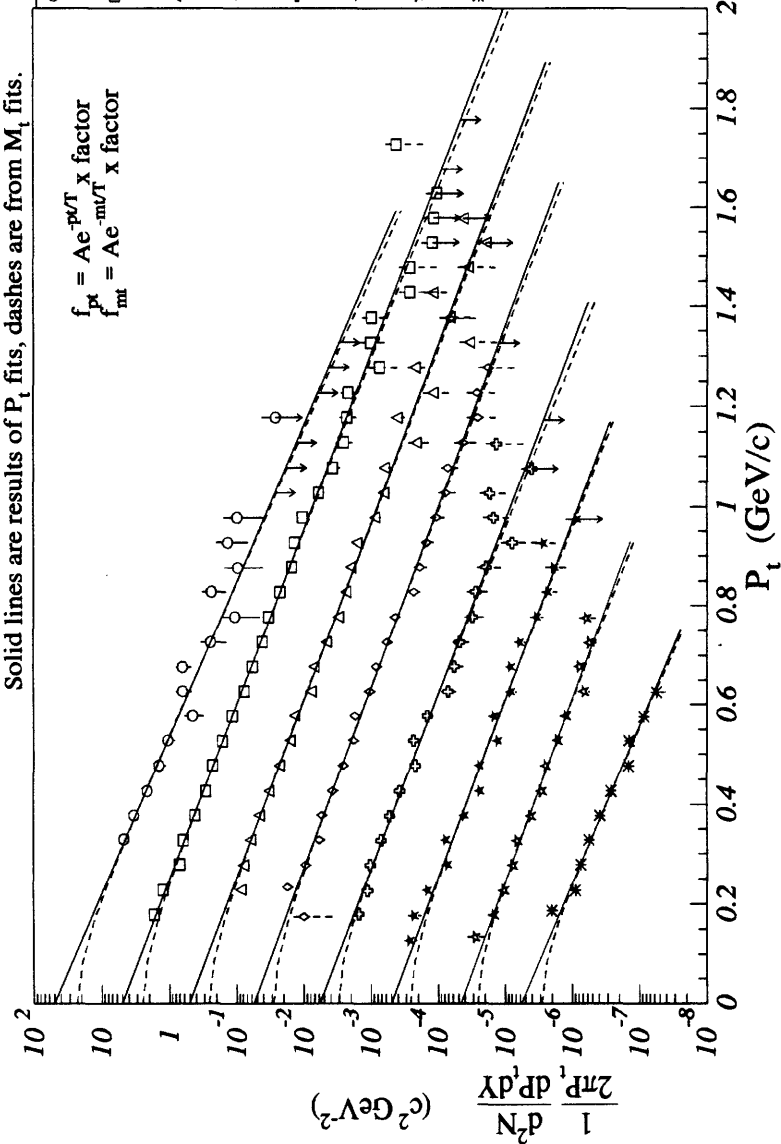
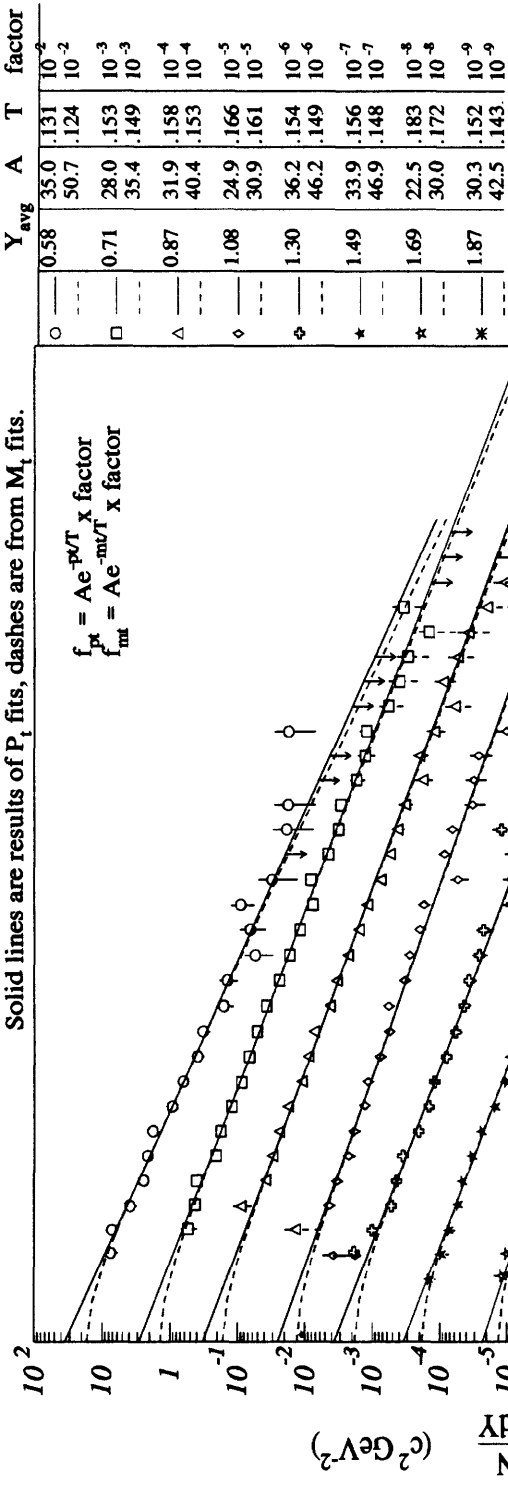


Figure C-6: Yield Summary for $^{16}\text{O} + ^{197}\text{Au}$ CENT1: π^-

$^{16}\text{O} + \text{Au}$ CENT2: Yield Summary π^+

Solid lines are results of P_t fits, dashes are from M_t fits.



Symbol	Y _{avg}	A	T	factor
○	0.58	35.0	.131	10 ⁻²
□	0.71	50.7	.124	10 ⁻²
△	0.87	28.0	.153	10 ⁻³
◇	1.08	35.4	.149	10 ⁻³
☆	1.30	31.9	.158	10 ⁻⁴
☆	1.49	40.4	.153	10 ⁻⁴
☆	1.69	24.9	.166	10 ⁻⁵
☆	1.87	30.9	.161	10 ⁻⁵
☆	1.87	36.2	.154	10 ⁻⁶
☆	1.87	46.2	.149	10 ⁻⁶
☆	1.87	33.9	.156	10 ⁻⁷
☆	1.87	46.9	.148	10 ⁻⁷
☆	1.87	22.5	.183	10 ⁻⁸
☆	1.87	30.0	.172	10 ⁻⁸
☆	1.87	30.3	.152	10 ⁻⁹
☆	1.87	42.5	.143	10 ⁻⁹

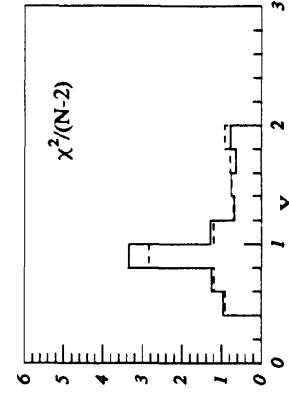
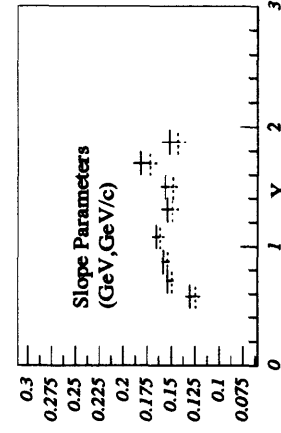
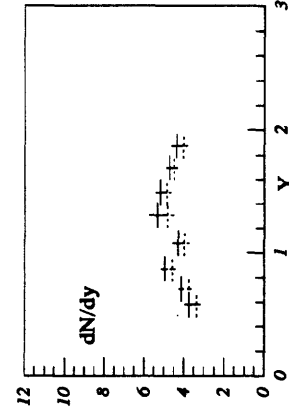
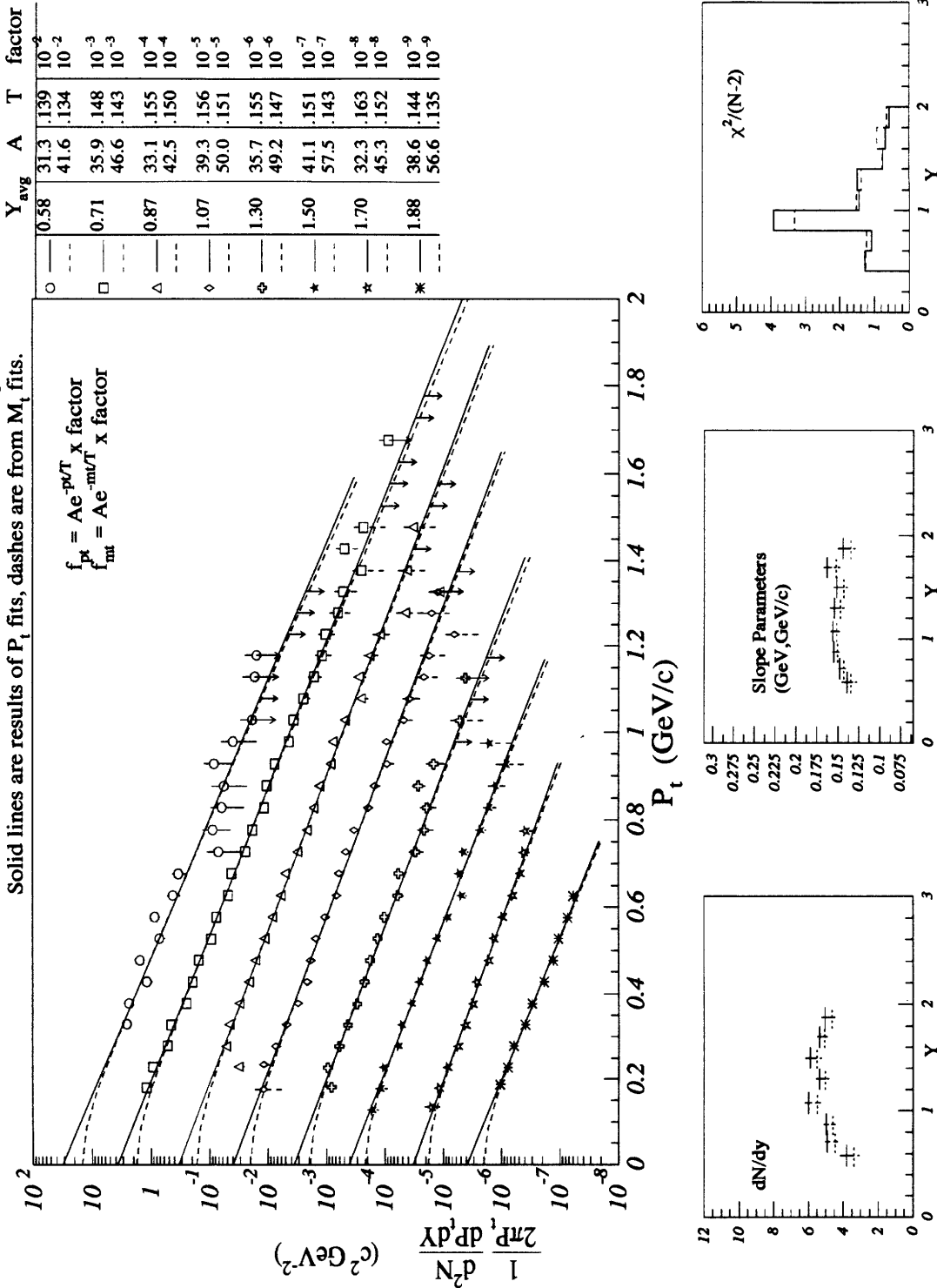


Figure C-7: Yield Summary for $^{16}\text{O} + ^{197}\text{Au}$ CENT2: π^+

$^{16}\text{O} + \text{Au}$ CENT2 : Yield Summary π^-

Solid lines are results of P_t fits, dashes are from M_t fits.

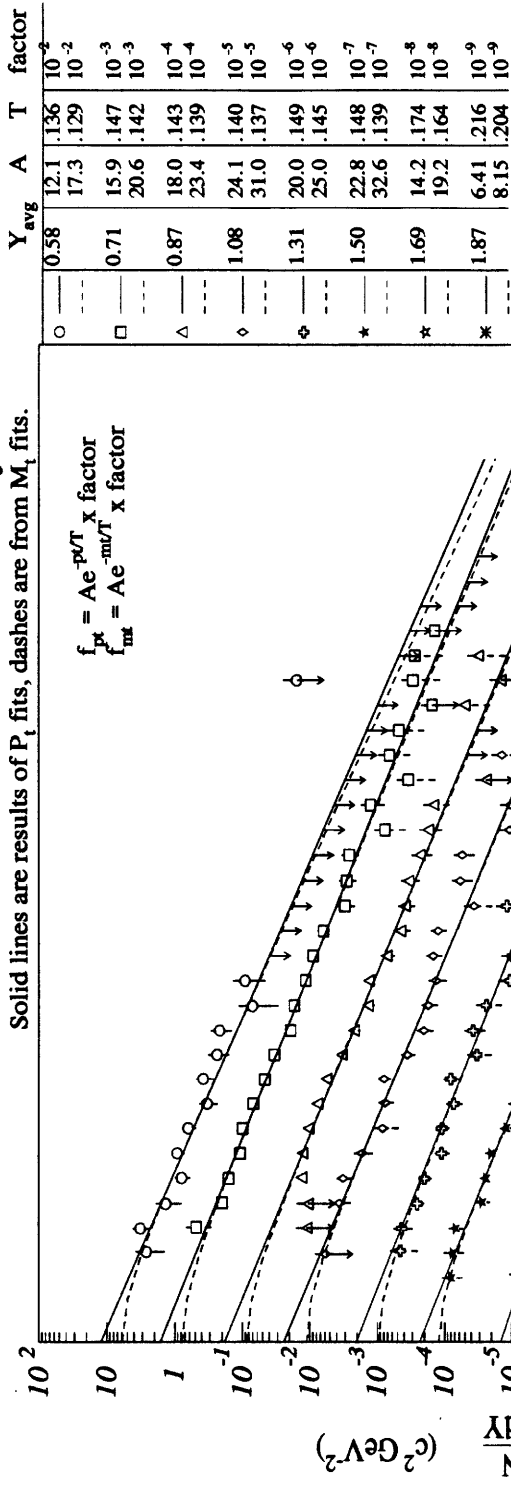


Y	Y_{avg}	A	T	factor
0	0.58	31.3	.139	10^{-2}
1	0.71	41.6	.134	10^{-2}
2	0.87	35.9	.148	10^{-3}
3	0.87	46.6	.143	10^{-3}
4	1.07	33.1	.155	10^{-4}
5	1.07	42.5	.150	10^{-4}
6	1.30	39.3	.156	10^{-5}
7	1.30	50.0	.151	10^{-5}
8	1.50	35.7	.155	10^{-6}
9	1.50	49.2	.147	10^{-6}
10	1.70	41.1	.151	10^{-7}
11	1.70	57.5	.143	10^{-7}
12	1.88	32.3	.163	10^{-8}
13	1.88	45.3	.152	10^{-8}
14	1.88	38.6	.144	10^{-9}
15	1.88	56.6	.135	10^{-9}

Figure C-8: Yield Summary for $^{16}\text{O} + ^{197}\text{Au}$ CENT2: π^-

$^{16}\text{O} + \text{Au}$ MID : Yield Summary π^+

Solid lines are results of P_t fits, dashes are from M_t fits.



$$f_{pt} = Ae^{-pT/T} \times \text{x factor}$$

$$f_{mt} = Ae^{-mT/T} \times \text{x factor}$$

Symbol	Y_{avg}	A	T	factor
○	0.58	12.1	.136	10^{-2}
□	0.71	17.3	.129	10^{-2}
△	0.87	15.9	.147	10^{-3}
◇	1.08	20.6	.142	10^{-3}
◆	1.31	18.0	.143	10^{-4}
♣	1.50	23.4	.139	10^{-4}
♠	1.69	24.1	.140	10^{-5}
♣	1.87	31.0	.137	10^{-5}
♠	1.87	20.0	.149	10^{-6}
♣	1.87	25.0	.145	10^{-6}
♠	1.87	22.8	.148	10^{-7}
♣	1.87	32.6	.139	10^{-7}
♠	1.87	14.2	.174	10^{-8}
♣	1.87	19.2	.164	10^{-8}
♠	1.87	6.41	.216	10^{-9}
♣	1.87	8.15	.204	10^{-9}

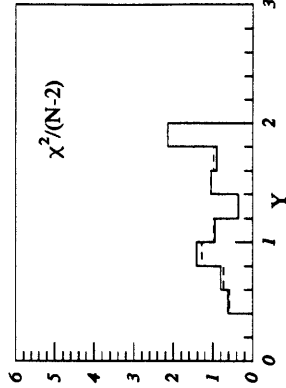
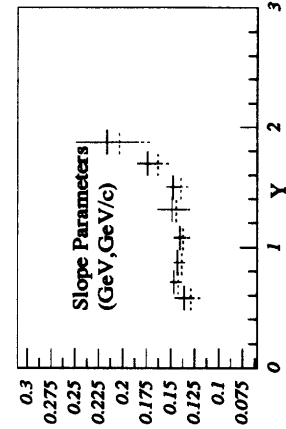
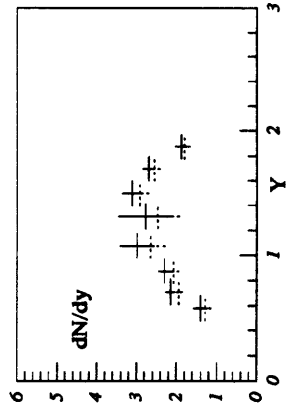


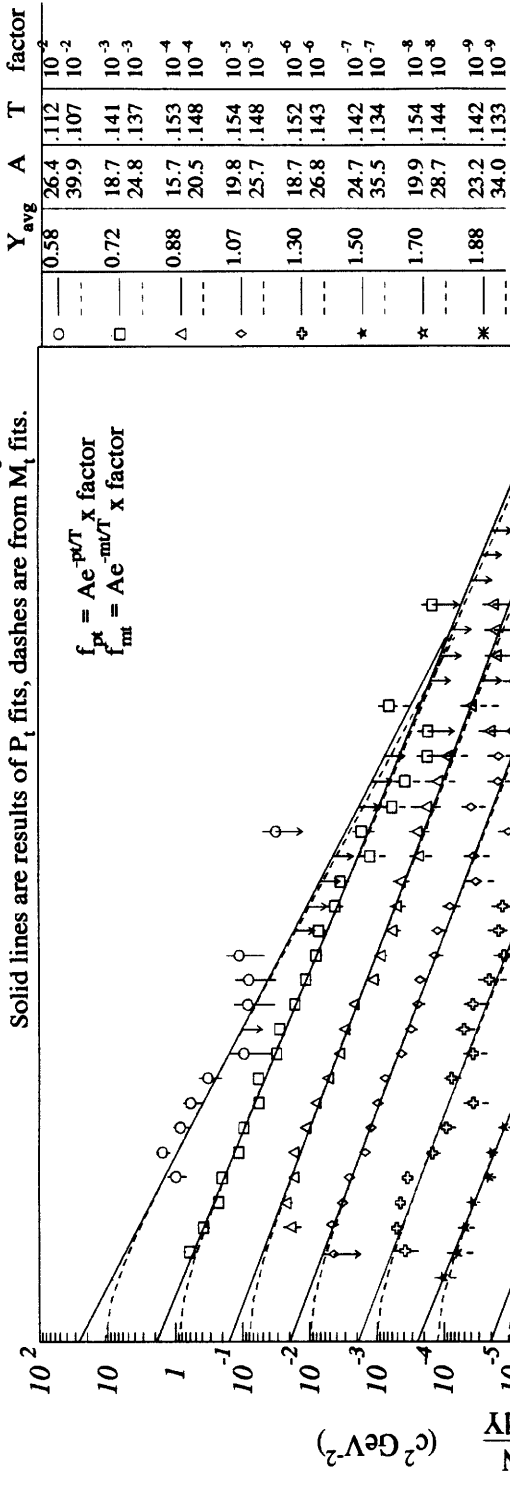
Figure C-9: Yield Summary for $^{16}\text{O} + ^{197}\text{Au}$ MID: π^+

$^{16}\text{O} + \text{Au}$ MID : Yield Summary π^-

Solid lines are results of P_t fits, dashes are from M_t fits.

$$f_{pk} = A e^{-p_t/T} \times \text{factor}$$

$$f_{mt} = A e^{-m_t/T} \times \text{factor}$$



Symbol	Y_{avg}	A	T	factor
○	0.58	26.4	.112	10^{-2}
□	0.72	39.9	.107	10^{-2}
△	0.88	18.7	.141	10^{-3}
◇	1.07	24.8	.137	10^{-3}
⊕	1.30	15.7	.153	10^{-4}
★	1.50	20.5	.148	10^{-4}
✱	1.70	19.8	.154	10^{-5}
✱	1.88	25.7	.148	10^{-5}
✱	1.88	18.7	.152	10^{-6}
✱	1.88	26.8	.143	10^{-6}
✱	1.88	24.7	.142	10^{-7}
✱	1.88	35.5	.134	10^{-7}
✱	1.88	19.9	.154	10^{-8}
✱	1.88	28.7	.144	10^{-8}
✱	1.88	23.2	.142	10^{-9}
✱	1.88	34.0	.133	10^{-9}

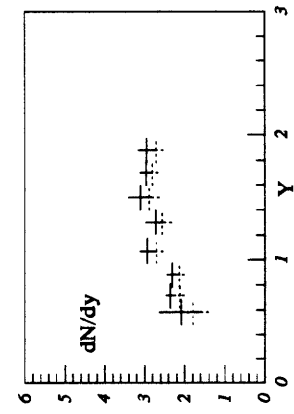
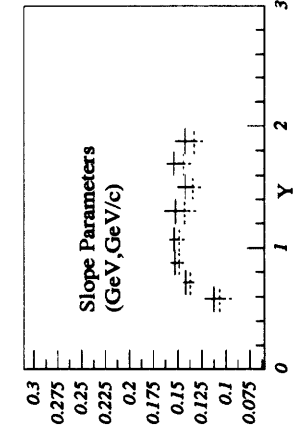
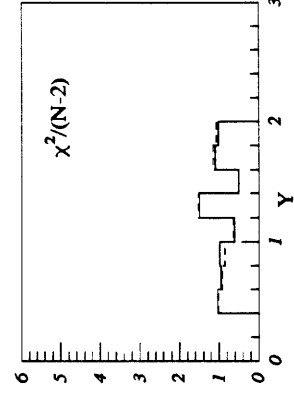
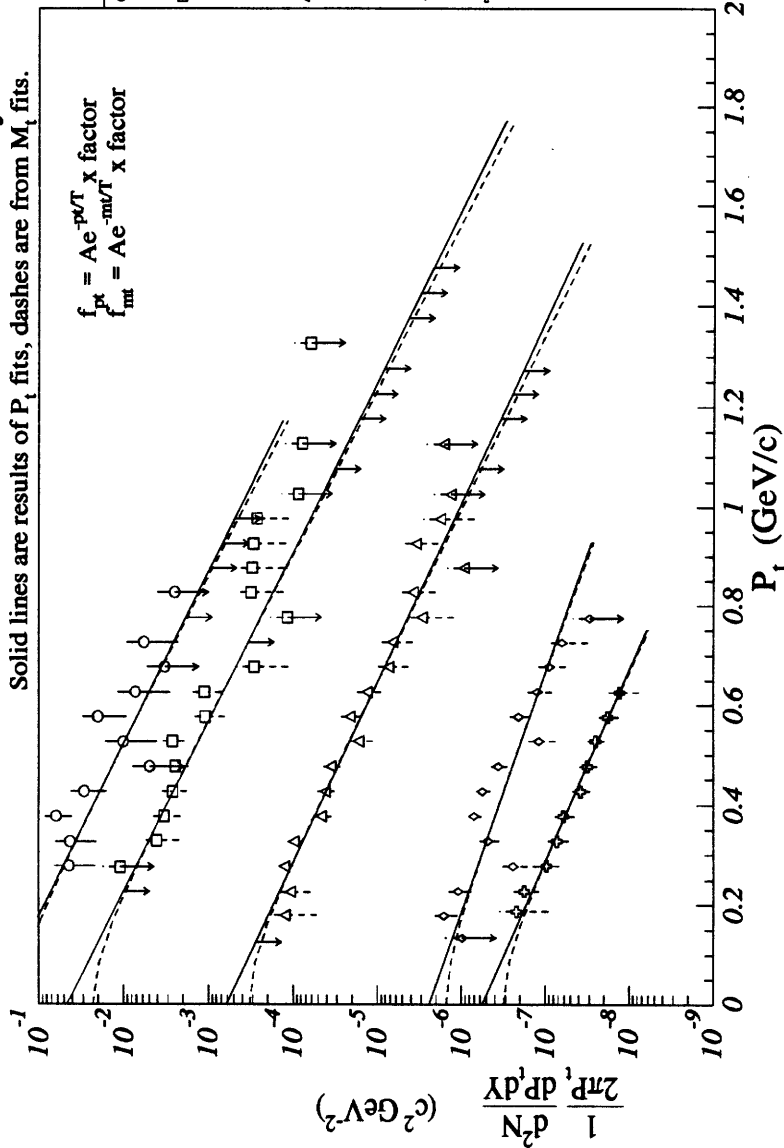


Figure C-10: Yield Summary for $^{16}\text{O} + ^{197}\text{Au}$ MID: π^-

$^{16}\text{O} + \text{Au}$ PERP1 : Yield Summary π^+

Solid lines are results of P_t fits, dashes are from M_t fits.



	Y_{avg}	A	T	factor
○	0.75	3.19	.151	10^{-3}
□	0.89	4.33	.144	10^{-3}
△	1.30	6.07	.157	10^{-6}
◇	1.69	2.37	.210	10^{-8}
⊕	1.87	5.59	.167	10^{-9}

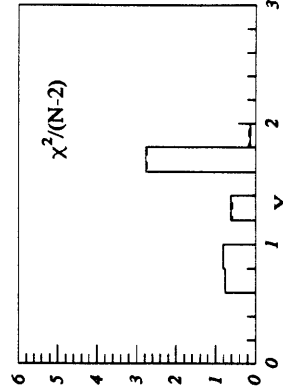
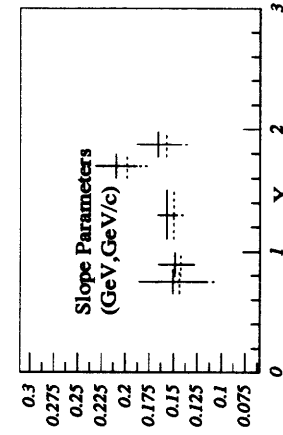
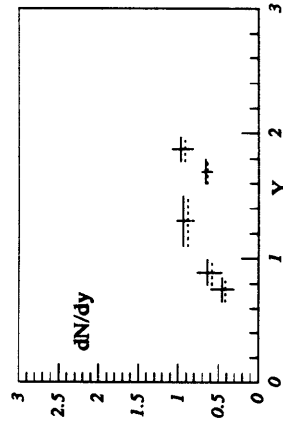


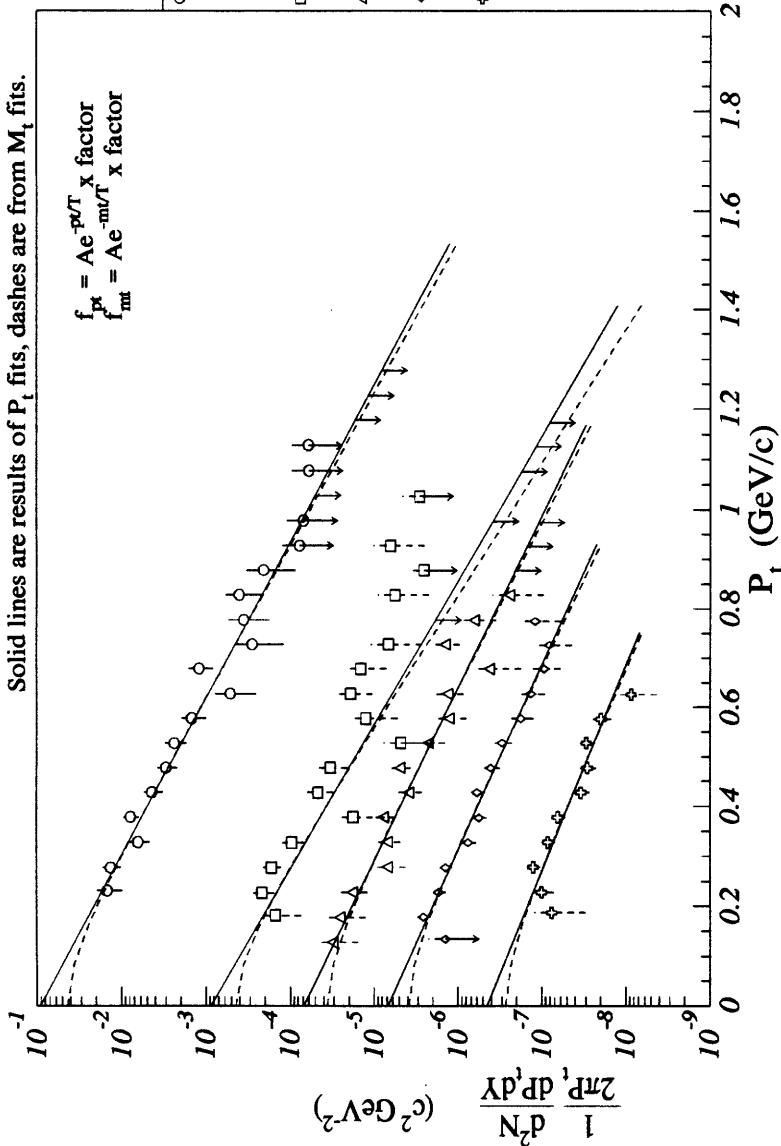
Figure C-11: Yield Summary for $^{16}\text{O} + ^{197}\text{Au}$ PERP1: π^+

$^{16}\text{O} + \text{Au}$ PERP1 : Yield Summary π^-

Solid lines are results of P_t fits, dashes are from M_t fits.

$$f_{pt} = A e^{-pT} \times \text{factor}$$

$$f_{mt} = A e^{-mT} \times \text{factor}$$



Symbol	Y _{avg}	A	T	factor
○	0.95	8.99	.137	10 ⁻⁴
○	---	12.4	.131	10 ⁻⁴
□	1.30	8.66	.126	10 ⁻⁶
□	---	14.8	.115	10 ⁻⁶
△	1.50	6.75	.151	10 ⁻⁷
△	---	9.40	.144	10 ⁻⁷
◇	1.70	6.77	.162	10 ⁻⁸
◇	---	9.59	.152	10 ⁻⁸
⊕	1.88	4.45	.180	10 ⁻⁹
⊕	---	6.16	.167	10 ⁻⁹

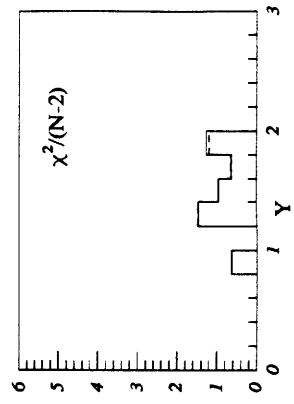
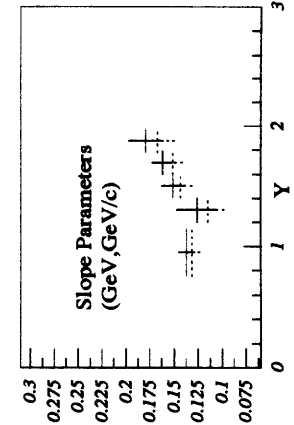
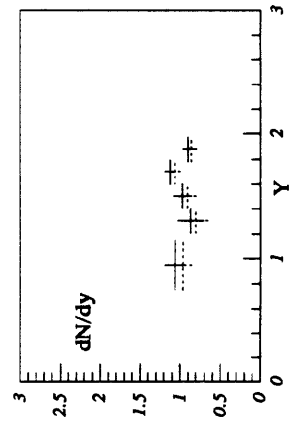


Figure C-12: Yield Summary for $^{16}\text{O} + ^{197}\text{Au}$ PERP1: π^-

Appendix D

Yield Summary: $^{16}\text{O} + ^{27}\text{Al} : \text{Kaons}$

$^{16}\text{O} + \text{Al}$ Inelastic Cross-Section Summary for K^-

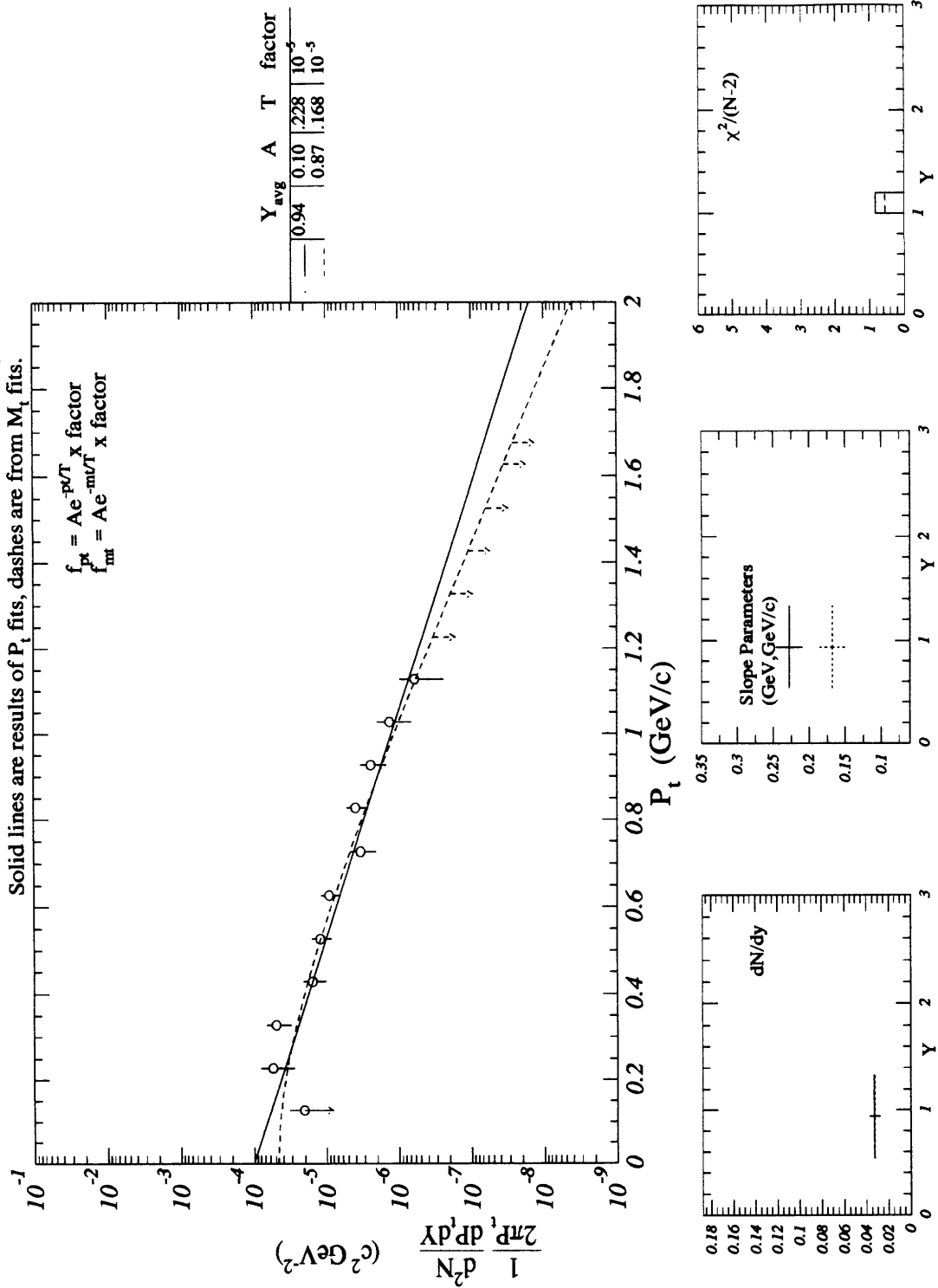


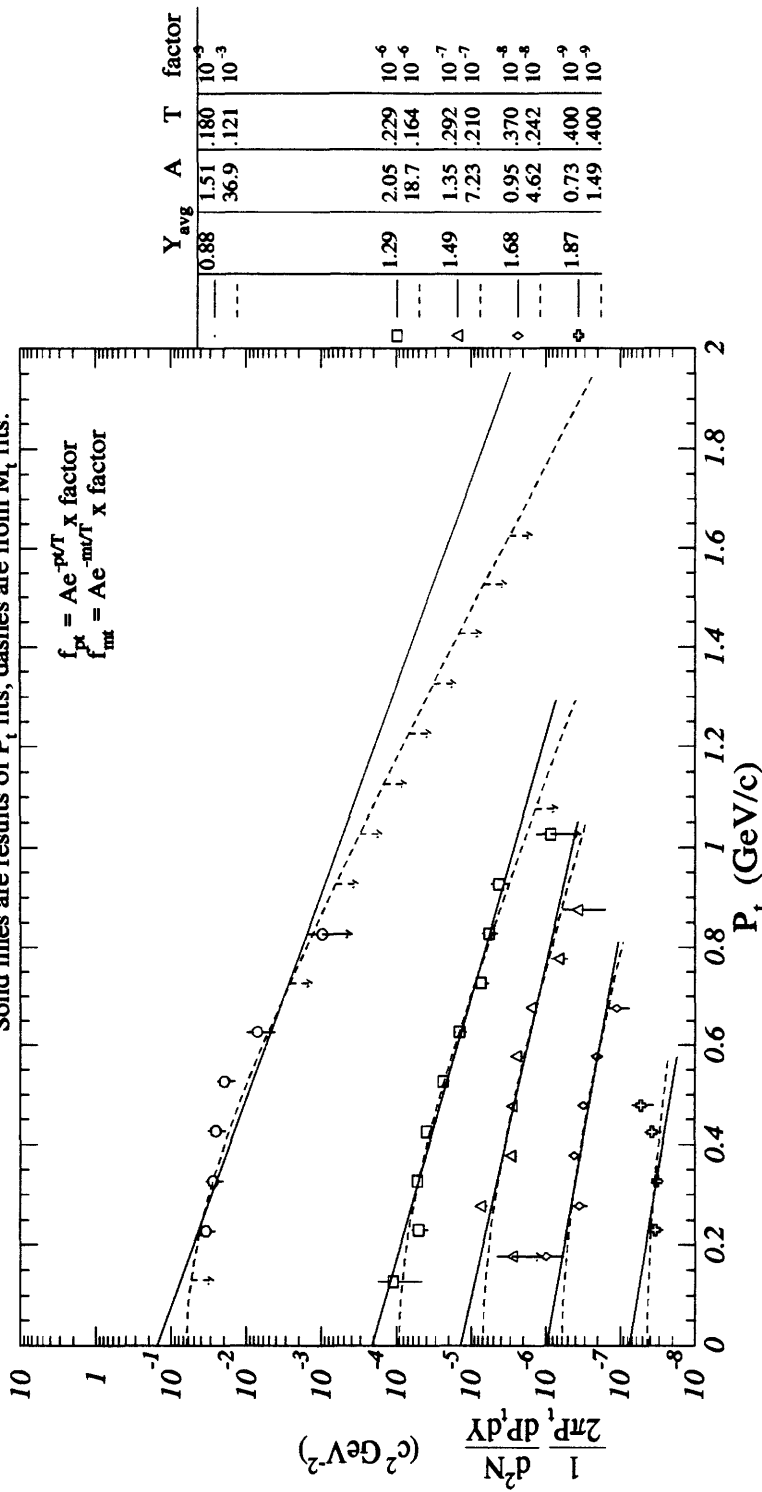
Figure D-1: Yield Summary for $^{16}\text{O} + ^{27}\text{Al}$ INEL: K^-

$^{16}\text{O} + \text{Al TMA}$: Yield Summary K^+

Solid lines are results of P_t fits, dashes are from M_t fits.

$$f_{\text{fit}} = A e^{-pT/T} \times \text{factor}$$

$$f_{\text{fit}} = A e^{-mT/T} \times \text{factor}$$



Y	A	T	factor
0.88	1.51	.180	10^{-9}
---	36.9	.121	10^{-3}
□	1.29	2.05	10^{-6}
---	18.7	.164	10^{-6}
△	1.49	1.35	10^{-7}
---	7.23	.210	10^{-7}
◇	1.68	0.95	10^{-8}
---	4.62	.242	10^{-8}
◇	1.87	0.73	10^{-9}
---	1.49	.400	10^{-9}

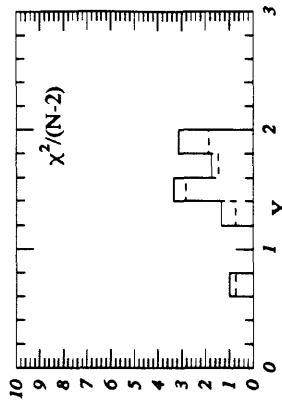
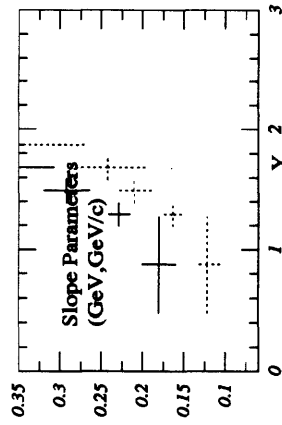
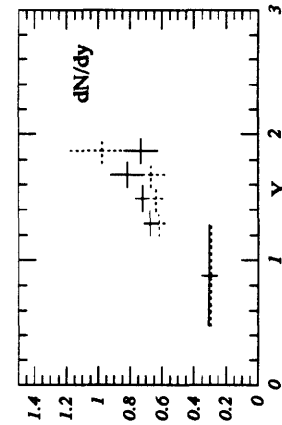


Figure D-2: Yield Summary for $^{16}\text{O} + ^{27}\text{Al TMA}$: K^+

¹⁶O+Al TMA : Yield Summary K⁻

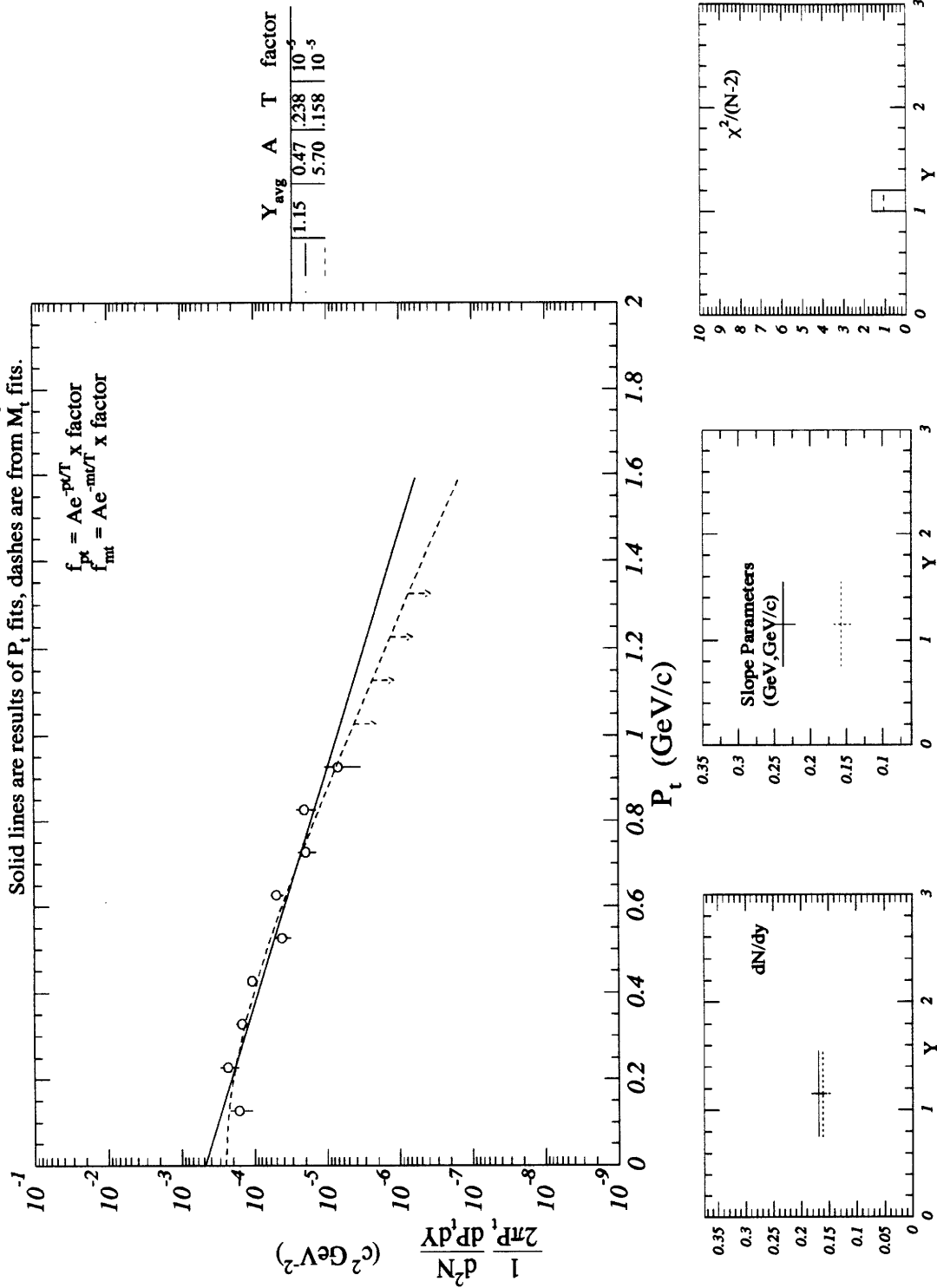


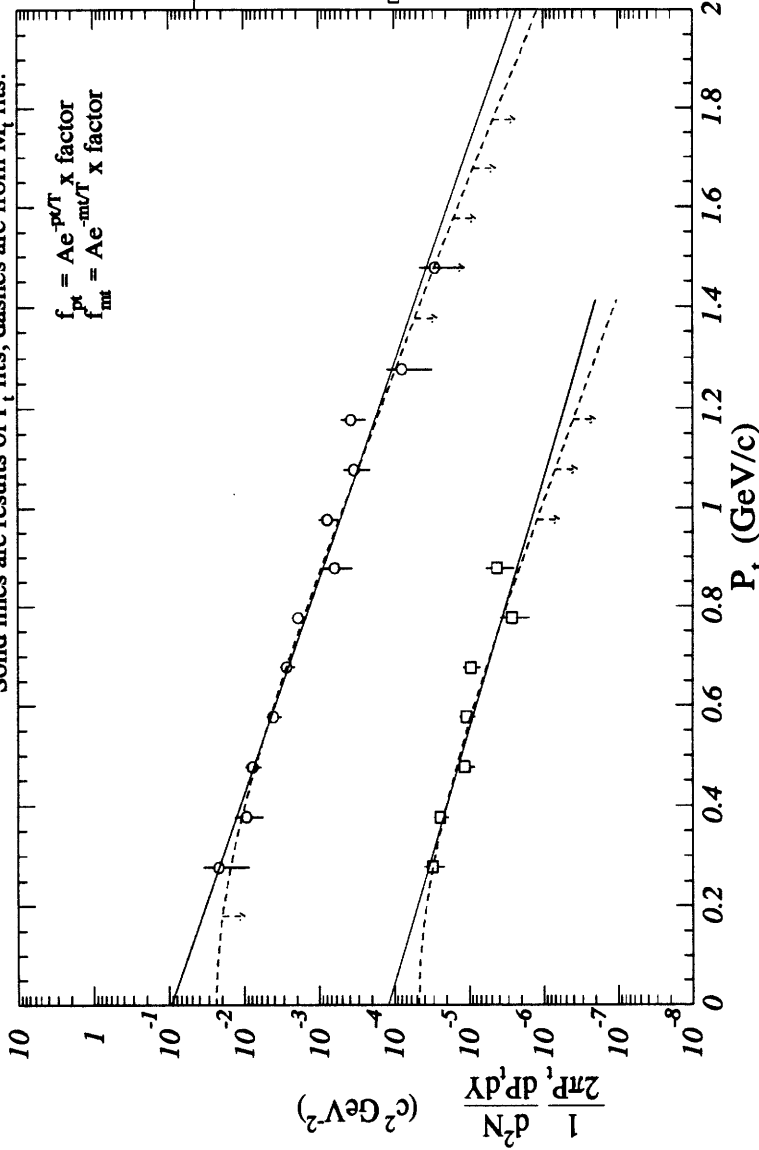
Figure D-3: Yield Summary for ¹⁶O + ²⁷Al TMA: K⁻

¹⁶O+Al CENT2: Yield Summary K+

Solid lines are results of P_t fits, dashes are from M_t fits.

$$f_{pt} = Ae^{-pT} \times \text{x factor}$$

$$f_{mt} = Ae^{-mT} \times \text{x factor}$$



Y	avg	A	T	factor
1	0.69	0.93	.188	10^{-3}
2	5.50	.158		10^{-3}
1	1.27	1.20	.221	10^{-6}
2	9.71	.163		10^{-6}

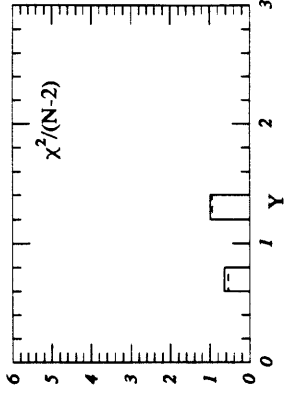
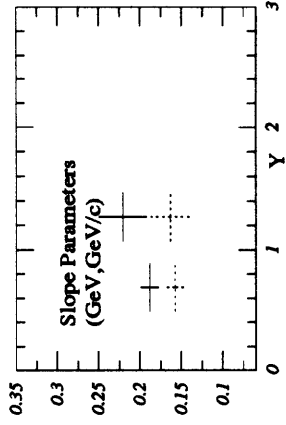
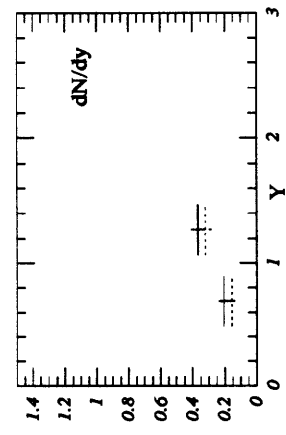


Figure D-4: Yield Summary for ¹⁶O + ²⁷Al CENT2: K+

Appendix E

Yield Summary: $^{16}\text{O} + ^{64}\text{Cu}$:

Kaons

$^{16}\text{O} + \text{Cu}$ Inelastic Cross-Section Summary for K^+

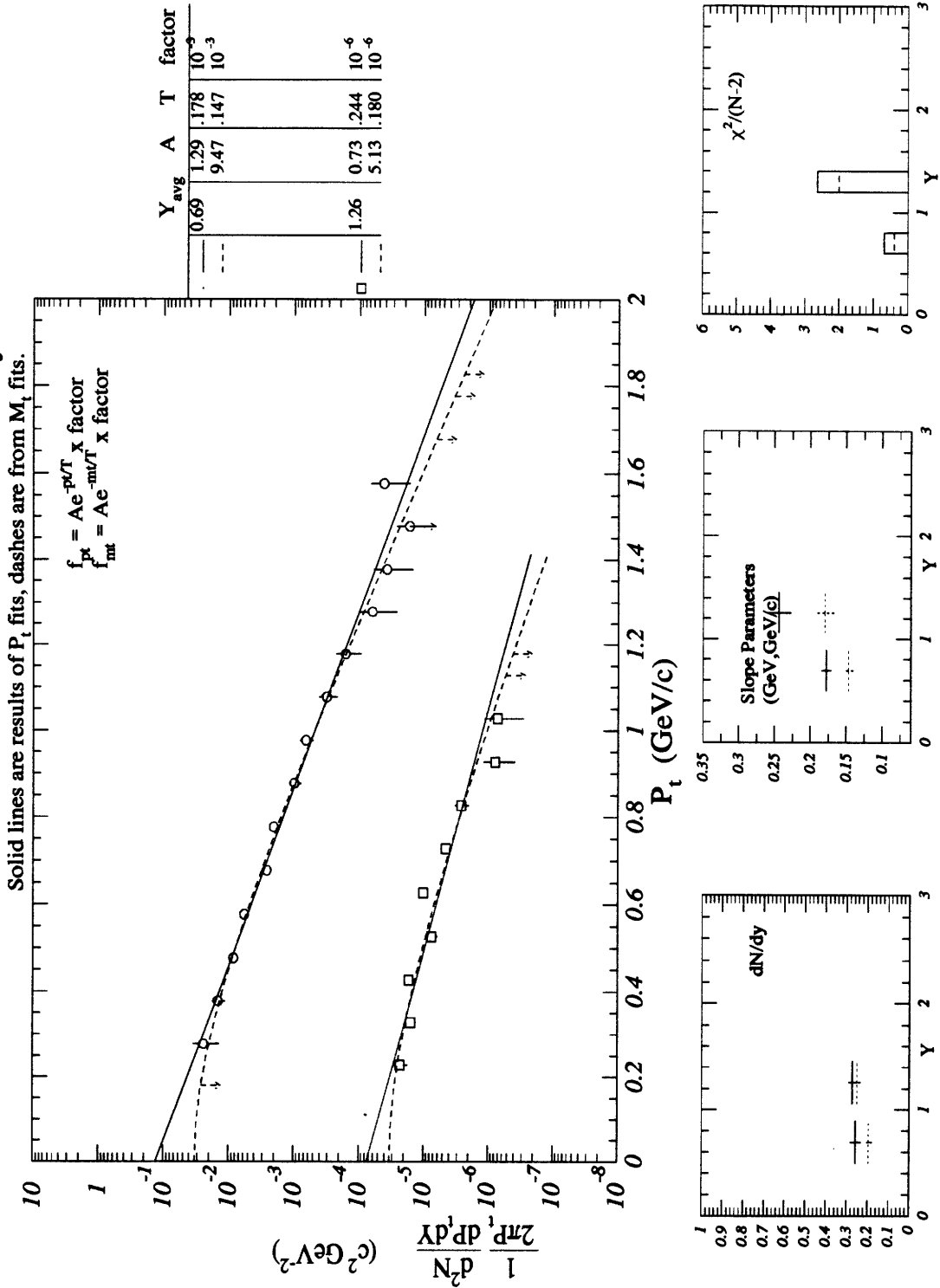


Figure E-1: Yield Summary for $^{16}\text{O} + ^{64}\text{Cu}$ INEL: K^+

$^{16}\text{O} + \text{Cu}$ Inelastic Cross-Section Summary for K^-

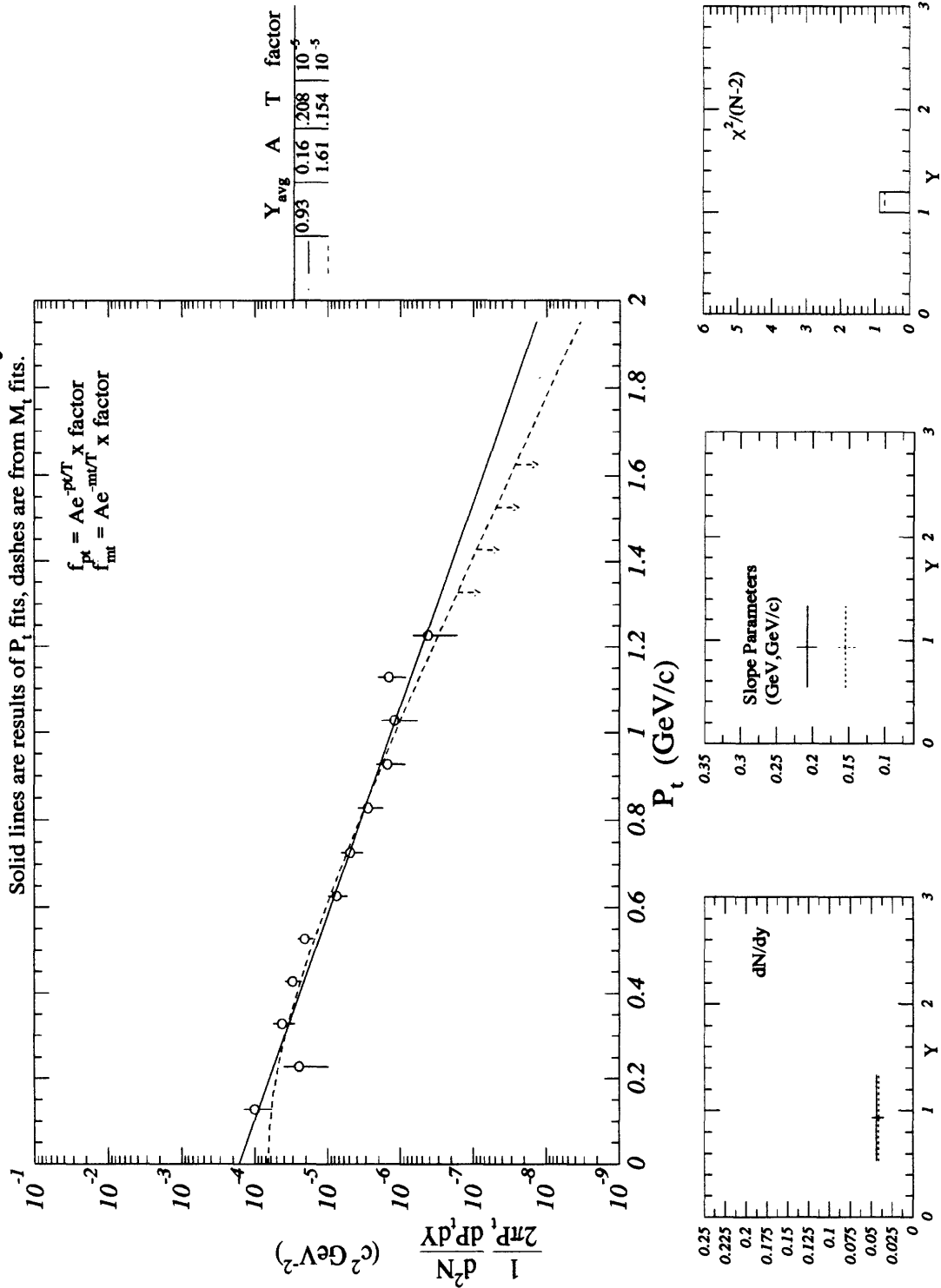
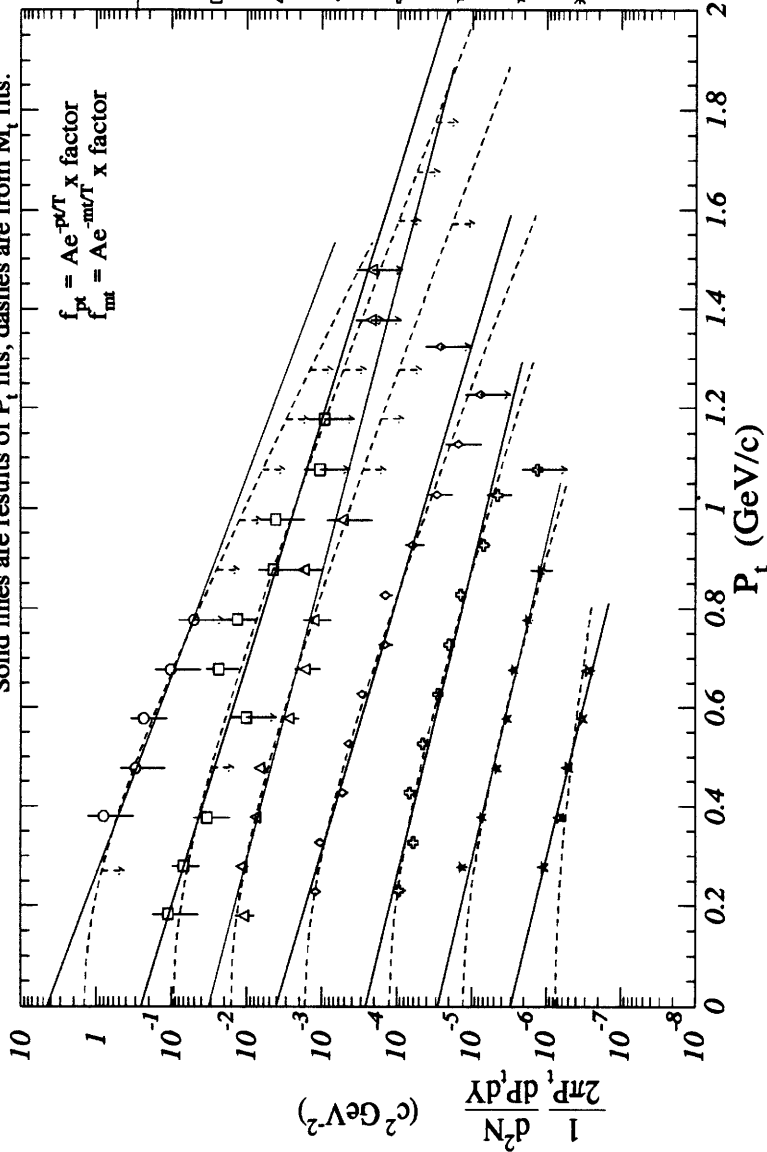


Figure E-2: Yield Summary for $^{16}\text{O} + ^{64}\text{Cu}$ INEL: K^-

$^{16}\text{O}+\text{Cu TMA} : \text{Yield Summary K}^+$

Solid lines are results of P_t fits, dashes are from M_t fits.



Y	Y _{avg}	A	T	factor
□	0.54	4.43	.175	10^{-2}
□	0.69	71.0	.127	10^{-2}
□	0.69	2.49	.213	10^{-3}
□	0.90	17.7	.168	10^{-3}
△	0.90	3.14	.252	10^{-4}
△	1.09	29.4	.170	10^{-4}
△	1.09	4.03	.221	10^{-5}
△	1.29	33.0	.165	10^{-5}
△	1.29	2.60	.269	10^{-6}
△	1.49	14.4	.202	10^{-6}
△	1.49	2.79	.278	10^{-7}
△	1.67	13.6	.209	10^{-7}
△	1.67	2.95	.268	10^{-8}
△	0.00	2.58	.400	10^{-8}
△	0.00	.000	.000	10^{-9}

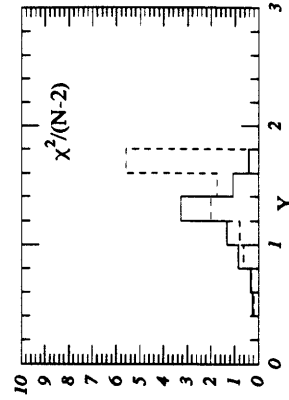
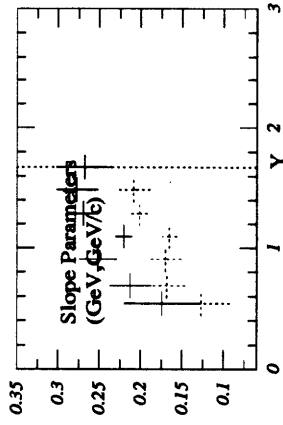
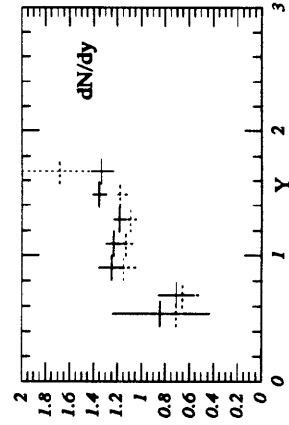


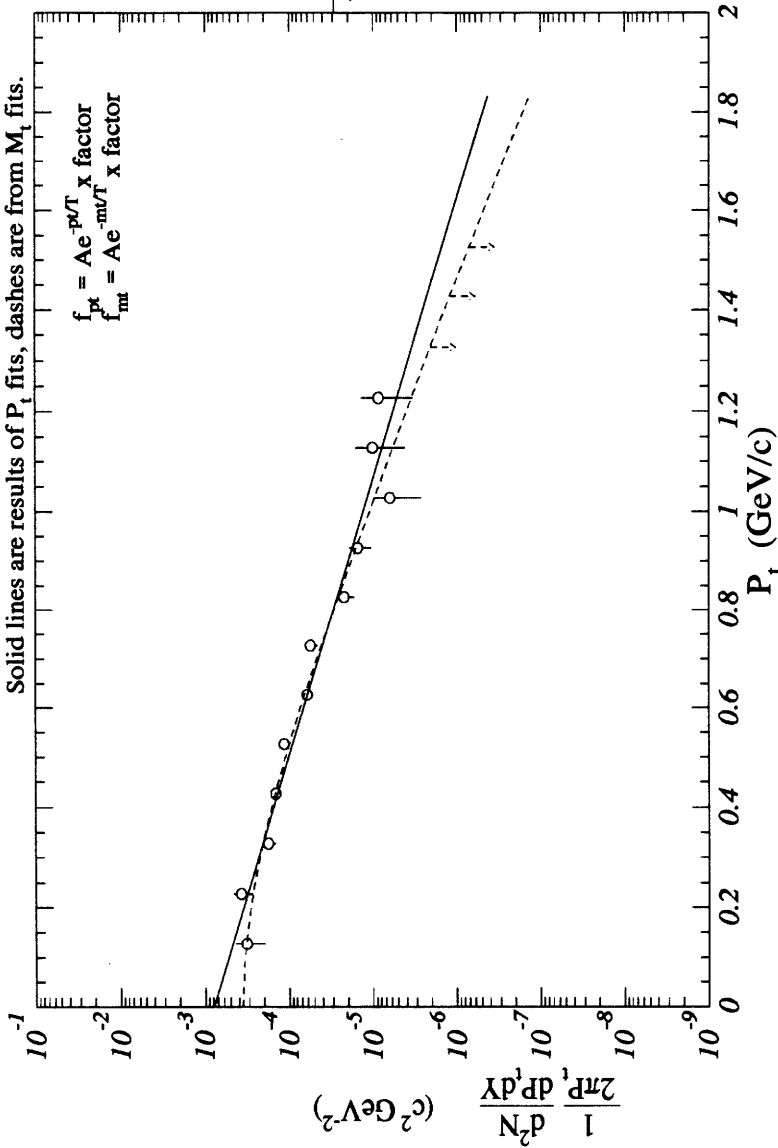
Figure E-3: Yield Summary for $^{16}\text{O} + ^{64}\text{Cu TMA}: \text{K}^+$

$^{16}\text{O} + \text{Cu TMA}$: Yield Summary K^-

Solid lines are results of P_t fits, dashes are from M_t fits.

$$f_{pt} = A e^{-p_t/T} \quad \text{x factor}$$

$$f_{mt} = A e^{-m_t/T} \quad \text{x factor}$$



	Y_{avg}	A	T factor
—	1.06	0.79	$243 \cdot 10^{-5}$
- - -		5.68	$178 \cdot 10^{-5}$

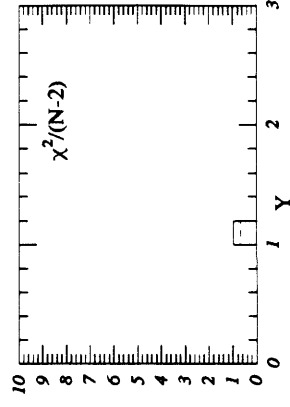
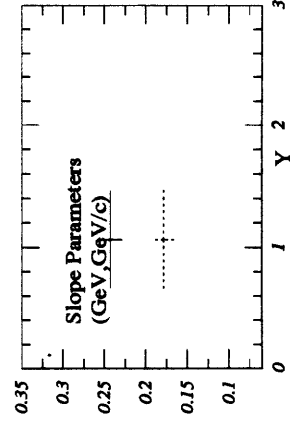
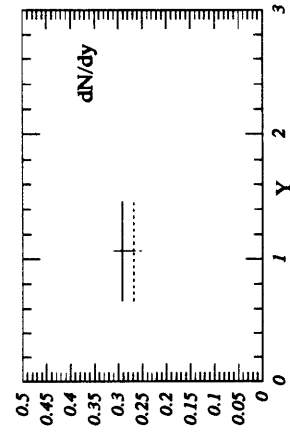


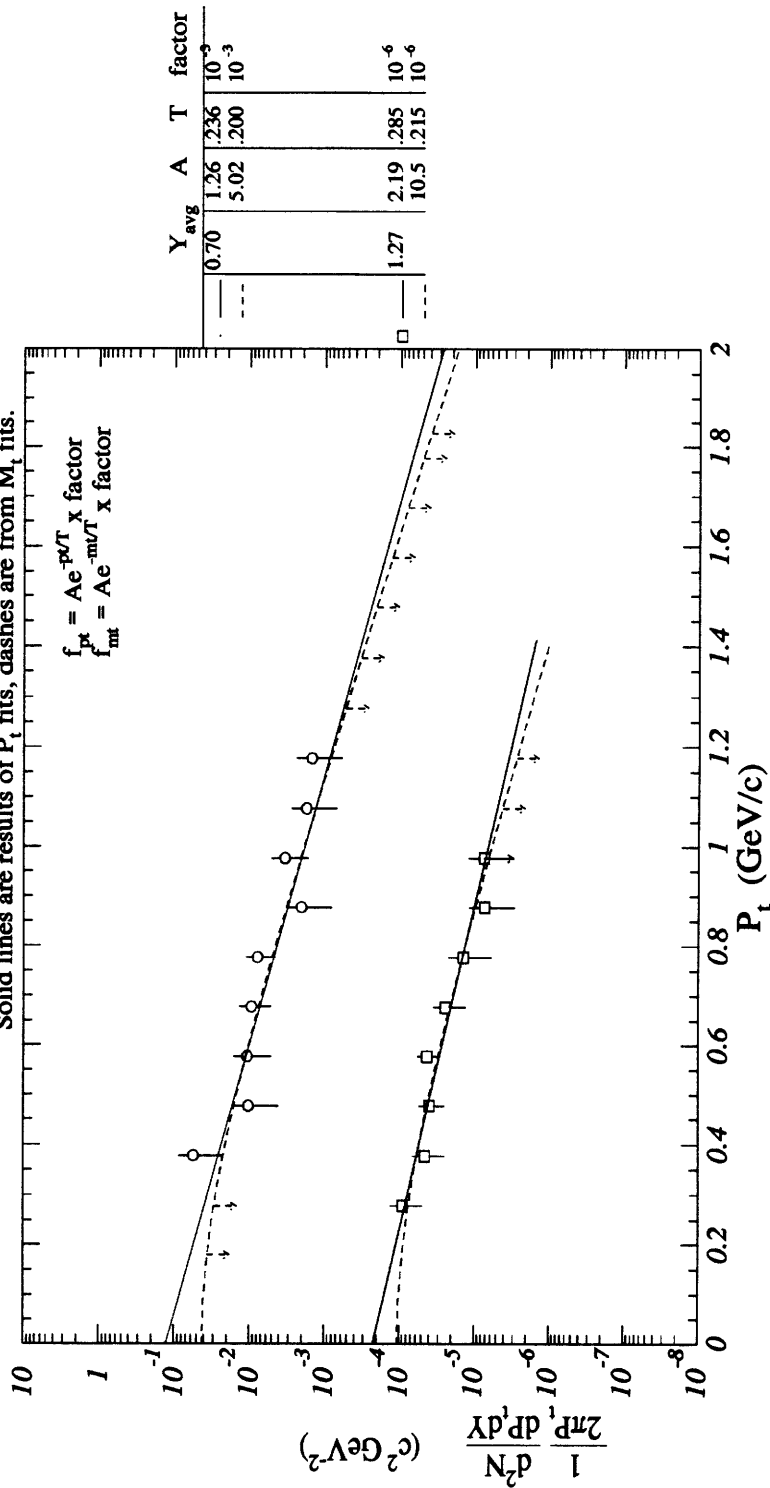
Figure E-4: Yield Summary for $^{16}\text{O} + ^{64}\text{Cu TMA: K}^-$

$^{16}\text{O} + \text{Cu}$ CENT1 : Yield Summary K^+

Solid lines are results of P_t fits, dashes are from M_t fits.

$$f_{\text{fit}} = A e^{-P_t/T} \times \text{factor}$$

$$f_{\text{fit}} = A e^{-m_T/T} \times \text{factor}$$



Y _{avg}	A	T	factor
0.70	1.26	.236	10^{-9}
	5.02	.200	10^{-3}
1.27	2.19	.285	10^{-6}
	10.5	.215	10^{-6}

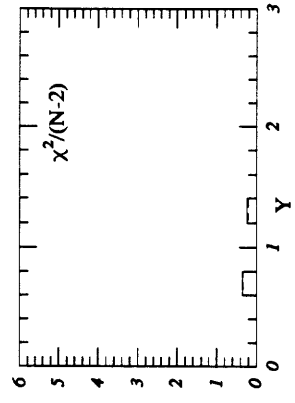
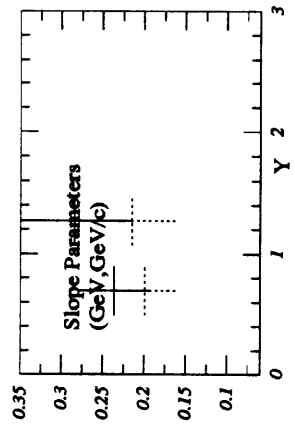
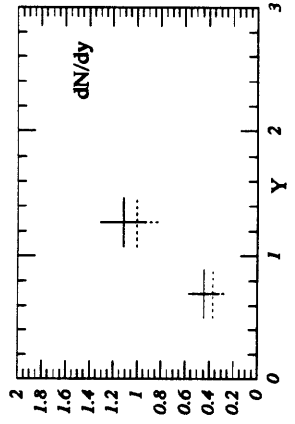


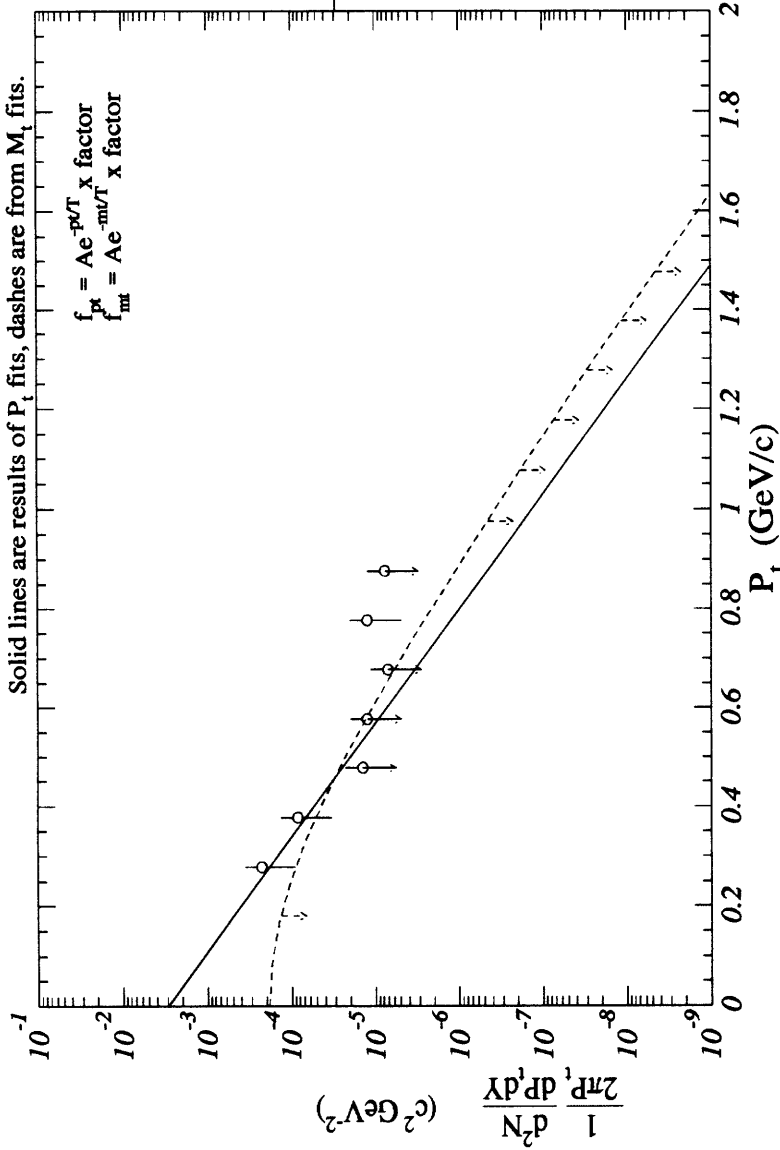
Figure E-5: Yield Summary for $^{16}\text{O} + ^{64}\text{Cu}$ CENT1: K^+

¹⁶O+Cu CENT1 : Yield Summary K-

Solid lines are results of P_t fits, dashes are from M_t fits.

$$f_{pt} = A e^{-pT/T} \times \text{x factor}$$

$$f_{mt} = A e^{-mT/T} \times \text{x factor}$$



	Y_{avg}	A	T factor
—	0.93	2.92	100
- - -		25.5	100
			10^{-5}

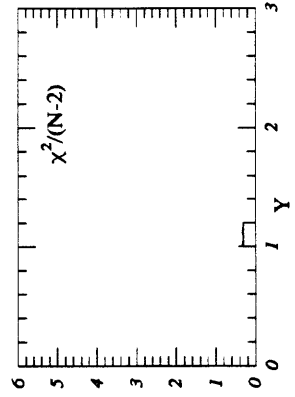
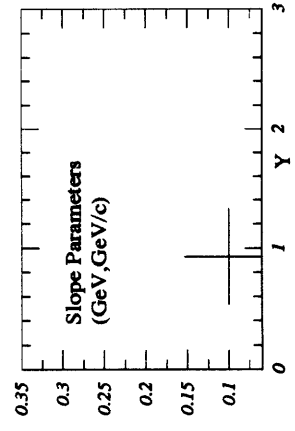
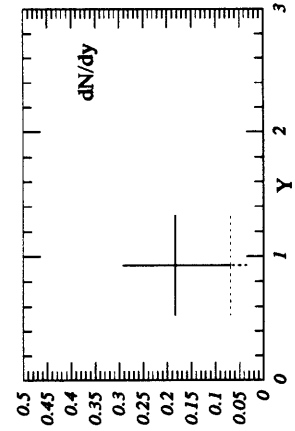


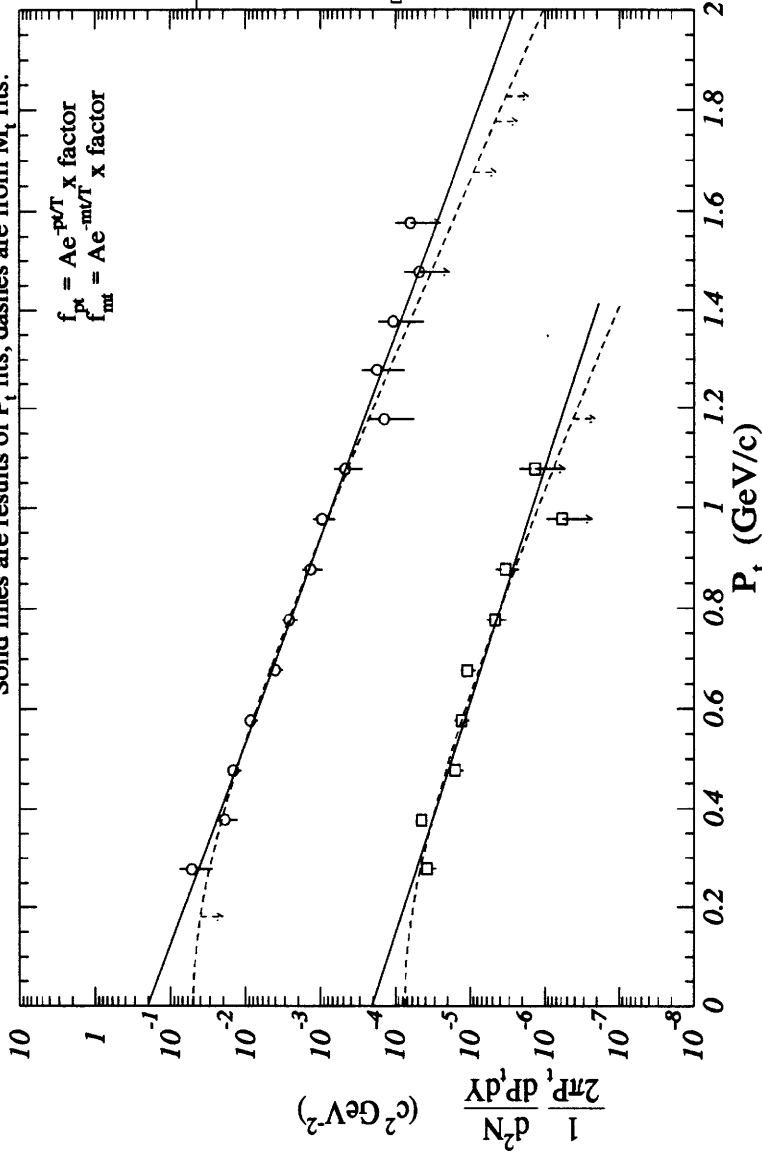
Figure E-6: Yield Summary for ¹⁶O + ⁶⁴Cu CENT1: K-

¹⁶O+Cu CENT2: Yield Summary K+

Solid lines are results of P_t fits, dashes are from M_t fits.

$$f_{pt} = Ae^{-pT/T} \times \text{x factor}$$

$$f_{mt} = Ae^{-mT/T} \times \text{x factor}$$



Y _{avg}	A	T	factor
0.70	1.98	.177	10 ⁻³
	15.0	.145	10 ⁻³
1.26	2.05	.202	10 ⁻⁶
	19.9	.151	10 ⁻⁶

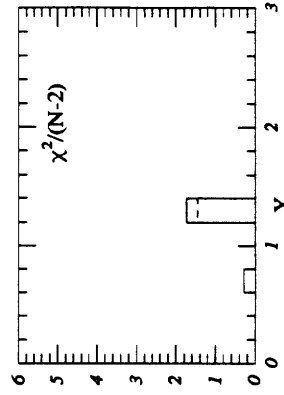
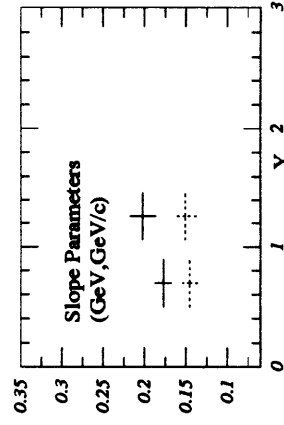
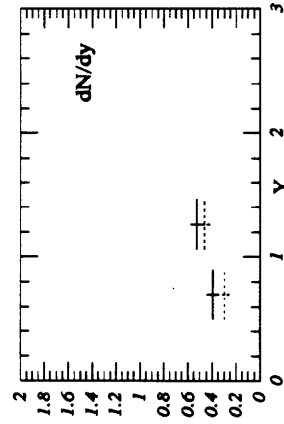


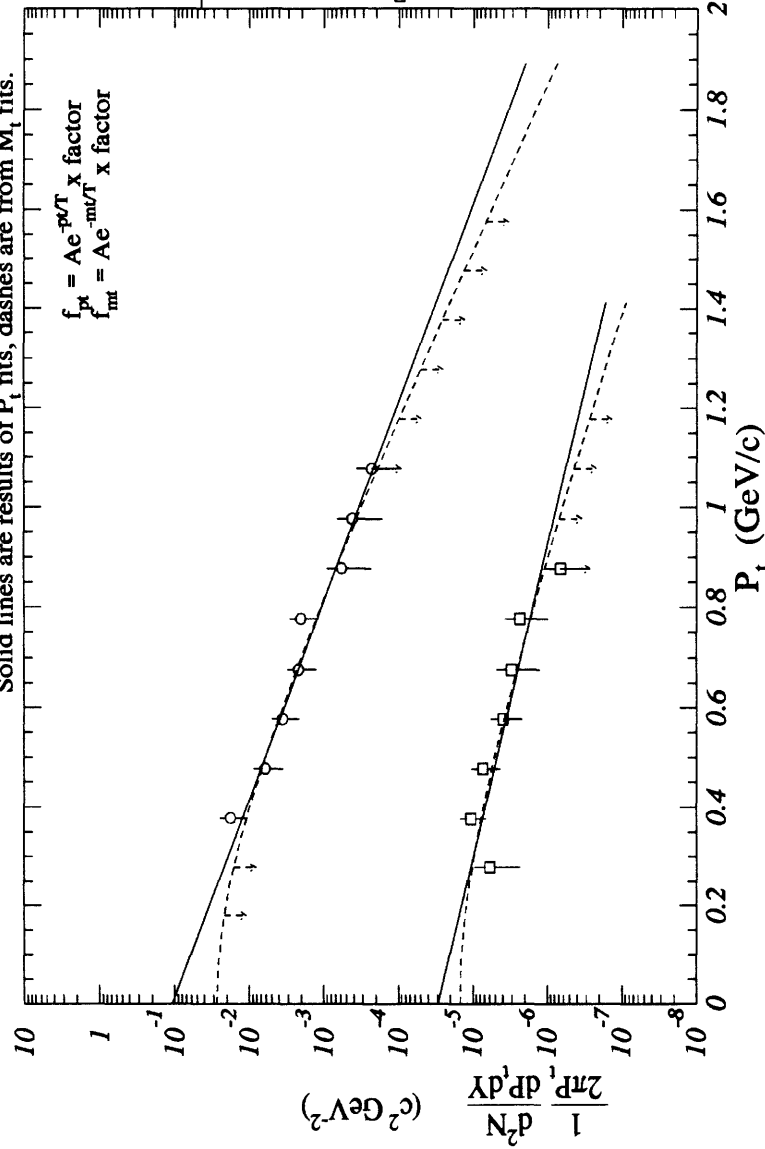
Figure E-7: Yield Summary for ¹⁶O + ⁶⁴Cu CENT2: K+

$^{16}\text{O} + \text{Cu}$ MID : Yield Summary K^+

Solid lines are results of P_t fits, dashes are from M_t fits.

$$f_{pt} = A e^{-pT/T} \times \text{factor}$$

$$f_{mt} = A e^{-mT/T} \times \text{factor}$$



	Y_{avg}	A	T	factor
—	0.74	1.06	.174	10^{-3}
- - -		9.36	.139	10^{-3}
□	1.27	0.29	.274	10^{-6}
- - -		1.84	.196	10^{-6}

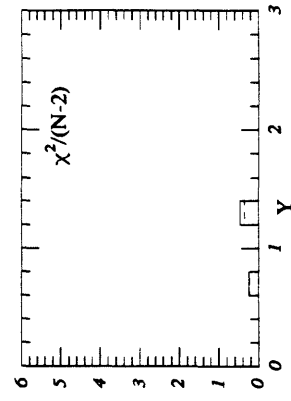
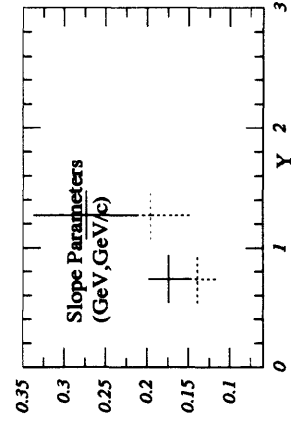
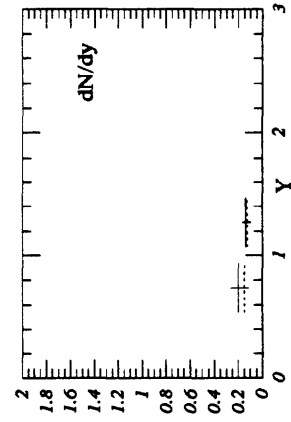


Figure E-8: Yield Summary for $^{16}\text{O} + ^{64}\text{Cu}$ MID: K^+

Appendix F

Yield Summary: $^{16}\text{O} + ^{197}\text{Au}$:

Kaons

$^{16}\text{O} + \text{Au}$ Inelastic Cross-Section Summary for K^+

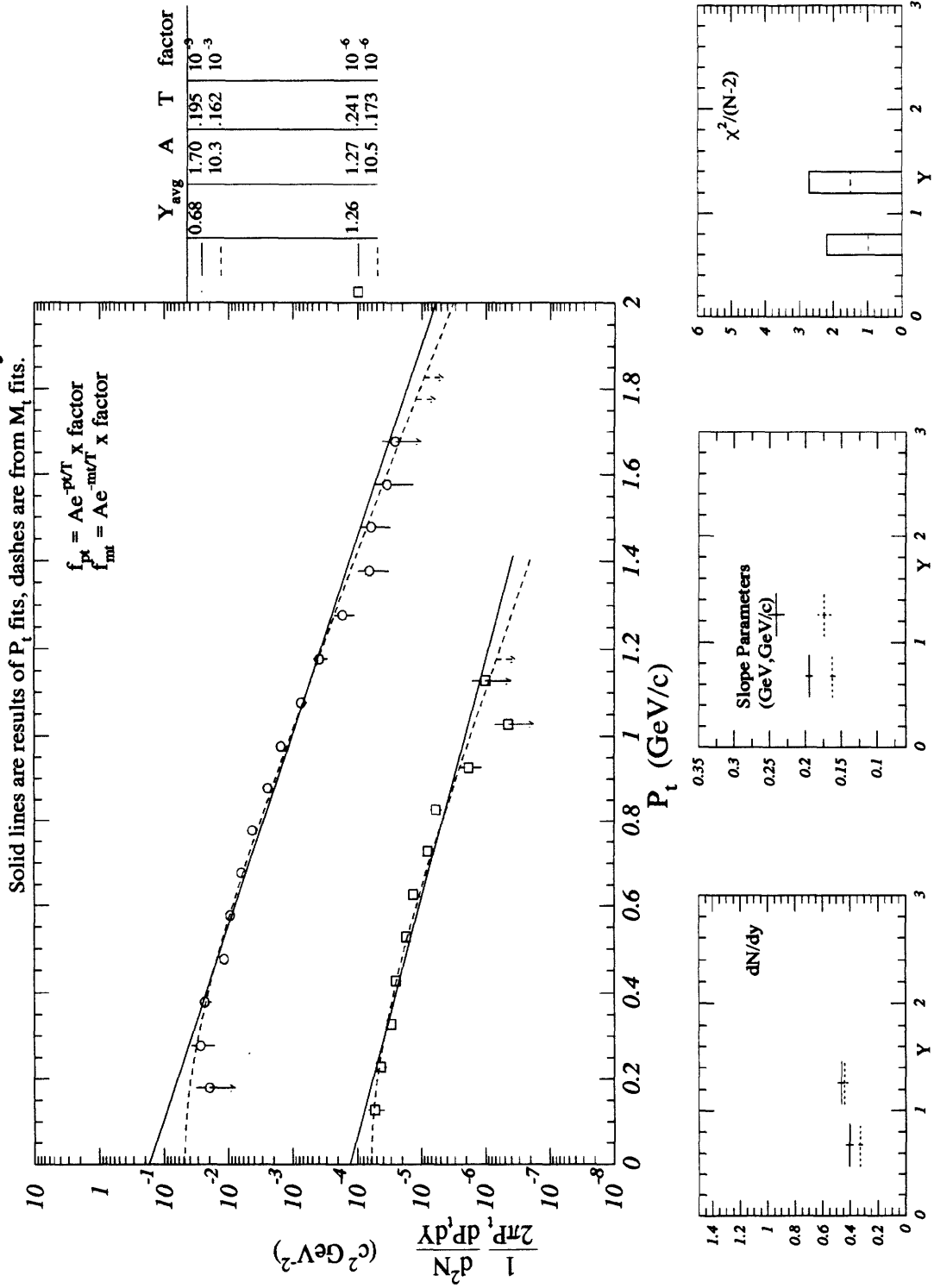


Figure F-1: Yield Summary for $^{16}\text{O} + ^{197}\text{Au}$ INEL: K^+

¹⁶O+Au Inelastic Cross-Section Summary for K⁻

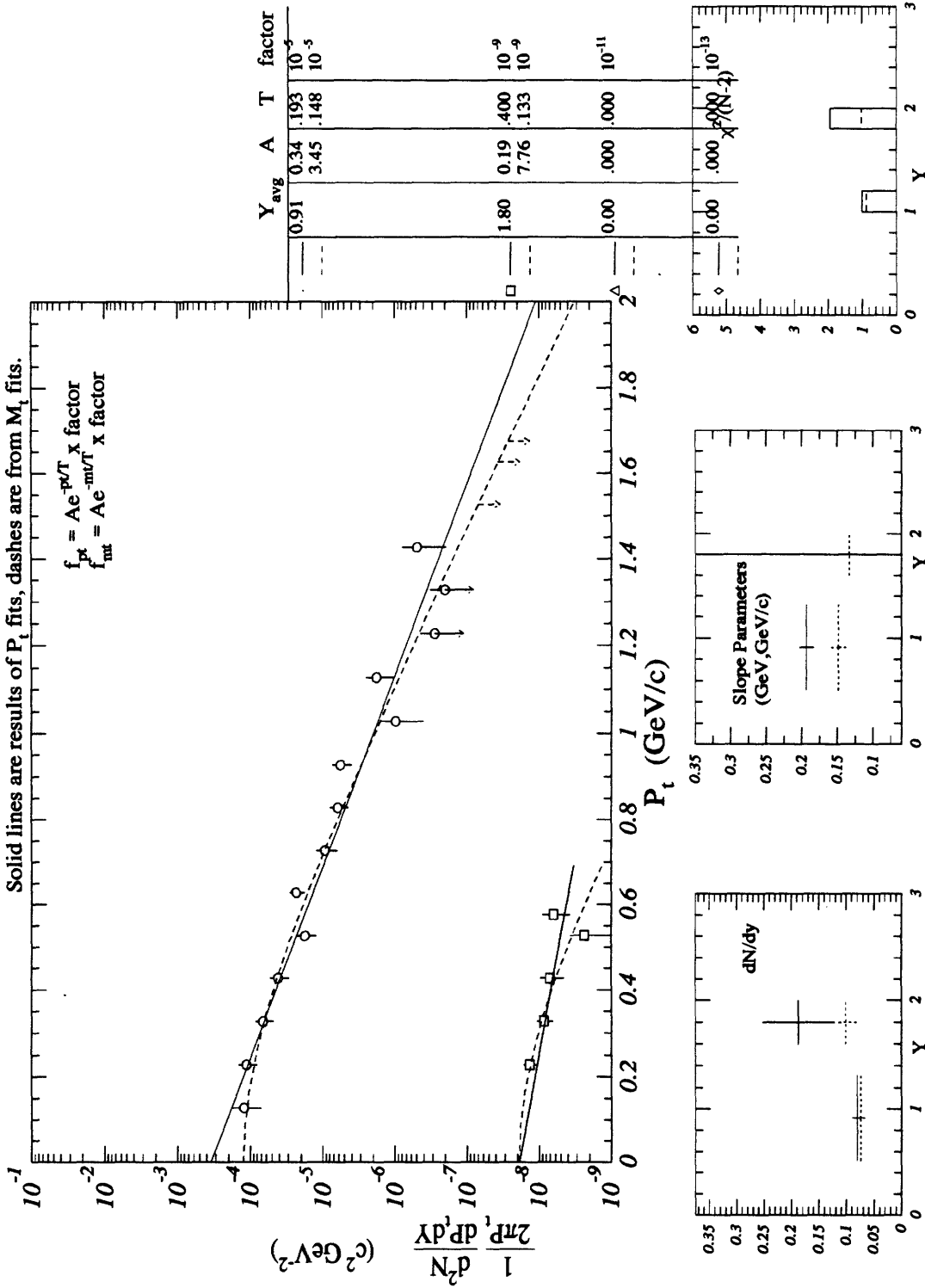


Figure F-2: Yield Summary for ¹⁶O + ¹⁹⁷Au INEL: K⁻

$^{16}\text{O} + \text{Au TMA} : \text{Yield Summary K}^+$

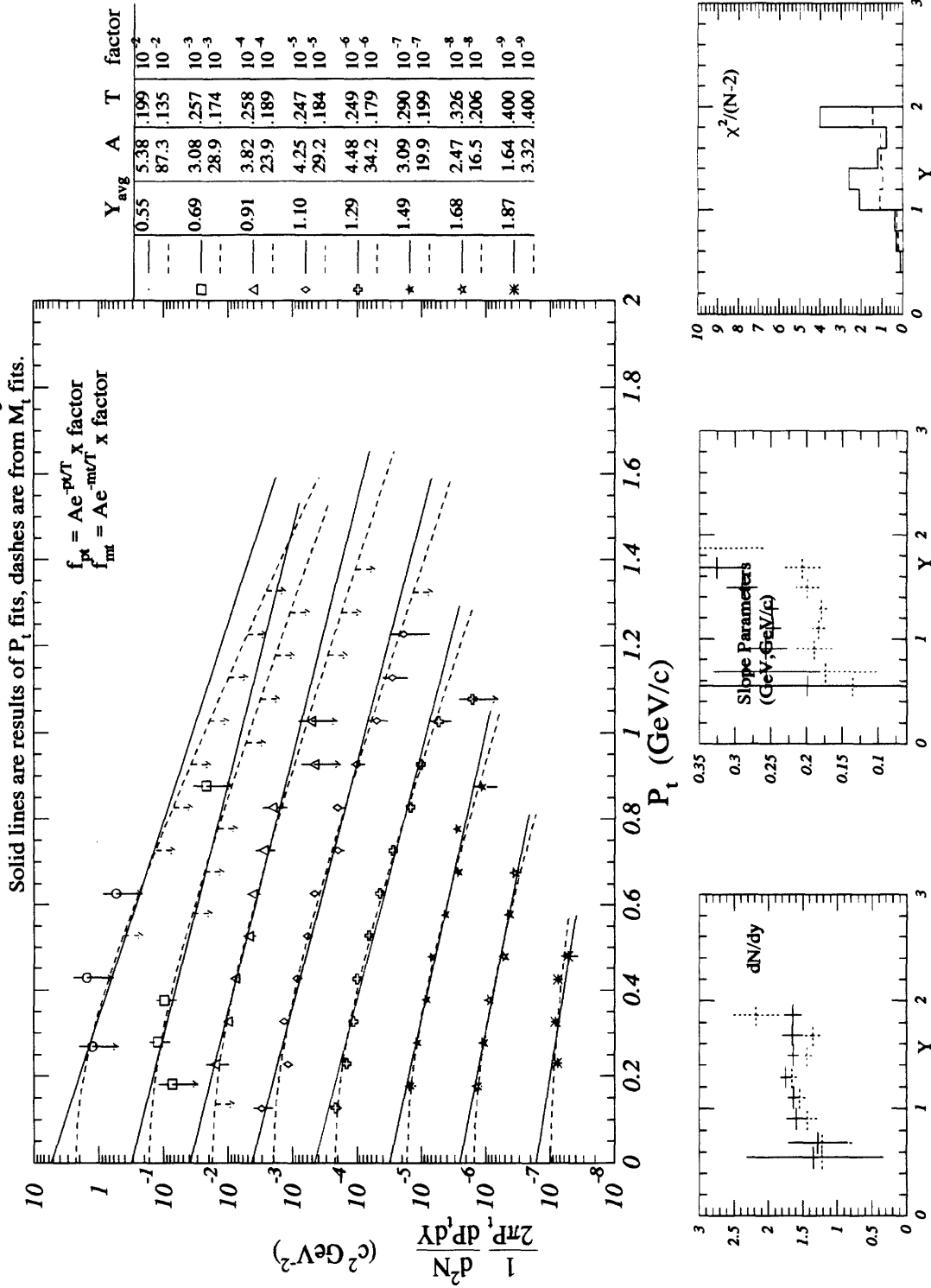


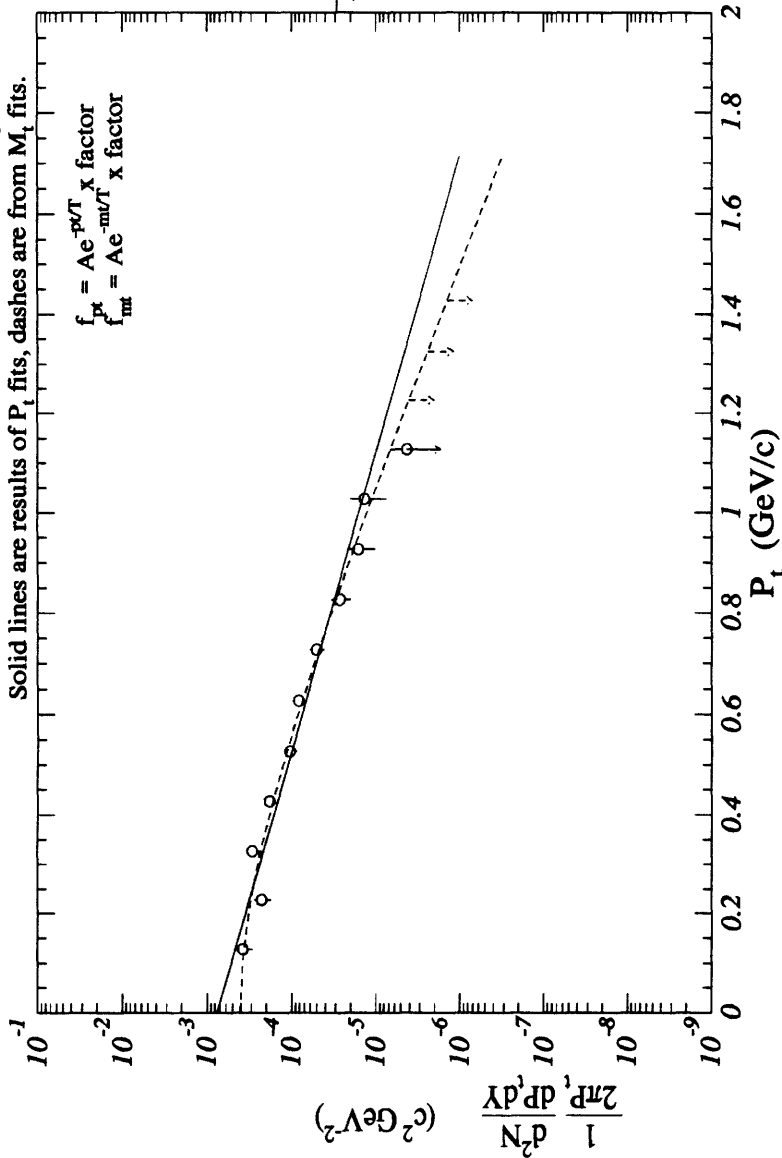
Figure F-3: Yield Summary for $^{16}\text{O} + ^{197}\text{Au TMA}: \text{K}^+$

$^{16}\text{O} + \text{Au TMA}$: Yield Summary K^-

Solid lines are results of P_t fits, dashes are from M_t fits.

$$f_{\text{fit}} = A e^{-P_t/T} \quad \text{x factor}$$

$$f_{\text{fit}} = A e^{-m_T/T} \quad \text{x factor}$$



	Y_{avg}	A	T factor
—	1.12	0.75	.259 10^{-5}
- - -		6.23	.180 10^{-5}

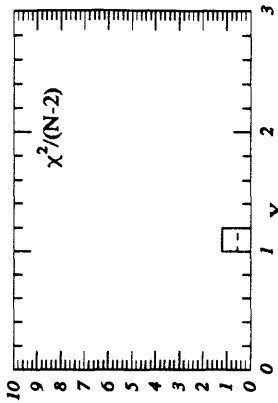
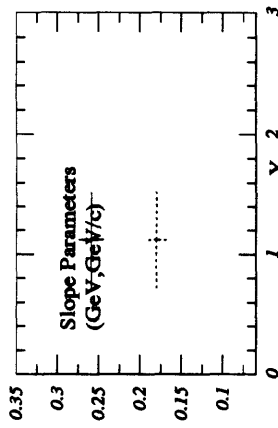
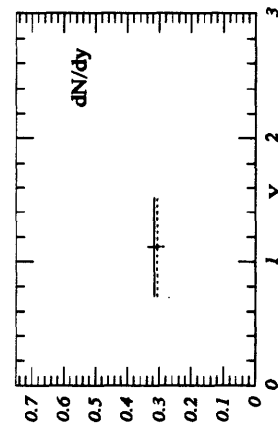


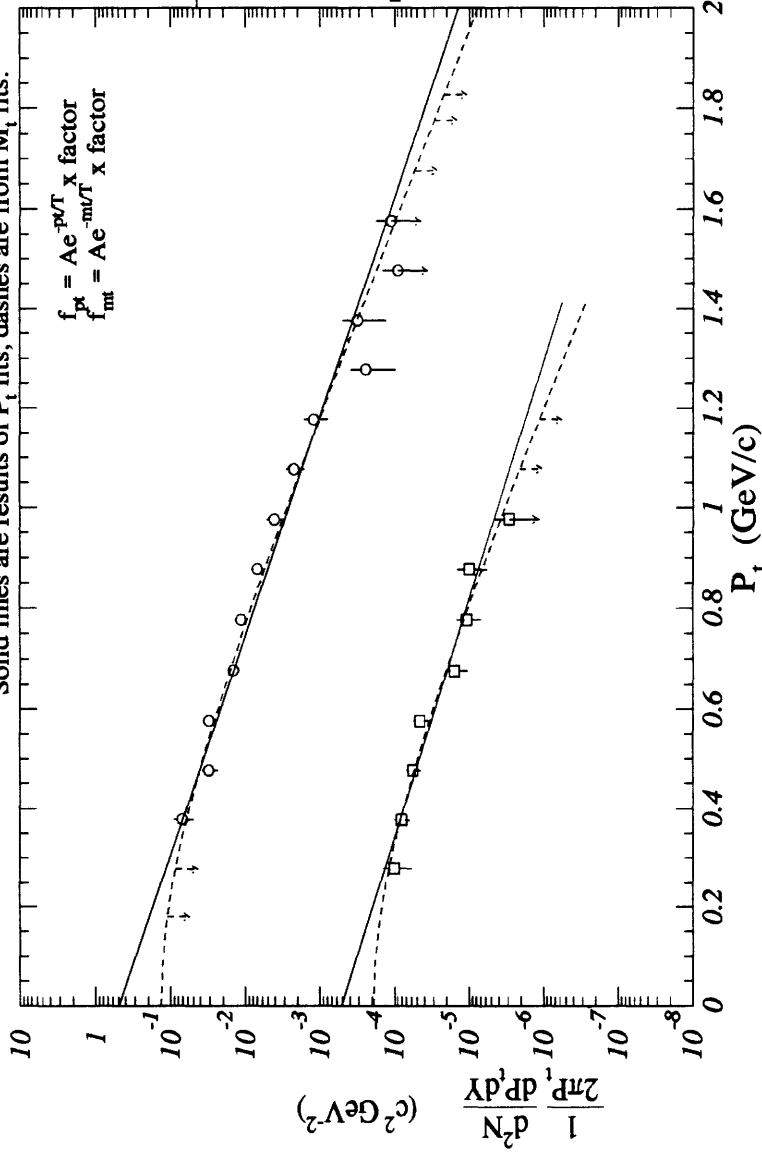
Figure F-4: Yield Summary for $^{16}\text{O} + ^{197}\text{Au TMA}$: K^-

$^{16}\text{O} + \text{Au}$ CENT1 : Yield Summary K^+

Solid lines are results of P_t fits, dashes are from M_t fits.

$$f_{\text{fit}} = A e^{-p_t/T} \times \text{factor}$$

$$f_{\text{mt}} = A e^{-m_t/T} \times \text{factor}$$



	Y_{avg}	A	T	factor
—	0.68	4.91	.191	10^{-3}
- - -		29.5	.160	10^{-3}
□	1.26	5.08	.207	10^{-6}
- - -		48.6	.153	10^{-6}

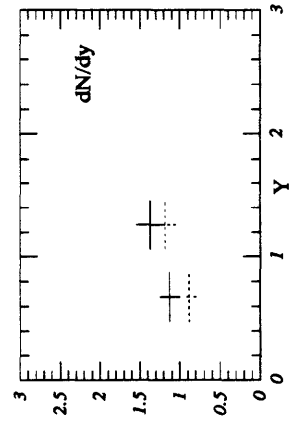
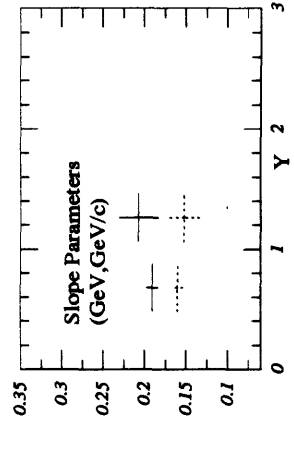
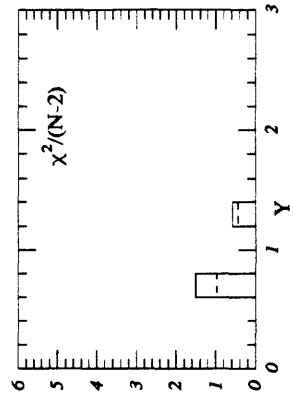


Figure F-5: Yield Summary for $^{16}\text{O} + ^{197}\text{Au}$ CENT1: K^+

¹⁶O+Au CENT1 : Yield Summary K-

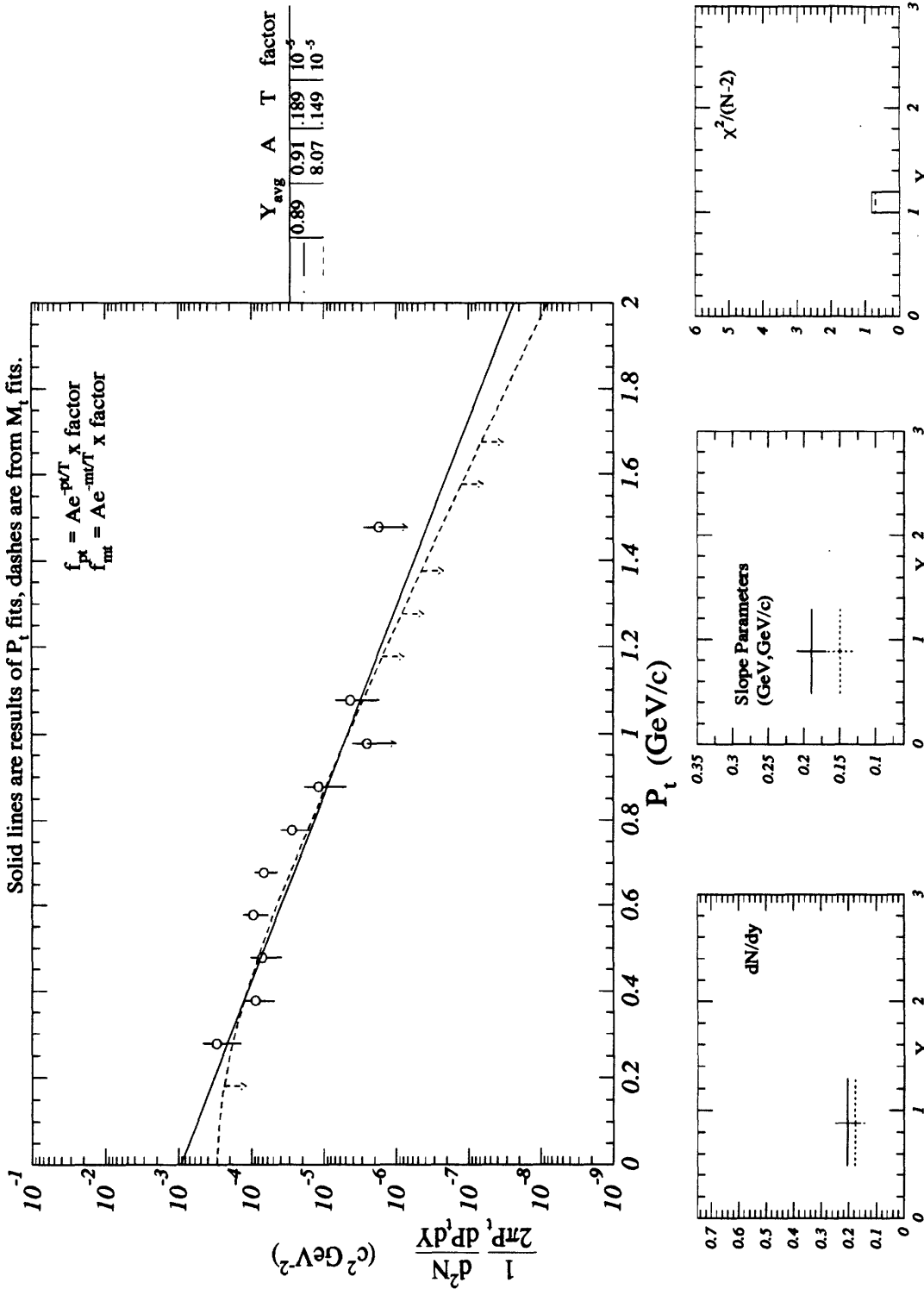


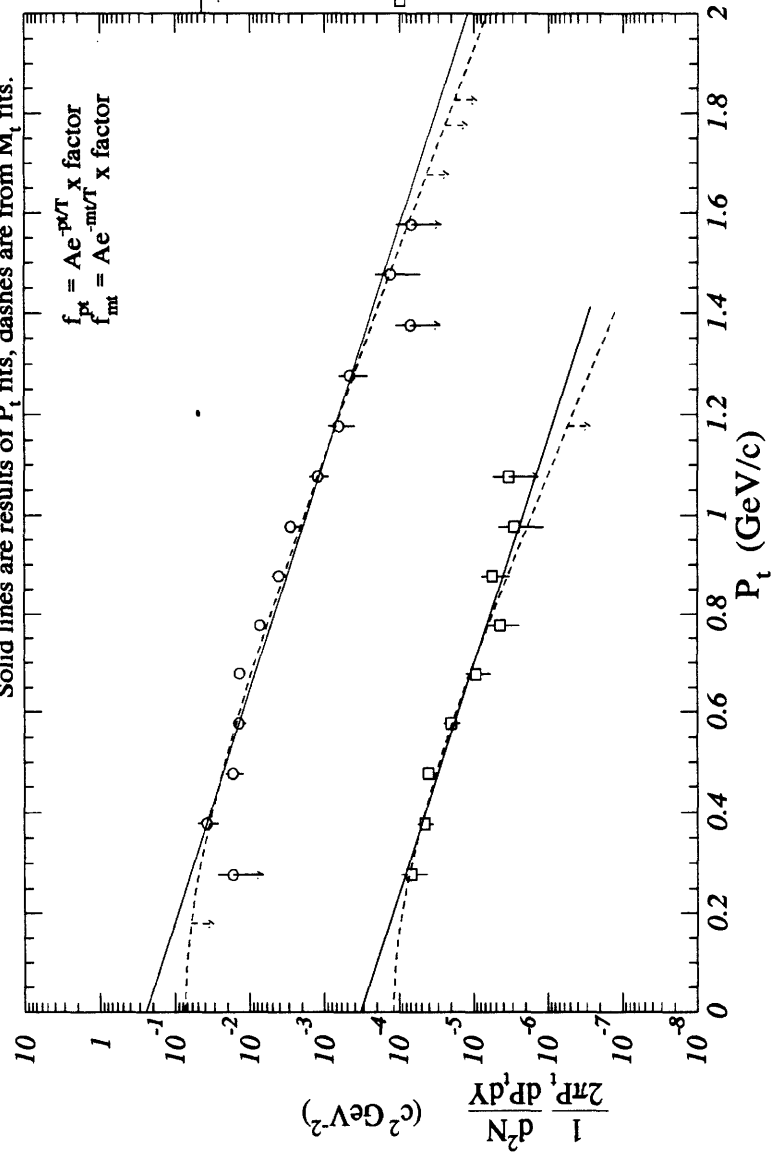
Figure F-6: Yield Summary for ¹⁶O + ¹⁹⁷Au CENT1: K-

¹⁶O+Au CENT2: Yield Summary K+

Solid lines are results of P_t fits, dashes are from M_t fits.

$$f_{px} = Ae^{-pT/T} \times \text{factor}$$

$$f_{mt} = Ae^{-mT/T} \times \text{factor}$$



Y _{AVG}	A	T factor
0.67	2.41	.202
	13.9	.168
1.26	3.27	.199
	36.4	.145

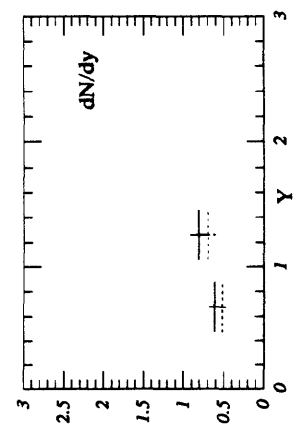
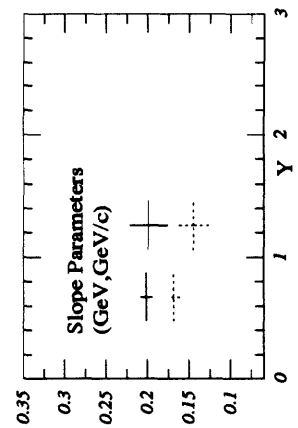
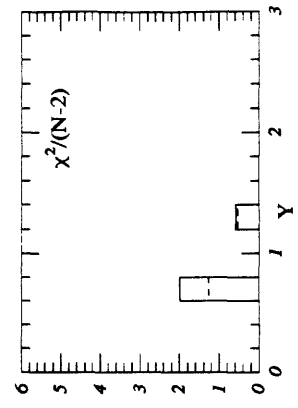


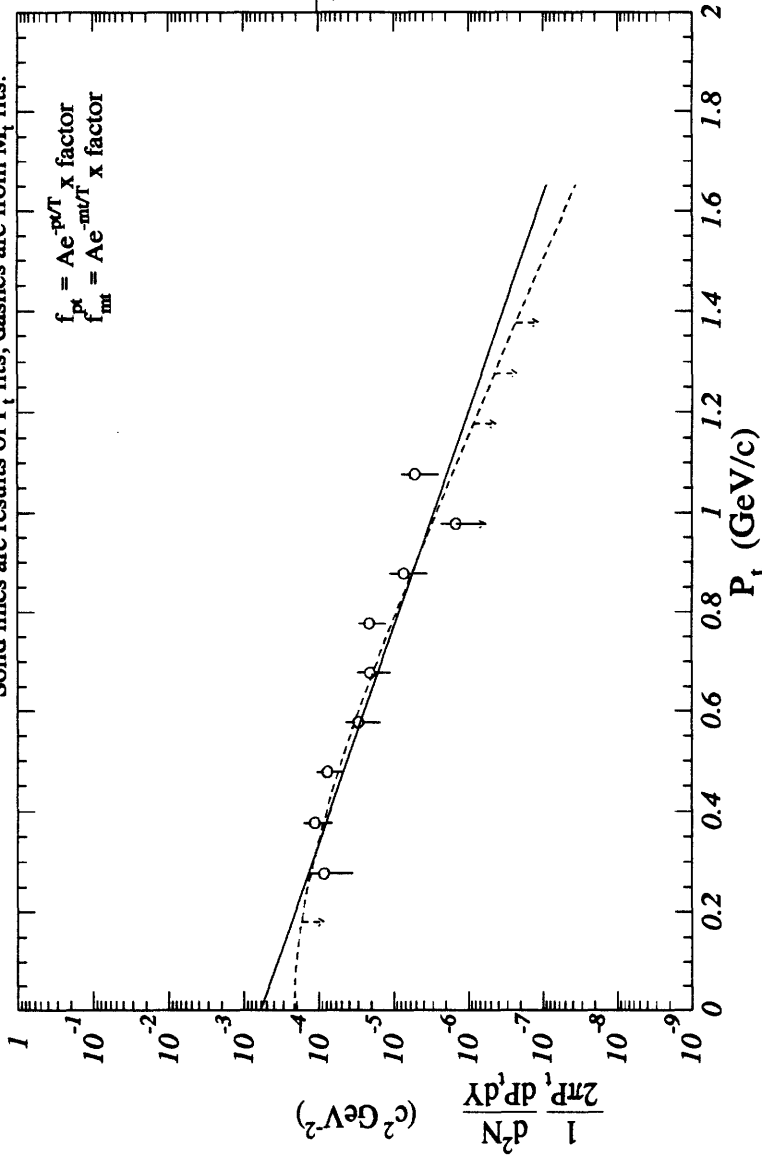
Figure F-7: Yield Summary for ¹⁶O + ¹⁹⁷Au CENT2: K⁺

$^{16}\text{O} + \text{Au}$ CENT2 : Yield Summary K⁻

Solid lines are results of P_t fits, dashes are from M_t fits.

$$f_{pt} = A e^{-p_t/T} \times \text{x factor}$$

$$f_{mt} = A e^{-m_t/T} \times \text{x factor}$$



	Y_{avg}	A	T	factor
—	0.92	0.60	1.187	10^{-5}
- - -	7.02	1.141	10	10^{-5}

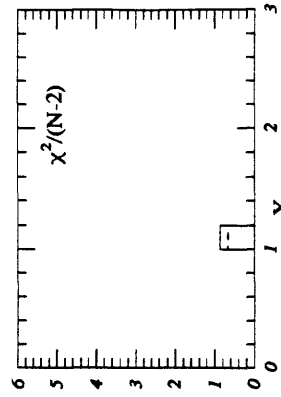
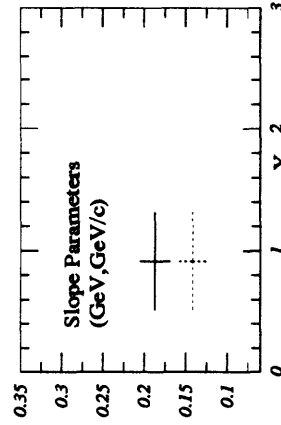
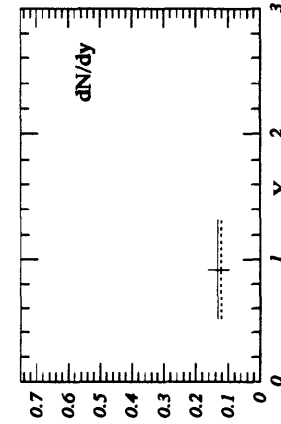


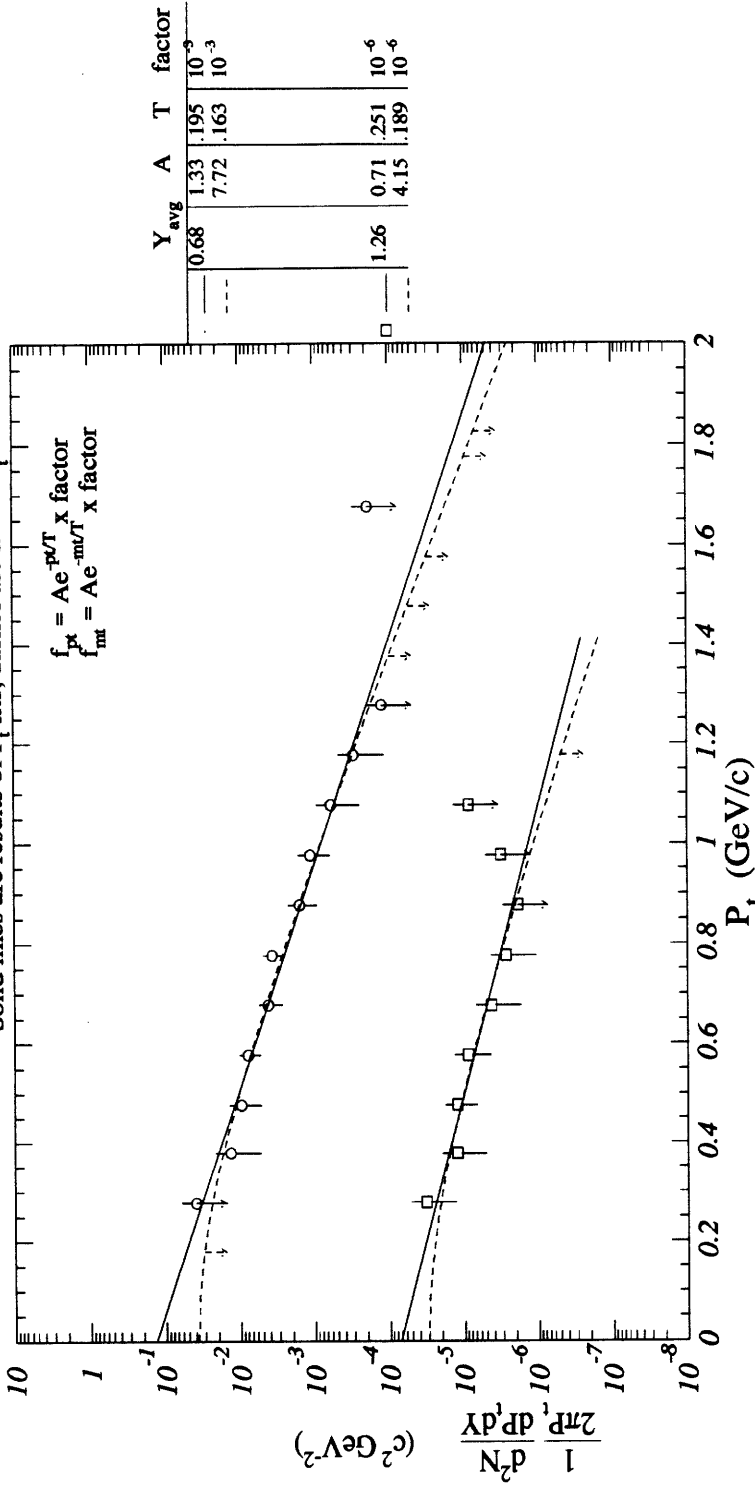
Figure F-8: Yield Summary for $^{16}\text{O} + ^{197}\text{Au}$ CENT2: K⁻

$^{16}\text{O} + \text{Au}$ MID : Yield Summary K^+

Solid lines are results of P_t fits, dashes are from M_t fits.

$$f_{pt} = A e^{-P_t/T} \times \text{factor}$$

$$f_{mt} = A e^{-m_t/T} \times \text{factor}$$



	Y_{avg}	A	T	factor
—	0.68	1.33	.195	10^{-9}
- - -	7.72	.163		10^{-3}
□	1.26	0.71	.251	10^{-6}
○		4.15	.189	10^{-6}

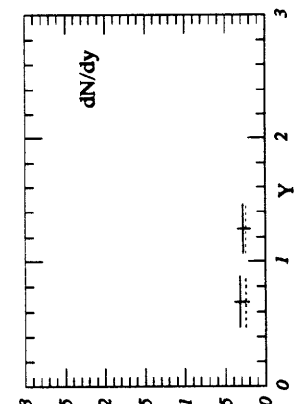
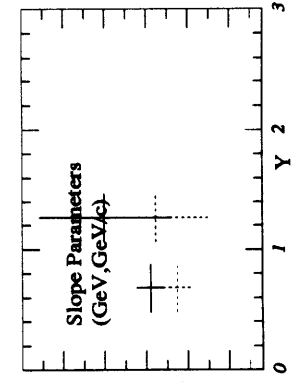
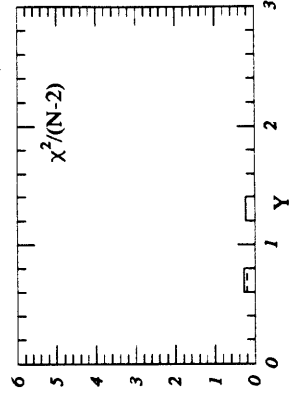


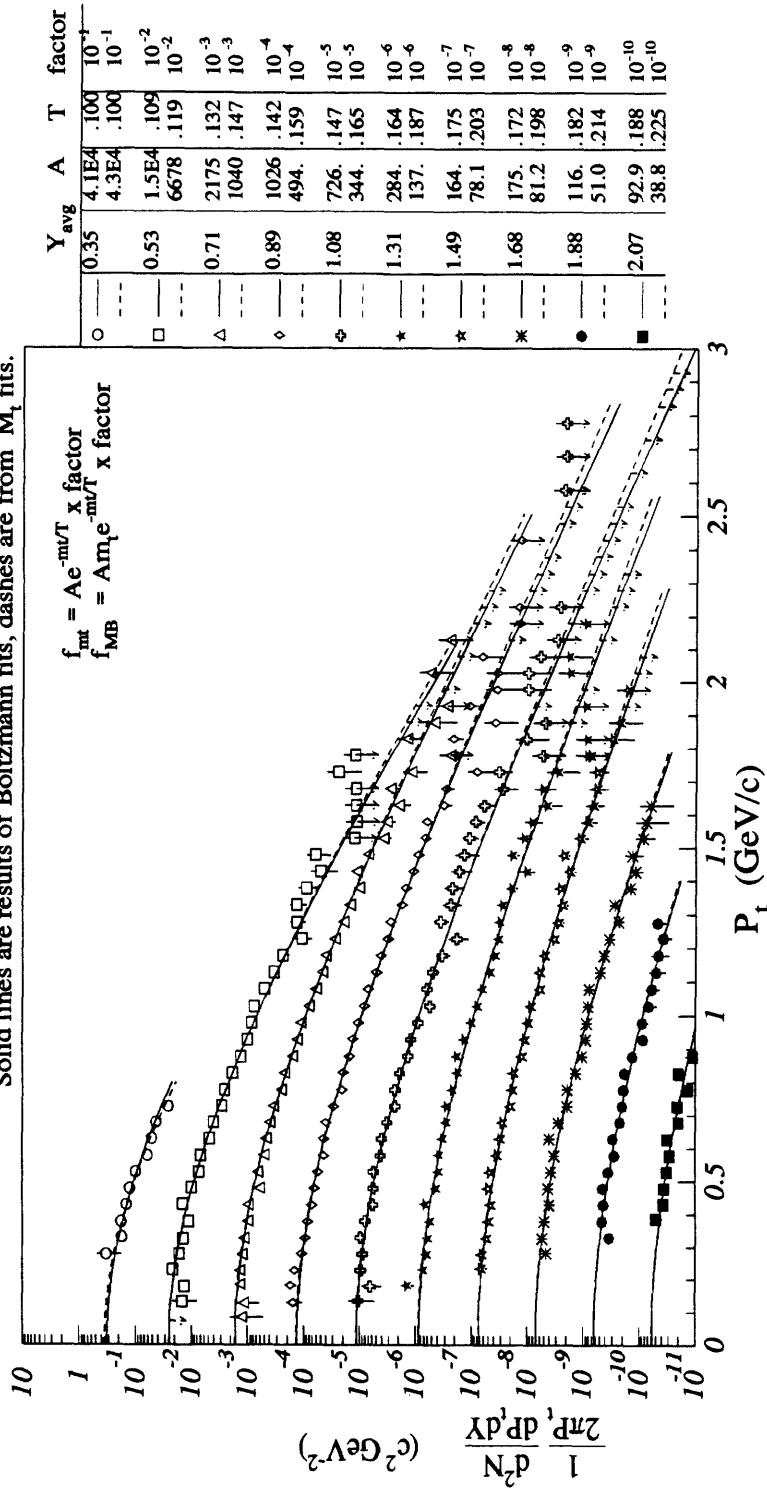
Figure F-9: Yield Summary for $^{16}\text{O} + ^{197}\text{Au}$ MID: K^+

Appendix G

Yield Summary: ^{16}O + A Protons

$^{16}\text{O} + \text{Al}$ Inelastic Cross-Section Summary for Protons

Solid lines are results of Boltzmann fits, dashes are from M_1 fits.



Y	avg	A	T	factor
○	0.35	4.1E4	.100	10^{-1}
□	0.53	4.3E4	.100	10^{-1}
△	0.71	1.5E4	.109	10^{-2}
◇	0.89	6678	.119	10^{-2}
◇	0.89	2175	.132	10^{-3}
◇	0.89	1040	.147	10^{-3}
◇	0.89	1026	.142	10^{-4}
◇	0.89	494	.159	10^{-4}
◇	1.08	726	.147	10^{-5}
◇	1.08	344	.165	10^{-5}
◇	1.31	284	.164	10^{-6}
◇	1.31	137	.187	10^{-6}
◇	1.49	164	.175	10^{-7}
◇	1.68	78.1	.203	10^{-7}
◇	1.68	175	.172	10^{-8}
◇	1.68	81.2	.198	10^{-8}
◇	1.88	116	.182	10^{-9}
◇	1.88	51.0	.214	10^{-9}
◇	2.07	92.9	.188	10^{-10}
◇	2.07	38.8	.225	10^{-10}

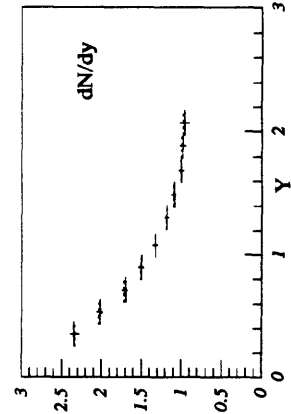
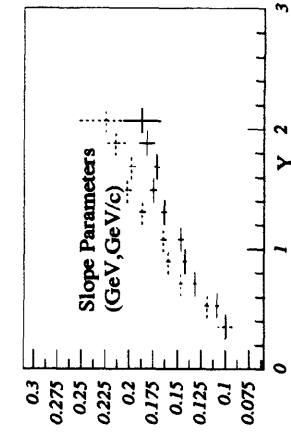
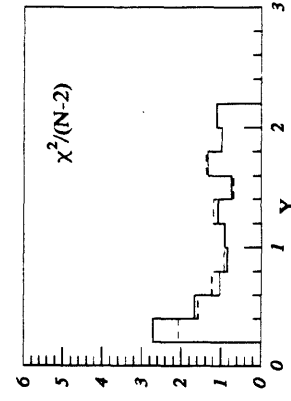


Figure G-1: Yield Summary for $^{16}\text{O} + ^{27}\text{Al}$ INEL: Protons

$^{16}\text{O} + \text{Al TMA}$: Yield Summary Protons

Solid lines are results of Boltzmann fits, dashes are from M_t fits.

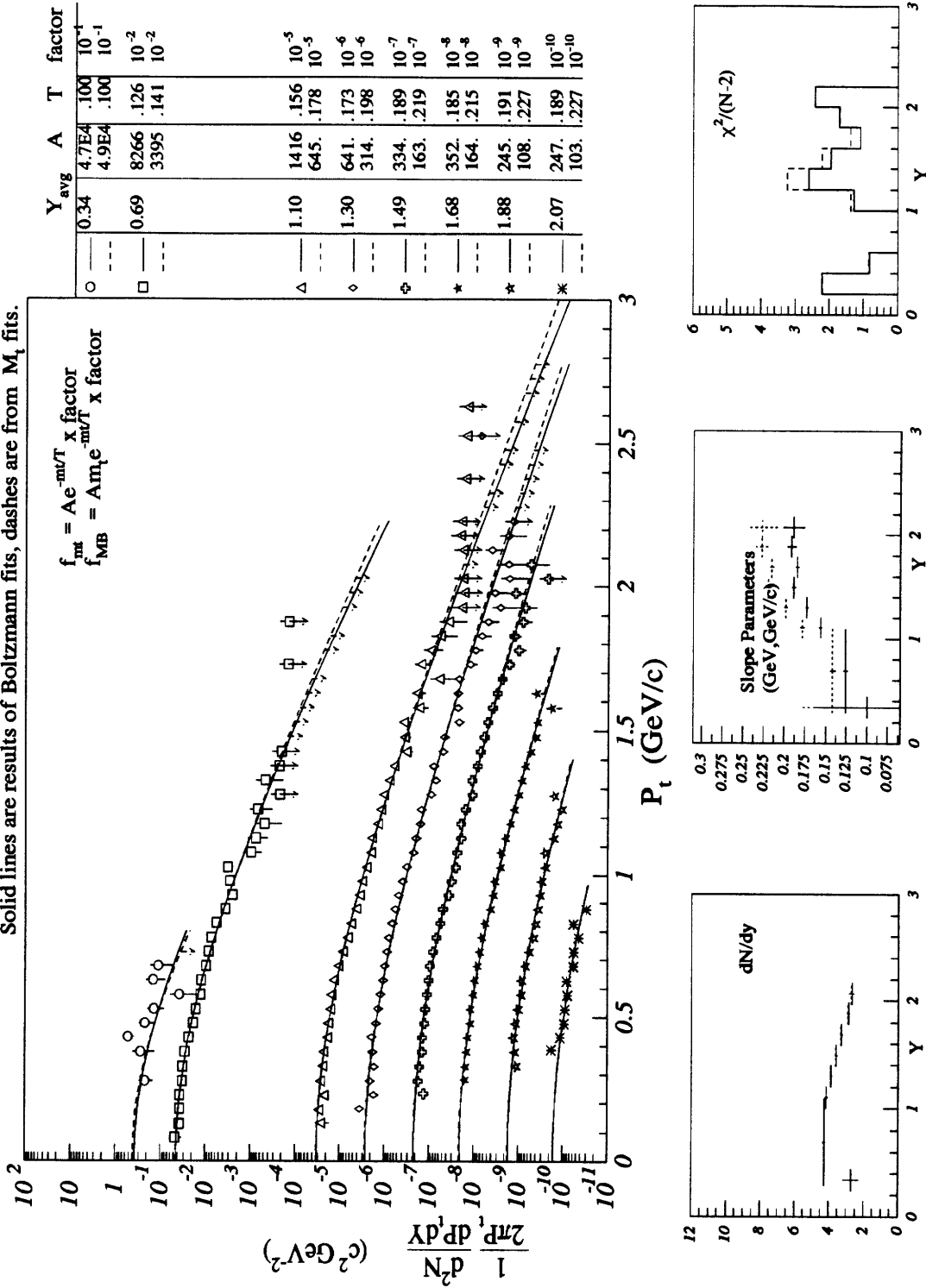
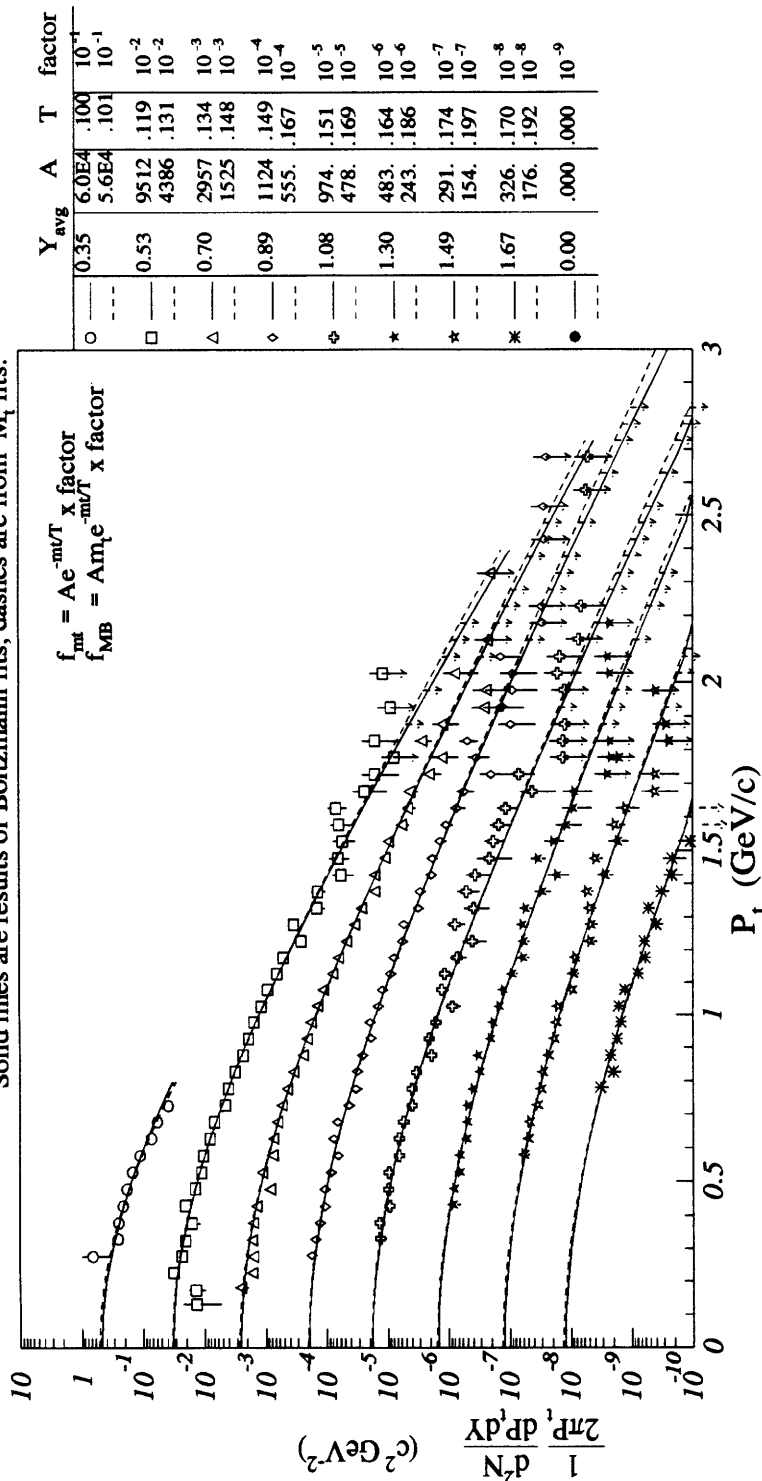


Figure G-2: Yield Summary for $^{16}\text{O} + ^{27}\text{Al TMA}$: Protons

$^{16}\text{O} + \text{Al}$ CENT2 : Yield Summary Protons

Solid lines are results of Boltzmann fits, dashes are from M_T fits.



Y _{avg}	A	T	factor
0.35	6.0E4	.100	10 ⁻¹
0.53	5.6E4	.101	10 ⁻¹
0.70	9512	.119	10 ⁻²
0.89	4386	.131	10 ⁻²
1.08	2957	.134	10 ⁻³
1.30	1525	.148	10 ⁻³
1.49	1124	.149	10 ⁻⁴
1.67	555	.167	10 ⁻⁴
1.70	974	.151	10 ⁻⁵
1.76	478	.169	10 ⁻⁵
1.86	483	.164	10 ⁻⁶
1.97	243	.186	10 ⁻⁶
2.00	291	.174	10 ⁻⁷
2.00	154	.197	10 ⁻⁷
2.00	326	.170	10 ⁻⁸
2.00	176	.192	10 ⁻⁸
2.00	.000	.000	10 ⁻⁹

$$f_{MB} = A e^{-m_T/T} \times \text{factor}$$

$$f_{fit} = A e^{-m_T/T} \times \text{factor}$$

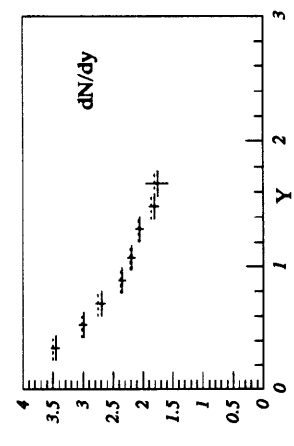
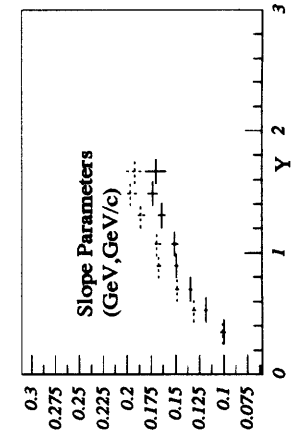
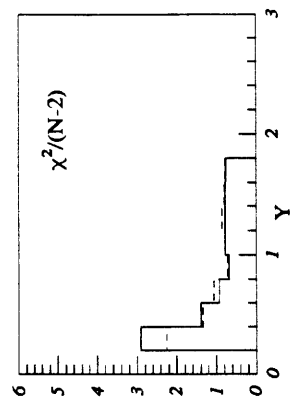


Figure G-3: Yield Summary for $^{16}\text{O} + ^{27}\text{Al}$ CENT2: Protons

$^{16}\text{O} + \text{Al MID}$: Yield Summary Protons

Solid lines are results of Boltzmann fits, dashes are from M_T fits.

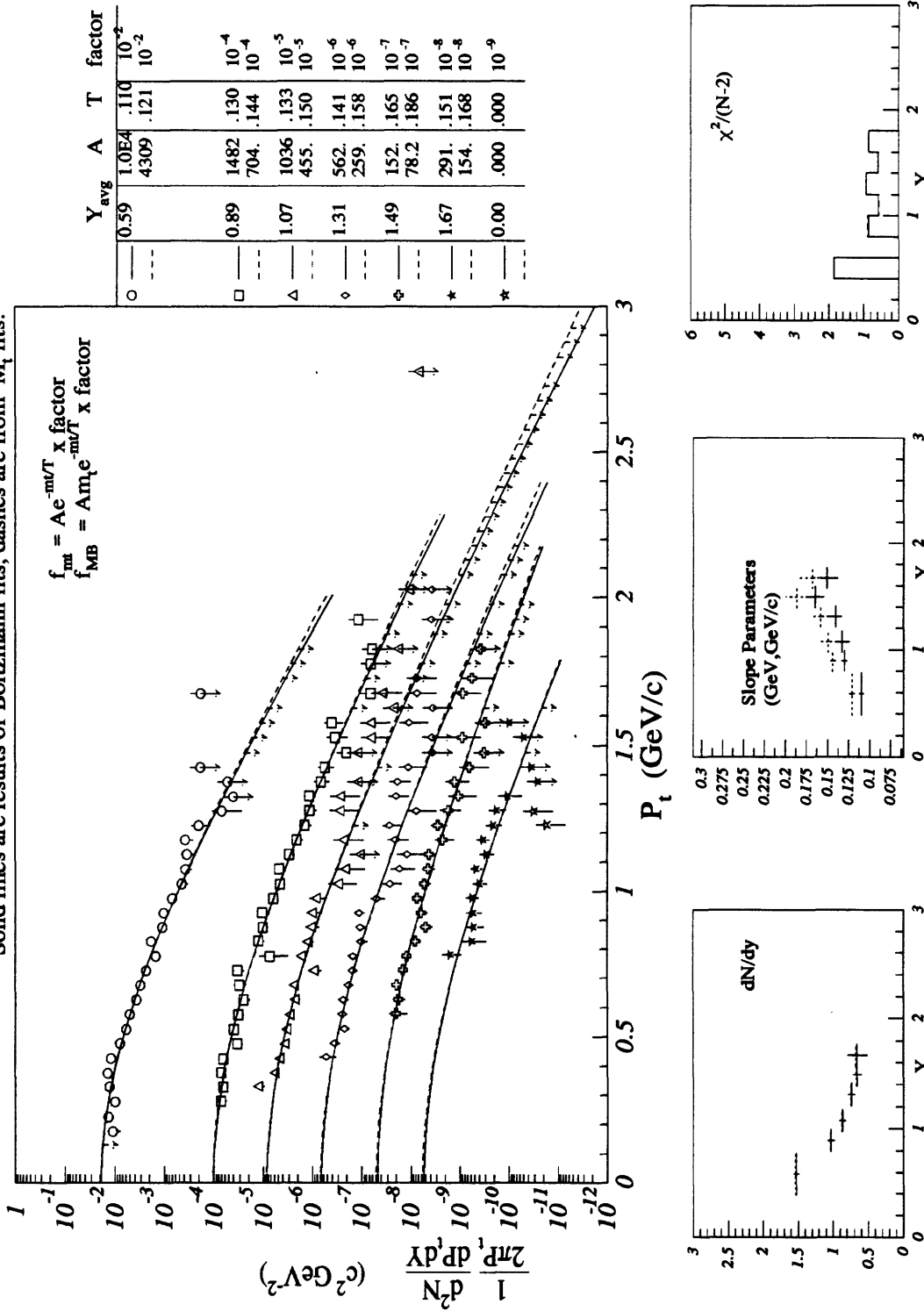


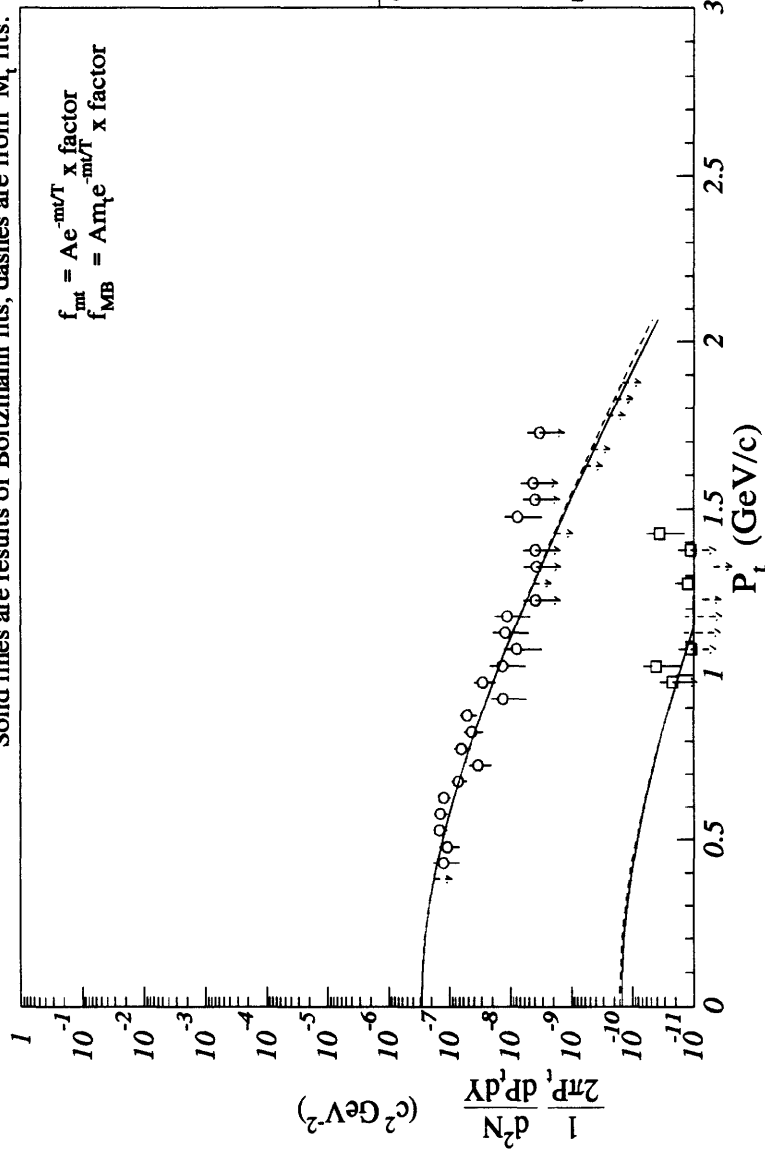
Figure G-4: Yield Summary for $^{16}\text{O} + ^{27}\text{Al}$ MID: Protons

¹⁶O + Al PERP1 : Yield Summary Protons

Solid lines are results of Boltzmann fits, dashes are from M_t fits.

$$f_{MB} = A m_t e^{-m_t/T} \times \text{factor}$$

$$f_{int} = A e^{-m_t/T} \times \text{factor}$$



Symbol	Y _{avg}	A	T factor
○	1.31	303	.136 10 ⁻⁶
---	---	136	.153 10 ⁻⁶
□	1.75	38.9	.171 10 ⁻⁹
---	---	20.8	.194 10 ⁻⁹

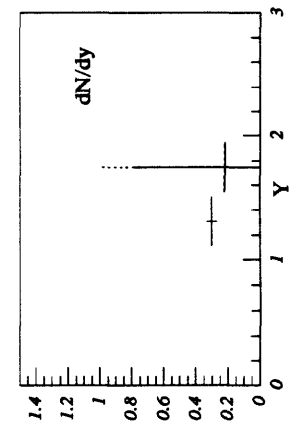
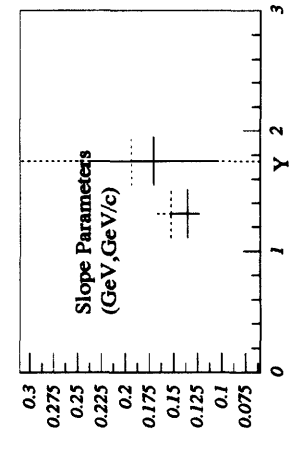
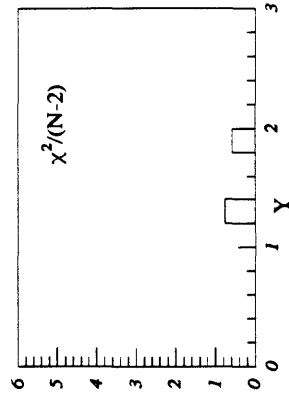


Figure G-5: Yield Summary for ¹⁶O + ²⁷Al PERP1: Protons

$^{16}\text{O} + \text{Cu}$ Inelastic Cross-Section Summary for Protons

Solid lines are results of Boltzmann fits, dashes are from M_t fits.

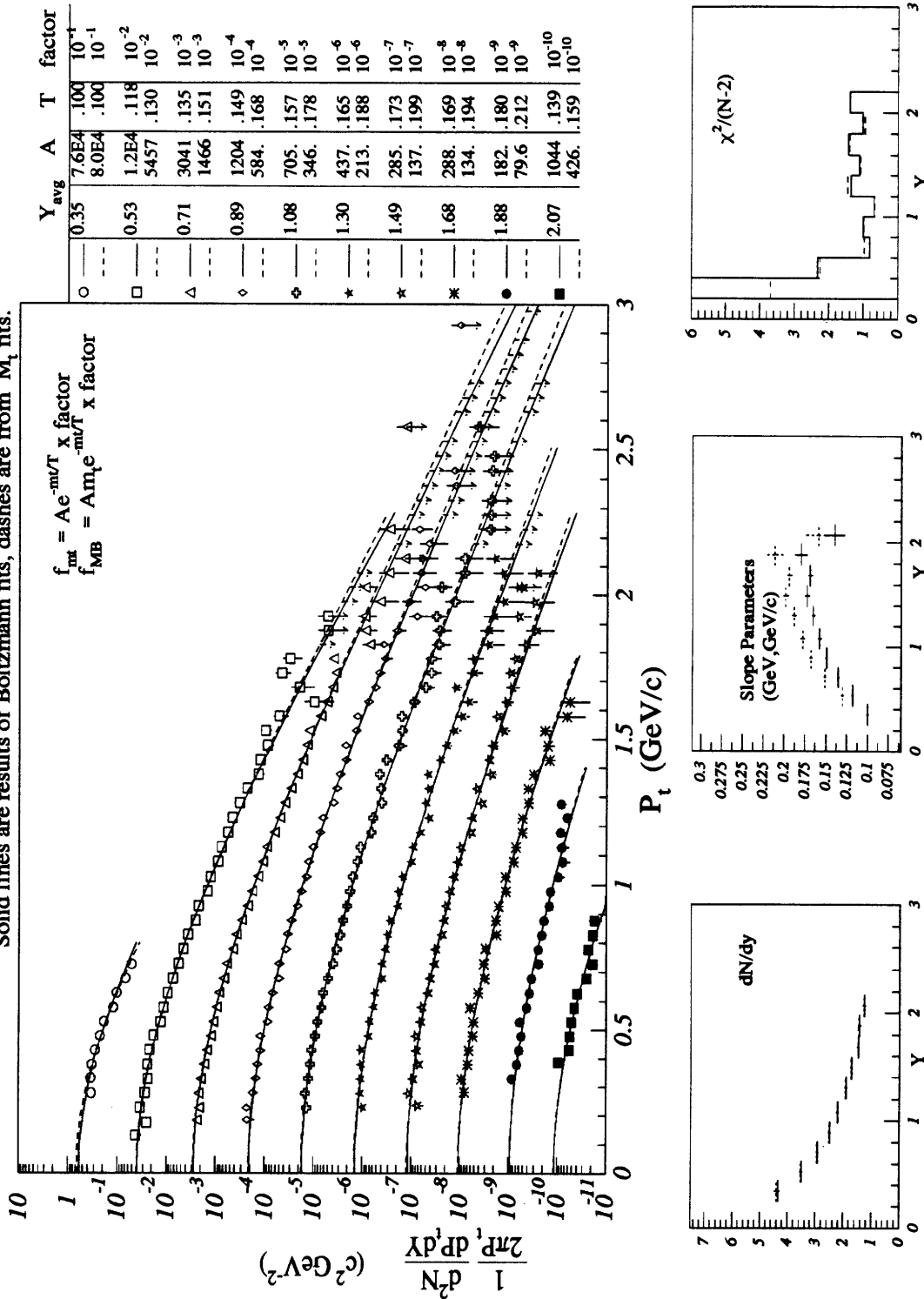
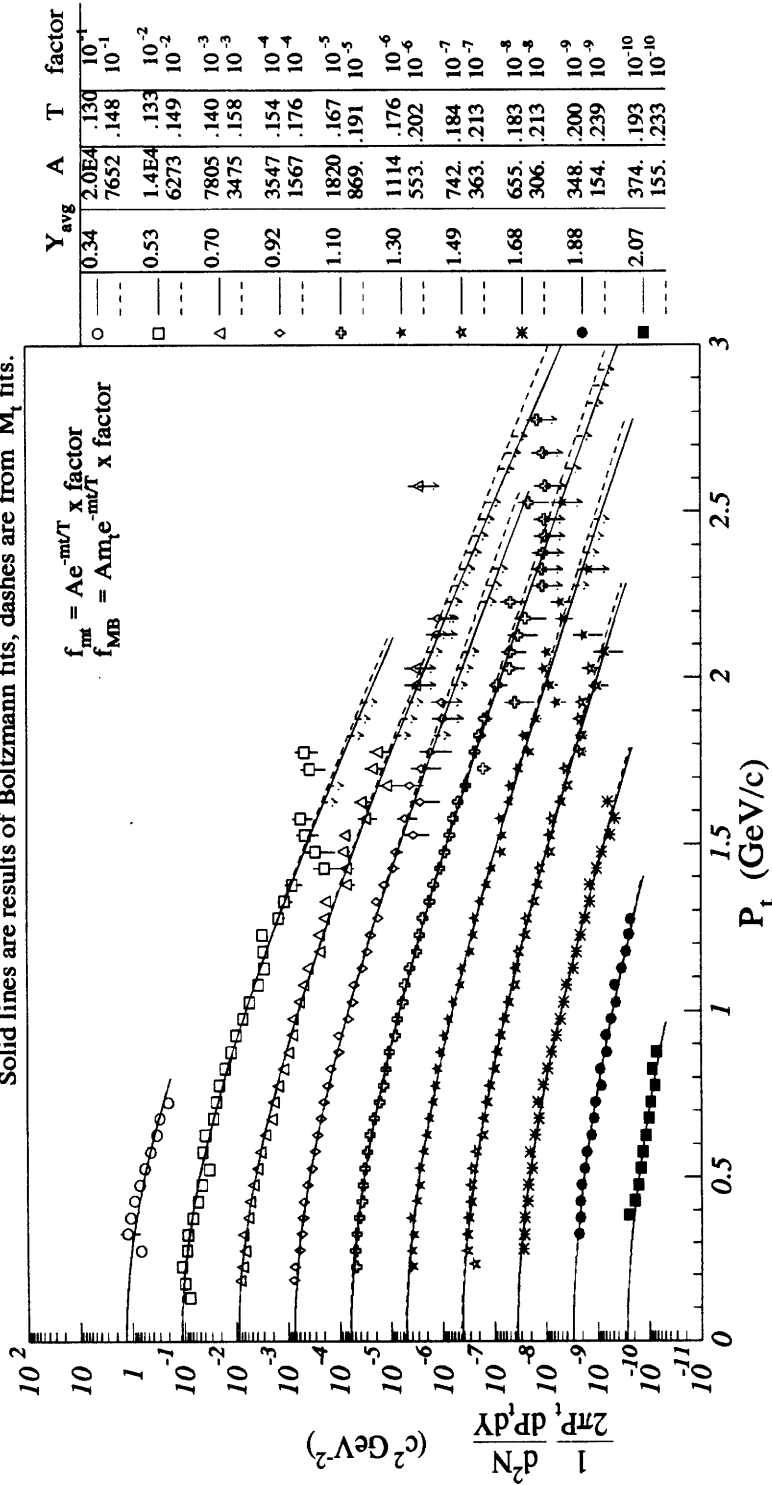


Figure G-6: Yield Summary for $^{16}\text{O} + ^{64}\text{Cu}$ INEL: Protons

$^{16}\text{O} + \text{Cu TMA}$: Yield Summary Protons

Solid lines are results of Boltzmann fits, dashes are from M_T fits.



Y	Y _{avg}	A	T	factor
0	0.34	2.0E4	.130	10 ⁻¹
	---	7652	.148	10 ⁻¹
1	0.53	1.4E4	.133	10 ⁻²
	---	6273	.149	10 ⁻²
2	0.70	7805	.140	10 ⁻³
	---	3475	.158	10 ⁻³
3	0.92	3547	.154	10 ⁻⁴
	---	1567	.176	10 ⁻⁴
4	1.10	1820	.167	10 ⁻⁵
	---	869.	.191	10 ⁻⁵
5	1.30	1114	.176	10 ⁻⁶
	---	553.	.202	10 ⁻⁶
6	1.49	742.	.184	10 ⁻⁷
	---	363.	.213	10 ⁻⁷
7	1.68	655.	.183	10 ⁻⁸
	---	306.	.213	10 ⁻⁸
8	1.88	348.	.200	10 ⁻⁹
	---	154.	.239	10 ⁻⁹
9	2.07	374.	.193	10 ⁻¹⁰
	---	155.	.233	10 ⁻¹⁰

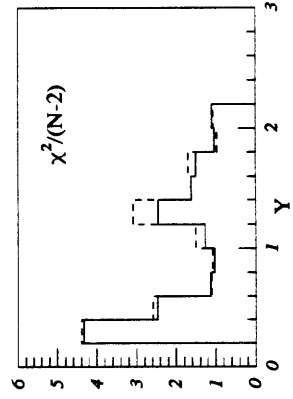
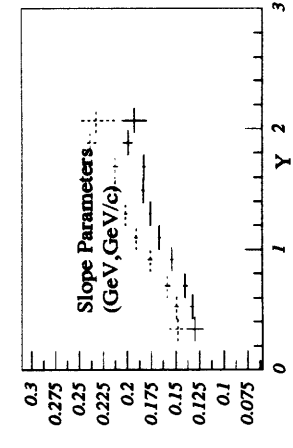
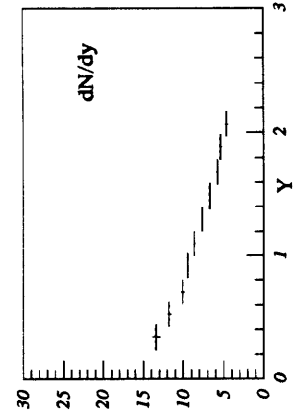


Figure G-7: Yield Summary for $^{16}\text{O} + ^{64}\text{Cu TMA}$: Protons

¹⁶O+Cu CENT1 : Yield Summary Protons

Solid lines are results of Boltzmann fits, dashes are from M_t fits.

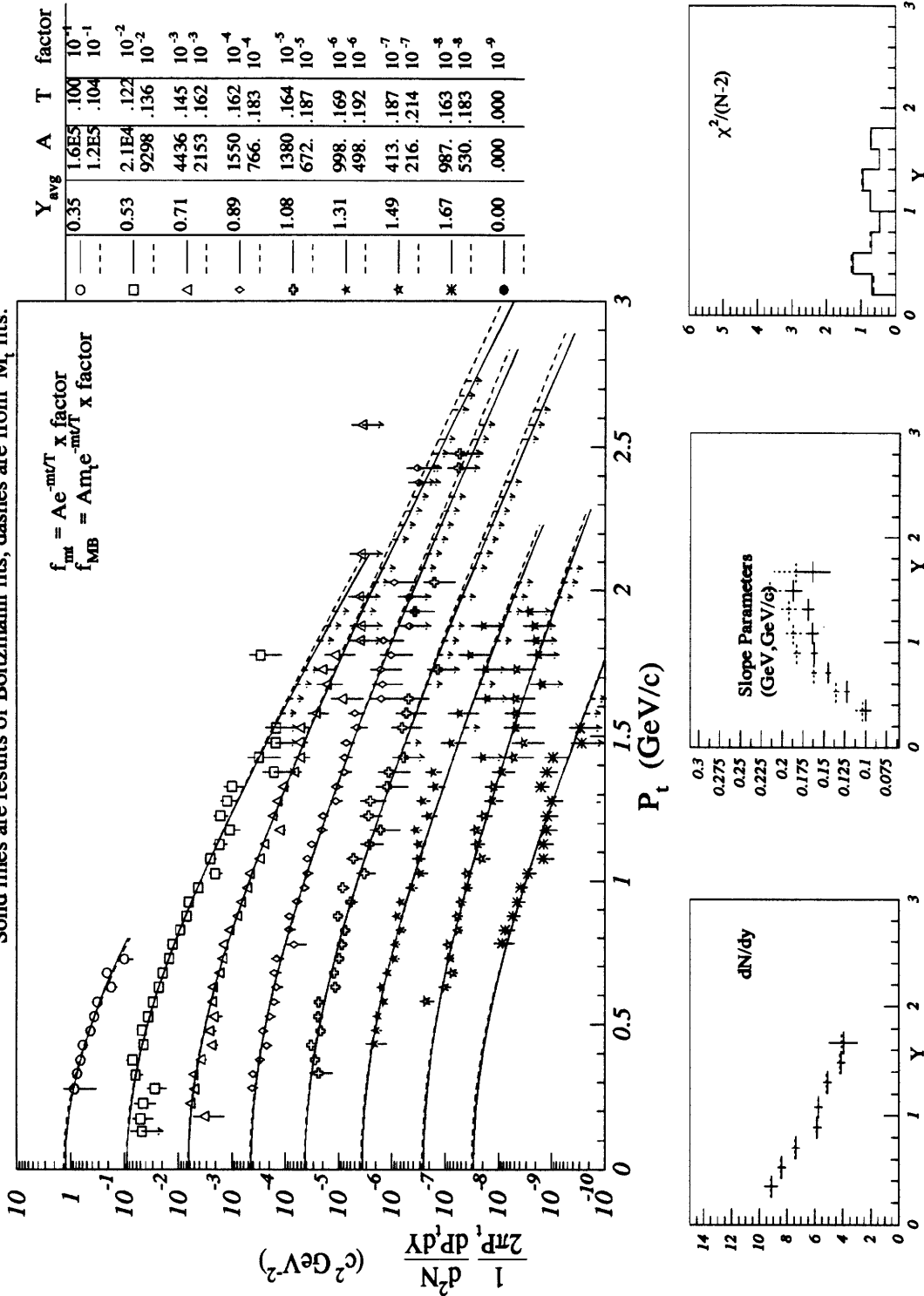
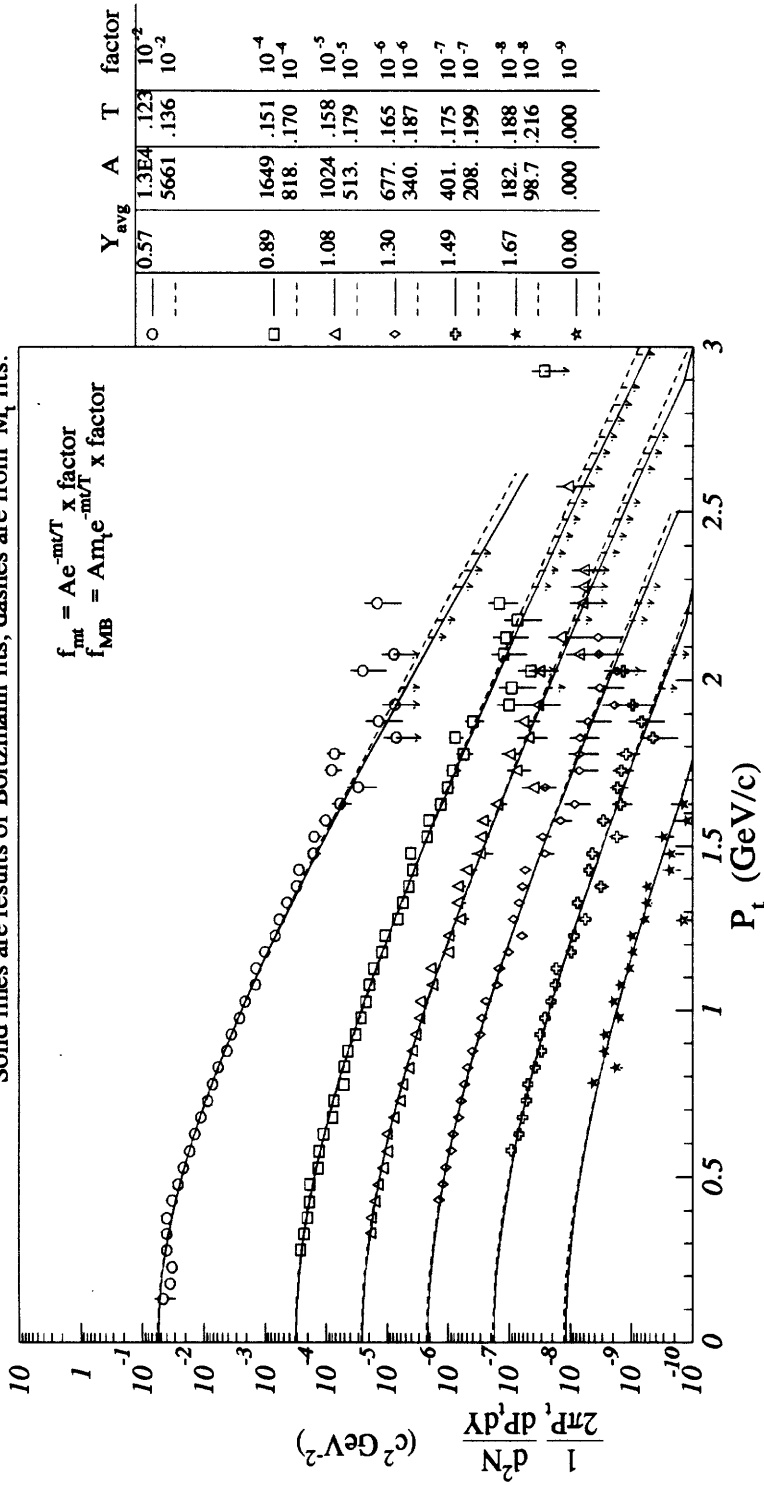


Figure G-8: Yield Summary for ¹⁶O + ⁶⁴Cu CENT1: Protons

¹⁶O+Cu CENT2: Yield Summary Protons

Solid lines are results of Boltzmann fits, dashes are from M_t fits.



$$f_{MB} = A e^{-m_T/T} \times \text{factor}$$

$$f_{MB} = A m_T e^{-m_T/T} \times \text{factor}$$

Y _{avg}	A	T	factor
0.57	1.3E4	.123	10 ⁻²
---	5661	.136	10 ⁻²
0.89	1649	.151	10 ⁻⁴
---	818	.170	10 ⁻⁴
1.08	1024	.158	10 ⁻⁵
---	513	.179	10 ⁻⁵
1.30	677	.165	10 ⁻⁶
---	340	.187	10 ⁻⁶
1.49	401	.175	10 ⁻⁷
---	208	.199	10 ⁻⁷
1.67	182	.188	10 ⁻⁸
---	98.7	.216	10 ⁻⁸
0.00	.000	.000	10 ⁻⁹

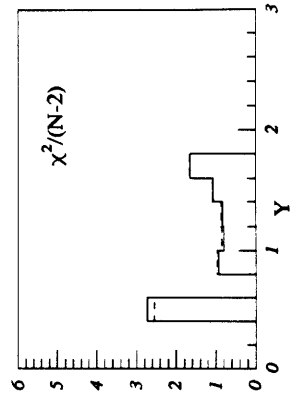
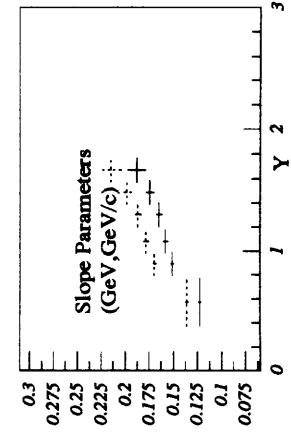
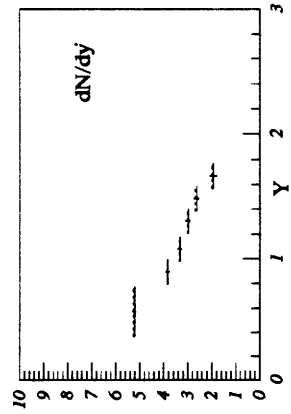
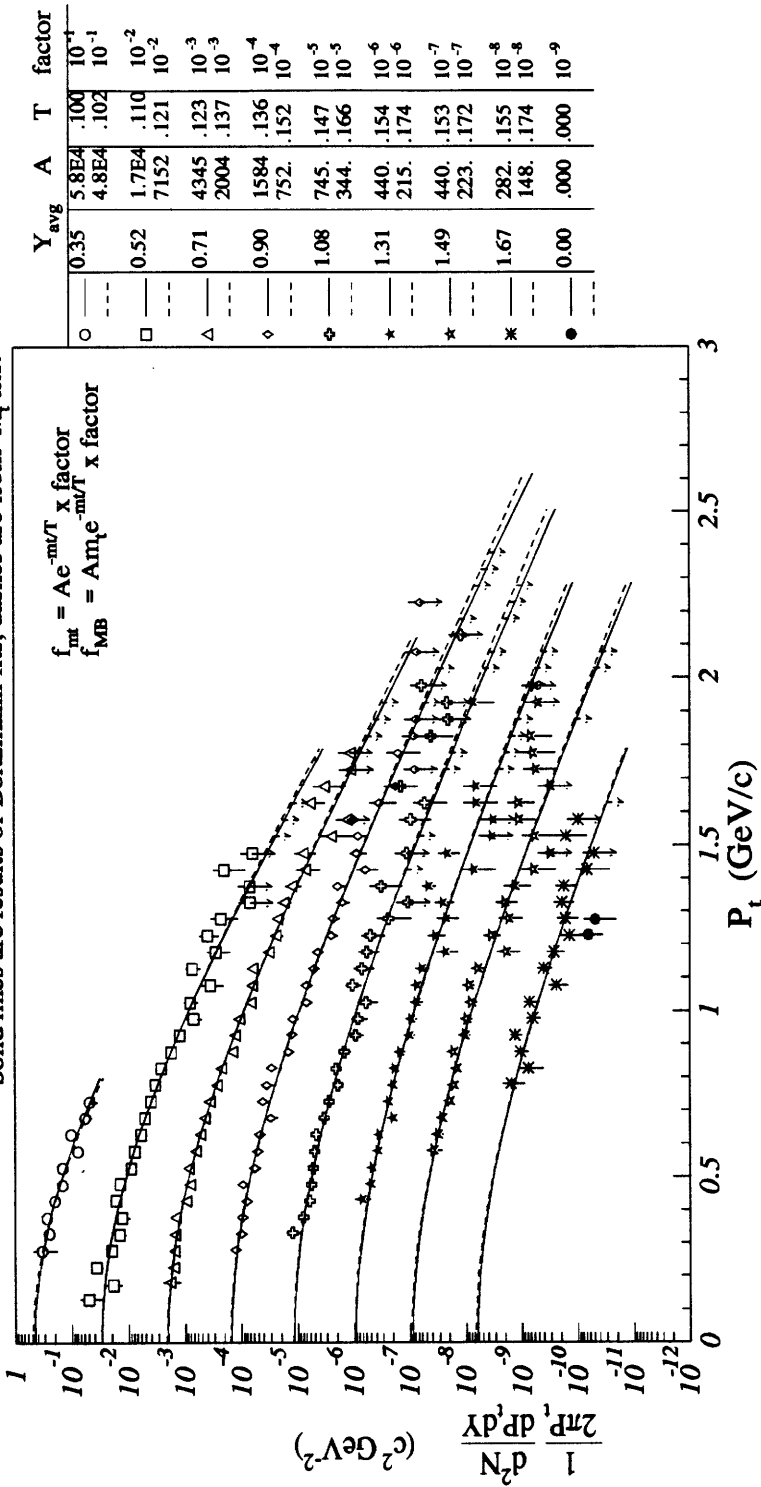


Figure G-9: Yield Summary for ¹⁶O + ⁶⁴Cu CENT2: Protons

¹⁶O+Cu MID : Yield Summary Protons

Solid lines are results of Boltzmann fits, dashes are from M_t fits.



Symbol	Y_{avg}	A	T	factor
○	0.35	5.8E4	.100	10^{-1}
□	0.52	4.8E4	.102	10^{-1}
△	0.71	1.7E4	.110	10^{-2}
◇	0.90	7152	.121	10^{-2}
◆	1.08	4345	.123	10^{-3}
◇	1.31	2004	.137	10^{-3}
◇	1.49	1584	.136	10^{-4}
◇	1.67	752	.152	10^{-4}
◇	1.85	745	.147	10^{-5}
◇	2.03	344	.166	10^{-5}
◇	2.21	440	.154	10^{-6}
◇	2.39	215	.174	10^{-6}
◇	2.57	440	.153	10^{-7}
◇	2.75	223	.172	10^{-7}
◇	2.93	282	.155	10^{-8}
◇	3.11	148	.174	10^{-8}
◇	3.29	.000	.000	10^{-9}

$$f_{MB} = A m_t e^{-m_t/T} \times \text{factor}$$

$$f_{fit} = A e^{-m_t/T} \times \text{factor}$$

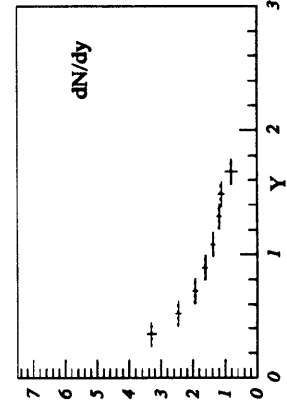
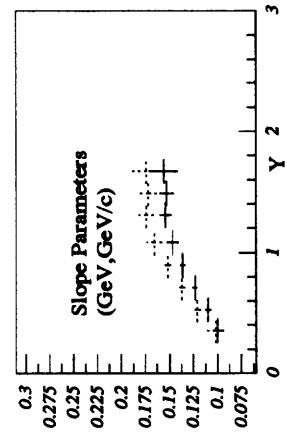
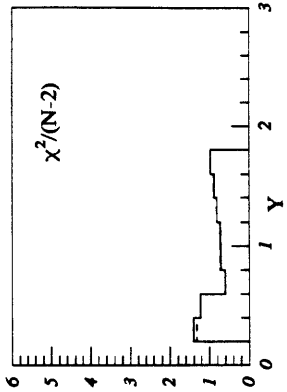


Figure G-10: Yield Summary for ¹⁶O + ⁶⁴Cu MID: Protons

$^{16}\text{O} + \text{Cu}$ PERP1 : Yield Summary Protons

Solid lines are results of Boltzmann fits, dashes are from M_t fits.

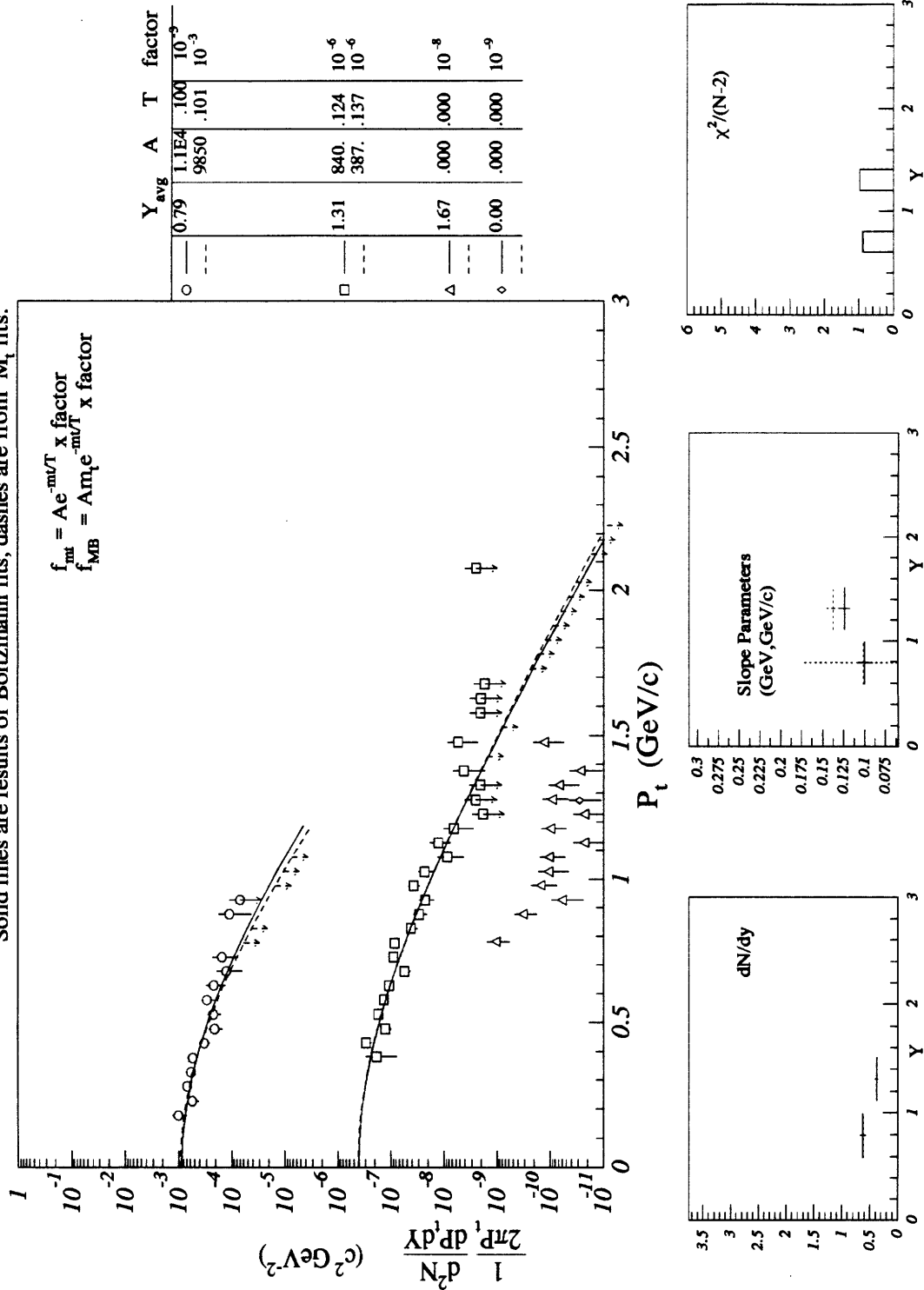
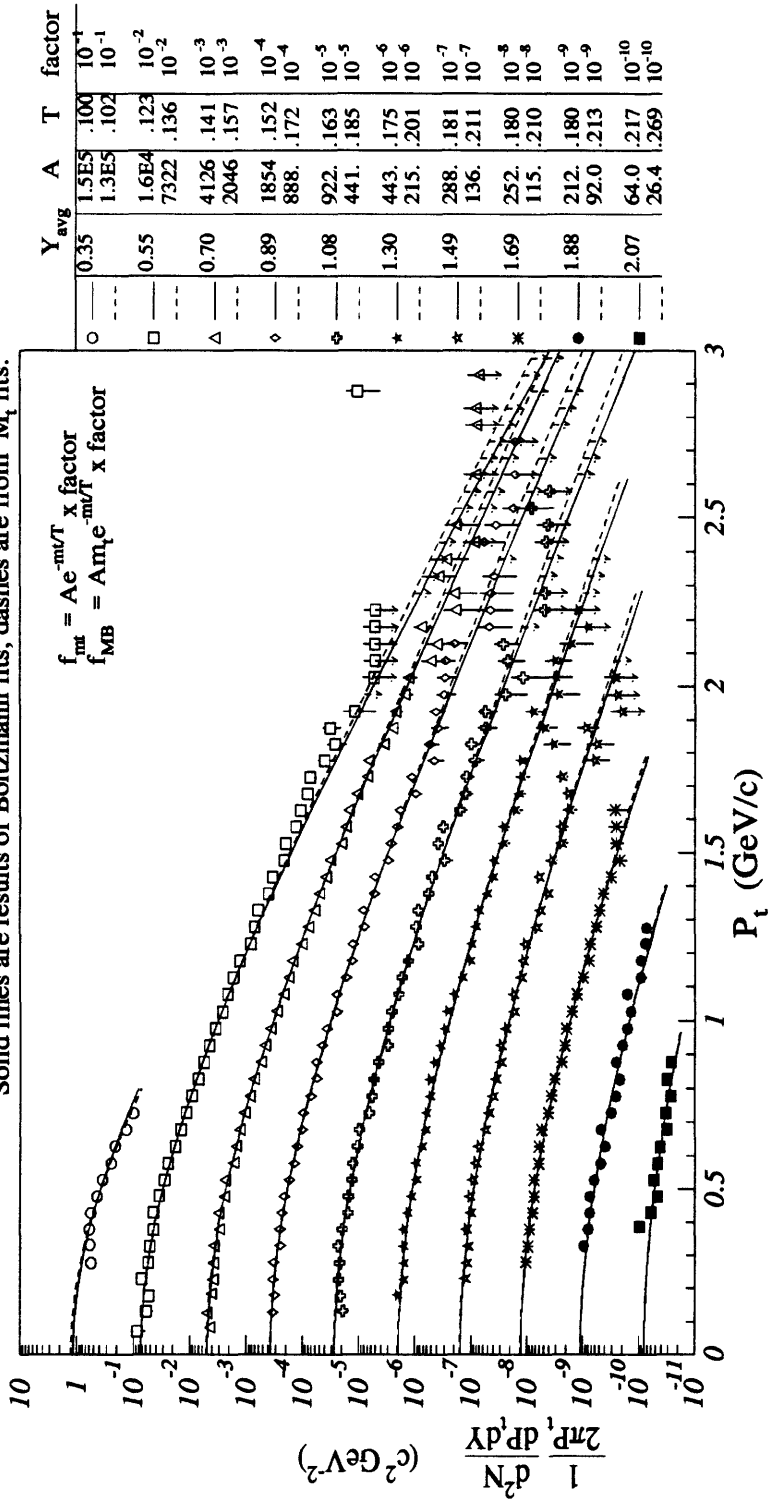


Figure G-11: Yield Summary for $^{16}\text{O} + ^{64}\text{Cu}$ PERP1: Protons

$^{16}\text{O} + \text{Au}$ Inelastic Cross-Section Summary for Protons

Solid lines are results of Boltzmann fits, dashes are from M_t fits.



Y avg	A	T	factor
0.35	1.5E5	.100	10^{-1}
0.55	1.3E5	.102	10^{-1}
0.70	1.6E4	.123	10^{-2}
0.89	7322	.136	10^{-2}
1.08	4126	.141	10^{-3}
1.30	2046	.157	10^{-3}
1.49	1854	.152	10^{-4}
1.69	888	.172	10^{-4}
1.88	922	.163	10^{-5}
2.07	441	.185	10^{-5}
	443	.175	10^{-6}
	215	.201	10^{-6}
	288	.181	10^{-7}
	136	.211	10^{-7}
	252	.180	10^{-8}
	115	.210	10^{-8}
	212	.180	10^{-9}
	92.0	.213	10^{-9}
	64.0	.217	10^{-10}
	26.4	.269	10^{-10}

$$\frac{f_{MB}}{f_{MT}} = A e^{-mT} \times \text{factor}$$

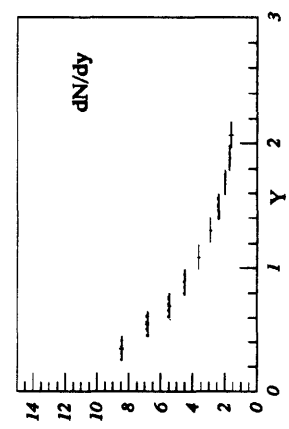
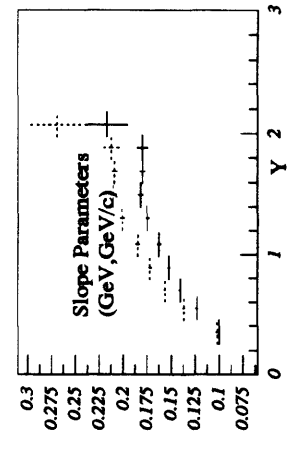
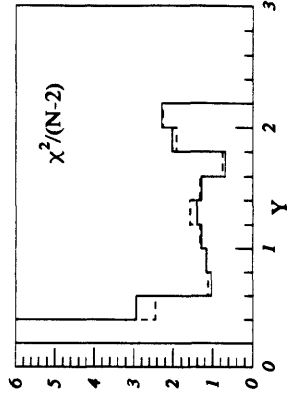
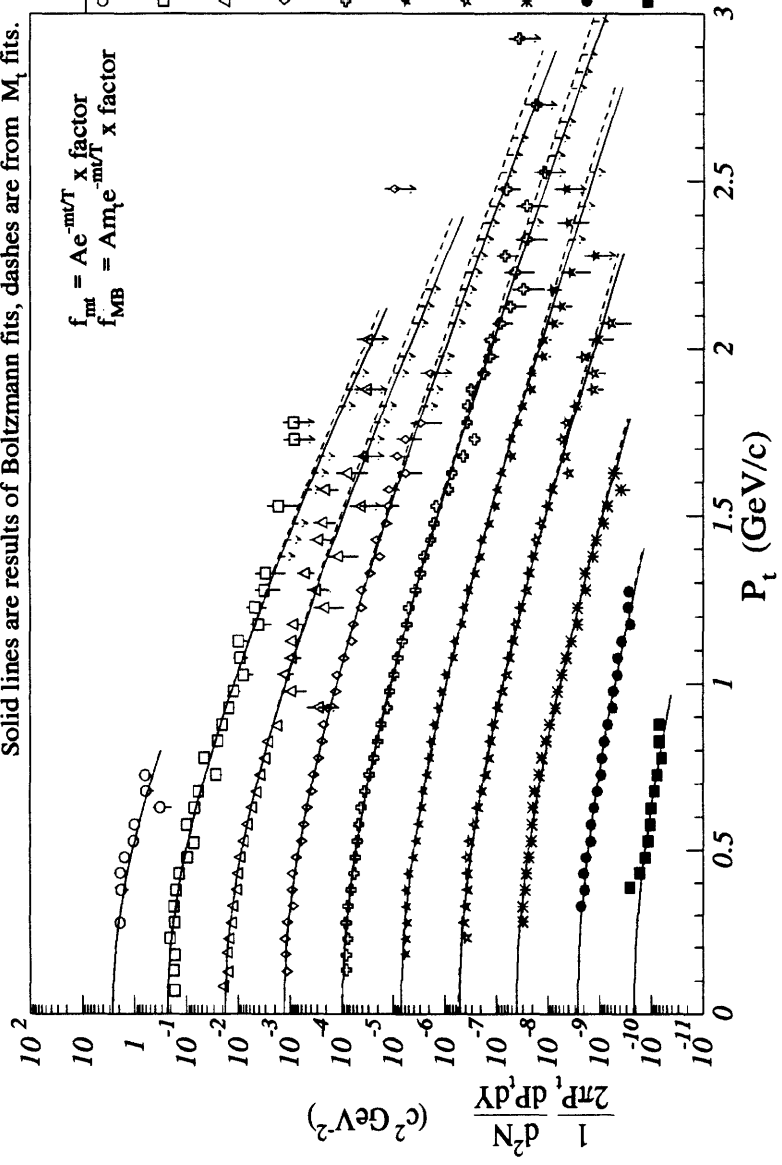


Figure G-12: Yield Summary for $^{16}\text{O} + ^{197}\text{Au}$ INEL: Protons

$^{16}\text{O} + \text{Au TMA}$: Yield Summary Protons

Solid lines are results of Boltzmann fits, dashes are from M_t fits.



Y	Y _{avg}	A	T	factor
○	0.34	5.9E4	.123	10 ⁻¹
□	0.53	2.3E4	.139	10 ⁻¹
△	0.70	3.5E4	.129	10 ⁻²
◇	0.91	1.5E4	.146	10 ⁻²
◇	0.70	1.5E4	.141	10 ⁻³
◇	0.91	6093	.161	10 ⁻³
◇	0.91	5267	.158	10 ⁻⁴
◇	0.91	2307	.182	10 ⁻⁴
◇	1.10	2541	.170	10 ⁻⁵
◇	1.10	1200	.195	10 ⁻⁵
◇	1.30	1301	.181	10 ⁻⁶
◇	1.30	638	.209	10 ⁻⁶
◇	1.49	896	.185	10 ⁻⁷
◇	1.49	425	.215	10 ⁻⁷
◇	1.69	673	.186	10 ⁻⁸
◇	1.69	311	.217	10 ⁻⁸
◇	1.88	239	.211	10 ⁻⁹
◇	1.88	105	.256	10 ⁻⁹
◇	2.07	251	.200	10 ⁻¹⁰
◇	2.07	104	.243	10 ⁻¹⁰

$$\frac{f_{\text{fit}}}{f_{\text{MB}}} = \frac{Ae^{-m_t/T}}{A_m e^{-m_t/T}} \times \text{factor}$$

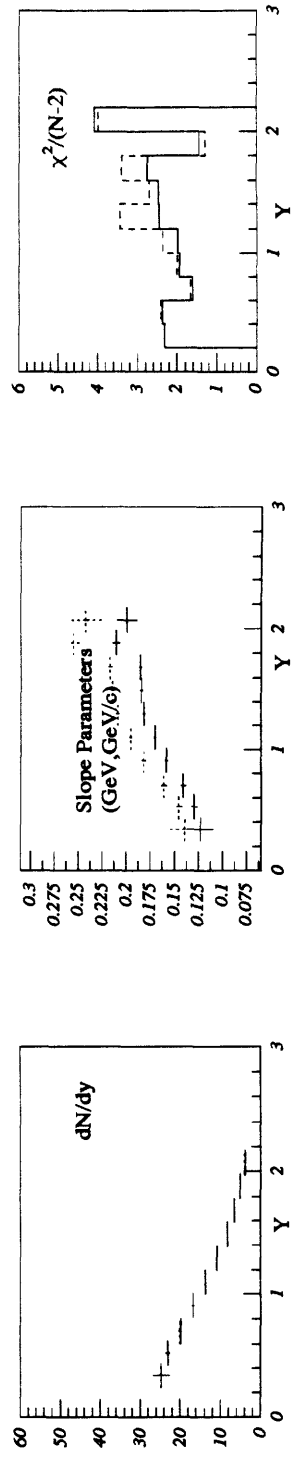


Figure G-13: Yield Summary for $^{16}\text{O} + ^{197}\text{Au TMA}$: Protons

¹⁶O+Au CENT1 : Yield Summary Protons

Solid lines are results of Boltzmann fits, dashes are from M₁ fits.

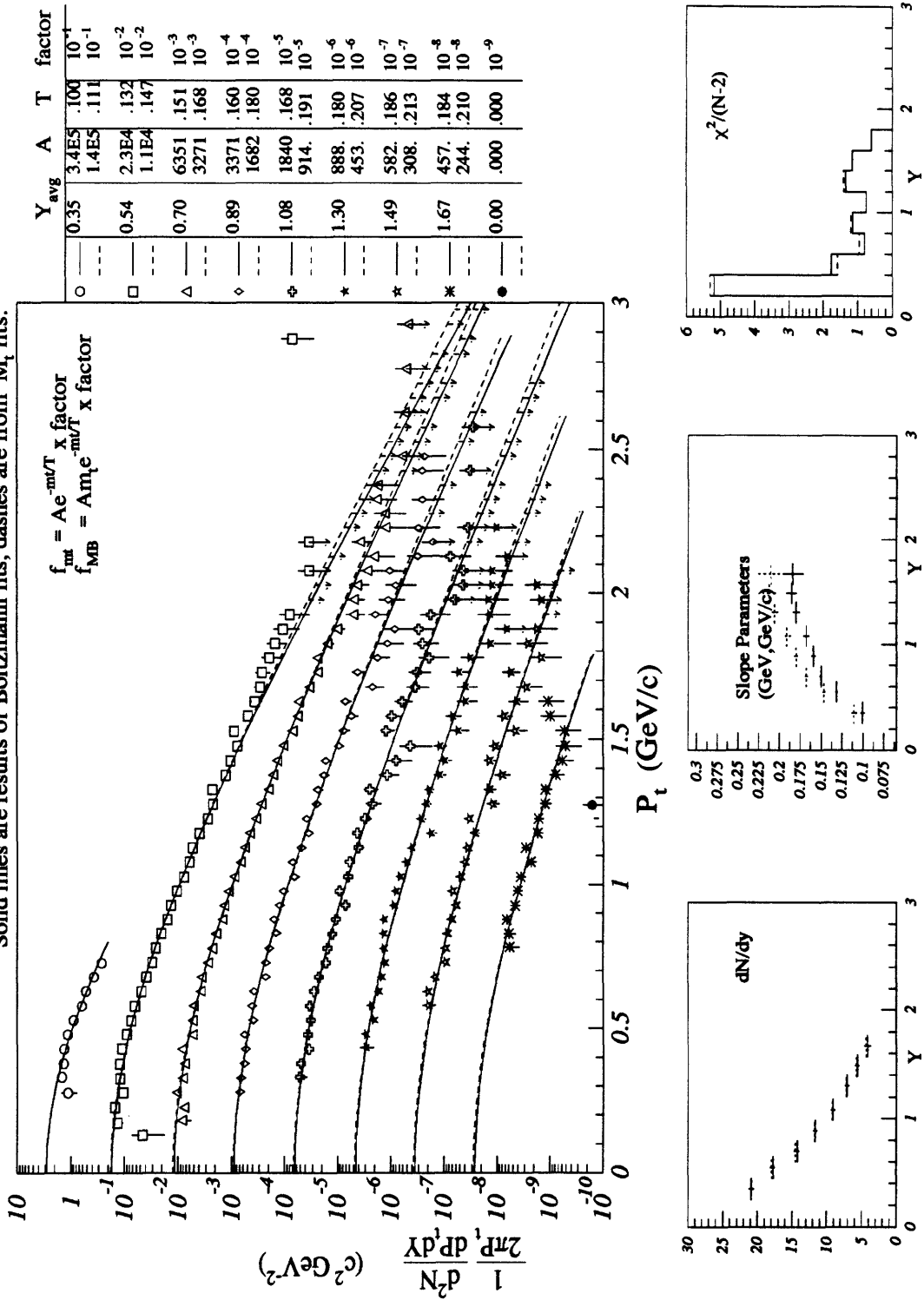
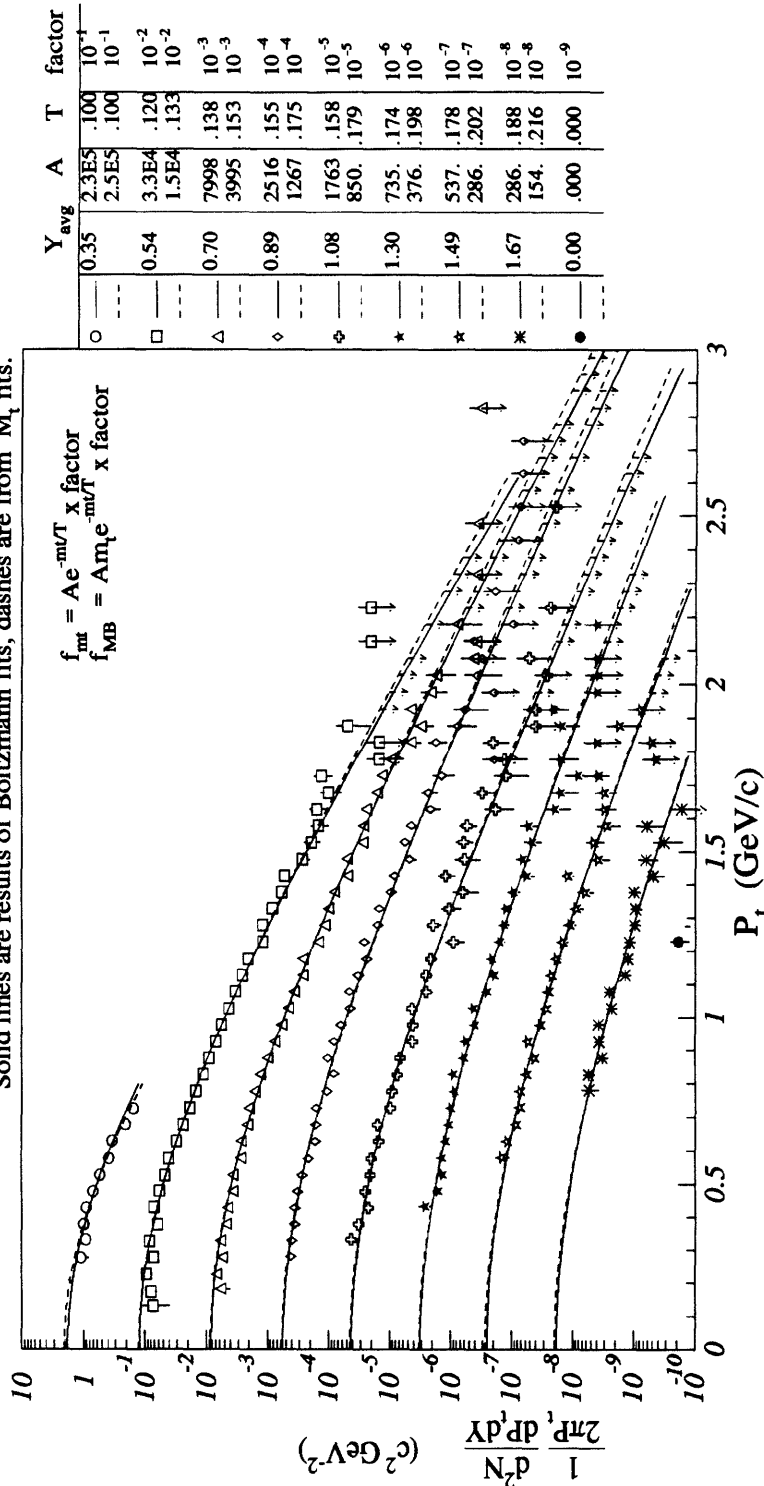


Figure G-14: Yield Summary for ¹⁶O + ¹⁹⁷Au CENT1: Protons

$^{16}\text{O} + \text{Au CENT2}$: Yield Summary Protons

Solid lines are results of Boltzmann fits, dashes are from M_t fits.



Y	Y _{avg}	A	T	factor
0	0.35	2.3E5	.100	10 ⁻¹
1	0.54	2.5E5	.100	10 ⁻¹
2	0.70	3.3E4	.120	10 ⁻²
3	0.89	1.5E4	.133	10 ⁻²
0	0.70	7998	.138	10 ⁻³
1	0.89	3995	.153	10 ⁻³
2	1.08	2516	.155	10 ⁻⁴
3	1.30	1267	.175	10 ⁻⁴
0	1.08	1763	.158	10 ⁻⁵
1	1.30	850	.179	10 ⁻⁵
2	1.49	735	.174	10 ⁻⁶
3	1.67	376	.198	10 ⁻⁶
0	1.49	537	.178	10 ⁻⁷
1	1.67	286	.202	10 ⁻⁷
2	0.00	286	.188	10 ⁻⁸
3	0.00	154	.216	10 ⁻⁸
0	0.00	.000	.000	10 ⁻⁹

$$f_{mt} = A e^{-m_t/T} \times \text{factor}$$

$$f_{MB} = A m_t e^{-m_t/T} \times \text{factor}$$

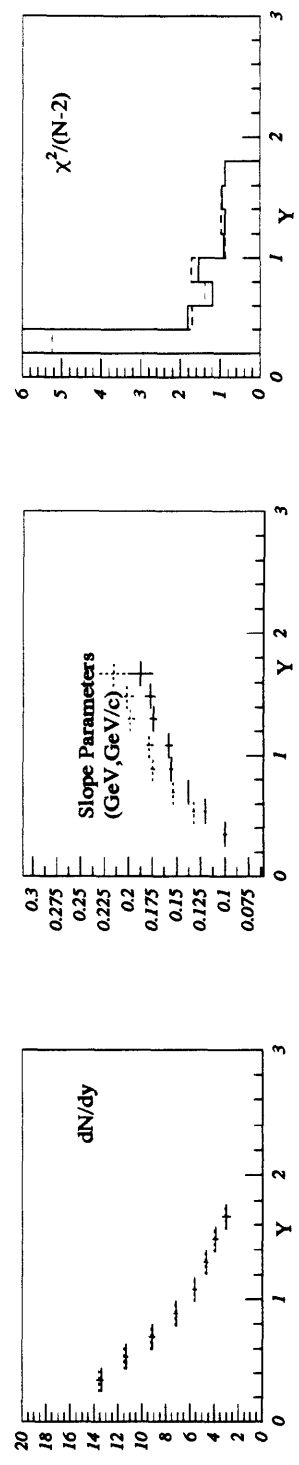
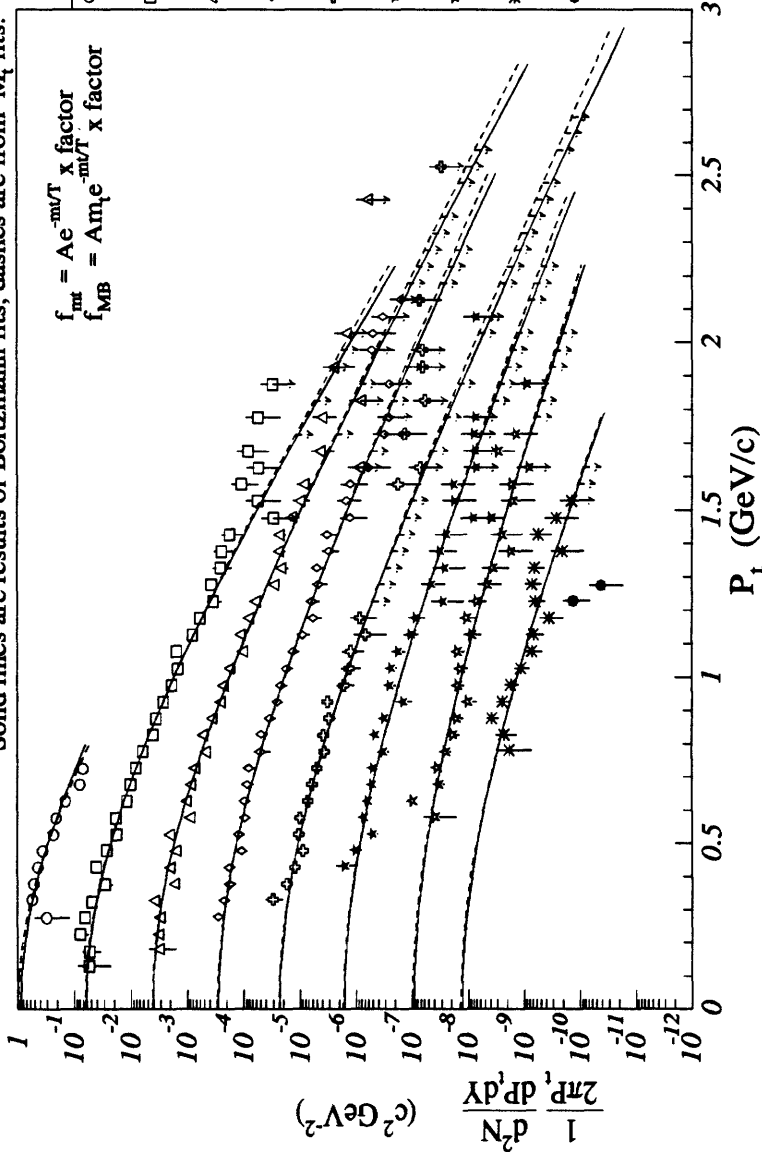


Figure G-15: Yield Summary for $^{16}\text{O} + ^{197}\text{Au CENT2}$: Protons

$^{16}\text{O} + \text{Au}$ MID : Yield Summary Protons

Solid lines are results of Boltzmann fits, dashes are from M_t fits.



Y	A	T	factor
○	0.35	1.1E5	.100
□	0.53	1.2E5	.100
△	0.70	3.7E4	.109
◇	0.89	1.7E4	.119
◇	1.08	8471	.124
◇	1.31	4146	.136
◇	1.49	2526	.139
◇	1.67	1198	.156
◇	0.00	2009	.140
◇	0.00	913	.157
◇	0.00	605	.160
◇	0.00	297	.182
◇	0.00	157	.185
◇	0.00	82.7	.212
◇	0.00	420	.164
◇	0.00	221	.185
◇	0.00	.000	.000
◇	0.00	.000	10 ⁻¹
◇	0.00	.000	10 ⁻²
◇	0.00	.000	10 ⁻³
◇	0.00	.000	10 ⁻⁴
◇	0.00	.000	10 ⁻⁵
◇	0.00	.000	10 ⁻⁶
◇	0.00	.000	10 ⁻⁷
◇	0.00	.000	10 ⁻⁸
◇	0.00	.000	10 ⁻⁹

$$f_{MB} = A e^{-m_t/T} \times \text{factor}$$

$$f_{MB} = A m_t e^{-m_t/T} \times \text{factor}$$

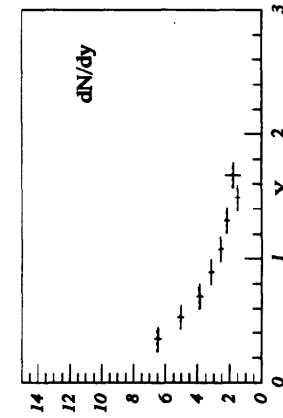
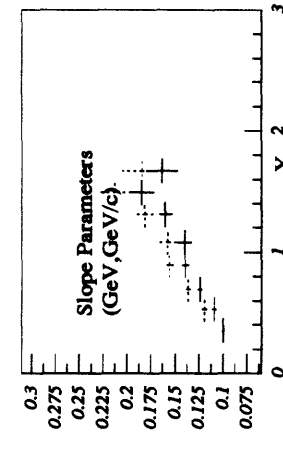
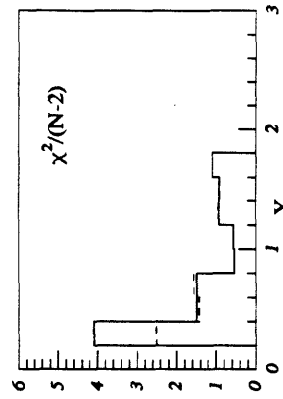
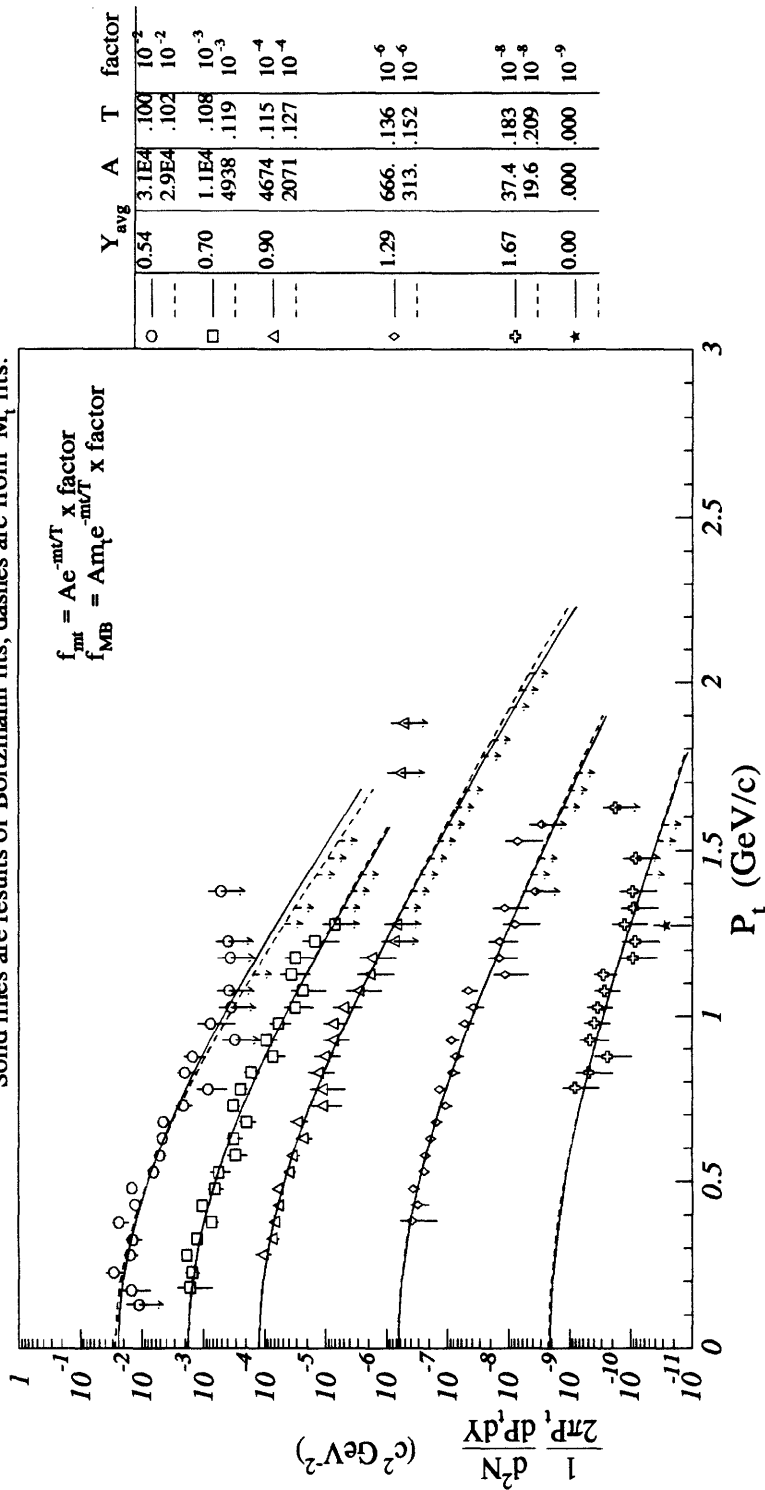


Figure G-16: Yield Summary for $^{16}\text{O} + ^{197}\text{Au}$ MID: Protons

¹⁶O+Au PERP1 : Yield Summary Protons

Solid lines are results of Boltzmann fits, dashes are from M_T fits.



$$f_{MB} = A e^{-m_T/T} \times \text{factor}$$

$$f_{int} = A e^{-m_T/T} \times \text{factor}$$

Centrality	Y _{avg}	A	T	factor
0	0.54	3.1E4	.100	10 ⁻²
1	0.70	2.9E4	.102	10 ⁻²
2	0.90	1.1E4	.108	10 ⁻³
3	1.29	4938	.119	10 ⁻³
4	1.67	4674	.115	10 ⁻⁴
5	0.00	2071	.127	10 ⁻⁴
6	0.00	666	.136	10 ⁻⁶
7	0.00	313	.152	10 ⁻⁶
8	0.00	37.4	.183	10 ⁻⁸
9	0.00	19.6	.209	10 ⁻⁸
10	0.00	.000	.000	10 ⁻⁹

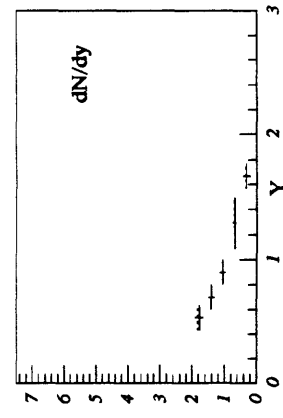
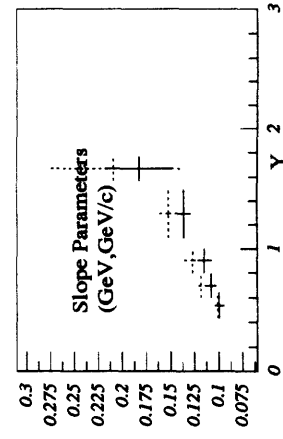
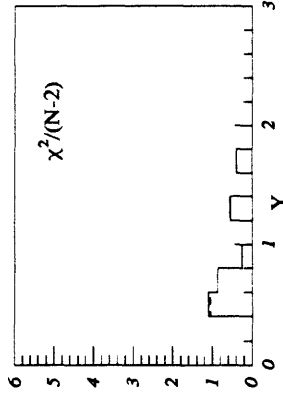


Figure G-17: Yield Summary for ¹⁶O + ¹⁹⁷Au PERP1: Protons

Appendix H

Yield Summary: $^{28}\text{Si} + ^{27}\text{Al} : \pi$

²⁸Si+Al CENT1 : Yield Summary π^+

Solid lines are results of P_t fits, dashes are from M_t fits.

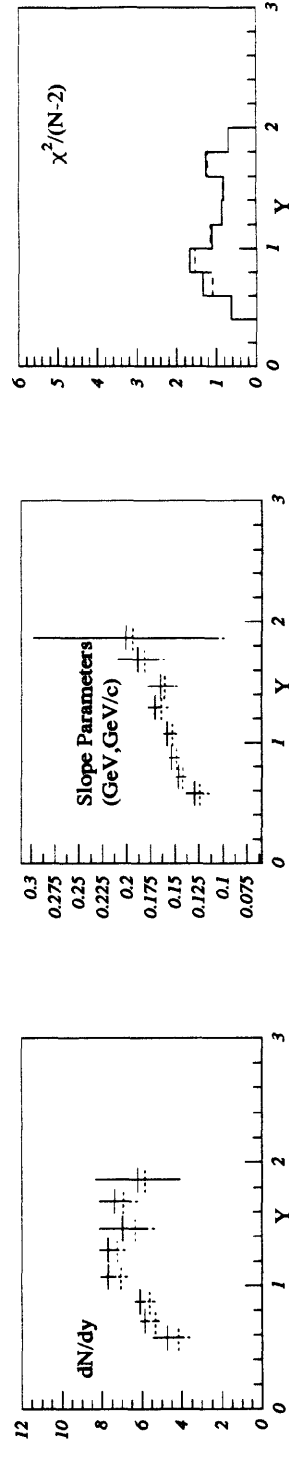
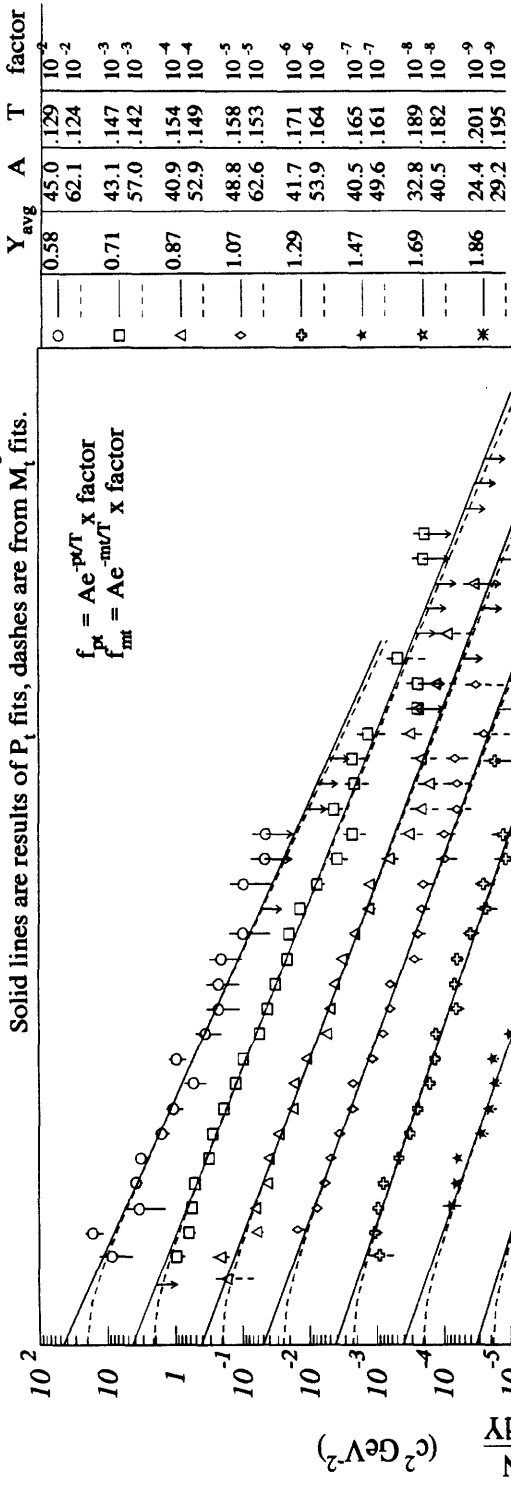
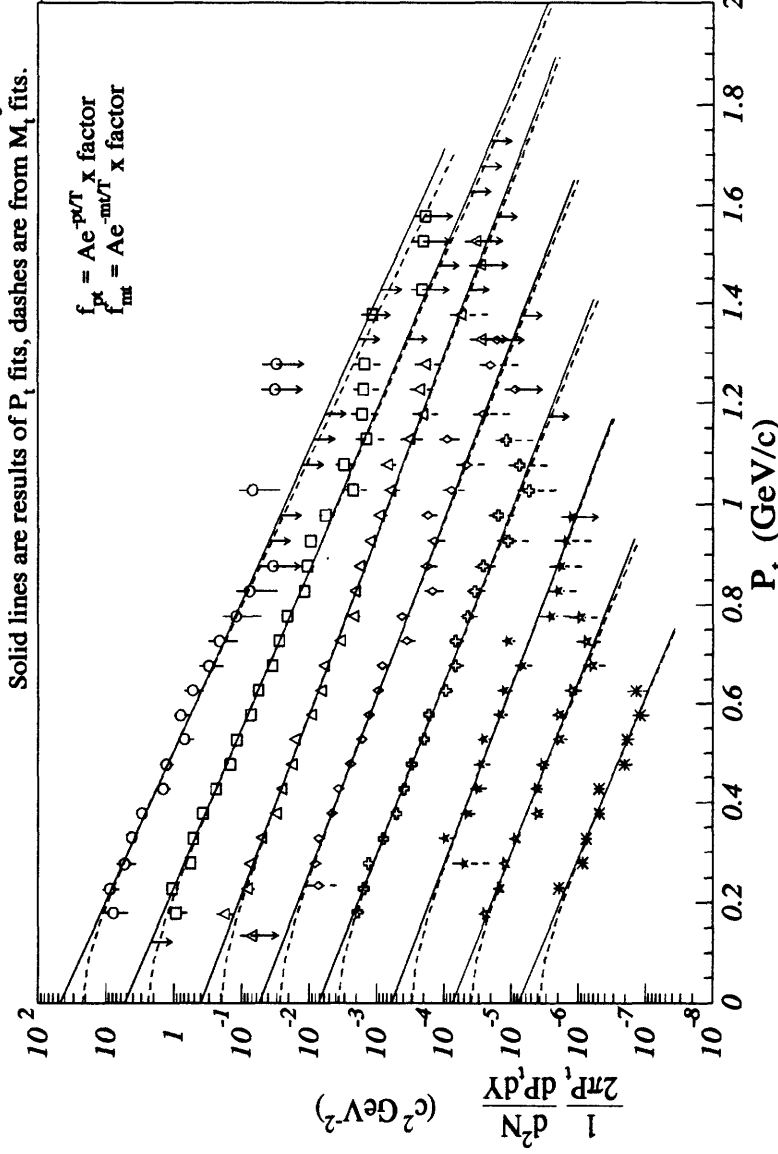


Figure H-1: Yield Summary for ²⁸Si + ²⁷Al CENT1: π^+

$^{28}\text{Si} + \text{Al}$ CENT1 : Yield Summary π^-

Solid lines are results of P_t fits, dashes are from M_t fits.

Symbol	Y_{avg}	A	T	factor
○	0.58	45.8	.131	10^{-2}
□	0.71	67.2	.124	10^{-2}
△	0.87	51.7	.139	10^{-3}
◇	0.87	66.1	.135	10^{-3}
◇	1.07	39.4	.157	10^{-4}
◇	1.07	49.5	.152	10^{-4}
◇	1.29	53.4	.154	10^{-5}
◇	1.29	68.6	.149	10^{-5}
◇	1.48	71.3	.150	10^{-6}
◇	1.48	95.7	.144	10^{-6}
*	1.70	59.6	.155	10^{-7}
*	1.70	74.9	.150	10^{-7}
*	1.88	72.1	.150	10^{-8}
*	1.88	106.	.140	10^{-8}
*	1.88	76.3	.141	10^{-9}
*	1.88	106.	.134	10^{-9}



$$f_{\text{pr}} = A e^{-pT} \times \text{factor}$$

$$f_{\text{mt}} = A e^{-mT} \times \text{factor}$$

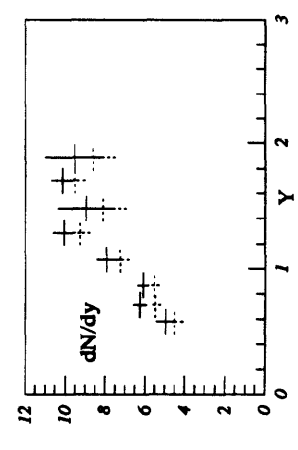
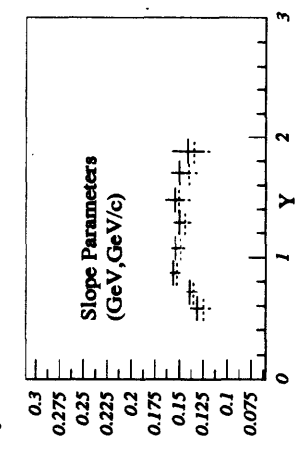
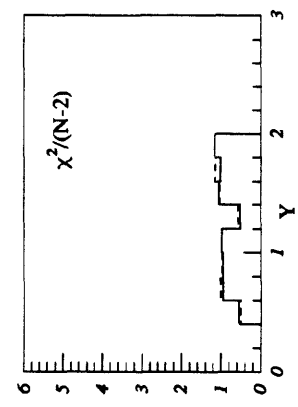
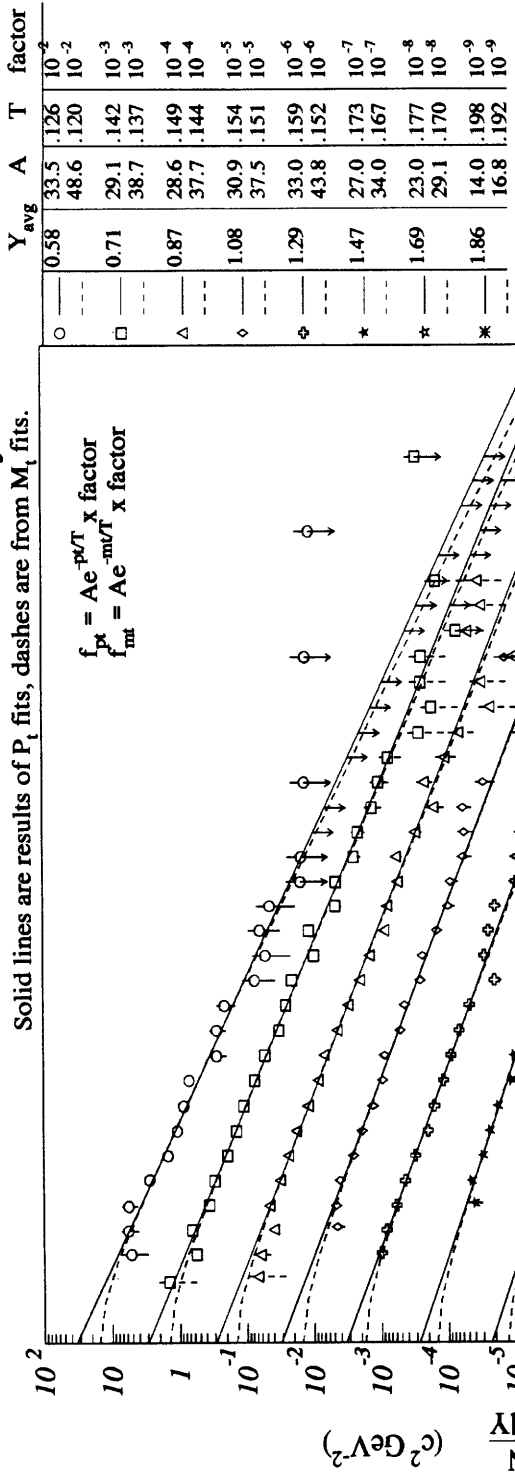


Figure H-2: Yield Summary for $^{28}\text{Si} + ^{27}\text{Al}$ CENT1: π^-

²⁸Si+Al CENT2 : Yield Summary π^+

Solid lines are results of P_t fits, dashes are from M_t fits.



$$f_{pt} = A e^{-p_t/T} \times \text{x factor}$$

$$f_{mt} = A e^{-m_t/T} \times \text{x factor}$$

Yield	Y_{avg}	A	T	factor
○	0.58	33.5	.126	10^{-2}
□	0.71	48.6	.120	10^{-2}
△	0.87	29.1	.142	10^{-3}
◇	1.08	38.7	.137	10^{-3}
◇	1.29	28.6	.149	10^{-4}
◇	1.47	37.7	.144	10^{-4}
◇	1.69	30.9	.154	10^{-5}
◇	1.86	37.5	.151	10^{-5}
◇	1.86	33.0	.159	10^{-6}
◇	1.86	43.8	.152	10^{-6}
◇	1.86	27.0	.173	10^{-7}
◇	1.86	34.0	.167	10^{-7}
◇	1.86	23.0	.177	10^{-8}
◇	1.86	29.1	.170	10^{-8}
◇	1.86	14.0	.198	10^{-9}
◇	1.86	16.8	.192	10^{-9}

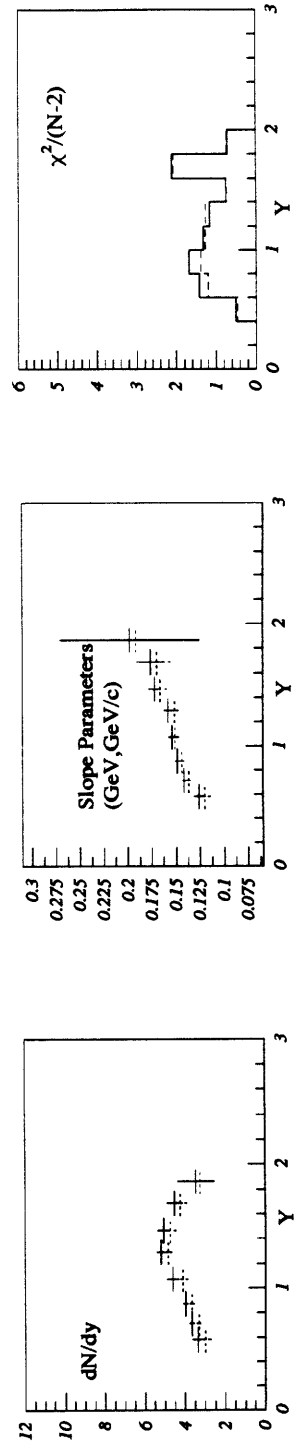
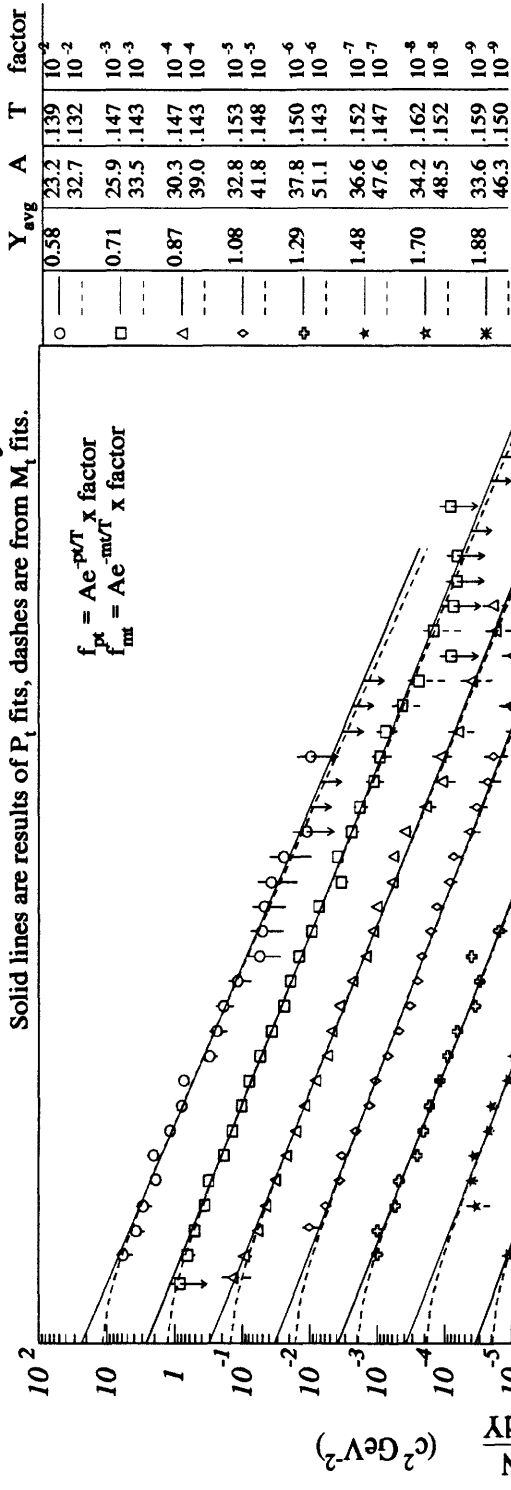


Figure H-3: Yield Summary for ²⁸Si + ²⁷Al CENT2: π^+

²⁸Si+Al CENT2 : Yield Summary π^-

Solid lines are results of P_t fits, dashes are from M_t fits.



$$f_{\pi^-} = A e^{-pT} \times \text{factor}$$

$$f_{\text{mt}} = A e^{-mT} \times \text{factor}$$

Symbol	Y _{avg}	A	T	factor
○	0.58	23.2	.139	10 ⁻²
□	0.71	32.7	.132	10 ⁻²
△	0.87	25.9	.147	10 ⁻³
◇	1.08	33.5	.143	10 ⁻³
☆	1.29	30.3	.147	10 ⁻⁴
☆	1.48	39.0	.143	10 ⁻⁴
☆	1.70	32.8	.153	10 ⁻⁵
☆	1.88	41.8	.148	10 ⁻⁵
☆	1.88	37.8	.150	10 ⁻⁶
☆	1.88	51.1	.143	10 ⁻⁶
☆	1.88	36.6	.152	10 ⁻⁷
☆	1.88	47.6	.147	10 ⁻⁷
☆	1.88	34.2	.162	10 ⁻⁸
☆	1.88	48.5	.152	10 ⁻⁸
☆	1.88	33.6	.159	10 ⁻⁹
☆	1.88	46.3	.150	10 ⁻⁹

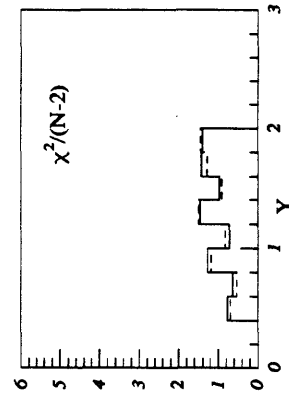
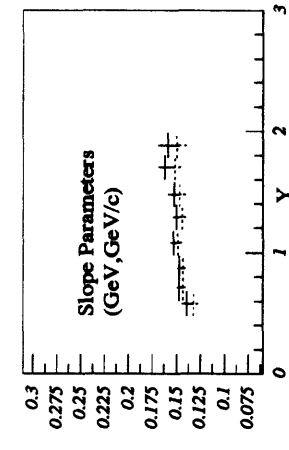
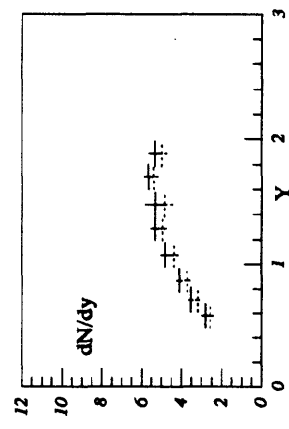


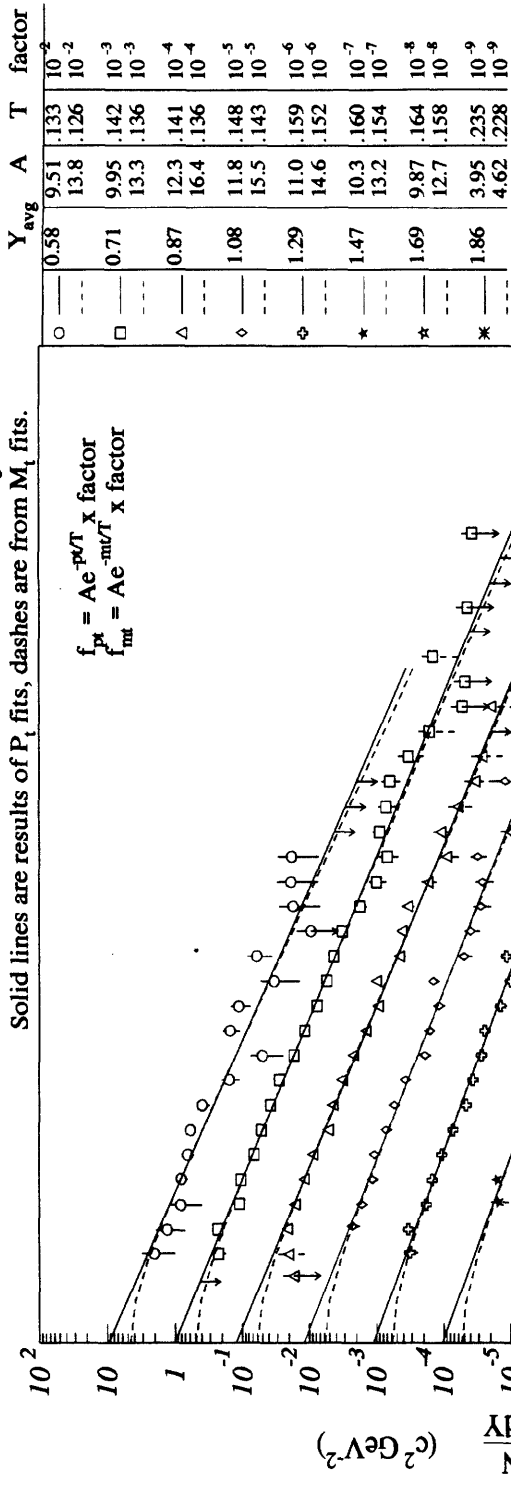
Figure H-4: Yield Summary for ²⁸Si + ²⁷Al CENT2: π^-

²⁸Si+Al MID : Yield Summary π^+

Solid lines are results of P_t fits, dashes are from M_t fits.

$$f_{pt} = Ae^{-pT} \times \text{x factor}$$

$$f_{mt} = Ae^{-mT} \times \text{x factor}$$



Symbol	Y_{avg}	A	T	factor
○	0.58	9.51	.133	10^{-2}
□	0.71	13.8	.126	10^{-2}
△	0.87	9.95	.142	10^{-3}
◇	1.08	13.3	.136	10^{-3}
☆	1.29	12.3	.141	10^{-4}
☆	1.47	16.4	.136	10^{-4}
☆	1.69	11.8	.148	10^{-5}
☆	1.86	15.5	.143	10^{-5}
☆	1.86	11.0	.159	10^{-6}
☆	1.86	14.6	.152	10^{-6}
☆	1.86	10.3	.160	10^{-7}
☆	1.86	13.2	.154	10^{-7}
☆	1.86	9.87	.164	10^{-8}
☆	1.86	12.7	.158	10^{-8}
☆	1.86	3.95	.235	10^{-9}
☆	1.86	4.62	.228	10^{-9}

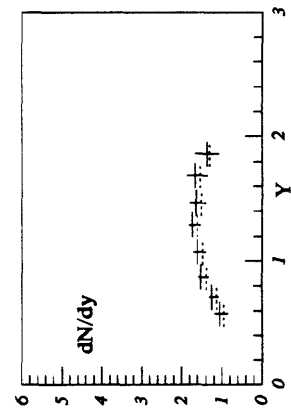
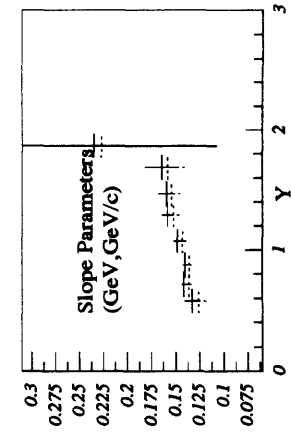
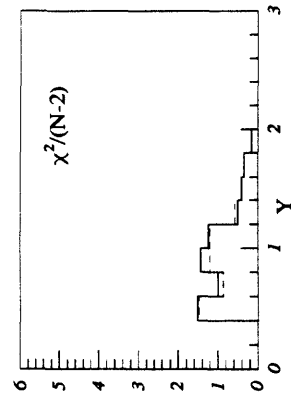
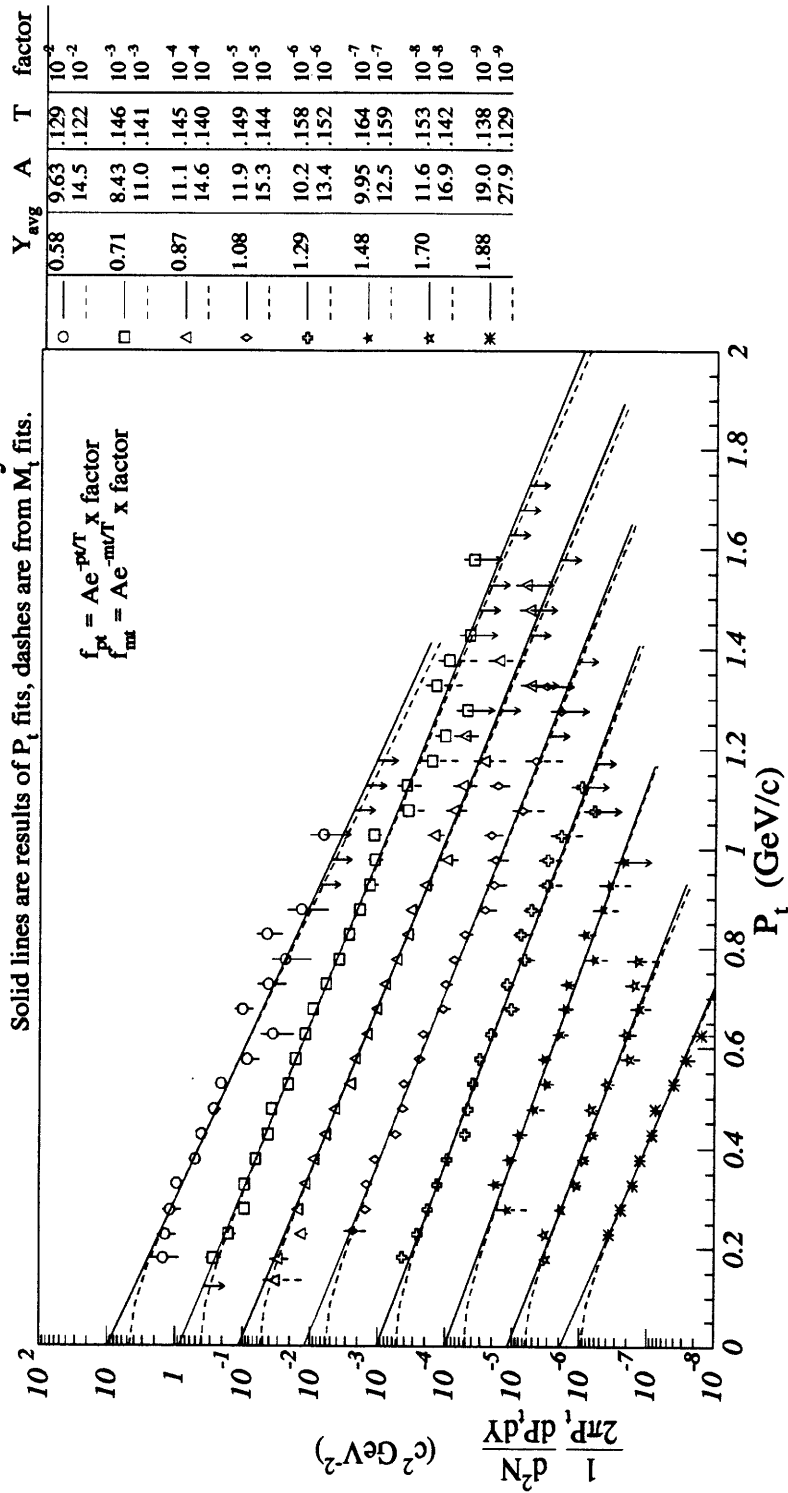


Figure H-5: Yield Summary for ²⁸Si + ²⁷Al MID: π^+

$^{28}\text{Si} + \text{Al}$ MID : Yield Summary π^-

Solid lines are results of P_t fits, dashes are from M_t fits.



$$f_{pt} = A e^{-pT/T} \times \text{factor}$$

$$f_{mt} = A e^{-mT/T} \times \text{factor}$$

Symbol	Y_{avg}	A	T	factor
○	0.58	9.63	.129	10^{-2}
□	0.71	14.5	.122	10^{-2}
△	0.87	8.43	.146	10^{-3}
◇	1.08	11.0	.141	10^{-3}
◆	1.29	11.1	.145	10^{-4}
♣	1.48	14.6	.140	10^{-4}
★	1.70	11.9	.149	10^{-5}
✱	1.88	15.3	.144	10^{-5}
✳	1.70	10.2	.158	10^{-6}
✴	1.88	13.4	.152	10^{-6}
✵	1.70	9.95	.164	10^{-7}
✶	1.88	12.5	.159	10^{-7}
✷	1.70	11.6	.153	10^{-8}
✸	1.88	16.9	.142	10^{-8}
✹	1.70	19.0	.138	10^{-9}
✺	1.88	27.9	.129	10^{-9}

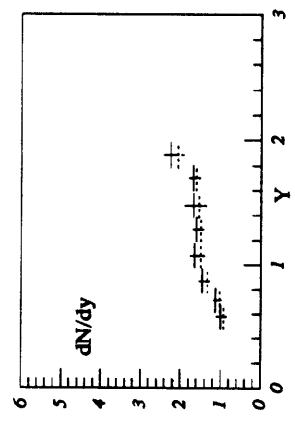
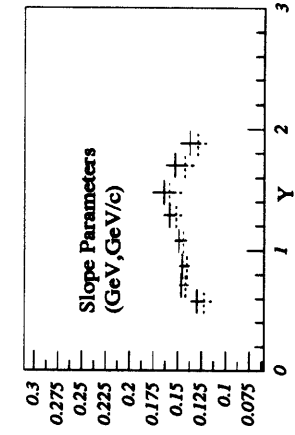
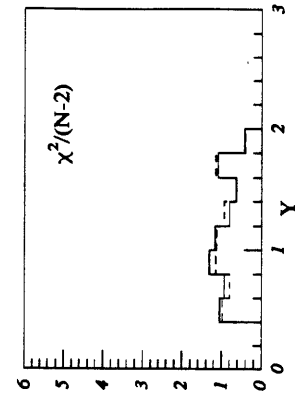


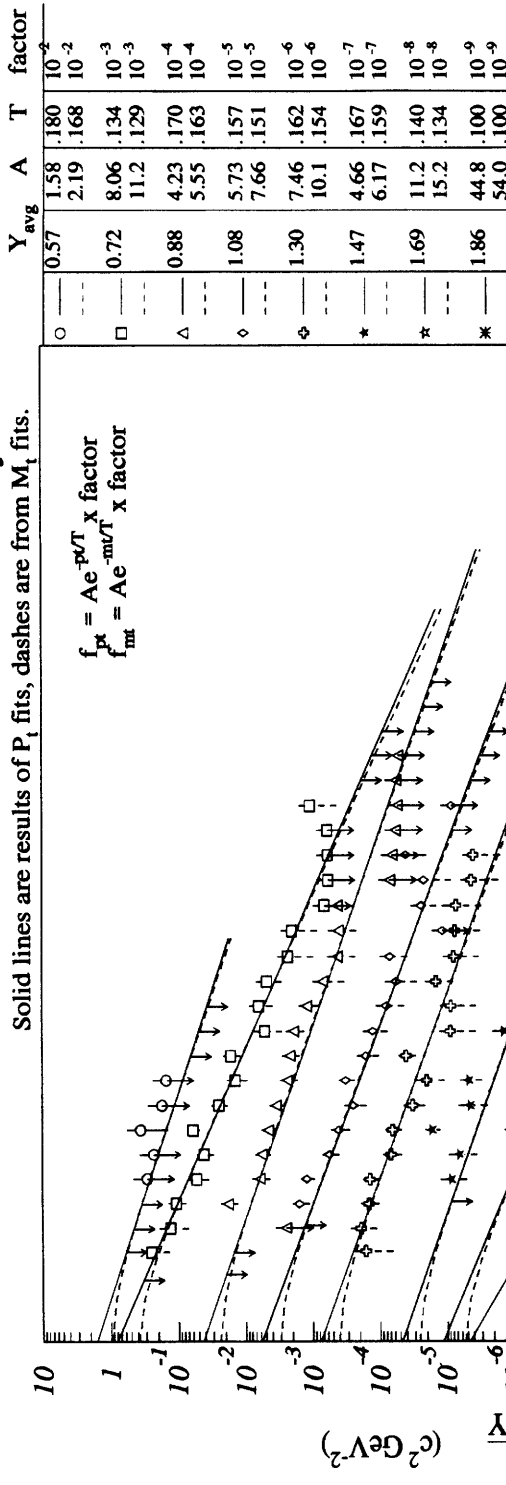
Figure H-6: Yield Summary for $^{28}\text{Si} + ^{27}\text{Al}$ MID: π^-

$^{28}\text{Si} + ^{27}\text{Al}$ PERP1 : Yield Summary π^+

Solid lines are results of P_t fits, dashes are from M_t fits.

$$f_{\pi^+} = A e^{-p/T} \times \text{factor}$$

$$f_{\text{fit}} = A e^{-m_p/T} \times \text{factor}$$



Symbol	Y_{avg}	A	T	factor
○	0.57	1.58	.180	10^{-2}
□	0.72	2.19	.168	10^{-2}
△	0.88	8.06	.134	10^{-3}
◇	1.08	11.2	.129	10^{-3}
◇	1.08	4.23	.170	10^{-4}
◇	1.08	5.55	.163	10^{-4}
◇	1.08	5.73	.157	10^{-5}
◇	1.08	7.66	.151	10^{-5}
◇	1.30	7.46	.162	10^{-6}
◇	1.30	10.1	.154	10^{-6}
★	1.47	4.66	.167	10^{-7}
★	1.47	6.17	.159	10^{-7}
★	1.69	11.2	.140	10^{-8}
★	1.69	15.2	.134	10^{-8}
★	1.86	44.8	.100	10^{-9}
★	1.86	54.0	.100	10^{-9}

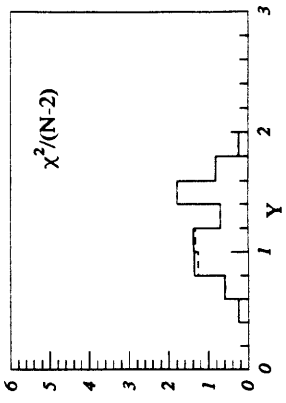
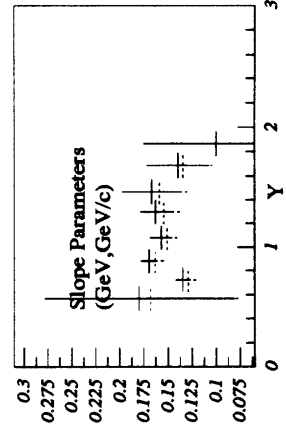
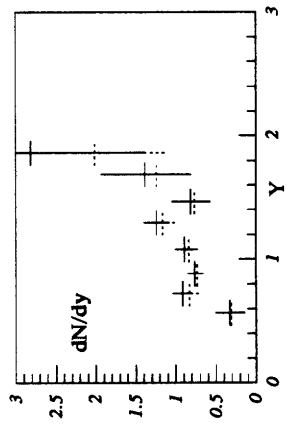
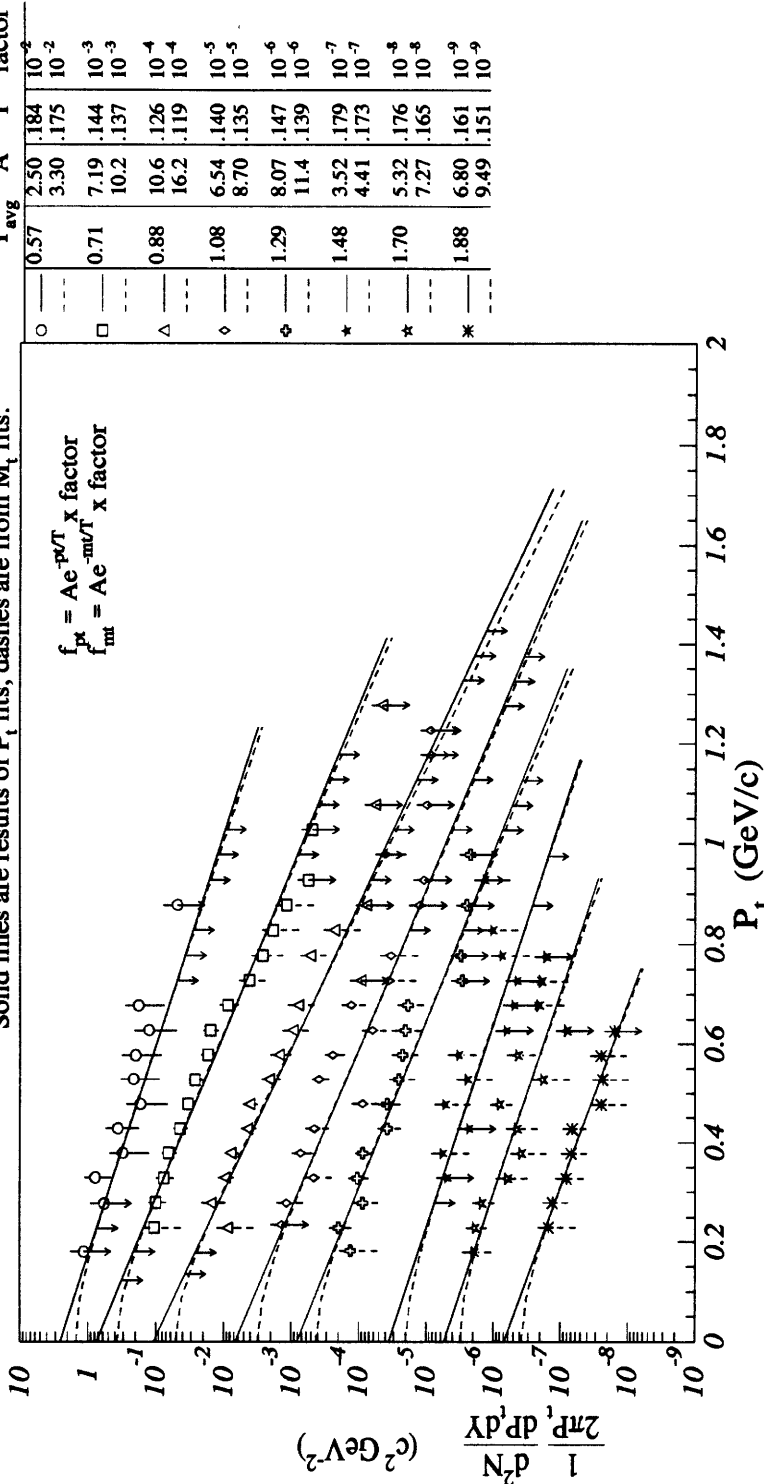


Figure H-7: Yield Summary for $^{28}\text{Si} + ^{27}\text{Al}$ PERP1: π^+

$^{28}\text{Si} + ^{27}\text{Al}$ PERP1 : Yield Summary π^-

Solid lines are results of P_t fits, dashes are from M_t fits.



$$f_{pt} = A e^{-pT/\Gamma} \times \text{x factor}$$

$$f_{mt} = A e^{-mT/\Gamma} \times \text{x factor}$$

	Y_{avg}	A	T	factor
○	0.57	2.50	.184	10^{-2}
□	0.71	3.30	.175	10^{-2}
△	0.88	7.19	.144	10^{-3}
◇	1.08	10.2	.137	10^{-3}
◆	1.29	10.6	.126	10^{-4}
♣	1.48	16.2	.119	10^{-4}
★	1.70	6.54	.140	10^{-5}
✱	1.88	8.70	.135	10^{-5}
		8.07	.147	10^{-6}
		11.4	.139	10^{-6}
		3.52	.179	10^{-7}
		4.41	.173	10^{-7}
		5.32	.176	10^{-8}
		7.27	.165	10^{-8}
		6.80	.161	10^{-9}
		9.49	.151	10^{-9}

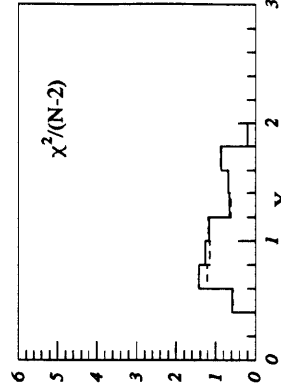
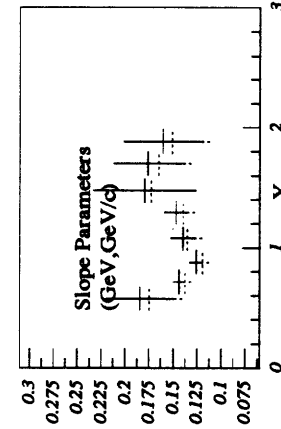
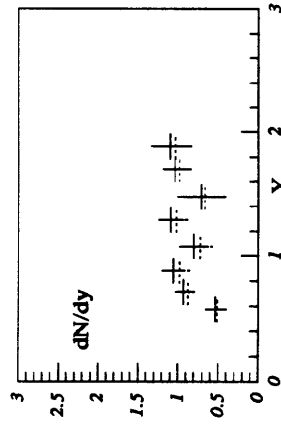


Figure H-8: Yield Summary for $^{28}\text{Si} + ^{27}\text{Al}$ PERP1: π^-

Appendix I

Yield Summary: $^{28}\text{Si} + ^{64}\text{Cu} : \pi$

²⁸Si+Cu CENT1 : Yield Summary π^+

Solid lines are results of P_t fits, dashes are from M_t fits.

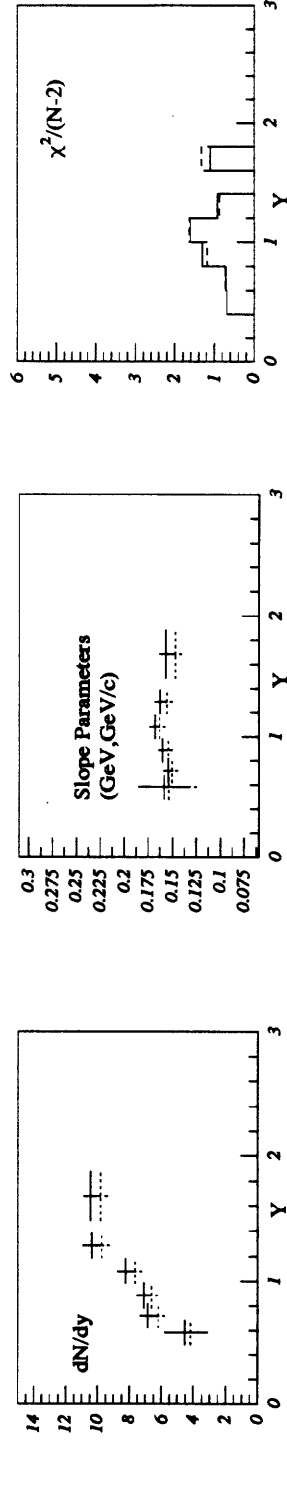
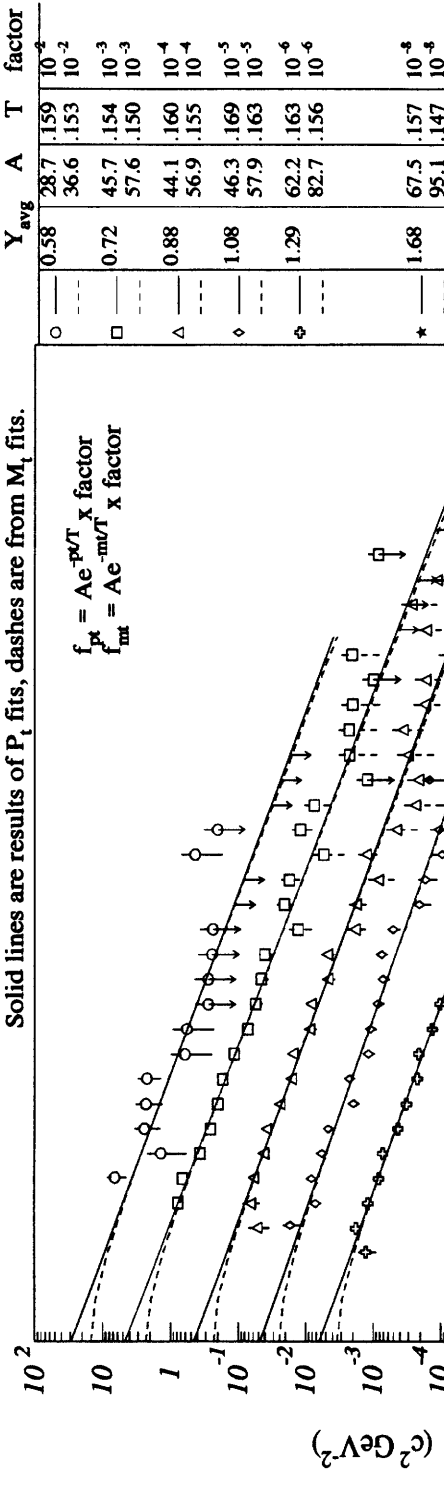


Figure I-1: Yield Summary for ²⁸Si + ⁶⁴Cu CENT1: π^+

²⁸Si+Cu CENT1 : Yield Summary π^-

Solid lines are results of P_t fits, dashes are from M_t fits.

$$f_{pt} = A e^{-pT} \times \text{factor}$$

$$f_{mt} = A e^{-mT} \times \text{factor}$$

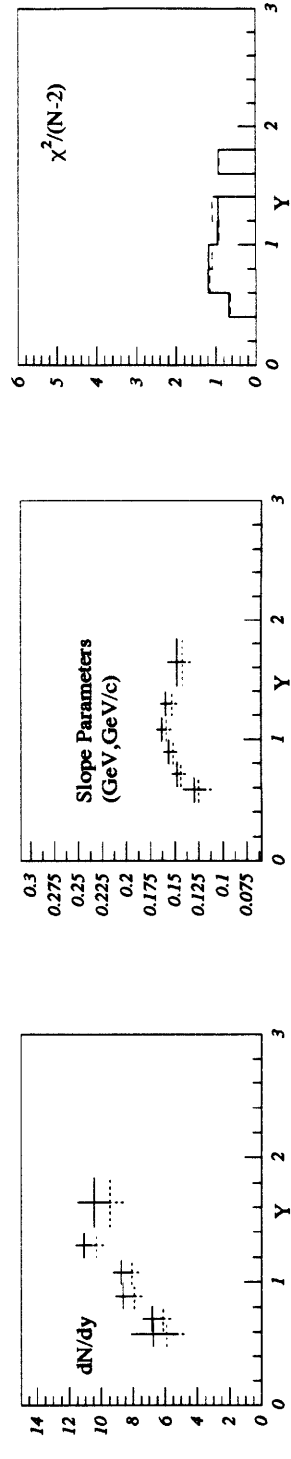
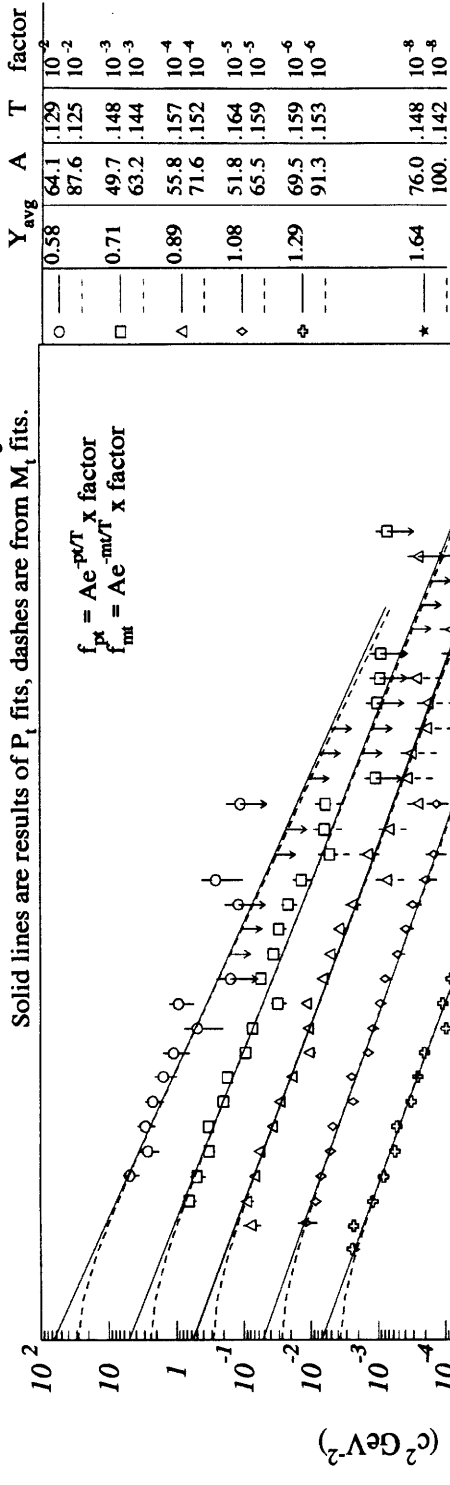


Figure I-2: Yield Summary for ²⁸Si + ⁶⁴Cu CENT1: π^-

²⁸Si+Cu CENT2 : Yield Summary π^+

Solid lines are results of P_t fits, dashes are from M_t fits.

Symbol	Y_{avg}	A	T	factor
○	0.58	42.3	.131	10^{-2}
□	0.72	57.2	.127	10^{-2}
△	0.89	30.5	.153	10^{-3}
◇	1.08	38.8	.149	10^{-3}
◇	1.29	31.9	.160	10^{-4}
◇	1.48	40.4	.156	10^{-4}
◇	1.70	36.9	.159	10^{-5}
◇	1.88	46.8	.154	10^{-5}
◇	1.88	42.7	.159	10^{-6}
◇	1.88	57.1	.152	10^{-6}
◇	1.88	28.4	.179	10^{-7}
◇	1.88	35.2	.173	10^{-7}
◇	1.88	38.8	.164	10^{-8}
◇	1.88	54.9	.153	10^{-8}
◇	1.88	36.8	.168	10^{-9}
◇	1.88	50.4	.158	10^{-9}

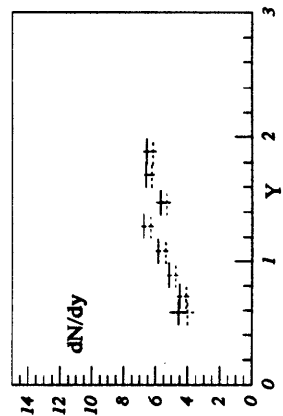
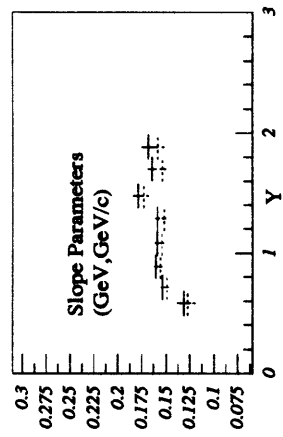
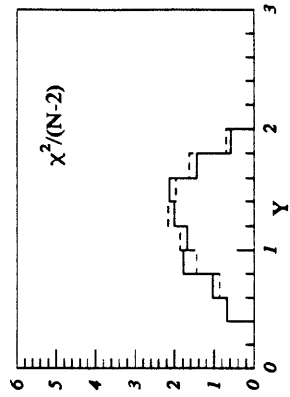
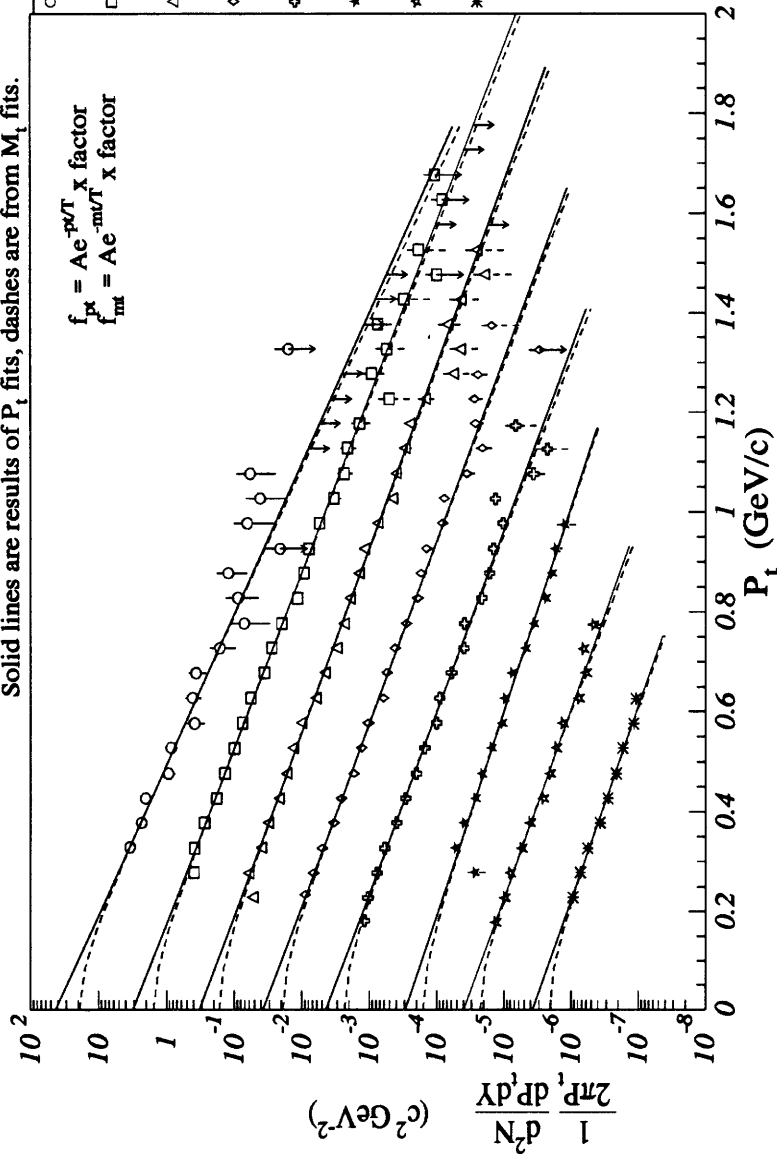
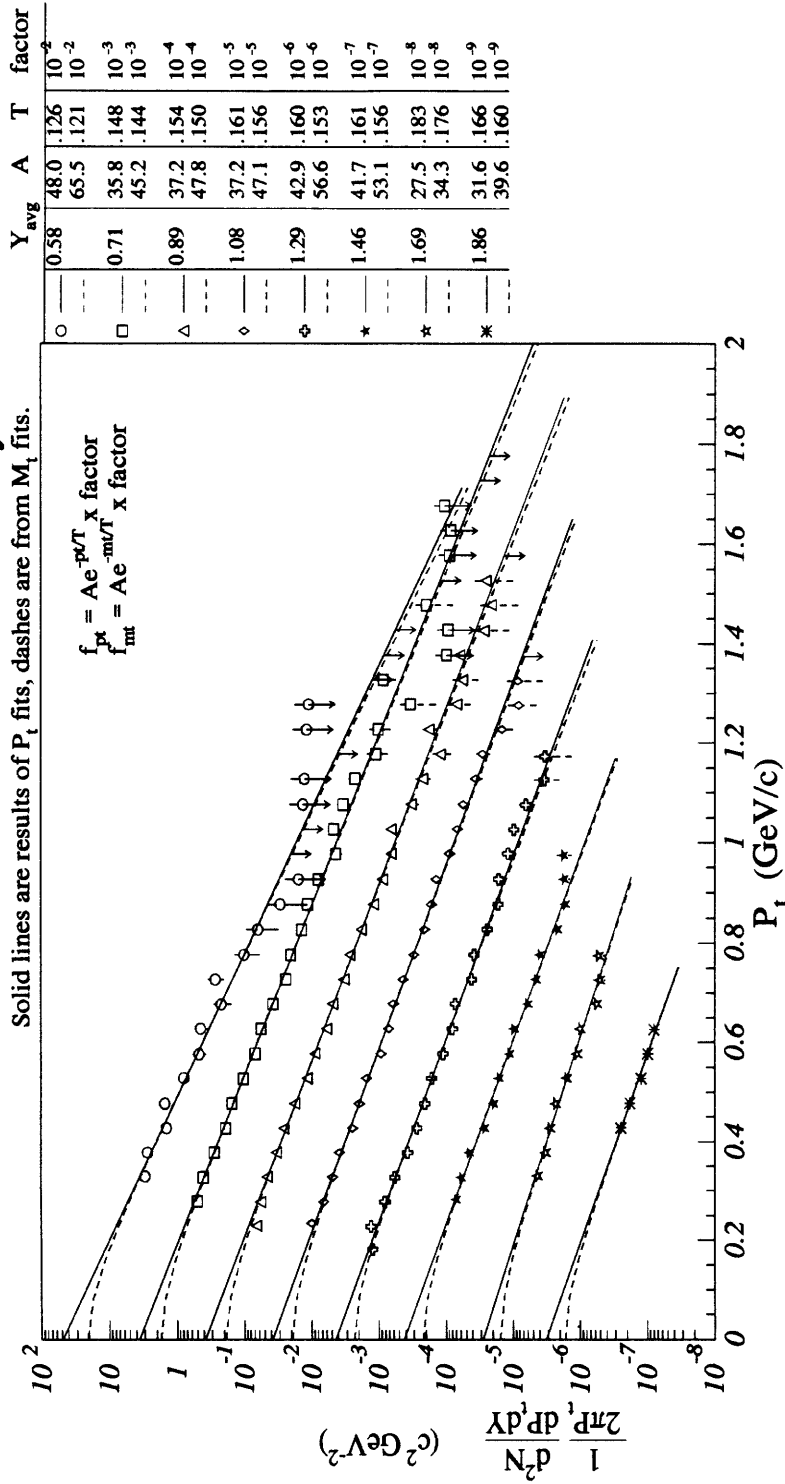


Figure I-3: Yield Summary for ²⁸Si + ⁶⁴Cu CENT2: π^+

²⁸Si+Cu CENT2: Yield Summary π^-

Solid lines are results of P_t fits, dashes are from M_t fits.



$$f_{pt} = A e^{-pT} \times \text{x factor}$$

$$f_{mt} = A e^{-mT} \times \text{x factor}$$

Symbol	Y_{avg}	A	T	factor
○	0.58	48.0	.126	10^{-2}
□	0.71	65.5	.121	10^{-2}
△	0.89	35.8	.148	10^{-3}
◇	1.08	45.2	.144	10^{-3}
☆	1.29	37.2	.154	10^{-4}
☆	1.46	47.8	.150	10^{-4}
☆	1.69	37.2	.161	10^{-5}
☆	1.86	47.1	.156	10^{-5}
☆	1.86	42.9	.160	10^{-6}
☆	1.86	56.6	.153	10^{-6}
☆	1.86	41.7	.161	10^{-7}
☆	1.86	53.1	.156	10^{-7}
☆	1.86	27.5	.183	10^{-8}
☆	1.86	34.3	.176	10^{-8}
☆	1.86	31.6	.166	10^{-9}
☆	1.86	39.6	.160	10^{-9}

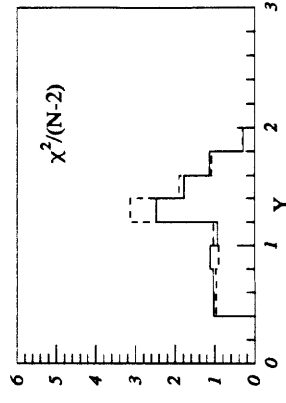
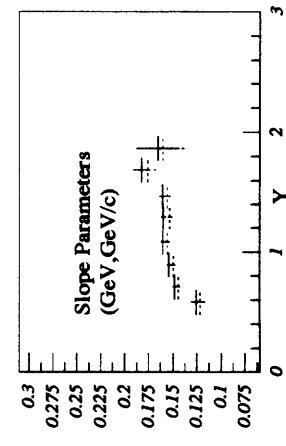
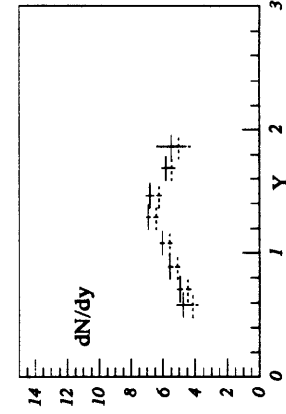


Figure I-4: Yield Summary for ²⁸Si + ⁶⁴Cu CENT2: π^-

²⁸Si+Cu MID : Yield Summary π^+

Solid lines are results of P_t fits, dashes are from M_t fits.

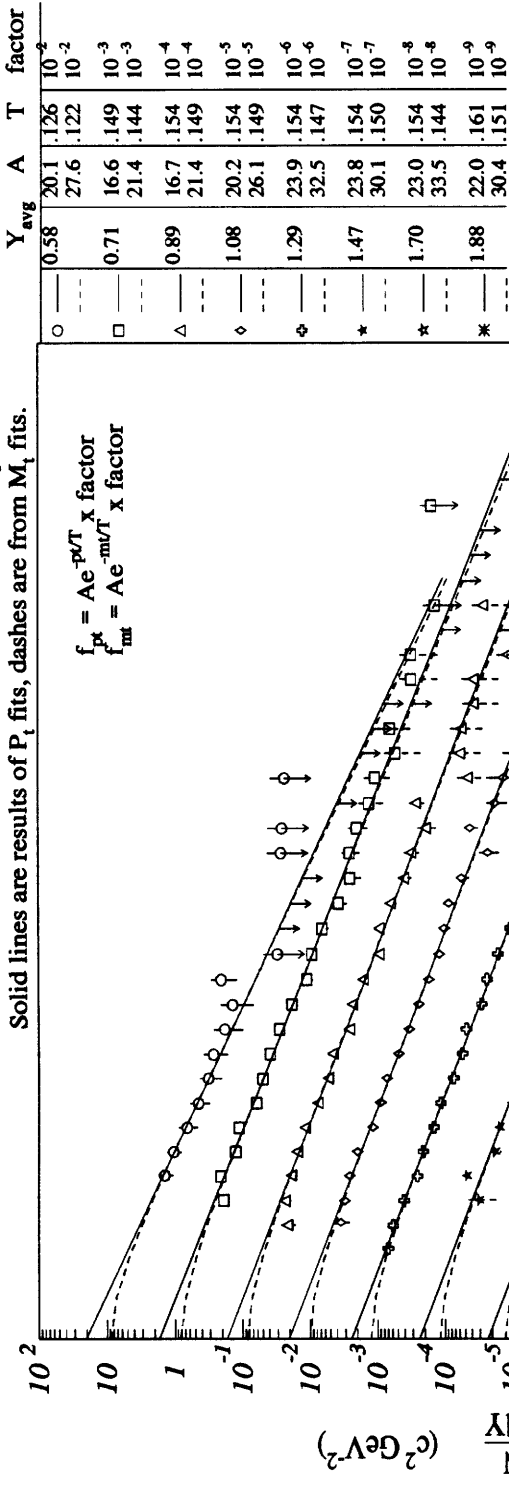
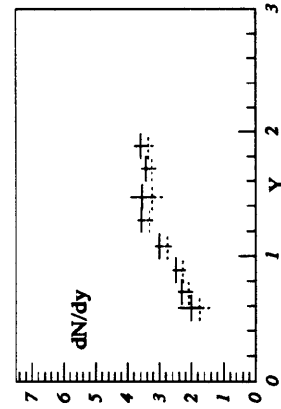
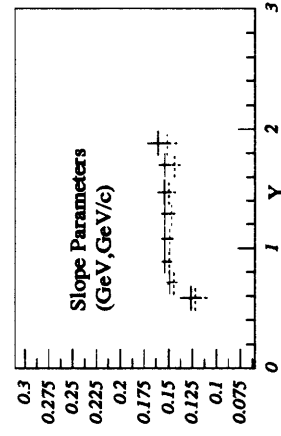
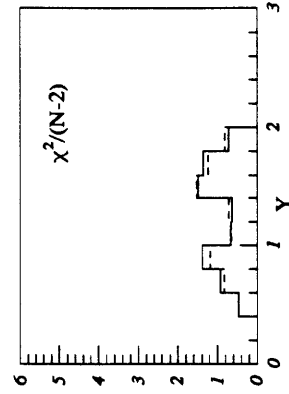


Figure I-5: Yield Summary for ²⁸Si + ⁶⁴Cu MID: π^+

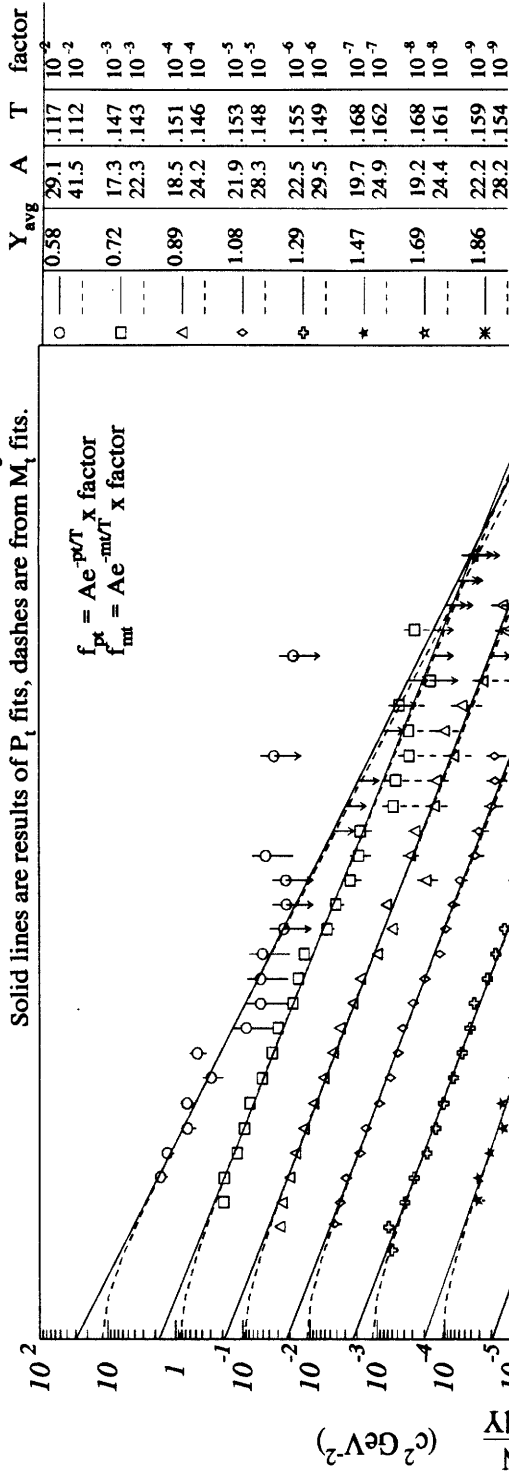


$^{28}\text{Si} + \text{Cu}$ MID : Yield Summary π^-

Solid lines are results of P_t fits, dashes are from M_t fits.

$$f_{pt} = Ae^{-pT/T} \times \text{factor}$$

$$f_{mt} = Ae^{-mT/T} \times \text{factor}$$



Symbol	Y_{avg}	A	T	factor
○	0.58	29.1	.117	10^{-2}
□	0.72	41.5	.112	10^{-2}
△	0.89	17.3	.147	10^{-3}
◇	1.08	22.3	.143	10^{-3}
◆	1.29	18.5	.151	10^{-4}
★	1.47	24.2	.146	10^{-4}
★	1.69	21.9	.153	10^{-5}
★	1.86	28.3	.148	10^{-5}
★	1.86	22.5	.155	10^{-6}
★	1.86	29.5	.149	10^{-6}
★	1.86	19.7	.168	10^{-7}
★	1.86	24.9	.162	10^{-7}
★	1.86	19.2	.168	10^{-8}
★	1.86	24.4	.161	10^{-8}
★	1.86	22.2	.159	10^{-9}
★	1.86	28.2	.154	10^{-9}

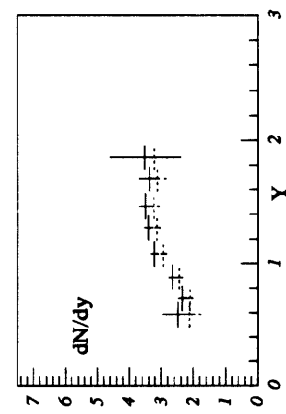
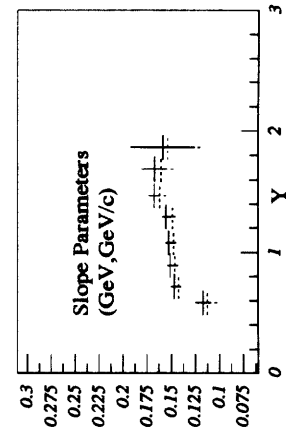
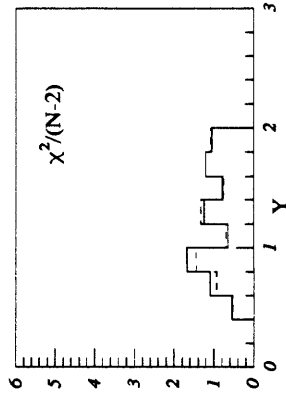


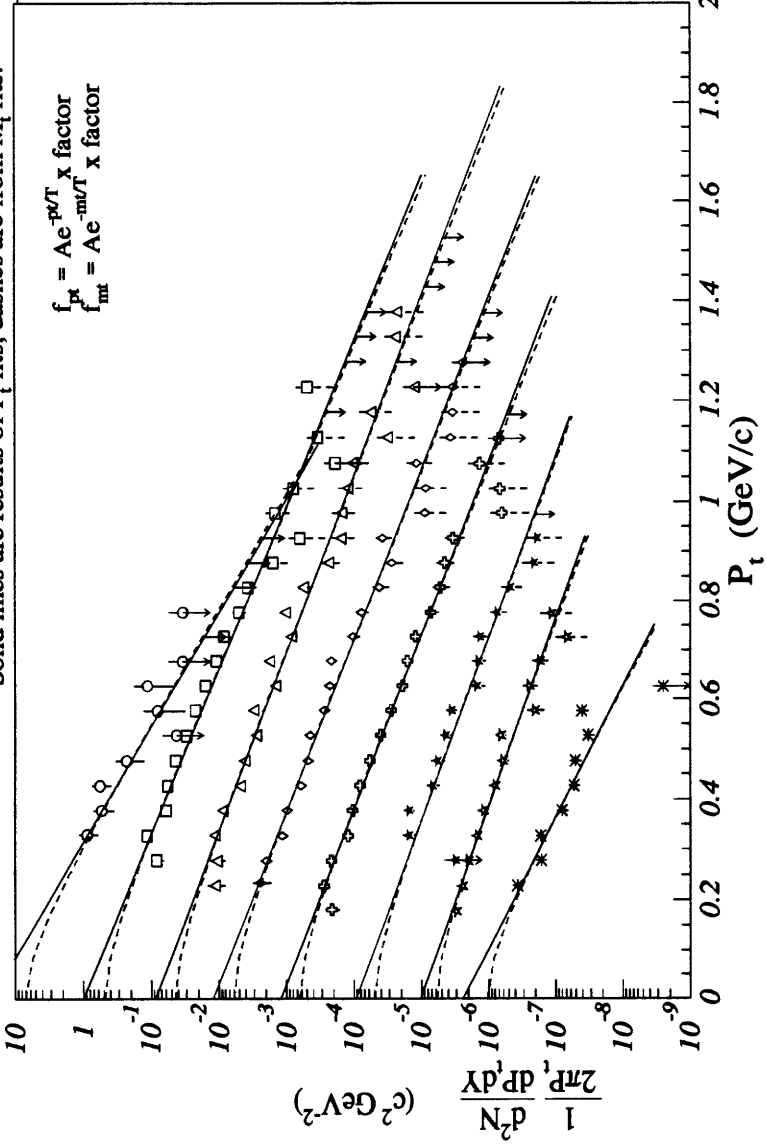
Figure I-6: Yield Summary for $^{28}\text{Si} + ^{64}\text{Cu}$ MID: π^-

²⁸Si+Cu PERP1 : Yield Summary π^+

Solid lines are results of P_t fits, dashes are from M_t fits.

$$f_{\pi^+} = Ae^{-pT} \times \text{x factor}$$

$$f_{m\pi} = Ae^{-mT} \times \text{x factor}$$



Symbol	Y_{avg}	A	T	factor
○	0.58	22.7	.100	10^{-2}
□	0.72	28.3	.100	10^{-2}
△	0.89	9.89	.143	10^{-3}
◇	1.08	13.0	.139	10^{-3}
⊕	1.29	8.57	.156	10^{-4}
*	1.47	11.0	.151	10^{-4}
*	1.70	12.0	.150	10^{-5}
*	1.88	15.5	.145	10^{-5}
*	1.88	12.0	.152	10^{-6}
*	1.88	16.4	.145	10^{-6}
*	1.88	9.11	.160	10^{-7}
*	1.88	11.9	.154	10^{-7}
*	1.88	10.1	.165	10^{-8}
*	1.88	14.4	.154	10^{-8}
*	1.88	23.8	.114	10^{-9}
*	1.88	37.6	.108	10^{-9}

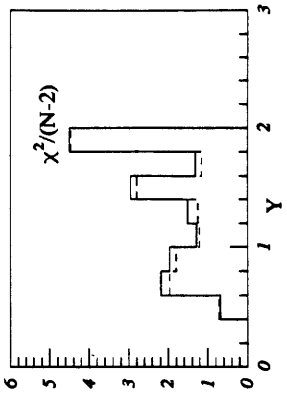
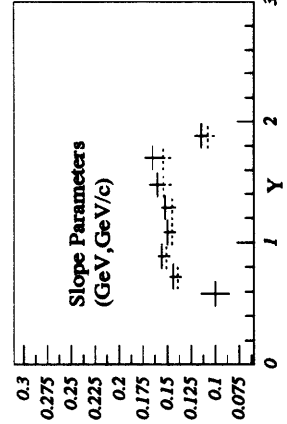
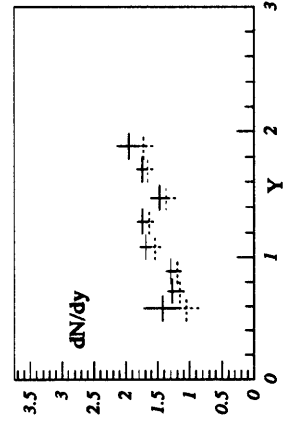
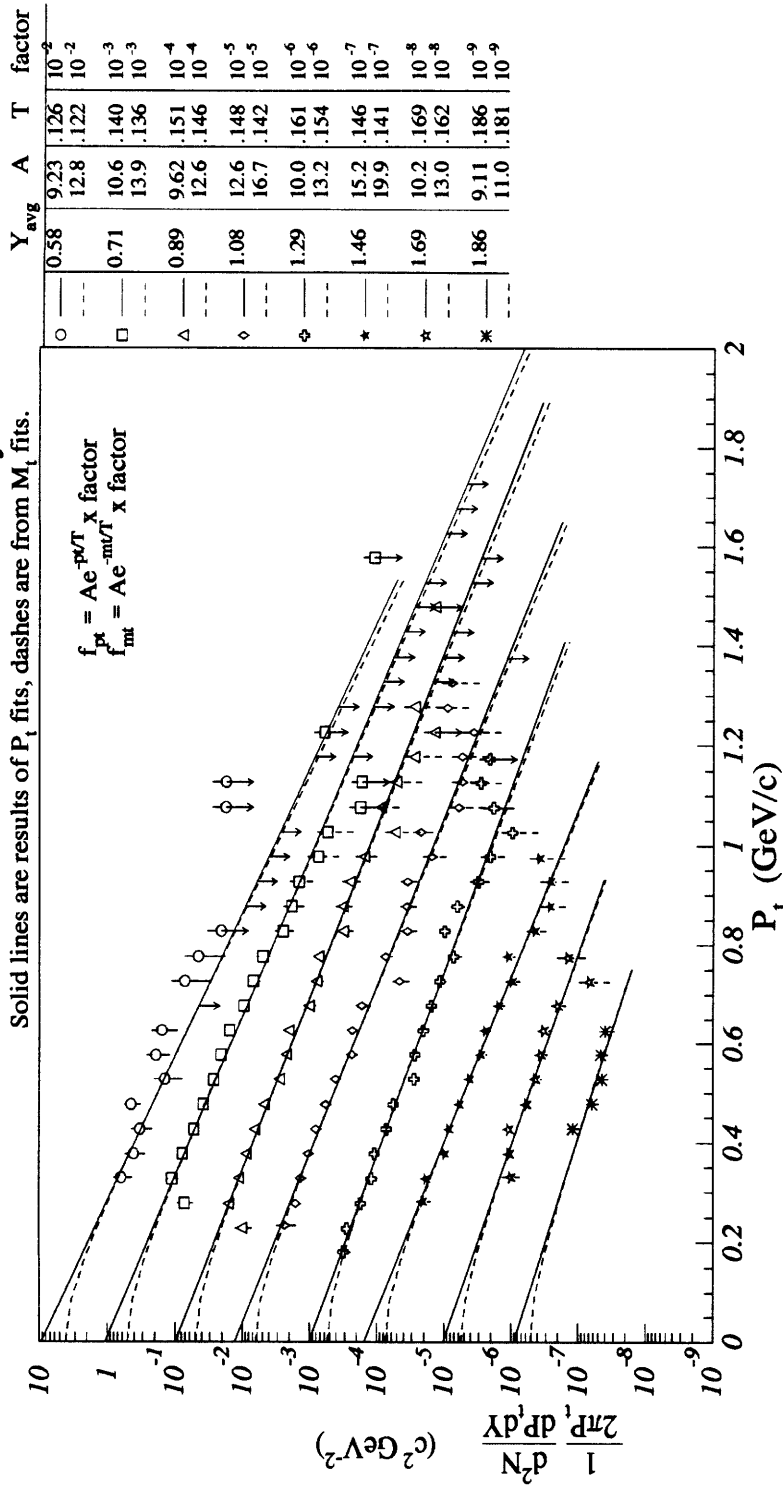


Figure I-7: Yield Summary for ²⁸Si + ⁶⁴Cu PERP1: π^+

$^{28}\text{Si} + \text{Cu}$ PERP1 : Yield Summary π^-

Solid lines are results of P_t fits, dashes are from M_t fits.



$$\begin{aligned} f_{pt} &= A e^{-pT} \times \text{factor} \\ f_{mt} &= A e^{-mT} \times \text{factor} \end{aligned}$$

Symbol	Y_{avg}	A	T	factor
○	0.58	9.23	.126	10^{-2}
□	0.71	12.8	.122	10^{-2}
△	0.89	10.6	.140	10^{-3}
◇	1.08	13.9	.136	10^{-3}
⊕	1.29	9.62	.151	10^{-4}
*	1.46	12.6	.146	10^{-4}
*	1.69	12.6	.148	10^{-5}
*	1.86	16.7	.142	10^{-5}
*	1.29	10.0	.161	10^{-6}
*	1.46	13.2	.154	10^{-6}
*	1.69	15.2	.146	10^{-7}
*	1.86	19.9	.141	10^{-7}
*	1.29	10.2	.169	10^{-8}
*	1.46	13.0	.162	10^{-8}
*	1.69	9.11	.186	10^{-9}
*	1.86	11.0	.181	10^{-9}

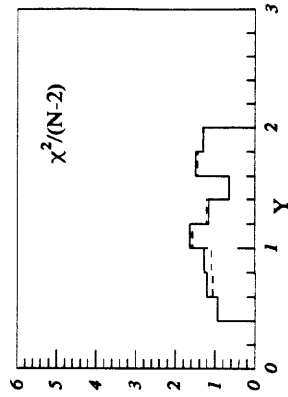
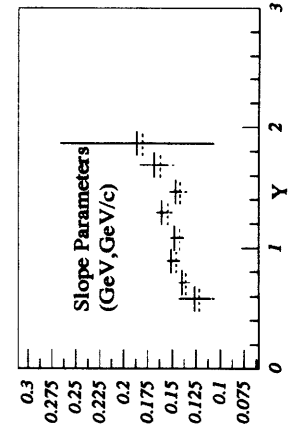
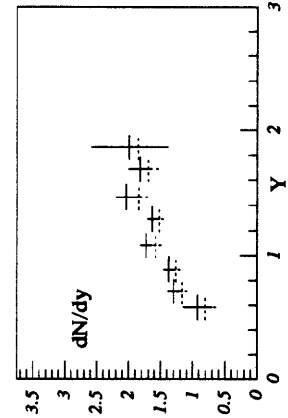


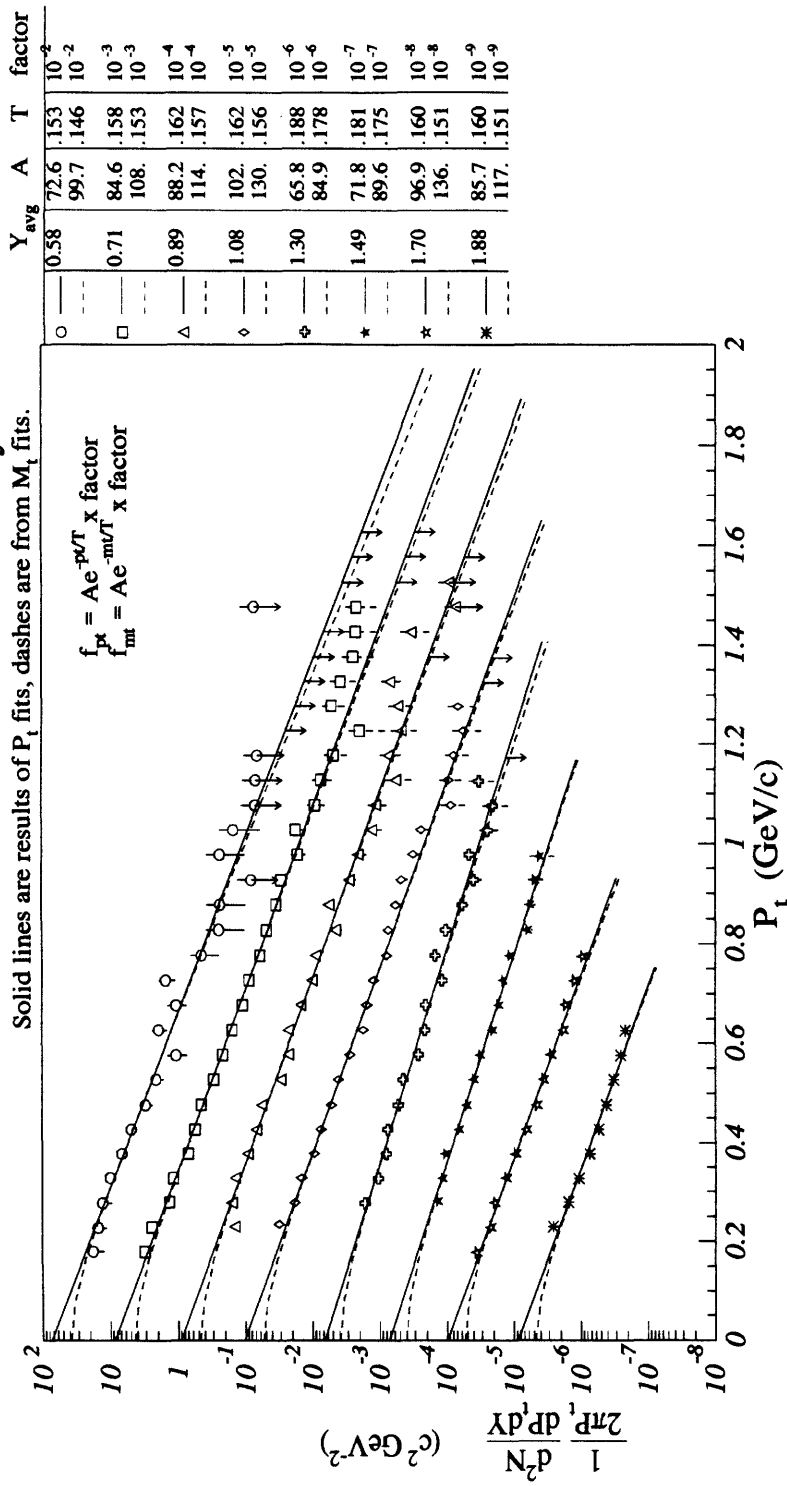
Figure I-8: Yield Summary for $^{28}\text{Si} + ^{64}\text{Cu}$ PERP1: π^-

Appendix J

Yield Summary: $^{28}\text{Si} + ^{197}\text{Au} : \pi$

$^{28}\text{Si} + \text{Au}$ CENT1 : Yield Summary π^+

Solid lines are results of P_t fits, dashes are from M_t fits.



$$f_{pt} = A e^{-pT/T} \times \text{x factor}$$

$$f_{mt} = A e^{-mT/T} \times \text{x factor}$$

Symbol	Y_{avg}	A	T	factor
○	0.58	72.6	.153	10^{-2}
□	0.71	99.7	.146	10^{-2}
△	0.89	84.6	.158	10^{-3}
◇	1.08	108.	.153	10^{-3}
☆	1.30	88.2	.162	10^{-4}
*	1.49	114.	.157	10^{-4}
⋆	1.70	102.	.162	10^{-5}
⋆	1.88	130.	.156	10^{-5}
⋆	1.88	65.8	.188	10^{-6}
⋆	1.88	84.9	.178	10^{-6}
⋆	1.88	71.8	.181	10^{-7}
⋆	1.88	89.6	.175	10^{-7}
⋆	1.88	96.9	.160	10^{-8}
⋆	1.88	136.	.151	10^{-8}
⋆	1.88	85.7	.160	10^{-9}
⋆	1.88	117.	.151	10^{-9}

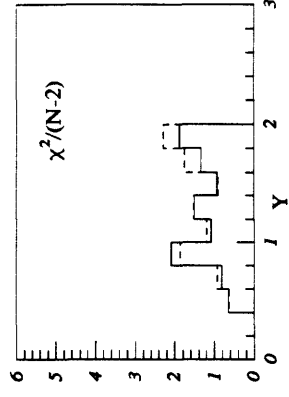
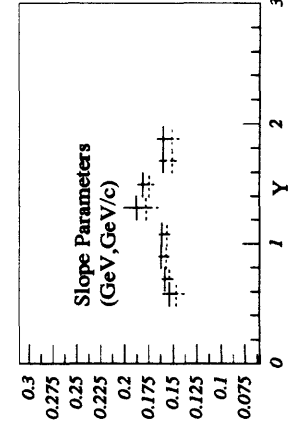
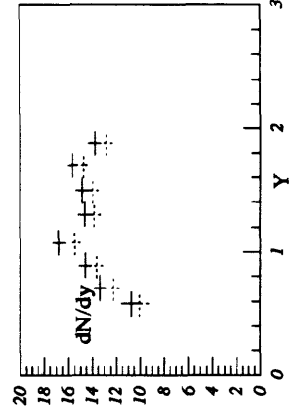
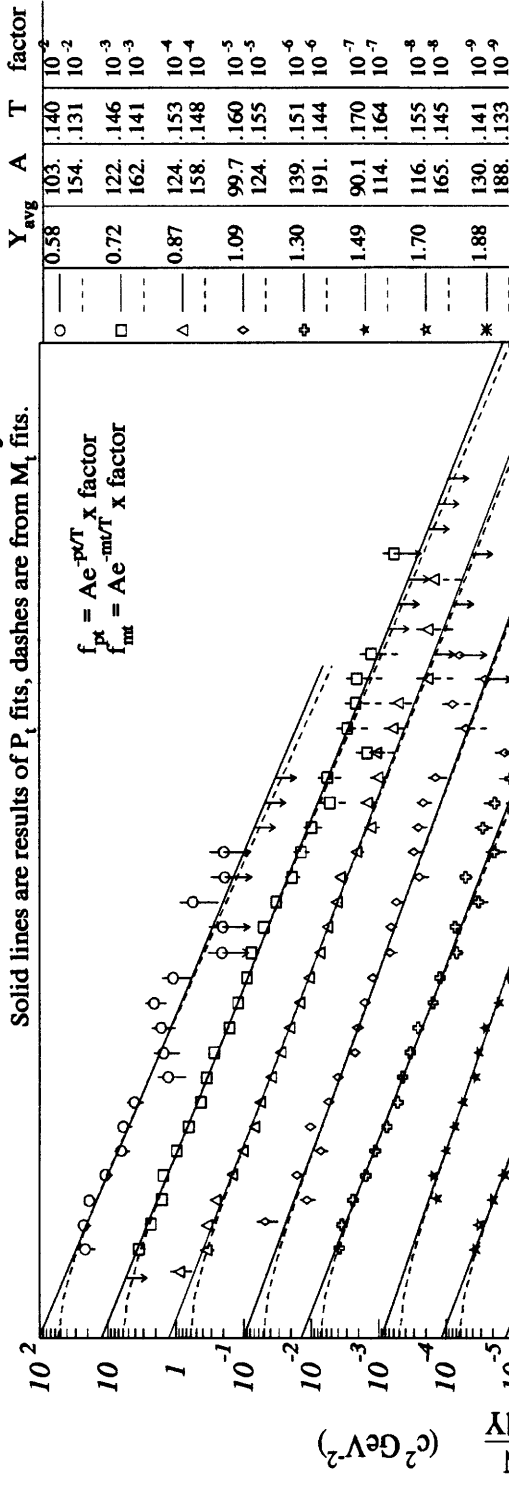


Figure J-1: Yield Summary for $^{28}\text{Si} + ^{197}\text{Au}$ CENT1: π^+

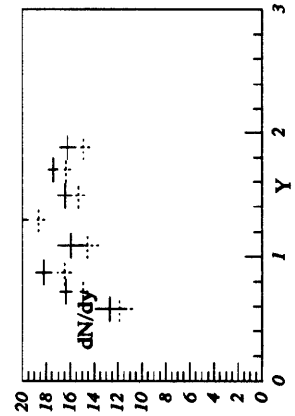
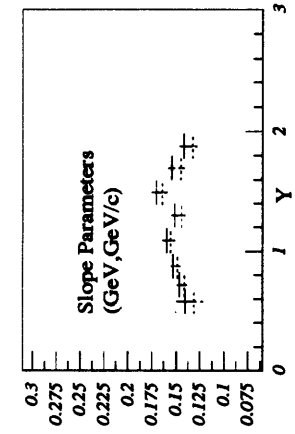
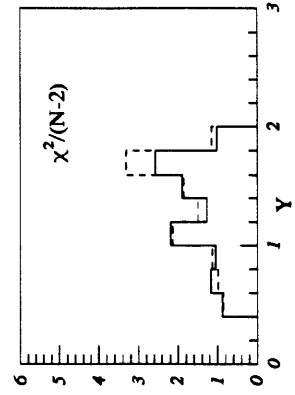
$^{28}\text{Si} + \text{Au}$ CENT1 : Yield Summary π^-

Solid lines are results of P_t fits, dashes are from M_t fits.



Symbol	Y_{avg}	A	T	factor
○	0.58	103.	.140	10^{-2}
□	0.72	154.	.131	10^{-2}
△	0.87	122.	.146	10^{-3}
◇	1.09	162.	.141	10^{-3}
◇	1.30	124.	.153	10^{-4}
◇	1.30	158.	.148	10^{-4}
◇	1.30	99.7	.160	10^{-5}
◇	1.30	124.	.155	10^{-5}
◇	1.30	139.	.151	10^{-6}
◇	1.30	191.	.144	10^{-6}
◇	1.49	90.1	.170	10^{-7}
◇	1.49	114.	.164	10^{-7}
◇	1.70	116.	.155	10^{-8}
◇	1.70	165.	.145	10^{-8}
◇	1.88	130.	.141	10^{-9}
◇	1.88	188.	.133	10^{-9}

Figure J-2: Yield Summary for $^{28}\text{Si} + ^{197}\text{Au}$ CENT1: π^-

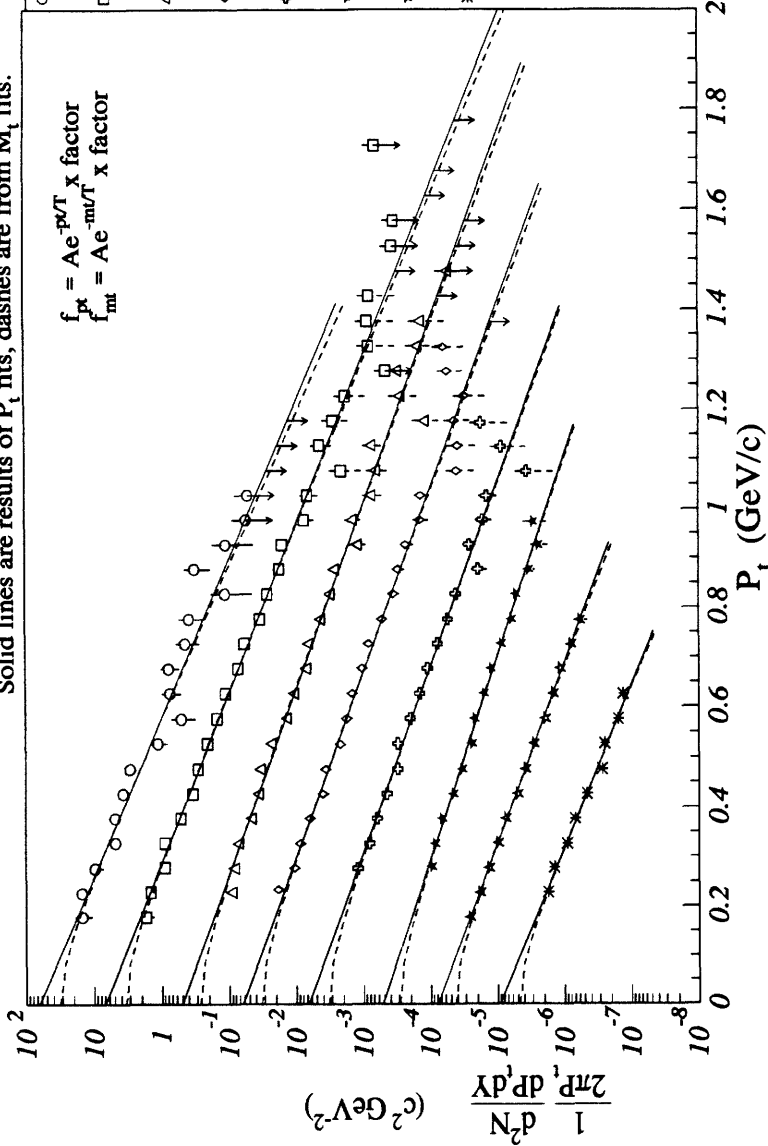


$^{28}\text{Si} + \text{Au}$ CENT2 : Yield Summary π^+

Solid lines are results of P_t fits, dashes are from M_t fits.

$$f_{\pi^+} = A e^{-pT/\Gamma} \times \text{x factor}$$

$$f_{m_t} = A e^{-m_t/\Gamma} \times \text{x factor}$$



Symbol	Y_{avg}	A	T	factor
○	0.58	63.4	.138	10^{-2}
□	0.70	91.4	.131	10^{-2}
△	0.89	69.0	.147	10^{-3}
◇	1.08	90.4	.143	10^{-3}
◇	1.30	50.4	.161	10^{-4}
◇	1.30	64.9	.156	10^{-4}
◇	1.30	62.6	.161	10^{-5}
◇	1.30	79.7	.156	10^{-5}
◇	1.30	65.5	.162	10^{-6}
◇	1.30	79.8	.158	10^{-6}
*	1.49	51.3	.177	10^{-7}
*	1.49	64.2	.171	10^{-7}
*	1.70	77.0	.158	10^{-8}
*	1.70	109.	.148	10^{-8}
*	1.88	92.1	.142	10^{-9}
*	1.88	134.	.133	10^{-9}

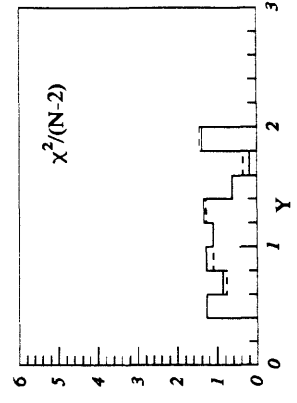
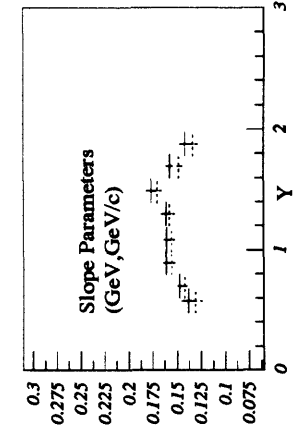
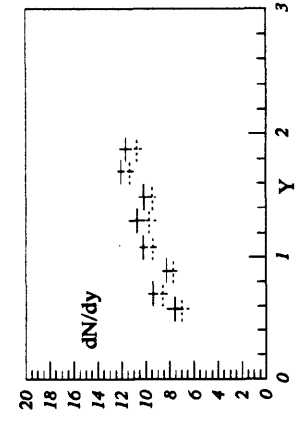
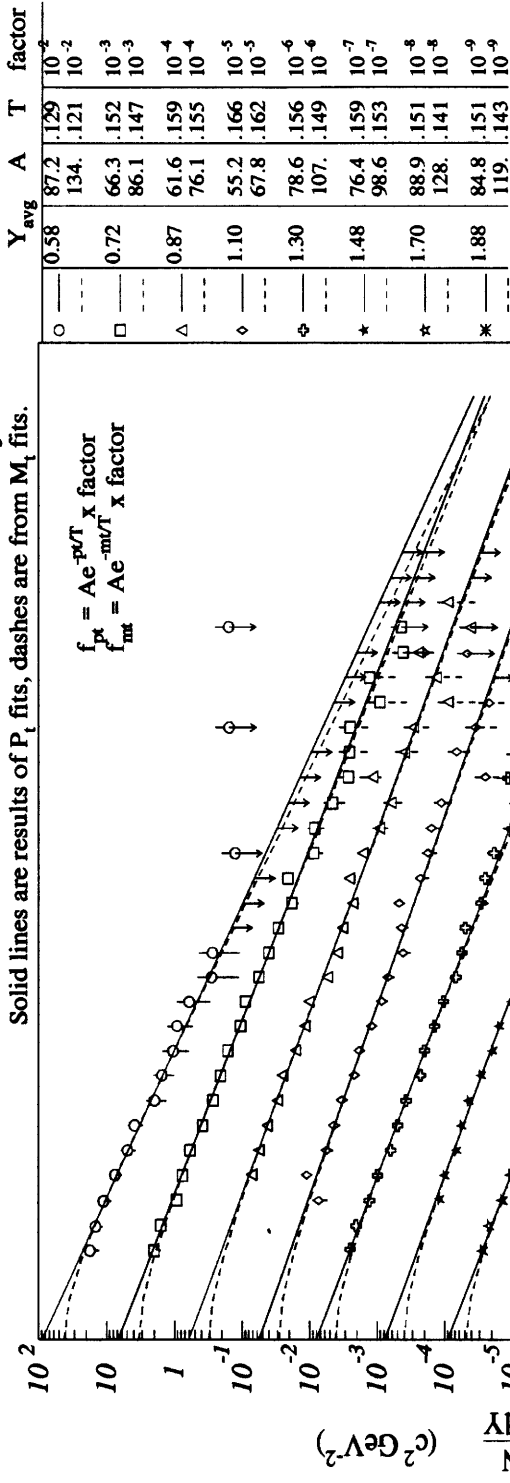


Figure J-3: Yield Summary for $^{28}\text{Si} + ^{197}\text{Au}$ CENT2: π^+

²⁸Si+Au CENT2 : Yield Summary π^-

Solid lines are results of P_t fits, dashes are from M_t fits.



Symbol	Y_{avg}	A	T	factor
○	0.58	87.2	.129	10^{-2}
□	0.72	134.	.121	10^{-2}
△	0.87	66.3	.152	10^{-3}
◇	1.10	86.1	.147	10^{-3}
◆	1.30	61.6	.159	10^{-4}
⊕	1.48	76.1	.155	10^{-4}
★	1.70	55.2	.166	10^{-5}
✱	1.88	67.8	.162	10^{-5}
✳	1.88	78.6	.156	10^{-6}
✴	1.88	107.	.149	10^{-6}
✵	1.88	76.4	.159	10^{-7}
✶	1.88	98.6	.153	10^{-7}
✷	1.88	88.9	.151	10^{-8}
✸	1.88	128.	.141	10^{-8}
✹	1.88	84.8	.151	10^{-9}
✺	1.88	119.	.143	10^{-9}

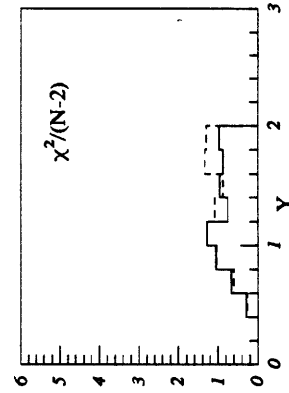
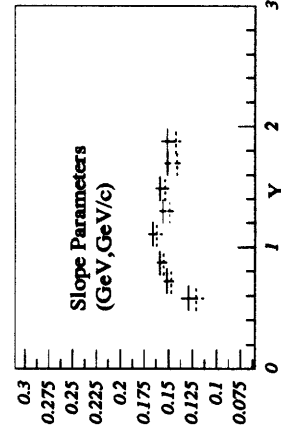
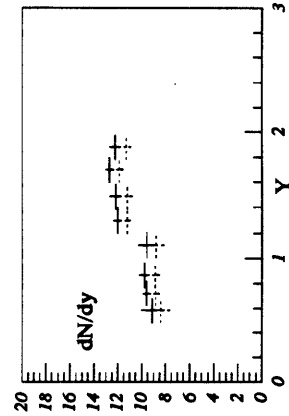
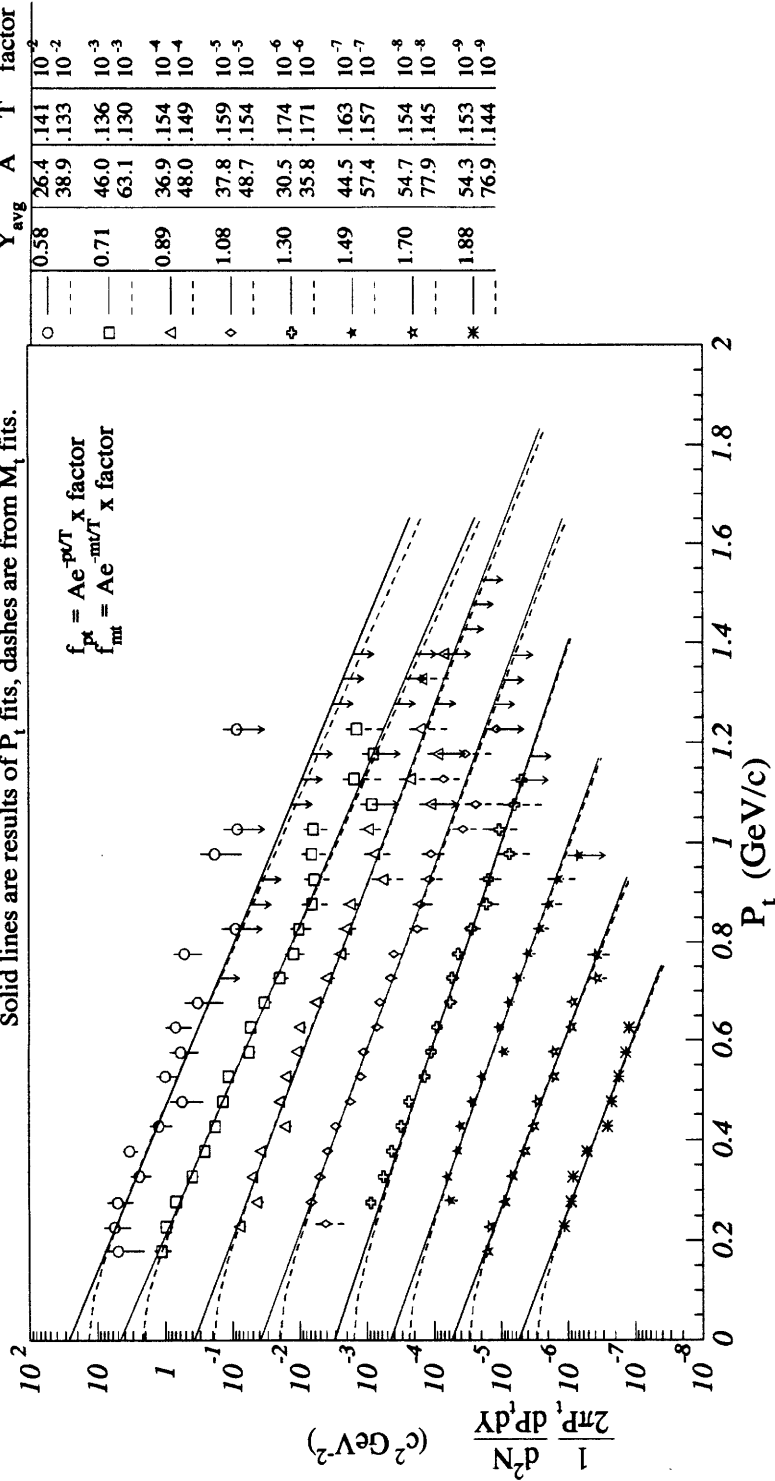


Figure J-4: Yield Summary for ²⁸Si + ¹⁹⁷Au CENT2: π^-

²⁸Si+Au MID : Yield Summary π^+

Solid lines are results of P_t fits, dashes are from M_t fits.



$$f_{pt}^{\pi^+} = A e^{-pT/T} \times \text{x factor}$$

$$f_{mt}^{\pi^+} = A e^{-mT/T} \times \text{x factor}$$

Symbol	Y _{avg}	A	T	factor
○	0.58	26.4	.141	10 ⁻²
□	0.71	38.9	.133	10 ⁻³
△	0.89	46.0	.136	10 ⁻³
◇	1.08	63.1	.130	10 ⁻³
☆	1.30	36.9	.154	10 ⁻⁴
☆	1.49	48.0	.149	10 ⁻⁴
☆	1.70	37.8	.159	10 ⁻⁵
☆	1.88	48.7	.154	10 ⁻⁵
☆	1.30	30.5	.174	10 ⁻⁶
☆	1.49	35.8	.171	10 ⁻⁶
☆	1.70	44.5	.163	10 ⁻⁷
☆	1.88	57.4	.157	10 ⁻⁷
☆	1.30	54.7	.154	10 ⁻⁸
☆	1.49	77.9	.145	10 ⁻⁸
☆	1.70	54.3	.153	10 ⁻⁹
☆	1.88	76.9	.144	10 ⁻⁹

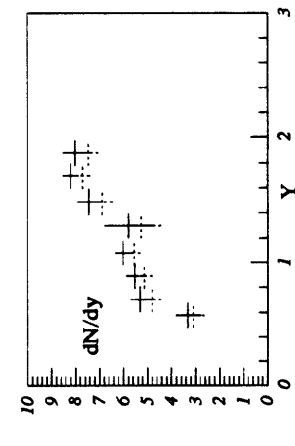
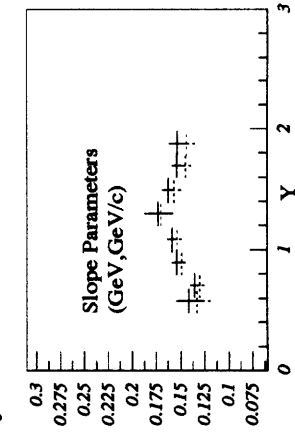
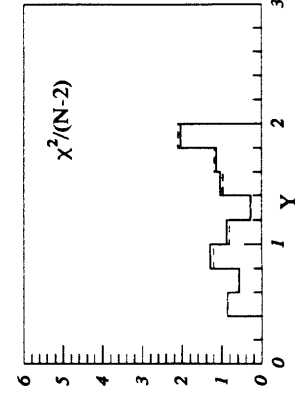


Figure J-5: Yield Summary for ²⁸Si + ¹⁹⁷Au MID: π^+

$^{28}\text{Si} + ^{197}\text{Au}$ MID : Yield Summary π^-

Solid lines are results of P_t fits, dashes are from M_t fits.

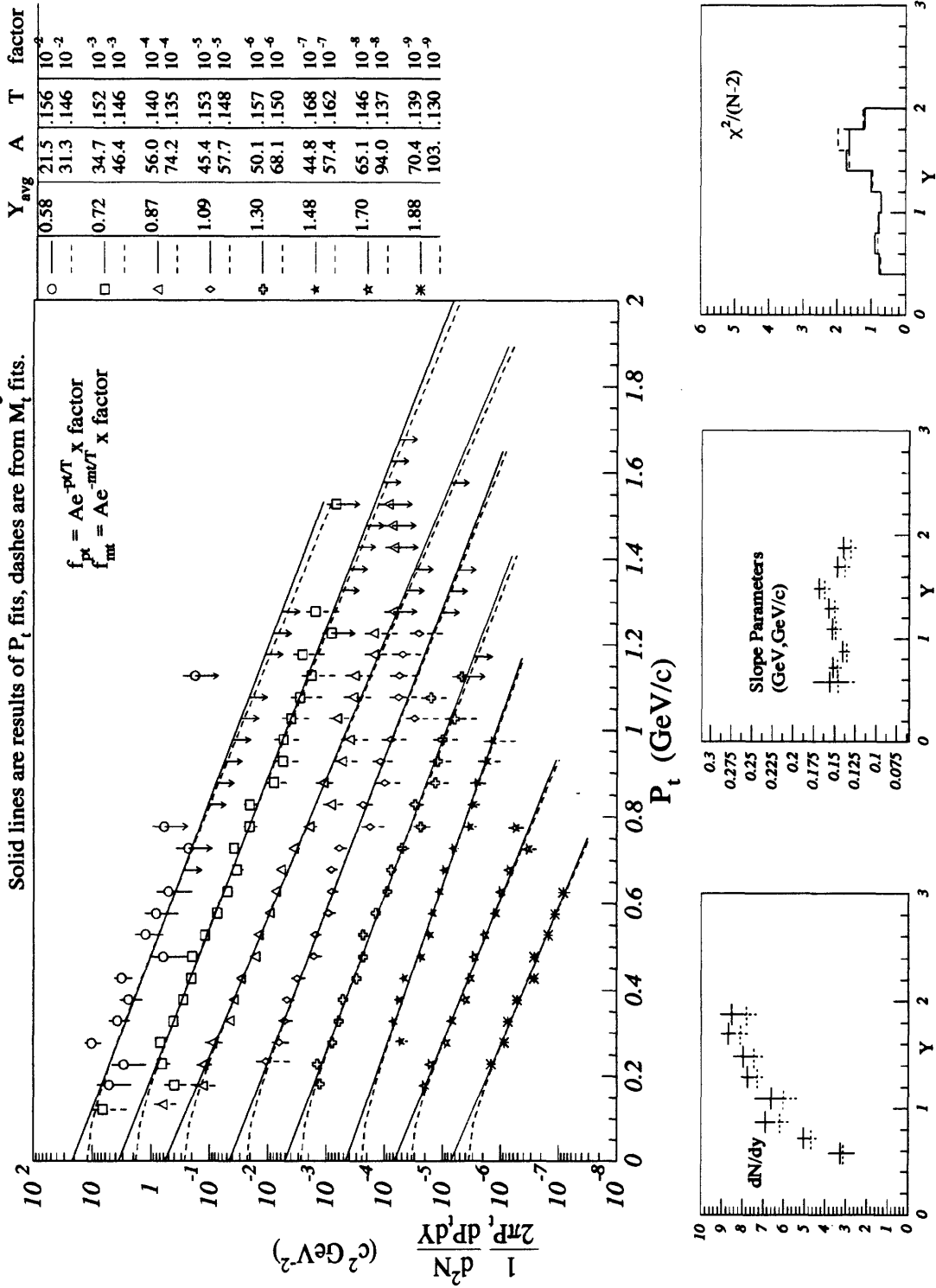


Figure J-6: Yield Summary for $^{28}\text{Si} + ^{197}\text{Au}$ MID: π^-

$^{28}\text{Si} + \text{Au}$ PERP1 : Yield Summary π^+

Solid lines are results of P_t fits, dashes are from M_t fits.

Symbol	Y_{avg}	A	T	factor
○	0.57	6.01	.168	10^{-2}
□	0.71	8.15	.160	10^{-2}
△	0.89	12.9	.147	10^{-3}
		17.8	.141	10^{-3}
		17.6	.142	10^{-4}
		23.9	.137	10^{-4}
◇	1.38	20.9	.151	10^{-7}
		28.3	.144	10^{-7}

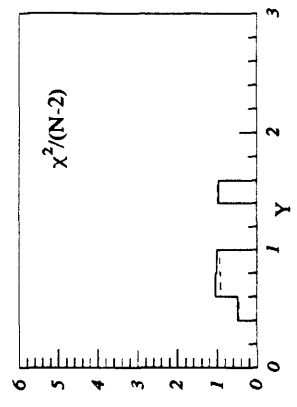
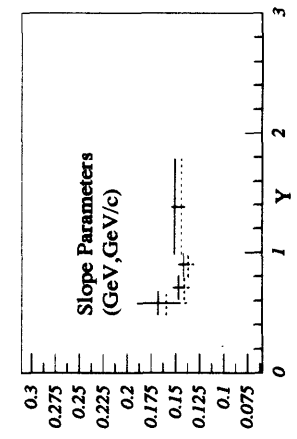
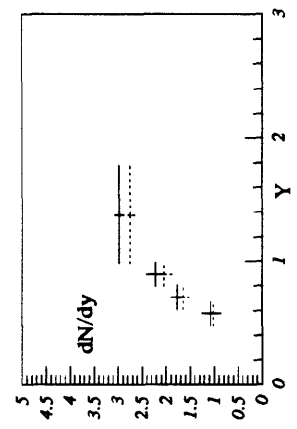
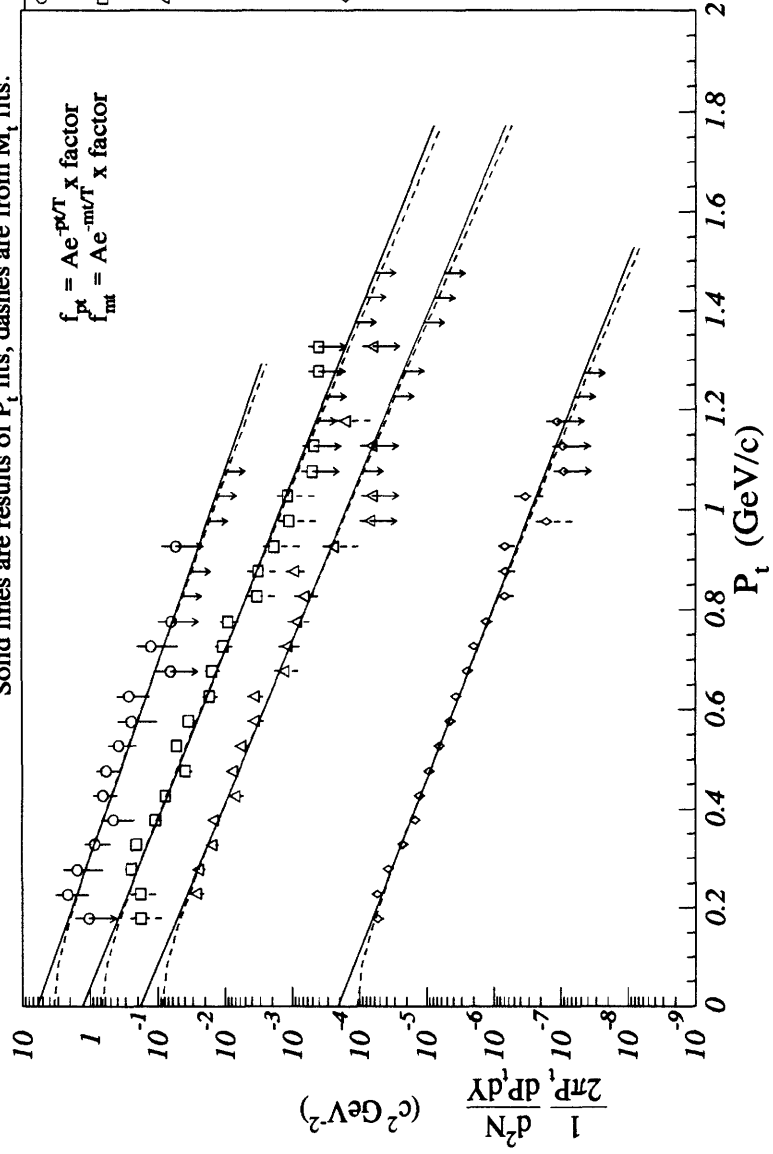


Figure J-7: Yield Summary for $^{28}\text{Si} + ^{197}\text{Au}$ PERP1: π^+

²⁸Si+Au PERP1 : Yield Summary π^-

Solid lines are results of P_t fits, dashes are from M_t fits.

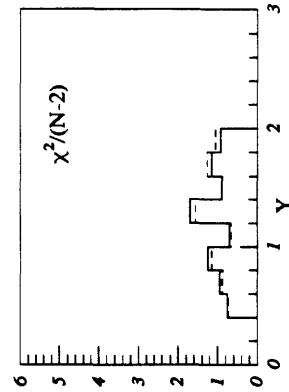
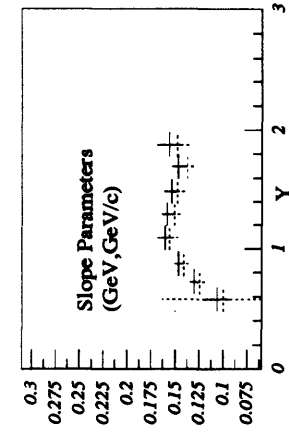
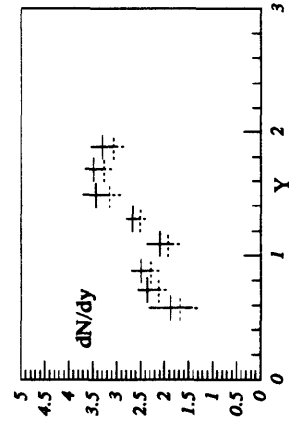
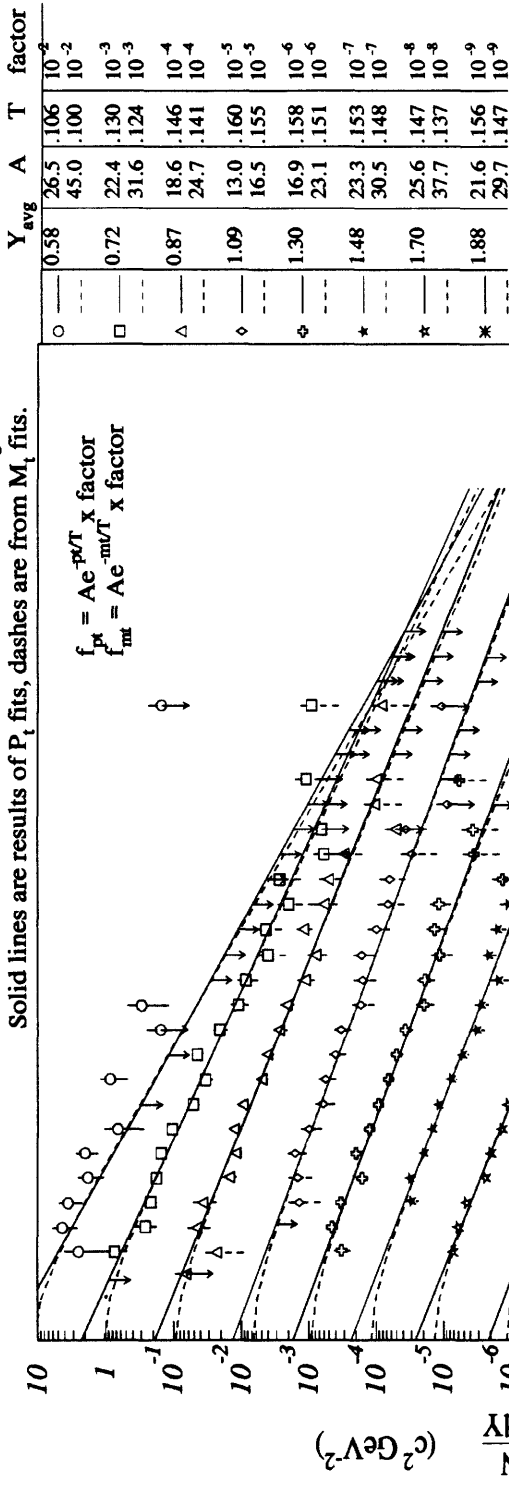


Figure J-8: Yield Summary for ²⁸Si + ¹⁹⁷Au PERP1: π^-

Appendix K

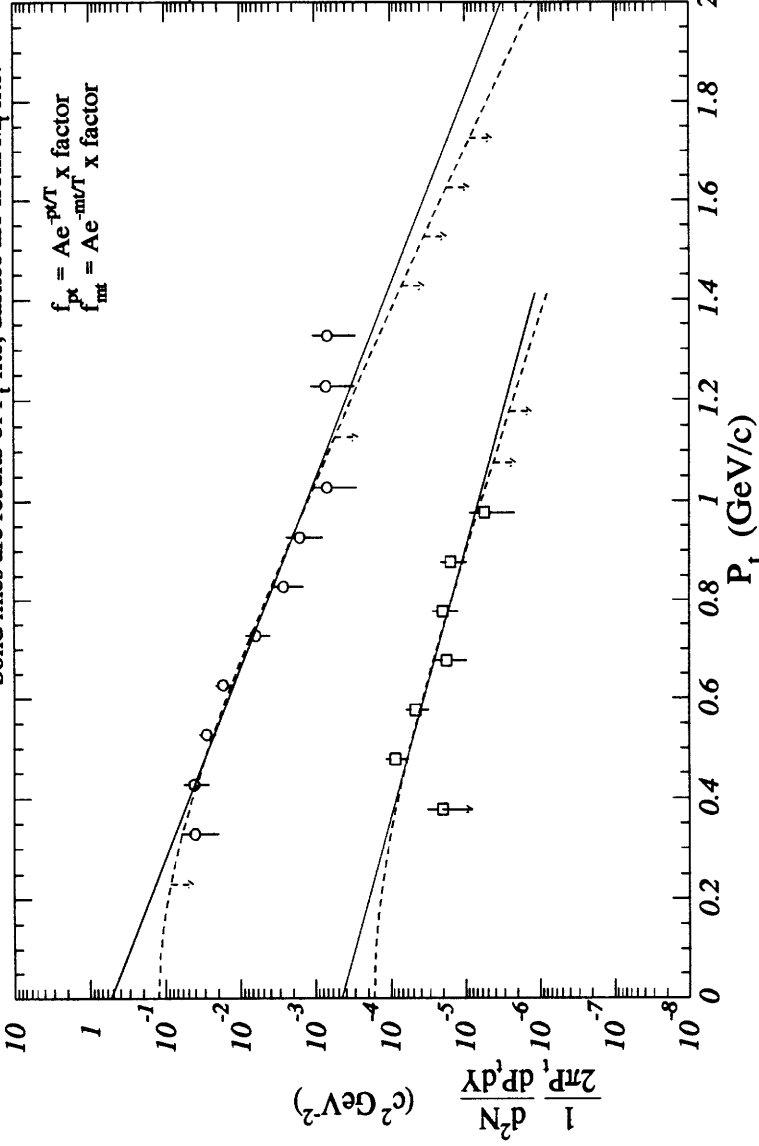
Yield Summary: $^{28}\text{Si} + ^{27}\text{Al} : \text{Kaons}$

²⁸Si+Al CENT1 : Yield Summary K+

Solid lines are results of P_t fits, dashes are from M_t fits.

$$f_{pt} = A e^{-pT} \times \text{factor}$$

$$f_{mt} = A e^{-mvT} \times \text{factor}$$



Y _{avg}	A	T	factor
0.68	5.27	.166	10 ⁻³
47.2	.136		10 ⁻³
1.23	4.50	.236	10 ⁻⁶
	23.7	.187	10 ⁻⁶

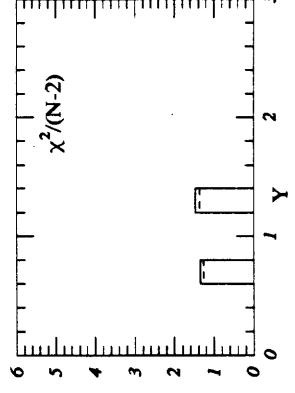
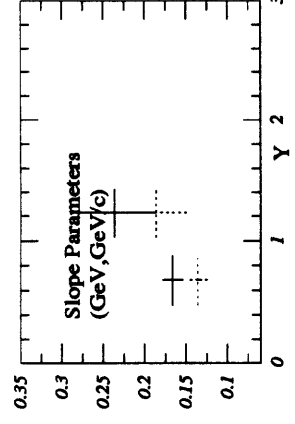
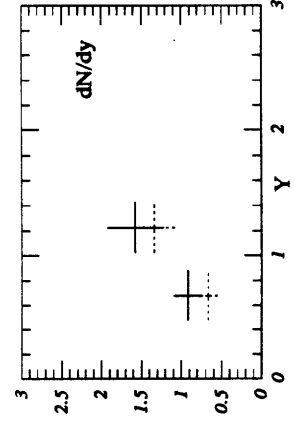


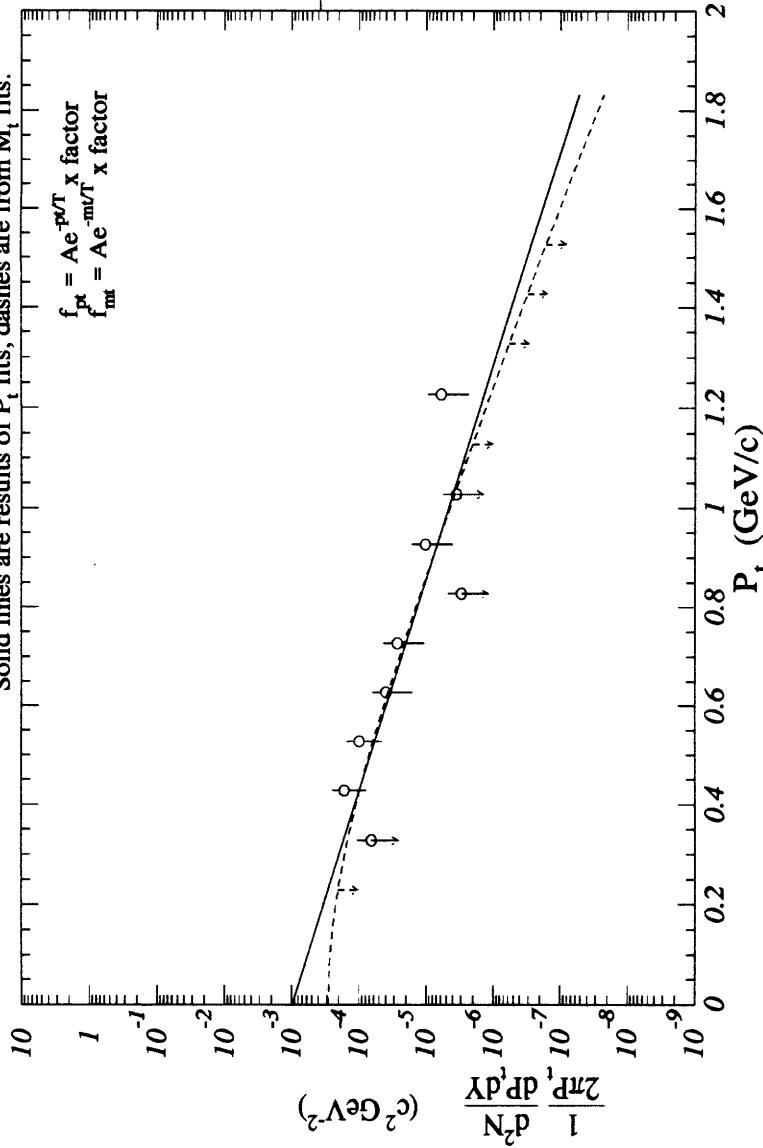
Figure K-1: Yield Summary for ²⁸Si + ²⁷Al CENT1: K+

²⁸Si+Al CENT1 : Yield Summary K-

Solid lines are results of P_t fits, dashes are from M_t fits.

$$f_{pt} = Ae^{-pT} \times \text{x factor}$$

$$f_{mt} = Ae^{-mT} \times \text{x factor}$$



Y _{avg}	A	T factor
0.88	0.96	.187 10 ⁻⁵
7.87	.149	10 ⁻⁵

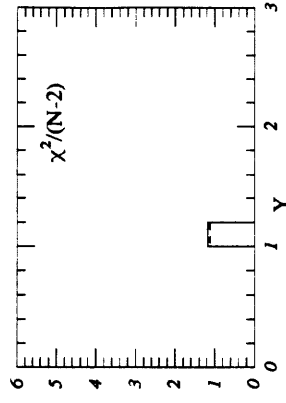
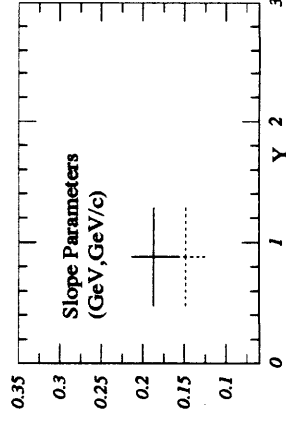
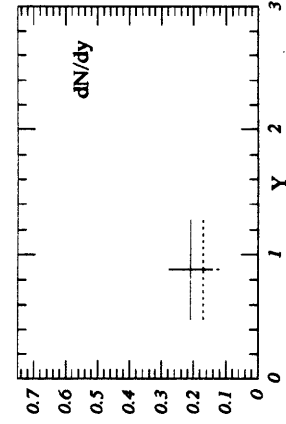


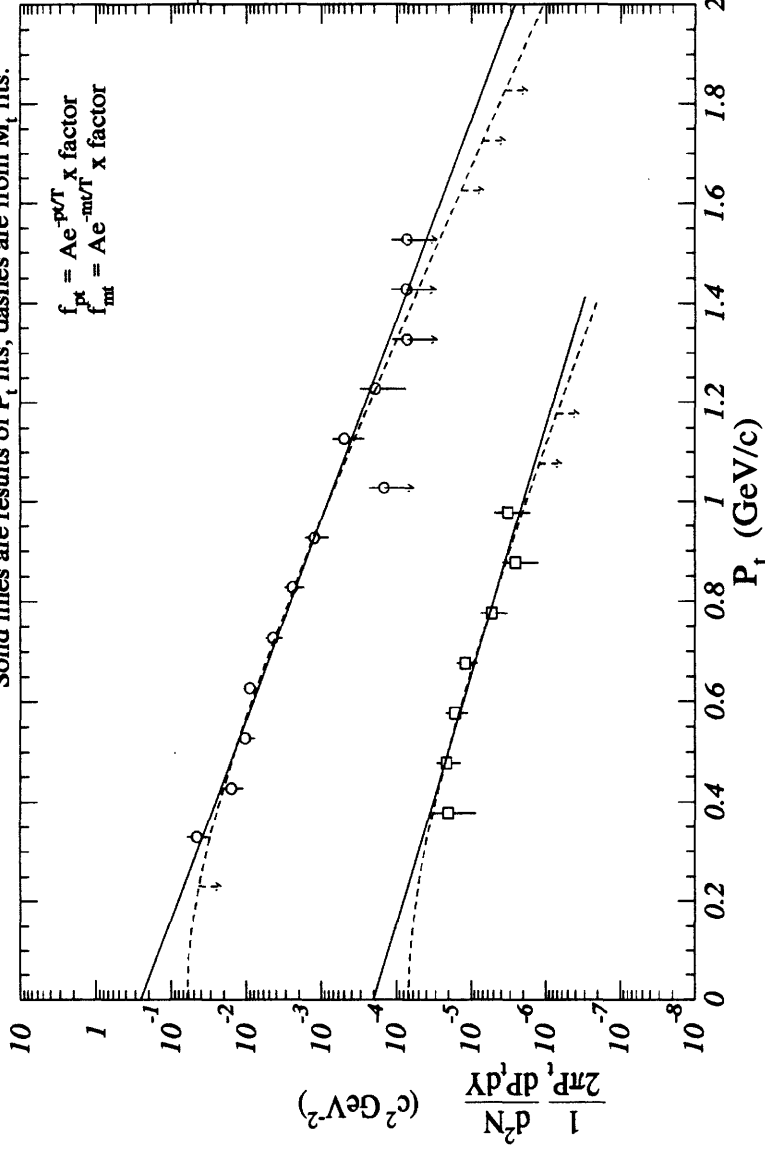
Figure K-2: Yield Summary for ²⁸Si + ²⁷Al CENT1: K-

²⁸Si + ²⁷Al CENT2: Yield Summary K+

Solid lines are results of P_t fits, dashes are from M_t fits.

$$f_{pt} = Ae^{-pT/\Gamma} \times \text{x factor}$$

$$f_{mt} = Ae^{-mT/\Gamma} \times \text{x factor}$$



Y _{avg}	A	T	factor
0.68	2.50	.174	10 ⁻³
1.23	19.4	.143	10 ⁻³
	2.01	.216	10 ⁻⁶
	12.3	.171	10 ⁻⁶

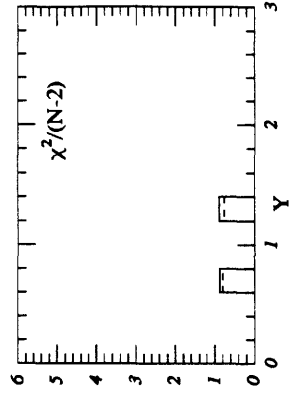
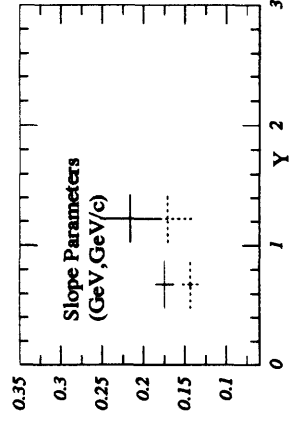
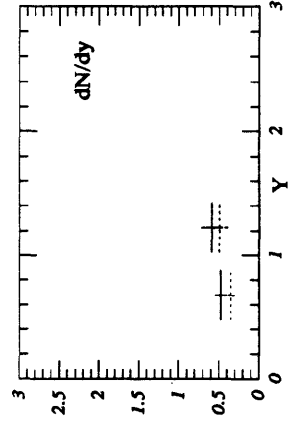


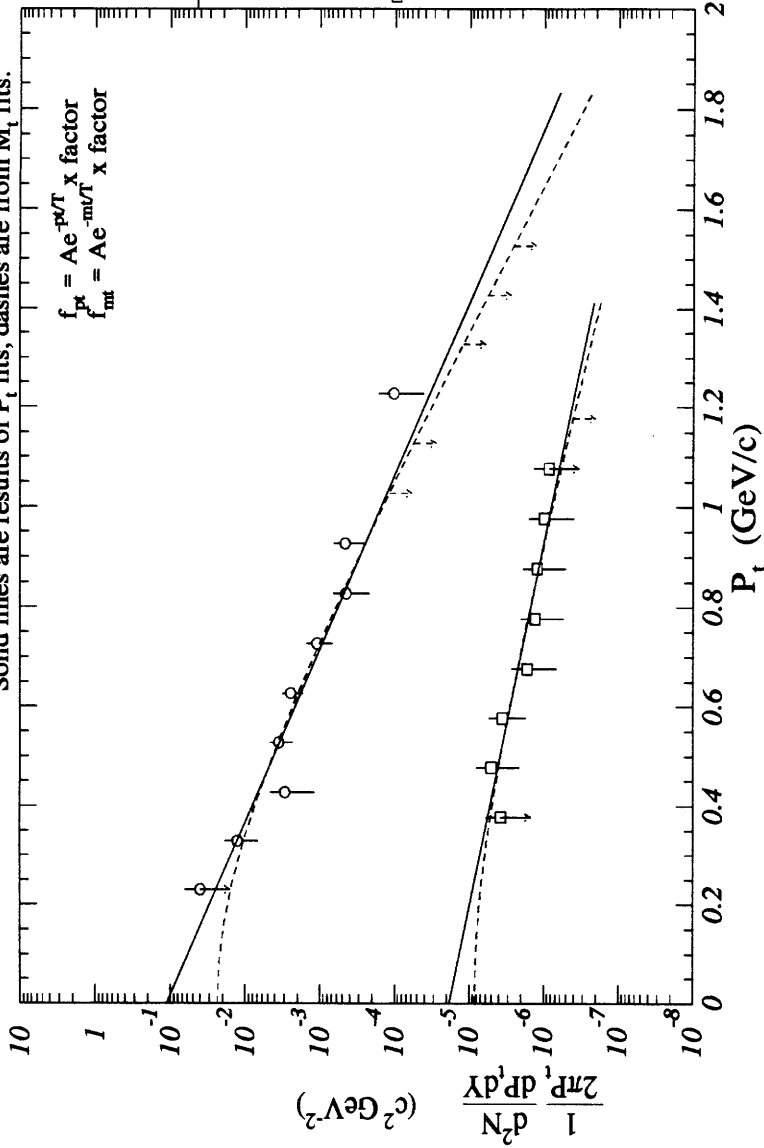
Figure K-3: Yield Summary for ²⁸Si + ²⁷Al CENT2: K+

²⁸Si + ²⁷Al MID : Yield Summary K⁺

Solid lines are results of P_t fits, dashes are from M_t fits.

$$f_{pt} = A e^{-p/T} \times \text{factor}$$

$$f_{mt} = A e^{-m/T} \times \text{factor}$$



Y _{avg}	A	T	factor
0.68	1.12	.151	10 ⁻⁹
	13.6	.122	10 ⁻³
1.23	0.18	.318	10 ⁻⁶
	0.57	.258	10 ⁻⁶

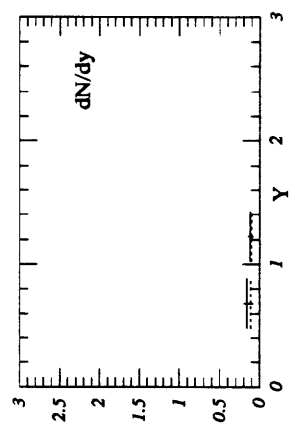
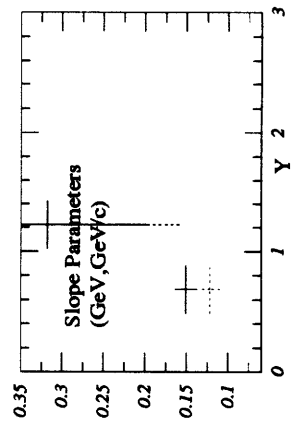
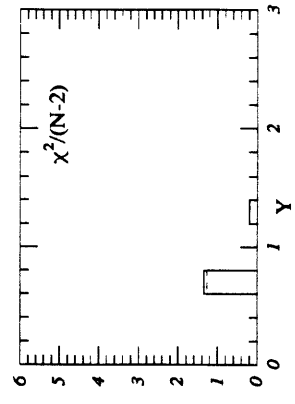


Figure K-4: Yield Summary for ²⁸Si + ²⁷Al MID: K⁺

Appendix L

Yield Summary: $^{28}\text{Si} + ^{64}\text{Cu}$:

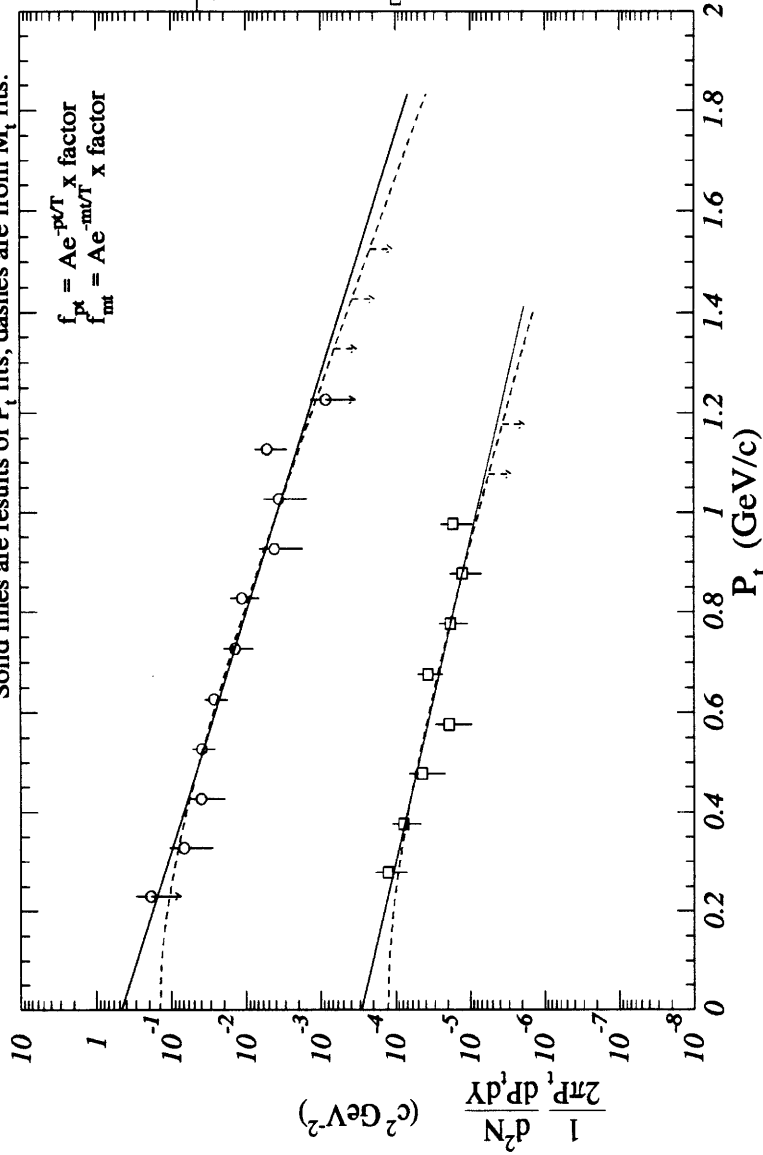
Kaons

²⁸Si+Cu CENT1 : Yield Summary K+

Solid lines are results of P_t fits, dashes are from M_t fits.

$$f_{pk} = Ae^{-pT} x \text{ factor}$$

$$f_{mt} = Ae^{-mT} x \text{ factor}$$



	Y_{avg}	A	T	factor
○	0.71	4.61	.207	10^{-9}
□	1.24	2.82	.281	10^{-6}
○	25.8	.171		10^{-3}
□	12.1	.219		10^{-6}

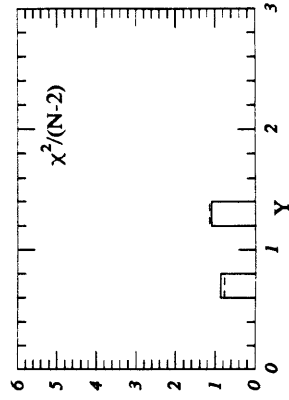
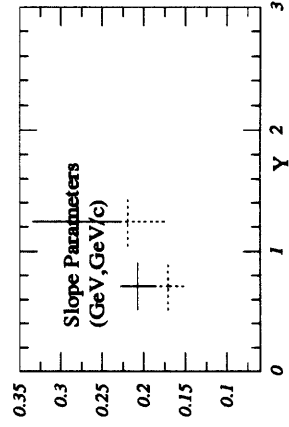
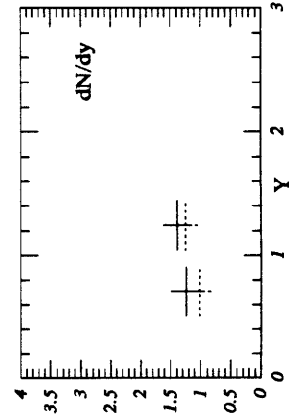


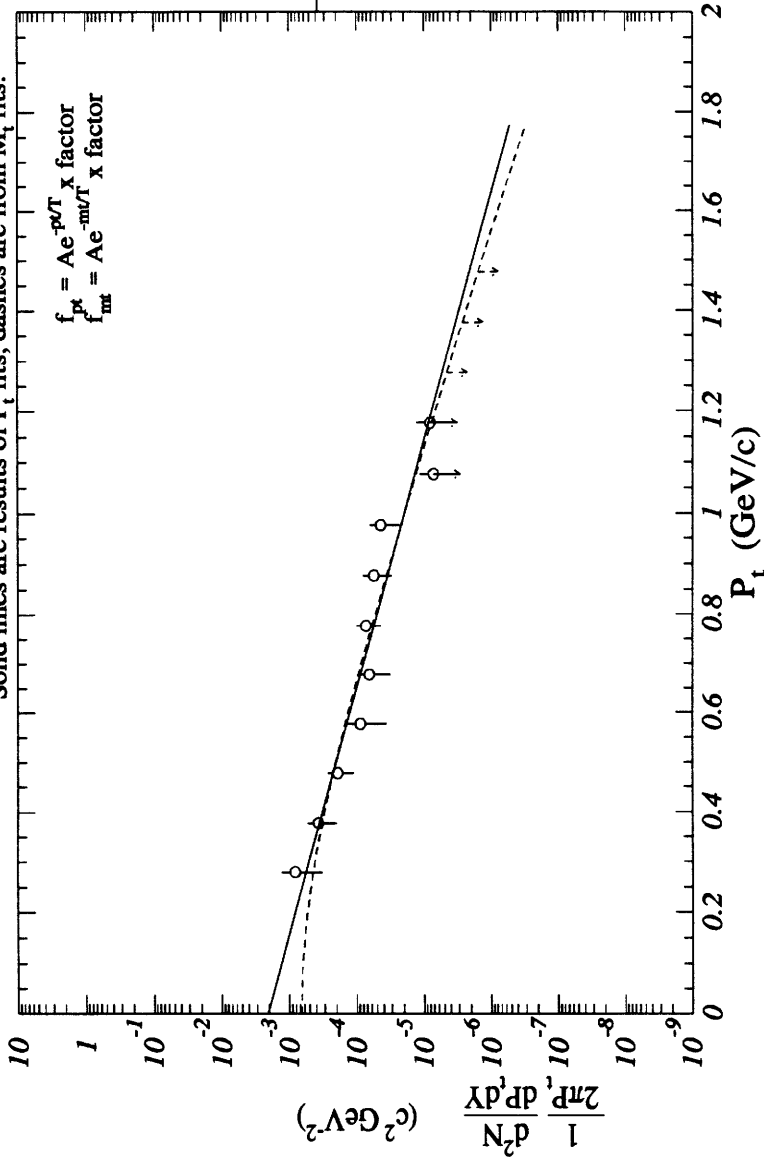
Figure L-1: Yield Summary for ²⁸Si + ⁶⁴Cu CENT1: K+

²⁸Si+Cu CENT1 : Yield Summary K-

Solid lines are results of P_t fits, dashes are from M_t fits.

$$f_{int} = Ae^{-p/T} \times \text{x factor}$$

$$f_{ext} = Ae^{-mv/T} \times \text{x factor}$$



	Y _{avg}	A	T	factor
—	0.92	2.07	.214	10 ⁻⁵
- - -	11.2	.175		10 ⁻⁵

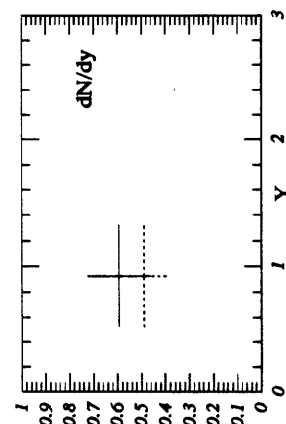
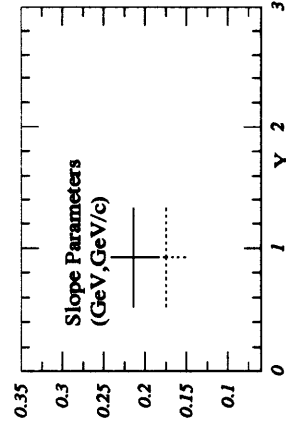
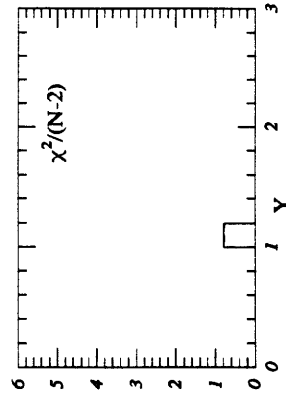


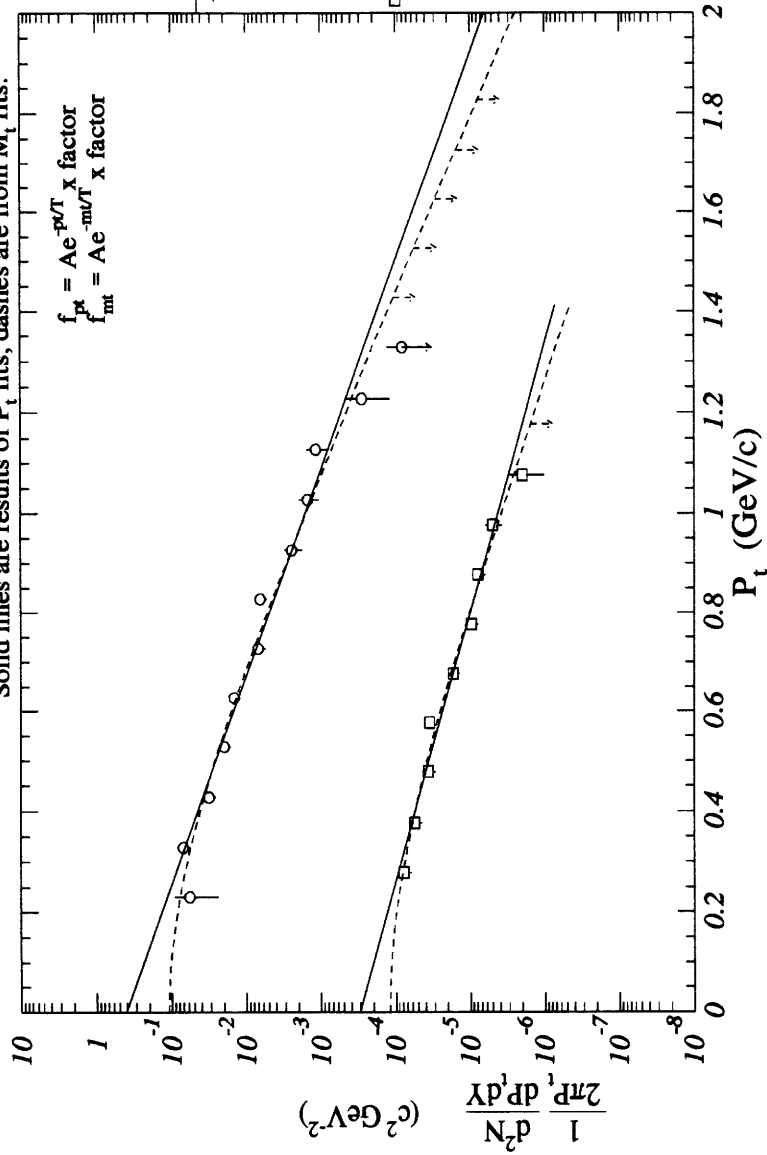
Figure L-2: Yield Summary for ²⁸Si + ⁶⁴Cu CENT1: K-

²⁸Si+Cu CENT2: Yield Summary K+

Solid lines are results of P_t fits, dashes are from M_t fits.

$$f_{pt} = Ae^{-pT/T} \times \text{x factor}$$

$$f_{mt} = Ae^{-mT/T} \times \text{x factor}$$



Y _{avg}	A	T	factor
0.70	4.02	1.81	10 ⁻³
	31.9	1.46	10 ⁻³
1.23	3.03	2.34	10 ⁻⁶
	19.0	1.79	10 ⁻⁶

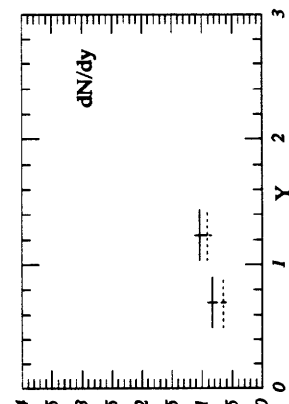
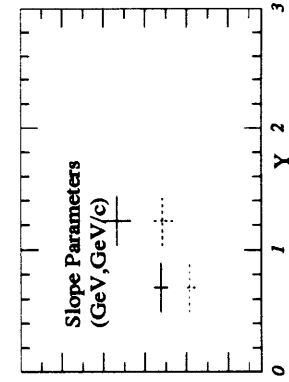
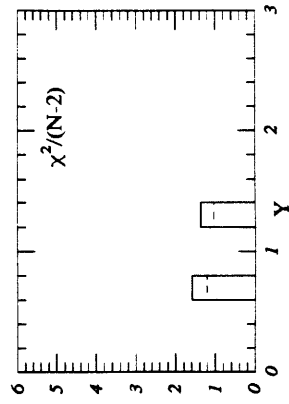
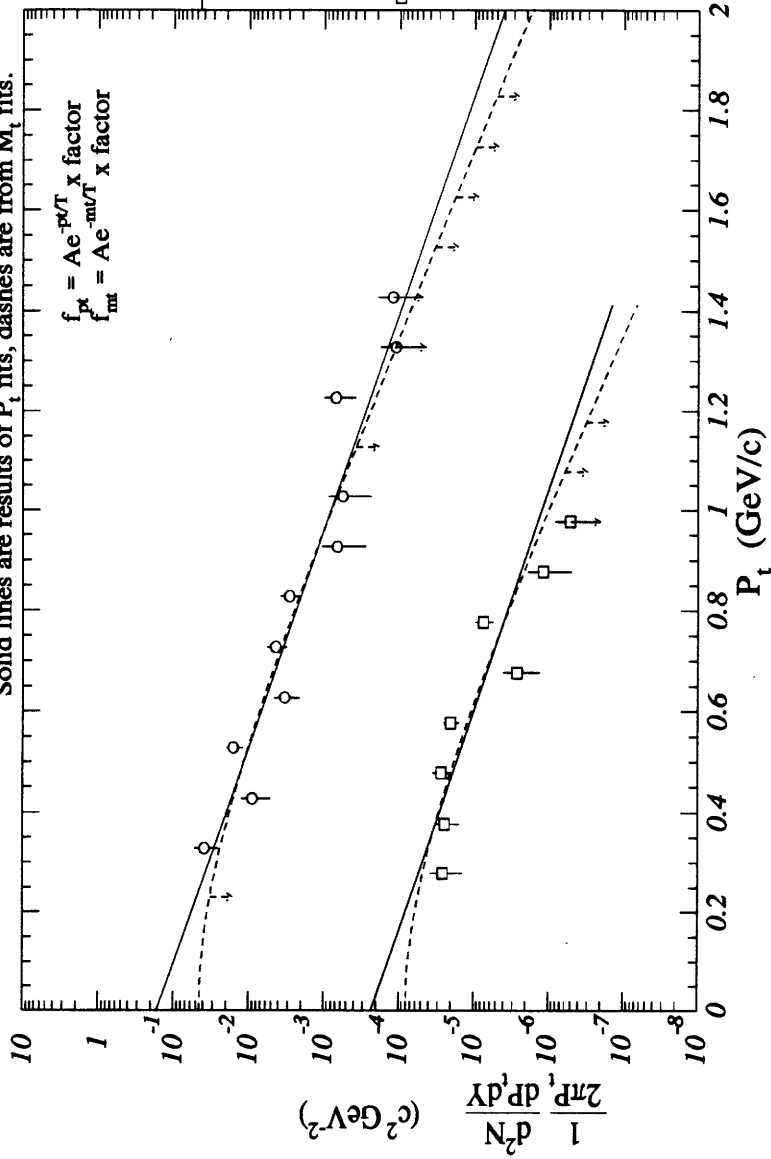


Figure L-3: Yield Summary for ²⁸Si + ⁶⁴Cu CENT2: K+

$^{28}\text{Si} + \text{Cu MID} : \text{Yield Summary } \text{K}^+$

Solid lines are results of P_t fits, dashes are from M_t fits.



$$f_{pt}^{\text{K}^+} = A e^{-P_t/T} \times \text{factor}$$

$$f_{mt}^{\text{K}^+} = A e^{-m v/T} \times \text{factor}$$

Y _{avg}	A	T	factor
0.70	1.62	.188	10^{-3}
	11.4	.153	10^{-3}
1.23	2.31	.191	10^{-6}
	26.7	.141	10^{-6}

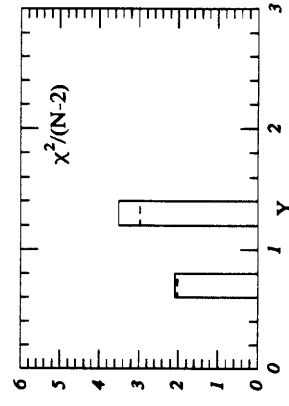
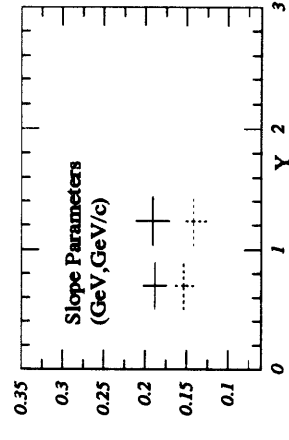
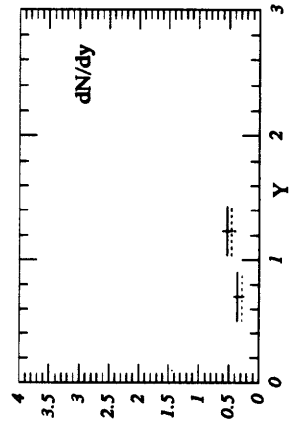


Figure L-4: Yield Summary for $^{28}\text{Si} + ^{64}\text{Cu MID}: \text{K}^+$

Appendix M

Yield Summary: $^{28}\text{Si} + ^{197}\text{Au}$:

Kaons

²⁸Si+Au CENT1 : Yield Summary K⁺

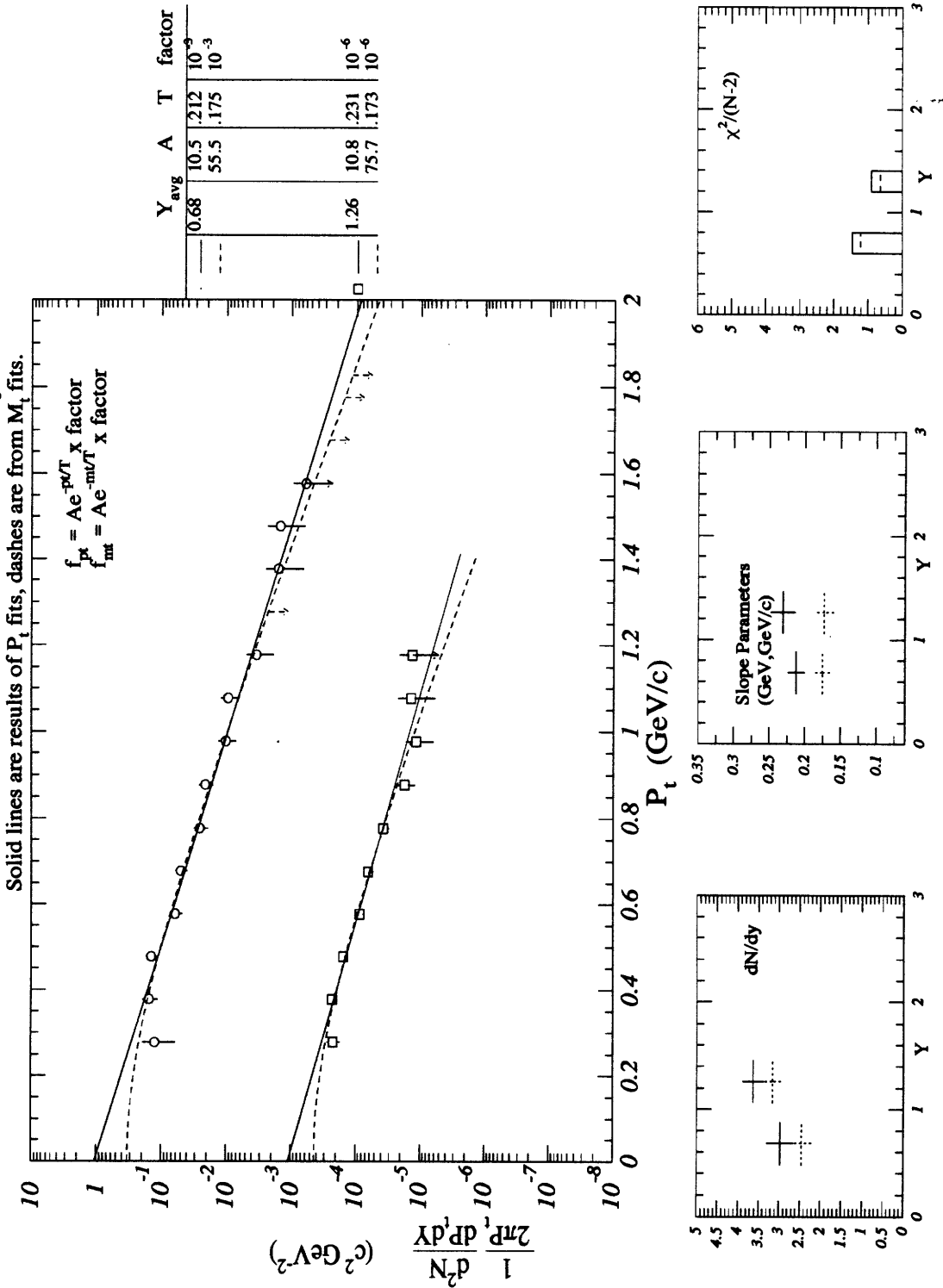


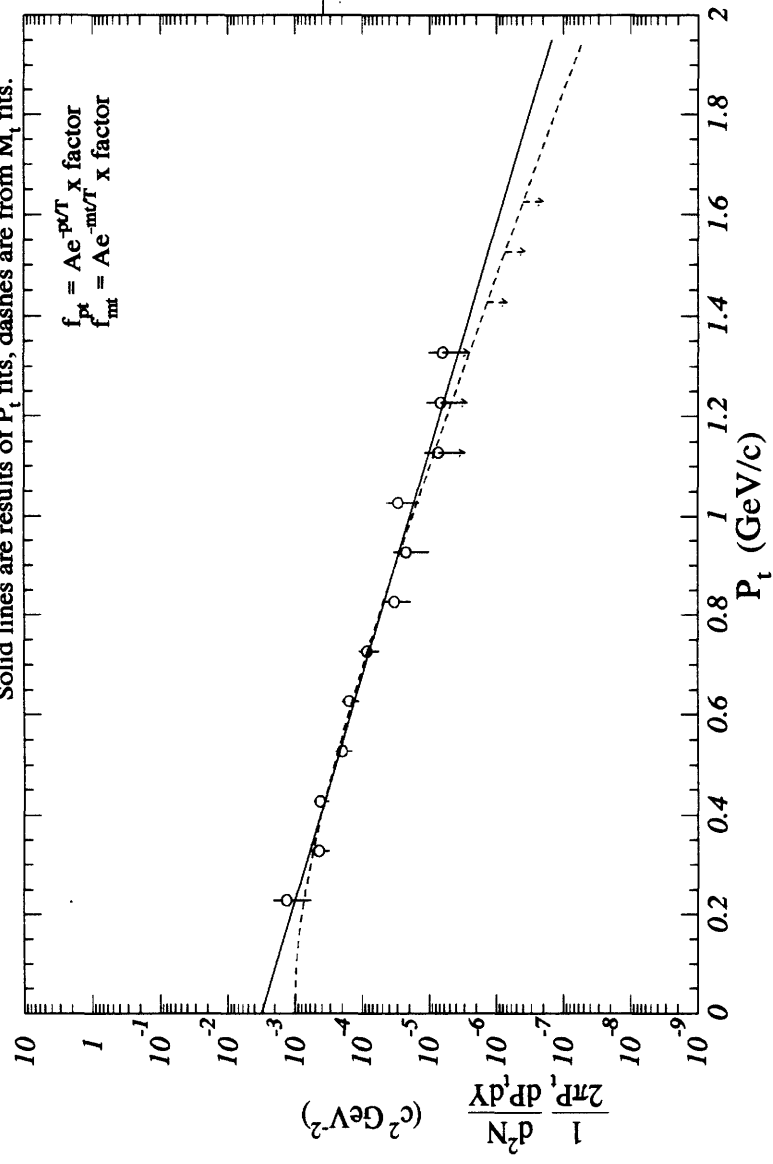
Figure M-1: Yield Summary for ²⁸Si + ¹⁹⁷Au CENT1: K⁺

²⁸Si+Au CENT1 : Yield Summary K-

Solid lines are results of P_t fits, dashes are from M_t fits.

$$f_{pt}^x = A e^{-p_t/T} \times \text{x factor}$$

$$f_{mt}^x = A e^{-m_t/T} \times \text{x factor}$$



Y _{avg}	A	T factor
0.95	3.13	196 10 ⁻⁵
	24.9	154 10 ⁻⁵

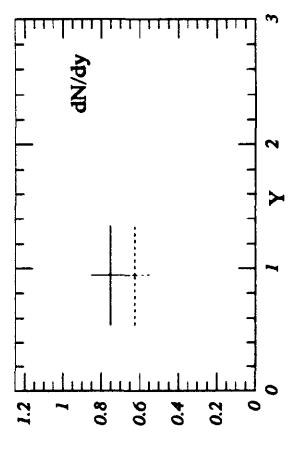
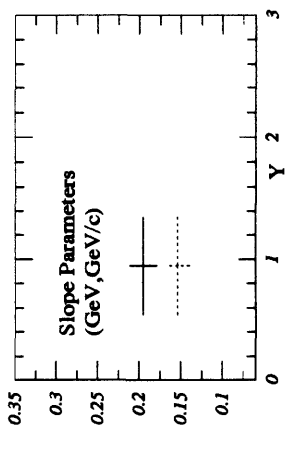
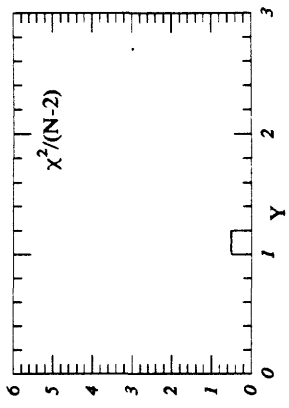


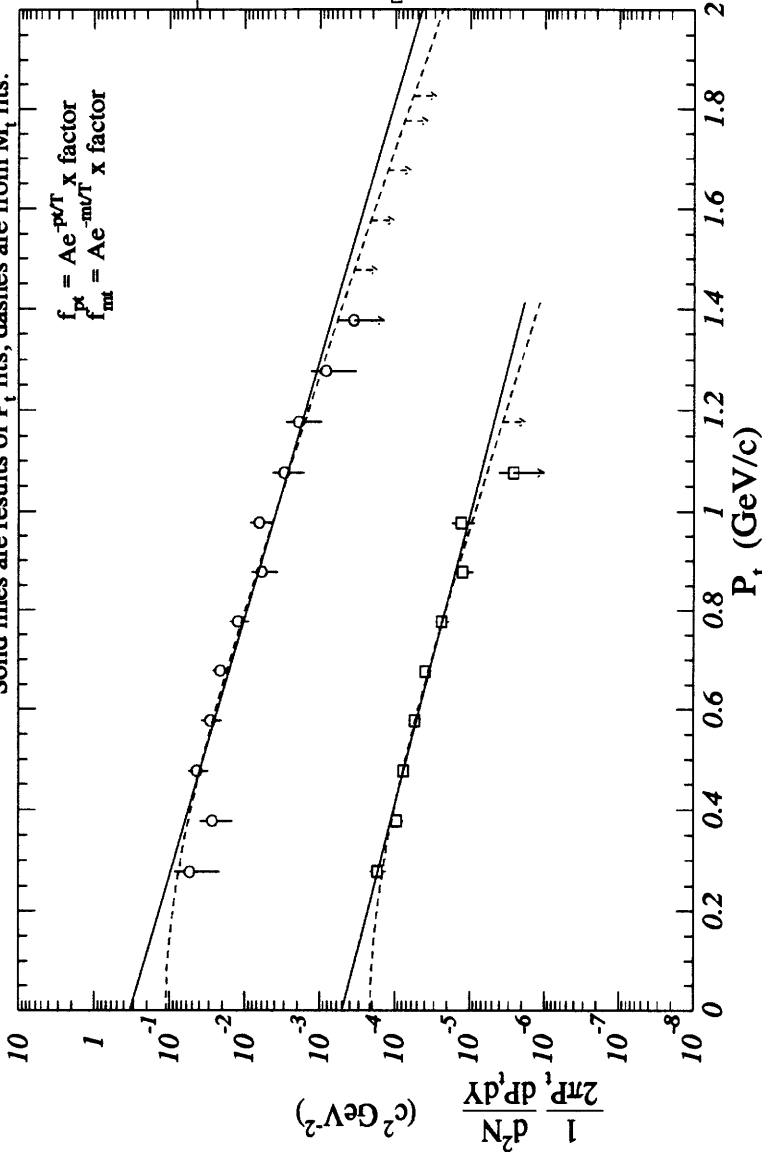
Figure M-2: Yield Summary for ²⁸Si + ¹⁹⁷Au CENT1: K-

²⁸Si+Au CENT2: Yield Summary K+

Solid lines are results of P_t fits, dashes are from M_t fits.

$$f_{pt}^x = A e^{-p_t/T} \quad x \text{ factor}$$

$$f_{mt}^x = A e^{-m_t/T} \quad x \text{ factor}$$



Y _{avg}	A	T	factor
0.68	3.27	.224	10 ⁻³
1.25	16.3	.184	10 ⁻³
	4.98	.252	10 ⁻⁶
	27.5	.193	10 ⁻⁶

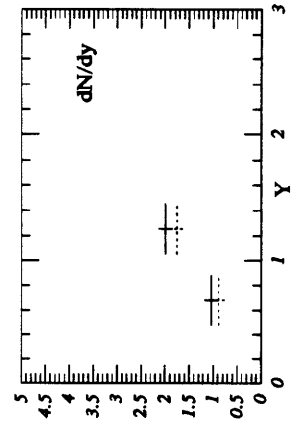
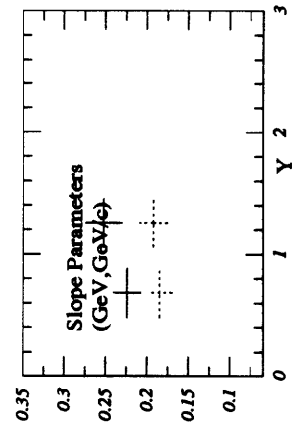
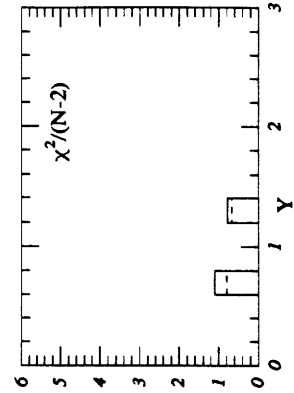


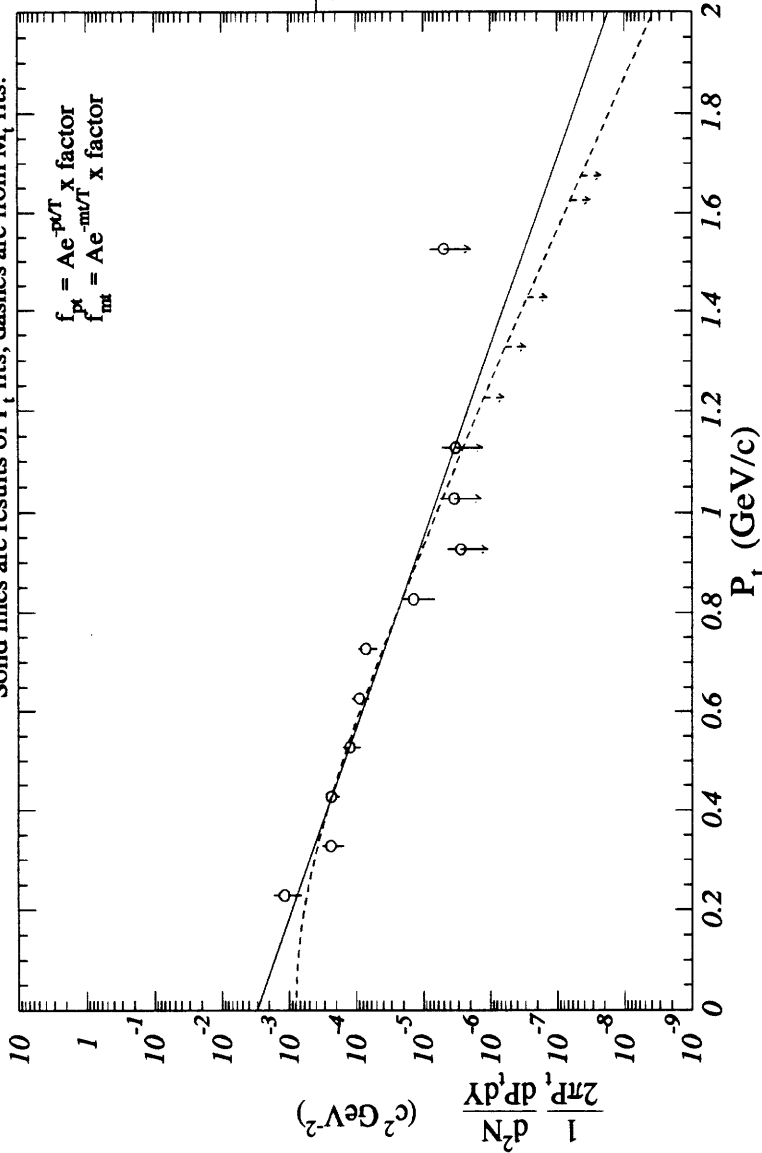
Figure M-3: Yield Summary for ²⁸Si + ¹⁹⁷Au CENT2: K+

$^{28}\text{Si} + \text{Au}$ CENT2 : Yield Summary K^-

Solid lines are results of P_t fits, dashes are from M_t fits.

$$f_{pt} = A e^{-pT/T} \times \text{factor}$$

$$f_{mt} = A e^{-mT/T} \times \text{factor}$$



Y_{avg}	A	T	factor
0.93	2.94	1.166	10^{-5}
	39.1	1.127	10^{-5}

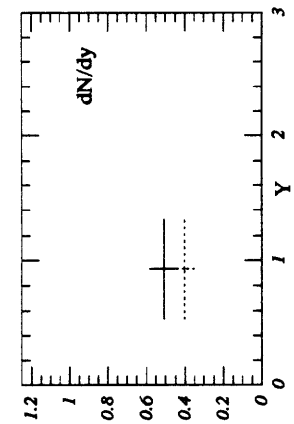
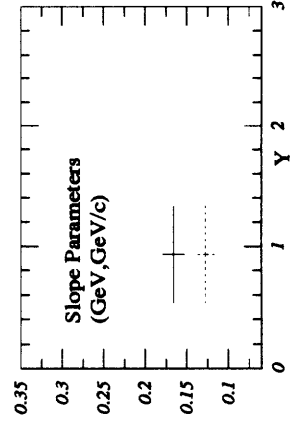
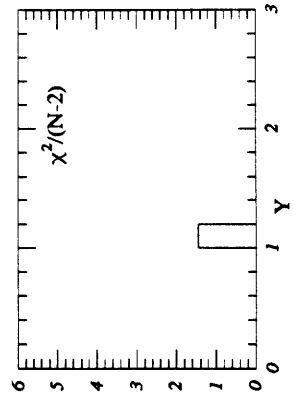


Figure M-4: Yield Summary for $^{28}\text{Si} + ^{197}\text{Au}$ CENT2: K^-

Appendix N

Yield Summary: $^{28}\text{Si} + \text{A} : \text{Protons}$

²⁸Si+Al CENT1 : Yield Summary Protons

Solid lines are results of Boltzmann fits, dashes are from M_T fits.

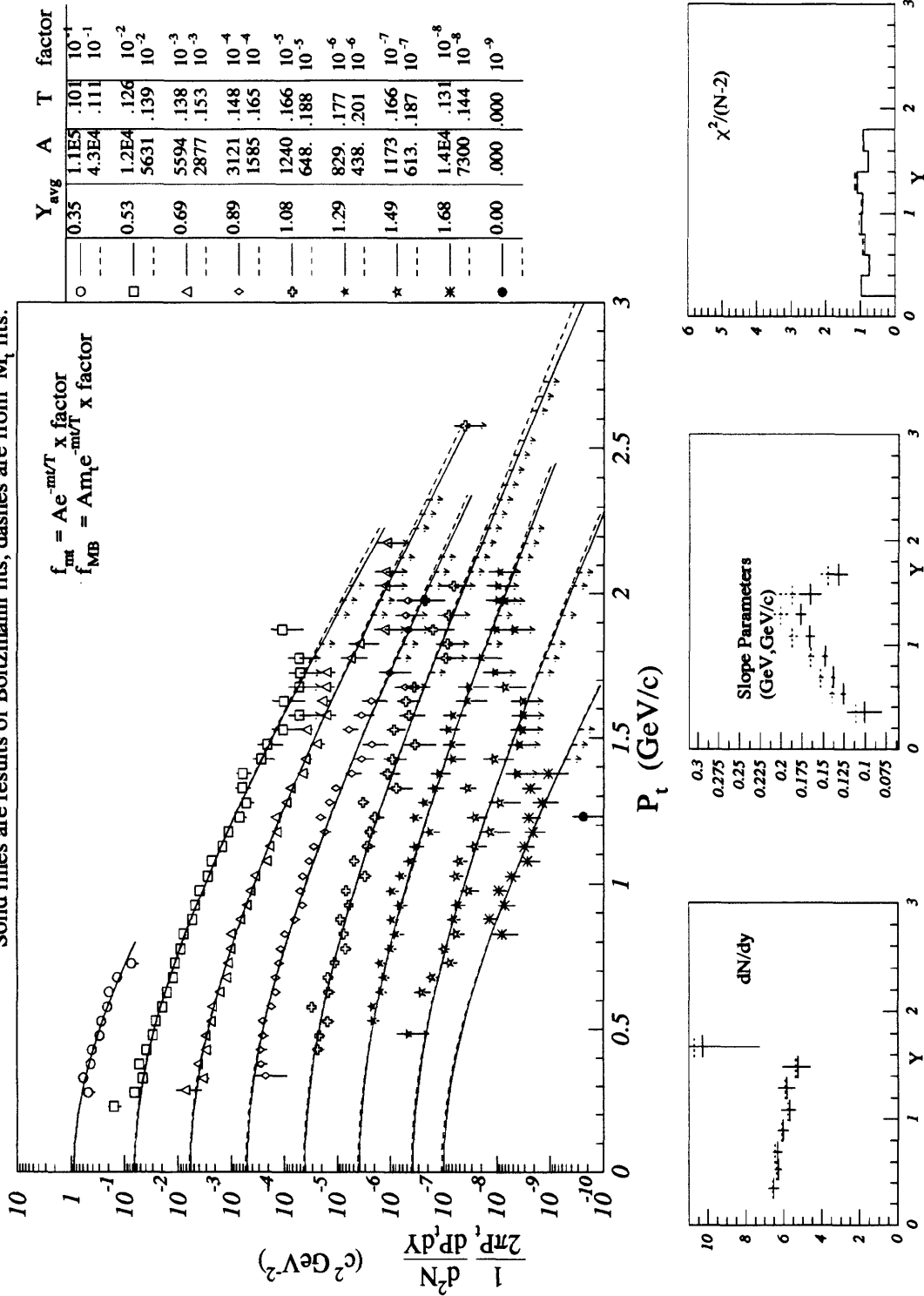


Figure N-1: Yield Summary for ²⁸Si + ²⁷Al CENT1: Protons

²⁸Si+Al CENT2: Yield Summary Protons

Solid lines are results of Boltzmann fits, dashes are from M_1 fits.

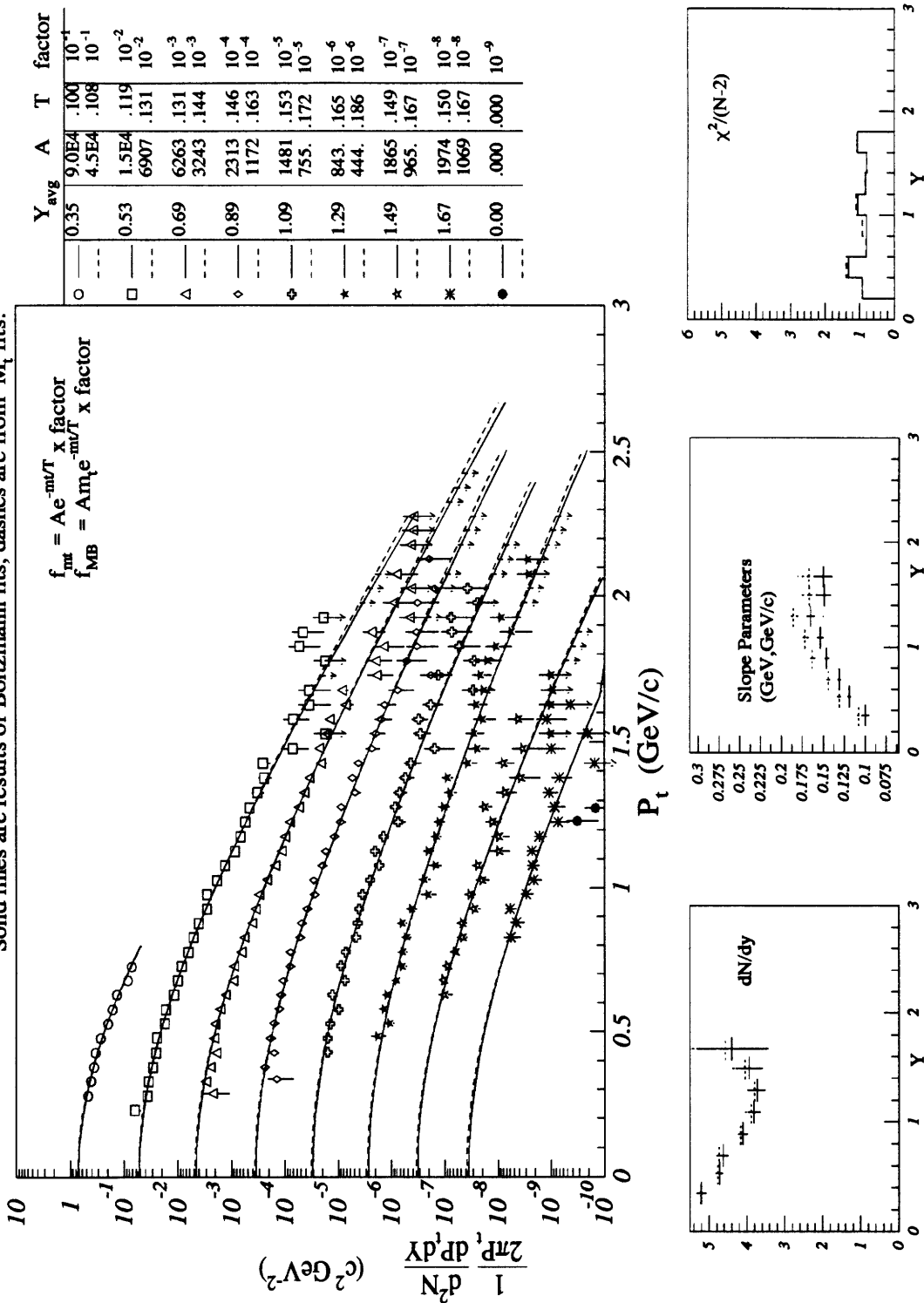


Figure N-2: Yield Summary for ²⁸Si + ²⁷Al CENT2: Protons

²⁸Si + Al MID : Yield Summary Protons

Solid lines are results of Boltzmann fits, dashes are from M_t fits.

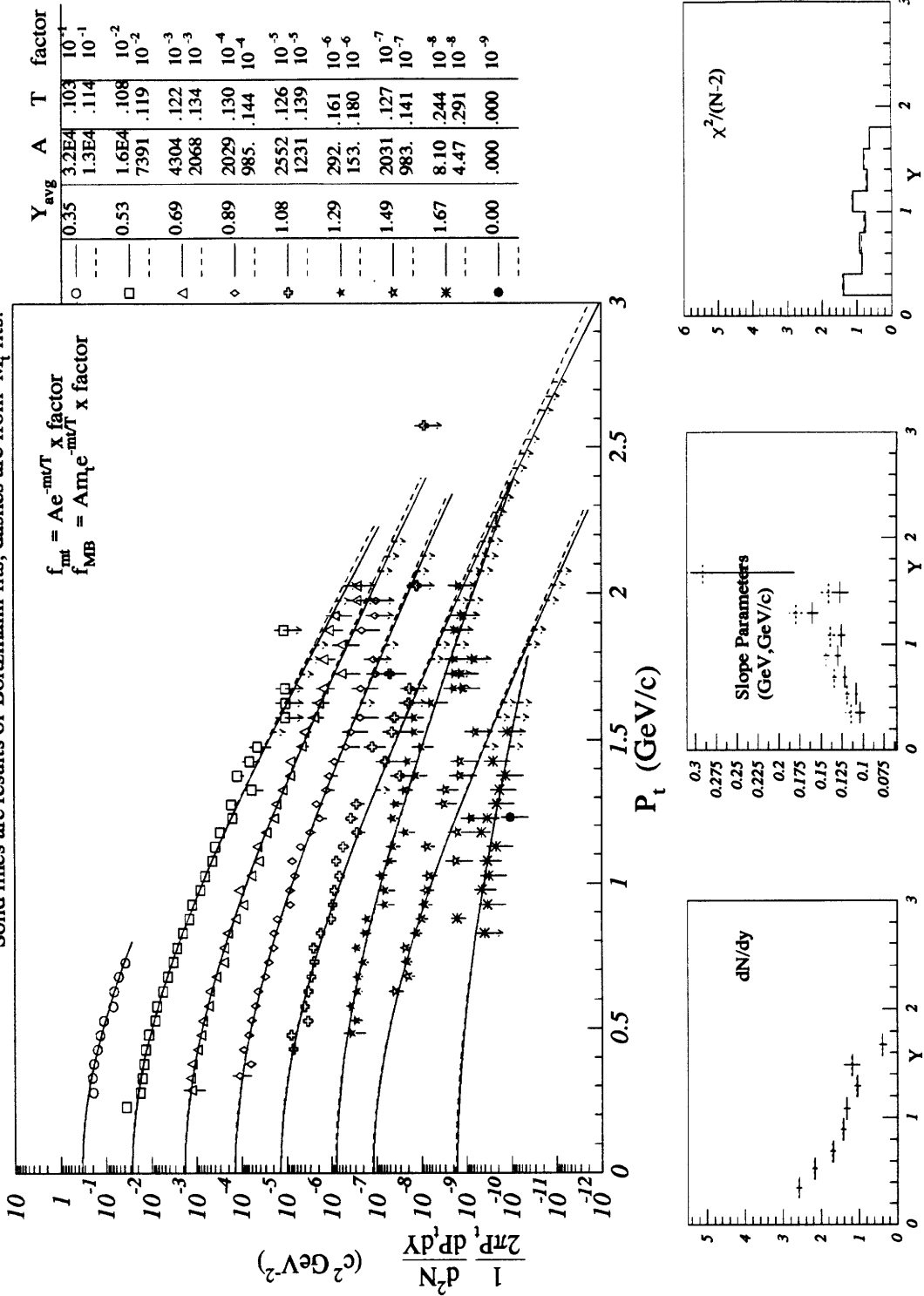
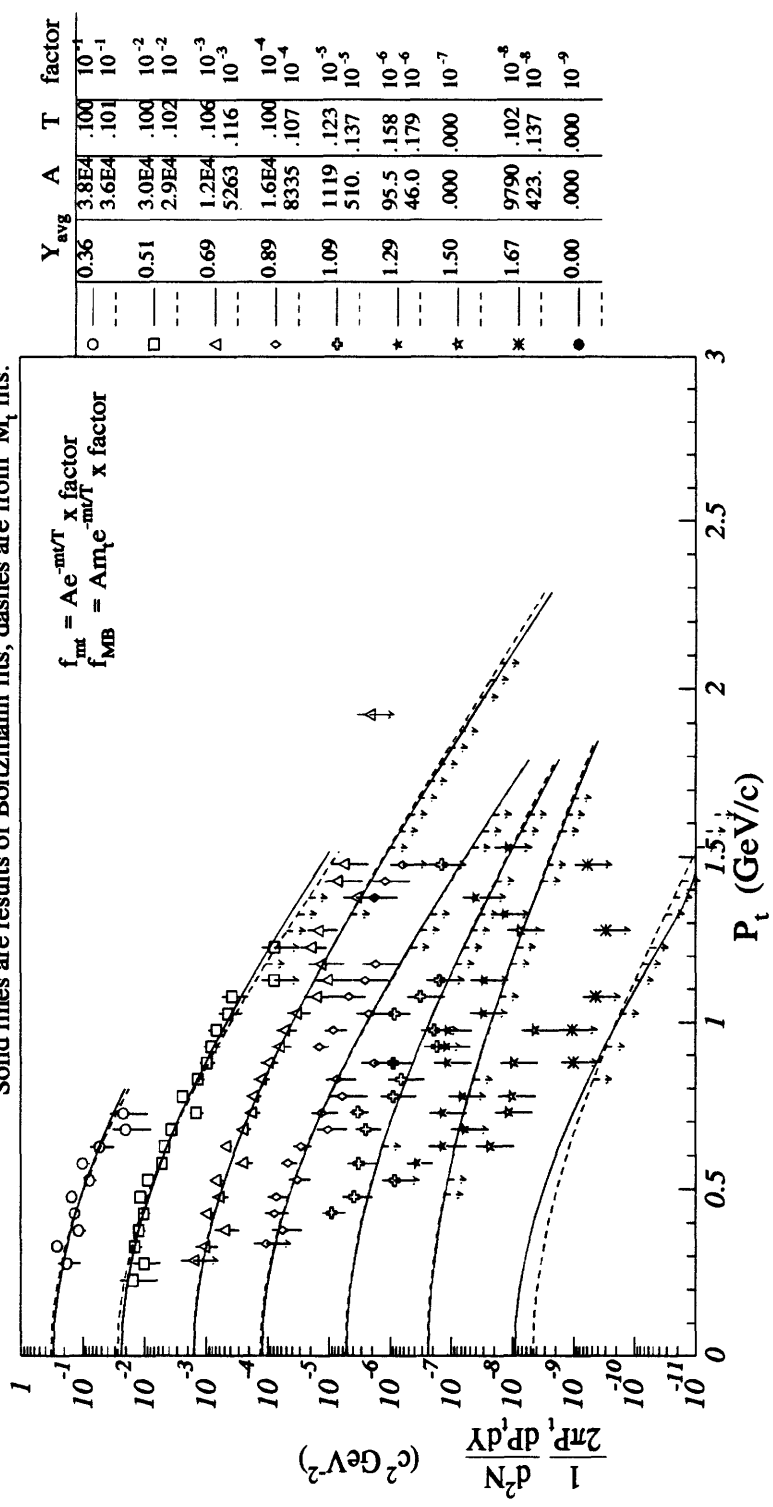


Figure N-3: Yield Summary for ²⁸Si + ²⁷Al MID: Protons

²⁸Si+Al PERP1 : Yield Summary Protons

Solid lines are results of Boltzmann fits, dashes are from M_t fits.



Y	Y _{avg}	A	T	factor
○	0.36	3.8E4	.100	10 ⁻¹
□	0.51	3.6E4	.101	10 ⁻¹
△	0.69	3.0E4	.100	10 ⁻²
◇	0.89	2.9E4	.102	10 ⁻²
◆	1.09	1.2E4	.106	10 ⁻³
♣	1.29	5263	.116	10 ⁻³
♠	1.50	1.6E4	.100	10 ⁻⁴
♣	1.67	8335	.107	10 ⁻⁴
♠	1.67	1119	.123	10 ⁻⁵
♠	1.67	510	.137	10 ⁻⁵
♠	1.67	95.5	.158	10 ⁻⁶
♠	1.67	46.0	.179	10 ⁻⁶
♠	1.67	.000	.000	10 ⁻⁷
♠	1.67	9790	.102	10 ⁻⁸
♠	1.67	423	.137	10 ⁻⁸
♠	1.67	.000	.000	10 ⁻⁹

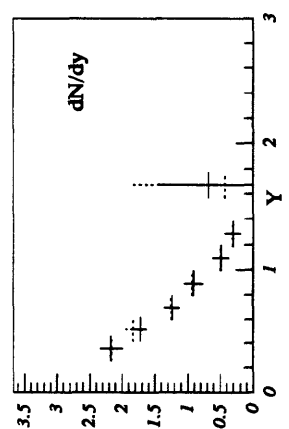
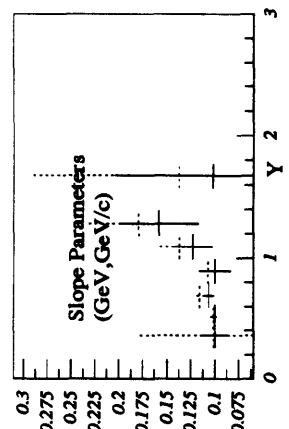
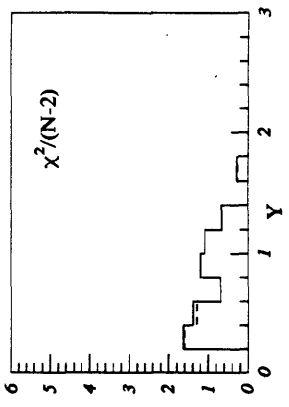
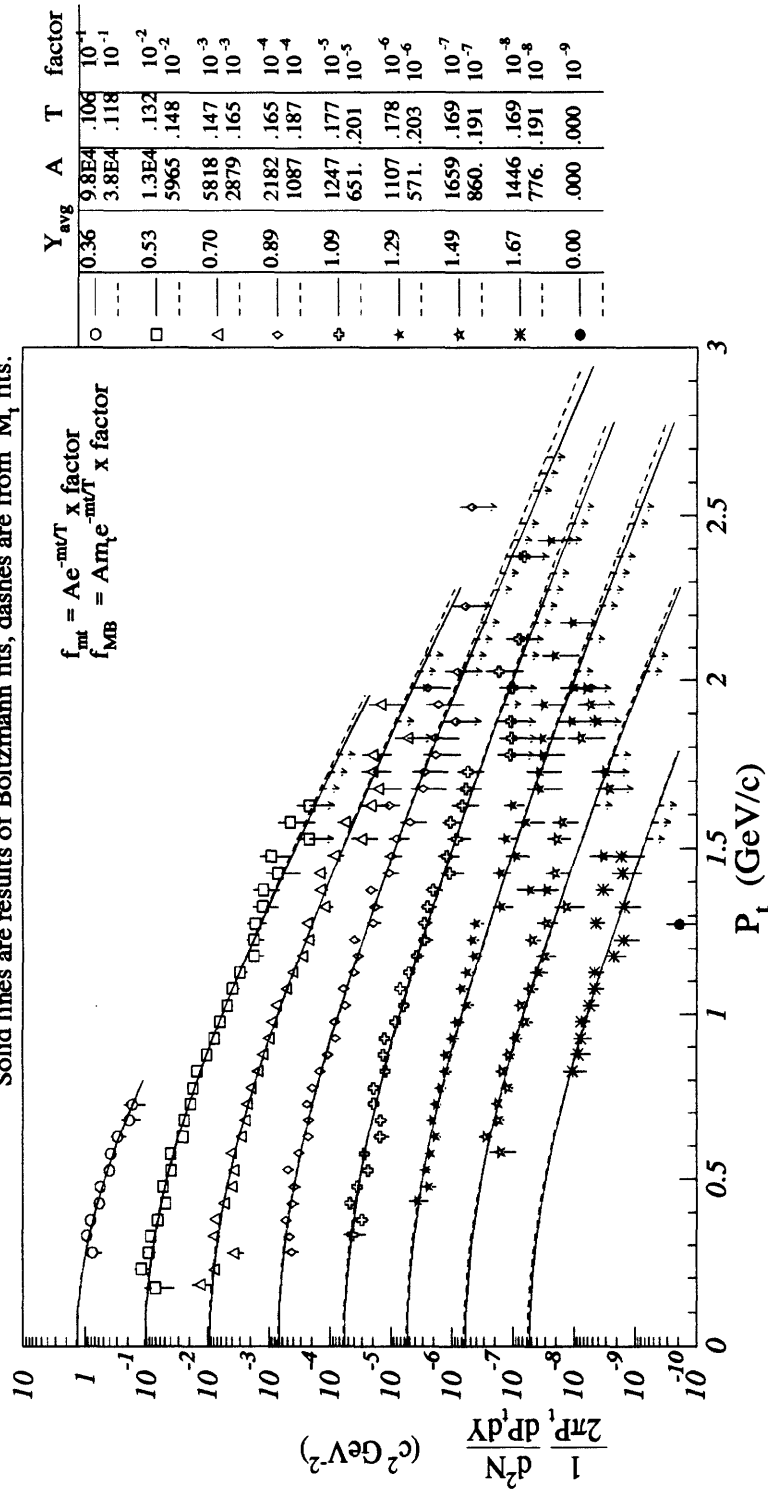


Figure N-4: Yield Summary for ²⁸Si + ²⁷Al PERP1: Protons

²⁸Si+Cu CENT1 : Yield Summary Protons

Solid lines are results of Boltzmann fits, dashes are from M_T fits.



Y avg	A	T	factor
0.36	9.8E4	.109	10 ⁻¹
---	3.8E4	.118	10 ⁻¹
0.53	1.3E4	.132	10 ⁻²
---	5965	.148	10 ⁻²
0.70	5818	.147	10 ⁻³
---	2879	.165	10 ⁻³
0.89	2182	.165	10 ⁻⁴
---	1087	.187	10 ⁻⁴
1.09	1247	.177	10 ⁻⁵
---	651.	.201	10 ⁻⁵
1.29	1107	.178	10 ⁻⁶
---	571.	.203	10 ⁻⁶
1.49	1659	.169	10 ⁻⁷
---	860.	.191	10 ⁻⁷
1.67	1446	.169	10 ⁻⁸
---	776.	.191	10 ⁻⁸
0.00	.000	.000	10 ⁻⁹

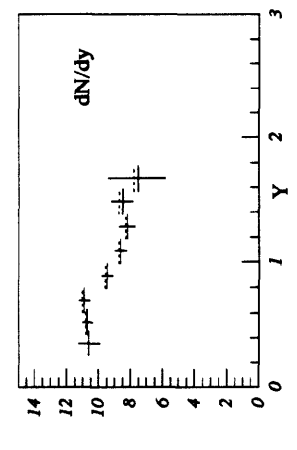
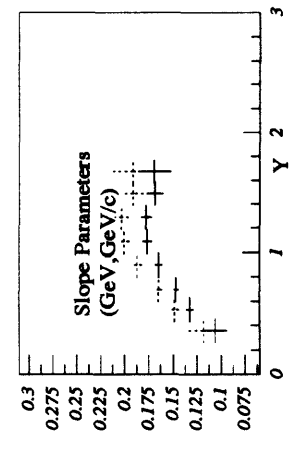
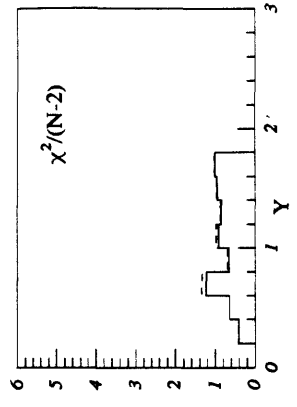
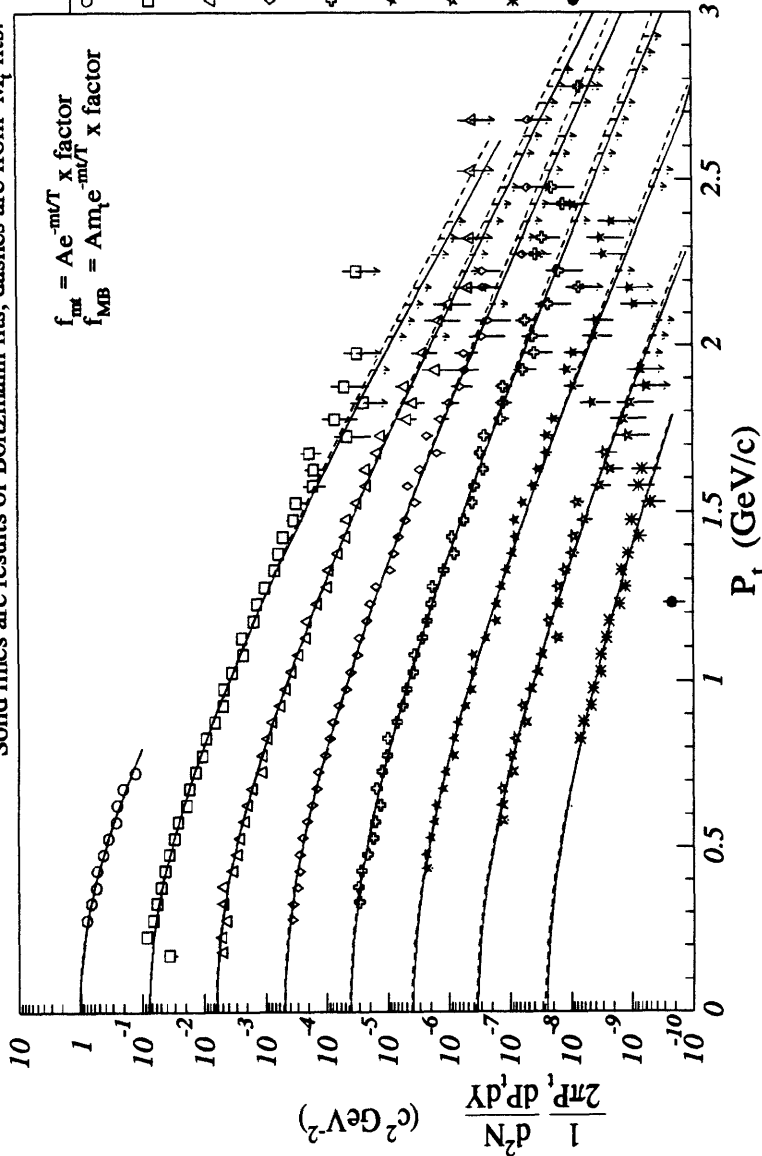


Figure N-5: Yield Summary for ²⁸Si + ⁶⁴Cu CENT1: Protons

²⁸Si+Cu CENT2 : Yield Summary Protons

Solid lines are results of Boltzmann fits, dashes are from M_t fits.



$$f_{MB} = A e^{-mT} \times \text{factor}$$

$$f_{MB} = A m e^{-mT} \times \text{factor}$$

Symbol	Y_{avg}	A	T	factor
○	0.36	4.8E4	.112	10^{-1}
□	0.54	1.9E4	.125	10^{-1}
△	0.70	1.3E4	.128	10^{-2}
◇	0.89	5626	.143	10^{-2}
○	1.08	4978	.142	10^{-3}
◇	1.29	2461	.158	10^{-3}
★	1.49	2038	.157	10^{-4}
★	1.67	1030	.177	10^{-4}
★	1.67	1145	.168	10^{-5}
★	1.67	593.	.191	10^{-5}
★	1.67	1126	.168	10^{-6}
★	1.67	593.	.189	10^{-6}
★	1.67	847.	.172	10^{-7}
★	1.67	445.	.195	10^{-7}
★	1.67	326.	.195	10^{-8}
★	1.67	177.	.224	10^{-8}
●	0.00	.000	.000	10^{-9}

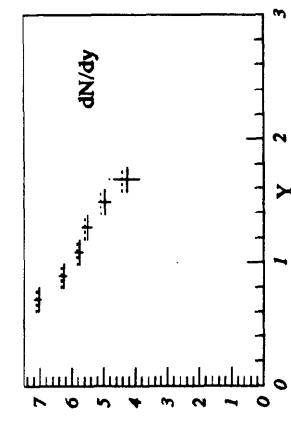
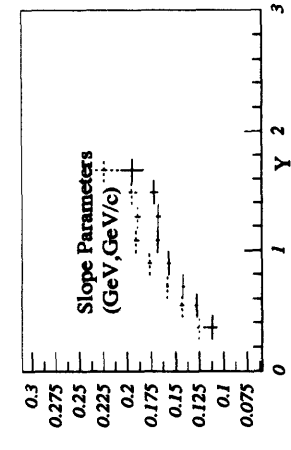
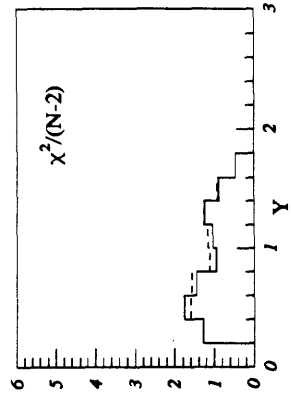


Figure N-6: Yield Summary for ²⁸Si + ⁶⁴Cu CENT2: Protons

²⁸Si+Cu MID : Yield Summary Protons

Solid lines are results of Boltzmann fits, dashes are from M_t fits.

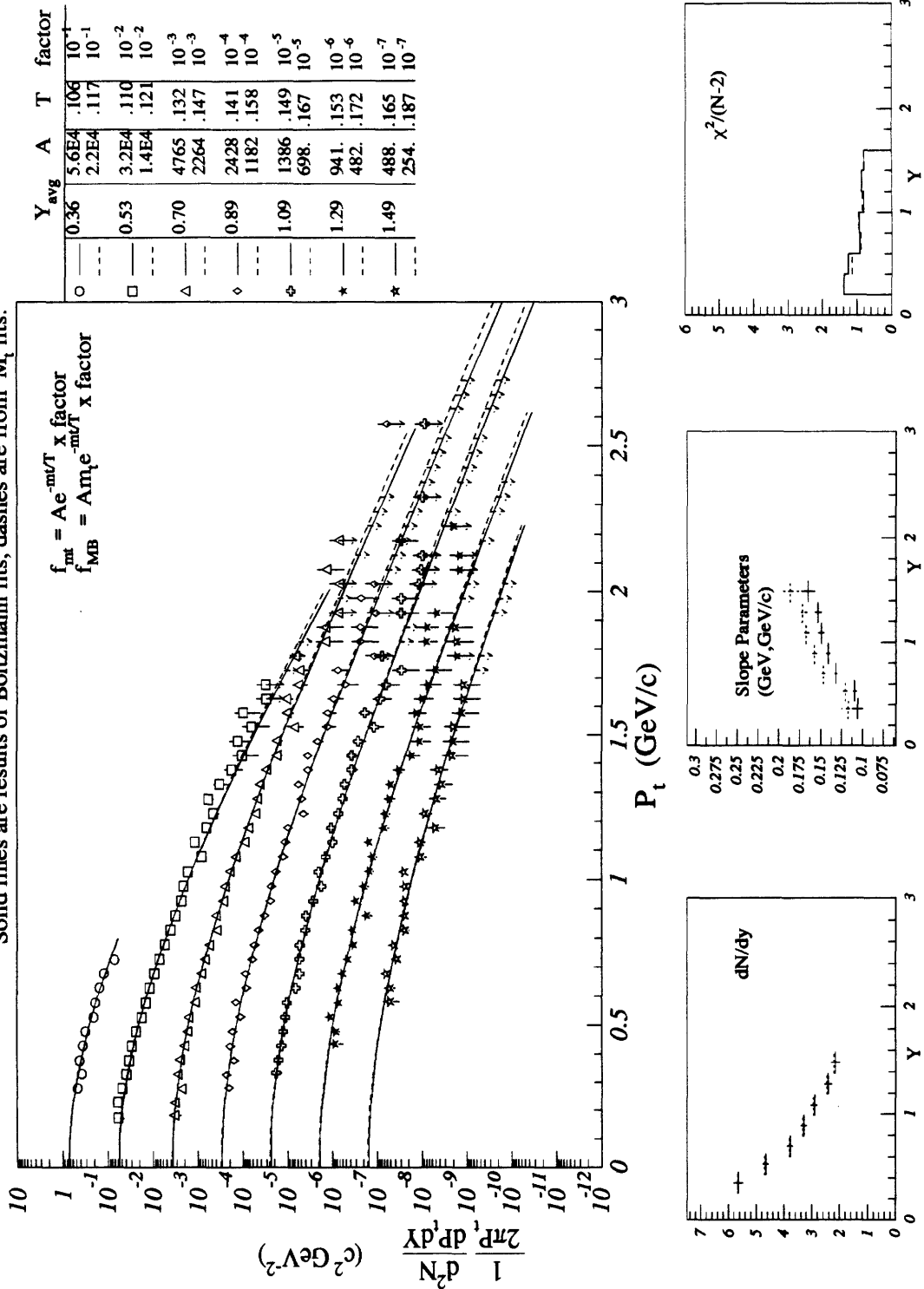
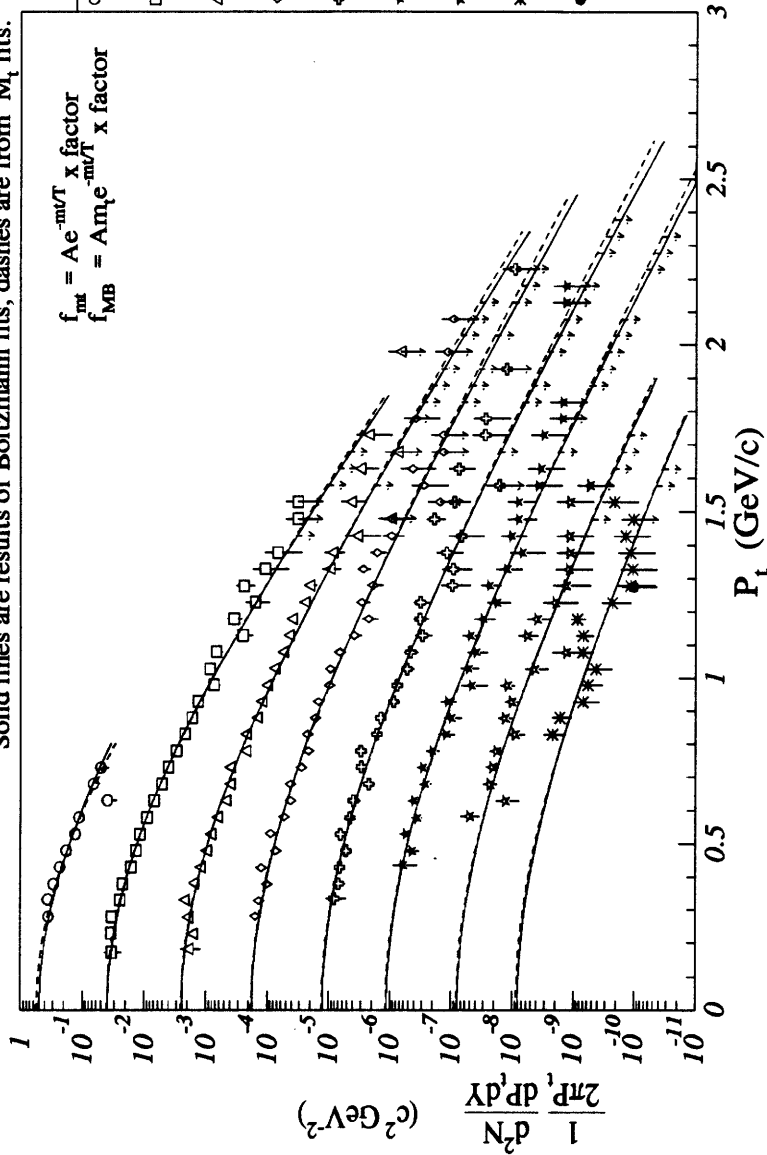


Figure N-7: Yield Summary for ²⁸Si + ⁶⁴Cu MID: Protons

²⁸Si+Cu PERP1 : Yield Summary Protons

Solid lines are results of Boltzmann fits, dashes are from M_T fits.



Y	Y _{avg}	A	T	factor
○	0.36	6.2E4	.100	10 ⁻¹
□	0.53	6.5E4	.100	10 ⁻¹
△	0.70	5.0E4	.100	10 ⁻²
◇	0.90	2.2E4	.109	10 ⁻²
◇	1.09	1.1E4	.113	10 ⁻³
◇	1.29	4933	.124	10 ⁻³
◇	1.49	2927	.128	10 ⁻⁴
◇	1.67	1386	.141	10 ⁻⁴
◇	1.85	1619	.132	10 ⁻⁵
◇	2.03	762	.147	10 ⁻⁵
◇	2.21	1207	.136	10 ⁻⁶
◇	2.39	590	.151	10 ⁻⁶
◇	2.57	614	.142	10 ⁻⁷
◇	2.75	304	.159	10 ⁻⁷
◇	2.93	411	.152	10 ⁻⁸
◇	3.11	223	.170	10 ⁻⁸
◇	3.29	.000	.000	10 ⁻⁹

$$f_{MB} = A e^{-m_T/T} \times \text{factor}$$

$$f_{fit} = A e^{-m_T/T} \times \text{factor}$$

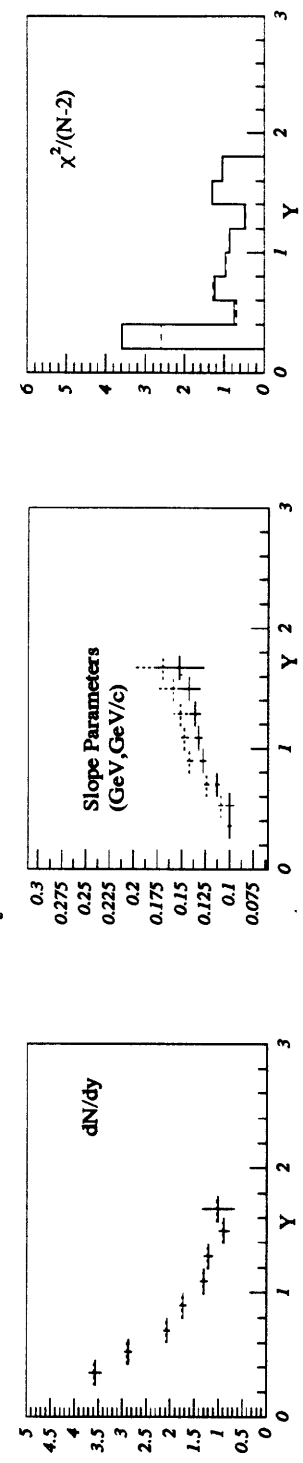


Figure N-8: Yield Summary for ²⁸Si + ⁶⁴Cu PERP1: Protons

²⁸Si+Au CENT1 : Yield Summary Protons

Solid lines are results of Boltzmann fits, dashes are from M_T fits.

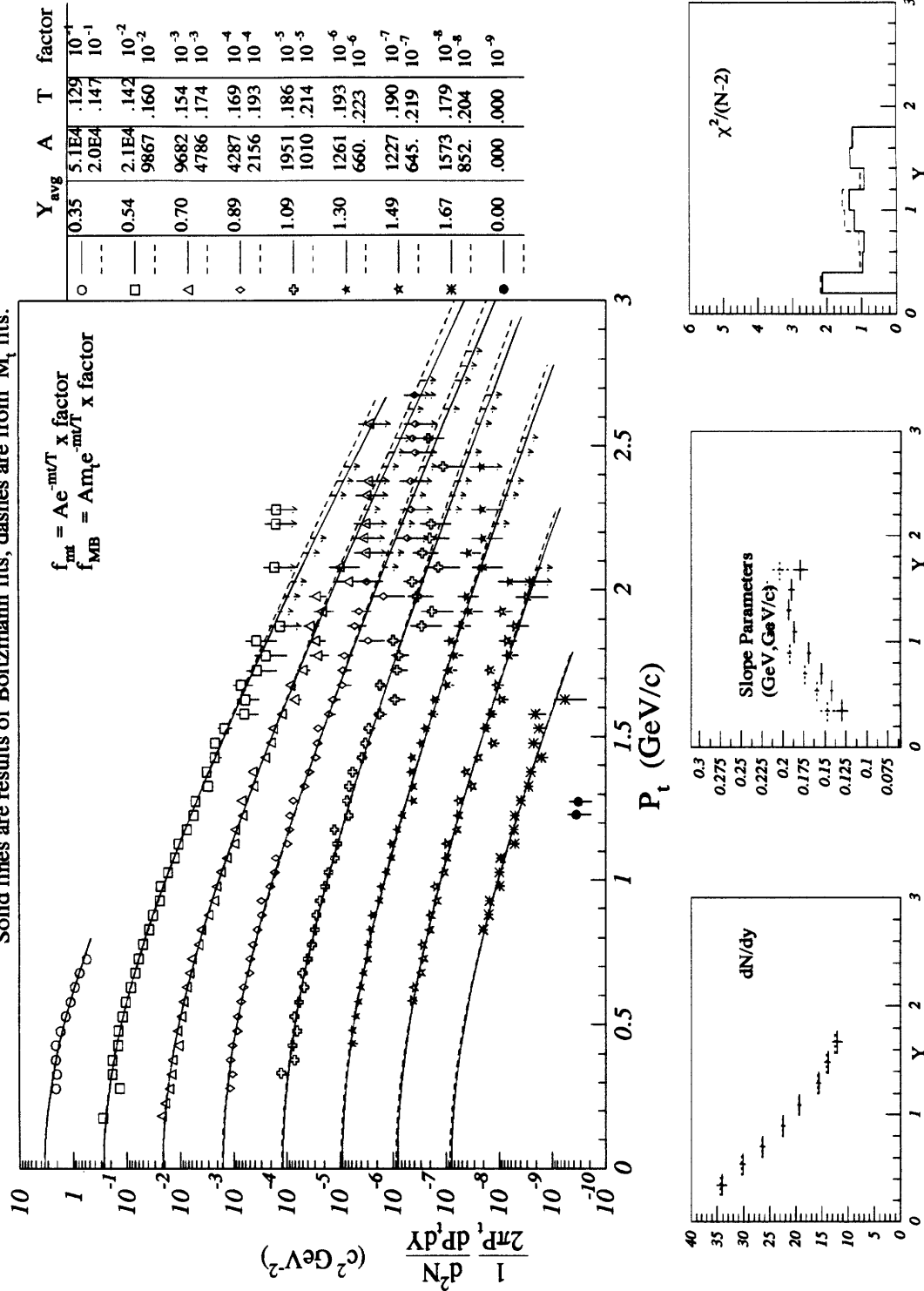


Figure N-9: Yield Summary for ²⁸Si + ¹⁹⁷Au CENT1: Protons

²⁸Si+Au CENT2 : Yield Summary Protons

Solid lines are results of Boltzmann fits, dashes are from M_t fits.

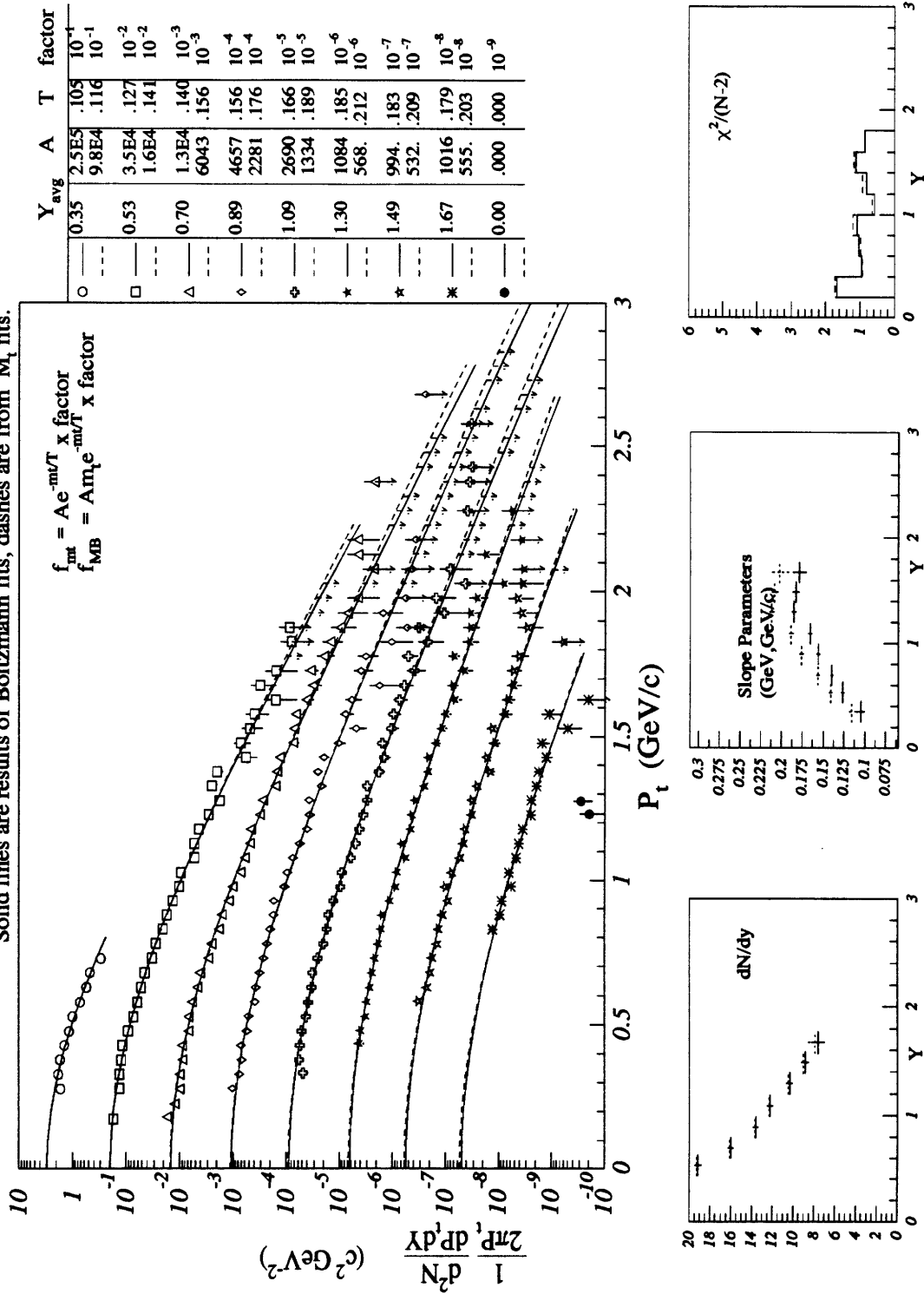
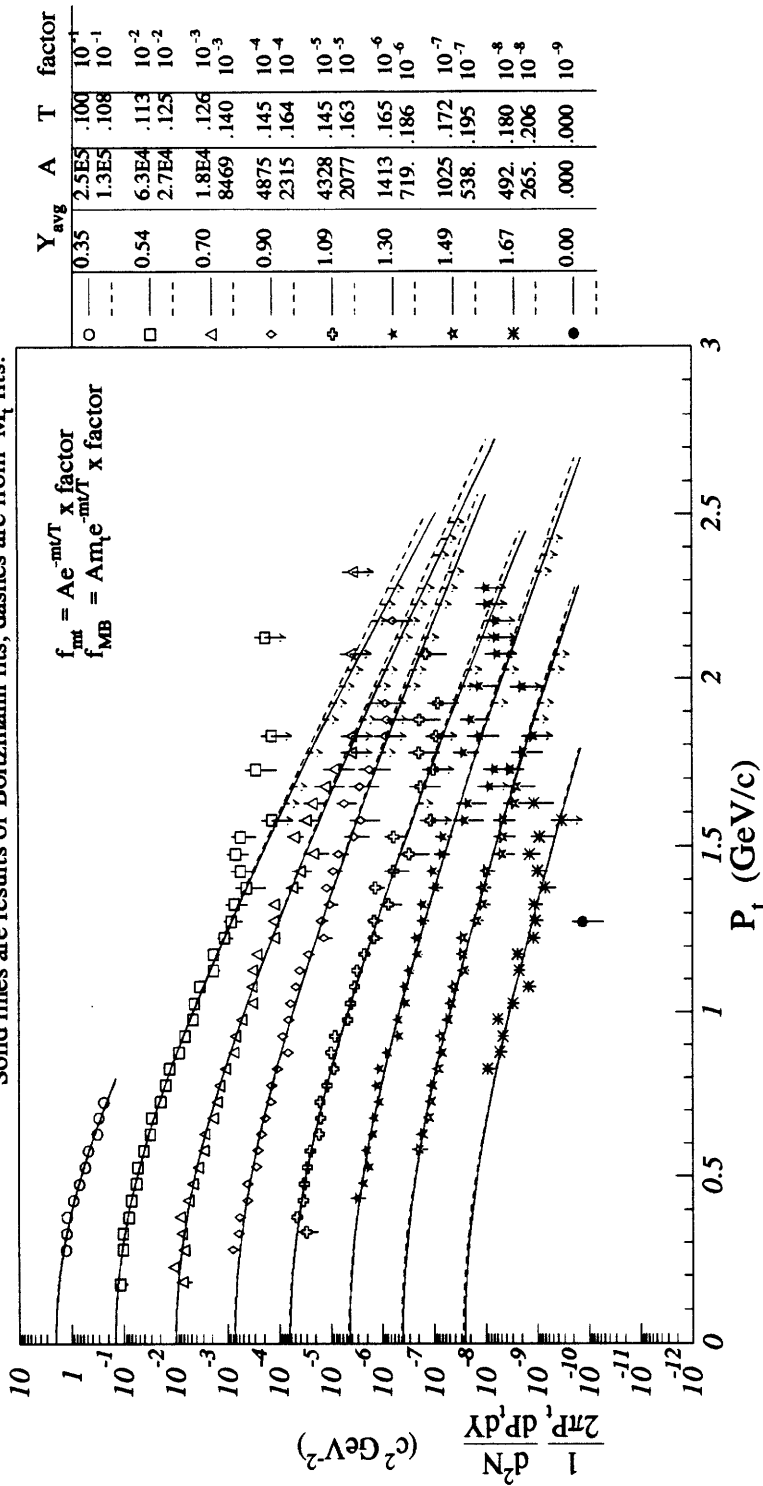


Figure N-10: Yield Summary for ²⁸Si + ¹⁹⁷Au CENT2: Protons

²⁸Si+Au MID : Yield Summary Protons

Solid lines are results of Boltzmann fits, dashes are from M_T fits.



Y	Y _{avg}	A	T	factor
0	0.35	2.5E5	.100	10 ⁻¹
0.5	0.54	1.3E5	.108	10 ⁻¹
1	0.70	6.3E4	.113	10 ⁻²
1.5	0.90	2.7E4	.125	10 ⁻²
2	1.30	1.8E4	.126	10 ⁻³
2.5	1.49	8469	.140	10 ⁻³
3	1.67	4875	.145	10 ⁻⁴
		2315	.164	10 ⁻⁴
		4328	.145	10 ⁻⁵
		2077	.163	10 ⁻⁵
		1413	.165	10 ⁻⁶
		719	.186	10 ⁻⁶
		1025	.172	10 ⁻⁷
		538	.195	10 ⁻⁷
		492	.180	10 ⁻⁸
		265	.206	10 ⁻⁸
		.000	.000	10 ⁻⁹

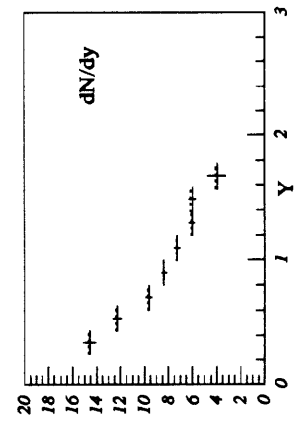
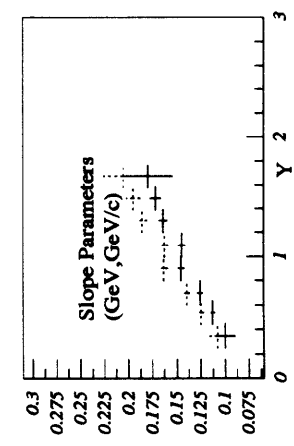
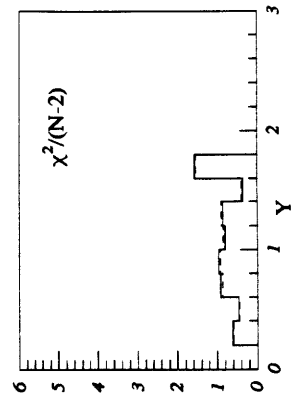
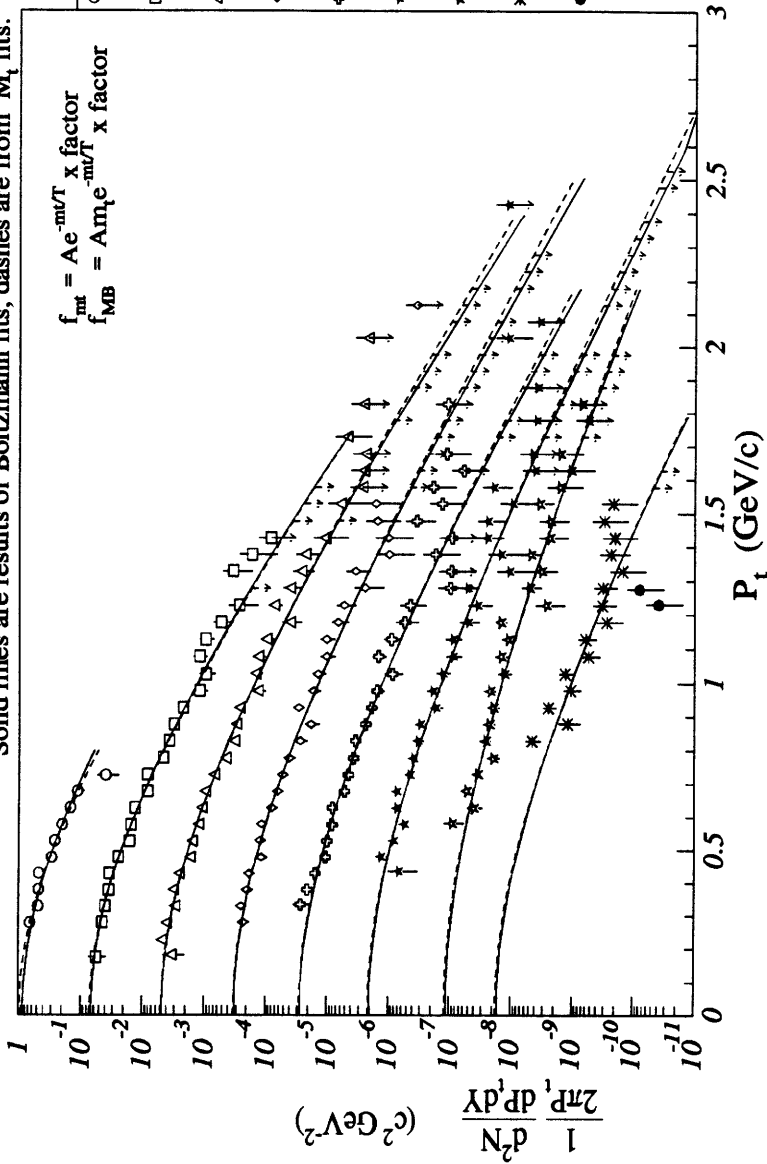


Figure N-11: Yield Summary for ²⁸Si + ¹⁹⁷Au MID: Protons

²⁸Si+Au PERP1 : Yield Summary Protons

Solid lines are results of Boltzmann fits, dashes are from M_t fits.



Symbol	Y_{avg}	A	T	factor
○	0.35	1.1E5	.100	10 ⁻¹
□	0.52	1.2E5	.100	10 ⁻¹
△	0.70	8.5E4	.100	10 ⁻²
◇	0.90	4.5E4	.107	10 ⁻²
◆	1.09	2.1E4	.113	10 ⁻³
♣	1.29	9741	.124	10 ⁻³
♠	1.49	7146	.123	10 ⁻⁴
♣	1.67	3257	.136	10 ⁻⁴
♠	0.00	5198	.125	10 ⁻⁵
♣	0.00	2372	.139	10 ⁻⁵
♠	0.00	1698	.141	10 ⁻⁶
♣	0.00	822	.157	10 ⁻⁶
♠	0.00	253	.176	10 ⁻⁷
♣	0.00	134	.200	10 ⁻⁷
♠	0.00	1675	.137	10 ⁻⁸
♣	0.00	876	.151	10 ⁻⁸
♠	0.00	.000	.000	10 ⁻⁹

$$f_{MB} = A e^{-m_t/T} \quad x \text{ factor}$$

$$f_{fit} = A e^{-m_t/T} \quad x \text{ factor}$$

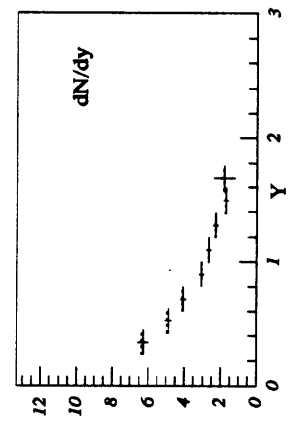
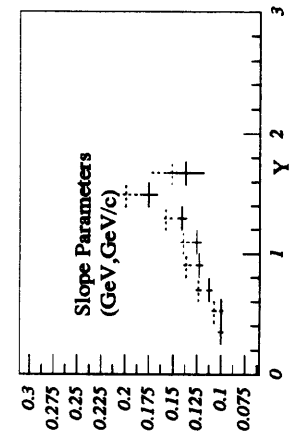
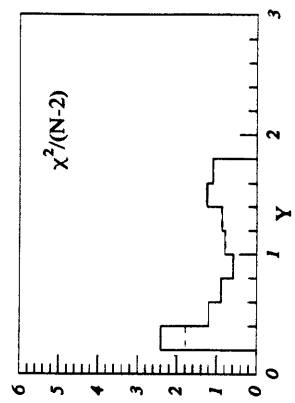


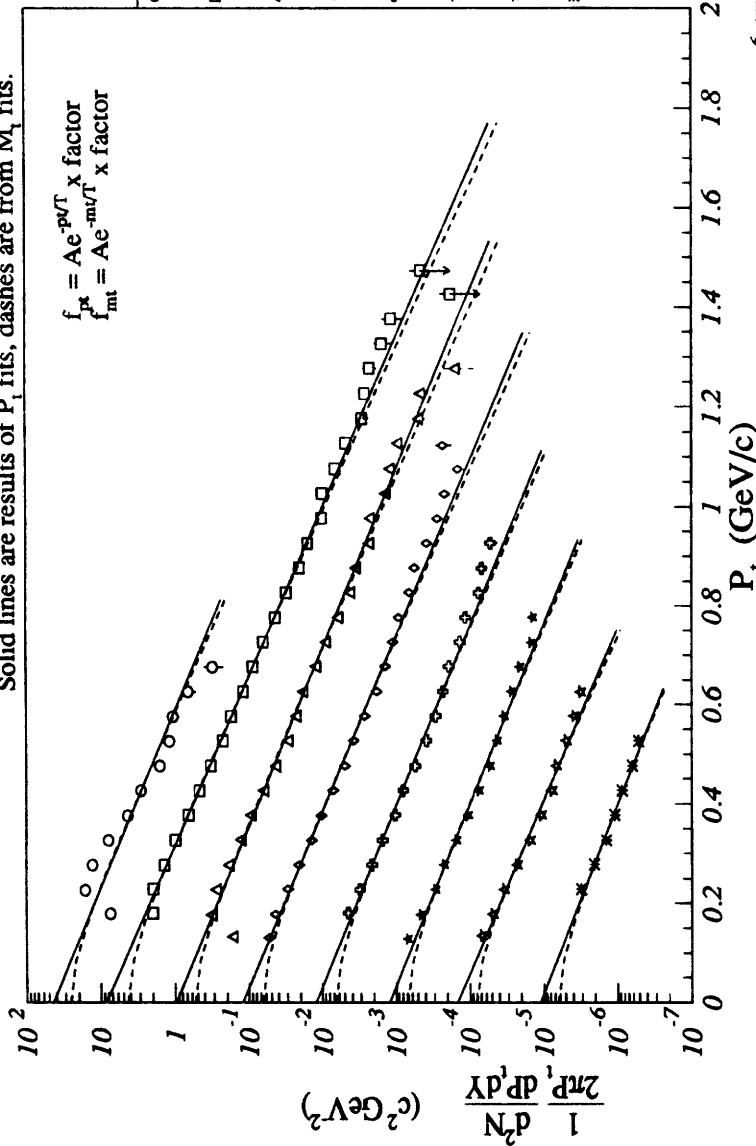
Figure N-12: Yield Summary for ²⁸Si + ¹⁹⁷Au PERP1: Protons

Appendix O

Yield Summary: $^{197}\text{Au} + ^{197}\text{Au} : \pi$

⁷⁹Au+Au Inelastic Cross-Section Summary for π^+

Solid lines are results of P_t fits, dashes are from M_t fits.



$$f_{\pi^+} = A e^{-p_T/T} \times \text{factor}$$

$$f_{\text{mt}} = A e^{-m_T/T} \times \text{factor}$$

Y	Y _{avg}	A	T	factor
0	0.57	43.7	.156	10 ⁻²
1	0.70	67.9	.142	10 ⁻²
2	0.88	84.8	.148	10 ⁻³
3	1.09	116.	.141	10 ⁻³
4	1.29	97.2	.156	10 ⁻⁴
5	1.50	139.	.147	10 ⁻⁴
6	1.69	122.	.153	10 ⁻⁵
7	1.87	172.	.145	10 ⁻⁵
8	1.50	123.	.157	10 ⁻⁶
9	1.69	169.	.149	10 ⁻⁶
10	1.50	124.	.158	10 ⁻⁷
11	1.69	176.	.148	10 ⁻⁷
12	1.50	145.	.151	10 ⁻⁸
13	1.69	221.	.139	10 ⁻⁸
14	1.50	111.	.164	10 ⁻⁹
15	1.69	157.	.153	10 ⁻⁹

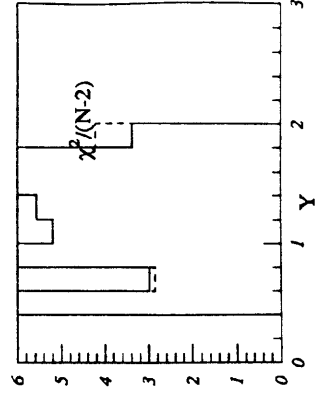
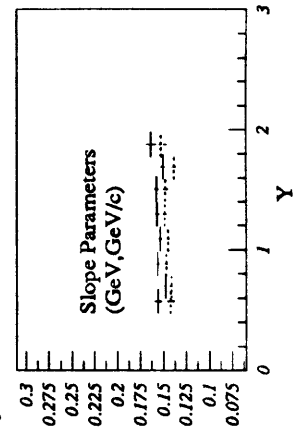
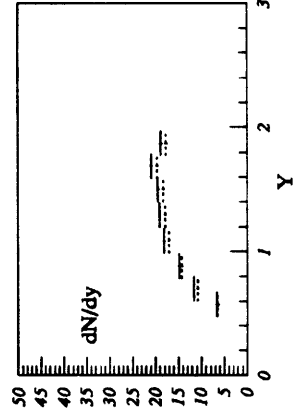
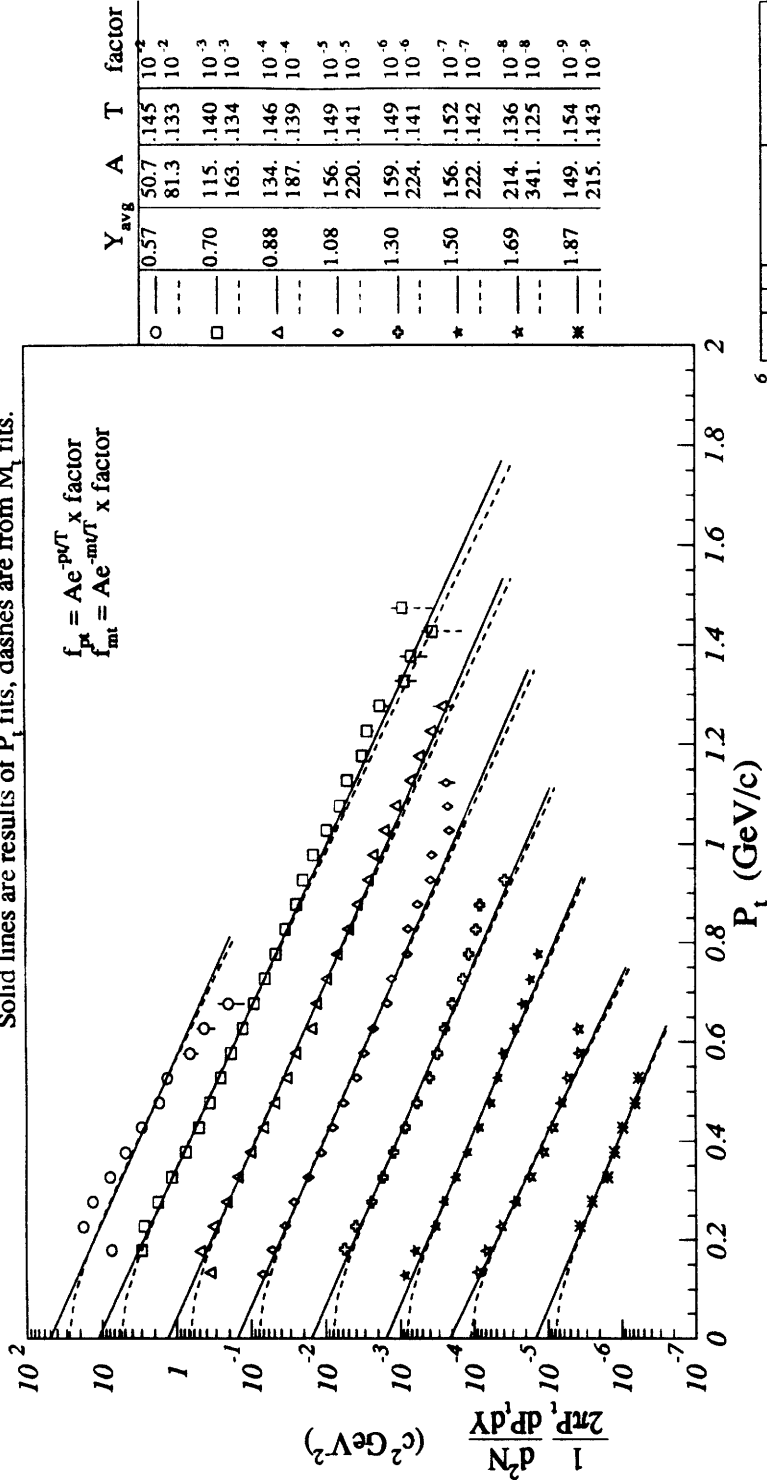


Figure O-1: Yield Summary for ¹⁹⁷Au + ¹⁹⁷Au INEL: π^+

⁷⁹Au+Au Inelastic Cross-Section Summary for π^-

Solid lines are results of P_t fits, dashes are from M_t fits.



$$f_{P_t} = A e^{-P_t/T} \quad \text{x factor}$$

$$f_{M_t} = A e^{-m_t/T} \quad \text{x factor}$$

Y	Y _{avg}	A	T	factor
0	0.57	50.7	.145	10 ⁻²
1	0.70	81.3	.133	10 ⁻²
2	0.88	115.	.140	10 ⁻³
3	1.08	163.	.134	10 ⁻³
4	1.30	134.	.146	10 ⁻⁴
5	1.50	187.	.139	10 ⁻⁴
6	1.69	156.	.149	10 ⁻⁵
7	1.87	220.	.141	10 ⁻⁵
8	1.30	159.	.149	10 ⁻⁶
9	1.50	224.	.141	10 ⁻⁶
10	1.69	156.	.152	10 ⁻⁷
11	1.87	222.	.142	10 ⁻⁷
12	1.69	214.	.136	10 ⁻⁸
13	1.87	341.	.125	10 ⁻⁸
14	1.87	149.	.154	10 ⁻⁹
15	1.87	215.	.143	10 ⁻⁹

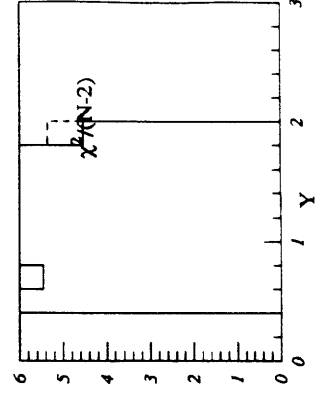
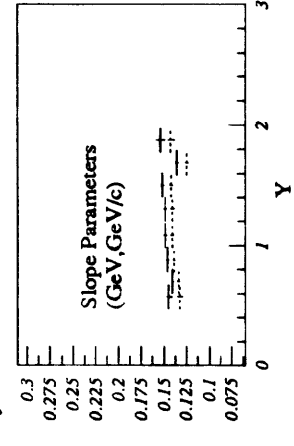
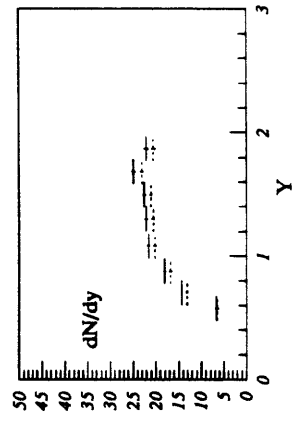
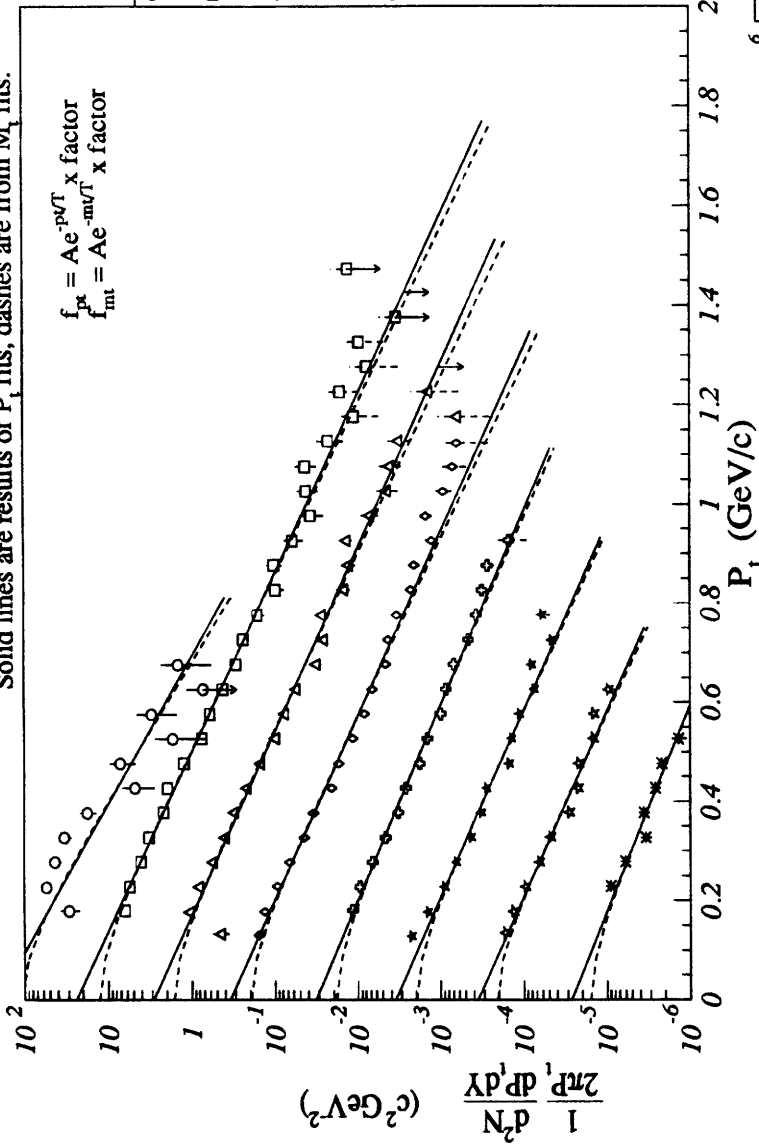


Figure O-2: Yield Summary for ¹⁹⁷Au + ¹⁹⁷Au INEL: π^-

⁷⁹Au+Au ZCALBAR : Yield Summary π^+

Solid lines are results of P_t fits, dashes are from M_t fits.



$$f_{pt} = Ae^{-pT} \times \text{factor}$$

$$f_{mt} = Ae^{-mT} \times \text{factor}$$

Symbol	Y_{avg}	A	T factor
○	0.57	208.	1.30×10^{-2}
□	0.70	356.	1.18×10^{-2}
△	0.89	242.	1.57×10^{-3}
◇	1.09	325.	1.50×10^{-3}
◇	1.29	287.	1.61×10^{-4}
◇	1.50	410.	1.51×10^{-4}
◇	1.69	349.	1.61×10^{-5}
◇	1.87	490.	1.51×10^{-5}
◇	1.29	325.	1.70×10^{-6}
◇	1.50	436.	1.61×10^{-6}
◇	1.69	354.	1.63×10^{-7}
◇	1.87	486.	1.54×10^{-7}
◇	1.29	359.	1.62×10^{-8}
◇	1.50	529.	1.49×10^{-8}
◇	1.69	268.	1.81×10^{-9}
◇	1.87	364.	1.69×10^{-9}

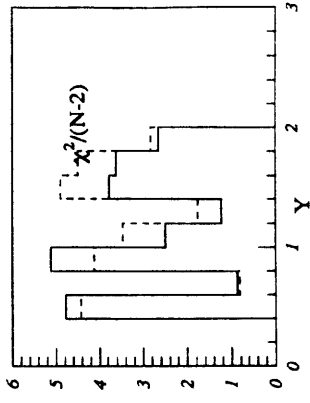
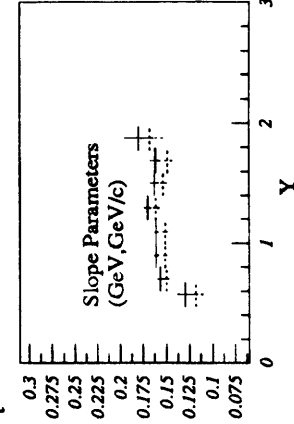
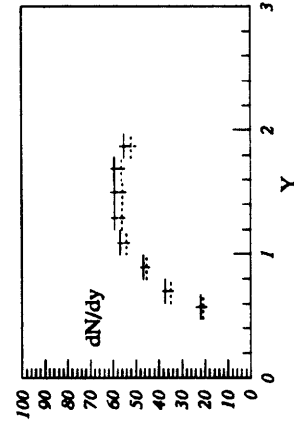
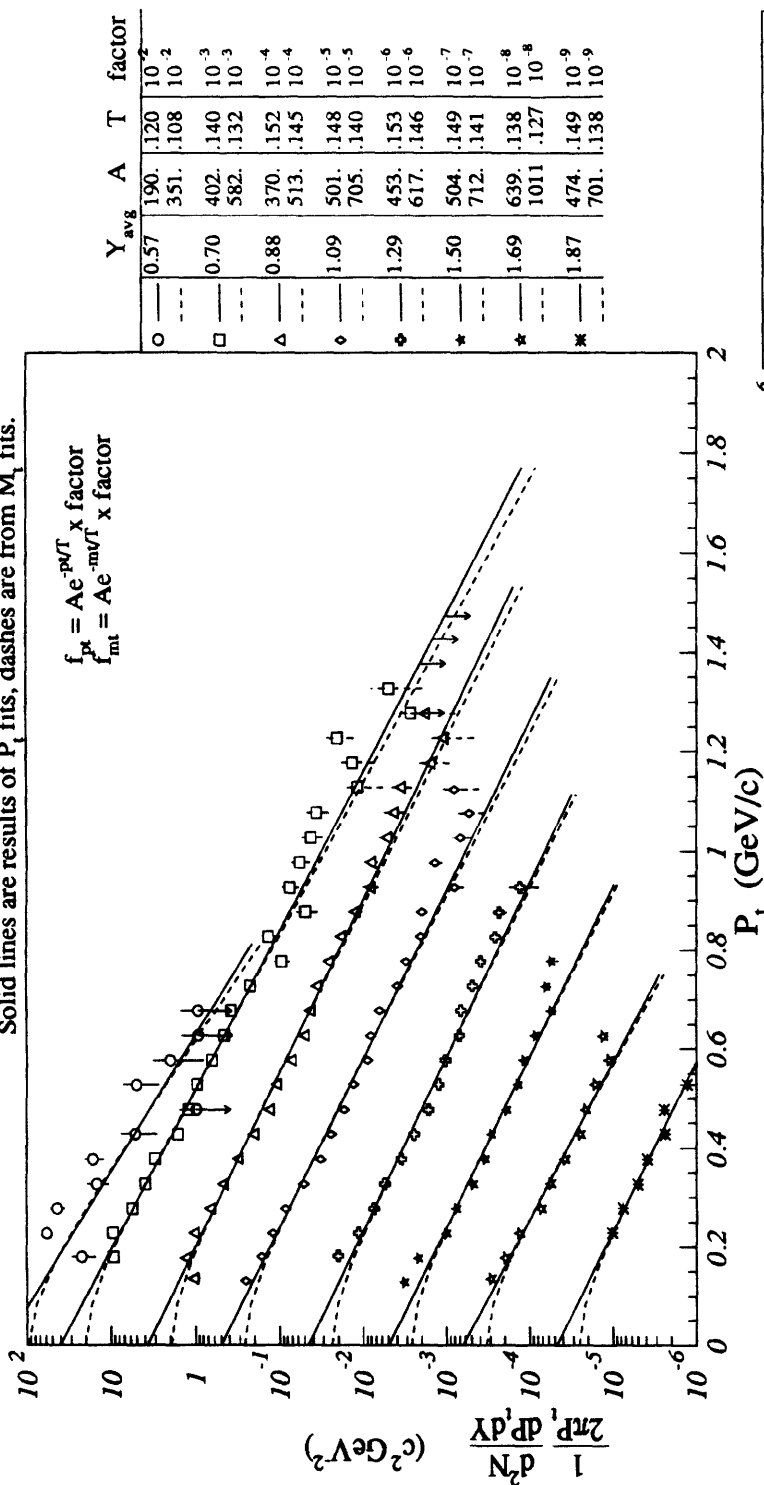


Figure O-3: Yield Summary for ¹⁹⁷Au + ¹⁹⁷Au ZCALBAR: π^+

⁷⁹Au+Au ZCALBAR : Yield Summary π^-

Solid lines are results of P_t fits, dashes are from M_t fits.



$$f_{pi} = A e^{-pT/T} \times \text{factor}$$

$$f_{mt} = A e^{-mT/T} \times \text{factor}$$

Symbol	Y _{avg}	A	T	factor
○	0.57	190.	.120	10 ⁻²
○	---	351.	.108	10 ⁻²
□	0.70	402.	.140	10 ⁻³
□	---	582.	.132	10 ⁻³
△	0.88	370.	.152	10 ⁻⁴
△	---	513.	.145	10 ⁻⁴
◇	1.09	501.	.148	10 ⁻⁵
◇	---	705.	.140	10 ⁻⁵
♣	1.29	453.	.153	10 ⁻⁶
♣	---	617.	.146	10 ⁻⁶
*	1.50	504.	.149	10 ⁻⁷
*	---	712.	.141	10 ⁻⁷
*	1.69	639.	.138	10 ⁻⁸
*	---	1011.	.127	10 ⁻⁸
*	1.87	474.	.149	10 ⁻⁹
*	---	701.	.138	10 ⁻⁹

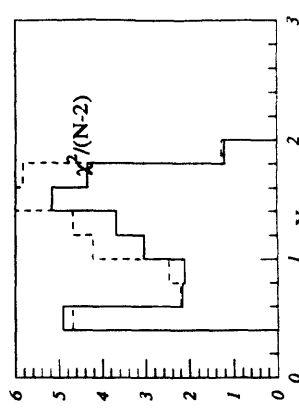
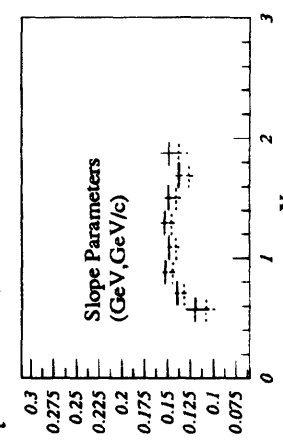
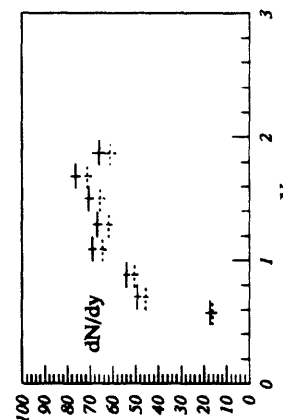
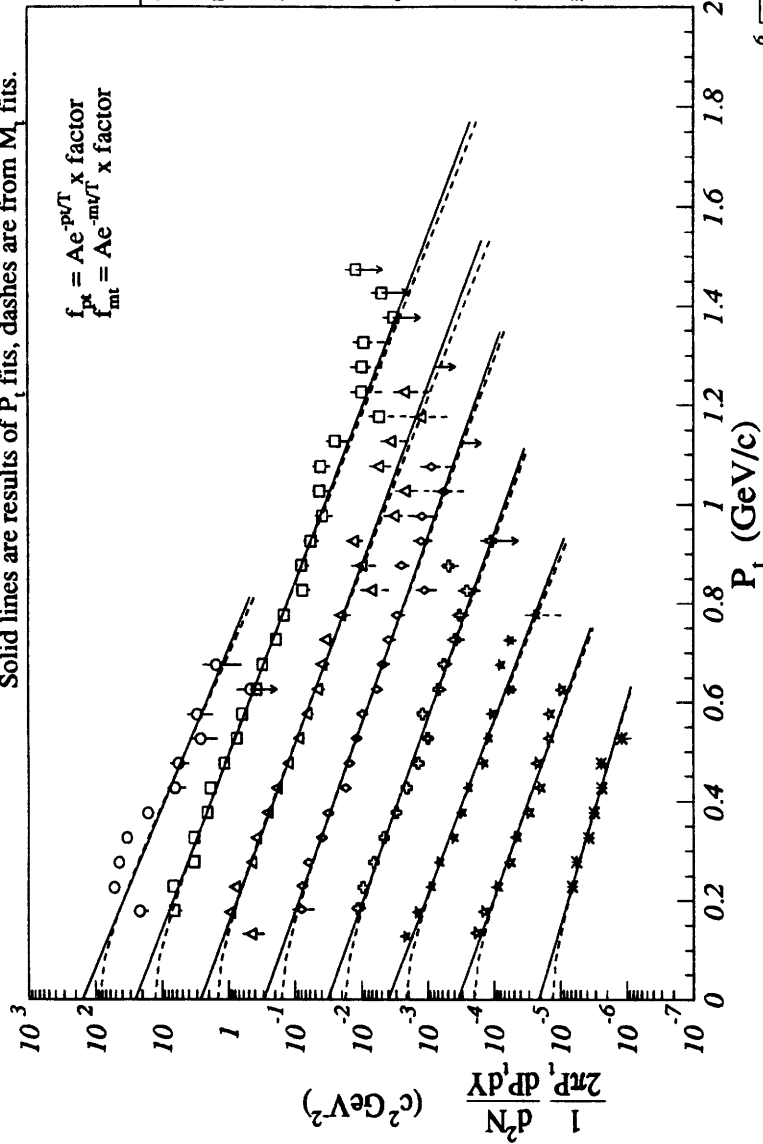


Figure O-4: Yield Summary for ¹⁹⁷Au + ¹⁹⁷Au ZCALBAR: π^-

⁷⁹Au+Au Upper 0-4%σ_{inel} : Yield Summary π⁺

Solid lines are results of P_t fits, dashes are from M_t fits.



$$f_{\pi^+} = A e^{-p_T/T} \times \text{factor}$$

$$f_{\text{mt}} = A e^{-m_T/T} \times \text{factor}$$

Centrality	Y _{avg}	A	T	factor
0-10%	0.57	159.	.140	10 ⁻²
10-20%	0.69	261.	.127	10 ⁻²
20-30%	0.89	334.	.152	10 ⁻³
30-40%	1.08	382.	.148	10 ⁻⁴
40-50%	1.30	296.	.164	10 ⁻⁵
50-60%	1.51	388.	.157	10 ⁻⁵
60-70%	1.69	326.	.162	10 ⁻⁶
70-80%	1.87	439.	.154	10 ⁻⁶
80-90%	1.87	398.	.152	10 ⁻⁷
90-100%	1.87	577.	.142	10 ⁻⁷
90-100%	1.87	349.	.163	10 ⁻⁸
90-100%	1.87	506.	.151	10 ⁻⁸
90-100%	1.87	216.	.196	10 ⁻⁹
90-100%	1.87	288.	.182	10 ⁻⁹

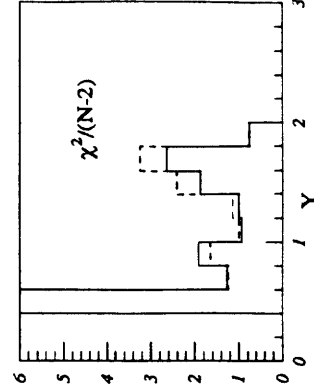
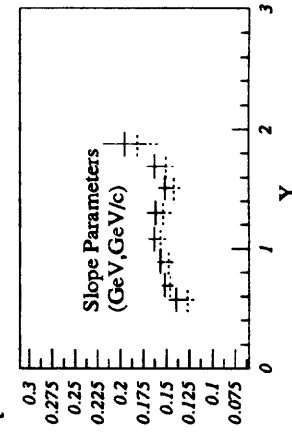
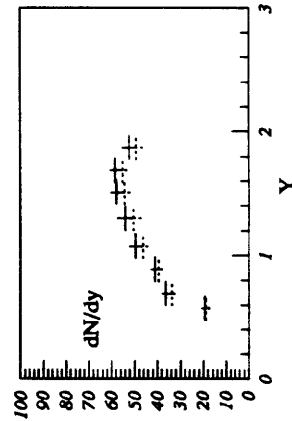


Figure O-5: Yield Summary for ¹⁹⁷Au + ¹⁹⁷Au 0 - 4 % σ_{inel} : π⁺

⁷⁹Au+Au Upper 0-4%σ_{inel} : Yield Summary π⁻

Solid lines are results of P_t fits, dashes are from M_t fits.

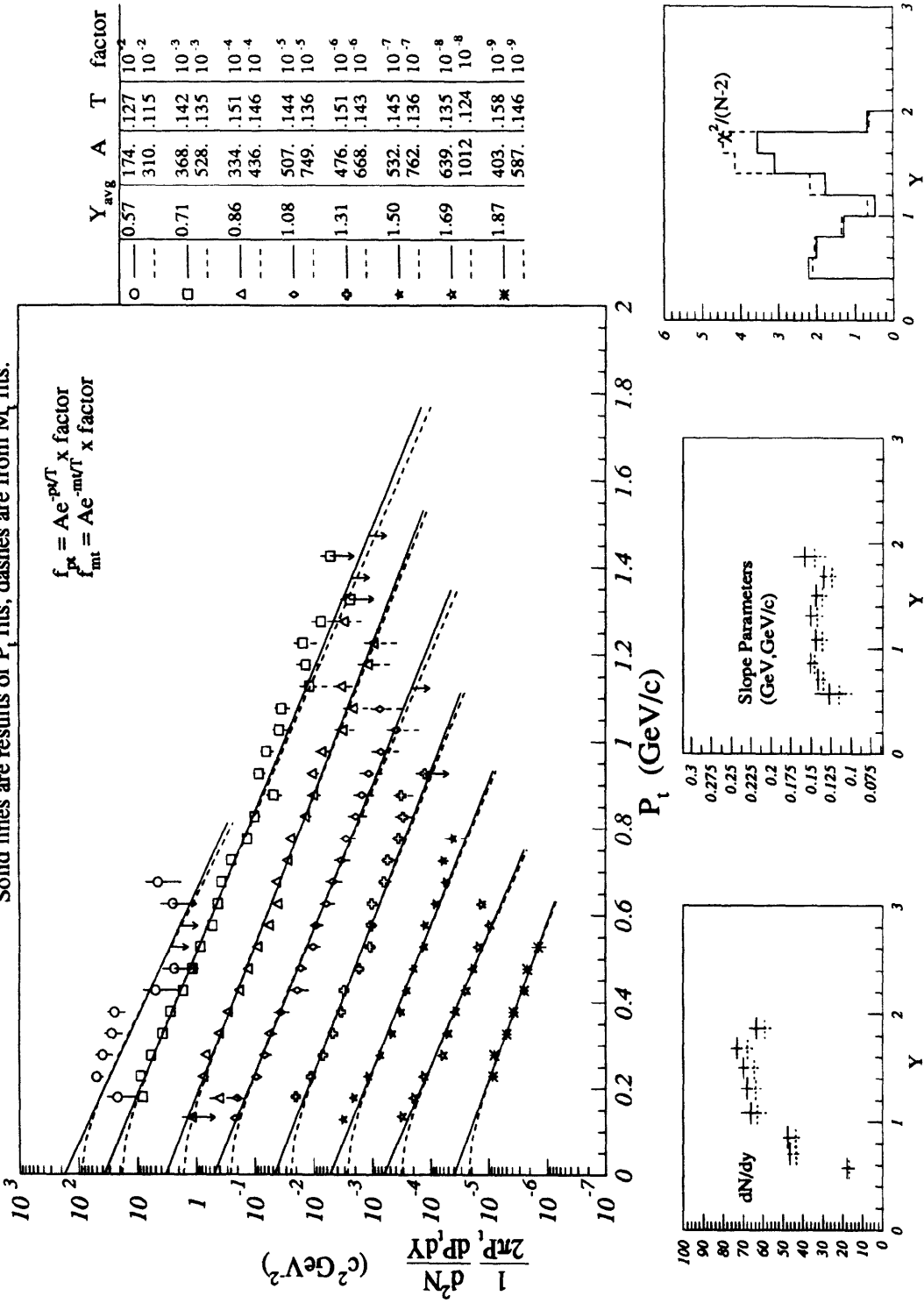
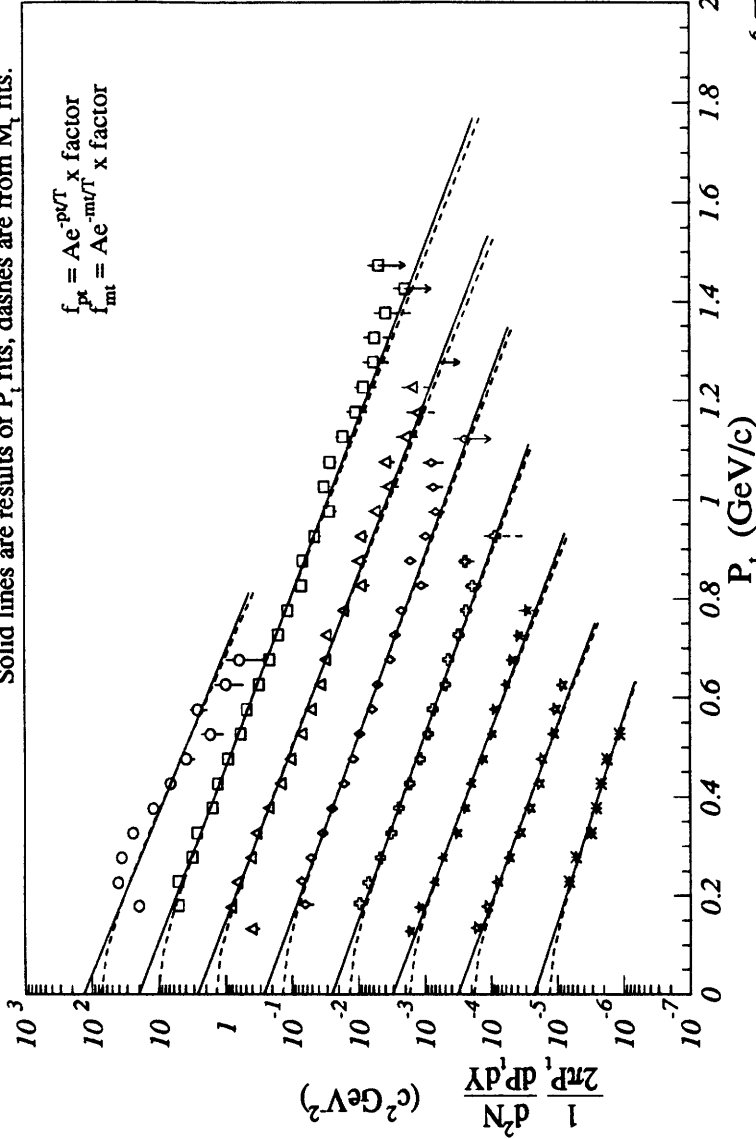


Figure O-6: Yield Summary for ¹⁹⁷Au + ¹⁹⁷Au 0 - 4 % σ_{inel} : π⁻

Symbol	Y _{avg}	A	T	factor
○	0.57	174.	.127	10 ⁻²
○	---	310.	.115	10 ⁻²
□	0.71	368.	.142	10 ⁻³
□	---	528.	.135	10 ⁻³
△	0.86	334.	.151	10 ⁻⁴
△	---	436.	.146	10 ⁻⁴
◇	1.08	507.	.144	10 ⁻⁵
◇	---	749.	.136	10 ⁻⁵
♣	1.31	476.	.151	10 ⁻⁶
♣	---	668.	.143	10 ⁻⁶
★	1.50	532.	.145	10 ⁻⁷
★	---	762.	.136	10 ⁻⁷
★	1.69	639.	.135	10 ⁻⁸
★	---	1012.	.124	10 ⁻⁸
★	1.87	403.	.158	10 ⁻⁹
★	---	587.	.146	10 ⁻⁹

$^{79}\text{Au} + \text{Au}$ Upper 0-10% σ_{inel} : Yield Summary π^+

Solid lines are results of P_t fits, dashes are from M_t fits.



$$f_{\text{pt}} = A e^{-pT/\Lambda} \times \text{factor}$$

$$f_{\text{mt}} = A e^{-mT/\Lambda} \times \text{factor}$$

Symbol	Y_{avg}	A	T	factor
○	0.57	133.	.142	10^{-2}
□	0.69	203.	.152	10^{-3}
△	0.89	268.	.146	10^{-3}
◇	1.08	266.	.158	10^{-5}
◇	1.30	354.	.151	10^{-5}
◇	1.30	253.	.162	10^{-6}
◇	1.51	339.	.154	10^{-6}
★	1.51	312.	.155	10^{-7}
★	1.69	447.	.145	10^{-7}
★	1.69	321.	.157	10^{-8}
★	1.87	476.	.145	10^{-8}
★	1.87	224.	.180	10^{-9}
★	1.87	306.	.167	10^{-9}

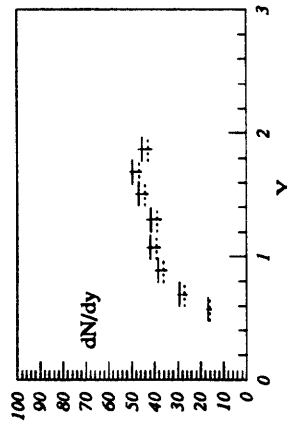
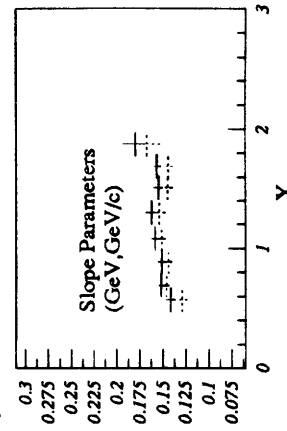
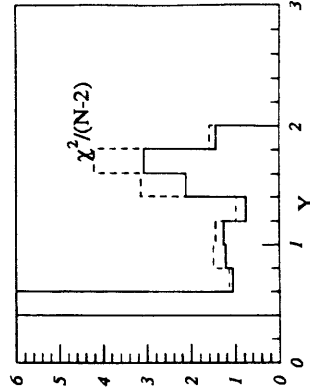
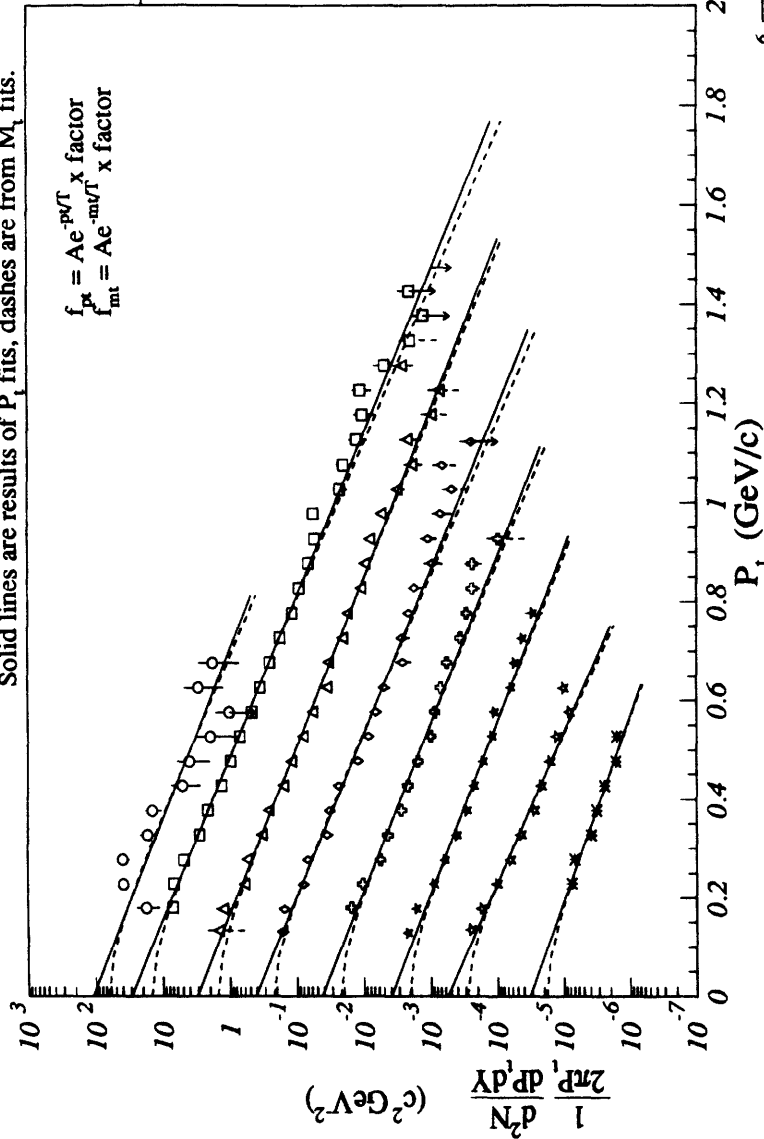


Figure O-7: Yield Summary for $^{197}\text{Au} + ^{197}\text{Au}$ 0 - 10 % σ_{inel} : π^+

⁷⁹Au+Au Upper 0-10%σ_{inel}: Yield Summary π⁻

Solid lines are results of P_t fits, dashes are from M₁ fits.



$$f_{pt} = A e^{-P_t/T} \times \text{factor}$$

$$f_{int} = A e^{-m_T/T} \times \text{factor}$$

Y	Y _{avg}	A	T	factor
0	0.57	111.	.149	10 ⁻²
1	0.71	179.	.135	10 ⁻²
2	0.86	293.	.143	10 ⁻³
3	0.86	417.	.136	10 ⁻³
4	1.08	310.	.148	10 ⁻⁴
5	1.08	406.	.143	10 ⁻⁴
6	1.31	415.	.143	10 ⁻⁵
7	1.31	627.	.134	10 ⁻⁵
8	1.50	428.	.147	10 ⁻⁶
9	1.50	613.	.139	10 ⁻⁶
10	1.69	393.	.152	10 ⁻⁷
11	1.69	557.	.143	10 ⁻⁷
12	1.87	562.	.133	10 ⁻⁸
13	1.87	900.	.122	10 ⁻⁸
14	1.87	325.	.164	10 ⁻⁹
15	1.87	464.	.151	10 ⁻⁹

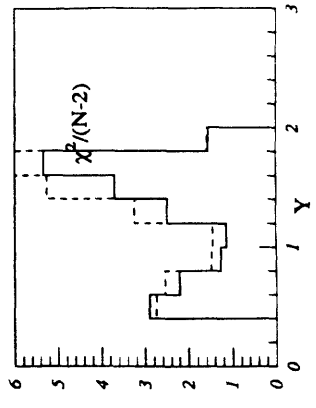
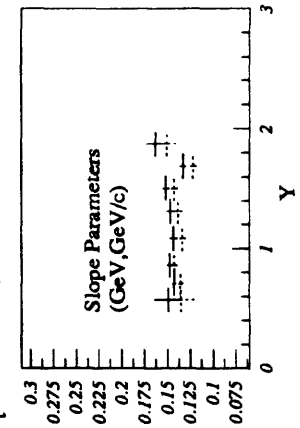
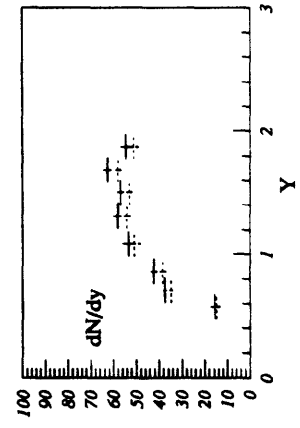
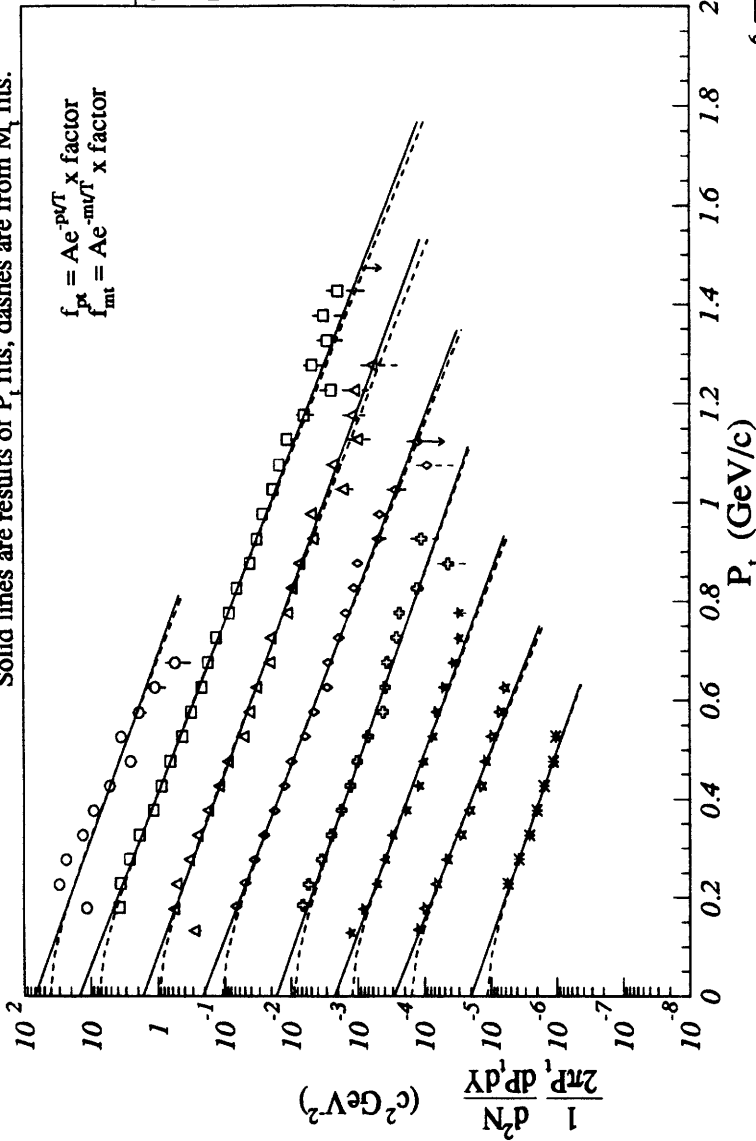


Figure O-8: Yield Summary for ¹⁹⁷Au + ¹⁹⁷Au 0 - 10 % σ_{inel}: π⁻

⁷⁹Au+Au Upper 10-30%σ_{inel} : Yield Summary π⁺

Solid lines are results of P_t fits, dashes are from M_t fits.



$$f_{pt} = Ae^{-pT/\Gamma} \times \text{factor}$$

$$f_{mt} = Ae^{-mT/\Gamma} \times \text{factor}$$

Symbol	Y _{avg}	A	T	factor
○	0.57	69.5	.163	10 ⁻²
□	0.69	106.	.149	10 ⁻²
△	0.89	151.	.151	10 ⁻³
◇	1.08	198.	.145	10 ⁻³
◆	1.30	169.	.159	10 ⁻⁴
★	1.51	242.	.150	10 ⁻⁴
☆	1.69	213.	.153	10 ⁻⁵
✱	1.87	286.	.146	10 ⁻⁵
✳	1.30	170.	.167	10 ⁻⁶
✴	1.51	227.	.158	10 ⁻⁷
✵	1.69	324.	.147	10 ⁻⁷
✶	1.87	289.	.148	10 ⁻⁸
✷	1.87	444.	.136	10 ⁻⁸
✸	1.87	201.	.166	10 ⁻⁹
✹	1.87	283.	.154	10 ⁻⁹

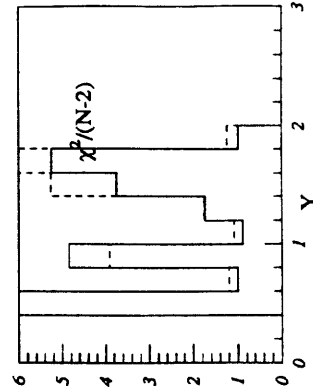
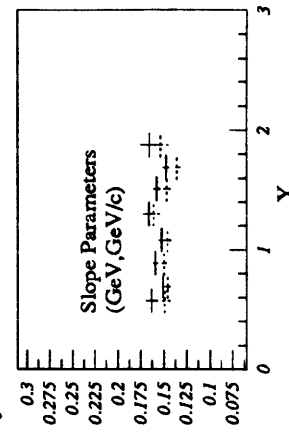
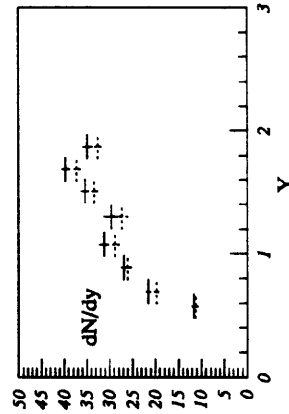


Figure O-9: Yield Summary for ¹⁹⁷Au + ¹⁹⁷Au 10 - 30 % σ_{inel} : π⁺

$^{79}\text{Au} + \text{Au}$ Upper 10-30% σ_{inel} : Yield Summary π^-

Solid lines are results of P_t fits, dashes are from M_t fits.

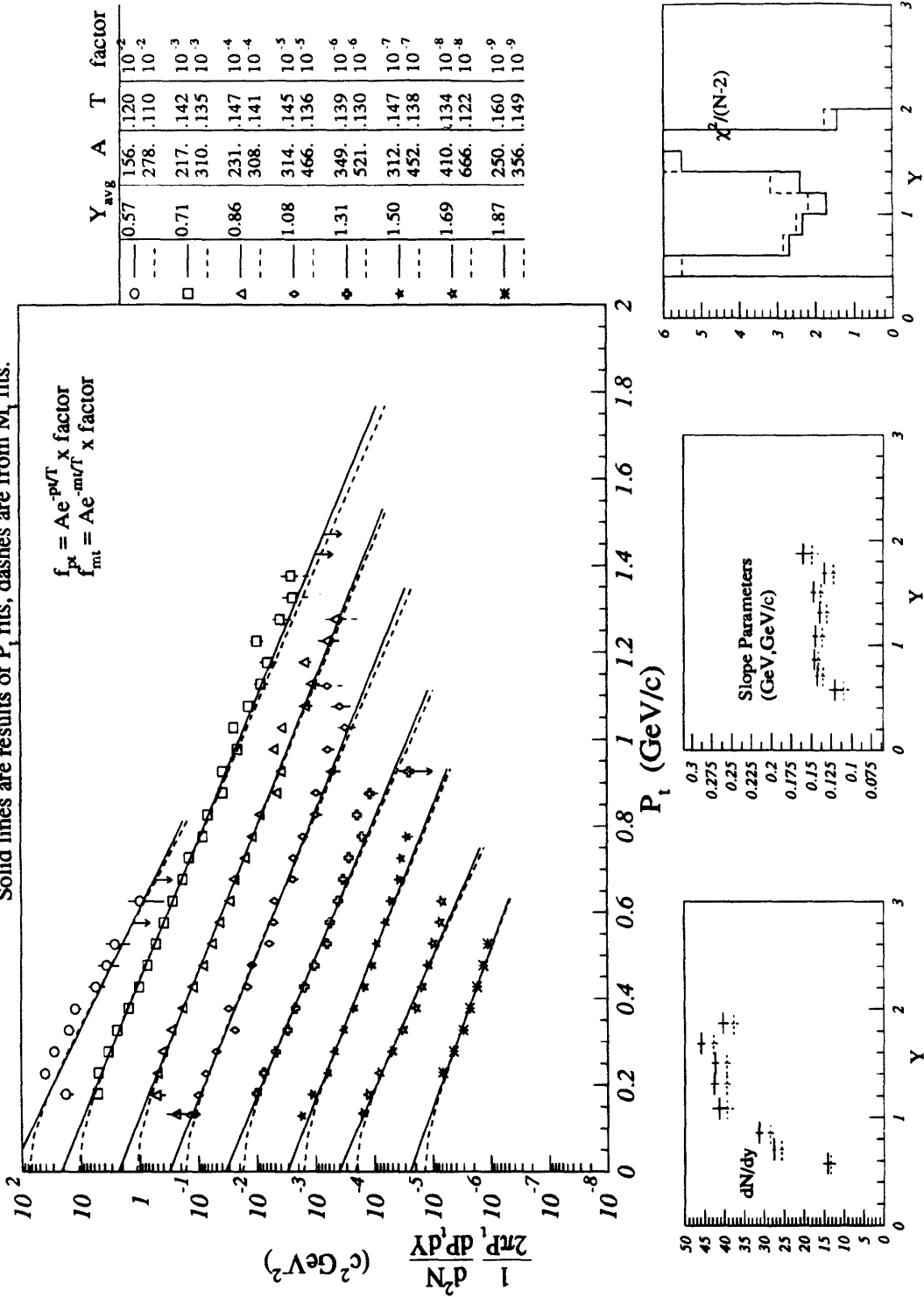
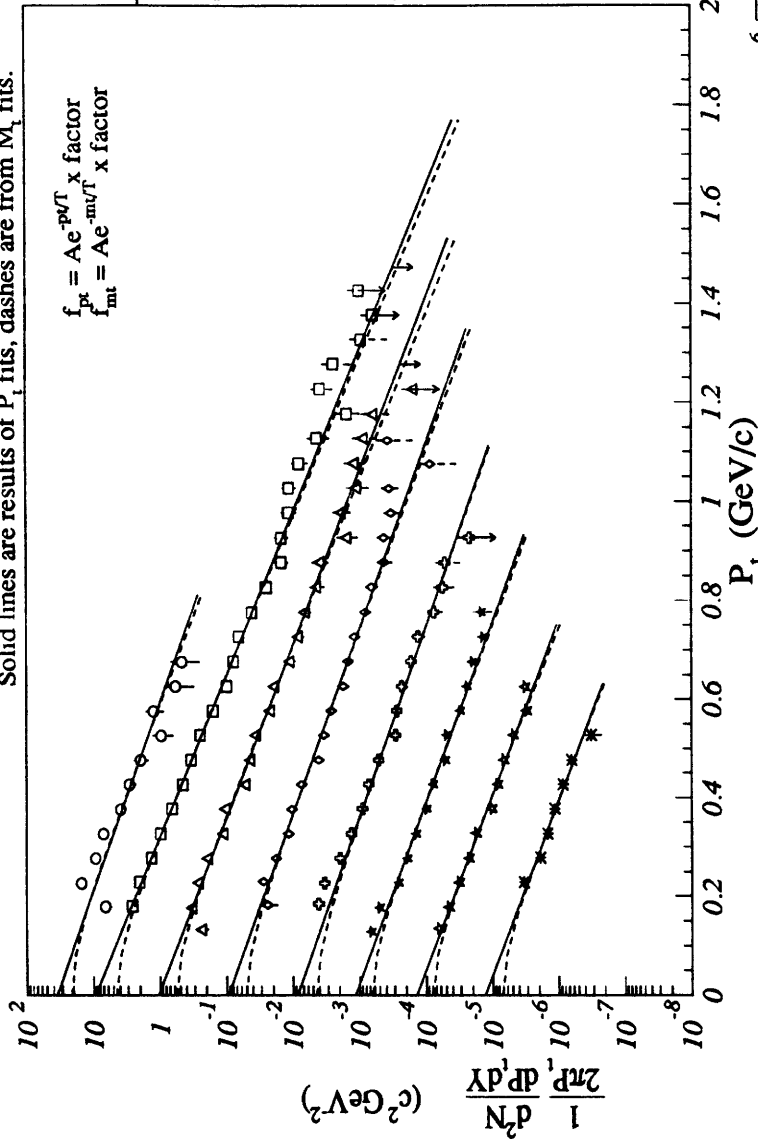


Figure O-10: Yield Summary for $^{197}\text{Au} + ^{197}\text{Au}$ 10 - 30 % σ_{inel} : π^-

⁷⁹Au+Au Upper 30-50% σ_{inel} : Yield Summary π^+

Solid lines are results of P_t fits, dashes are from M_t fits.



$$f_{pt} = Ae^{-pt/\Gamma} \times \text{factor}$$

$$f_{mt} = Ae^{-m_t/\Gamma} \times \text{factor}$$

Symbol	Y_{avg}	A	T	factor
○	0.57	35.7	.165	10^{-2}
□	0.69	53.9	.151	10^{-2}
△	0.89	93.1	.143	10^{-3}
◇	1.08	125.	.137	10^{-3}
◇	1.30	104.	.152	10^{-4}
◇	1.51	149.	.144	10^{-4}
◇	1.69	94.7	.162	10^{-5}
◇	1.87	125.	.156	10^{-5}
◇	1.30	86.2	.167	10^{-6}
◇	1.51	105.	.163	10^{-6}
◇	1.69	117.	.159	10^{-7}
◇	1.87	164.	.149	10^{-7}
◇	1.30	140.	.153	10^{-8}
◇	1.51	212.	.141	10^{-8}
◇	1.69	132.	.153	10^{-9}
◇	1.87	192.	.142	10^{-9}

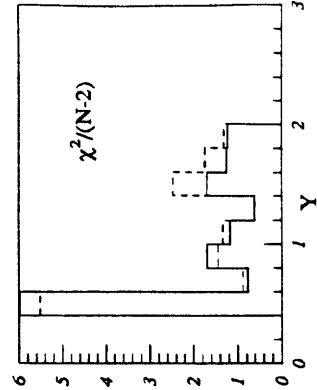
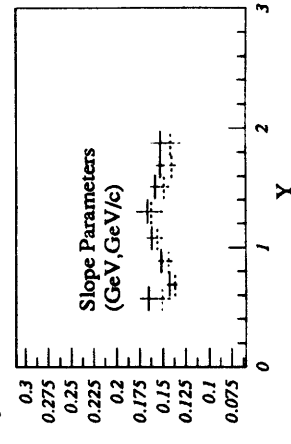
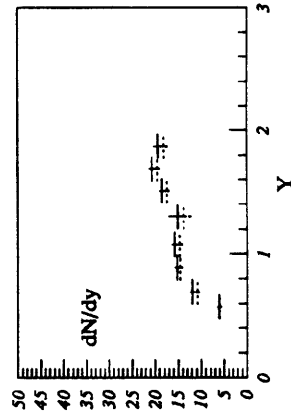
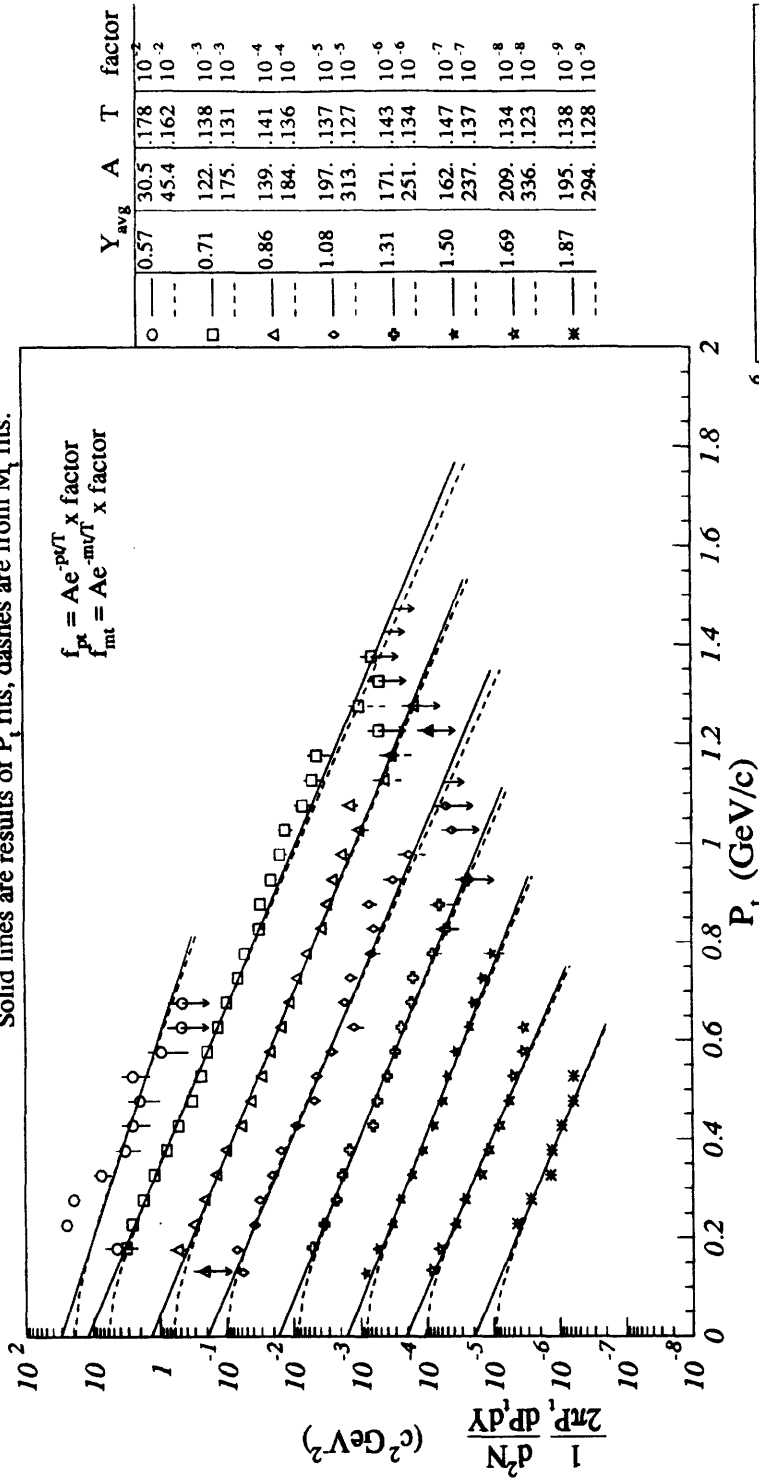


Figure O-11: Yield Summary for ¹⁹⁷Au + ¹⁹⁷Au 30 - 50 % σ_{inel} : π^+

⁷⁹Au+Au Upper 30-50%σ_{inel} : Yield Summary π⁻

Solid lines are results of P_t fits, dashes are from M_t fits.



$$f_{pt} = A e^{-P_t/T} \times \text{factor}$$

$$f_{mt} = A e^{-m_T/T} \times \text{factor}$$

Y _{avg}	A	T factor
○	0.57	30.5 .178 10 ⁻²
□	0.71	45.4 .162 10 ⁻²
△	0.86	122. .138 10 ⁻³
◇	1.08	175. .131 10 ⁻³
◇	1.31	139. .141 10 ⁻⁴
◇	1.31	184. .136 10 ⁻⁴
◇	1.50	197. .137 10 ⁻⁵
◇	1.50	313. .127 10 ⁻⁵
◇	1.50	171. .143 10 ⁻⁶
◇	1.50	251. .134 10 ⁻⁶
◇	1.50	162. .147 10 ⁻⁷
◇	1.50	237. .137 10 ⁻⁷
◇	1.69	209. .134 10 ⁻⁸
◇	1.69	336. .123 10 ⁻⁸
◇	1.87	195. .138 10 ⁻⁹
◇	1.87	294. .128 10 ⁻⁹

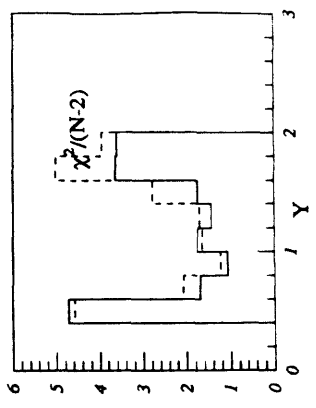
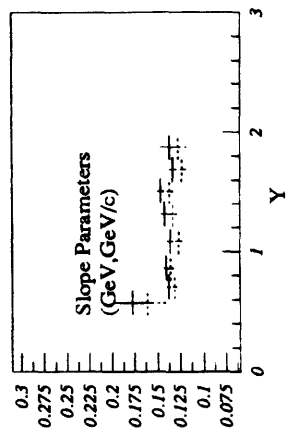
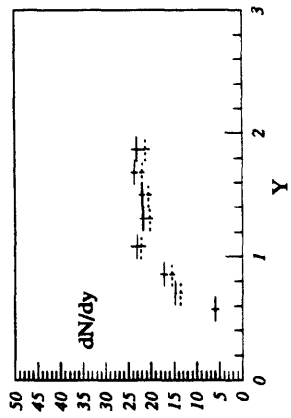
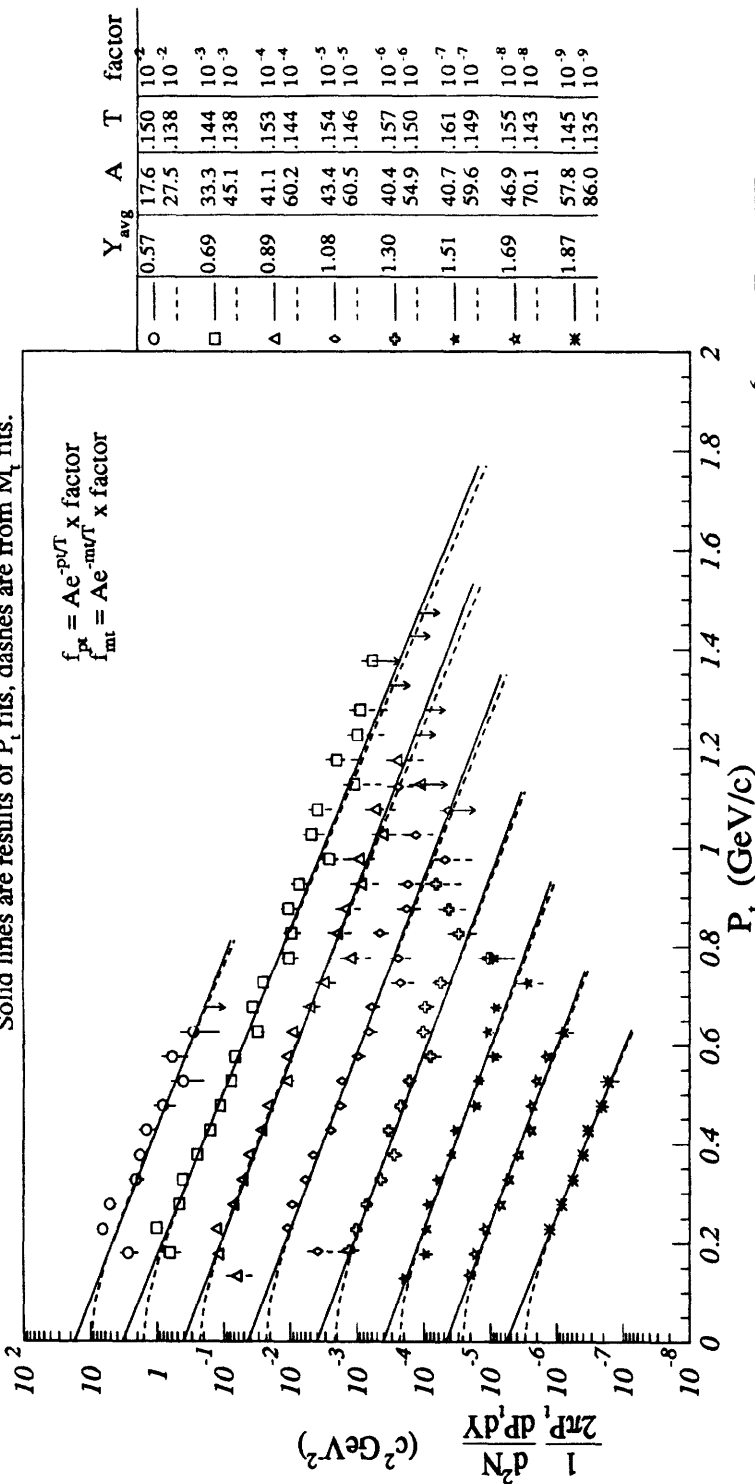


Figure O-12: Yield Summary for ¹⁹⁷Au + ¹⁹⁷Au 30 - 50 % σ_{inel} : π⁻

⁷⁹Au+Au Upper 50-70%σ_{inel} : Yield Summary π⁺

Solid lines are results of P_t fits, dashes are from M_t fits.



$$f_{pt} = A e^{-pT/\Lambda} \times \text{factor}$$

$$f_{mt} = A e^{-mT/\Lambda} \times \text{factor}$$

Y	Y _{avg}	A	T	factor
0	0.57	17.6	.150	10 ⁻²
1	0.69	27.5	.138	10 ⁻²
2	0.89	33.3	.144	10 ⁻³
3	0.89	45.1	.138	10 ⁻³
4	1.08	41.1	.153	10 ⁻⁴
5	1.08	60.2	.144	10 ⁻⁴
6	1.30	43.4	.154	10 ⁻⁵
7	1.30	60.5	.146	10 ⁻⁵
8	1.51	40.4	.157	10 ⁻⁶
9	1.51	54.9	.150	10 ⁻⁶
10	1.69	40.7	.161	10 ⁻⁷
11	1.69	59.6	.149	10 ⁻⁷
12	1.87	46.9	.155	10 ⁻⁸
13	1.87	70.1	.143	10 ⁻⁸
14	1.87	57.8	.145	10 ⁻⁹
15	1.87	86.0	.135	10 ⁻⁹

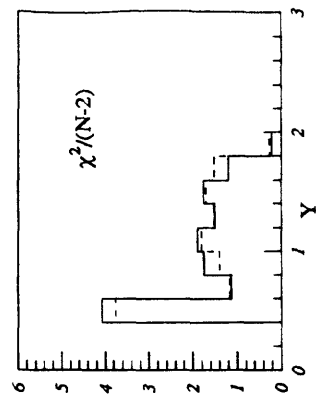
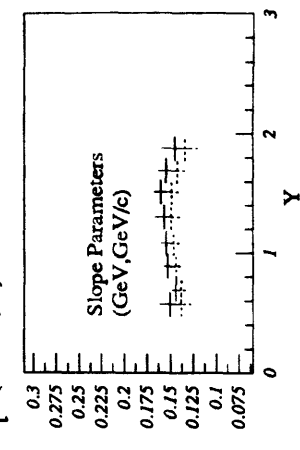
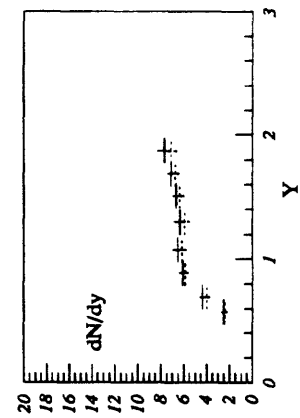
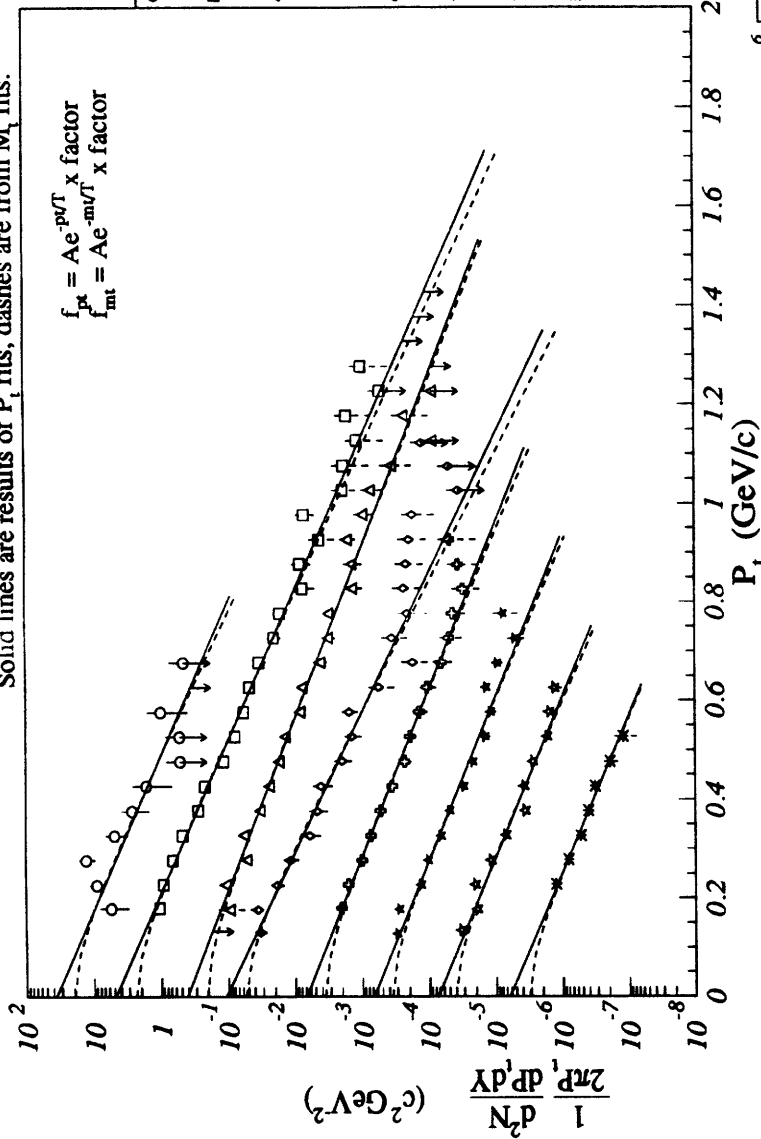


Figure O-13: Yield Summary for ¹⁹⁷Au + ¹⁹⁷Au 50 - 70 % σ_{inel} : π⁺

⁷⁹Au+Au Upper 50-70% σ_{inel} : Yield Summary π^-

Solid lines are results of P_t fits, dashes are from M_t fits.



$$f_{pt} = Ae^{-p_t/\Gamma} \times \text{factor}$$

$$f_{mt} = Ae^{-m_t/\Gamma} \times \text{factor}$$

Symbol	Y_{avg}	A	T	factor
○	0.57	36.6	.135	10^{-2}
□	0.71	48.4	.133	10^{-3}
△	0.86	41.6	.151	10^{-4}
◇	1.08	109.	.123	10^{-5}
◇	1.31	68.5	.147	10^{-6}
★	1.50	67.7	.144	10^{-7}
★	1.69	75.4	.141	10^{-8}
★	1.87	63.2	.137	10^{-9}

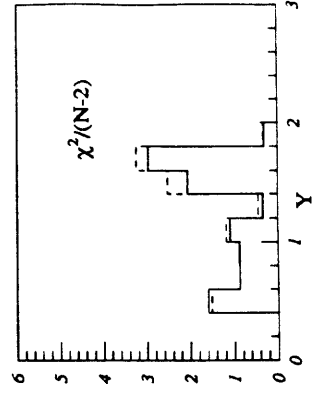
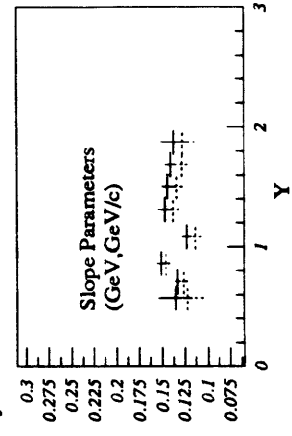
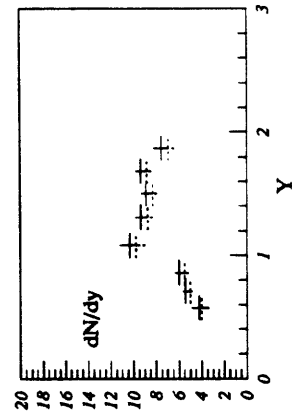


Figure O-14: Yield Summary for ¹⁹⁷Au + ¹⁹⁷Au 50 - 70 % σ_{inel} : π^-

⁷⁹Au+Au Upper 70-90% σ_{inel} : Yield Summary π^+

Solid lines are results of P_t fits, dashes are from M_t fits.

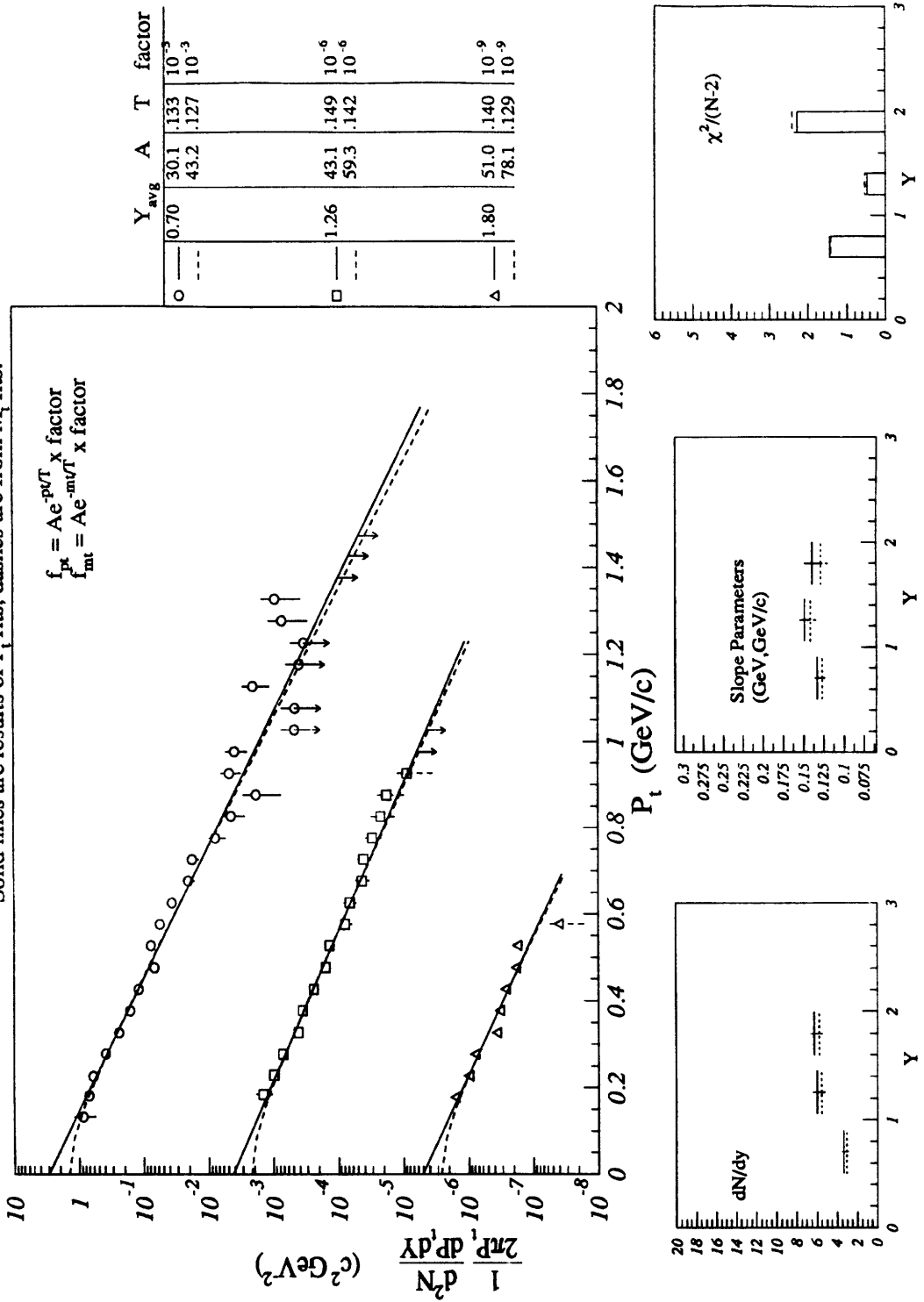


Figure O-15: Yield Summary for ¹⁹⁷Au + ¹⁹⁷Au 70 - 90 % σ_{inel} : π^+

⁷⁹Au+Au Upper 70-90%σ_{inel} : Yield Summary π⁻

Solid lines are results of P_T fits, dashes are from M_T fits.

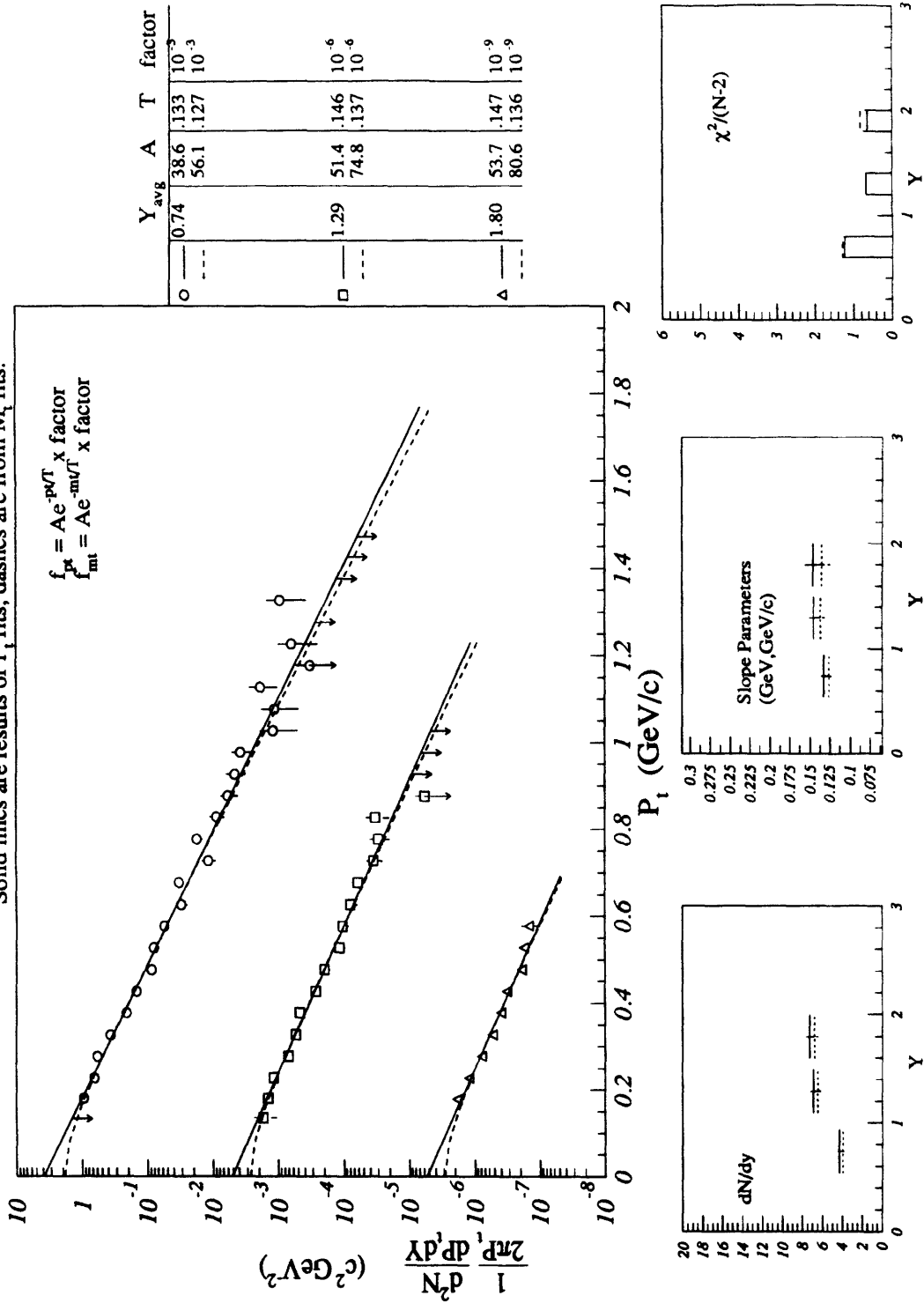


Figure O-16: Yield Summary for ¹⁹⁷Au + ¹⁹⁷Au 70 - 90 % σ_{inel} : π⁻

Appendix P

Yield Summary: $^{197}\text{Au} + ^{197}\text{Au}$:

Kaons

⁷⁹Au+Au Inelastic Cross-Section Summary for K⁺

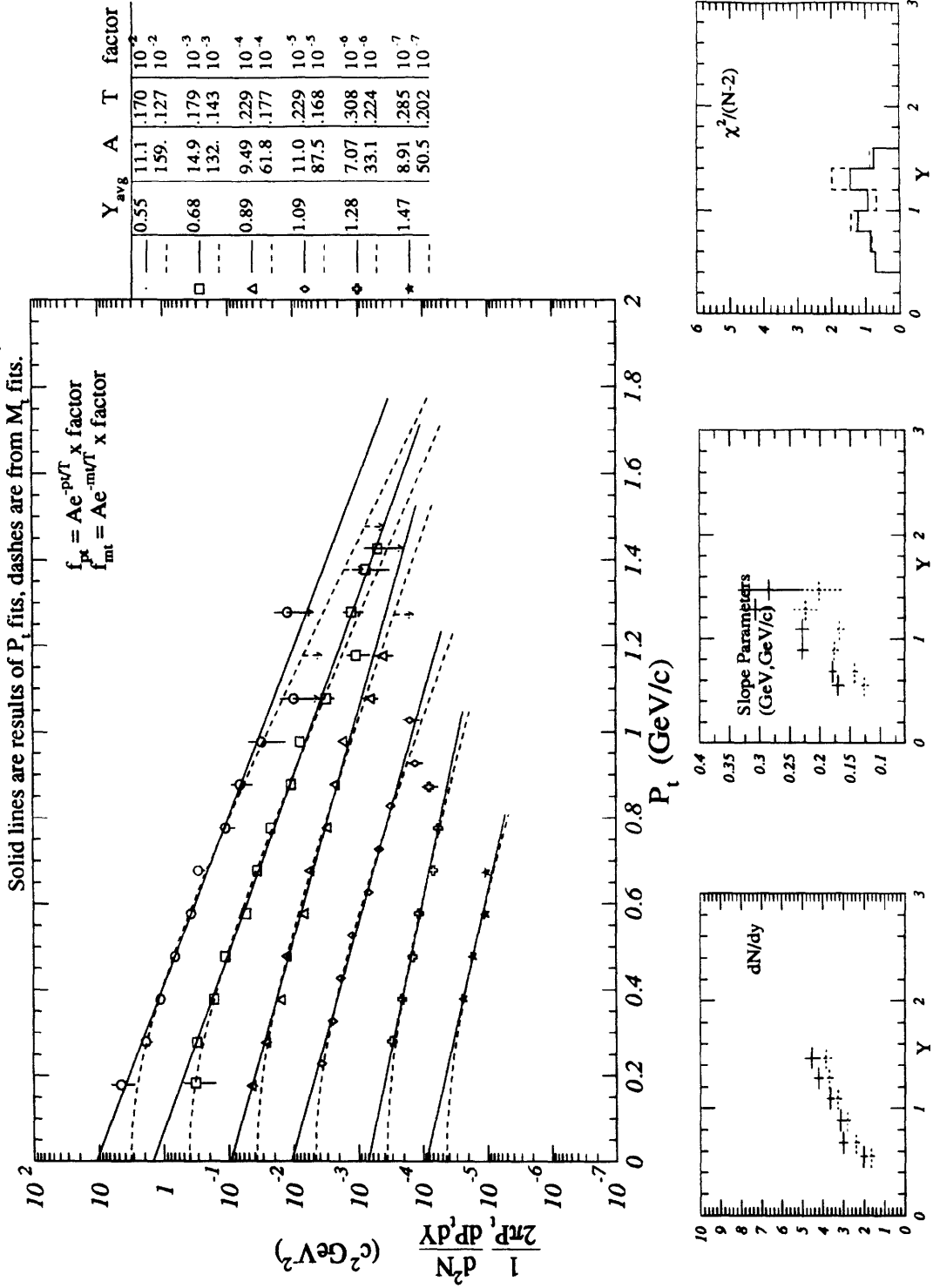


Figure P-1: Yield Summary for ¹⁹⁷Au + ¹⁹⁷Au INEL: K⁺

⁷⁹Au+Au Inelastic Cross-Section Summary for K⁻

Solid lines are results of P_t fits, dashes are from M_t fits.

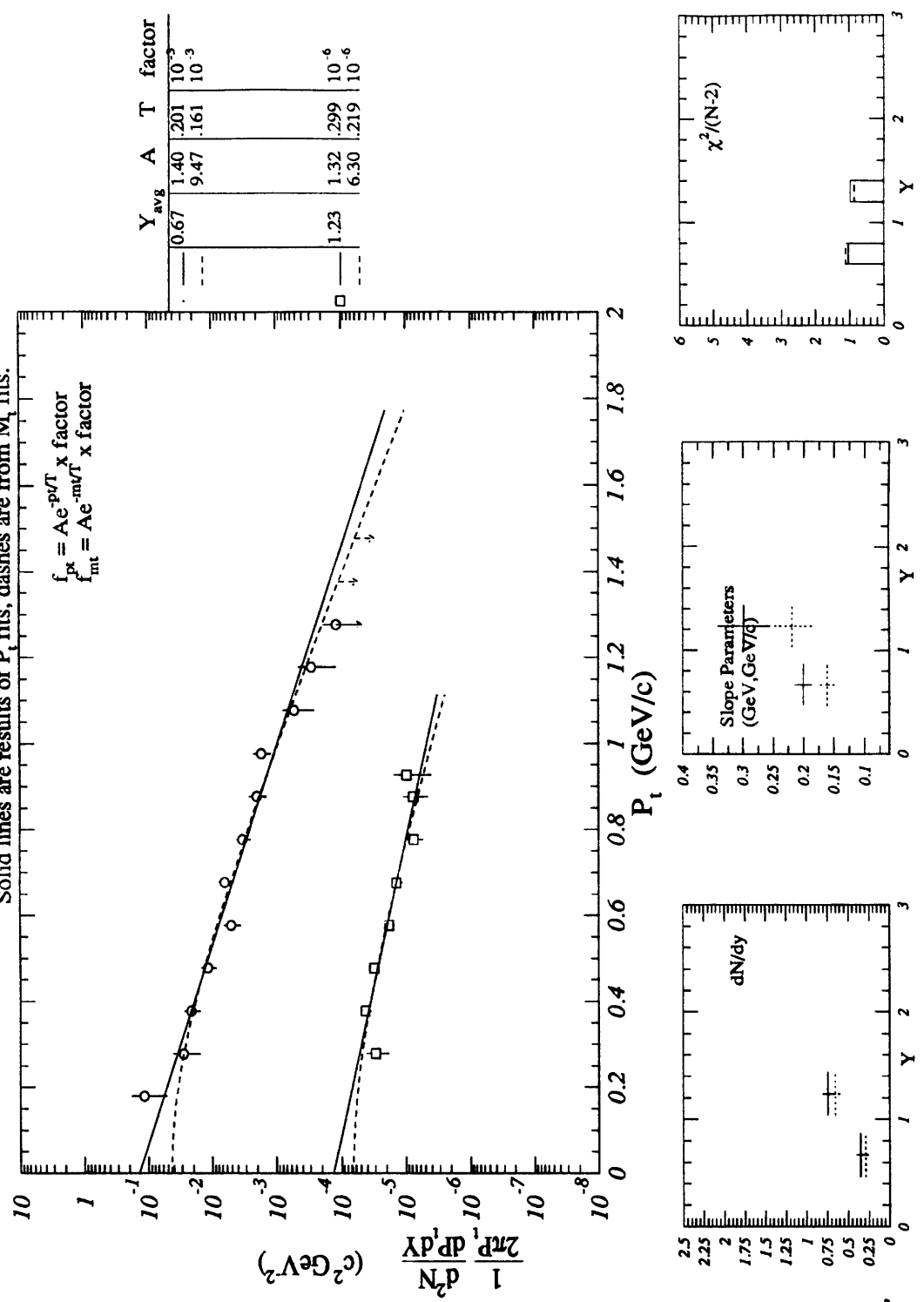


Figure P-2: Yield Summary for ¹⁸⁷Au + ¹⁹⁷Au INEL: K⁻

⁷⁹Au+Au ZCALBAR : Yield Summary K+

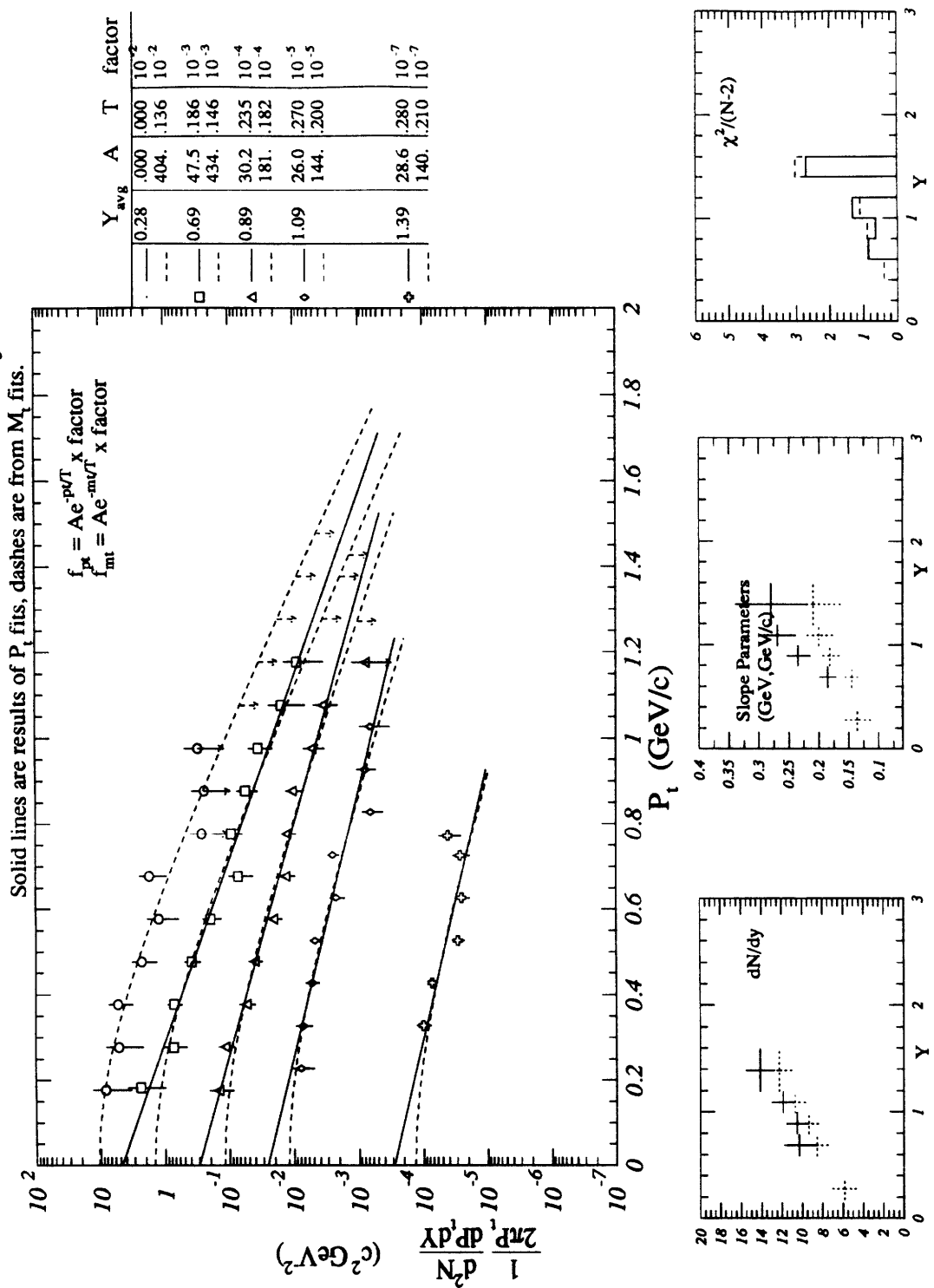


Figure P-3: Yield Summary for ¹⁹⁷Au + ¹⁹⁷Au ZCALBAR: K+

⁷⁹Au+Au ZCALBAR : Yield Summary K-

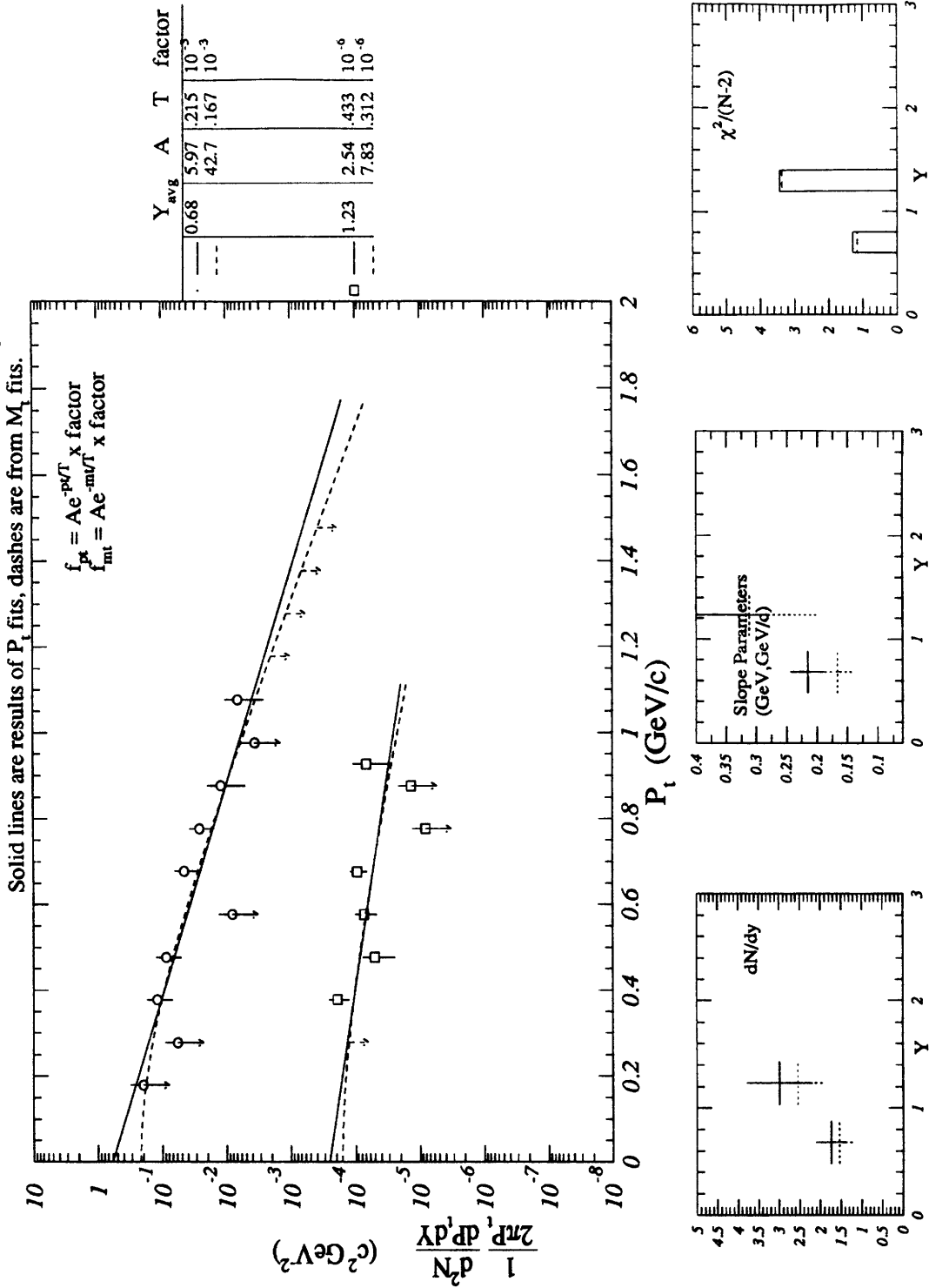


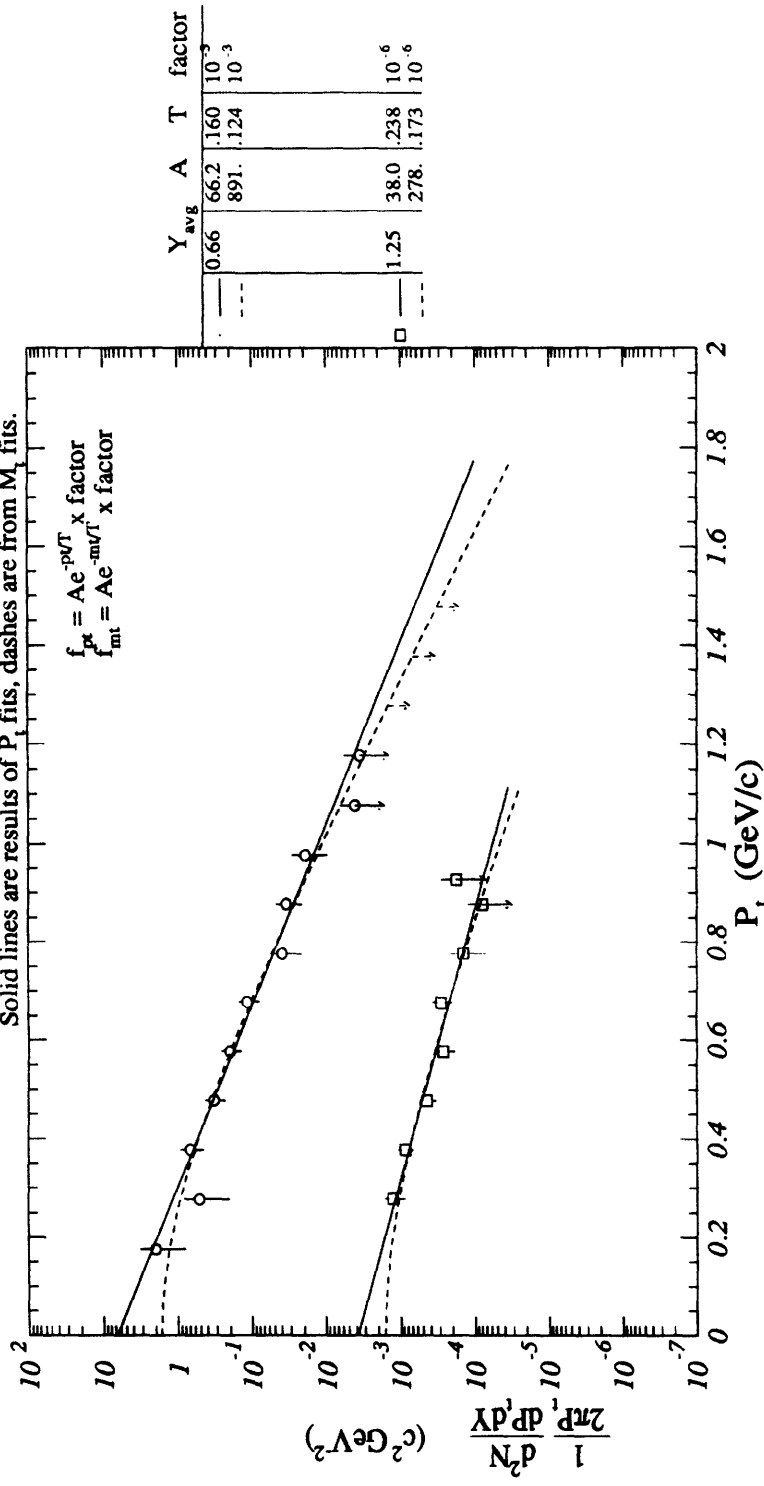
Figure P-4: Yield Summary for ¹⁹⁷Au + ¹⁹⁷Au ZCALBAR: K-

⁷⁹Au+Au Upper 0-4%σ_{inel} : Yield Summary K⁺

Solid lines are results of P_t fits, dashes are from M_t fits.

$$f_{pt} = Ae^{-pT} \times \text{x factor}$$

$$f_{mt} = Ae^{-mvT} \times \text{x factor}$$



Y _{avg}	A	T factor
0.66	66.2	.160 10 ⁻³
---	891.	.124 10 ⁻³
1.25	38.0	.238 10 ⁻⁶
---	278.	.173 10 ⁻⁶

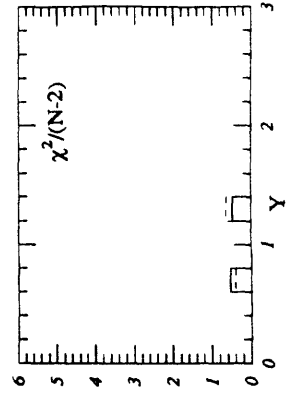
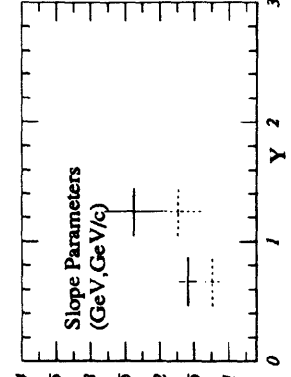
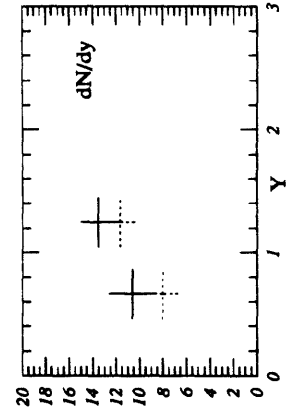


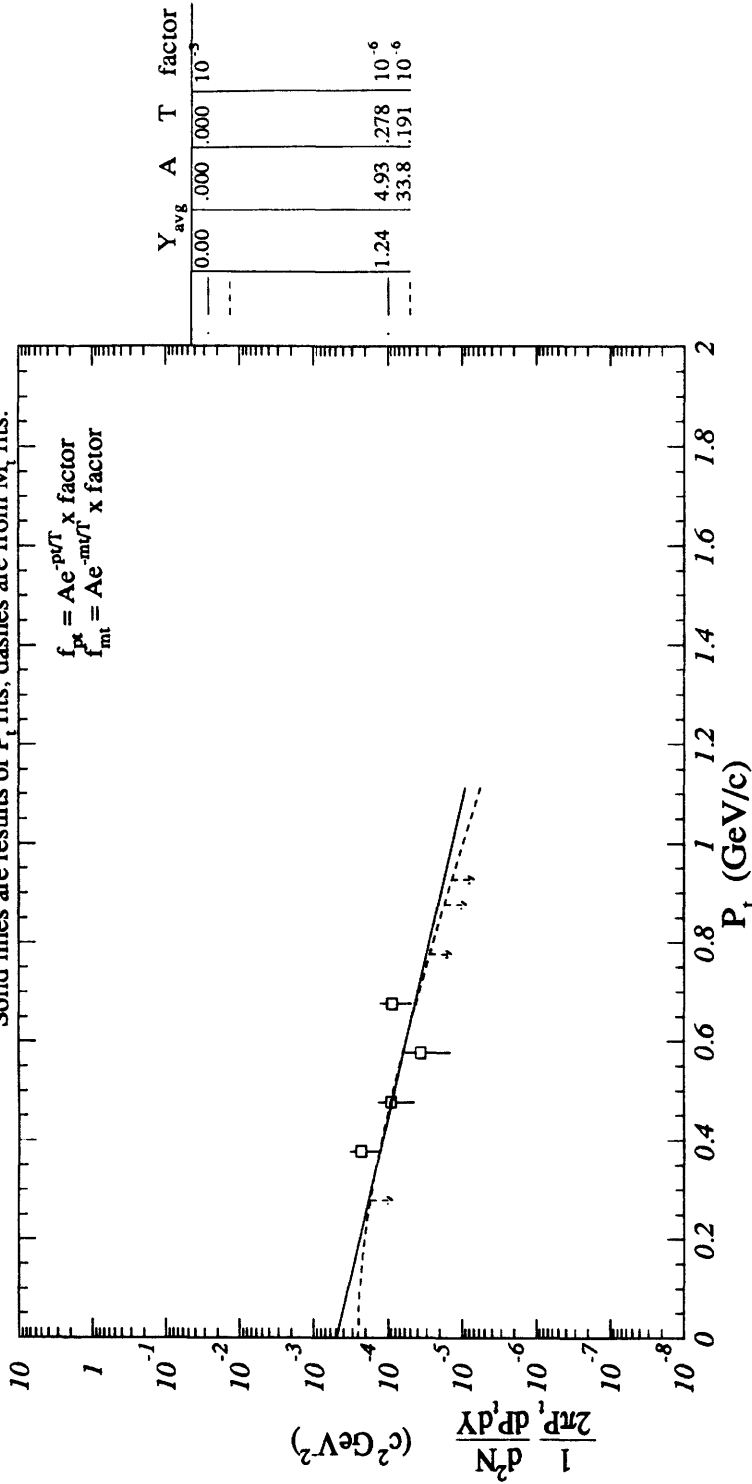
Figure P-5: Yield Summary for ¹⁹⁷Au + ¹⁹⁷Au 0 - 4 % σ_{inel} : K⁺

⁷⁹Au+Au Upper 0-4%σ_{inel} : Yield Summary K⁻

Solid lines are results of P_t fits, dashes are from M_t fits.

$$f_{pt} = A e^{-pT/\lambda} \times \text{factor}$$

$$f_{mt} = A e^{-mT/\lambda} \times \text{factor}$$



Y _{avg}	A	T	factor
0.00	.000	.000	10 ⁻³
1.24	4.93	.278	10 ⁻⁶
	33.8	.191	10 ⁻⁶

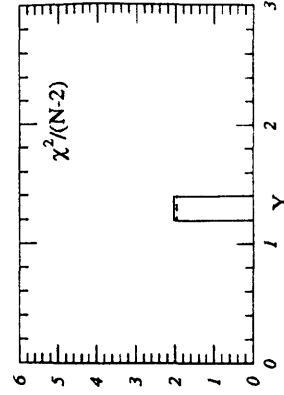
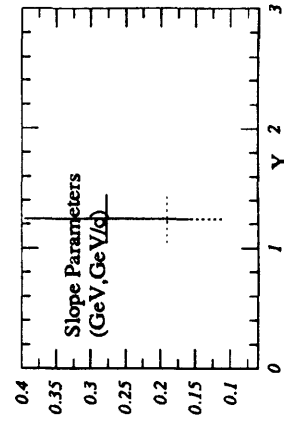
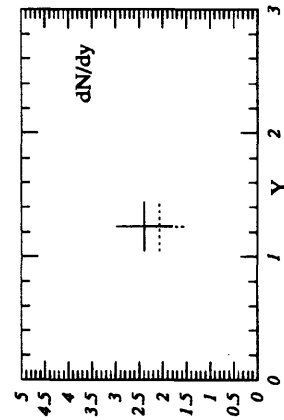


Figure P-6: Yield Summary for ¹⁹⁷Au + ¹⁹⁷Au 0 - 4 % σ_{inel} : K⁻

⁷⁹Au+Au Upper 0-10%σ_{inel} : Yield Summary K⁺

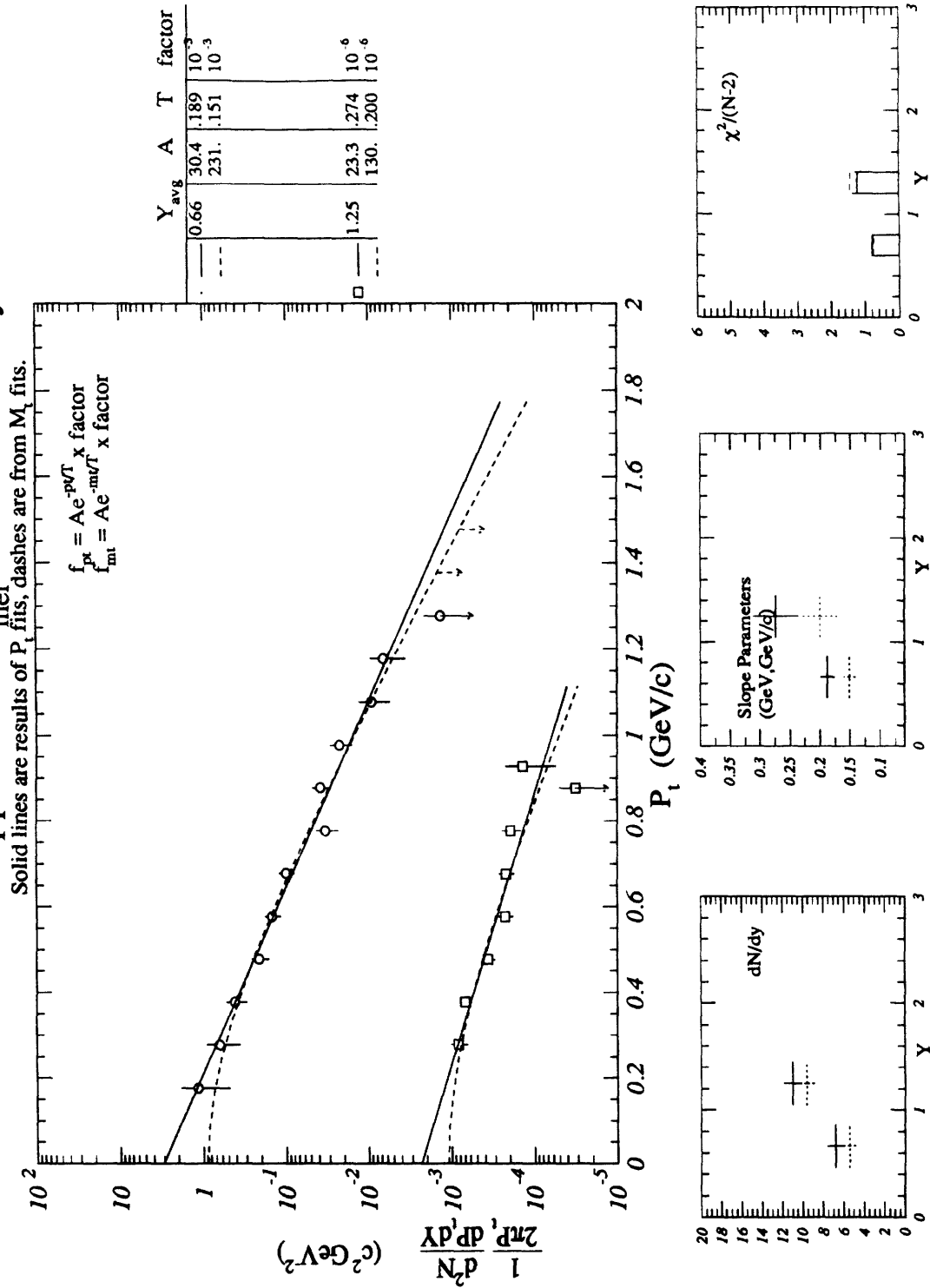


Figure P-7: Yield Summary for ¹⁹⁷Au + ¹⁹⁷Au 0 - 10 % σ_{inel} : K⁺

⁷⁹Au+Au Upper 0-10%σ_{inel} : Yield Summary K⁻

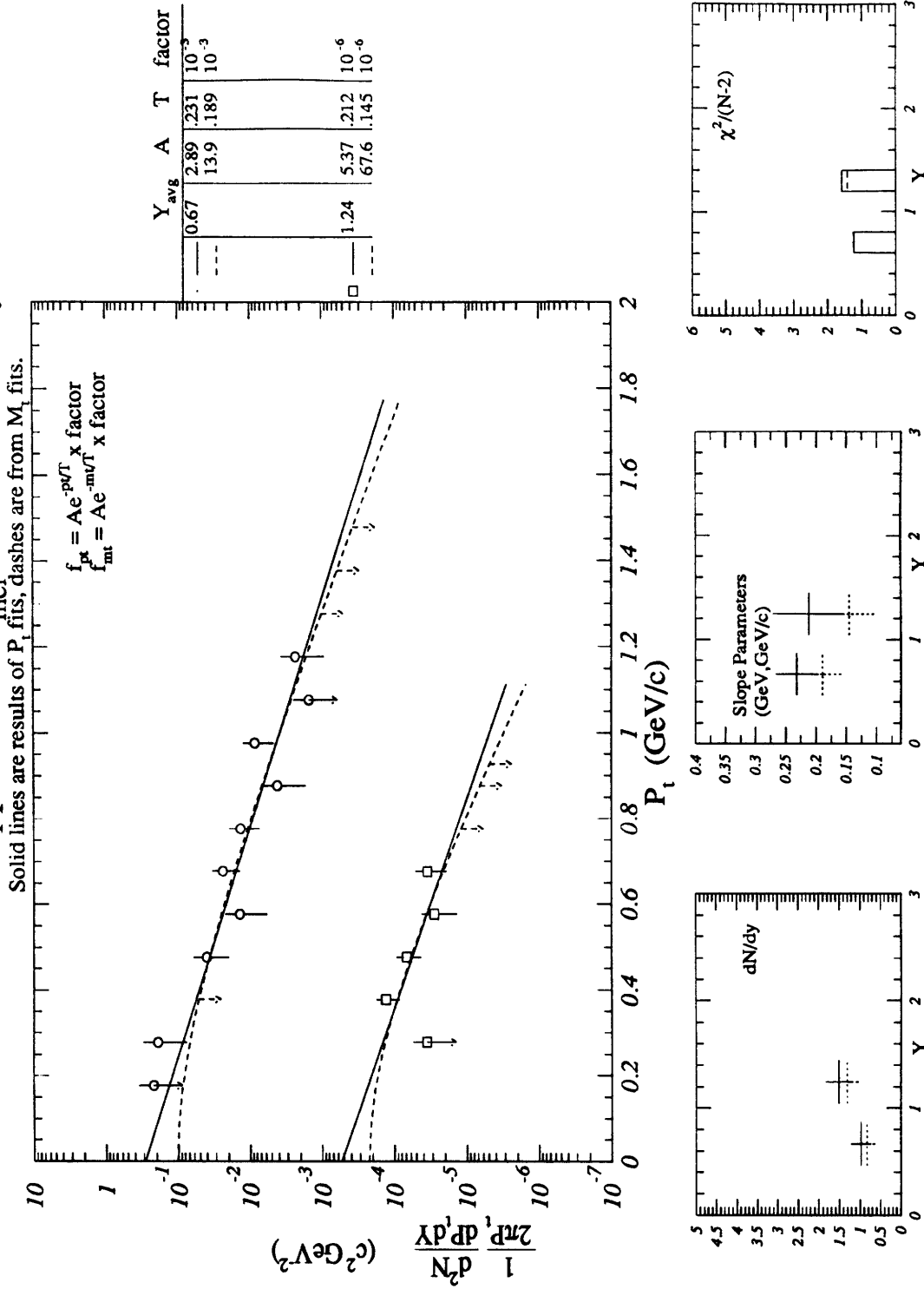


Figure P-8: Yield Summary for ¹⁹⁷Au + ¹⁹⁷Au 0 - 10 % σ_{inel} : K⁻

⁷⁹Au+Au Upper 10-30% σ_{inel} : Yield Summary K+

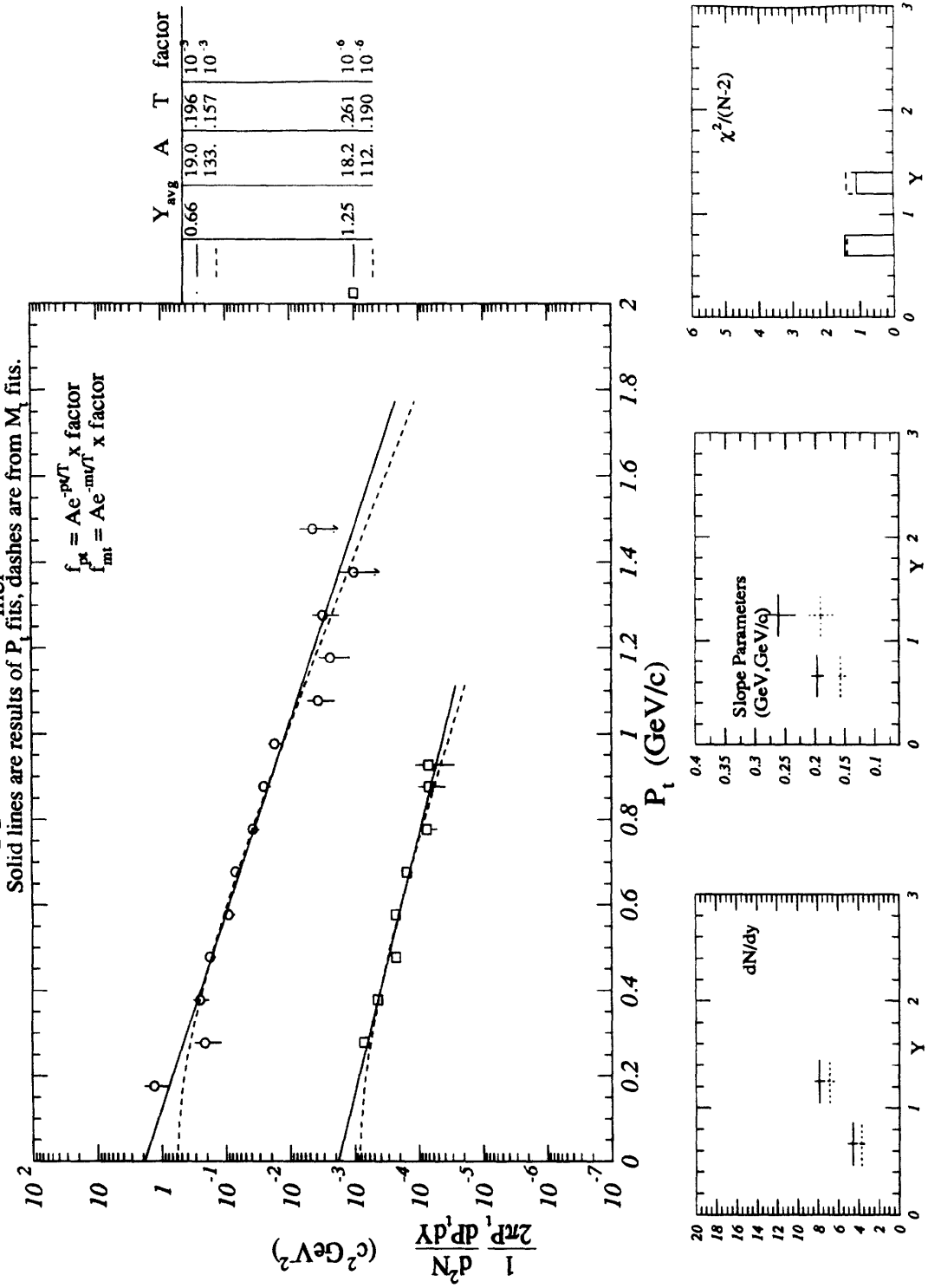


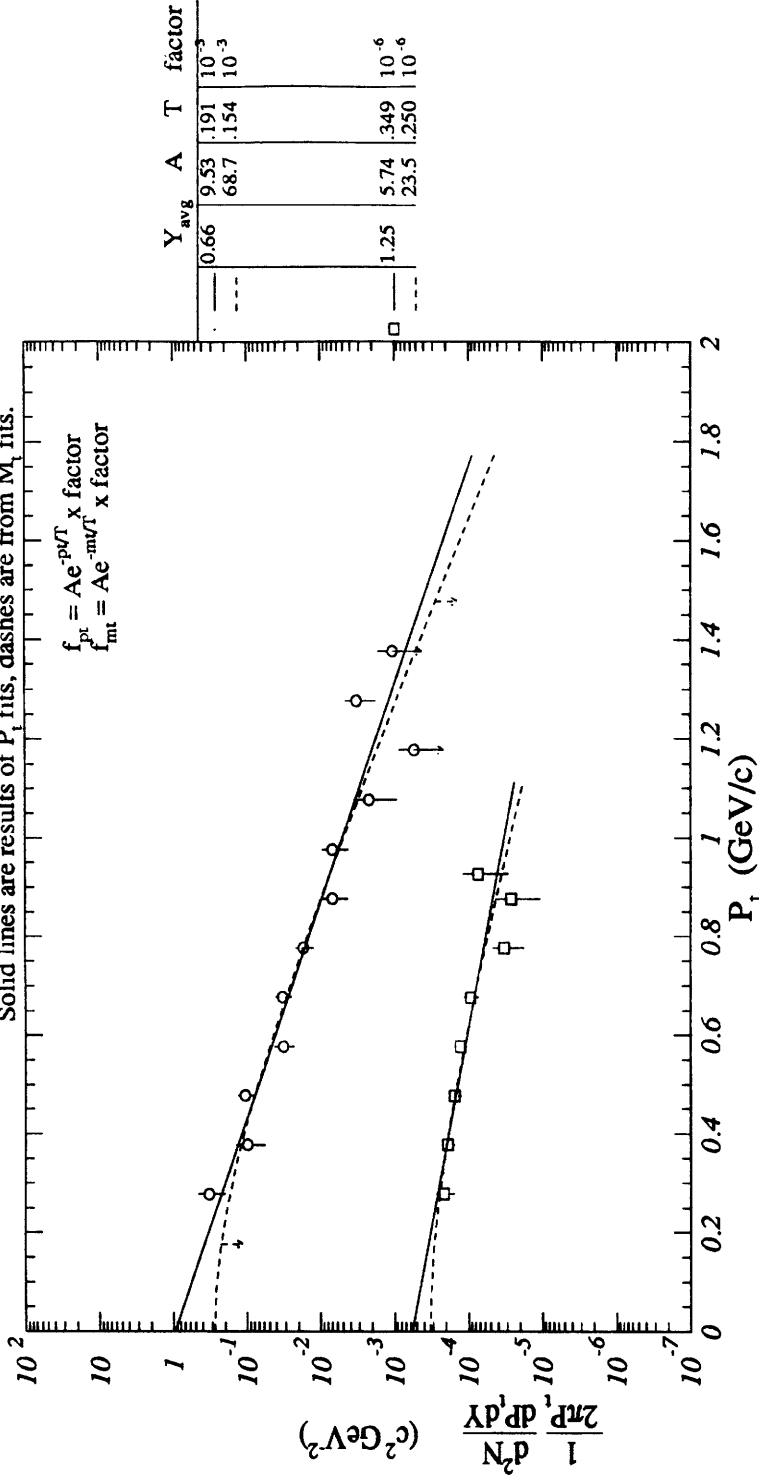
Figure P-9: Yield Summary for ¹⁹⁷Au + ¹⁹⁷Au 10 - 30 % σ_{inel} : K+

⁷⁹Au+Au Upper 30-50%σ_{inel} : Yield Summary K⁺

Solid lines are results of P_t fits, dashes are from M_t fits.

$$f_{pt} = A e^{-p_t/T} \times \text{factor}$$

$$f_{mt} = A e^{-m_t/T} \times \text{factor}$$



Y _{avg}	A	T	factor
0.66	9.53	.191	10 ⁻³
---	68.7	.154	10 ⁻³
1.25	5.74	.349	10 ⁻⁶
---	23.5	.250	10 ⁻⁶

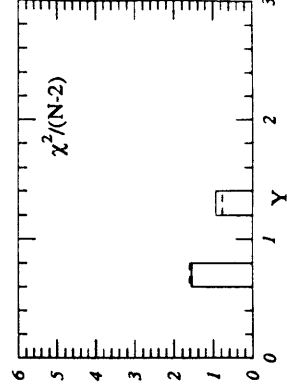
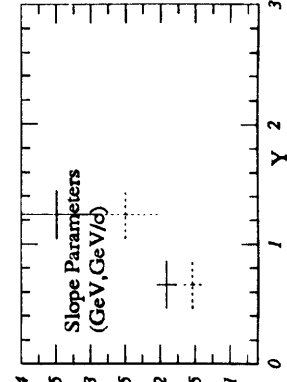
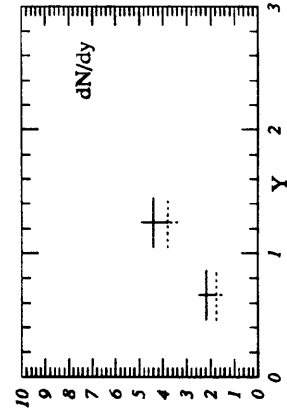
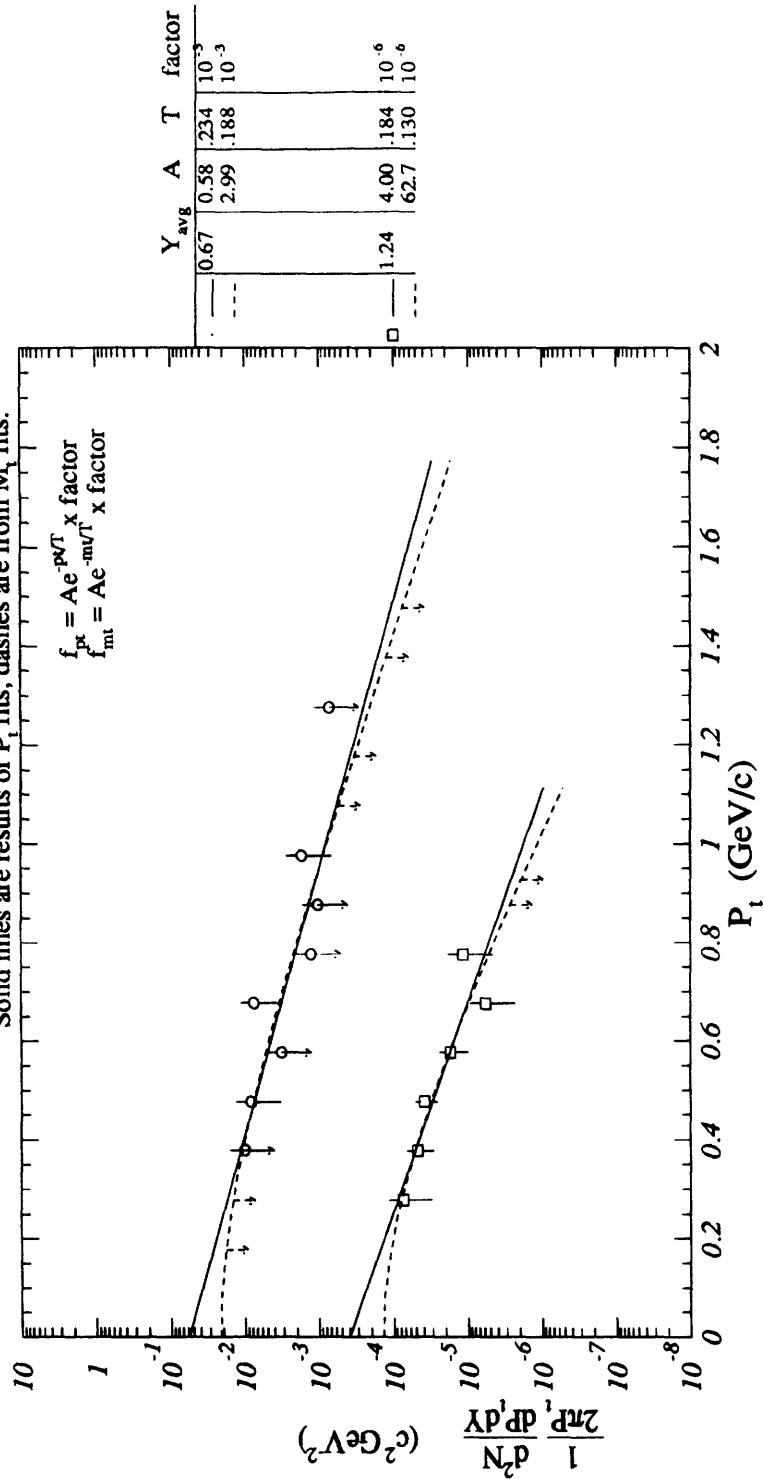


Figure P-10: Yield Summary for ¹⁹⁷Au + ¹⁹⁷Au 30 - 50 % σ_{inel} : K⁺

⁷⁹Au+Au Upper 30-50%σ_{inel} : Yield Summary K⁻

Solid lines are results of P_t fits, dashes are from M_t fits.



$$f_{pt} = Ae^{-pT} \times \text{x factor}$$

$$f_{mt} = Ae^{-mT} \times \text{x factor}$$

Y _{avg}	A	T	factor
0.67	0.58	.234	10 ⁻³
2.99	1.88	.188	10 ⁻³
1.24	4.00	.184	10 ⁻⁶
	62.7	.130	10 ⁻⁶

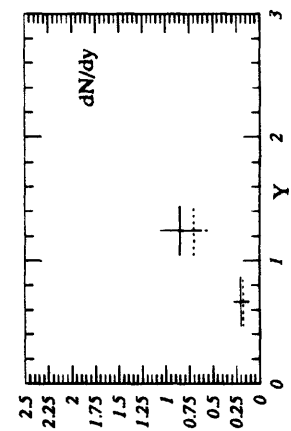
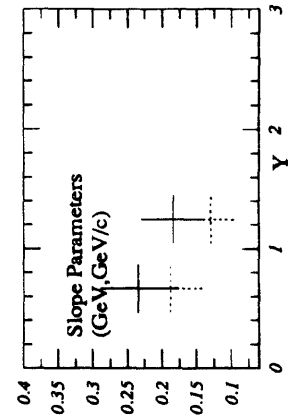
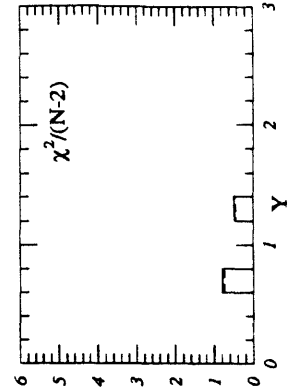


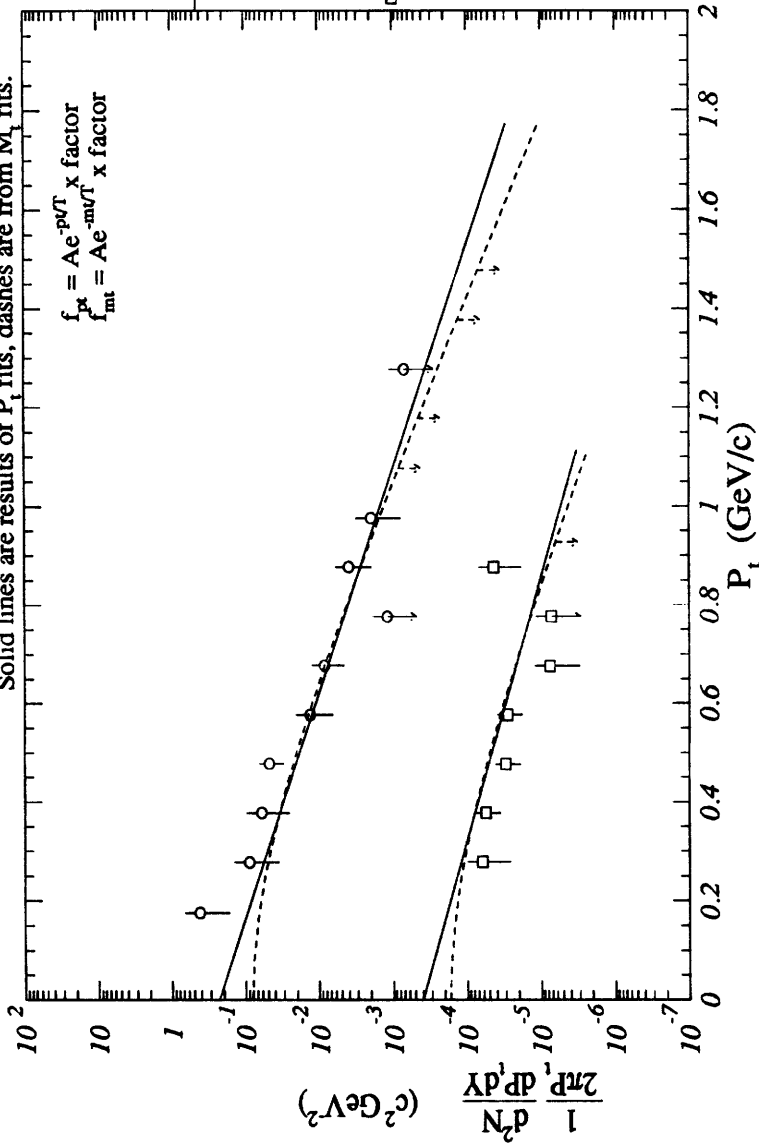
Figure P-11: Yield Summary for ¹⁹⁷Au + ¹⁹⁷Au 30 - 50 % σ_{inel} : K⁻

$^{79}\text{Au} + \text{Au}$ Upper 50-70% σ_{inel} : Yield Summary K^+

Solid lines are results of P_t fits, dashes are from M_t fits.

$$f_{\text{pt}} = A e^{-pT} \times \text{x factor}$$

$$f_{\text{mt}} = A e^{-mT} \times \text{x factor}$$



	Y_{avg}	A	T	factor
○	0.65	2.32	1.197	10^{-3}
□	1.09	4.01	1.232	10^{-6}
		21.5	1.151	10^{-3}
		31.5	1.169	10^{-6}

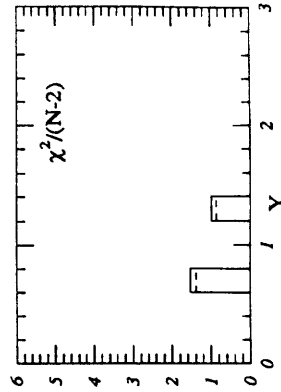
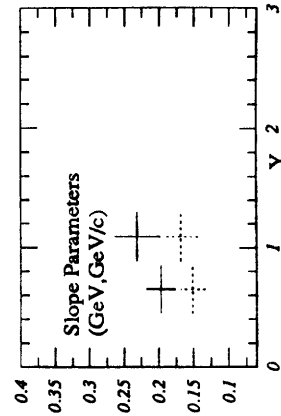
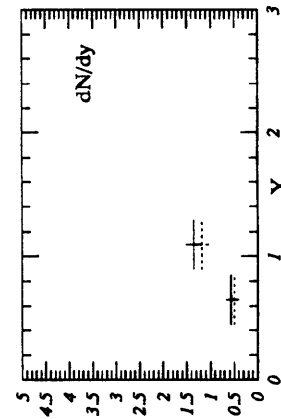


Figure P-12: Yield Summary for $^{197}\text{Au} + ^{197}\text{Au}$ 50 - 70 % σ_{inel} : K^+

⁷⁹Au+Au Upper 70-90%σ_{inel} : Yield Summary K⁺

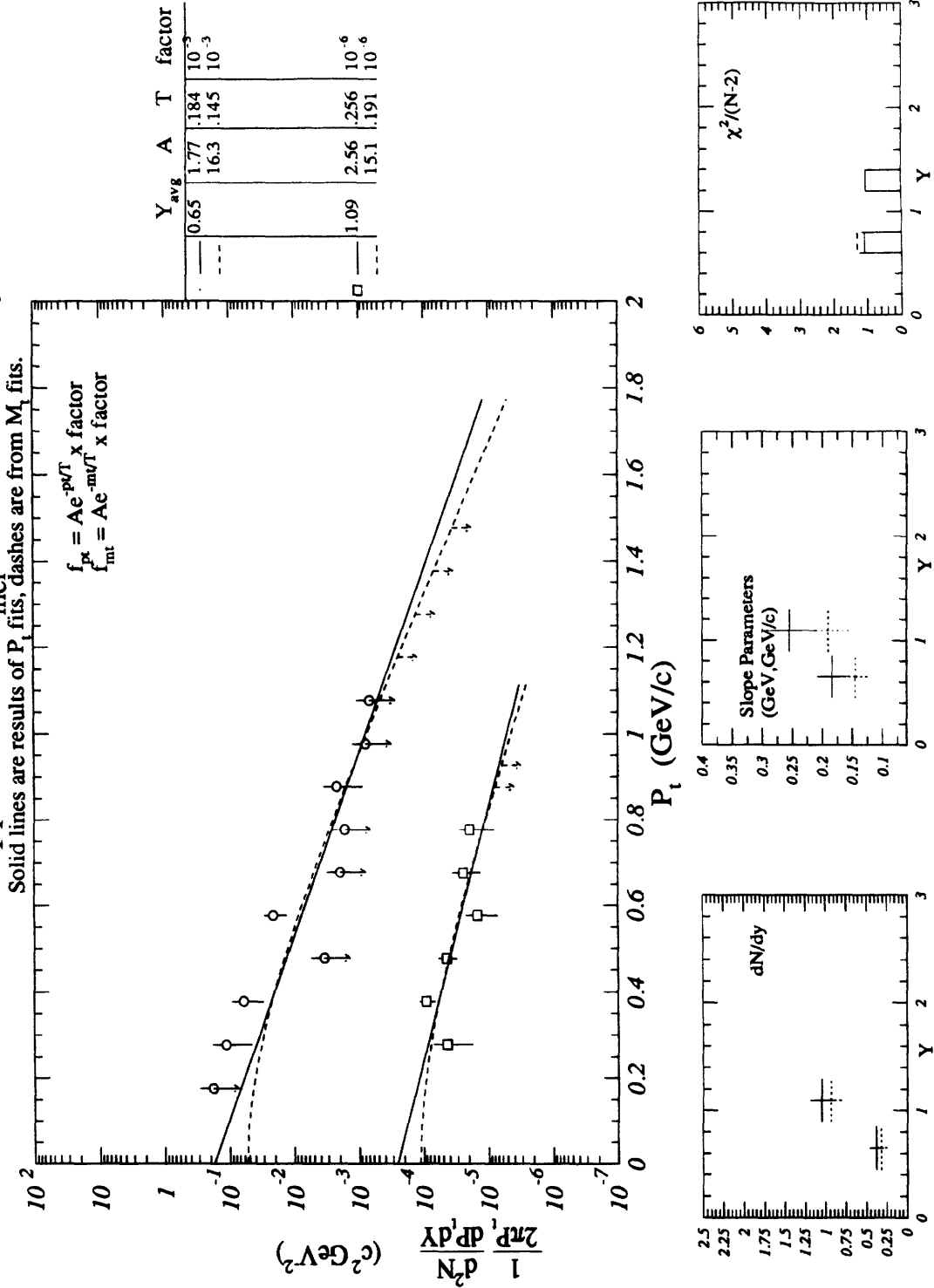


Figure P-13: Yield Summary for ¹⁹⁷Au + ¹⁹⁷Au 70 - 90 % σ_{inel} : K⁺

Appendix Q

Yield Summary: $^{197}\text{Au} + ^{197}\text{Au}$:

Protons

¹⁹⁷Au+Au Inelastic Cross-Section Summary for Protons

Solid lines are results of Boltzmann fits, dashes are from M_T fits.

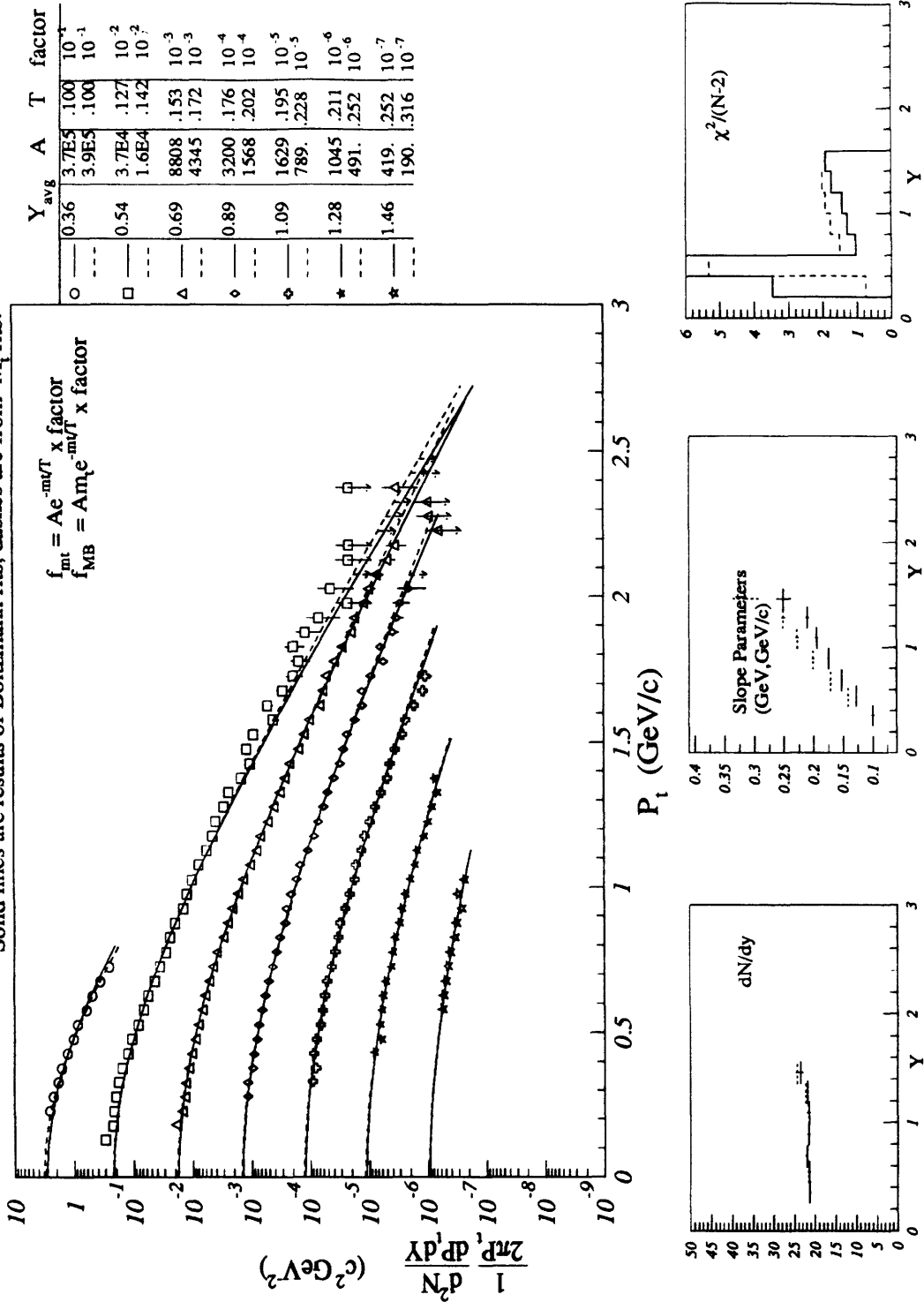
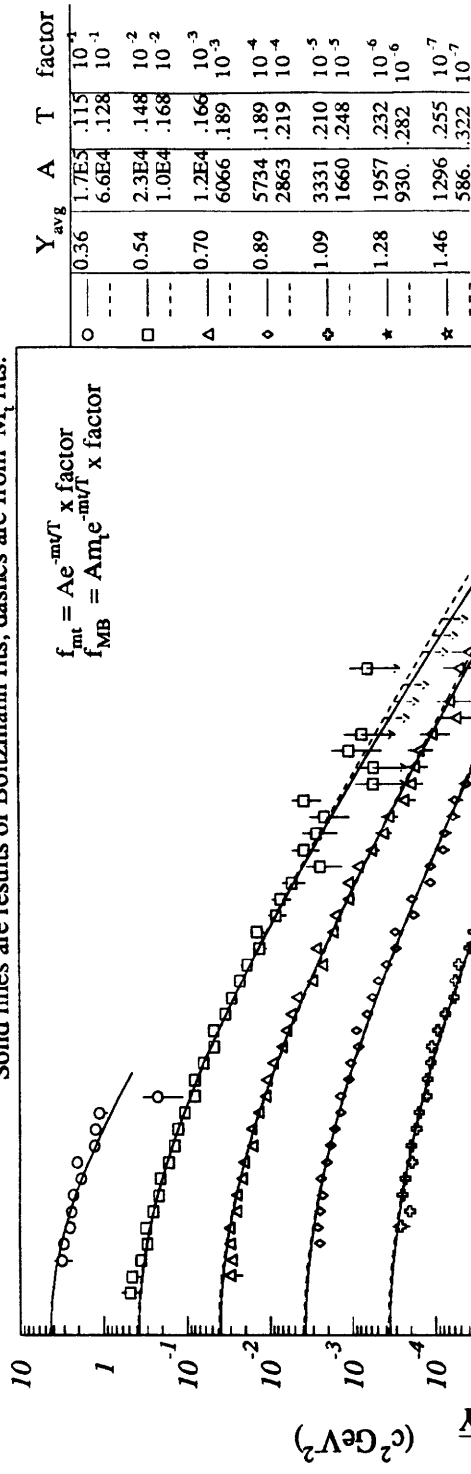


Figure Q-1: Yield Summary for ¹⁹⁷Au + ¹⁹⁷Au INEL: Protons

¹⁹⁷Au+Au ZCALBAR : Yield Summary Protons

Solid lines are results of Boltzmann fits, dashes are from M_T fits.



Centrality	Y_{avg}	A	T	factor
0	0.36	1.7E5	.115	10^{-1}
1	0.54	6.6E4	.128	10^{-1}
2	0.70	2.3E4	.148	10^{-2}
3	0.89	1.0E4	.168	10^{-2}
4	1.09	1.2E4	.166	10^{-3}
5	1.28	6066	.189	10^{-3}
6	1.46	5734	.189	10^{-4}
7	1.28	2863	.219	10^{-4}
8	1.09	3331	.210	10^{-5}
9	1.28	1660	.248	10^{-5}
10	1.46	1957	.232	10^{-6}
11	1.28	930	.282	10^{-6}
12	1.46	1296	.255	10^{-7}
13	1.46	586	.322	10^{-7}

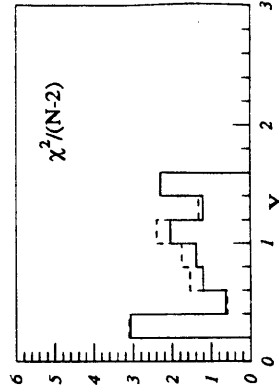
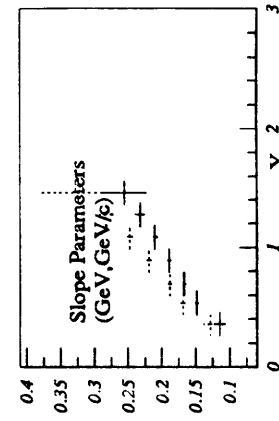
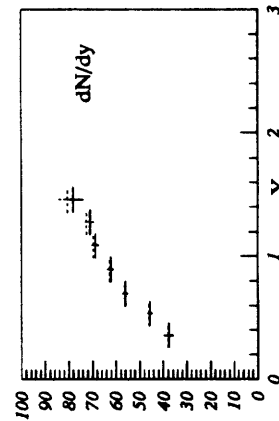


Figure Q-2: Yield Summary for ¹⁹⁷Au + ¹⁹⁷Au ZCALBAR: Protons

¹⁹⁷Au+Au Upper 0-4%σ_{inel} : Yield Summary Protons

Solid lines are results of Boltzmann fits, dashes are from M_s fits.

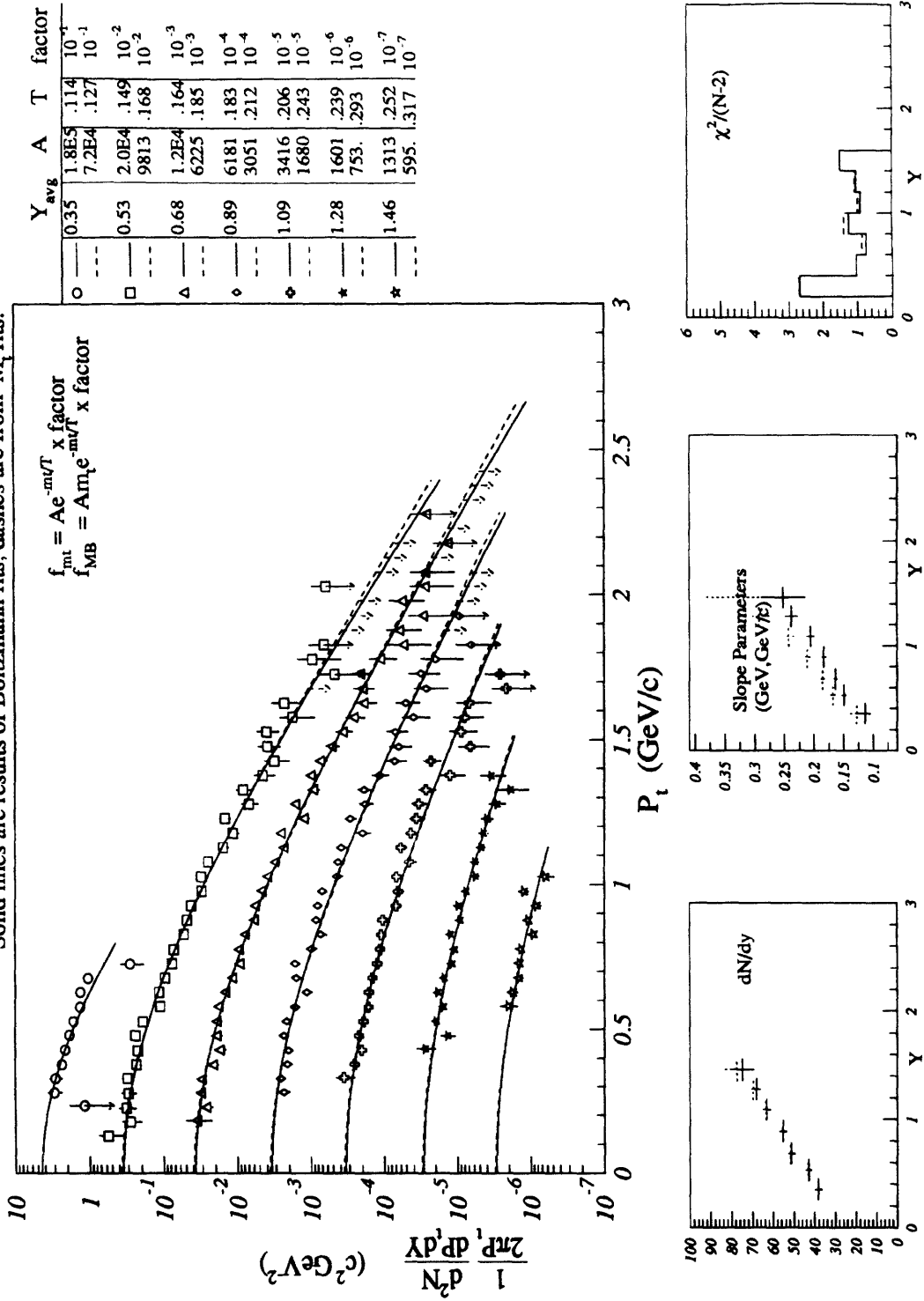


Figure Q-3: Yield Summary for ¹⁹⁷Au + ¹⁹⁷Au 0 - 4 % σ_{inel} : Protons

$^{197}\text{Au}+\text{Au}$ Upper 0-10% σ_{inel} : Yield Summary Protons

Solid lines are results of Boltzmann fits, dashes are from M_T fits.

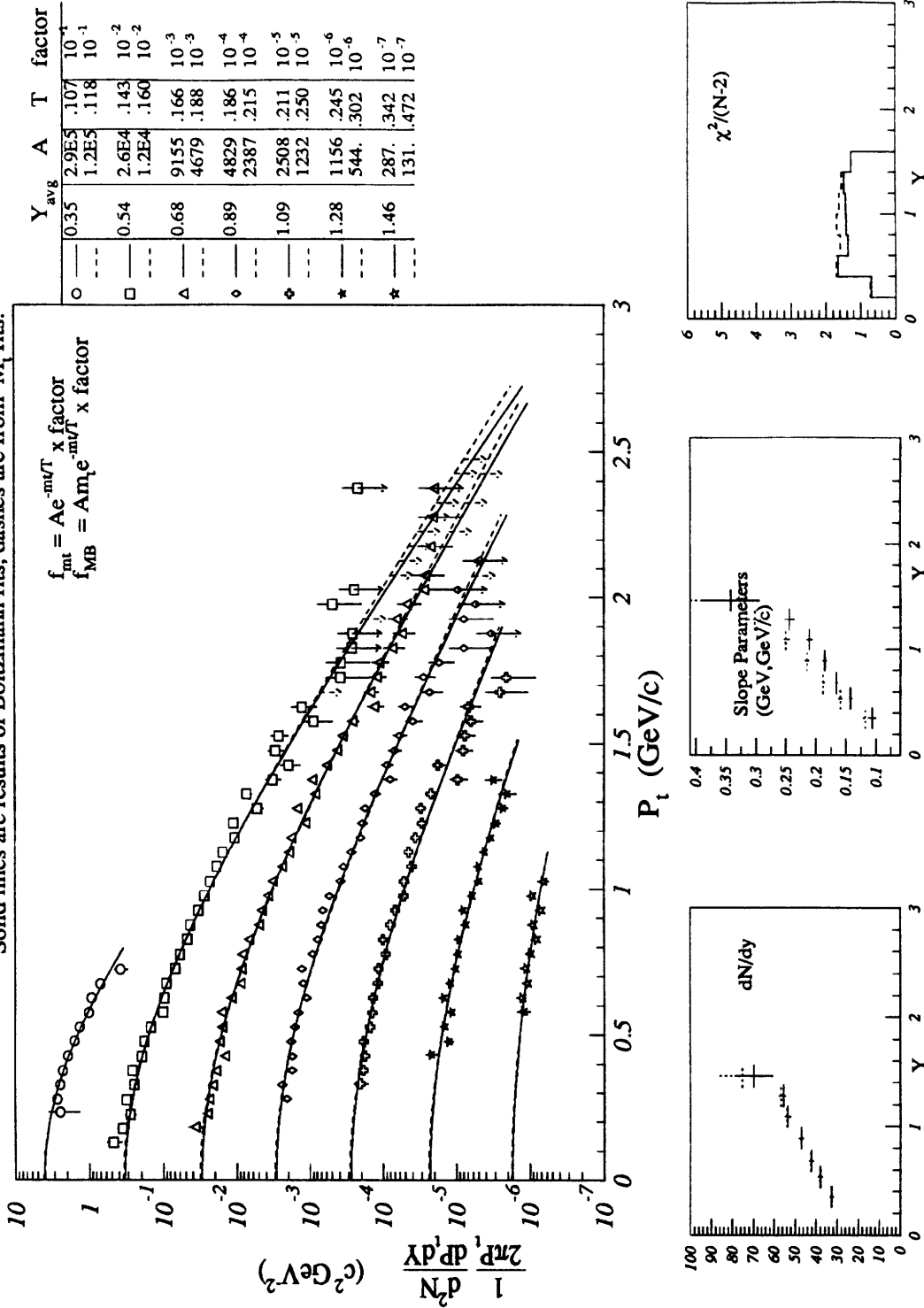


Figure Q-4: Yield Summary for $^{197}\text{Au} + ^{197}\text{Au}$ 0 - 10 % σ_{inel} : Protons

¹⁹⁷Au+Au Upper 10-30%σ_{inel} : Yield Summary Protons

Solid lines are results of Boltzmann fits, dashes are from M_t fits.

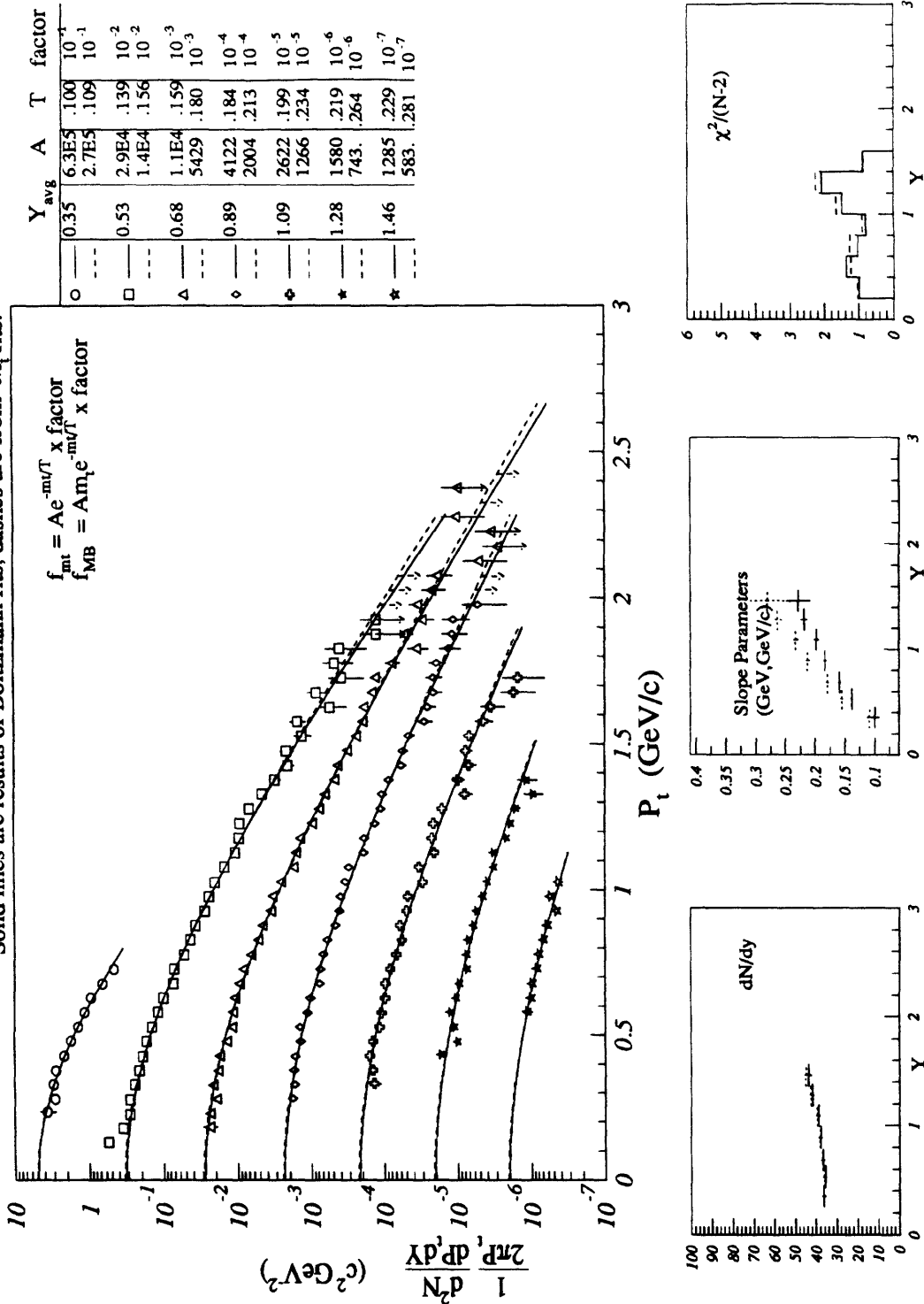
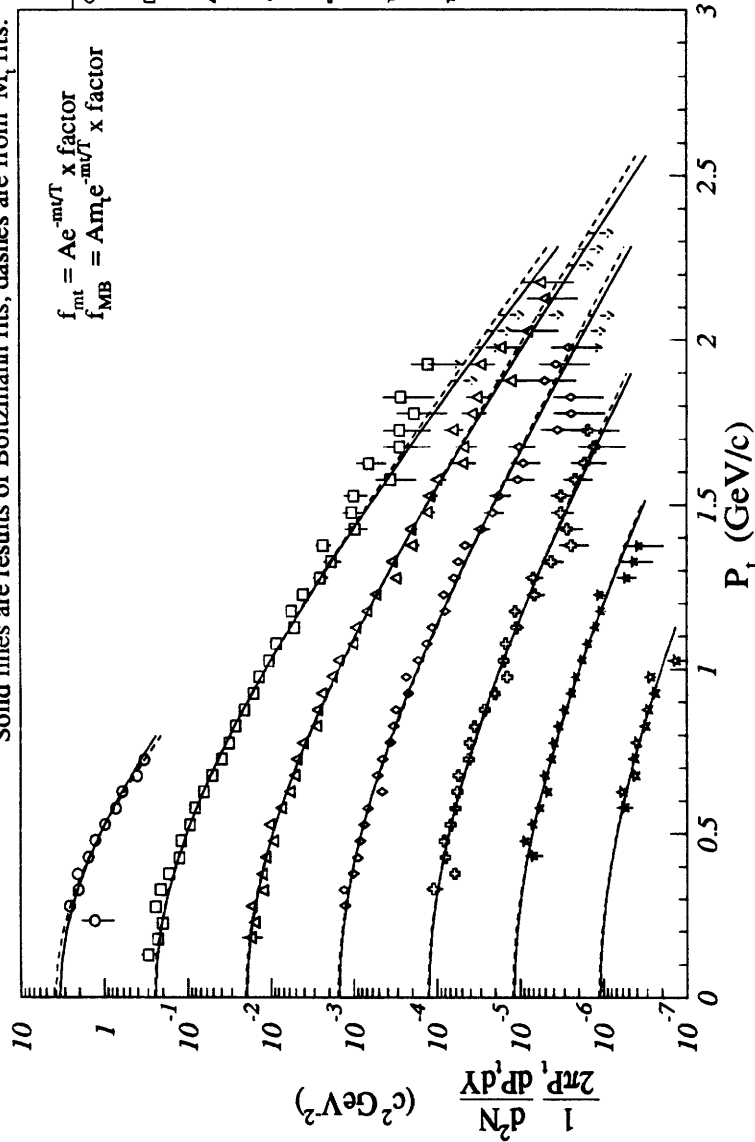


Figure Q-5: Yield Summary for ¹⁹⁷Au + ¹⁹⁷Au 10 - 30 % σ_{inel} : Protons

$^{197}\text{Au}+\text{Au}$ Upper 30-50% σ_{inel} : Yield Summary Protons

Solid lines are results of Boltzmann fits, dashes are from M_T fits.



Symbol	Y_{avg}	A	T	factor
○	0.35	4.3E5	.100	10^{-1}
□	0.53	4.6E5	.100	10^{-1}
△	0.69	2.0E4	.126	10^{-2}
◇	0.89	1.2E4	.147	10^{-3}
⊕	1.09	5989	.165	10^{-3}
⊙	1.28	4164	.169	10^{-4}
⊛	1.46	2037	.193	10^{-4}
⊠	1.46	2229	.184	10^{-5}
⊡	1.46	1050	.214	10^{-5}
⊞	1.46	1496	.197	10^{-6}
⊚	1.46	702	.232	10^{-6}
⊛	1.46	1090	.208	10^{-7}
⊠	1.46	498	.249	10^{-7}

$$f_{\text{int}} = Ae^{-m_T/T} \times \text{factor}$$

$$f_{\text{MB}} = A m_T e^{-m_T/T} \times \text{factor}$$

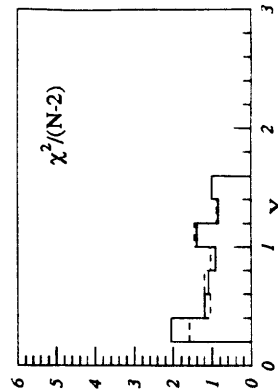
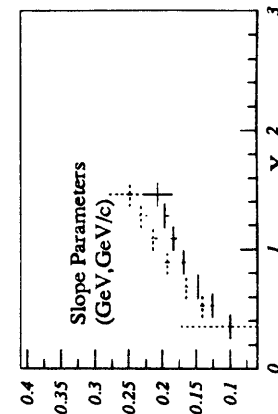
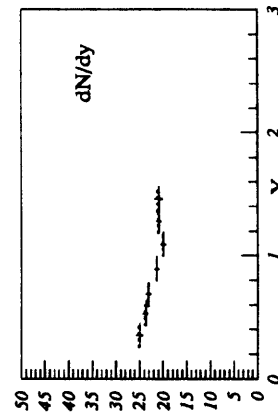


Figure Q-6: Yield Summary for $^{197}\text{Au} + ^{197}\text{Au}$ 30 - 50 % σ_{inel} : Protons

$^{197}\text{Au} + ^{197}\text{Au}$ Upper 50-70% σ_{inel} : Yield Summary Protons

Solid lines are results of Boltzmann fits, dashes are from M_T fits.

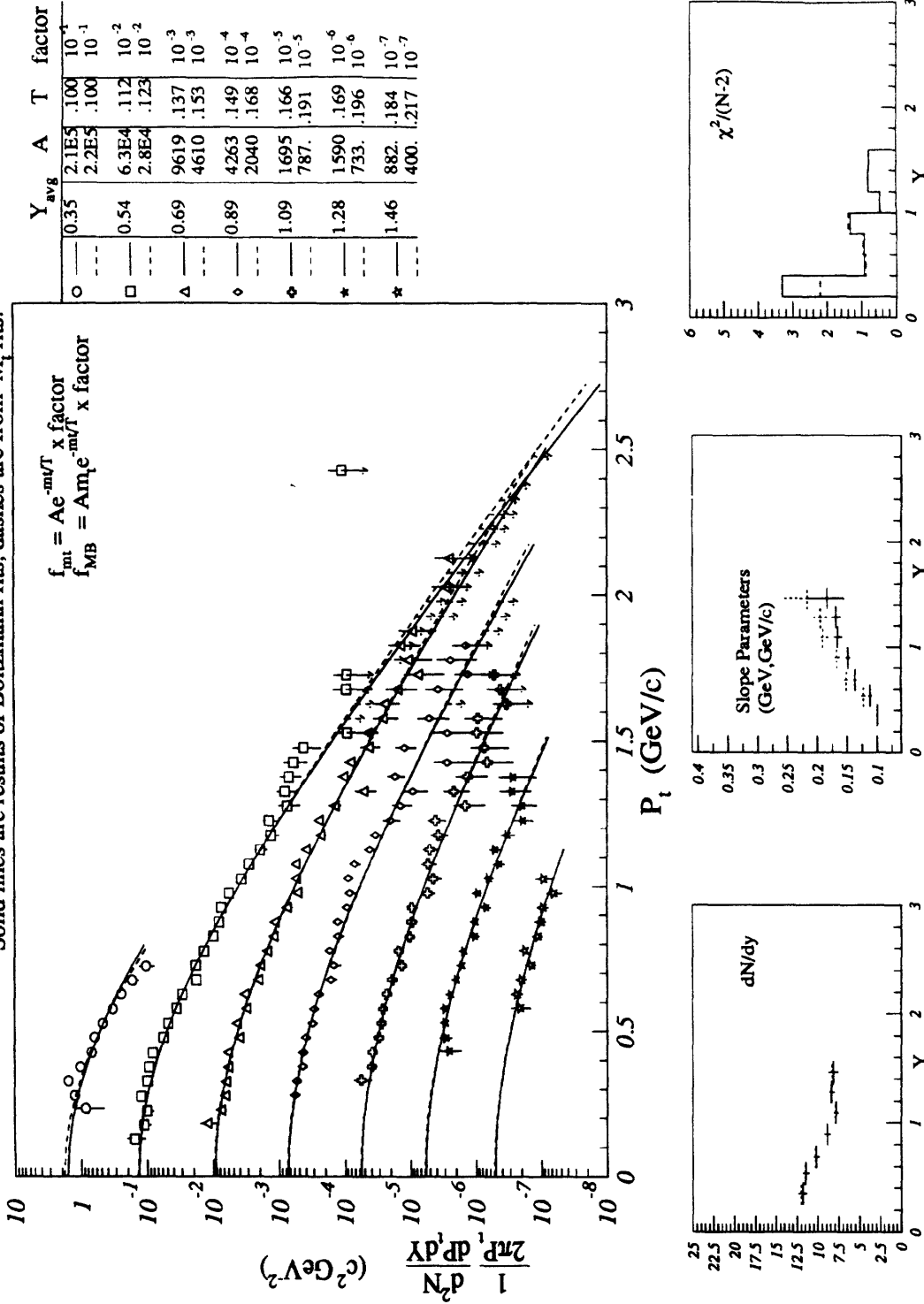
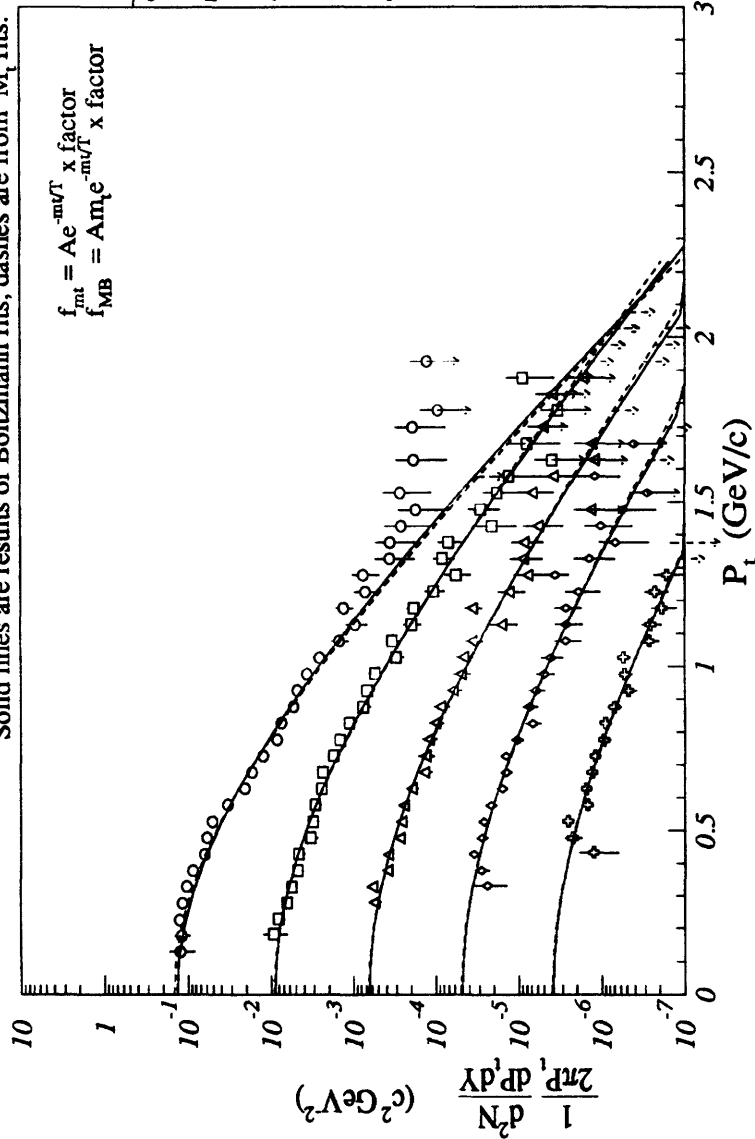


Figure Q-7: Yield Summary for $^{197}\text{Au} + ^{197}\text{Au}$ 50 - 70 % σ_{inel} : Protons

$^{197}\text{Au} + \text{Au}$ Upper 70-90% σ_{inel} : Yield Summary Protons

Solid lines are results of Boltzmann fits, dashes are from M_T fits.



$$f_{\text{MB}}^{\text{fit}} = A m_T e^{-m_T/T} \times \text{factor}$$

Symbol	Y _{avg}	A	T	factor
○	0.53	1.7E5	.100	10 ⁻²
○	---	1.1E5	.105	10 ⁻²
□	0.69	1.8E4	.124	10 ⁻³
□	---	8638	.137	10 ⁻³
△	0.89	5703	.140	10 ⁻⁴
△	---	2644	.157	10 ⁻⁴
◇	1.09	2010	.157	10 ⁻⁵
◇	---	923	.180	10 ⁻⁵
⊕	1.28	1107	.168	10 ⁻⁶
⊕	---	512	.193	10 ⁻⁶

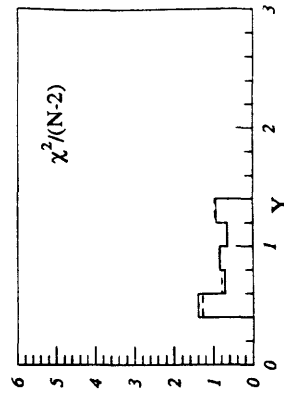
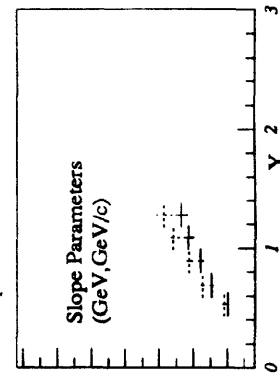
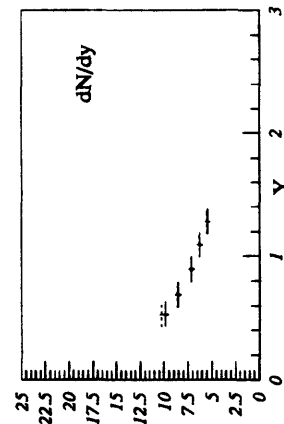


Figure Q-8: Yield Summary for $^{197}\text{Au} + ^{197}\text{Au}$ 70 - 90 % σ_{inel} : Protons

Bibliography

- [Abb90th] T. Abbott. *Search for Intermittency in Central Collisions of $^{16}\text{O} + \text{Cu}$ at 14.6 A·GeV/c*. Ph. D. Thesis, Univ. of Cal. Riverside (1990).
- [Abb87] E802 Collaboration, T. Abbott et al. "Measurement of energy emission from O + A and p + A collisions at 14.6 GeV/c per nucleon with a lead glass array", *Phys. Lett.*, **197**(1987)p. 285.
- [Abb89] E802 Collaboration, T. Abbott et al. "A single arm spectrometer detector for high energy heavy-ion experiments", *Nucl. Inst. Meth.* **A290**(1990)p. 41-60.
- [Abb92a] E802 Collaboration, T. Abbott et al. "Measurement of particle production in proton-induced reactions at 14.6 A·GeV/c", *Phys. Rev. D* **11**(1992).
- [Abb92b] E802 Collaboration, T. Abbott et al. "Bose-Einstein Correlations ins Si + Al and Si + Au collisions at 14.6 A · GeV/c", *Phys. Rev. Lett.* **70**(1993).
- [Abb92c] E802 Collaboration, T. Abbott et al. "Centrality dependence of K⁺ and π^+ multiplicites from $^{28}\text{Si} + \text{A}$ collisions at 14.6 A·GeV/c ." *Phys. Lett. B.* **291**(1992)p. 341.
- [Abb94] E802 Collaboration, T. Abbott et al. "Charged Hadron Distributions in Central and Peripheral $^{28}\text{Si} + \text{A}$ collisions at 14.6 A·GeV/c." Submitted to *Phys. Rev. C*.
- [Ak89] Y. Akiba. *Measurement of Energy Emission from O + A Collisions at 14.6 GeV/c per Nucleon*. Ph. D. Thesis. Univ. of Tokyo (1989).

- [Alp75] B. Alper, et al. *Nucl. Phys.* **B100**(1975)p. 237.
- [And87] B. Anderson, B. Gustafson, and B. Nilsson-Almqvist. *Nucl. Phys.* **B281**(1987)p. 289.
- [Ant73] Antinuci, et al. *Lett. Al Nuo. Cim.* **6**(1973)p. 121.
- [Ant75] D. Antreasyan, et al. *Phys. Rev.* **D19**(1979)p. 764.
- [Bak83] P.R. Baker. *Nuc. Inst. and Meth. in Phys. Res.* **221**(1984)p. 437.
- [Beav89] D. Beavis, et al. *Nucl. Inst. and Meth.* **A281**(1989)p. 367.
- [Bev69] P.R. Bevington. *Data reduction and error analysis for the physical sciences.* McGraw-Hill, Inc (1969)p. 62.
- [Bial74] A. Bialas and C. Czyz. *Phys. Lett.* **51B**(1974)p. 179.
- [Bjo83] J.D. Bjorken. *Phys. Rev.* **D27**(1983)p. 454.
- [Blo90] M. Bloomer. *Energy and Baryon Densities in $^{28}\text{Si} + A$ Collisions at 14.6 A·GeV/c.* Ph. D. Thesis, MIT (1991).
- [Bus84] W. Busa and A.S. Goldhaber. *Phys. Lett.* **139B**(1984)p. 235.
- [Bus88] W. Busa and R. Ledoux. *Ann Rev. Nucl. Sci.* **18**(1988)p. 119.
- [CDF156] D. Quarrie, B. Troemel. Internal CDF memo: YBOS Programmers Reference Manual. #156 Vol(4.00).
- [Cian93] V. Cianciolo. *Bose-Einstein correlations for kaons in relativistic heavy-ion collisions at 14.6 A·GeV/c.* Ph. D. Thesis, MIT (1994).
- [Chi79] S.A. Chin and A.K. Kerman. *Phys. Rev. Lett.* **43**(1979)p. 1292.
- [Col91] B. A. Cole. *Particle Production of High Transverse Momentum in Nucleus-Nucleus Collisions at the AGS.* Ph. D. Thesis, MIT (1992).

- [Cos90] J.B. Costales. *Antiproton Production in Central Nucleus-Nucleus Collisions at 14.6 GeV/A*. Ph. D.Thesis, MIT (1990).
- [Cron75] J.W. Cronin, et al. *Phys. Rev.* **D11**(1975)p. 3105.
- [Carr89] P.A. Carruthers and J. Rafelski. *Hadronic Matter in Collisions*. World Scientific, Singapore 1989.
- [Drij81] D. Drijard, et al. *Z. Phy C. Part. and Fields* **9**(1981)p. 293.
- [E802-17] M. J. Tannenbaum. "How I learned to love the fireball model (at St. Malo)", Internal E802 Memo #17, BNL, 1988.
- [E802-39] R. Debbe and O. Hansen. "Note on Cross-Section and Number of Particles". Internal E802 Memo #39, BNL, 1989.
- [E802-40] J. Cummings, et al. "More on ZCAL's Response: Position Determination and Collimation Effects", Internal E802 Memo #40, BNL, 1989.
- [E802-54] G.S.F.Stephans. "Tracking Chamber Geometry Arrays and Data", Internal E802 Memo # 54 ,BNL, 1991.
- [PZ,91] C.Parsons and D. Zachary. "The CSPAW User's Manual", Internal E859 Memo, E859 Memo 6, BNL, 1992.
- [MRSZ,92] D. Morrison, P.Rothschild, T.Sung, D.Zachary. "Cross Section Details", Internal E859 Memo, E859 Memo 7, BNL, 1992.
- [E859memip] G.S.F. Stephans. "Timing Memo", Internal E859 Memo (in progress).
- [Fah79] E. Fahri and R.L. Jaffe. *Phys. Rev. Lett.* **D30**(1984)p. 2379.
- [Gav91a] S. Gavin. *Nucl. Phys.* **B351**(1991)p. 561.
- [Gav91b] S. Gavin, P.V. Ruuskanen. *Nucl. Phys. Lett.* **B262**(1991)p. 326.

- [Gre75] D.E. Greiner, et al. *Phys. Rev. Lett.* **35**(1975)p. 152.
- [Gor91] M. Gorenstein and S. Nan Yang. *Phy. Rev. C.* **44**(1991)p. 2875.
- [Goss78] J. Gosset, et al. *Phys. Rev.* **C18**(1978)p. 844.
- [Grö78] H. Grössler et. al. *Nucl. Phys.* **B32**(1978)p. 1.
- [Gyul87] M. Gyulassy. *CERN preprint*, CERN-Th 4794/87.
- [Gyul81] M. Gyulassy. *Nucl. Phys.* **A362**(1981)p. 503.
- [Harr89] NA35 Collaboration, J. Harris. *Nucl. Phys.* **A498**(1989)p. 133c.
- [Hein89] U. Heinz, K.S. Lee and E. Schnedermann. Preprint TPR-89-23 (1989).
- [HIP93-go] M. Gonin. Heavy-ion physics at the AGS HIPAGS'93 : Laboratory For Nuclear Science, MIT (1993).
- [HIP93:-ka] S. Kahana. Heavy-ion physics at the AGS HIPAGS'93: Laboratory For Nuclear Science, MIT (1993)p. 265.
- [HIP93-sor] H. Sorge. Heavy-ion physics at the AGS HIPAGS'93: Laboratory For Nuclear Science, MIT (1993)p. 283.
- [Hua90] H.Z. Huang. *Semi-Inclusive and Inclusive Spectra for Charged Pions, Kaons and Protons from Proton-Nucleus and Silicon-Nucleus Collision at AGS Energy*. Ph D. Thesis, MIT (1990).
- [Koc86] P. Koch, B. Müller, and J. Rafelski. *Phy. Rep.* **142**(1986)p. 167.
- [Kur92] K. Kurita. *Particle production study in proton-nucleus and central oxygen-nucleus collisions at 14.6 A-GeV/c*. Ph. D.Thesis, Columbia University (1992).
- [JANCSO,77] G. Jansco, et al. *Nucl. Phys.* **B124**(1977)p. 1.
- [Land53] L.D. Landau. *Izv. Akad. Nauk. (SSSR)* **26**(1954)p. 529.

- [Land56] L.D. Landau. *Nuo. Cim. Suppl.* **3**(1953)p. 15. (Also see *Collected papers of L.D. Landau*, ed. D.Ter Harr (New York: Gordon and Breach ,1965).
- [Lee76] T.D. Lee. *Rev. of Mod. Phy.* **47**(1976)p. 267.
- [Lee90] K.S. Lee, U. Heinz, E. Schnedermann. *Z. Phys, C Part. and Fields* **48**(1990)p. 525-541.
- [Lee88] K.S. Lee, M.J. Rhoades-Brown and U. Heinz. *Phys. Rev.* **C37**(1988)p. 1463.
- [Lev87] M.J. Levine, W.A. Watson. Distributed data acquisition for E802: I the front end. Internal BNL Report. BNL- 39808, BNL (1988).
- [Morr90] R. Morris. *Bose-Einstein correlation measurements in 14.6 A-GeV/c nucleus-nucleus collisions.* Ph. D. Thesis, MIT (1990).
- [Morr94] D. Morrison. *Strange particle production in in 14.6 A-GeV/c nucleus-nucleus collisions.* Ph. D. Thesis, MIT (1994).
- [Mosk92] B. Moskowitz. Private Communication.
- [Nag91] S. Nagamiya. *Nucleus-Nucleus collisions in the BNL-AGS Energy Domain. Lecture Notes for Relativistic Heavy-Ion Collisions.* Symposium/Workshop: June 1989, Beijing, P.R. China.
- [Nag92] S. Nagamiya. *Nucl. Phys.* **A544**(1992)p. 5c.
- [Nat92-Cs] L.P. Csernai, L.B. Bravina and E.E. Zabrodin. " Particle Production in Highly Excited Matter." *NATO ASI Series. Series B: Physics* Vol. 303.
- [Nat92-He] U. Heinz. *ibid.*
- [Nat92-Gu] H. Gutbrod. *ibid.*
- [Nat92-Zi] J. Zimányi. *ibid.*

- [Nil87] B. Nilsson-Almqvist and E. Stenlund. *Comput. Phys. Comm.* **43**(1987)p. 387.
- [Pan92] Y. Pang, T.J. Schalgel, S.H. Kehana. *Phy. Rev. Lett.* **68**(1992)p. 2743.
- [Par92] C.Parsons. *Strange particle production in 14.6 A·GeV/c nucleus-nucleus collisions*. Ph. D. Thesis, MIT (1992).
- [PPDB80] Particle properties data booklet from Review of particle properties *Rev. of Mod. Phy.* **52**(1980).
- [QM83-Ja] M. Jacob. Proceedings of the Third International Conference of Ultra-Rel. Nucleus-Nucleus Collision-Quark Matter '83 September 26-30, 1983, Brookhaven National Laboratory, ed. T. Ludlam and H.E. Wegner Preprint. *Nucl. Phys.*(1984)p. 7.
- [QM86] Proceedings of the Fifth International Conference of Ultra-Rel. Nucleus-Nucleus Collision-Quark Matter '86 April 13-17, 1986, Asilomar, CA, ed. L.S. Schroeder and M. Gyulassy, *Nucl. Phys.* **A461**(1987).
- [QM91-Sa] H.Satz. Proceedings of the Ninth International Conference of Ultra-Rel. Nucleus-Nucleus Collisions-Quark Matter '91 November 11-15, 1991, Gatlinburg, Tennessee, ed. T.C. Awes, F.E. Obenshain, F.Plasil *Nucl. Phys.* **A544**(1992)p. 378c.
- [QM91-Gu] H.Gutbrod. *ibid* p. 357c.
- [QM91-Ra] J. Rafelski. *ibid* p. 279c.
- [QM91-zaj] W.A. Zajc. *ibid*.
- [QM93-Sa] M. Gonin. Proceedings of the Tenth International Conference of Ultra-Rel. Nucleus-Nucleus Collisions-Quark Matter '93 June 20-24, 1993, Borlange, Sweden.
- [Raf82] J. Rafelski and B. Müller. *Phys. Rev. Lett.* **48**(1982)p. 1066.; J.Rafelski. *Nucl. Phys.* **A418**(1984)p. 215c.

- [Raf91] J. Rafelski. *Phys. Lett.* **B262**(91)p. 333.
- [Rei65] F. Reif. *Statistical and Thermal Physics*. McGraw-Hill(1965)p. 152-153.
- [Roth94] P. Rothschild. *Rapidity Dependence of Anti-Proton Production in Relativistic Heavy Ion collisions at 14.6 A·GeV/c*. Ph. D.Thesis, MIT (1994).
- [Sar89] M.Sarubra. *Cluster Production in Relativistic Heavy-Ion Collisions*. Ph. D.Thesis, MIT (1989).
- [Schl92] T.J. Schalgel, S.H. Kahana, Y. Pang. *Phys. Rev. Lett.* **68**(1992)p. 3290.
- [Shur80] E.V. Shuryak. *Phys. Rep.* **61**(1980).
- [Shur91] E.V. Shuryak. *Nucl. Phys.* **A533** (1991)p. 761.
- [Soll91] J. Sollfrank, P. Koch,, U. Heinz. *Z. Phys, C -Part. and Fields* **52**(1991)p. 593.
- [Sol94] R. Soltz. *Two pion correlation measurement for Si+X at 14.6 A·GeV/c and Au + Au at 11.6 A·GeV/c*. Ph. D. Thesis, MIT (1994).
- [Sol94b] R. Soltz. Private communication.
- [Sor89] H.Sorge, H. Stöcker , W. Greiner. *Nucl. Phys.* **A498**(1989)p. 567c.
- [Stev93] G. Stevens. Private communication.
- [Sun94] T. Sung. *Strange Particle Production*. Ph. D.Thesis, MIT (1994).
- [Sun] T. Sung. Private communication.
- [UA1-82] UA1 Coll. *Phys. Lett.* **B118**(1982)p. 167.
- [Wad87] B. Wadsworth, et al. Trigger Supervisor: Managing trigger conditions in a high energy physics experiment. Internal BNL Report BNL- 39806, BNL (1987).
- [Wei76] W.Weise and G.E. Brown. *Phys. Rep.* **27**(1976)p. 1.

[Wern88] K.Werner. *Phys. Lett.* **B208**(1988)p. 520.

[Witt84] E. Witten. *Phys. Rev.* **D30**(1984)p. 272.

[Vut92] V. Vutsadakis. *Proton - proton correlations in 14.6 A·GeV/c nucleus-nucleus collisions*. Ph. D.Thesis, MIT (1992).

[Wan93] U. Wang. *Production of ϕ mesons in central Si + Au collisions at 14.6 A·GeV/c*. Ph. D.Thesis, Columbia University, (1994).

Acknowledgements

I would like to thank the numerous people who have supported me throughout the past four and a half years. First, I would like to thank Steve Steadman, my advisor and co-spokesman for E866. I appreciate his enthusiasm for heavy-ion physics and I appreciate the time he gave me in helping shape-up this work. I am also grateful for Craig Ogilvie for his advice and vision for the field and his sincere care for students. George Stephans has also inspired me in his knowledge and professionalism in the field.

I am very grateful to Peter Rothschild and Ted Sung. They are both much more than office mates. Over the past five years we have become the best of friends and the memories we share working together will never be forgotten.

The Heavy-Ion group at MIT is quite large but I would like to thank everyone who has taken a part in making this research possible. First, I would like to thank Vince Cianciolo, Dave Morrison, and Ron Soltz. Together they made the analysis effort possible and they did an incredible job on E859. I would like to thank Chuck Parsons for his input into this work. Chuck Parsons is a very creative individual who has my respect. I would also like to thank Brian Cole, Matt Bloomer, and Vas Vutsadakas as well.

I am grateful to Dave Woodruff, who came to the rescue so many times when unusual computer errors arose. I would also like to thank Marjory Neal, Barb Corbisier, Walter Kehoe, Mark Baker and Gunter Roland as well.

There are many people at BNL that I would like to thank. First, I would like to thank Chellis Chasman and Hideki Hamagaki who are also co-spokesmen for E866. I also thank Bruce Moskowitz for the enjoyable physics discussions we have had together. I also thank Flemming Videabeck, Ziping Chen, J. Cumming, M. Gonin, S. Gushue, and O. Vossnack, to name only a few.

I have made many other friends over my years at MIT, and I would like to take the

opportunity to thank some of them. I would first like to thank Cedric Login. Cedric has been a constant companion during my work here. I wish him well in his research efforts as he completes his Ph. D. in electrical engineering at M.I.T.. His friendship is priceless. I also would like to thank Scott Sweeney, Harris Gilliam, José Elizondo, Aaron Cárdenas, Trevor Mendez, Ethan Wenger, Mark Wintersmith, Bryan Klassen, and Mike Domroese, and Rob Grace

I would also like to thank Howard and Ann Loree, John and Karen Oates, Brian and Caryn Homet, Dean and Kim Farmer, Vic and Julie Gobbell, Roy and Chelly Larson, Gregg and Cathy Marutzky, and Yuri Sung.

I would like to thank the following people who have helped proofread this work; Sharon Belville, Susan Park, Robert LaChance, and William DeShazer.

I would also like to thank the following for their help over the months while I was writing my thesis; Mark Shelly, Patti Kellett, Joanne Liu, Jim Ryan, Kristine Drobot, Lisa Chou, Lisa Sopata, Parquita Barton, Michael Metzger, Susan Park, Sajjan Sharma, Jude Federspiel, Charlotte Huang, Piper Keables, Randy Sanders, Kim Oakberg, Michael Lee, Mark Rawizza, Drew Henshaw, Robert LaChance, Andrew Romain, Natashya Trejo, Wendell Stallings, Danielle Dunlap, Chelsea Wilkin, Amber Smith, Helen Kang, Lynn Jean-Denis, John Clark, Aubrey Burton.

Others that have been a part of my life over the years at MIT are Ann Renaud, Jacque, M. et Mme Renaud. I also thank Renée Balog and Nadine Barrett for their friendship.

Lastly, I thank my family, especially my parents, William and Betty Zachary. I also thank my brothers and sister, Mark, Kurt and Dawn. I thank my grandparents, Grandma and Grandpa Zachary. I have received my first telescope from Grandpa Zachary in 1969...the rest was history. I thank Grandma and Grandpa Blendin as well. I began to appreciate experimental physics after passing so many hours in Grandpa Blendin's shop in N. Redington Beach, Florida.

Biographical Note

Daniel S. Zachary was born on 9 January, 1963 in Pontiac Michigan. He grew up in the city of Walled Lake, Michigan and attended Walled Lake High School. In 1980, he moved to Muscatine, Iowa and completed high school in Muscatine. In 1981, he attended Iowa State University. The following year, he attended the University of Michigan. In 1983, he transferred to the Massachusetts Institute of Technology and completed his Bachelor degree in Physics. He worked with Prof. Rainer Weiss at MIT's Gravity Labs. In the following year, he received his Master of Science in physics after working on the automation of the Explosive Transient Camera system with Dr. George Ricker. Afterwards, his research efforts included work on the Large Volume Detector with Prof. Irwin Pless before joining the Heavy-Ion group in 1989.

Daniel and the Golden Beam

We Higgs come in sizes large and small,
But Dan may be the strongest one of all.

Mere cosmics he did scornfully disdain,
“Go Heavy Ions!” was his new refrain.
Small oxygen, he also found restrictive.
Soon, hefting bigger beams became addictive.

Low kaon stats made careful technique crucial.
The clever answer, study yields fiducial.
If we approach a thermaliz'ed state,
Should kaons over pions saturate?

With energy and matter concentrated,
The QGP (our Grail) is contemplated.
The CERN Pb-beamers must be getting tense,
To see our protons piling up so dense.

With Dan, the Midas tale reverses pieces.
He put his touch on gold and made a thesis.